Kinetic Physics with Solar Wind Heavy Ions Measured at 1 AU

Dissertation
zur Erlangung des Doktorgrades
der Mathematisch-Naturwissenschaftlichen Fakultät
der Christian-Albrechts-Universität zu Kiel
vorgelegt von Nils Peter Janitzek
Kiel, 2021

Erster Gutachter:	Prof. Dr. Robert Wimmer-Schweingruber
Zweiter Gutachter:	Prof. Dr. Holger Kersten
Tag der mündlichen Prüfung:	24.01.2020

SUMMARY

One possibility to study kinetic processes such as particle acceleration, transport and thermalization in the solar wind are in-situ measurements of ion velocity distribution functions (VDFs). In particular the extension of the VDF analysis to the wide range of heavy ions (with atomic number $Z \geq 2$) allows to investigate the dependence of the underlying processes on the particles' mass and charge in a systematical way. In this thesis we analyze nonthermal signatures in the velocity distribution functions of solar wind heavy ions, in particular differential speeds and thermal speed ratios between the heavy ions and the solar wind protons. For our investigation we utilize measurements that were conducted with the Charge Element Isotope Analysis System (CELIAS) experiment onboard the Solar and Heliospheric Observatory (SOHO) that is located at the Lagrange Point L1 at a distance of about one astronomical unit (1 AU) from the Sun. The measurement data is recorded during a relatively short period around solar minimum between DOY 174 and 220 in 1996. The SOHO/CELIAS experiment is one of only a few instrument suites located in the undisturbed solar wind, far away from planetary magnetospheres, that is able to measure a wide range of solar wind heavy ion species with relatively high counting statistics and fast measurement cadence. Our studies include both the investigation of long-term speed spectra in the form of accumulated count rates over the full measurement period and the analysis of short-term speed distributions, so-called 1D-reduced velocity distribution functions, that are recorded with the intrinsic cadence of the CELIAS/CTOF (Charge-Time-Of-Flight) sensor of about 5 minutes.

The most comprehensive investigated ion set in the long-term data analysis consists of 69 ion species, of which 28 are measured with sufficient counting statistics to yield a physically conclusive speed spectrum for the investigated slow wind case with well-defined simultaneously measured proton speed between 330 and 340 km/s. Among these 28 species, 27 ion species are measured with differential speeds of $\Delta v_{ip} \pm 5\,\mathrm{km/s}$ with respect to the measured mean proton speed of 335 km/s. This is consistent with the hypothesis of equal speeds among all these ion species within the estimated systematic measurement uncertainties. In the less frequently observed fast wind 21 ion species were measured with sufficient counting statistics to yield a physically conclusive long-term speed spectrum under the condition of a well-defined simultaneously measured proton speed between 500 and 510 km/s . Among these 21 species, 16 ion species were measured with differential speeds $\Delta v_{ip} \in [15\,\mathrm{km/s}, 30\,\mathrm{km/s}]$ with respect to the measured mean proton speed of 505 km/s. Such differential speeds are estimated to lie beyond the systematic uncertainties for most of these species, so that these

ions stream significantly faster than the solar wind protons. In particular the 11 most reliably measured ion species C^{4+}, C^{5+}, O^{6+}, O^{7+}, Ne^{8+}, Si^{7+} - Si^{9+} and Fe^{9+} - Fe^{11+} with estimated systematic measurement uncertainties of less than 10 km/s are all measured with $\Delta v_{ip} \in [15\,\mathrm{km/s}, 30\,\mathrm{km/s}]$. From the analyzed short-term data we derived about 10^4 1D-reduced velocity distribution functions, respectively, for an ion set of 28 species which was systematically reduced compared to the long-term data to ensure a statistically stable analysis despite the low counting statistics. The statistical analysis of the mean speeds of the 8 ion species C^{4+}, O^{6+}, Si^{7+} - Si^{9+} and Fe^{9+} - Fe^{11+} with the lowest systematic bias ($\lesssim 10$) km/s and sufficient counting statistics in the short-term data yields a very similar differential speed pattern for all these ion species in dependence of the simultaneously measured mean proton speed: We find constant or slowly increasing differential speeds $-10\,\mathrm{km/s} \leq \Delta v_{ip} \leq 15\,\mathrm{km/s}$ for each species in the slow and intermediate proton speed regime between $v_p \in [320\,\mathrm{km/s}, 480\,\mathrm{km/s}]$ before a steep increase of about 20 km/s occurs at a proton mean speed of $v_p \approx 480\,\mathrm{km/s}$ after which all ion species reach a nearly constant plateau of positive differential speeds between 15 and 35 km/s, respectively. This finding is supported by the derived time series of heavy ion mean speeds compared to the proton mean speeds which shows that significant positive differential speeds over longer time periods of several hours to days could only be measured in the two observed fast wind streams on DOY 185-186 and DOY 213-216 in 1996. In comparison to the proton speed dependency we find an equally clear but smoother dependency of the short-term differential speeds on the ion-proton collisional age ($A_{C,ip}$), which might indicate that Coulomb collisions play an important role in the relaxation of this nonthermal signature in a wider range of solar wind regimes. Finally, combining the short-term differential speeds in the fast wind with the systematic uncertainty analysis from the long-term spectra analysis, we find that the data is consistent both with a decreasing trend of the mean differential speeds with increasing mass-per-charge down to $\Delta(\langle \Delta v_{ip} \rangle)/(\Delta m/q) \approx -5\,(\mathrm{e\,km})/(\mathrm{amu\,s})$ as well as with a constant mean differential speed of $\langle \Delta v_{ip} \rangle \approx 25\,\mathrm{km/s}$ for all ion species regardless of the ion species mass-per-charge. However, a significant increase of the differential speed with increasing mass-per-charge can be excluded.

For the thermal speeds, we find both from the long-term and short-term data analysis that the heavy ion thermal speeds in the fast wind are several times higher than in the slow wind. The more precise short-term data analysis for the thermal speeds of Si^{7+}, Si^{8+} and Fe^{9+} - Fe^{11+} yields that in the collisionless wind ($\log_{10}(A_{C,ip}) \lesssim 0$), that can be mainly associated with fast and intermediate wind speeds, we find for all ion species nearly constant most frequently observed thermal speed ratios between $v_{i,th}/v_{p,th} = 0.85 \pm 0.1$ and $v_{i,th}/v_{p,th} = 1.0 \pm 0.1$. In the collisional wind ($\log_{10}(A_{C,ip}) > 0$) we see that all speed ratios decrease to values on the order of 0.5. This could be interpreted as the beginning of a thermalization between the ion species due to Coulomb collisions.

ZUSAMMENFASSUNG

Eine Möglichkeit kinetische Prozesse wie Teilchen-Beschleunigung, -Transport und -Thermalisierung im Sonnenwind zu untersuchen ist die in-situ Messung von Ionen-Geschwindigkeitsverteilungen (VDFs). Insbesondere die Ausweitung der VDF-Analyse auf einen weiten Bereich von Schweren Sonnenwindionen (mit Ordnungszahl $Z \geq 2$) erlaubt es die Abhängigkeit der zugrundeliegenden Prozesse von Teilchenmasse und Teilchenladung zu untersuchen. In dieser Arbeit analysieren wir die nichtthermischen Signaturen in den Geschwindigkeitsverteilungen Schwerer Sonnenwindionen, insbesondere Differenz-Geschwindigkeiten und Verhältnisse Thermischer Geschwindigkeiten zwischen den Schweren Ionen und den Sonnenwindprotonen. Für unsere Untersuchungen verwenden wir Messungen des Charge Element Isotope Analysis System (CELIAS) - Experiments an Bord des Solar and Heliospheric Observatory (SOHO), welches sich am Lagrange-Punkt L1 befindet und daher einen Abstand zur Sonne von etwa einer Astronomischen Einheit (1 AE) hat. Die Messdaten wurden während einer relativ kurzen Zeitperiode zwischen Tag 174 und Tag 220 im Jahr 1996 in zeitlicher Nähe zum Solaren Minimum aufgenommen. Das CELIAS-Experiment ist eines der wenigen Instrumentenpakete, das sich im ungestörten Sonnenwind, d.h. weit entfernt von planetaren Magnetosphären, befindet und dazu in der Lage ist einen weiten Bereich von Schweren Sonnenwindionen-Spezies mit hoher Zählstatistik und Kadenz zu messen. Unsere Untersuchungen bestehen zum einen aus der Analyse von Langzeit-Geschwindigkeitsspektren in Form von akkumulierten Zählraten über den gesamten Messzeitraum und zum anderen aus der Untersuchung von Kurzzeit-Geschwindigkeitsverteilungen, sogenannten 1D-reduzierten Geschwindigleitsverteilungen, die mit der intrinsischen Kadenz des CELIAS/CTOF (Charge-Time-Of-Flight) sensors von etwa 5 Minuten aufgenommen wurden. Das umfangreichste Set an untersuchten Ionen in der Analyse der Langzeit-Geschwindigkeitspektren besteht aus 69 Ionen-Spezies, von denen 28 Spezies mit ausreichender Zählstatistik gemessen wurden um im untersuchten Szenario des Langsamen Sonnenwindes, mit wohldefinierter gleichzeitig gemessener Protonen-Geschwindigkeit zwischen 330 und 340 km/s, physikalisch sinnvolle Geschwindigkeitsspektren zu erhalten. Von diesen 28 Ionen-Spezies wurden 27 Spezies mit Differenz-Geschwindigkeiten von $\Delta v_{ip} \pm 5$ km/s im Vergleich zur mittleren Protonengeschwindigkeit von 335 km/s gemessen. Dies ist konsistent mit der Hypothese von identischen Geschwindigkeiten all dieser Ionen-Spezies im Rahmen der ermittelten systematischen Messunsicherheiten. Im seltener beobachteten Schnellen Sonnenwind wurden 21 Ionen mit hinreichender Zählstatistik gemessen um physikalisch sinnvolle Langzeit-Geschwindigkeitsspektren unter der Bedingung einer

wohldefinierten gleichzeitig gemessenen Protonengeschwindigkeit zwischen 500 und 510 km/s zu erhalten. Von diesen 21 Ionen-Spezies wurden 16 Spezies mit Differenz-Geschwindigkeiten von $\Delta v_{ip} \in [15\,\mathrm{km/s}, 30\,\mathrm{km/s}]$ im Vergleich zur mittleren Protonengeschwindigkeit von 335 km/s gemessen. Dies sind Differenz-Geschwindigkeiten außerhalb der ermittelten Messunsicherheiten für die meisten dieser Spezies und daher strömen diese signifikant schneller als die Sonnenwindprotonen. Insbesondere die 11 am zuverlässigsten vermessenen Ionen-Spezies C^{4+}, C^{5+}, O^{6+}, O^{7+}, Ne^{8+}, Si^{7+} - Si^{9+} und Fe^{9+} - Fe^{11+} mit ermittelten systematischen Messunsicherheiten von unter 10 km/s wurden alle mit einer Differenz-Geschwindigkeit $\Delta v_{ip} \in [15\,\mathrm{km/s}, 30\,\mathrm{km/s}]$ gemessen.

Aus den analysierten Kurzzeit-Daten wurden für ein Ionen-Set von 28 Spezies jeweils etwa 10^4 1D-reduzierte Geschwindigkeitsverteilungen erzeugt. Im Vergleich zu den Langzeit-Daten wurde das Ionen-Set systematisch reduziert um trotz der geringen Zählstatistik eine statistisch stabile Analyse zu ermöglichen. Die statistische Analyse der mittleren Geschwindigkeiten der 8 Ionen-Spezies mit dem geringsten systematischen Bias und hinreichend hoher Zählstatistik C^{4+}, O^{6+}, Si^{7+} - Si^{9+} und Fe^{9+} - Fe^{11+} ergibt ein sehr ähnliches Muster für die ermittelten mittleren Differenz-Geschwindigkeiten in Abhängigkeit von der zeitgleich gemessenen mittleren Protonen-Geschwindigkeit: Wir finden konstante oder schwach ansteigende mittlere Differenz-Geschwindigkeiten $-10\,\mathrm{km/s} \leq \Delta v_{ip} \leq 15\,\mathrm{km/s}$ für jede der Ionen-Spezies im Langsamen und Mittelschnellen Windregime $v_p \in [320\,\mathrm{km/s}, 480\,\mathrm{km/s}]$, bevor ein steiler Anstieg von etwa 20 km/s bei einer mittleren Protonengeschwindigkeit von $v_p \approx 480\,\mathrm{km/s}$ auftritt, nach welchem alle Ionen-Spezies ein Geschwindigkeits-Plateau von annähernd konstanten positiven mittleren Differenz-Geschwindigkeiten zwischen 15 und 35 km/s erreichen. Dieses Ergebnis ist in Einklang mit der erzeugten Zeitreihe der mittleren Geschwindigkeiten der Schweren Ionen im Vergleich zu den mittleren Geschwindigkeiten der Protonen, die zeigt, dass signifikante positive Differenz-Geschwindigkeiten über längere Zeiträume von mehreren Stunden bis Tagen nur während der beiden beobachteten Schnellen Sonnenwind-Ströme an den Tagen 185-186 und 213-216 im Jahr 1996 gemessen wurden. Im Vergleich zur Protonengeschwindigkeits-Abhängigkeit finden wir eine ebenso klare, aber kontinuierlichere Abhängigkeit der Kurzzeit-Differenzgeschwindigkeiten von der Ion-Proton Collisional Age $(A_{C,ip})$ was bedeuten könnte dass Coulomb-Kollisionen eine wichtige Rolle für die Relaxation dieser nichtthermischen Signatur in einem weiteren Bereich von Sonnenwindregimen spielen könnten. Schließlich finden wir aus der Kombination der Kurzzeit-Differenzgeschwindigkeiten und der Analyse der systematischen Fehler in der Langzeitspektren-Analyse, dass die Messdaten sowohl mit einem absteigenden Trend der mittleren Differenz-Geschwindigkeit mit ansteigender Masse-pro-Ladung bis hinunter zu $\Delta(\langle \Delta v_{ip} \rangle)/(\Delta m/q)$

$\approx -5\,\mathrm{e\,km/(amu\,s)}$ vereinbar sind, als auch mit einer konstanten mittleren Differenz-Geschwindigkeit von $\langle \Delta v_{ip} \rangle \approx 25\,\mathrm{km/s}$ für alle Ionen-Spezies unabhängig von ihrer Masse-pro-Ladung. Ein signifikanter Anstieg der Differenz-Geschwindigkeit mit ansteigender Masse-pro-Ladung kann jedoch ausgeschlossen werden.
Betreffend der Thermischen Geschwindigkeiten finden wir sowohl in der Langzeit- als auch in der Kurzzeit-Datenanalyse, dass die Thermischen Geschwindigkeiten der Schweren Ionen im Schnellen Sonnenwind um ein Vielfaches höher sind als im Langsamen Sonnenwind. Die im Vergleich für die Thermischen Geschwindigkeiten viel präzisere Kurzzeit-Datenanalyse für Si^{7+}, Si^{8+} und Fe^{9+} - Fe^{11+} ergibt, dass wir im kollisionslosen Sonnenwind ($\log_{10}(A_{C,ip}) \lesssim 0$), der hauptsächlich mit Mittleren bis Schnellen Sonnenwindgeschwindigkeiten assoziiert werden kann, Verhältnisse zwischen $\langle v_{i,th}/v_{p,th} \rangle = 0.85 \pm 0.1$ und $\langle v_{i,th}/v_{p,th} \rangle = 1.0 \pm 0.1$ zwischen den Thermischen Geschwindigkeiten der Ionen und den Protonen haben. Im kollisionsdominierten Wind ($\log_{10}(A_{C,ip}) > 0$), lässt sich hingegen erkennen, dass sich alle Verhältnisse der Thermischen Geschwindigkeiten zwischen den Schweren Sonnenwindionen und den Protonen bis zu einem Wert von ungefähr 0.5 verringern. Dies könnte als der Beginn einer Thermalisierung zwischen den kinetischen Temperaturen der Ionen-Spezies aufgrund von Coulomb-Kollisionen interpretiert werden.

Contents

Chapter 1

Kinetic Physics of the Solar Wind

1.1 The Solar Wind

Based on observations of comet tail accelerations, that could not be explained by the solar photon radiation pressure, in 1951 L. Biermann developed the concept of a continuous plasma stream from the Sun that was first called *solar corpuscular radiation* [Biermann, 1951] and which is today known as the solar wind. A few years later [Parker, 1958] presented a first model of the solar wind that could reproduce the high plasma outflow speeds of more than 500 km/s calculated by Biermann. This was achieved by assuming a stationary expansion of the solar corona instead of the previously common assumption that this outermost atmospheric layer of the Sun is in hydrostatic equilibrium. As depicted in Figure 1.1, the Parker model of the solar wind predicts outflow speeds between 200 and 800 km/s for coronal temperatures on the order of $T_C \approx 10^6$ K which is in good agreement with the coronal temperatures that were inferred already in the 1940s from spectroscopic measurements of the solar corona (see [Aschwanden, 2005] and references therein).
In the beginning of the 1960s the existence of the solar wind could be proven independently with in-situ particle measurements by the Russian Luna-1 and US-American Mariner-2 missions [Gringauz, 1960, Snyder C. W., 1963]. The plasma experiment on Mariner-2 measured almost the entire solar wind speed range that was predicted by the Parker model from speeds below 300 km/s to about 800 km/s [Snyder C. W., 1963]. This speed range is confirmed up to today by all following missions and thus can be considered as the regular solar wind speed range. Mariner-2 measurements also revealed the two major ion components of the solar wind as protons (H^+) and alpha particles (He^{2+}) that have relative abundances of 95% and 5% in the average solar wind.

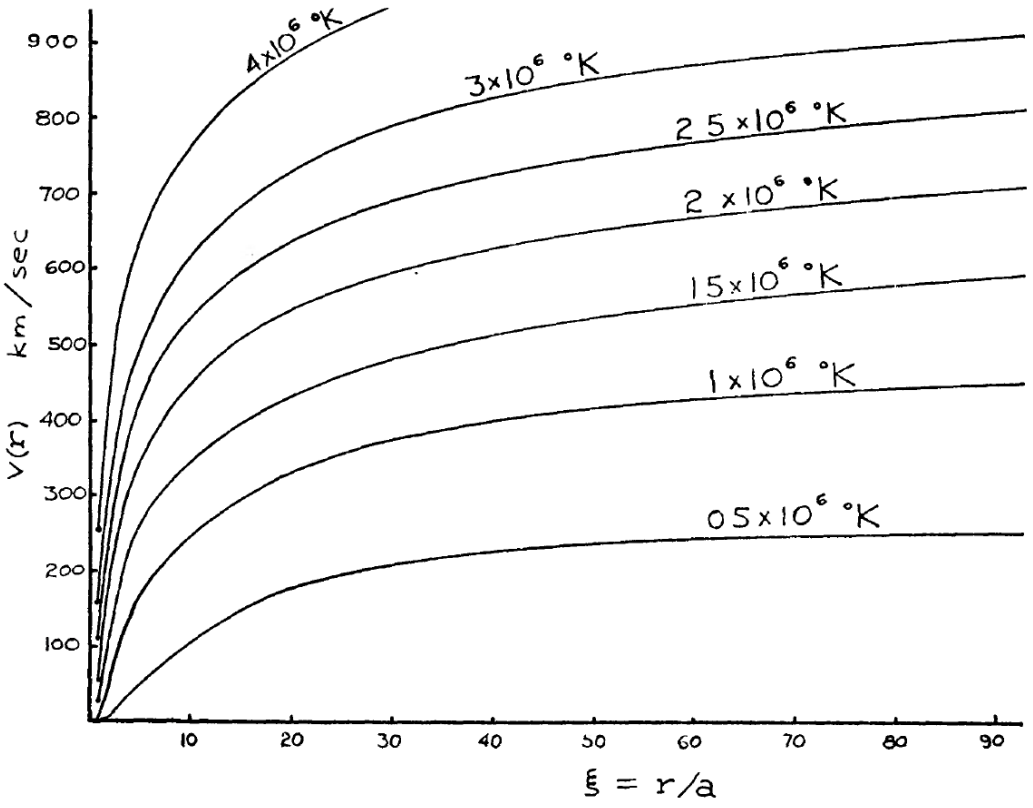

FIGURE 1.1: Predicted solar wind outflow speed v in dependence of the distance to the solar center r for coronal temperatures $T_C = 0.5 \cdot 10^6$ K - $T_C = 4 \cdot 10^6$ K. The speeds are calculated as spherically symmetric hydrodynamic expansion velocity of an isothermal solar corona. The distance is given in units of the solar radius a, which has been approximated as $a = 10^6$ km. The figure is taken from [Parker, 1958].

The Parker model based on the radial expansion of the plasma also has implications for the topology of the magnetic field in the solar wind. This magnetic field is generated by processes within the Sun [Dikpati and Gilman, 2008] and can be regarded in a first approximation (for the quiet Sun) as a dipole field perpendicular to the ecliptic plane of the heliosphere. The B-field expands from the solar surface, the photosphere, through the Sun's atmosphere out into interplanetary space. At a certain distance from the Sun, the local kinetic pressure in the surrounding plasma

$$p_{kin} = nk_B T \,, \tag{1.1}$$

depending on the plasma temperature T and particle number density n, overcomes the local magnetic pressure

$$p_{mag} = \frac{B^2}{2\mu_0} \,, \tag{1.2}$$

where $B = |\underline{B}|$ is the magnitude of the ambient magnetic field and μ_0 is the vacuum permeability. At this point, where the so-called plasma beta parameter $\beta = p_{kin}/p_{mag}$

becomes larger than 1, the trajectories of the charged plasma particles are no longer confined to the solar magnetic field but instead the particles start to stream out radially from the Sun and carry the magnetic field lines with them. The B-field is said to be *frozen* into the plasma from this point on and the surface that is defined by $\beta = 1$ is termed the *source surface* of the solar wind. It is estimated to be located at a distance of $R_0 \gtrsim 1R_S$ above the Sun's surface where $R_s \approx 7 \cdot 10^5$ km is the solar radius (see Figure 1.2). The Parker model yields that the acceleration of the solar wind happens in a region close to the source surface that is narrow compared to heliospheric scales of at least several astronomical units (1 AU $\approx 1.5 \cdot 10^8$ km). From there on, the wind streams with nearly constant speed outwards in accordance with the speed profiles in Figure 1.1. Based on this approximation of constant speed one finds for the heliospheric steady state B-field that the field lines form an Archimedean spiral and their orientation (or winding angle) ϕ in the ecliptic plane at a radial distance $R \geq R_0$ relative to the center of the Sun is given by:

$$\tan(\phi) = \phi_0 - \frac{\omega}{v} R \tag{1.3}$$

where $\omega = 2\pi/25.38\,\mathrm{d}$ is the (sidereal) angular speed corresponding to the solar rotation, v is the assumed constant flow speed of the solar wind and ϕ_0 is the azimuth angle at $R = R_0$ which is by definition of the particle outflow direction perpendicular to the source surface. The magnetic field $\underline{B}(R, \phi) = \underline{B}_r + \underline{B}_\phi$ at any location $\underline{r} = (R, \phi)$ in the ecliptic plane can then be calculated as

$$\underline{B}_r(R) = B_0 \left(\frac{R_0}{R}\right)^2 \underline{e}_r \tag{1.4}$$

and

$$\underline{B}_\phi(R, \phi) = B_0 \left(\frac{\omega}{v}\right) (R - R_0) \left(\frac{R}{R_0}\right)^2 \underline{e}_\phi \tag{1.5}$$

where $B_0 = |\underline{B}_0|$ is the magnitude of the magnetic field on the source surface and $\underline{e}_r$ and $\underline{e}_\phi$ are the radial and azimuthal unit vectors in polar coordinates, respectively. As we can see from Eq. 1.3 the mean magnetic field direction in the ecliptic plane varies with the distance to the Sun and also to some extent with the solar wind speed. For instance at the Lagrange-point L1 that is corotating with the Earth at a solar distance of $R_{L1} \approx 1\,\mathrm{AU}$, we find for a solar wind speed of 400 km/s a mean B-field angle of $\phi = -45^\circ$ with respect to the selected radial solar wind outflow direction $\phi_0 = 0$ if we substitute the sidereal angular speed by the synodical angular speed $\widetilde{\omega} = 2\pi/27.28\,\mathrm{d}$.

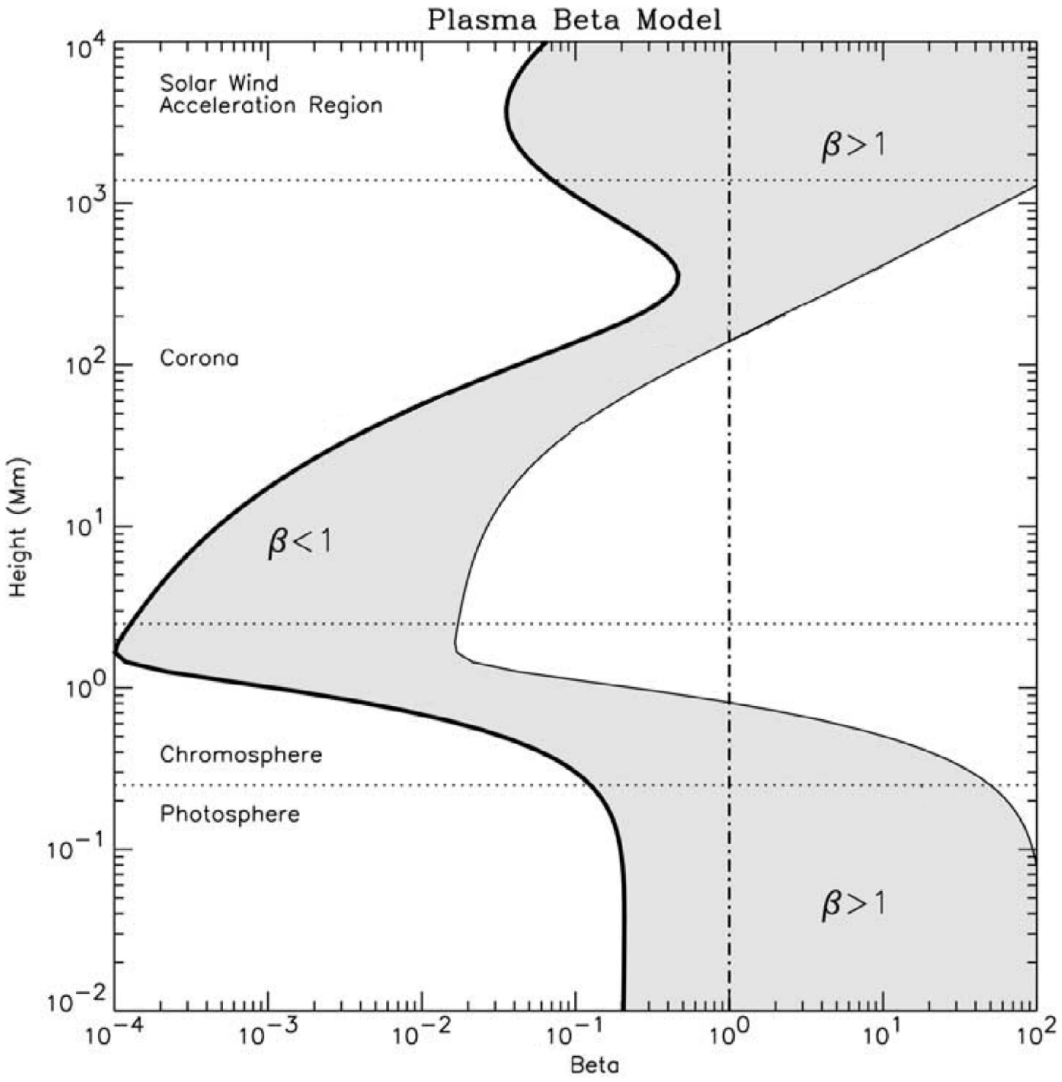

FIGURE 1.2: Modeled plasma beta parameter as a function of the height in the solar atmosphere. The figure is taken from [Gary, 2001].

Since the establishment of the Parker model more than 60 years have passed and a number of missions dedicated to the Sun and the solar wind were launched, among them Helios, Ulysses, SOHO, ACE, Hinode, SDO, STEREO, and recently Parker(!) Solar Probe. These missions, together with particular experiments on planetary missions such as the famous Apollo-11 [Geiss, 1972] solar wind foil experiment, contributed to reveal a much more detailed picture of the solar wind i.e. by determining the kinetic properties of its main constituents at different distances from the Sun [Marsch et al., 1982a,b, Steinberg et al., 1996, Gary et al., 2000], discovering and describing the heavy element component from helium to nickel [Aschwanden, 2005, Bochsler, 2007], analyzing the wind's source regions [McComas et al., 2000, Cranmer, 2002] or unveiling the global 3-dimensional structure of the solar wind over the solar cycle [McComas et al., 2000, 2003].

In the simplest scheme the solar wind is divided into two classes that are related historically to the typical observed speeds and are therefore called *fast wind* and *slow wind*. The slow wind is typically measured at velocities around 300 km/s up to velocities of about 400 km/s while the fast wind is usually measured at speeds above 500 km/s and reaches up to about 800 km/s [Prölss, 2004, Feldman, 2005]. Naturally, one also measures intermediate speeds for which the classical distinction can be ambiguous and there exist alternative classification schemes [Xu and Borovsky, 2015] that are currently also investigated with machine learning techniques [Heidrich-Meisner and Wimmer-Schweingruber, 2018]. Yet, for the purpose of this work it is sufficient to keep the two-class scheme that, besides its terminology, is nowadays based on more criteria than just the solar wind speed. Fast and Slow wind are also different in elemental and charge state composition of the so-called *heavy minor elements* with atomic number $Z > 2$ and relative abundances below 10^{-3} compared to solar wind hydrogen: While both wind types show an enhancement of so-called low-FIP elements (with a first ionization potential below $U_{FIP} \lesssim 10\,\mathrm{V}$ such as calcium, magnesium, silicon, and iron) compared to the photospheric composition, in the slow wind the over-representation of low-FIP elements is with a factor of about 3 much stronger pronounced than in the fast wind with a factor of about 1.5 [Bochsler, 2007]. Finally, the typical slow and fast wind streams also differ in the observed charge states of the heavy elements. One has to note that the (final) charge state of an ion that is measured in the solar wind is determined in the solar corona [Geiss and Gloeckler, 1995, Aellig, 1997] where the higher particle densities yield short ionization and recombination times so that the mean charge state of a species can adapt to the plasma temperature, while the rapidly decreasing densities in the solar wind cause a so-called *freezing* of the charge states independent of the local plasma temperature. As one observes higher ion charge states in the slow wind compared to the fast wind [von Steiger et al., 2000], which links the slow wind to higher coronal temperatures, these observations pose a serious problem to the Parker model.
An alternative approach to understand the nature of the slow and fast wind is to look for its respective origin on the Sun by comparing in-situ kinetic and composition measurements with remote sensing observations of the solar corona. Within the ecliptic the back-mapping of small scale structures in the in-situ data back to the corona might be ambiguous but with Ulysses for the first time solar wind in-situ measurements out of the ecliptic were possible and as can be seen from Figure 1.3 one can recognize a simple large scale pattern of the solar wind outflow kinetics for the quiet Sun (in the left panel). It becomes clear that at quiet conditions the fast wind originates from extended regions at high latitudes while at low latitudes primarily slower wind is observed. By the comparison with EUV and soft X-ray images of the corona (e.g. SOHO/EIT, SDO/AIA) the source regions of the fast wind can be identified as the so-called *coronal holes*, which

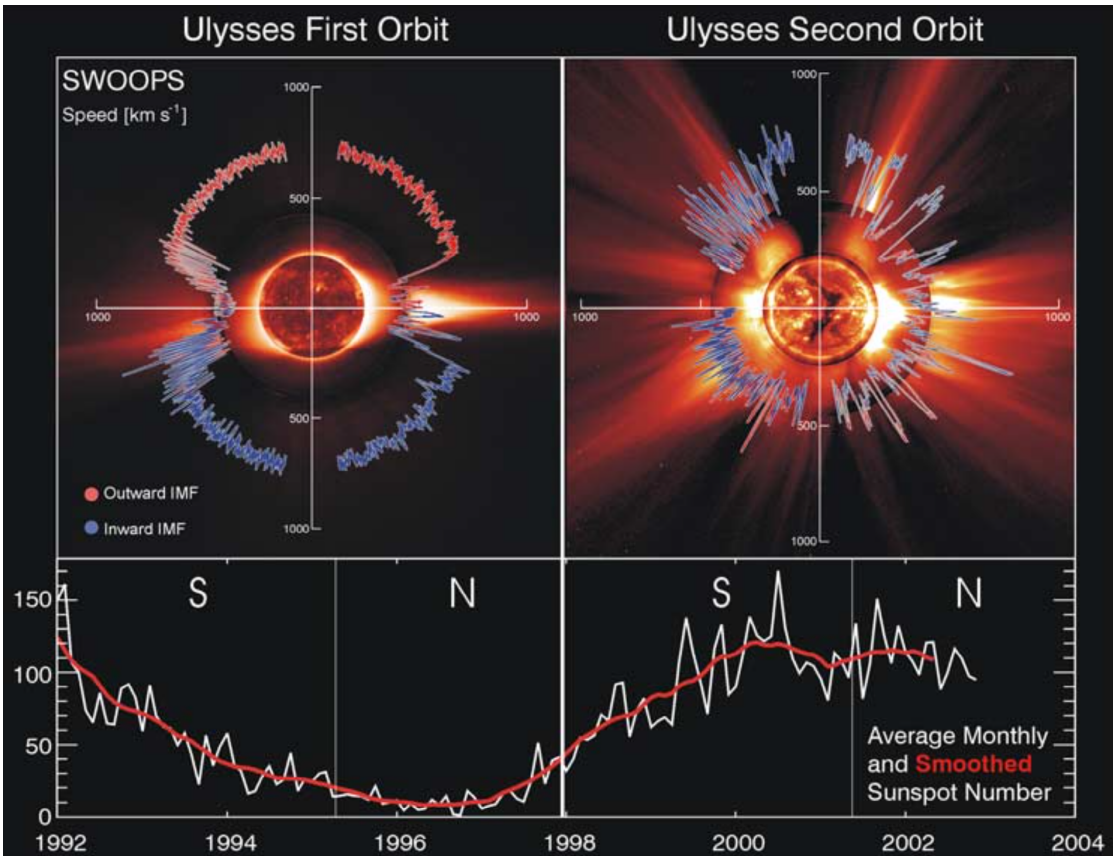

FIGURE 1.3: Upper panels: solar wind speed measured with the SWOOPS instrument onboard the Ulysses spacecraft on its first (left) and second (right) orbit plotted as a function of the Ulysses orbit latitude (in blue and red for the different magnetic polarity). As can be seen from the time-line of the sunspot number in the two lower panels, Ulysses' first orbit occurred mostly during solar minimum where the solar magnetic field can be well-approximated by a dipole field. In this situation the measured solar wind speed shows a clear latitudinal pattern: At higher latitudes above 30° a relatively constant fast wind with $700\,\mathrm{km/s} < v < 800\,\mathrm{km/s}$ is measured while at lower latitudes primarily slow wind $v \lesssim 400\,\mathrm{km/s}$ is measured interrupted by occasional faster wind streams with speeds up to about 600 km/s. In the second orbit that coincided with solar maximum, the measured solar wind speed does not show any clear large scale pattern as the result of the ongoing change of magnetic field polarity that leads to a complex magnetic field structure all over the corona and in the heliosphere. Furthermore, at high solar activity the Sun frequently emits spontaneously large plasma structures into interplanetary space. These are termed *interplanetary coronal mass ejections* (ICMEs) and add additional complexity to the situation. The Ulysses speed observations are plotted over images characteristic of the corona at solar minimum on 17 August 1996 and solar maximum on 7 December 2000. From the center out, the images are composed of the recorded images by the Extreme Ultraviolet Imaging Telescope (EIT) on SOHO (spectral line: Fe XII at 195 Å), the Mauna Loa K-coronameter (spectral range: 700–950 nm), and the SOHO C2 Large Angle Spectrometric Coronagraph (white light). The figure is taken from [McComas et al., 2003].

are extended regions of nearly radial magnetic fields in the corona which thus allow an efficient outflow of the plasma. As this causes low plasma density and temperatures in this regions they look darker at typical wavelengths of UV and soft X-ray images of the corona [Cranmer, 2002].

We note, that the established link between the fast wind and low coronal temperature is consistent with the trend in the coronal freeze-in temperatures obtained from heavy ion in-situ composition measurements, but it is in contradiction with the Parker model[1], and therefore illustrates the need for a better theoretical model. Besides the mean outflow speeds also the in-situ measured kinetic temperatures of the fast solar wind ions are not well-understood as one measures about mass-proportional (or even over mass-proportional) temperatures [Marsch et al., 1982a,b, Hefti, 1998a, von Steiger and Zurbuchen, 2006, Tracy et al., 2015] for the heavy ions with increasing particle mass while one expects equal temperatures for a thermal equilibrium. As these high heavy ion temperatures are already observed in the corona, they might also provide a key-observation for the still unsolved *coronal heating problem* that expresses the fact that the corona is up to three orders of magnitude hotter than the photosphere and chromosphere, although the energy that is released from the Sun's core has to pass through these colder lower atmospheric layers to reach and heat the corona. Finally, the origin of the slow wind is another problem as the theoretical confinement of the plasma due to the strong magnetic field should prohibit the efficient release of plasma at low magnitudes where the slow wind is measured in-situ.

All described problems occur already for the simpler case of low solar activity, but the situation becomes even more complex for the active Sun (see right panel in Figure 1.3) where the solar magnetic field is in the middle of its polarity change that occurs approximately every 11 years [Hathaway, 2015]. At high solar activity the magnetic field structure is more complex allowing for different solar wind speed regimes at all latitudes. Furthermore, the Sun frequently emits spontaneously large plasma structures into interplanetary space, called ICMEs, that can be accompanied by the release of high energetic particles via flares or can create these particle populations through shock acceleration of the ambient plasma on their way out through the heliosphere [Schrijver and Siscoe, 2010]. ICMEs rarely happen during solar minimum which coincides with the period of the SOHO/CELIAS observations and they are most probably related to completely different initial acceleration processes than the classical continuous solar wind [Antiochos et al., 1999]. Therefore, they are not part of this work, although they are sometimes considered as its own solar wind class termed *transients* [Xu and Borovsky, 2015].

[1]The Parker model, however, still explains successfully the large scale heliospheric magnetic field by Eq. 1.3 - 1.5.

To solve the problem of solar wind acceleration and heating in the fast wind, over the last five decades more elaborated models of solar wind evolution have been developed, that proposed a variety of processes to accelerate the plasma in accordance with the existing observations (see [Marsch, 2006] and references therein). A promising class of mechanisms involves wave-particle interaction such as turbulent heating by Alfvén waves [Perez and Chandran, 2013, Hoppock et al., 2018] or resonant wave particle interaction with ion-cyclotron waves [McKenzie and Marsch, 1982, Isenberg and Hollweg, 1983, Isenberg et al., 2001, TU and Marsch, 1997]. The latter might evolve through a turbulence cascade from low-frequency Alfvén waves originating from the photospheric convection motion [Cranmer and van Ballegooijen, 2005, Suzuki and Inutsuka, 2006]. Alternatively, the high-frequency ion-cyclotron waves could be created directly through reconnection of the flaring network in the lower transition region [Marsch, 2006, Axford, W.I., McKenzie, J.F., 1997].
In order to test and restrict these acceleration and heating models as well as further models of solar wind transport and thermalization, precise measurements of the solar wind kinetic properties are needed. In particular the systematic measurements of solar wind minor ion species might yield additional information just by the fact that the heavy ions span a wide range in mass and charge and therefore couple differently to electromagnetic fields in the plasma. Furthermore, as these particles are in most cases negligible in terms of their number and mass density in the solar wind, their implementation into current models as test-particles might be realized relatively easy. Before we come to the measurement of these heavy minor ions with SOHO/CELIAS, in the following we give a short introduction into the theoretical framework of kinetic solar wind description and discuss possible mechanism of solar wind acceleration, heating, transport and thermalization.

1.2 Kinetic Description of the Solar Wind

As a plasma the solar wind is a many-body system and therefore its adequate description requires a statistical treatment. In the following we will rely mainly on the so-called *kinetic* plasma description[2] that is based on probability distribution functions $f(\underline{r}, \underline{v})$ that are defined in general in the 6-dimensional phase space composed of the 3 dimensions $\underline{r} = (x, y, z)$ and $\underline{v} = (v_x, v_y, v_z)$ in position and velocity space, respectively. The state of the plasma particle ensemble is fully described when we know the evolution of $f(\underline{r}, \underline{v})$ over time. As the particle measurements that we discuss are all obtained at one point in (position) space, the phase space distribution becomes a velocity

[2] The kinetic description has to be distinguished from the magneto-hydrodynamic (MHD) description that treats the plasma as a magnetized fluid.

distribution function (VDF) : $f(\underline{v})$. In theory f is often treated as a continuous function assuming large particle counting statistics ($N_p \to \infty$). In this limit a one-species plasma in thermal equilibrium is described by a Maxwellian VDF:

$$f(\underline{v}) = f(v_x, v_y, v_z) = \left(\frac{m}{2k_B T}\right)^{3/2} \exp\left[-\frac{m((v_x - v_{x0})^2 + (v_y - v_{y0})^2 + (v_z - v_{z0})^2)}{2k_B T}\right], \tag{1.6}$$

where $\langle \underline{v} \rangle = (v_{x0}, v_{y0}, v_{z0})$ is the species' mean velocity, m is the mass of the plasma species, k_B is the Boltzmann constant and T is the kinetic temperature of the plasma which is given for the three dimensional distribution by

$$T = \frac{3mv_{th}^2}{2k_B} \tag{1.7}$$

with the thermal speed v_{th}. When the situation reduces to one dimension as it is approximately the case when one measures along a well-defined given axis (x) in velocity space, the Maxwellian distribution reduces to

$$f(v_x) = \left(\frac{m}{2k_B T_x}\right)^{1/2} \exp\left[-\frac{m(v_x - v_{x0})^2}{2k_B T}\right] \tag{1.8}$$

and the temperature along the given axis is then given by

$$T_x = \frac{mv_{th,x}^2}{2k_B} \tag{1.9}$$

with the corresponding thermal speed $v_{th,x}$. We note that Eq. 1.8 has the mathematical form of a Gaussian [3] distribution with most probable speed v_x and standard deviation $v_{th,x}$. If we have several particle species in the plasma, than the thermal equilibrium is only reached when each species on its own obeys a Maxwell distribution and in addition all species have the same mean velocity $\langle \underline{v} \rangle$ and the same kinetic temperature T, which is *not* equal to the same thermal speed due to the mass-dependence of T.

In contrast to theory, in the measured particle data we have finite (and often very limited) particle count statistics. Also in many cases the spaceborne instrumentation is not capable of measuring full 3-dimensional velocity distribution functions (simultaneously at all directions) so that our information is limited to certain measurement directions and certain model assumptions have to be made to infer the full picture

[3] Note that Eq. 1.8 should not be confused with the Maxwell distribution for the speed magnitude $v = |\underline{v}|$, that is just Eq. 1.6 transformed to spherical coordinates with the shift in coordinate-system origin $v_{x0} = v_{y0} = v_{z0} := 0$ that leads to an asymmetrical distribution in v due to the additional factor v^2 that arises from the transformation.

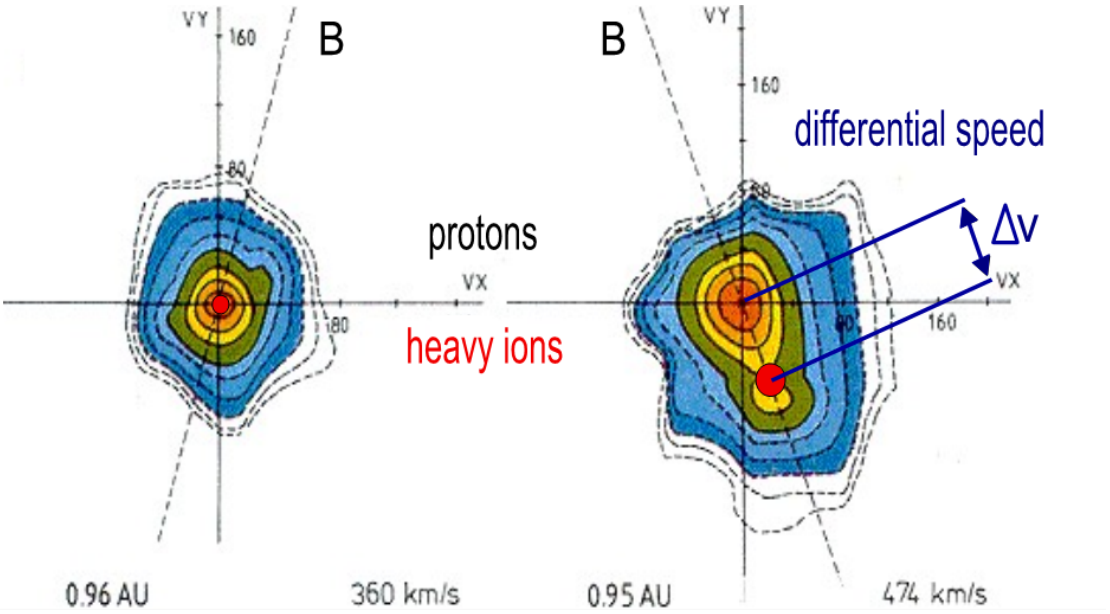

FIGURE 1.4: Measurements of 2-dimensional VDFs of the solar wind protons (black contour lines with orange to blue contour filling) recorded with the HELIOS E1 Plasma Experiment for two measurement periods at approximately 1 AU in the slow (left panel) and (somewhat) faster wind (right panel) with proton mean speeds of $\langle v_p \rangle = 360$ km/s and $\langle v_p \rangle = 474$ km/s, respectively. The 2D-cuts are done along the zenith angle of the magnetic field vector. Orange fillings mark the highest phase space densities and the contour lines correspond to a factor of 0.8, 0.6,0.4 and 0.2 times the maximum phase space density (solid lines) and logarithmically spaced to 0.1, 0.032, 0.001, 0.0032 and 0.001 times the maximum phase space density (dashed lines). The integration period of the VDFs is $\Delta t \leq 20$ s. To illustrate the differential streaming between protons and heavy ions we overlaid schematically the center of mass of a typical alpha particle VDF observed by Helios for both cases as red circles. We see that the proton VDF shows clear nonthermal features in the faster wind case compared to the approximately Maxwellian VDF shape in the slow wind, which can be recognized best by the pronounced asymmetry along the local magnetic field direction $\underline{B}$ which is primarily caused by the so-called proton beam. The alpha particles show a differential velocity that is also directed along the magnetic field but its magnitude Δv is smaller than the proton beam differential speed. The figure is adapted after [Marsch, 2012].

from the measurements. In particular, most heavy ion measurements are restricted to 1-dimensional measurements along a certain instrument axis that then result in the 1D-reduced VDFs that we obtain e.g. with SOHO/CELIAS/CTOF and which can be described approximately with Eq. 1.8 and Eq. 1.9 (see section 2.4).

One of the few experiments that measure 3-dimensional particle VDFs that can be well-resolved for protons and alpha particles is the E1 plasma experiment onboard the Helios twin-spacecraft [Marsch et al., 1982a]. In Figure 1.4 we depict solar wind proton 2D-VDFs measured with Helios in the ecliptic plane at approximately 1 AU in the slow (left panel, $\langle v_p \rangle = 360$ km/s) and intermediate speed regime (right panel, $\langle v_p \rangle = 474$ km/s). In both panels we overlaid schematically the typical center of mass for the simultaneously measured alpha particles with a red circle. While the measured VDF in the slow wind is nearly isotropic, the VDF measured at intermediate speeds shows

a pronounced elongation along the in-situ magnetic field that is measured simultaneously with the particles by the Helios fluxgate magnetometer. This nonthermal feature is primarily (but not entirely) the result of a second minor proton component, the so-called proton beam, that streams ahead of the core proton distribution if one follows the field line outwards in the solar wind center of mass frame. The alpha particle center of mass also streams ahead of the proton core distribution with a differential speed $\Delta v \lesssim v_A$ measured along the B-field which is typically a bit less than the core beam differential speed and comparable but lower than the ambient Alfvén speed [Marsch et al., 1982a] . In general it is not surprising that the differential velocity of the nonthermal ion populations are aligned with the magnetic field as any perpendicular velocity component leads to a gyro-motion of the population that cannot be resolved in time with our measurements and thus contributes to the apparent perpendicular temperature.
In this work we aim to determine the differential speed Δv_{ip} between protons and heavy minor ions ($Z > 2$) at 1 AU with the SOHO/CELIAS experiment. Depending on the expected underlying processes it is yet under debate whether the relevant differential speed should be measured from the proton core mean speed to the minor ion species mean speed as illustrated in Figure 1.4 or from the overall center of mass speed (including the alphas and the proton beam) to the minor species mean speed. As the CELIAS Proton Monitor only provides moment measurements of the protons and CELIAS/CTOF only measures 1D-reduced heavy ion VDFs, in any case we have to calculate Δv_{ip} in this study as the speed difference between the mean proton speed and the mean heavy ion speed both measured in the spacecraft frame (see section 2.4).
In Figure 1.5 we show the same 2-dimensional solar wind proton VDFs as in Figure 1.4 but this time we overlaid typical thermal speeds for alpha particles by sketching the highest two contour lines of the alphas both for the slow wind case (left panel) and the faster wind case (right panel). In the right panel the thermal speeds for the proton (core) VDF and ion (core) VDF are approximately equal which translates into the *nonthermal* feature of about mass-proportional temperatures while in the slow wind in the left panel the thermal speed of the heavy ion VDF is about a factor of 2 lower than the proton thermal speed indicating a temperature ratio that is close to thermal equilibrium. Note that for the comparison of the slow and faster wind case, the proton thermal speed should be calculated ideally from the core only, as the beam is a separate nonthermal feature by itself. This assumes a very good separation between proton core and the beam population, which is not achieved with most proton experiments and neither by the CELIAS Proton Monitor.
Despite the measurements of 3-dimensional VDFs, a second outstanding feature of the Helios mission was its highly elliptical orbit in the ecliptic plane that allowed measurements of the solar wind as close as 0.3 AU. We know now from these measurements

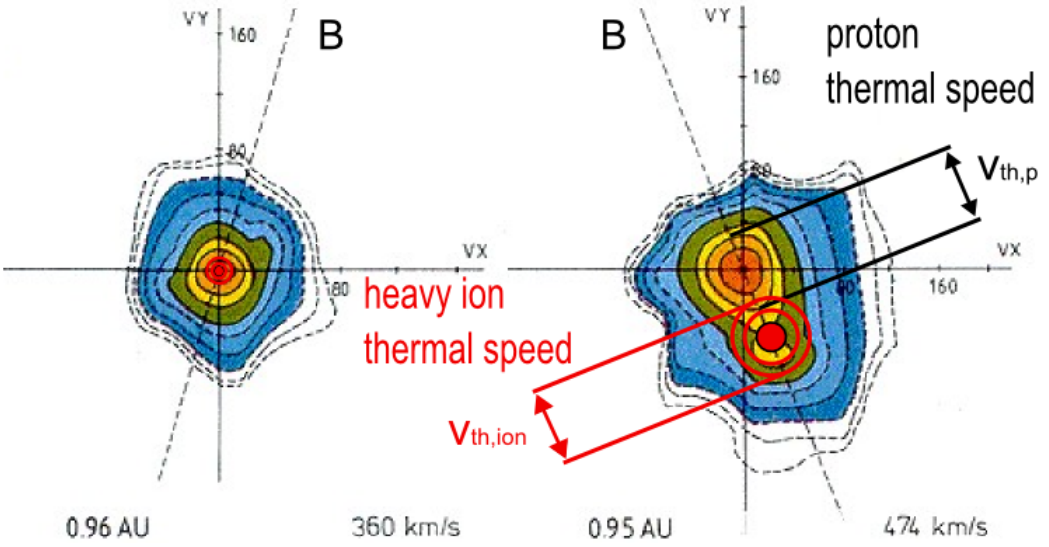

FIGURE 1.5: Same measurements of 2-dimensional VDFs of the solar wind protons (black contour lines with orange to blue contour filling) as in Figure 1.4. The sketched alpha species VDFs are again overlaid schematically (red concentric circles) only to illustrate approximately thermal (left) and nonthermal (right) ratios between heavy ion and proton thermal speeds. In the faster wind case in the right panel the thermal speed of the sketched alpha (core) VDF has approximately equal thermal speed as the proton (core) VDF which translates into the *nonthermal* feature of about mass-proportional temperatures while in the slow wind in the left panel the thermal speed of the heavy ion VDF is sketched about a factor of 2 lower than the proton thermal speed indicating a temperature ratio that is close to thermal equilibrium. The figure is adapted after [Marsch, 2012].

[Marsch et al., 1982a] that the in-situ observed differential speed between alpha particles and protons shows a systematical behavior in dependence of both the solar wind speed regime and the distance to the Sun. While for the slow wind at proton speeds between $v_p \approx 300$ km/s and 400 km/s no differential speed was observed, for faster wind above $v_p \approx 400$ km/s an increasing differential speed with decreasing distance to the Sun was found. In the fastest wind between $v_p \approx 600$ km/s and $v_p \approx 800$ km/s differential speeds of $v_{\alpha,p} \approx 150$ km/s were measured at 0.3 AU which decreased to values of $v_{\alpha,p} \approx 40$ km/s close to 1 AU. Comparable values of $\Delta v_{\alpha,p}$ in the vicinity of 1 AU were found from observations by several spacecraft, eg from ISEE-1 [Schmidt et al., 1980], WIND [Steinberg et al., 1996, Kasper et al., 2008, 2017] and ACE [Berger et al., 2011]. Concerning the preferential heating of alpha particles both mass-proportional and even over-mass proportional alpha particle temperatures were found between 0.3 and 1 AU e.g. from Helios [Marsch et al., 1982b], WIND [Kasper et al., 2008, 2017] [Maruca et al., 2013], and ACE [Tracy et al., 2015]. Besides differential streaming and temperature differences between ion species, there is the third typical nonthermal VDF feature of

temperature anisotropy with differences between the parallel and perpendicular temperature of a given species with respect to the magnetic field that are commonly observed for solar wind protons and alpha particles [Marsch et al., 1982a,b, Kasper et al., 2008, Maruca et al., 2013]. Unfortunately, this feature cannot be observed at all with SOHO/CELIAS due to the lack of a magnetometer onboard SOHO and the impossibility to extrapolate the B-field direction from other spacecraft on short timescales comparable to the frequency of directional change for longer measurement periods.
We finally emphasize that the discussed nonthermal features that shall be investigated with the SOHO/CELIAS data are not only of interest by themselves in terms of fundamental collisionless plasma physics but instead as pointed out by [Neugebauer et al., 1994] they might play a key role to better understand the "solar wind acceleration itself" and to gain deeper insights into "interplanetary processes such as instabilities and wave-particle interaction". These links between the measured particle VDFs and such fundamental processes in the solar wind are discussed in the following two sections. We start with the discussion of ion-cyclotron resonance as a possible candidate process for solar wind acceleration close to the Sun which can simultaneously create the observed nonthermal VDF features throughout the inner heliosphere.

1.3 Ion-Cyclotron Resonance as Candidate Mechanism for Solar Wind Acceleration and Heating

From a theoretical perspective one of the most investigated acceleration processes among the wave-particle interaction-based mechanisms is ion-cyclotron resonance. This is justified by the fact that the process can simultaneously create all three observed nonthermal VDF features that we discussed in the previous section: Differential speeds between solar wind heavy ion species and the bulk protons, preferential heating of the heavy ion VDFs as well as temperature anisotropies for all ion species so that $T_\perp > T_\parallel$. As the occurrence of the resonance itself depends on the gyrofrequency of the involved ions, one might further expect a distinct behavior of the ion species depending on their mass-per-charge values. Therefore, ion-cyclotron resonance is a natural candidate process to be investigated with a solar wind time-of-flight mass spectrometer such as CTOF that is able to measure a wider range of heavy ion species both in mass and charge. In the following we describe shortly the basic concept of ion-cyclotron resonance and discuss some theoretical model predictions. In this whole section 1.3 we follow closely an early paper on resonant wave acceleration of minor ions by [McKenzie and Marsch, 1982] and the review article on fast solar wind acceleration by [Hollweg and Isenberg, 2002].

The Single Particle-Wave Scenario of Resonant Ion-Cyclotron Interaction

The motion of charged particles in a magnetic field can be decomposed into a translational motion along the magnetic field lines and a circular gyro-motion perpendicular to the field lines. The gyrofrequency of the particle is linked to its mass m and charge q as well as to the local B-field magnitude $B = |\vec{B}|$ as

$$\Omega = \frac{qB}{m} \,. \tag{1.10}$$

Due to their gyro-motion the ions in the solar wind can interact (exchange momentum and energy) with circularly left-hand-polarized so-called ion-cyclotron waves in the plasma if the resonance condition is fulfilled (see e.g. [Hollweg and Isenberg, 2002]):

$$\omega(k_\parallel) - k_\parallel v_\parallel = n\Omega \,. \tag{1.11}$$

The term on the left side of Eq. 1.11 describes the Doppler-shifted wave frequency that is seen by the ion that moves with the speed $v_\parallel$ parallel to the magnetic field and which can be expressed as a function of the parallel wave number $k_\parallel$.

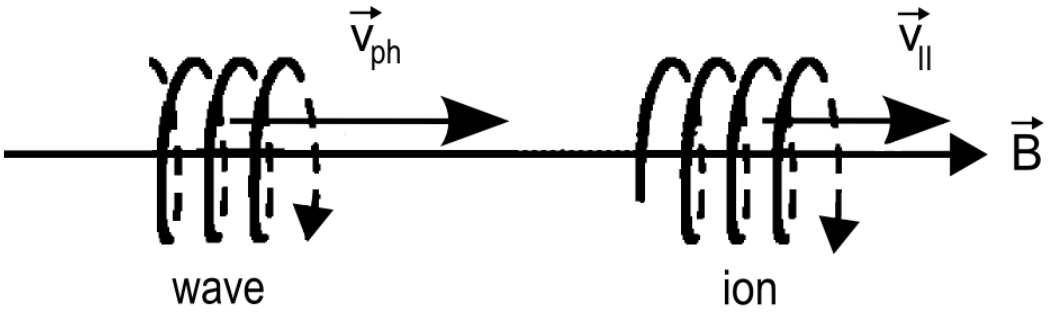

FIGURE 1.6: Schematic illustration of resonant wave-particle interaction between an ion with parallel velocity $\underline{v}_\parallel$ to the background magnetic field $\underline{B}$ and an over-taking ion-cyclotron wave that is propagating parallel to the magnetic field with an outward phase speed $v_{ph} > v_\parallel$. The figure is adapted after [Tsurutani and Lakhina, 1997].

While the integer n on the right side of the equation indicates that higher orders of resonance can occur at higher wave frequencies we concentrate in the following on the first order resonance $n = 1$ and for additional simplicity we only discuss waves that move parallel to the magnetic field so that we abbreviate $k := k_\parallel$.
If a gyrating ion encounters a wave with matching frequency ω as shown in Figure 1.6

the ion is accelerated in a direction perpendicular to $\underline{B}$ as it sees the corotating electric field $\underline{\delta E}(t)$ of the wave as a DC electric field in its own rest frame. The particle can thus increase or decrease secularly its perpendicular speed $v_\perp$ over its gyro orbit depending on the phase difference ϕ between the rotating wave E-field vector and its own perpendicular speed component at the moment of encounter. The rate of the ion's energy gain/loss over the time Δt while it is traveling a distance ΔL on its gyro-orbit can be written as:

$$\frac{\delta E_{kin}}{\Delta t} = \frac{q\delta E_\perp \Delta L}{\Delta t}\cos\phi = q\delta E_\perp v_\perp \cos(\phi) \tag{1.12}$$

where $\delta E_\perp$ is the wave's transverse electric field component and $v_\perp$ is the initial transverse ion speed along its gyro orbit. From Faraday's law we can relate the magnitudes of the electric and magnetic field vectors of the wave to each other

$$\delta E = \frac{\Omega}{k}\delta B \tag{1.13}$$

and thus express the change in the particle's squared perpendicular speed over the time Δt as a function of the wave's magnetic field δB:

$$v_\perp \delta v_\perp = \frac{q\Omega \delta B_\perp v_\perp}{mk}\cos(\phi)\Delta t\,. \tag{1.14}$$

We can now make use of the ion gyro-frequency definition in Eq. 1.10 to obtain the final expression

$$v_\perp \delta v_\perp = v_\perp \frac{\Omega^2}{k}\frac{\delta B_\perp}{B_0}\cos(\phi)\Delta t\,. \tag{1.15}$$

Due to the waves perpendicular magnetic field component and $\delta E \perp \delta B$ there is in general also a Lorentz force acting on the gyrating particles with magnitude

$$F_L = q v_\perp \delta B_\perp \tag{1.16}$$

which accelerates them parallel to the background magnetic field $\underline{B_0}$. Using again Eq. 1.10 we can write this change in the parallel speed over the same time Δt as

$$\delta v_\parallel = \frac{F_L}{m}\cdot\Delta t = v_\perp \Omega \frac{\delta B}{B}\cos(\phi)\Delta t\,. \tag{1.17}$$

With Eq. 1.15 and 1.17 the particle motion is completely described for all times as long as the ions remain in the adequate speed range to stay in resonance with the ion cyclotron wave(s). As the magnetic field is stationary in the frame moving with the wave, there should not be any work performed on the ions in this frame. We show that

the overall kinetic energy of the particles is conserved in this wave frame by calculating the total change of E_{kin} after any given time Δt:

$$\Delta E_{kin} = m(v_{\parallel}\delta v_{\parallel} + v_{\perp}\delta v_{\perp}) = mv_{\perp}\Omega\frac{\delta B_{\perp}}{B_0}\cos(\phi)\Delta t\left(v_{\parallel} + \frac{\Omega}{k}\right) = 0 \tag{1.18}$$

where we made use of the fact that in the wave frame the wave frequency ω is zero, so that we find from Eq. 1.11 for the parallel speed component of the particle

$$v_{\parallel} = -\frac{\Omega}{k}\,. \tag{1.19}$$

Model Predictions for Resonant Ion Acceleration and Heating

In the following we want to find a quantitative prediction of how strong the nonthermal VDF features can develop when we assume ion-cyclotron resonance as the dominant process. In particular we will see that certain limitations on the differential speed are already given by the resonance condition itself.
When we transform into the solar wind proton bulk rest frame so that $\langle \underline{v_p} \rangle := 0$ and restrict the situation again to parallel propagating waves ($|\underline{k}| = k_{\parallel}$) and to first-order resonance ($n = 1$) Eq. 1.11 becomes

$$\omega'(k) - k\Delta v = \Omega \tag{1.20}$$

where

$$\Delta v = |\Delta \underline{v}| = |\underline{v} - \langle \underline{v_p} \rangle| \tag{1.21}$$

is the differential speed that equals the magnitude of the differential velocity between the velocity of the interacting ion and the solar wind proton bulk velocity. Note that we can directly omit the parallel index for Δv as any differential speed component perpendicular to $\underline{B}$ would immediately start to gyrate around $\underline{B}$ as already mentioned in section 1.2. In analogy we made the same transformation for the wave frequency so that we find in Eq. 1.20 for the Doppler-shifted wave frequency in the solar wind proton (SW) frame

$$\omega'(k) = \omega - k\langle v_{p,\parallel} \rangle\,. \tag{1.22}$$

When we now assume in a first approximation that the ion-cyclotron waves are entirely carried by the solar wind bulk protons and thus are unaffected by the heavy ion species

we find in the SW frame for the dispersion relation [McKenzie and Marsch, 1982]:

$$k = \frac{\omega'}{v_A \sqrt{1 - \omega'/\Omega_p}} \tag{1.23}$$

where Ω_p is the proton gyro-frequency and v_A is the Alfvén speed

$$v_A = \frac{B}{\mu_0 \rho} \tag{1.24}$$

that can be calculated from the vacuum permeability μ_0, the magnitude of the background magnetic field B and the solar wind mass density ρ. Eq. 1.23 is known as the cold plasma dispersion relation for ion-cyclotron waves and fully describes these waves in the plasma as it links the wave-number to the wave frequency and thus also determines the wave phase speed (in the SW frame) for any given frequency by

$$v'_{ph} = \frac{\omega'}{k} \,. \tag{1.25}$$

If we solve Eq. 1.23 for ω' and plot it as a function of k as it is done in Figure 1.7 we see that the ion-cyclotron waves have lower phase speed the higher their wave number is and eventually cannot move anymore at the proton gyro frequency which is consistent with the complete dissipation of the wave energy to the thermal motion of the bulk protons that thus cannot longer carry the wave. When we also solve Eq. 1.20 for $\omega'(k)$ we obtain a linear function

$$\omega'_{\Delta v}(k) := \Omega'(k) = \Omega + \Delta v \cdot k \tag{1.26}$$

of the wave number with the gradient of the differential speed Δv and the offset given by the ion gyro-frequency Ω of the ion. In Figure 1.7, we sketched different linear functions $\omega'_{\Delta v}(k)$ for an alpha particle in dependence of its differential speed Δv with respect to the mean bulk proton speed. Thus for a given differential speed the resonance condition in Eq. 1.11 is fulfilled only at the intersections $(k, \omega)_{res}$ which represent waves with matching frequency and wave number. We see that for He^{2+} we find two intersections for all differential speeds below a certain differential speed Δv_{max} and one intersection in the limiting case $\Delta v = \Delta v_{max}$, while for $\Delta v > \Delta v_{max}$ no resonant interaction can occur. Thus, the particle cannot be accelerated to higher differential speeds by any resonant interaction with the existing ion-cyclotron waves and thus the resonant acceleration is self-limiting regardless of the available wave power. We also see that a proton can only interact resonantly with the waves as long as it is slower than $\langle v_p \rangle$ as its gyro-frequency cannot be reached by any ion-cyclotron wave carried by the proton bulk as discussed above. On the other hand, all minor ion species have a higher

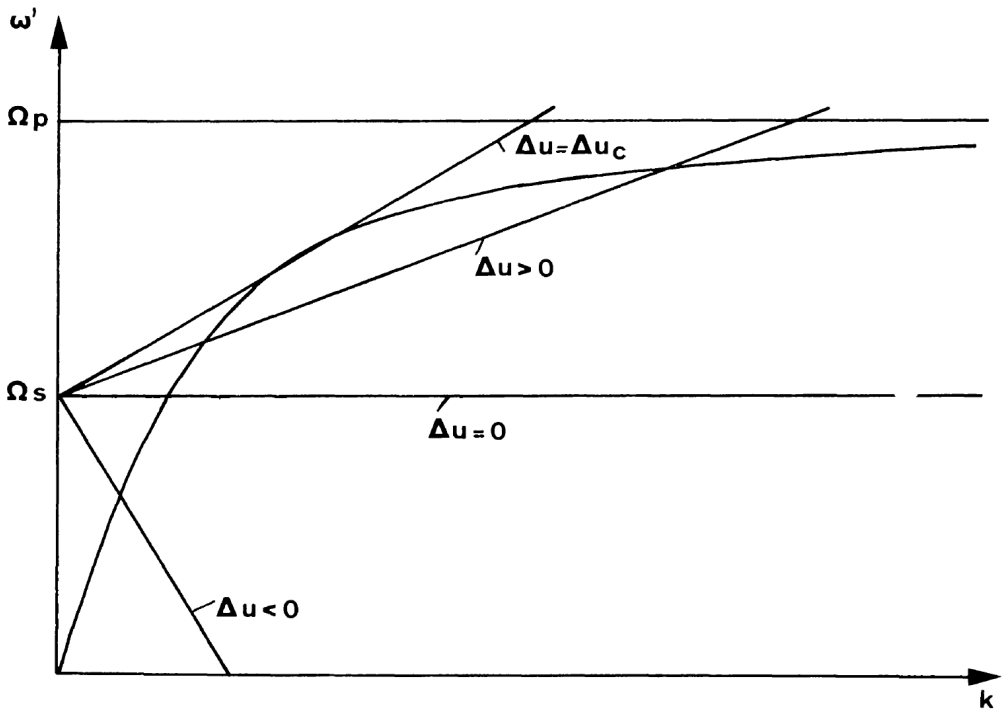

FIGURE 1.7: Visualization of the ion-cyclotron resonance condition in the solar wind plasma. The curved line marks the cold plasma dispersion relation $\omega'_w(k)$ of ion-cyclotron waves in the solar wind under the assumption that the waves are carried entirely by the solar wind bulk protons. Note that in this representation all frequencies $\omega'(k)$ are plotted in the solar wind (or proton bulk) rest frame, so that the Doppler-shifted resonance frequency $\Omega' = \Omega + k\Delta v$ of ions that move with a relative speed Δv to the proton bulk in this frame is given by a straight line with gradient Δv and frequency offset Ω. As the resonance condition 1.11 is only fulfilled at the intersection between Ω' and the dispersion relation $\omega'_w(k)$, we see that there is for each species a characteristic maximum differential speed given by the slope of the tangent where we only find exactly one intersection. Therefore the particles can only be accelerated to a certain maximum differential speed. For protons at arbitrary speeds this is the bulk speed as Ω_p is an asymptotic limit of $\omega'_w(k)$. For heavy ions with higher mass-per-charge their gyrofrequency Ω is lower and therefore they can be accelerated to characteristic m/q-dependent maximum positive differential speeds, before the resonance limits itself. The figure is taken from [McKenzie and Marsch, 1982]. Note that in the nomenclature of [McKenzie and Marsch, 1982] one has $\Delta u := \Delta v$ and $\Omega_s = \Omega$ is the gyrofrequency for each species.

mass-per-charge ratio and therefore lower gyro-frequencies than He^{2+}. As the dispersion relation is assumed to be independent of the solar wind heavy ions the differential speed cut-off of the minor ions due to the resonance condition occurs at even higher values than for the alpha particles $\Delta v_{max} > \Delta v^{\alpha}_{max}$. By solving Eq. 1.23 for ω', taking the partial derivative with respect to k and setting

$$\frac{\partial \omega'(k)}{\partial k} \stackrel{!}{=} \Omega + k \cdot \Delta v_{max} \tag{1.27}$$

we can obtain the differential cut-off speed for each heavy ion species in dependence of its gyro-frequency. This cut-off speed can be then expressed in dependence of the ions' charge-per-mass:

$$\Delta v_{max}(m,q) = \left[\frac{8 + 20 \cdot q/m - (q/m)^2 - (q/m)^{1/2} \cdot (8 + q/m)^{3/2}}{8}\right]^{1/2} v_A \,. \quad (1.28)$$

In Figure 1.8 we show the dependency of the predicted differential cut-off speed on the ion's charge-per-mass for a number of typical solar wind ion species where the discussed case of wave propagation parallel to the magnetic background field is the lower branch. The upper branch shows the analogous dependency for wave-propagation perpendicular to the magnetic field. The differential cut-off speeds are given relative to the Alfvén speed. We see the same qualitative behavior for parallel and perpendicular wave propagation with maximum differences of about 0.1 v_A between the branches. For the shown ion species the calculation yields maximum differential speeds of a bit more than 0.53 v_A for Fe^{12+} in the perpendicular case. For the lowest clearly observable iron charge state Fe^{7+} (not shown here, but see chapters 4 - 5) one expects a maximum differential speed of about 0.65 v_A for perpendicular wave propagation.
So far we could derive a quantitative prediction for the differential speeds based on a relatively simple analytic model of resonant ion-cyclotron interaction. However, when we go to a more realistic modeling of the solar wind plasma we have to include a number of effects that can change the obtained predictions significantly. One aspect to take into account is that the alpha particles represent on average about 5% of the number density and 20% of the mass-density of the solar wind and thus in general it is hard to justify treating them as test-particles. When one therefore assumes that the alpha particles are part of the solar wind background plasma in which the waves propagate, one has to modify the dispersion relation of the ion cyclotron waves which then is written as [Hollweg and Isenberg, 2002], [Gomberoff and Elgueta, 1991]:

$$(kv_A)^2 = \Omega_p \left[\frac{\omega^2}{\Omega_p - \omega} + \frac{2n_\alpha}{n_p}\frac{(\omega - kv_\alpha)^2}{\Omega_\alpha - (\omega - kv_\alpha)}\right] \quad (1.29)$$

where n_p and n_α are the proton and alpha particle number densities, Ω_α is the alpha particle gyro-frequency and v_α is the mean differential speed of the alpha particle population compared to the mean proton bulk speed v_p. As it is now clear that we do all calculations in the solar wind proton frame, we already denoted in Eq. 1.29 the wave frequency in this frame as $\omega' := \omega$. When one assumes zero (initial) differential speed between the protons and the alpha particles and a number density ratio of $n_\alpha/n_p = 0.075$ one obtains for the ion-cyclotron waves the dispersion relation depicted

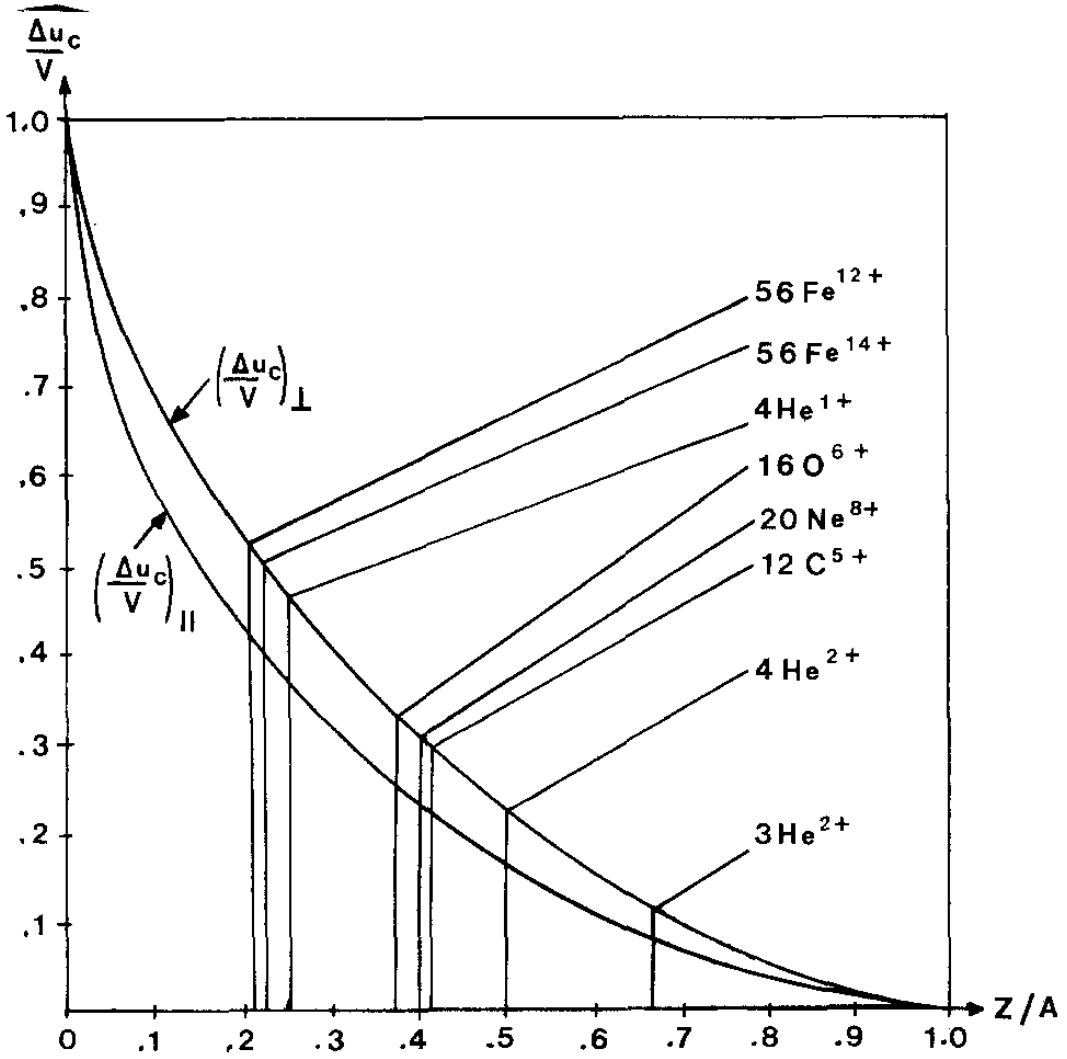

FIGURE 1.8: Characteristic differential speed cut-offs of heavy ion species due to ion-cyclotron resonance in units of the Alfvén speed for the scenario of the waves propagating parallel to the background magnetic field $\underline{B}$ (lower branch, as calculated after Eq. 1.28) and perpendicular to $\underline{B}$ (upper branch, not discussed here but see [McKenzie and Marsch, 1982, Hollweg and Isenberg, 2002]). The figure is taken from [McKenzie and Marsch, 1982]. Again we have in comparison to the text $\Delta u := \Delta v$ and $Z/A := q/m$.

in Figure 1.9. In the new situation we now have two branches indicating ion-cyclotron waves in two frequency bands. While a proton still can only interact resonantly with the waves when its speed is lower than v_p the depicted heavy minor ion O^{5+} can still be accelerated to positive differential speeds. In contrast to Figure 1.7 we note that, there is now even no upper limit of the O^{5+} differential speed as the ion can in principle switch from the lower to the higher resonance branch by resonating there with waves at high wave numbers $kv_A/\Omega_p > 4$ (not depicted here) after leaving the lower branch and then returning to infinitely low wave numbers on the upper branch with further increasing differential speed. In this context it becomes obvious that so far we did not

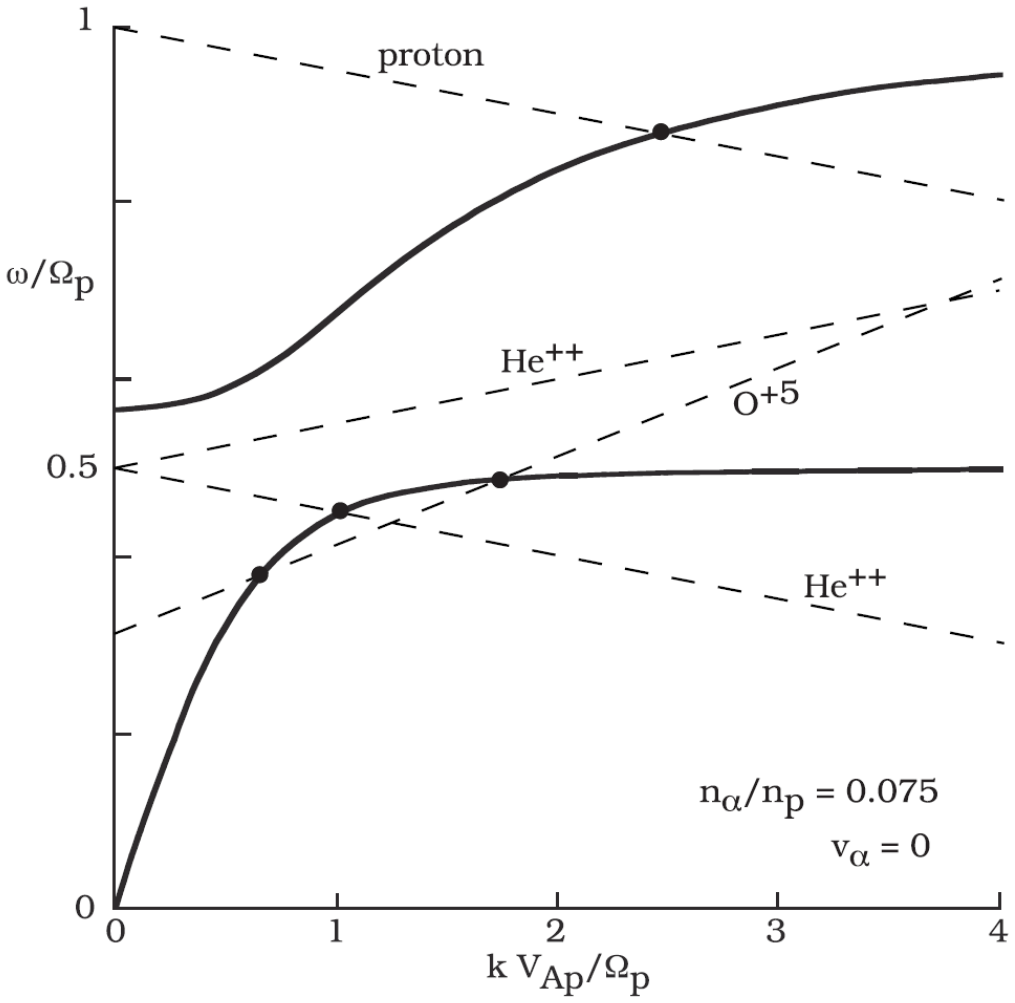

FIGURE 1.9: Visualization of the ion-cyclotron resonance condition in the solar wind plasma for the assumption that the ion-cyclotron waves are carried by both the solar wind bulk protons and alpha particles. The relative alpha particle number density is taken as 0.075 relative to the protons and no differential speed between these bulk species is assumed. The determination of a differential speed limit for heavy ions is more complex in this case as the different ion species can resonate in principle with two branches. However, one has to note that the acceleration at resonances with large values of k is low as one has to assume a decreasing wave power spectrum $P(k)$ with increasing k. The figure is taken from [Hollweg and Isenberg, 2002].

consider how much wave power is available at a given wave number (and branch). As the wave power spectrum $P(k)$ in a first approximation should decrease monotonically with increasing wave number one can estimate that the strongest acceleration occurs at the lowest wave numbers while at sufficiently high wave numbers no effective acceleration takes place anymore, which then can provide the differential speed cut-off. Any reasonable quantitative model therefore has to take into account the local wave spectrum in the solar wind at the acceleration site. Interestingly, in the given situation, He^{2+} cannot be accelerated from zero differential speed on, but those helium particles

that gained by some other mechanism already enough speed to resonate with the upper branch, can then be further accelerated by ion-cyclotron resonance. This observation underlines the potential importance of other processes that can act together or subsequently with ion-cyclotron resonance on providing efficient acceleration (and heating) for some ion species more than others.

After understanding the cause and basic characteristics of the differential speed cut-off, we can now fully understand the trajectory of a resonantly interacting heavy ion in velocity phase space that is depicted as an example for O^{5+} in Figure 1.10 together with the trajectory of a proton (H^+). The origin of the depicted velocity space is centered in the solar wind bulk proton frame and the situation obeys rotation symmetry with respect to the parallel speed axis, so that we can reduce the following discussion to $v_\perp \geq 0$. When the O^{5+} ion interacts with the ion-cyclotron wave it can gain or lose momentum and kinetic energy in the solar wind frame that is associated with a change in $v_\perp$ and $v_\parallel$. However, as discussed above, its kinetic energy in the frame moving with the wave is conserved so that during the resonant interaction its phase space trajectory is given by a semicircle centered around the phase speed v_{ph} of the wave. This means that the heavy ions become overall accelerated compared to the solar wind bulk protons as long as they interact with waves that are traveling outward faster than the solar wind bulk which is the typical situation. The radius of the semicircle is given by the magnitude of the relative velocity between the initial particle velocity at the moment when the wave encounters the particle and the wave phase velocity (here always directed along the magnetic field, so that $v_{ph,\perp} = 0$). Due to the discussed differential speed cut-off the ions cannot access all velocities on the semicircles. When we assume the simple scenario of the waves being carried entirely by the solar wind bulk protons, we find from the Eq. 1.28 that O^{5+} can reach a differential speed of $v_\parallel = 0.3\, v_A$, while we still have for proton $v_\parallel \leq 0$. A second main difference between H^+ and O^{5+} is that in the discussed scenarios in Figure 1.7 and 1.9 ion species with higher mass-per-charge tend to resonate with faster waves compared to those with lower mass-per-charge at least at moderate differential speeds. This is because their typical resonance wave numbers k_{res} are low compared to their respective resonance frequencies ω_{res} as a result of the rapid increase of the lower-branch dispersion relation at low values of k. This leads to larger semicircles for O^{5+} compared to H^+ which comes with the possibility to reach higher perpendicular speeds that in the shown case reach up to almost $0.7\, v_A$ for O^{5+} compared to about $0.3\, v_A$ for H^+.
In the wave frame the depicted situation is also known as the so-called pitch-angle scattering as the change between different states $(v_\parallel, v_\perp)$ under the condition of kinetic energy conservation has only one degree of freedom and can alternatively be fully described by the change of the pitch-angle θ which is the angle between the magnetic

field direction and the ion velocity vector. It can be expressed in terms of the particle's perpendicular and parallel speed component by

$$\tan(\theta) = \frac{v_\perp}{v_\parallel} \,. \tag{1.30}$$

This last observation can be utilized to generalize the single-particle description of ion-cyclotron resonance to a statistical model that allows the derivation of (average) acceleration and heating rates for a given heavy ion test-particle population in the solar wind. As discussed above, from Eq. 1.15 and 1.17 we can derive the evolution of the parallel and perpendicular speed component due to resonant ion-cyclotron interaction for a single test-particle in a coherent wave field. However, waves in the solar wind plasma are generally incoherent. Therefore, in the following the wave field is modeled by assuming each wave to be coherent for a length L but then it undergoes a random phase shift $\Delta\phi$ and this procedure is repeated N times within the time t. In this way, one can still use Eq. 1.15 and 1.17 to describe the change in the speed components during the coherent periods but in the end $\delta v_\parallel(N)$ and $\delta v_\perp(N)$ undergo a random walk which is equivalent to diffusion in velocity phase space. As discussed above, in the wave frame this diffusion can be described as diffusion in pitch-angle only. Thus, the temporal evolution of an ion test-particle population can be described with the common differential equation for pitch-angle diffusion:

$$\frac{\partial f(v,\mu)}{\partial t} = \frac{\partial}{\partial \mu}\left(D_{\mu\mu}\frac{\partial f(v,\mu)}{\partial \mu}\right) \tag{1.31}$$

where $v = \sqrt{v_\perp^2 + v_\parallel^2}$ is the magnitude of the heavy ion velocity in the solar wind frame, $\mu = \cos(\theta)$ is the cosine of the pitch-angle and $f(v,\mu)$ is the velocity distribution function (VDF) of the test-particle population parametrized by v and μ. From the described random walk scenario and Eq. 1.15 and 1.17 one derives after a few steps of straightforward calculation the pitch-angle diffusion coefficient $D_{\mu\mu}$

$$D_{\mu\mu} = \frac{(1-\mu^2)}{4|\mu|v}\left(\frac{q}{m}\right)^2 \delta B_\perp^2 L \tag{1.32}$$

with $L = t\Omega/(Nk)$ and the remaining quantities $\delta B_\perp$, Ω and k defined as in the beginning of this section in Eq. 1.10 - Eq. 1.14. The magnetic field of the ambient ion-cyclotron waves is related to the intensity spectrum of the waves via

$$\frac{v_{ph}\langle \delta B_\perp^2 \rangle}{2\mu_0} = I_B = \int_0^\infty I_B(k)dk \,, \tag{1.33}$$

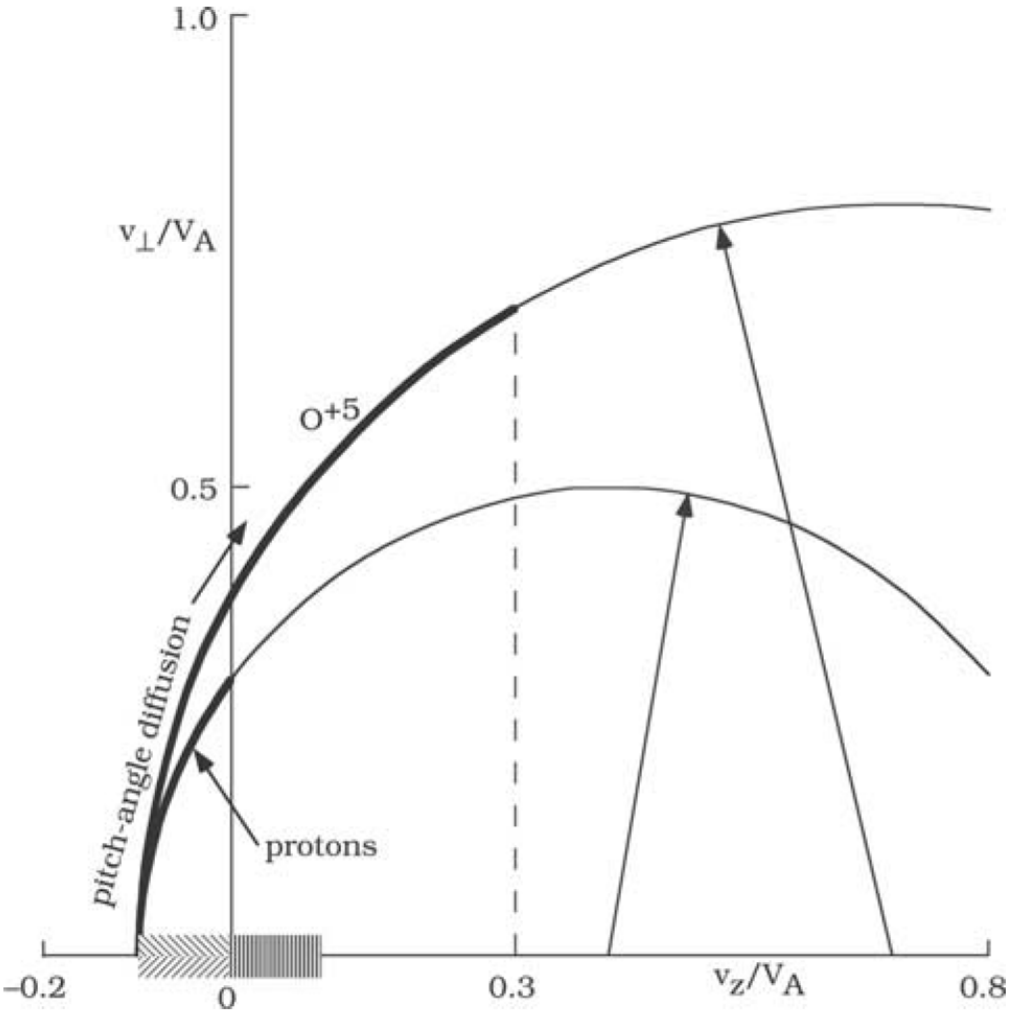

FIGURE 1.10: Visualization of acceleration and heating of solar wind ions (H^+ and O^{5+}) due to resonant wave-particle interaction depicted in velocity space parallel ($v_\parallel$) and perpendicular ($v_\perp$) to the ambient background magnetic field $\underline{B}$. The origin of the coordinate system moves with the solar wind bulk speed. Because the resonant ions conserve their kinetic energy in the frame moving with the ion-cyclotron wave after Eq. 1.18 they are restricted to semi-circles centered at the (parallel) wave velocity that is on average higher than the solar wind bulk parallel velocity. This trajectory in velocity space can be alternatively described by the change of particles' pitch-angle with respect to $\underline{B}$. As heavy ion species tend to resonate with faster waves than protons the two species are situated at different circles. Due to the differential speed cut-off, only a limited part of the respective semi-circles is accessible to the different species, that is marked fat here. Assuming an initial beam-like distribution of particles which are located approximately at the same point in velocity space, one can generate a spread of this distribution when one assumes an incoherent ion-cyclotron wave field with random wave phases ϕ as explained in the text. This process can be interpreted as pitch-angle diffusion or heating of the particle distribution that happens simultaneously with the acceleration process of the ions. In comparison to the text, the phase speed of the wave (which is aligned along the z-axis) is marked here as $v_{ph} := v_z$ and is given in units of the Alfvén speed. The figure is taken from [Hollweg and Isenberg, 2002].

where v_{ph} is the waves' phase speed, μ_0 is the vacuum permeability, and $I_B(k)$ is the spectral wave intensity density, i.e. the spectral wave power density $P_B(k)$ per unit area. Following [Hollweg and Isenberg, 2002] and [Kennel and Englemann, 1966] one can then substitute for the case of weak plasma turbulence

$$\delta B_\perp^2 L = \frac{2\pi\mu_0 I_B(k_{res})}{v_{ph}} \tag{1.34}$$

so that the diffusion coefficient reads

$$D_{\mu\mu} = \frac{\pi}{2}\frac{\mu_0(1-\mu^2)}{|\mu|\, v\, v_{ph}}\left(\frac{q}{m}\right)^2 I_B(k_{res}) \tag{1.35}$$

with $k_{res} = -\Omega/(\mu v)$.
To illustrate the behavior of a particle distribution in the presence of ion-cyclotron waves we consider a well-localized population in velocity space

$$f(v,\mu) = \frac{1}{2\pi v_{ph}^2}\delta(v-|V|)\delta(\mu+1) \tag{1.36}$$

that is described by a mono-energetic beam of particles that travels parallel to the background magnetic field with a speed V that is comparable to the phase speed of the waves. We can then calculate the perpendicular heating rate of $f(v,\mu)$ in analogy to an ordinary VDF moment calculation as

$$\frac{k_B dT_\perp}{dt} = \int \frac{mv_\perp^2}{2}\frac{\partial f(v,\mu)}{\partial t} d^3v = \frac{\pi\mu_0|V|q^2 I_B(k_{res})}{m\, v_{ph}} \tag{1.37}$$

where the actual calculation of the partial derivative $\partial f/\partial t$ is substituted by the calculation of the right term in Eq. 1.31. When we now assume, as often observed, a power-law for the wave spectrum in the relevant frequency range $I_B \propto k^{-\gamma}$ and use $V \approx v_{ph}$ together with Eq. 1.10 and Eq. 1.19, we find from Eq. 1.37 the relation:

$$k_B\frac{dT_\perp}{dt} \propto m\left(\frac{m}{q}\right)^{\gamma-2}|V|^{\gamma+1}\,. \tag{1.38}$$

Thus, the heating rate depends both on mass and charge of the ion species, the exponent of the wave power spectrum, and on the particle speed at which the ions can interact resonantly with the waves. We see that if all species had the same resonant speed V one would need values of $\gamma \geq 2$ to enable (over-) mass-proportional heating of the ions. Yet, heavy ions with high mass-per-charge ratios can reach higher differential speeds (see Eq. 1.28) and can also interact with faster waves (see Figure 1.10). Therefore, their preferential heating is produced also with typical solar wind wave spectra exponents that are somewhat lower than $\gamma = 2$.

For the resonant acceleration, a_{res}, of the same initial VDF $f(v,\mu)$ we obtain with the identical mathematical approach

$$a_{res} = \frac{dv_{\parallel}}{dt} \int v_{\parallel} \frac{\partial f(v,\mu)}{\partial t} d^3v = \frac{\pi \mu_0 \Omega^2 I_B(k_{res})}{v_{ph}\, B^2} \,. \tag{1.39}$$

Assuming again $V \approx v_{ph}$ and the same power-law $I_B(k) \propto k^{-\gamma}$ this expression gives the relation

$$a_{res} \propto \left(\frac{m}{q}\right)^{\gamma-2} |V|^{\gamma} \tag{1.40}$$

that shows a similar mass-per-charge dependence as the over-mass-proportional term of the heating rate. Both effects result from the strong dependency on the resonant wave numbers k_{res} that are linked to the ions' gyrofrequency.
To finally obtain a parallel heating rate we have to assume an initial thermal spread of $f(v,\mu)$. If one assumes in the simplest case a Bi-Maxwellian distribution (with in general $T_{\parallel} \neq T_{\perp}$) that initially rests in the solar wind frame, one obtains in a first approximation after [Hollweg and Isenberg, 2002]:

$$k_B \frac{dT_{\parallel}}{dt} = \frac{2k_B^2 T_{\perp}}{m v_{ph}^2} \left(\frac{dT_{\perp}}{dt}\right) \left[1 + \frac{T_{\parallel}}{T_{\perp}} k_0 \left(\frac{d\log(I_B(k))}{dk}\right)_{k_0}\right] \tag{1.41}$$

with $k_0 = \Omega/|v_{ph}|$. Thus, the parallel and perpendicular heating (or cooling) are coupled to each other.

The derived Eq. 1.38 - 1.40 rely in principle still on an early, but well-known model by [Isenberg and Hollweg, 1983] that is in relatively poor quantitative agreement with observations [Isenberg and Hollweg, 1983]. This might be caused by the fact that the model is still an oversimplified description of resonant ion-cyclotron as it does not take into account the subtleties of the dispersion relation in a multi-species plasma as shown in Figure 1.9. Another crucial point is also that the absorption of wave-energy by the particle species is not taken into account in a self-consistent manner, that would couple back to the wave power spectrum. Therefore, over the years more elaborated models [Isenberg et al., 2001, TU and Marsch, 1997] have been developed including subsequent stages[4] of (non-resonant) acceleration but they all rely on the described initial resonance mechanism that we illustrated.

[4]In particular the protons need to be accelerated finally by these non-resonant acceleration processes during the intial solar wind acceleration close to the Sun as we have seen that they cannot be accelerated through their bulk speed with the described resonant interaction. The crucial mechanism here is the acceleration of the protons along the magnetic field by the magnetic mirror force [Hollweg and Isenberg, 2002] which can efficiently transform the perpendicular speed component of the resonantly heated protons into an outward speed parallel to the magnetic field in the presence of fast expanding magnetic field structures (magnetic mirrors) as they can be assumed in coronal holes.

The models of resonant ion-cyclotron interaction give quantitative predictions of differential speeds and temperatures as well as acceleration and heating rates that depend only on the magnetic field fluctuations and the ions' mass and charge. Therefore, one can in principle test the proposed models with combined measurements of the B-field and the particle velocity distributions. Even when one only has the particle measurements (as in the case of SOHO, where no magnetometer is onboard) a restriction of the models can be made from the simultaneous measurement of different ion species as they all feel the same B-field.
Nevertheless, one should not forget that the largest part of, e.g., the solar wind acceleration happens close to the Sun and for instance the Helios measurements have shown that the differential speed decreases from 0.3 AU out to 1 AU [Marsch et al., 1982b]. Therefore, even if we find remnants from solar acceleration at 1 AU or local acceleration, these signatures are generally overlaid or regulated by other transport and thermalization processes that happen on the way out to 1 AU. Two known processes competing with ion acceleration and heating in the solar wind are 1) Coulomb collisions and 2) plasma instabilities that we briefly discuss in the next section.

1.4 Competing Processes in the Solar Wind

Coulomb Collisions

In their solar wind in-situ studies, [Marsch et al., 1982b] and [Livi et al., 1986] have shown that Coulomb collisions can play an important role in the shaping of ion VDFs in the slow wind. On the basis of proton and alpha particle data measured onboard the WIND spacecraft, [Maruca et al., 2013] suggest that the observed relaxation of differential temperatures between alpha particles and protons in the solar wind could be explained mainly by Coulomb interaction and [Kasper et al., 2017] argue that Coulomb collisions might be the fundamental process to regulate speed and temperature differences as well as proton temperature anisotropy beyond a few tens of solar radii away from the Sun, disregarding the solar wind speed. In this picture both fast and slow wind possibly exhibit nonthermal features close to the Sun, but by the time the plasma reaches 1 AU these signatures have vanished in the slow wind because its plasma has a higher typical Coulomb interaction rate ν and also needs a longer traveling time to arrive at the observation site. Assuming an approximately Gaussian proton VDF with

density n_p and temperature T_p the characteristic Coulomb collision rate ν_{pp} can be calculated analytically from the application of Rutherford scattering to proton-proton collisions as described in [Spitzer, 1962, 2013, Chhiber et al., 2016]:

$$\nu_{pp} = \left(8.77 \cdot 10^{-7} \cdot \frac{\mathrm{m}^3\mathrm{K}^{3/2}}{\mathrm{s}}\right)\left(\frac{n_p \lambda_{pp}}{T_p^{3/2}}\right) \tag{1.42}$$

where λ_{pp} is the Coulomb logarithm:

$$\lambda_{pp} = 2.51 + \ln\left[\left(\frac{1}{\mathrm{m}^{3/2}\mathrm{K}^{3/2}}\right)\left(\frac{T_p^{3/2}}{n_p^{1/2}}\right)\right] . \tag{1.43}$$

This Coulomb collision rate can be extended for collisions between heavy ions and protons to [Tracy et al., 2015, Hernandez and Marsch, 1985]:

$$\nu_{ip} = \left(0.35 \cdot \frac{\mathrm{m}^6}{\mathrm{s}^4}\right)\left(\frac{z_i^2 n_p \lambda_{ip}}{A_i (v_{th,i}^2 + v_{th,p}^2)^{3/2}} \cdot \frac{\phi(x)}{x}\right) \tag{1.44}$$

where

$$\lambda_{ip} = 23.0 - \ln\left[\left(\frac{1}{\mathrm{m}^{3/2}\mathrm{K}^{3/2}}\right)\left(\frac{A_i T_p + T_i}{z_i(1+A_i)}\right)\left(\frac{T_p}{n_p}\right)^{1/2}\right] \tag{1.45}$$

is the ion-proton generalization of λ_{pp} and z_i, A_i, T_i, and $v_{th,i}$ are the heavy ion charge in units of e, their mass number, kinetic temperature, and thermal speed, respectively. ϕ is the standard error function and x is the normalized differential speed between the heavy ions and the protons:

$$x = \frac{|v_{ip}|}{(v_{th,i}^2 + v_{th,p}^2)^{1/2}} . \tag{1.46}$$

Finally, we obtain the collisional age[5] $A_C = \nu\tau$ by multiplying the collision rate with the solar wind expansion time $\tau = R/v_{sw}$, where R is the distance the wind has travelled from the Sun to the measurement site. The term v_{sw} is the solar wind speed at the measurement site [Livi et al., 1986] and is typically approximated as the measured proton speed v_p. As one can see from Eq. (1.42) - (1.46) we can deduce both the proton-proton collisional age

$$A_{C,pp} = \frac{\nu_{pp} R}{v_p} \tag{1.47}$$

[5] In [Kasper et al., 2017] this quantity is named Coulomb number N_C, to distinguish it from an introduced more elaborated calculation of collisional age A_C, taking into account the variation of in-situ parameters $x_i(r)$ over the solar wind traveling distance R.

and ion-proton collisional age

$$A_{C,ip} = \frac{\nu_{ip} R}{v_p} \tag{1.48}$$

from the moments of the proton and heavy ion VDFs measured in-situ with CELIAS and are therefore capable to relate the measured differential speeds to these quantities.

Kinetic Plasma Instabilities

All kinetic plasma states that deviate from thermal equilibrium, (i. e. Maxwellian VDFs with equal temperature and flow speed for a multiple species plasma) are not in their minimum, or *thermal* energy state. If the deviations from the thermal state exceed a certain characteristic threshold the plasma state becomes unstable and part of the excessive kinetic particle energy in the system is released by the emission of plasma waves that grow exponentially and can then again interact with the particles. These (kinetic) plasma instabilities therefore are thought to play an important role in the regulation of the discussed nonthermal features such as differential speeds or temperature anisotropies [Gary et al., 2000]. The investigation of plasma instabilities in space plasma physics is a complex topic in itself and the number of classified instabilities is large (see e.g. [Matteini et al., 2013, Gary, 1992] and references therein) so that we restrict ourselves to one example: [Gary et al., 2000] have shown that the so-called alpha-proton magnetosonic instability could play a key-role in the regulation of the differential speed between protons and alpha particles even beyond Earth orbit by a comparison of Kinetic-MHD hybrid-simulations and in-situ observations of protons and alpha particles in the polar fast wind with Ulysses SWOOPS [Bame, S. and McComas., 1992] at 1.6 AU $\leq$ R $\leq$ 1.8 AU (upper panel) and 1.45 AU $\leq$ R $\leq$ 1.6 AU (lower panel), respectively. In Figure 1.11 the calculated differential speed threshold for the instability growth rate exponent $\gamma_m/\Omega = 0.001$ from the simulations is shown as the thick black line that obeys the relation

$$\frac{\Delta v_{\alpha p}}{v_A} = \frac{1.38}{\beta_{\parallel,p}^{0.17}} \tag{1.49}$$

in dependence of the local solar wind plasma β-parameter parallel to the in-situ magnetic field that is calculated from protons only. As we can see the calculated threshold confines reasonably well the observed differential speeds shown as a scatter plot over a wider range of values for $\beta_{\parallel,p}$ which shows its applicability to a range of fast wind plasma conditions. However, at low $\beta_{\parallel,p}$ an additional empirical relation is needed to

explain the confinement of the data in $(\Delta v, \beta_{\parallel,p})$-space, which is given as

$$\frac{\Delta v_{\alpha p}}{v_A} = 1.4 \cdot \sqrt{\beta_{\parallel,p}}\,. \tag{1.50}$$

and marked as the dashed line in Figure 1.11. When now the Alfvén speed decreases with increasing radial distance as observed in the Helios measurements, the calculated differential speed threshold reduces the absolute differential streaming of the alpha particles and therefore due to the instability a part of the streaming energy is redistributed and the simulations suggest that it goes into the heating of the alpha particles while the solar wind is propagating outward [Gary et al., 2000]. [Li and Habbal, 2000] conclude in their study that a similar (ion-proton) magnetic instability should be able to equally reduce the differential speed of heavy minor ions and simultaneously heat them when they have similar gyro-frequencies as He^{2+} and investigate in their simulation the case of O^{6+}. Precise differential speed and temperature measurements of heavy minor ions, could be therefore useful to further restrict these models. However, up to date there exist no sufficiently accurate more-dimensional VDF measurements of minor heavy ions from which one can get reliable estimates of a temperature anisotropy $v_{th,i,\parallel}/v_{th,i,\perp} > 1$ that is commonly used as an additional indicator of the ion-proton magnetosonic instability [Gary et al., 2000, Li and Habbal, 2000].

In summary, the situation in the inner heliosphere and in particular at 1 AU is complex. From a theoretical point of view we can have simultaneously acting

1. acceleration and heating mechanisms such as resonant ion-cyclotron interaction that are able to provide momentum and energy to the solar wind particles from the solar corona on and simultaneously create nonthermal features in the ion VDFs,

2. Coulomb collisions that constantly aim to thermalize the solar wind plasma,

3. plasma instabilities that can regulate the observed nonthermal features while the wind is propagating outward.

To disentangle all these processes in order to finally determine the mechanisms that actually dominate the acceleration, heating, transport and thermalization of the solar wind (in certain regions) we need precise systematic in-situ measurements of the particle VDFs and electromagnetic fields at selected sites and solar distances throughout the heliosphere (and ideally in the corona). In particular, we showed that certain promising acceleration and heating processes such as ion-cyclotron resonance are sensitive to the mass and charge of the solar wind ion species and the same applies to Coulomb

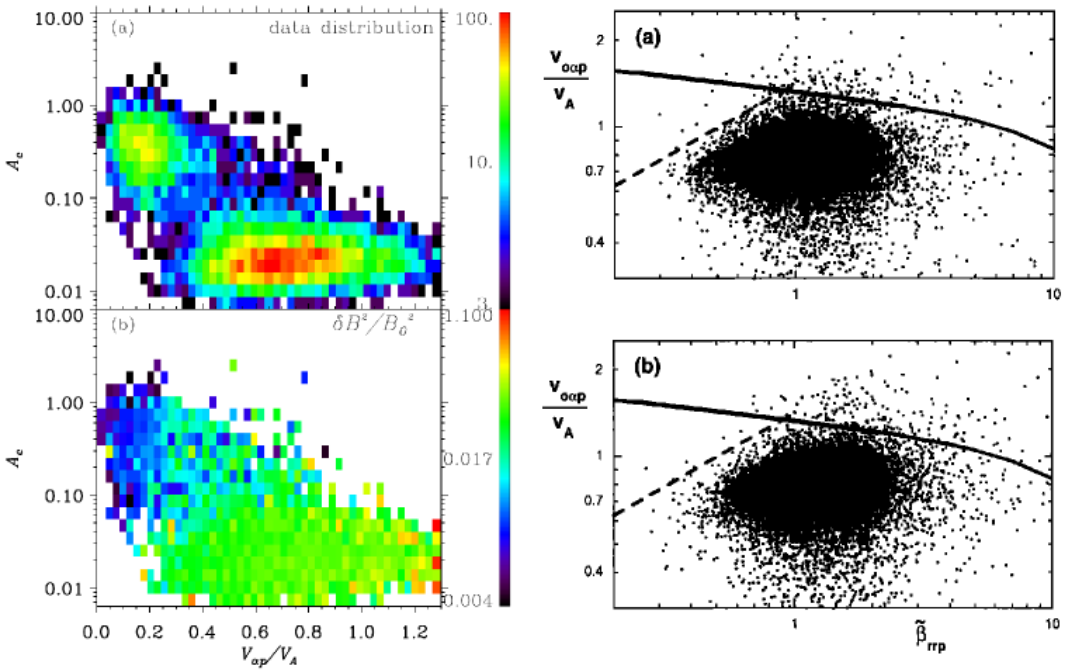

FIGURE 1.11: Left panel: Both Coulomb collisions and wave-particle interaction might regulate the differential speed $v_{\alpha p}$ (given in units of the local Alfvén speed). The wave-particle acceleration processes depend on the wave power, related to the relative B-field fluctations $\delta B/B_0$ while the Coulomb collisions are quantified in terms of the collisional age A_C. The figure is taken from [Bourouaine et al., 2011]. Right panel: Simulated differential speed boundary between alpha particles and protons due to the alpha-proton magnetosonic instability and the observed differential speeds with Ulysses/Swoops. The subscript 'rr' refers to the fact that only time intervals were utilized for the analysis in which the magnetic field is co-aligned with the radial direction from the Sun. This is due to the fact that the (parallel) ion temperatures can be determined most accurately along the instrument axis, pointing radially to the Sun. The figure is taken from [Gary et al., 2000].

collisions and certain ion instabilities such as the described ion-proton magnetosonic instability. Therefore, the systematic measurements of a wide range of minor heavy ion VDFs can provide crucial additional information to restrict and eventually distinguish between different proposed models, provided that the measurement inaccuracies are sufficiently small to resolve the expected features. In the following we give a short overview over the measurements of minor heavy ions in the solar wind up to date and formulate on this basis the scientific objectives for the systematic measurements of heavy ion kinetic properties with SOHO/CELIAS in this work.

1.5 Systematic Measurements of Heavy Ion Kinetic Properties

While the differential streaming between alpha particles and protons in the solar wind has been studied for several decades [Steinberg et al., 1996, Kasper et al., 2008, Marsch et al., 1981, Neugebauer and Snyder, 1966, Asbridge et al., 1976], there exist only a few independent speed measurements of heavy minor ions (with atomic number $Z>2$), which are several orders of magnitude less abundant than helium. Therefore, their precise measurement in the solar wind plasma requires very specific measurement instrumentation [Gloeckler, G. and Geiss., 1992, Hovestadt et al., 1995]. However, due to their low number density and their wide range in mass and charge, the minor ion species can be considered as perfectly suited test-particles to study possible mass- and charge-dependent acceleration and thermalization mechanisms in the solar wind.
From the early eighties on, case studies of the differential streaming of several relatively abundant minor ions such as O^{6+}, Si^{7+}, Fe^{9+} and Fe^{10+} [Hefti, 1998a, Schmidt et al., 1980, Ipavich et al., 1986] were conducted in fast streams in the vicinity of 1 AU and even in the inner heliosphere [Gershman et al., 2012], but until today the only systematic measurements of heavy ion differential speeds based on a wide set of solar wind ion species are available from the Solar Wind Ion Composition Spectrometer (SWICS) instrument on Ulysses [von Steiger and Zurbuchen, 2006, von Steiger et al., 1995] and from its twin instrument on the Advanced Composition Explorer (ACE) [Berger et al., 2011] . As mentioned before, Ulysses orbited the Sun in a highly elliptic polar orbit between 1.4 and 5.4 AU. During four extended time periods of the mission, corresponding to northern coronal hole wind, southern coronal hole wind and ecliptic wind at solar minimum and solar maximum, respectively, [von Steiger and Zurbuchen, 2006] analyzed the speeds of 35 heavy ion species spanning a range in mass-per-charge of $2.0 \leq m/q \leq 9.3$. The study is based on 1D-reduced heavy ion VDFs, derived from measurements of the absolute ion speed v_i with an integration time of two hours. While the authors do observe preferential heating of the heavy ions, they do not observe any signature of differential streaming, so that all ions were observed to flow at the proton speed during all observation periods. However, [von Steiger and Zurbuchen, 2006] state that this result is expected for most of the Ulysses orbit far beyond 1 AU, simply because the mean interplanetary B-field angle is almost perpendicular to the SWICS measurement axis and the differential streaming is supposed to act along the local B-field (compare section 2.4). Nevertheless, this result is in contradiction with the shown findings for the alpha-particles measured with SWOOPS [Gary et al., 2000] and there might be time periods where the B-field angle at the Ulysses orbit is sufficiently far off the nominal Parker angle. Also when Ulysses is above the solar poles the magnetic field should align reasonably well with the instrument measurement axis. In contrast

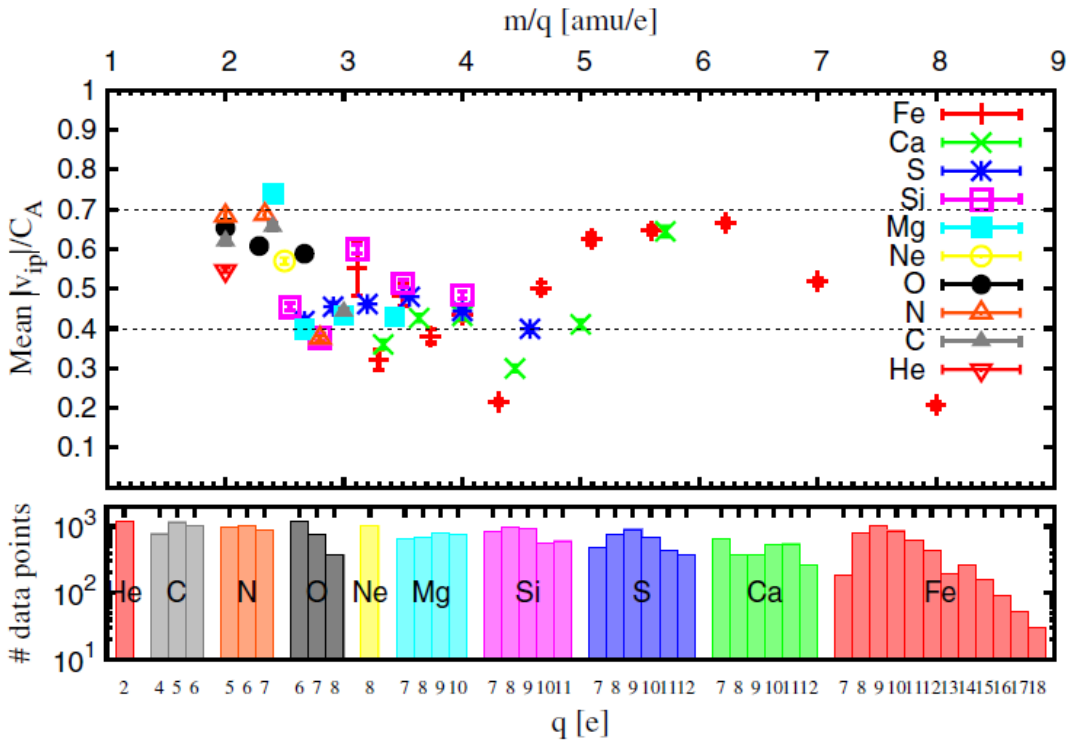

FIGURE 1.12: Mean differential speeds measured with ACE/SWICS after [Berger et al., 2011] in units of the local Alfvén speed as a function of mass-per-charge. The data is measured during two fast wind speeds around solar minimum in 2008. The error bars mark the statistical 1σ-standard error of the mean differential speed for each species.

to Ulysses, the ACE spacecraft is located at 1 AU on a halo orbit around L1. [Berger et al., 2011] used ACE/SWICS data to measure the differential speed between 44 heavy ion species in the mass-per-charge range $2.0 \leq m/q \leq 8.0$ and the solar wind protons. By analyzing the ion data in the intrinsic instrument resolution of 12 minutes and by correcting for the ambient magnetic field direction, the authors observed differential speeds for all analyzed ion species which were comparable in order of magnitude, but significantly lower than the local Alfvén speed and were found to lie between 0.2 and 0.8 v_A for all investigated ions (with 35 out of 44 ions between 0.4 and 0.7 v_A). A comparison of the heavy ion differential speeds showed no clear m/q-dependence as we can see in Figure 1.12.

While the differing results between the studies of [von Steiger and Zurbuchen, 2006] and [Berger et al., 2011] could be explained by the different measurement location and time resolution used in the analysis, the observations of differential streaming at 1 AU are not completely consistent either. In particular, there exist apparent differences between the ACE/SWICS results and the observations by [Hefti, 1998a] who analyzed the

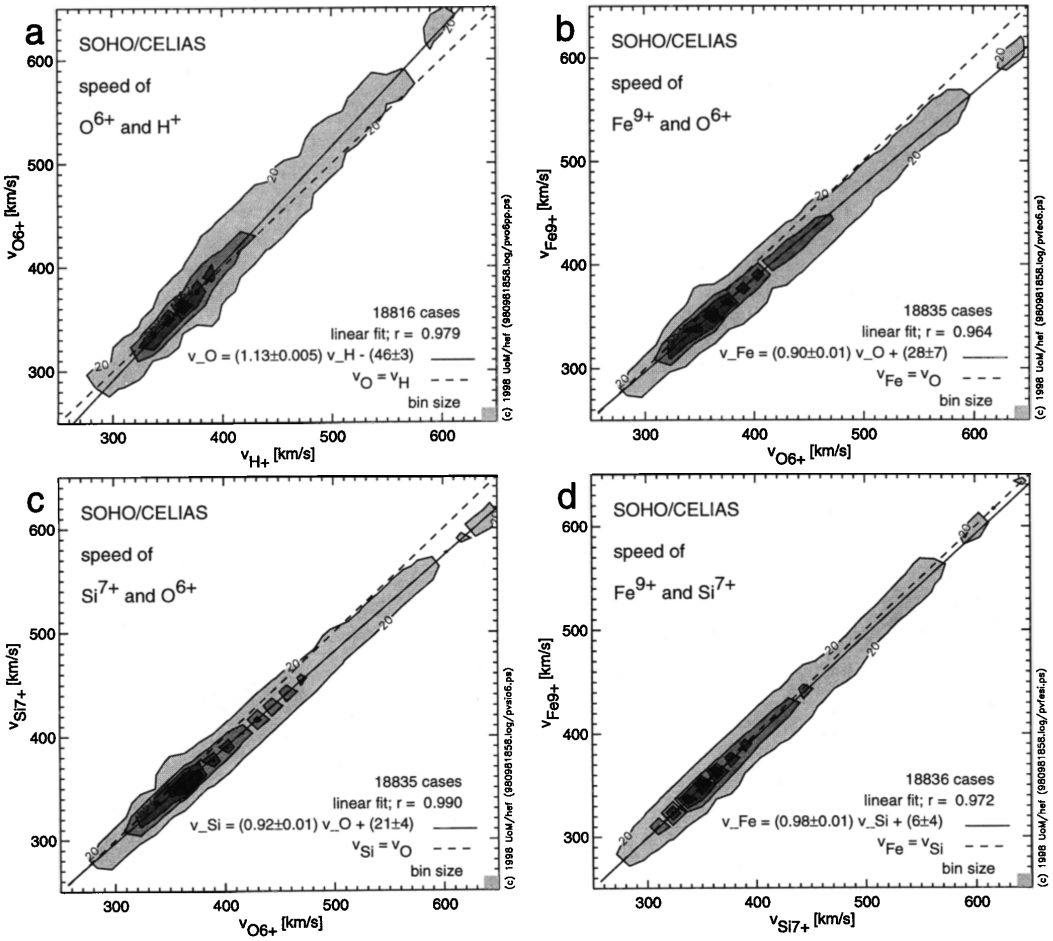

FIGURE 1.13: Heavy ion speeds measured with SOHO/CELIAS after [Hefti, 1998a]. The upper left 2D-histogram shows the measured speed of O^{6+} versus the simultaneously measured speed of the solar wind protons. In the other three panels the different heavy ion speeds for O^{6+}, Si^{7+} and Fe^{9+} are plotted against each other. On the whole [Hefti, 1998a] found significant differential speeds only for O^{6+} while Si^{7+} and Fe^{9+} stream at the same speed as the protons or at an even slightly lower speed.

differential streaming of several ion species measured with the CELIAS experiment onboard the SOHO spacecraft, which is also located in a halo orbit around L1. The study by [Hefti, 1998a] investigated heavy ion data from the CELIAS Charge-Time-of-Flight (CTOF) sensor with a time resolution of 10 minutes roughly covering the Carrington Rotations 1908 - 1912. Although CTOF is a time-of-flight mass spectrometer similar to the SWICS instruments and therefore capable to measure ions in a wide mass and mass-per-charge range, in the CELIAS study only three ion species O^{6+}, Si^{7+}, and Fe^{9+} were analyzed with the result that only O^{6+} showed systematic differential streaming compared to the solar wind bulk protons on the order of 20 km/s in the fast wind, while Si^{7+} and Fe^{9+} were reported to stream at the same speed as the protons or even slightly lower speed (see Figure 1.13). Unfortunately, the CELIAS/CTOF sensor was only in operation for a few months in 1996 due to a severe instrument failure on day of year (DOY) 230 in 1996, so that the study by [Hefti, 1998a] is the only one conducted

so far on kinetic properties of heavy ions measured with this instrument. However, the sensor's measurement principle provides very good charge-state separation facilitating precise identification of the heavy ion species while the unique combination of a high measurement cadence with a large geometry factor enables the measurement of heavy minor ions with relatively high counting statistics. By conducting a systematic analysis of solar wind ion kinetic properties including a wide range of heavy minor ion species in the mass-per-charge range between $2.3 \leq m/q \leq 8.0$, measured with the SOHO/CELIAS experiment, we aim to gain a better understanding of the kinetic processes in the solar wind at 1 AU.

1.6 Goals of this Work

To clarify the observational situation at 1 AU and provide restrictions for theoretical models of solar wind ion acceleration, heating, transport, and thermalization, with this work we aim to answer the following questions:

1. Do we observe differential streaming between the solar wind heavy ions and protons in the SOHO data?
   If so,
   (a) do we observe significant differential speeds for all ion species or only for particular species?
   (b) what is the sign and magnitude of the observed differential speeds?
   (c) do we observe a general trend depending on mass and charge of the ion species?
   (d) how does the differential speed depend on the ambient solar wind plasma conditions, in particular solar wind speed/type and collisional age?
2. Do we observe preferential heating of solar wind heavy ions compared to the solar wind protons in the SOHO data?
   If so,
   (a) are the heavy ions heated strictly mass-proportional or do we observe signatures of over- or under-mass-proportional heating?
   (b) how do the observed heavy ion temperatures depend on the ambient solar wind plasma conditions, in particular on solar wind speed/type and collisional age?

Chapter 2

Measurement Instrumentation and Data Products

2.1 The CELIAS Experiment onboard SOHO

The Solar and Heliospheric Observatory (SOHO) was designed to study the Sun, from its core to the atmosphere and the solar wind [Domingo et al., 1995] and thus its three principal science objectives are

1. the study of the solar interior,
2. the study of the heating mechanisms of the solar corona,
3. the investigation of the solar wind and its acceleration processes.

For these purposes the SOHO spacecraft is equipped with a comprehensive instrument suite that is depicted in Figure 2.1 and consists of remote-sensing and in-situ instruments, which add up to a total scientific payload of twelve experiments. Among the three in-situ particle experiments one finds the CELIAS (Charge, Elemental, and Isotope Analysis System) sensor suite which was built in a joint effort by the Max Planck Institute for Extraterrestrial Physics, the Max Planck Institute for Aeronomy (now the Max Planck Institute for Solar System Research), the University of Bern, the University of Maryland, the University of Braunschweig, and the University of Southern California. The CELIAS experiment has the objective to measure the energy distribution and composition (elemental, mass and charge state) of the solar wind in the energy range from about 0.1 to 1000 keV/e [Domingo et al., 1995, Hovestadt et al., 1995]. For this purpose it consists of four main sensors: The Charge-Time-OF-Flight (CTOF)

sensor, the Mass-Time-OF-Flight (MTOF) sensor, the Suprathermal Charge-Time-OF-Flight (STOF) sensor and the Proton Monitor (PM). CTOF, MTOF and STOF are illustrated in color in Figure 2.1 while the PM is a smaller device mounted on top of the MTOF monitor. For this work the only relevant sensors are CELIAS/CTOF and the CELIAS/PM, which are described in detail below.
The SOHO spacecraft was launched in December 1995 and is still in operation, although this is not the case for all experiments onboard. It is located on a halo orbit around L1 and is a 3-axis stabilized spacecraft, which means that both the CELIAS/PM and CELIAS/CTOF are pointed radially to the Sun to maximize their field of view for the approximately radially outward streaming solar wind.

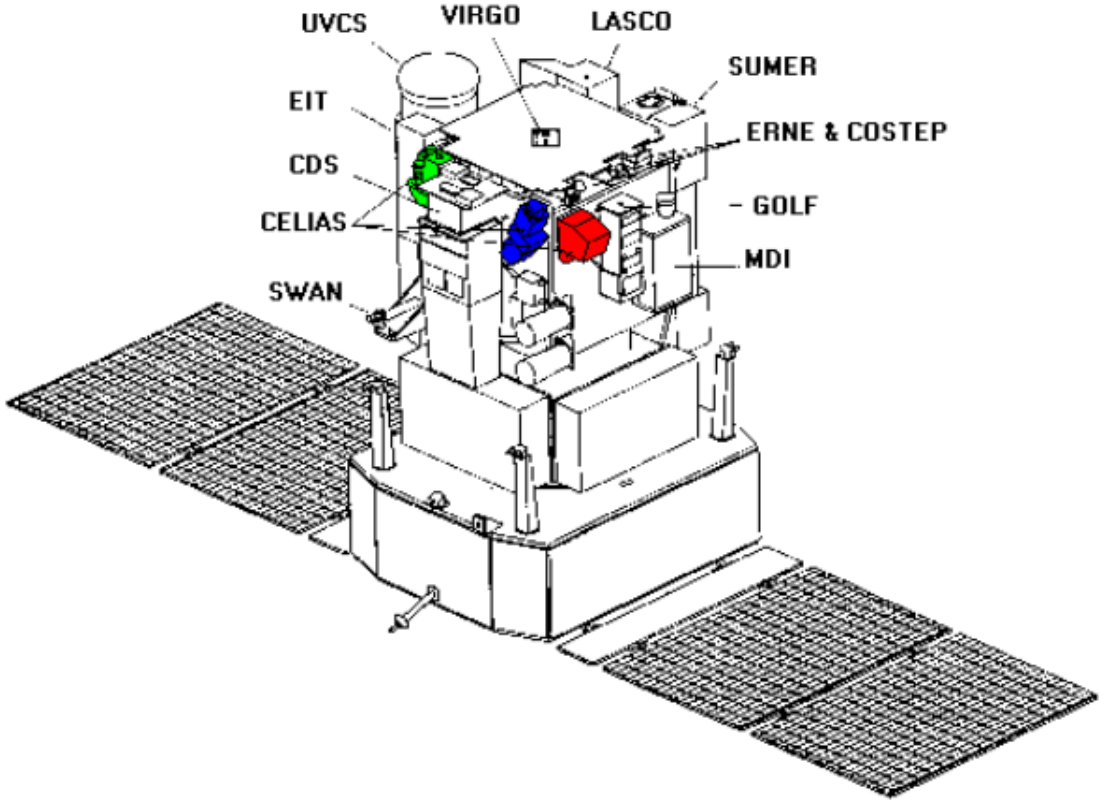

FIGURE 2.1: Schematic illustration of the SOHO Spacecraft with its scientific payload. The three CELIAS sensor units are colored: CTOF (green), MTOF (red), and STOF (blue). The Image is adapted after [Domingo et al., 1995].

2.2 The CELIAS/Charge-Time-Of-Flight Sensor

CTOF is a solar wind particle instrument that was built to measure the solar wind heavy minor ion species (with atomic number $Z > 2$) and is designed especially to resolve accurately the different solar wind charge states of these minor elements. By

blending out the solar wind protons and partially also the alpha particles, it could be designed with a high geometry factor that leads to relatively high counting statistics of the minor ion species in combination with a relatively fast measurement cadence of 5 minutes for these ions. Unfortunately, the instrument suffered a serious failure already on DOY 230, 1996, so that it recorded only data of several months around solar minimum in 1996. In the following we describe the instrument's principle of operation in greater detail.

Principle of Operation

The CELIAS/Charge-Time-Of-Flight (CTOF) sensor is a linear time-of-flight mass spectrometer based on the carbon-foil technique which is designed to detect heavy minor ions with $Z>2$ in the energy-per-charge range between 0.3 and 34.8 keV/e. The sensor measures the ions' mass, m, charge. q and speed, v. To derive these three quantities, three measurements are performed subsequently on an incident ion: First, in the CTOF entrance system the ion's energy-per-charge (Epq) value is determined by the Electrostatic Analyzer (ESA), which is a hemispherical capacitor, that the ion can only pass if its energy-per-charge is within the narrow Epq-passband of the analyzer which depends on the applied voltage between the capacitor electrodes[1]. Second, after being accelerated by a post-acceleration voltage the ion undergoes a time-of-flight (TOF) measurement. To trigger a start pulse for the TOF measurement the particle penetrates a thin carbon foil at the beginning of the TOF section from which secondary electrons are emitted that are then guided to a microchannel plate (MCP) detector. In a similar way a stop pulse is provided when the ion reaches a solid state detector (SSD) at the end of the TOF section by releasing secondary electrons from the SSD surface that are again detected by an MCP. Finally, the residual kinetic energy (ESSD) of the ion is measured in the solid state detector, which consists of a thin SiO_2 dead-layer on top of a sensitive silicon layer, where the ions fully stop.
Within one CTOF instrument cycle, which has a duration of about 5 minutes, the electrostatic analyzer steps through a sequence of up to 117 energy-per-charge values by changing the Epq-passband through the applied capacitor voltage:

$$U_0 \cdot r^{s_{max}-j} = \left(\frac{E}{q}\right)_j = \frac{1}{2} \cdot \frac{m}{q} \cdot v^2 \tag{2.1}$$

[1]Note, that the quantity on the left side of Eq. 2.1 $U_j = U_0 \cdot r^{116-j}$ that is given in the instrument description by [Hefti, 1998b] and [Aellig, 1998b] is not the actual voltage applied at the capacitor electrodes U_{app}, but absorbs already the so-called *analyzer constant* $C_A = R/2d$ which contains the radius R of the hemispherical analyzer and the distance between the capacitor electrodes d. This can be found from the equality of the electric force in an approximate plate capacitor ($R \gg d$) and the centripetal force:
$m\frac{v^2}{R} = q\frac{U_{app}}{d} \Leftrightarrow \frac{mv^2}{2q} = \frac{R}{2d} \cdot U_{app} = U_j = U_0 r^{s_{max}-j}$.

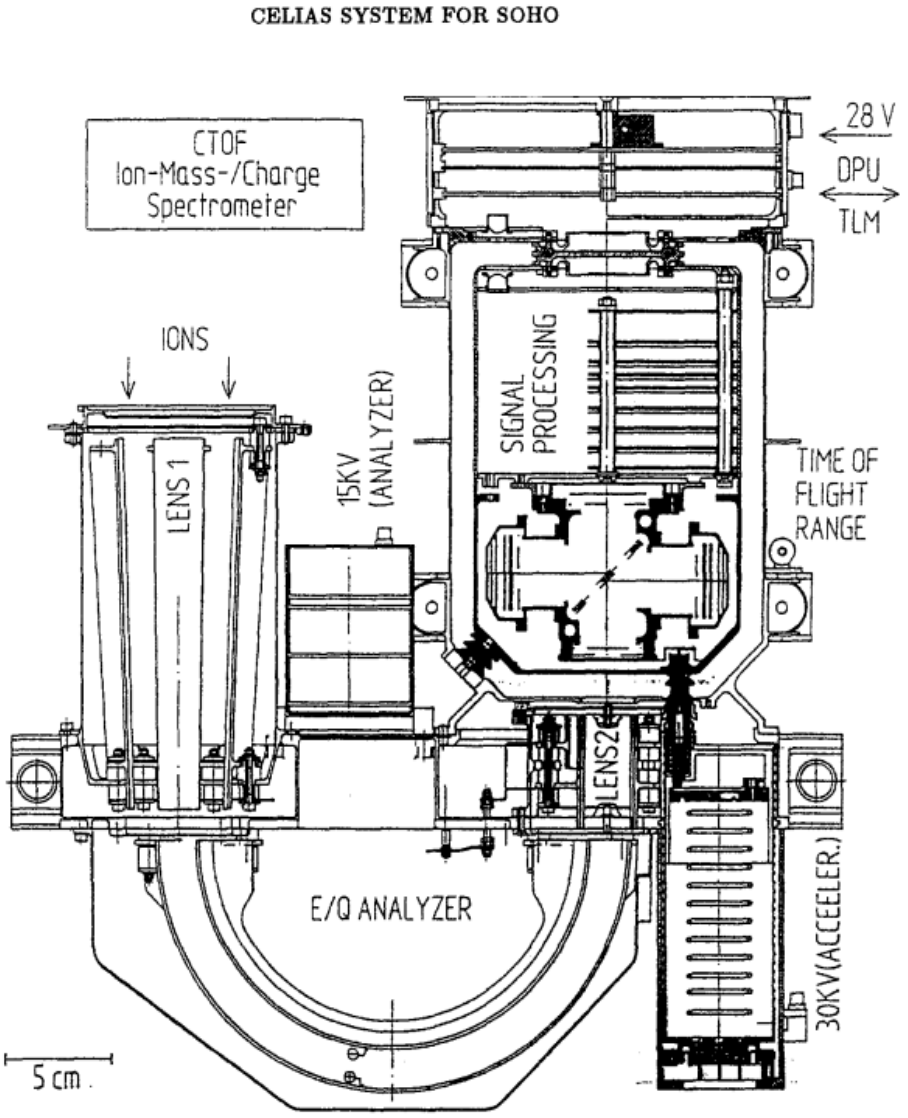

FIGURE 2.2: Cross-section of the CELIAS/CTOF sensor from [Hovestadt et al., 1995]. First the ions are focused by the quadrupole lens and pass through the electrostatic E/q-analyzer (ESA) in the entrance system if their energy-per-charge is appropriate. They are then further accelerated by a post-acceleration voltage and pass a thin carbon foil where the start pulse for the time-of-flight (TOF) measurement is triggered. Finally, the ions reach the solid state detector (SSD) at the end of the TOF section where they first trigger the stop pulse for the TOF measurement at the SSD surface and then deposit their residual kinetic energy within the SSD so that they fully stop.

where j is the ESA Epq-step number obtaining values from $s_{min} = 0$ to $s_{max} = 116$ while U_0 and r are constants given in appendix B in Table B.1 that allow the exponential stepping of the Epq-value. For a given ion species with fix mass and charge the Epq-stepping is equivalent to a scan in speed v as we see from Eq. 2.1, so that in principle we

obtain directly a speed distribution[2] from the ion count rate $N_{ij} = N_i(v_j)$ for any given ion species i measured over the range of Epq-steps. An important aspect of the CTOF operation principle is the fact that the ESA Epq-stepping is stopped when a certain limit of TOF start pulses (front start pulse rate (FSR) $\geq 10^5$ Hz) is reached which happens at low Epq-values (high Epq-step numbers j) in the alpha particle or proton VDF high-speed flank[3].

Yet, as CTOF measures different ion species simultaneously we need to derive the ions' mass and charge from their measured TOF and ESSD signals at each Epq-step in order to apply Eq. 2.1 . For any ion with mass m_i and charge q_i its residual energy after the post-acceleration[4] is well-defined for any given Epq-step j as

$$E_{acc}^{ij} := E_{acc}(q_i, j) = \left[\left(\frac{E}{q}\right)_j + U_{acc}\right] \cdot q_i \tag{2.2}$$

with U_{acc} defined in Table B.1, so that its speed after the post-acceleration reads

$$v_{acc}^{ij} := v_{acc}(m_i, q_i, j) = \sqrt{\frac{2E_{acc}^{ij}}{m_i}}\,. \tag{2.3}$$

Now, in an ideal instrument the solid state detector would measure the exact residual energy of the particle

$$\epsilon_{ij} = E_{acc}^{ij} \tag{2.4}$$

and its time-of-flight would be determined as

$$\tau_{ij} = \frac{L_\tau}{v_{acc}^{ij}} \tag{2.5}$$

where L_τ is the fix length of the TOF section between carbon foil and SSD surface. Thus, from the measured combined signals (τ, ϵ) one could unambiguously determine the ion's mass-per-charge by

$$\left(\frac{m}{q}\right)_i = \frac{2\tau_{ij}^2}{L_\tau^2}\left[\left(\frac{E}{q}\right)_j + U_{acc}\right] \tag{2.6}$$

[2] These speed distributions still have to be corrected for the difference in phase space coverage between the Epq-steps as it is explained below.

[3] As mentioned in chapter 1, this feature allows for a high geometry factor of the sensor without saturating or even damaging the instrument's internal particle detectors and electronics.

[4] The post-acceleration is necessary to allow a sufficient number of particles to trigger valid TOF and ESSD signals above the detection threshold. Thus, it increases dramatically the ion detection efficiency which is discussed in section 4.8.

and its mass by

$$m_i = \frac{2\tau_{ij}^2 \epsilon_{ij}}{L_\tau^2} \,. \tag{2.7}$$

with the known values L_τ and U_{acc} given in Table B.1 .
Yet, in the real measurement we have to take into account two phenomena that alter systematically the measured TOF and ESSD signals (see e.g. [Ziegler et al., 2008] and references therein). The first effect is the energy loss of the ions in the carbon foil due to the ion's interaction with the foil electrons and nuclei. This causes in a first instance a shift of the TOF signal to higher values, and in a second instance a shift of the ESSD signal to lower values as the ESSD measurement is not independent of the TOF measurement. The second effect is the so-called *pulse height defect* (PHD) in the SSD, which actually subsumes two phenomena [Oetliker, 1993a,b]: The energy loss of the ions in the SSD dead-layer which is analogous to the energy loss in the foil and the effect that part of the residual ion energy is lost to elastic interactions with the silicon nuclei in the sensitive SSD area and therefore is lost for the electron-hole pair creation. Thus, not the full residual energy of the ion is converted to an electronic energy signal which causes an additional shift of the observed ESSD signal to lower values. Both effects can be taken into account by transforming, Eq. (2.6) to:

$$\left(\frac{m}{q}\right)_i = \frac{2\tau_{ij}^2 \alpha_\tau}{L_\tau^2} \left[\left(\frac{E}{q}\right)_j + U_{acc}\right] \tag{2.8}$$

and Eq. (2.7) to:

$$m_i = \frac{2\tau_{ij}^2 \epsilon_{ij}}{\alpha_\epsilon L_\tau^2} \tag{2.9}$$

where the introduced factor α_τ is the ions' *residual kinetic energy fraction* after the carbon foil and the factor α_ϵ is the fraction of the ions' residual kinetic energy that is converted to an electronic signal in the SSD and which we denote as its *pulse height fraction*. Both factors can be only defined for a sample of measured ions in a statistical manner and depend on several quantities such as the atomic number Z of the ions, the speed v (or equivalently kinetic energy E_{kin}) of the ions prior to the carbon foil and SSD, the foil and SSD material, and the foil and SSD geometry, respectively. Therefore, α_τ and α_ϵ have to be determined in the instrument calibration for each relevant element[5] over the whole relevant energy range of the incident ions. As this is the starting point for the characterization of the CTOF response model in chapter 4 we only mention here that further effects that could potentially influence the observed ion peak signals such as

[5]Note, that both quantities do not depend on the charge q of the ions as the particles lose their initial charge state information already within the first few layers of the carbon foil [Ziegler et al., 2008].

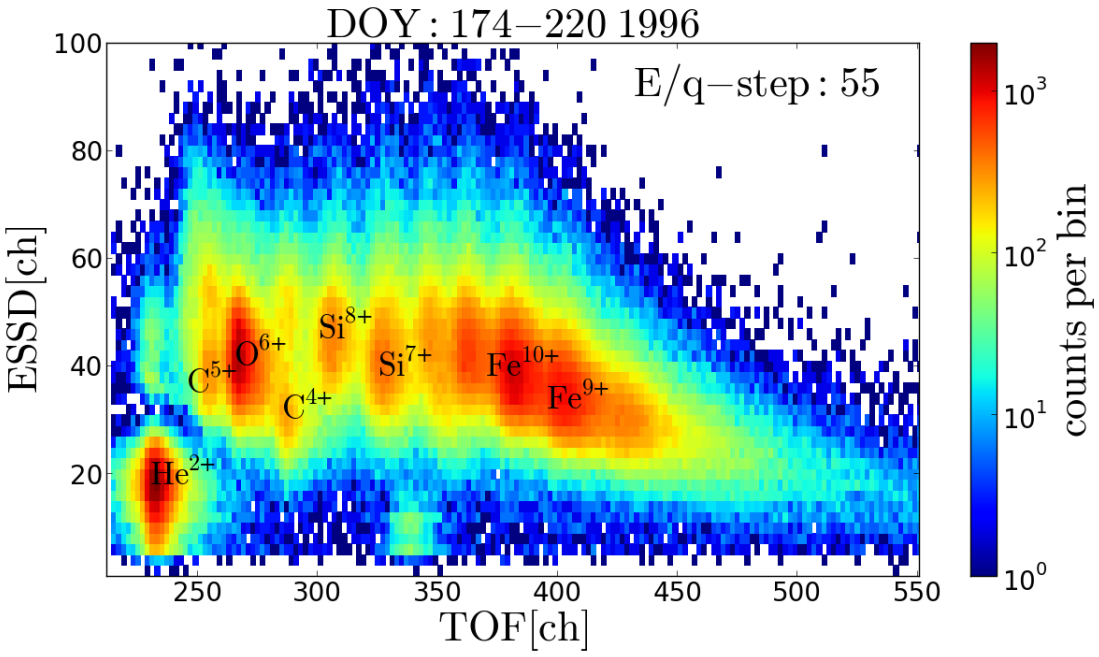

FIGURE 2.3: ET-matrix of the accumulated PHA data long-term counts for the whole measurement period DOY 174-220, 1996, at Epq-step 55. Note that these are only the transmitted counts due to the CTOF telemetry scheme as explained in the CTOF data products overview. The peaks of several more abundant ion species are well-recognizable by eye. For a fully calibrated ET-matrix with all ion species labeled see Figure 4.4 in chapter 4.

the finite energy acceptance of the ESA capacitor [Janitzek, 2014] or the read-out electronics [Hovestadt et al., 1995] could be shown to have negligible impact compared to the aforementioned effects.

In Figure 2.3 we show for Epq-step 55 a two-dimensional histogram of the transmitted TOF and ESSD signals that were measured with CTOF over the whole valid measurement period DOY 174-220 in 1996[6]. In the following we call these histograms ET-matrices for a given Epq-step accumulated over a given time-period which relates to a certain number of instrument cycles ($\approx$ 288 cycles per day). The TOF measurement is nominally resolved with 1024 channels while the ESSD measurement is resolved with 512 channels but the relevant solar wind events lie actually in a fraction of this total range (150 ch $< \tau <$ 600 ch, $\epsilon <$ 150 ch). Furthermore, we have to bin two channels together both in TOF and ESSD due to an artificial bit-pattern that creates a stronger (weaker) signal in every second channel in both the residual energy and time-of-flight signal. One can clearly recognize several peaks in the ET-matrix data that correspond to the positions of certain ion species as described in Eq. 2.8 and 2.9. But we can also

[6]For the definition of this valid subperiod of the CTOF measurements we refer to the subsection *CTOF Data Products Overview* further below in this section 2.2.

see that the widths of these peaks are large and thus overlap, so that in reality one cannot separate the different ion species deterministically as Eq. 2.8 and 2.9 suggest. The observed peak widths are mainly caused by the straggling of the ion species both in the carbon foil and the SSD which causes a broadening of both the TOF and ESSD signal[7] and which we did not consider so far.
Due to the straggling the ion identification has to be accomplished in a statistical way. Thus, Eq. 2.8 and Eq. 2.9 only hold when we regard the calculated values $(\tau, \epsilon) := (\tau_{ij}, \epsilon_{ij})$ as the most probable channels to be measured for an ion of a certain species i at a given Epq-step j or equivalently as the respective (central) ion peak position in the ET-matrix at the given Epq-step. The remaining channels that form the peak in the close ET-environment of $(\tau_{ij}, \epsilon_{ij})$ must be also taken into account to calculate the total count rate N_{ij} of a given ion species at a certain Epq-step. Also, due to the peak overlaps the measured count rate in a certain ET-channel includes in general contributions from different ion species. We assess these points in detail in the CTOF response model description in chapter 4.

CTOF Phase Space Coverage

After identifying the measured ion counts by their mass and charge, we finally obtain from Eq. 2.1 (total) count rates $N_{ij} = N(v_{ij})$ for every ion species i for all speeds v_{ij} that correspond to the 117 Epq-steps. However, these are not yet a physical phase space density (or VDF) in 1D velocity space, but have to be corrected for the different phase space coverage of the CTOF sensor both in 1D-velocity and -position space[8]. The electrostatic analyzer has a relative speed acceptance of $\delta v_{E/q}/v_{E/q} := \delta v_{E/q} = 0.0121$, which means that within the same measurement duration for all Epq-steps ($\approx 2.5\,\mathrm{s}$ per step for CTOF) we have for any given species a higher acceptance for particles measured at a higher speed v_{j+1} compared to those measured at a lower speed v_j by a relative factor:

$$\frac{N_{meas,j+1}}{N_{meas,j}} = \frac{\delta v_{E/q} v_{j+1}}{\delta v_{E/q} v_j} = \frac{v_{j+1}}{v_j} \tag{2.10}$$

so that we have to correct the measured count rates $N_j = N_{meas,j}$ with a factor $f_v \propto 1/v_j$ to make them comparable among the speeds v_j. This is the correction in velocity space. Similarly, particles with a higher speed can enter the CTOF sensor from a larger 'tube'

[7] See chapter 4 for a detailed discussion of the straggling in the carbon foil and approaches and its effects on the ion measurements.

[8] Note, that we only need to apply phase-space corrections in 1D velocity and position space as we can assume due to the large CTOF aperture [Hefti, 1998b] and the relatively narrow solar wind VDFs that we always measure the whole particle distribution in the directions perpendicular to the instrument axis regardless of the particle speed.

in position space. Assuming a constant speed of these particles over the short measurement duration of $\Delta t = 2.5\,\mathrm{s}$ we find for the correction factor again:

$$\frac{N_{meas,j+1}}{N_{meas,j}} = \frac{v_{j+1}\Delta t}{v_j \Delta t} = \frac{v_{j+1}}{v_j} \tag{2.11}$$

so that we obtain for the correction in position space also a factor $f_x \propto 1/v_j$, leading to an overall correction factor of $f_{xv} \propto 1/v_j^2$ that has to be multiplied with the measured count rates N_{ij} to derive the phase space densities (VDFs) $n(v_{ij})$ from which one can calculate the first and second moments to derive mean and thermal speeds.

CTOF Data Products Overview

The CTOF sensor data, as processed in the CELIAS digital processing unit (DPU), is sent down to Earth in four principal data products: the pulse height analysis (PHA) data, the matrix rates (MR) data, the matrix elements (ME) data and the sensor rates (SR) data. Unfortunately, the onboard algorithm for the post-processing of the measured raw data to the matrix rates product with the exact given parameters in [Hefti, 1998b] turned out to be valid only for DOY 174-220, 1996, so that we can only analyze the matrix rate data in this time period. Since also the PHA data is subject to this issue through the PHA base-rate correction, that is described at the end of this section, the whole study is limited to the aforementioned period DOY 174-220 in 1996. This is about a factor of 3 shorter than the time-period in the earlier CELIAS study by [Hefti, 1998a] and covers only about 1.7 Carrington Rotations.

CTOF Pulse Height Analysis Data

The most fundamental CTOF data product is the **pulse height analysis (PHA)** data which consists of the detected ion events for each CTOF 5-minute cycle time stamp with the events being represented by their Epq-step, TOF and ESSD channel. Note that not every ion reaches the SSD (with sufficient energy) to generate an electronic signal so that in these cases $E_{SSD} = 0$ and these events are classified as double coincidence events in contrast to the triple coincidence events for which ESSD ≥ 1 ch. In this whole study we only deal with triple coincidence data, so we always have the full Epq, TOF and ESSD information for the PHA events that we denote in the following directly as PHA counts. However, due to the limited telemetry budget the CELIAS DPU does not send the *full PHA* count data to Earth, but performs an onboard post-processing of all measured PHA events to the compressed *matrix rates* and *matrix elements* data products

that are discussed below. Yet, in order to be able to check the onboard assignment algorithm of the PHA counts to ion-specific matrix rate boxes, there is in addition also a limited number of raw PHA counts transmitted for each Epq-step within each CTOF cycle (see Figure 2.5), containing the full Epq, TOF, and ESSD information for these counts. Thus, the long-term PHA count rates depicted in Figure 2.3 are just the integrated counts of these *transmitted PHA* subsamples for all cycles at the given Epq-step 55.
These transmitted counts are selected according to a priority scheme which is based on a very rough onboard mass classification of the originally measured PHA counts using their TOF and ESSD information: double coincidence counts or counts with very low ESSD channels are classified as priority range PR0, while all other coincidences are classified within the priority ranges PR1 (anticipated iron range) to PR5 (anticipated helium range). As iron is less abundant than e.g. oxygen (PR4), almost every iron ion is selected to be transmitted down to Earth to be able to reconstruct the iron distribution with sufficient statistics, while for oxygen a smaller fraction is transmitted. For all priority ranges the so-called base-rate factor calculated as the number of measured counts divided by the number of transmitted counts has to be stored, so that in the end the true number of measured counts can be reconstructed from the transmitted PHA data (see appendix A). We note that these base-rate factors are not constant over time but also vary at each cycle and Epq-step with the ambient solar wind proton conditions to make sure to sample the species properly over varying solar wind speeds. We also note that within each priority range the selection of the events is completely independent of their Epq, TOF and ESSD to assure a statistical sample of the measured ions for unbiased reconstruction of the ion species count rates within this range.

CTOF Matrix Rate Data

During a given CTOF instrument cycle the onboard algorithm assigns the measured full PHA counts to 21 so-called *matrix rates* (MR0 - MR20) within 508 *matrix rate boxes* (MR-boxes) which we summarize in the following as **matrix rate (MR)** data. This assignment works as follows:
From the CTOF preflight calibration [Oetliker, 1993a, Hovestadt et al., 1995, Hefti, 1998b] one knows for each Epq-step the location of each ion species in the respective ET-matrix. By dividing the ET-matrices into ion-specific boxes and inverting the calibration, the CTOF onboard algorithm assigns after Eq. A.2 and A.8 a mass and mass-per-charge channel to each PHA count depending on its TOF and ESSD channel at the Epq-step of occurrence. Based on this combination of m and m/q channel the count can be already identified with a certain ion species and is sorted into the corresponding

MR-box. The MR-boxes are defined in terms of mass and mass-per-charge channel in the *CTOF Matrix Rates Box Definition* table in Figure A.10. Simultaneously, the count is assigned to one of 21 matrix rates, which represent basically a compressed speed binning compared to the 116 Epq-steps. The idea of the compression is of course to save telemetry budget. To achieve this goal with as little information loss as possible, the 21 matrix rates are designed to be centered always close to the most probable measured speeds of the heavy ion species (which naturally depends on the solar wind speed) and have the highest speed resolution at their central matrix rates where the core of the ion speed distributions is expected to be measured. Consequently, in the very low and high matrix rates, that correspond to the far flanks of the expected distributions where small count rates are anticipated, the speed resolution is low due to high compression ratios. To center the matrix rates properly around a highly probable heavy ion speed, an estimation of the heavy ion speed for the current CTOF cycle $\widetilde{v}_{swi}$ is calculated from the mean speed of the major iron species measured in the previous cycle (calculated onboard from the full PHA data before the compression). The central matrix rate 10 can be then linked to a certain *central Epq-step* j_c that for a given MR-box and estimated heavy ion speed $\widetilde{v}_{swi}$ is calculated as

$$j_c = 116 - \ln(\widetilde{v}_{swi}) \cdot V_1 + V_2 - (S+1)/2\,, \tag{2.12}$$

where $V_1 = 49.8516$ and $V_2 = -164$ are fixed algorithm values during the whole analyzed time period and $\widetilde{v}_{swi}$ is given in km/s. The remaining number S is a shift that corresponds to the given matrix box number of the selected species. This shift is defined for each box in the *Look-up Table for the CTOF Matrix Rates Center Step* in Figure A.11. This table has the same format as the *Matrix Box Definition* table in Figure A.10 so that box number and shift can be mapped to each other by position in the tables. All float values that appear in Eq. 2.12 by the application of the logarithm or by division are truncated to the next-lowest integer value.
For all of the 508 MR-boxes the 21 matrix count rates within MR0 - MR20 are then calculated onboard by binning together the full PHA count rates measured at the respective Epq-steps as shown in the compression scheme in Table 2.1:

The value $\widetilde{v}_{swi}$ is stored for each measurement cycle in the matrix rate data together with the 21 matrix count rates for each of the 508 matrix boxes[9], so that the matrix (count) rates can be reconverted to a Epq-spectrum after Eq. 2.12 and the scheme in Table 2.1. These Epq-spectra can then be transformed for every MR-box to a speed distribution, which is shown in the following chapter 3.

[9]Note that $\widetilde{v}_{swi}$ is stored in the same cycle (i) in which it is used for the calculation of the central Epq-step j_c and not in the cycle for which it was calculated (i-1).

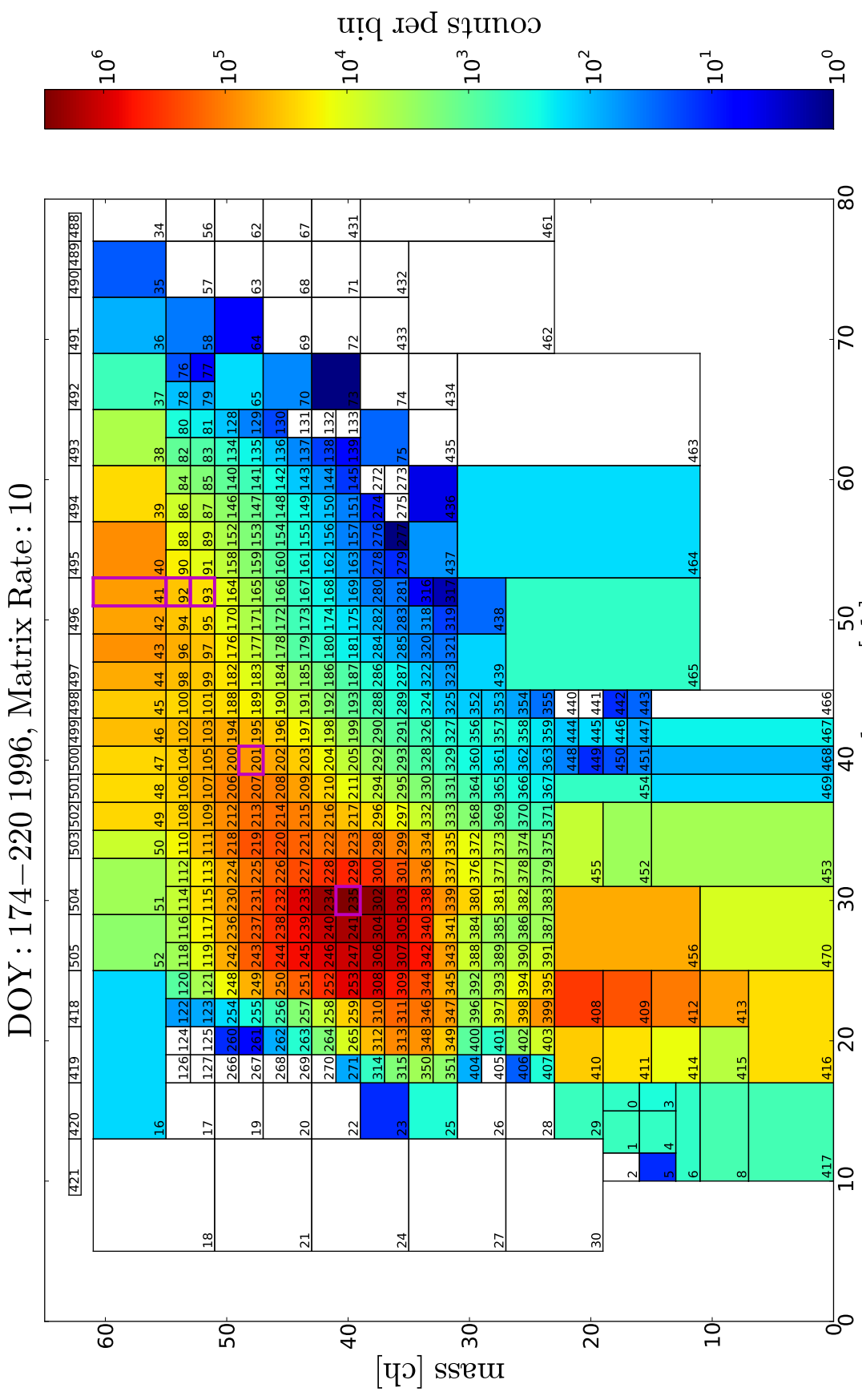

FIGURE 2.4: The accumulated matrix count rates of the CTOF MR data for the whole measurement period DOY 174-220 for matrix rate MR10. Note, that the assigned mass (m) and mass-per-charge (m/q) are still given in the nominal instrumental channels. The boxes 235, 201, and (41,92,93), that are framed magenta, are used for the derivation of the O^{6+}, Si^{7+} and Fe^{9+} velocity distribution functions from the matrix rate data in chapter 3.

matrix rate	0	1	2	3	4	5	6	7	8	9	10
lower step	0	j_c-33	j_c-24	j_c-16	j_c-12	j_c-8	j_c-6	j_c-4	j_c-2	j_c-1	j_c
upper step	j_c-32	j_c-25	j_c-17	j_c-13	j_c-9	j_c-7	j_c-5	j_c-3	j_c-2	j_c-1	j_c

matrix rate	11	12	13	14	15	16	17	18	19	20	
lower step	j_c+1	j_c+2	j_c+3	j_c+5	j_c+7	j_c+9	j_c+13	j_c+17	j_c+25	j_c+33	
upper step	j_c+1	j_c+2	j_c+4	j_c+6	j_c+8	j_c+12	j_c+16	j_c+24	j_c+32	STOP	

TABLE 2.1: Definition of the CTOF matrix rate binning in terms of Epq-steps with respect to the central Epq-step j_c.

In Figure 2.4 the CTOF matrix rate box scheme is depicted, containing in each box the accumulated counts for the full measurement period DOY 174-220, 1996 for matrix rate MR10. The scheme contains on the x-axis the increasing mass-per-charge channel and on the y-axis the increasing mass channel. Thus, every ion species can be identified with a certain (range of) predefined MR-box(es). The dominant O^{6+} peak centered around $m/q \approx 30$ and $m \approx 40$ can be well-recognized, while other ion species peaks are harder to determine by eye. Also note, that the He^{2+} peak ($m/q \approx 20$ and $m \approx 20$), which nominally should be more prominent than O^{6+} is less pronounced in the data, due to the frequent interruption of the ESA-stepping in the high-speed He^{2+} flank and the additional suppression in the onboard processing of He^{2+}. From the CTOF preflight calibration, [Hefti, 1998a] identified O^{6+} with box 235, Si^{7+} with box 201 and Fe^{9+} with the boxes 41, 92, and 93, that are all marked with a magenta frame in Figure 2.4 and which we also use in this work for the derivation of short-term velocity distribution functions from the CTOF matrix rate data. In this context we show the 21 matrix (count) rates for several MR-boxes in selected cycles under different solar wind conditions in the upper left panels of Figures 3.1 - 3.4 in chapter 3.

CTOF Matrix Element Data

The **matrix element (ME)** data is very similar to the matrix rate data, except for the fact that all counts within a certain MR-box are integrated during a given CTOF cycle over all Epq-steps, so that the spectral velocity information is lost. Instead the m and m/q resolution is doubled in both dimensions. Therefore the ME data is suitable for evaluating elemental or charge state abundances of specific ions, but cannot be utilized to deduce kinetic properties of the heavy ions.

CTOF Sensor Rate Data

Finally, the **sensor rate (SR)** data is not intended for concrete scientific utilization, but contains the raw output values of the different subsensors inside the CTOF instrument at each Epq-step during each CTOF cycle. In particular the data includes the E/q-analyzer voltage and operation status (scanning or stopped), the total number of triggered start and stop pulses in the TOF section, the number of SSD surface hits and the overall number of double and triple coincidence events. We used this data to follow in detail the configuration of the electrostatic analyzer and to cross-check the obtained PHA and MR count rates with the overall obtained number of events in the different subsensors during the cycles of the given measurement period.

Base-Rate Correction of the CTOF PHA Data

In Figure 2.3 we show the accumulated *transmitted PHA* long-term data counts for the measurement period DOY 174-220 for Epq-step 55. However, as explained in the previous section, these are just a subsample of the original raw measurement data, the *full PHA* counts. In Figure 2.5 we show the overall number of transmitted counts per CTOF cycle as a histogram. Before one can analyze the PHA data, one has to correct the given count rates in the ET-matrices with the corresponding base-rate factors, that contain the information how strong a given count rate in a certain priority range has been reduced due to the data compression. For most other instruments such as ACE/SWICS these base rates are explicitly given and stored together with the PHA data. However, for the case of CTOF this is not the case, as one can in principle reconstruct the base-rate factors F_{br} from the comparison between MR and PHA data. The base-rate factor reconstruction is described in appendix A and we just show an example of the base-rate reconstruction in Figure 2.6 for the accumulated long-term PHA counts in Epq-step 70. In the upper panel we see the ET-matrix with the transmitted (or uncorrected) PHA counts $C_{tr}(\tau, \epsilon)$ while in the lower panel we see the corrected PHA counts

$$C(\tau, \epsilon) = F_{br}(\tau, \epsilon) \cdot C_{tr}(\tau, \epsilon) \tag{2.13}$$

that can be seen as a reasonable approximation of the actually measured full PHA count rates for a sufficiently large statistical sample. We note for instance that the O^{6+} peak at ($\tau \approx 280\,\text{ch}, \epsilon \approx 40\,\text{ch}$) was strongly under-represented in count rate in the transmitted PHA data by almost 2 orders of magnitude while the Si^{7+} peak at ($\tau \approx 340\,\text{ch}, \epsilon \approx 40\,\text{ch}$) was (only) under-represented in count rate in the transmitted

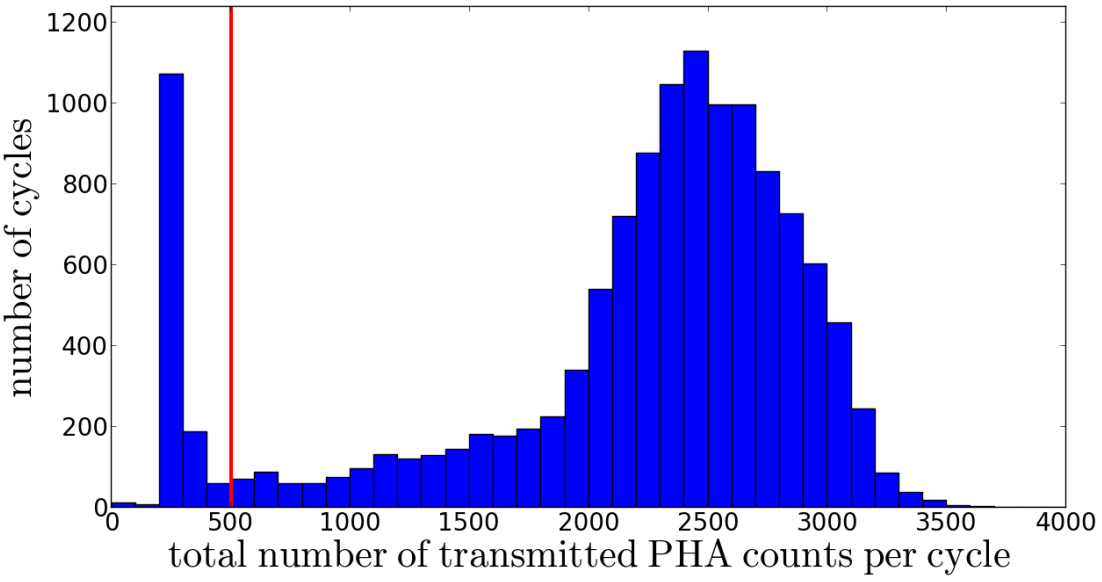

FIGURE 2.5: Histogram of the total number of transmitted PHA words per CTOF 5-minute cycle (for the whole ET-range and over all 117 Epq-steps). In most cases the telemetry limit of PHA words is between 2000 and about 3000, but also cycles with lower limits occur. The very low transmission numbers that form the peak between 200 and 400 PHA words are from cycles with strongly reduced CTOF telemetry budget due to internal budget changes between the CELIAS sensors. We excluded all cycles with less than 500 transmitted PHA counts from the PHA data analysis as it is not possible to reconstruct the base-rate factors reliably for these cycles.

PHA data by less than 1 order of magnitude. We also note that the artificial diagonal steps in count rate in the upper panel at the priority range borders between PR2[10] and PR3 and PR4 and PR5, respectively, have vanished in the lower panel, so that e.g. the O^{6+} peak has a more continuous shape now. Unfortunately, the counts in priority range 5 at the lowest ESSD values, including the He^{2+} peak at ($\tau \approx 240\,\mathrm{ch}, \epsilon \approx 10\,\mathrm{ch}$) cannot be reconstructed properly. This is due to an additional onboard algorithm that sorts out proton and alpha particle events based on their anticipated Epq, TOF and ESSD signal combination. This algorithm, that allows for a total suppression of the alpha particle and proton count rates of 90% and 100%, respectively, is referred to as *fast analog identification system* or PID in [Hovestadt et al., 1995], but is not documented in detail in the currently available instrument descriptions. In fact, the base-rate reconstruction causes an over-representation of the unsuppressed transmitted PHA counts in PR5 that lie at the border to PR4 causing an artificial step in this area of the ET-matrix that can be seen best in the C^{6+} peak at ($\tau \approx 240, \epsilon \approx 40$). In Figures A.5 - A.9 in the appendix we show in addition the base rate corrected PHA long-term count rates for the ET-matrices at Epq-steps 40, 50, 60 and 80 to give a representative overview of the successful reconstruction.

[10] For the definition of the Priority Ranges see Figure A.3 in the appendix.

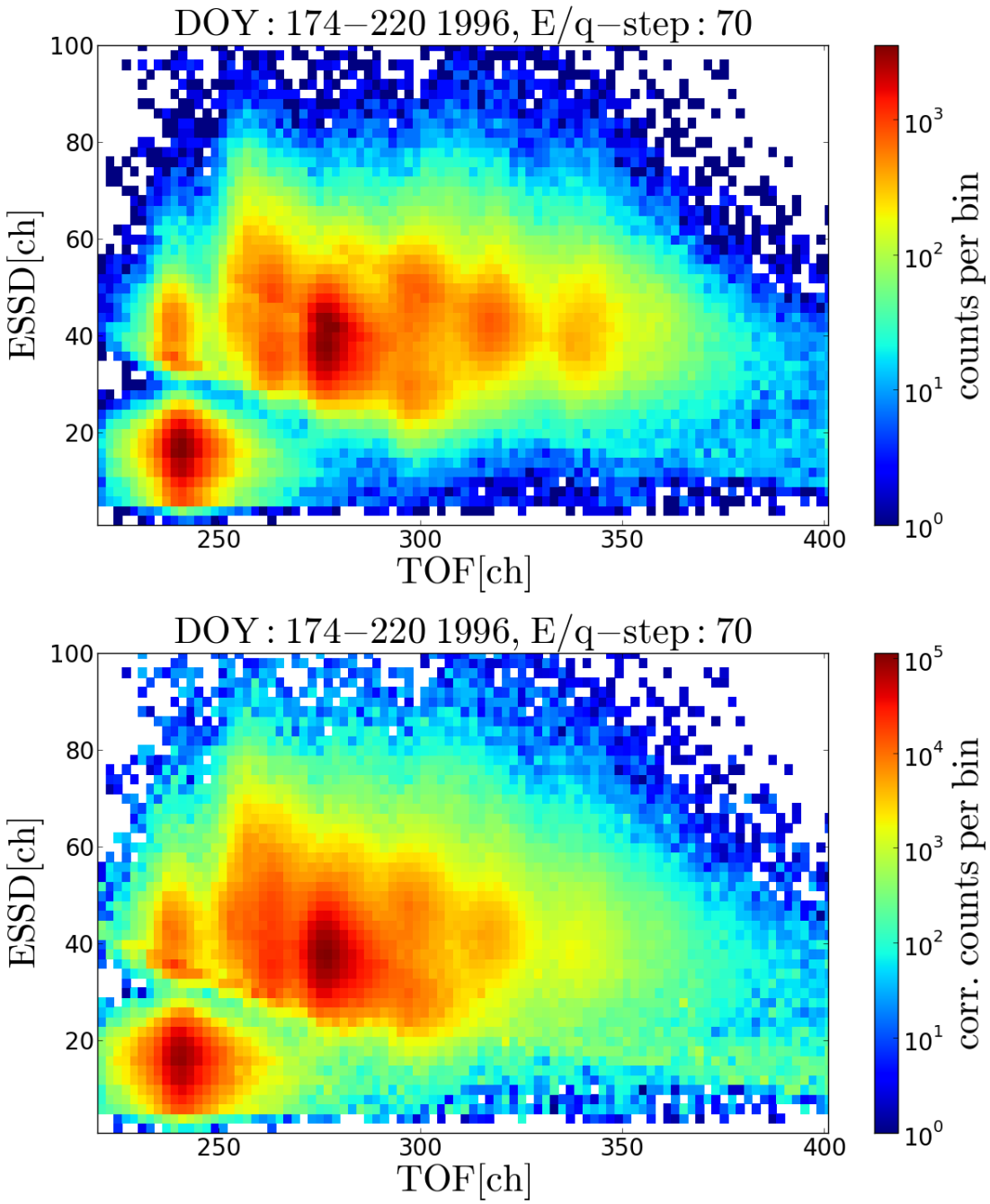

FIGURE 2.6: Comparison of the uncorrected (upper panel) and corrected (lower panel) count rates for the accumulated long-term PHA data (DOY 174-220) for Epq-step 70.

2.3 The CELIAS/Proton Monitor

The CELIAS Proton Monitor (PM) is integrated in the MTOF housing and measures routinely with a resolution of 30 seconds the solar wind proton mean speed $\langle v_p \rangle$[11], thermal speed $v_{th,p}$ and number density n_p as well as the solar wind flow direction in the plane perpendicular to the ecliptic plane [Ipavich et al., 1998]. Since the PM was originally designed to assist in the interpretation of MTOF data, it uses an electrostatic analyzer with a relatively wide energy bandwidth and angular acceptance which limits the accuracy of the derived solar wind proton bulk parameters. Yet, because the original SOHO Plasma Instrument was not incorporated in the final spacecraft payload configuration [Domingo et al., 1995], the CELIAS PM is the only SOHO sensor which measures the in-situ (proton) plasma parameters. Besides the electrostatic (E/q)-analyzer the PM contains a microchannel plate (MCP) with a two-dimensional cylindrically symmetric position sensing anode. The PM E/q-analyzer is stepped through six Epq-steps corresponding to a logarithmically (60% step size) increased deflection plate voltage between 0.3 and 3 kV within a total cycle time of 30 seconds. The proton speed information is derived from the radial position distribution of the incident protons on the sensing anode at each of the six Epq-steps while the zenith inflow direction is derived from the angular position. A schematic of the PM is shown in Figure 2.7.
For the utilized PM data in this study the proton mean speed and thermal speed is derived from a discrete moment calculation of the obtained 1D-reduced proton VDF, similar to the one that we apply in chapters 3, 5, and 6 for the derivation of the heavy ion mean and thermal speeds, while the number density is derived from a series of model fits applied to the measured proton distributions [Ipavich et al., 1998]. For the derived proton mean speeds [Ipavich et al., 1998] estimated the PM measurement accuracy by comparison with the speeds measured by the SWE instrument onboard the WIND spacecraft (see Figure 2.8). For the time period DOY 20 in 1996 to DOY 31 in 1997, the authors mapped the SOHO speed back to the WIND location which was on average 104 Earth radii closer to Earth in the X_{GSE} coordinate, corresponding to an average time delay of 26 minutes. For two hour averaged data periods they found a very good agreement of PM and SWE measurements with very low systematic deviations and statistical deviations of ($\sigma_{v_{p,rel}} \approx 2\%$). Due to the different measurement location of the two spacecraft one can assume that part of this deviation is real and therefore consider this value as upper limit of the measurement uncertainty.
Despite the former work, in a sanity check of the proton data for the time interval DOY

[11] For our analysis we used five-minute averaged PM moment data. As we cannot analyze the proton VDF in detail we always refer to the proton mean speed when mentioning the *proton speed* measured by the PM, and also abbreviate $v_p := \langle v_p \rangle$ in cases where no confusion is possible.

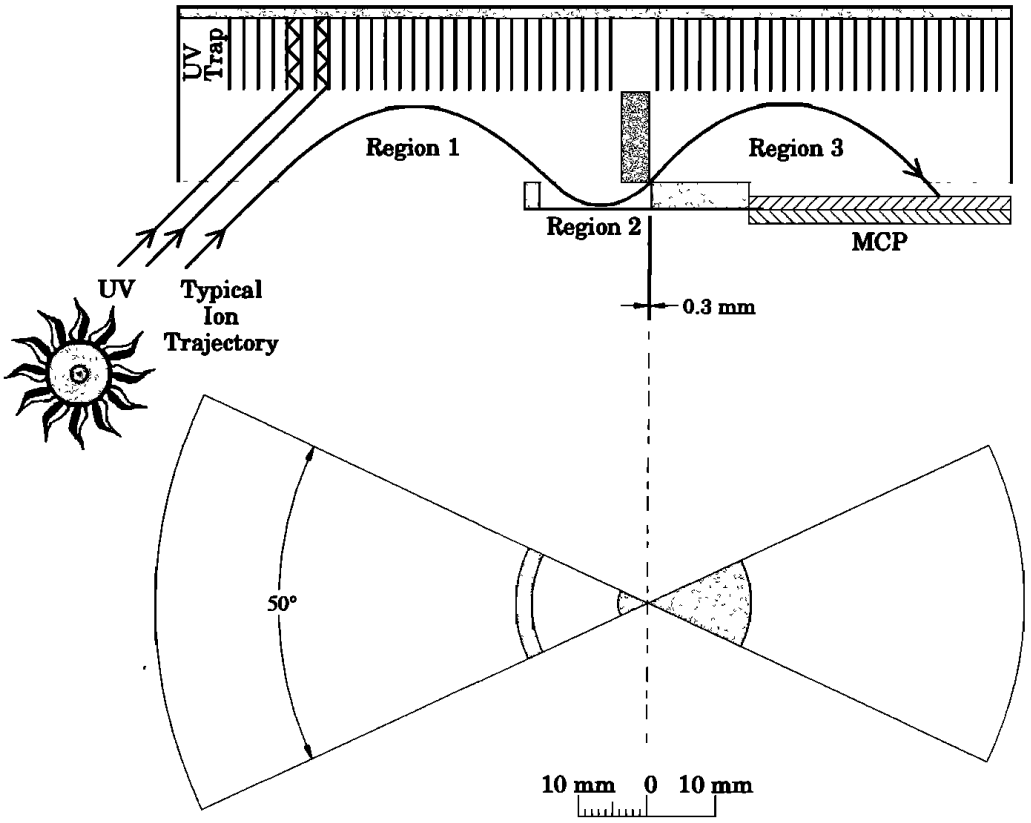

FIGURE 2.7: Schematic side view (upper panel) and front view (lower panel) of the SOHO CELIAS Proton Monitor (PM). The PM E/q analyzer consists of three 50° wedge-shaped parallel plate deflection regions, which are arranged such as to provide a high suppression of UV-photons given the relatively high PM geometry factor. The three regions are cylindrically symmetrical about a 0.3 mm diameter hole in the beryllium-copper sheet between region 2 and region 3. If a particle has the appropriate Epq-value at a given analyzer Epq-step it follows the typical ion trajectory as a result of the applied electric fields in regions 1 to 3 and finally triggers a signal in the MCP. The secondary electrons that are then released from the MCP create a localized signal in the cylindrically symmetrical anode that is situated 1 cm behind the MCP output. From the radial and angular position (R, θ) of the electron signal on the anode the speed and zenith incident angle information (in the plane perpendicular to the ecliptic) of the detected primary particle can be obtained simultaneously. The figure is taken from [Ipavich et al., 1998].

174-220 we observe a very sharp accumulation of thermal proton speeds at values of 20 and 21 km/s which coincides with an accumulation of certain proton speed values in the vicinity of 320 km/s (not shown here). Since we consider these increased occurrences for certain combinations of mean and thermal speed at the edge of the PM parameter range as potentially unphysical we systematically exclude all time stamps where we measure a thermal speed below 22 km/s, which automatically also excludes all time stamps with very low proton speeds $v_p \lesssim 325$ km/s (see Figure 6.3). Besides these minor irregularities the PM is operated successfully to the current date and the

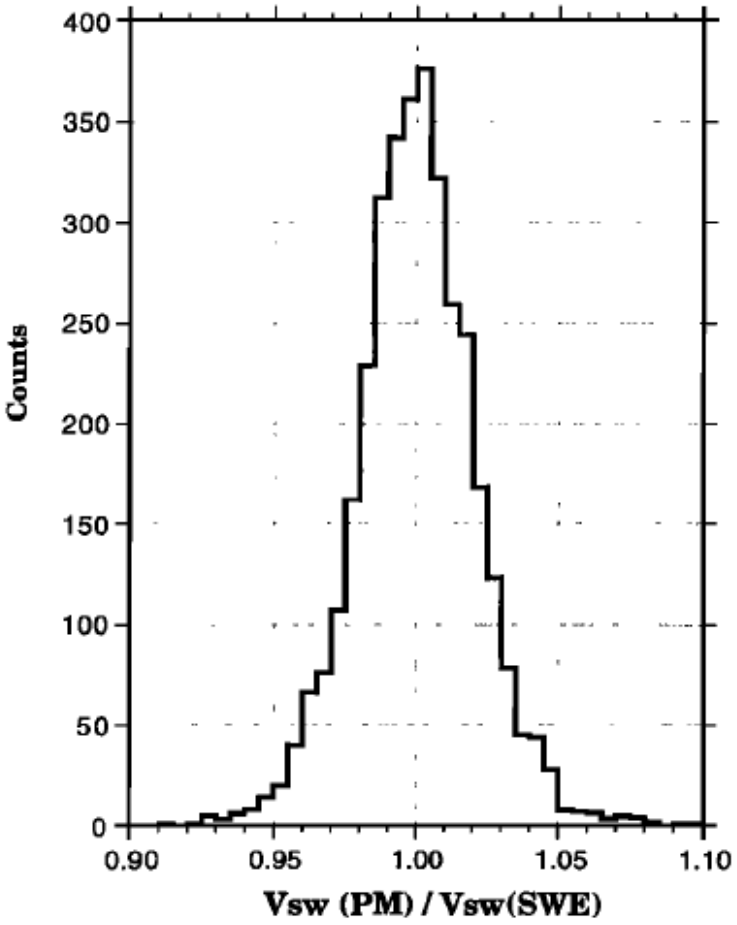

FIGURE 2.8: Observed case distribution of the ratios of proton mean speeds measured by the CELIAS Proton monitor (PM) on the SOHO spacecraft and the SWE instrument onboard the Wind spacecraft. The histogram contains 3479 cases (=speed ratios) calculated from 2-hour data averages for the time period DOY 20 in 1996 to DOY 31 in 1997 which fully includes the measurement period in this work. The figure is taken from [Ipavich et al., 1998].

instrument data can be downloaded from the University of Maryland website [12].

2.4 Measurement Geometry

In Figure 2.9 we show a schematic of the measurement geometry of solar wind heavy ions (brown vector $\underline{v}_i$) and protons (yellow vector $\underline{v}_p$) in two-dimensional velocity space ($v_\parallel, v_\perp$ with respect to the proton velocity) in the ecliptic plane at L1. The figure is taken from [Berger et al., 2011] and illustrates the measurements of solar wind ions at L1 with ACE/SWICS but is equivalently valid for the SOHO measurements in this study. Both the CELIAS Proton Monitor and CTOF measure the absolute value of the

[12] SOHO/CELIAS/MTOF/PM data and documentation can be found at *http://umtof.umd.edu/pm/*
.

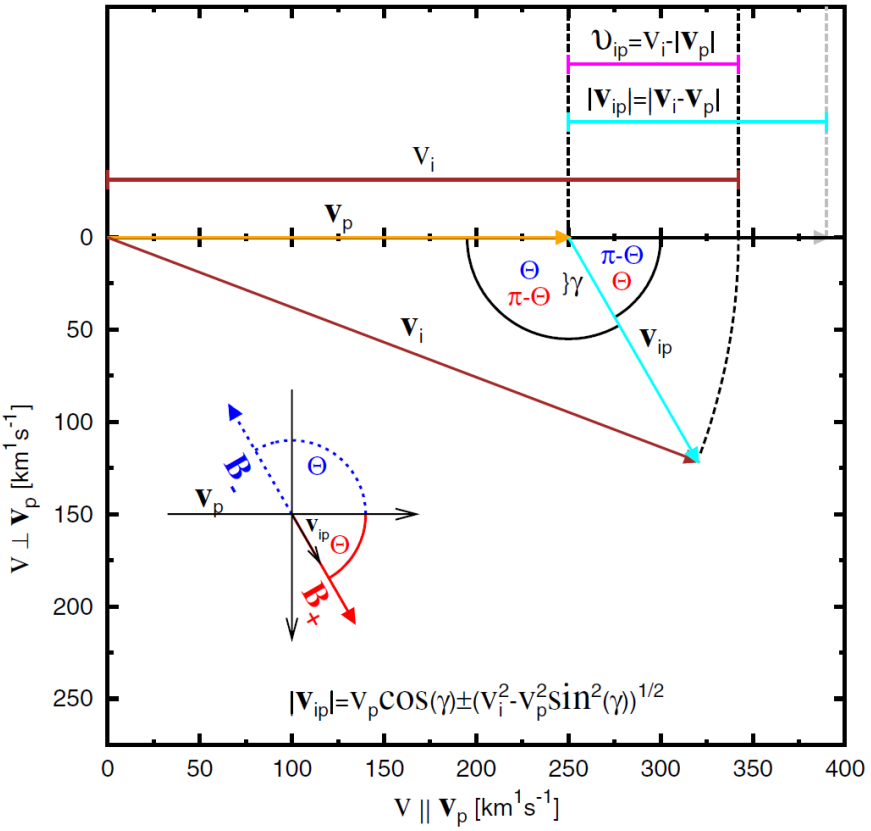

FIGURE 2.9: Measurement geometry for solar wind heavy ions (brown vector $\underline{v}_i$) and protons (yellow vector $\underline{v}_p$) in two-dimensional velocity space ($v_{\parallel}, v_{\perp}$ with respect to the proton velocity) in the ecliptic plane. The figure is taken from [Berger et al., 2011] and illustrates the measurements of solar wind ions at L1 with ACE/SWICS but is also valid for our SOHO measurements. Note, that the same geometrical relations between the shown ion velocities apply when we assume that the heavy ions flow approximately radially outwards from the Sun and instead the proton velocity shows a small deviation from the radial direction. This is often observed for the case of alfvénic waves that are carried by the protons while the heavy ions surf these waves (see e.g. [Marsch, 2006]).

ion speed and not the full velocity vector. Therefore, the magnitude of the differential velocity $\underline{v}_{ip}$ (also called differential speed $|\underline{v}_{ip}| = \Delta v_{ip} =: v_{ip}$) which is oriented along the in-situ magnetic field, is systematically underestimated as $v_{ip} = |\underline{v}_i| - |\underline{v}_p|$ (pink length bar) instead of $v_{ip} = |\underline{v}_i - \underline{v}_p|$ (cyan length bar). If the in-situ B-field angle θ is measured simultaneously with the particles the true differential speed v_{ip} can be reconstructed from the combination of both measurements with the equation in the bottom of Figure 2.9. Unfortunately, in the case of SOHO there are no in-situ magnetic field measurements conducted on the spacecraft, so that we cannot apply the given correction but have to have in mind that the absolute magnitudes of the differential speeds Δv_{ip} measured with CELIAS in this study are always lower limits of the actual differential speeds. As a rough estimation of the systematic bias that this geometrical effect

causes, one calculates that for an average Parker angle of $\theta = 45°$, the true differential speed Δv_{ip} is about a factor of $f_{geo} \approx 1/\cos(\theta) \approx 1.4$ times larger than the measured differential speed Δv_{ip}. For a first comparison of the SOHO/CELIAS and ACE/SWICS differential speed measurements we discuss these 'mean corrected' differential speeds $\Delta \widetilde{v}_{ip}$ in chapter 7.

We further note when measuring an extended 3D-VDF with time-of-flight mass spectrometers such as CTOF or SWICS, that the resulting 1D-VDFs are not exact 1D-cuts through the 3D VDFs, but rather integrate the count rate from all particles with the same speed. This is because particle velocities with a perpendicular component $v_\perp \neq 0$ are always bent onto the radial measurement axis and these integrated VDFs are called *1D-reduced VDFs*. Strictly speaking, these 1D-reduced VDFs of a Maxwellian distribution are not completely symmetrical anymore but have a more pronounced high-speed flank as they are basically Maxwellian distributions of the velocity magnitude $|\underline{v}|$ as discussed in section 1.2. However, due to the fact that the perpendicular thermal speeds are small compared to the mean speed of the distribution along the measurement axis, this effect is small and the thermal core of the distribution can be well-approximated with a Gaussian, that represents a 1D-Maxwellian, as shown in the long-term spectra in chapter 5. Finally, we note that any small occurring asymmetry is the same for all ion species, including the protons, when these have the same thermal speeds as it is approximately the case in the fast wind[13], so that no artificial differential speeds can be introduced into the measurement by this geometrical integration effect.

[13] In fact, the protons have slightly higher thermal speeds in the fast wind and much higher thermal speeds in the slow wind as shown in section 6.4. Therefore, any differential speed might be even slightly underestimated in the fast wind, while in the slow wind the observed faster streaming of the protons is in the right order to be explained by this integration effect. Unfortunately, we only have the proton VDF moments available in this study, so that this effect of a few km/s cannot be corrected here.

Chapter 3

A Critical Revision of Heavy Ion Differential Speeds Derived from CTOF Matrix Rate Data

In this section we utilize the CTOF matrix rate data to investigate the heavy ion short-term VDFs as it was originally intended by the CTOF data product design. In principle, we check whether we can reproduce the results of the earlier CELIAS study by [Hefti, 1998a]. As explained in section 2.2 we only can reconstruct the heavy ion speeds with the documented MR classification algorithm for the subperiod DOY 174-220 compared to the full analysis period in [Hefti, 1998a] between DOY 93 and 229 in 1996. However, statistically this subsample is large enough that a systematic differential streaming of a given ion species should be visible also in this data set, if it is a permanent feature in the covered solar wind (speed) regimes. We concentrate on the three relatively abundant heavy ion species analyzed in the earlier study by [Hefti, 1998a]: O^{6+}, Si^{7+}, Fe^{9+} as for these species we have reference MR-boxes from the CTOF preflight calibration [Hefti, 1998b].

3.1 Derivation of Heavy Ion Short-Term Velocity Distribution Functions from CTOF Matrix Rate Data

To illustrate the matrix rate data processing we use in the following the short-term count rates measured in CTOF cycle 170 on DOY 178, 1996, which is just an example case for a cycle measured in the slow wind. We take now all counts measured during this cycle in MR-box 235 for all 21 matrix rates MR0 - MR20 and convert them to a

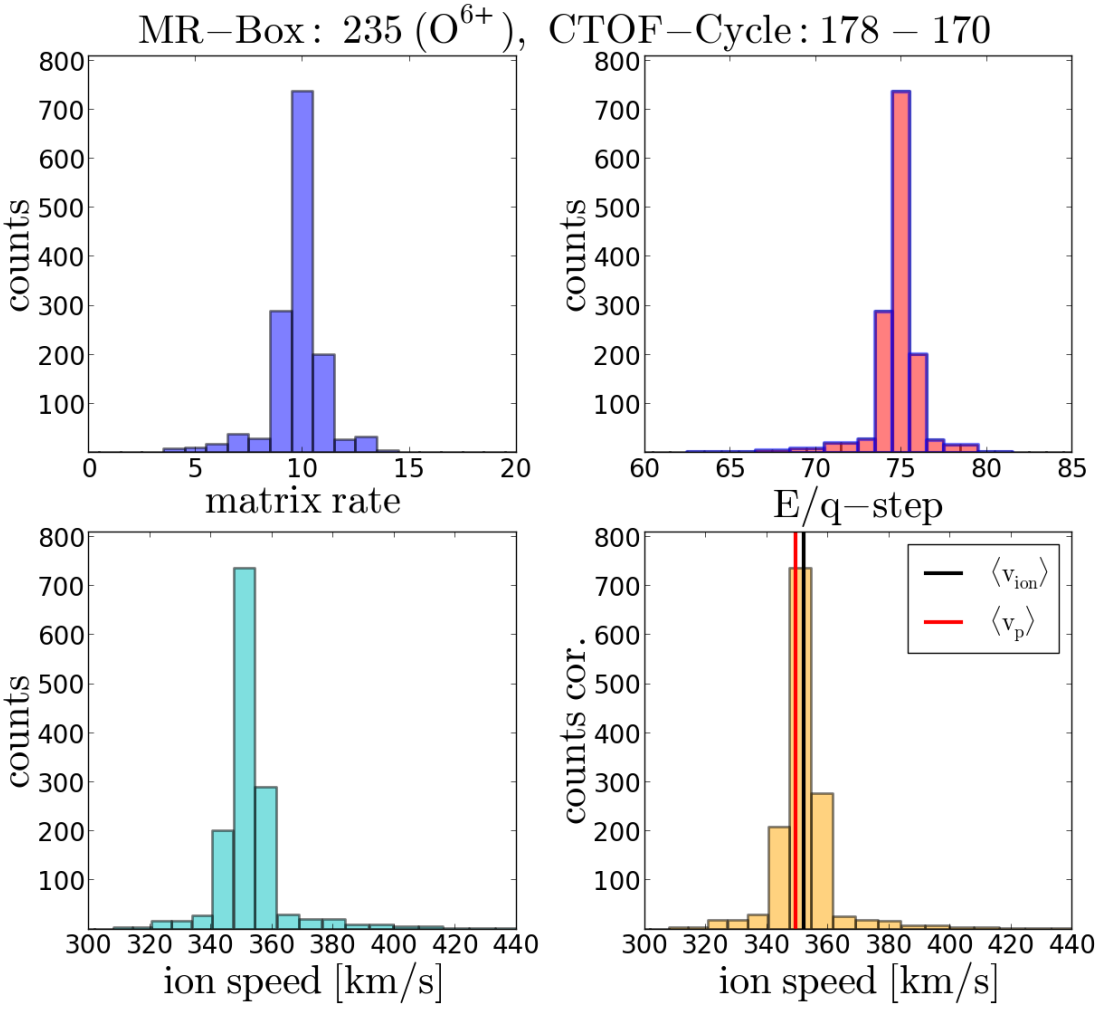

FIGURE 3.1: In the upper left panel we show the CTOF matrix rate spectrum for MR-box 235 at cycle 170 on DOY 178, 1996, as an example of the obtained matrix count rates that are measured in the slow solar wind. The selected MR-box is the same that was selected by [Hefti, 1998a] for the determination of the mean O^{6+} speed. As explained in the text one can convert this matrix rate spectrum to an Epq-step spectrum which is shown in the upper right panel. In the lower left panel we convert the Epq-spectrum into a speed spectrum. Finally, the measured spectrum is corrected for the systematic over-representation of fast particles. In terms of the kinetic plasma description this spectrum in the lower right panel can now be interpreted as a 1D-reduced velocity distribution function (VDF). In the depicted cycle the VDF yields a proton speed of $\langle v_p \rangle = 349\,\mathrm{km/s}$ (marked as red vertical bar in the lower right panel) and the calculated ion speed is $\langle v_{O^{6+}} \rangle = 352\,\mathrm{km/s}$ (marked as black vertical bar).

short-term 1D-reduced VDF for O^{6+}:

We first calculate after Eq. 2.12 the central Epq-step that corresponds to matrix rate MR10. For the given measurement cycle 170 on DOY 178, 1996 with estimated heavy ion speed $\widetilde{v}_{swi} = 345\,\mathrm{km/s}$ we find $c_j = 75$. Once we have the central Epq-step, we reconstruct the Epq-spectrum by inverting the scheme in Table 2.1 which can only be done in a unique way for the 5 Epq-steps that correspond to the 5 central matrix rates.

For the remaining Epq-steps we assume in a first approximation equal count rates for all Epq-steps that contribute to the same matrix rate. The complete translation from the matrix count (rate) spectra to Epq-step spectra for the discussed example is shown for O^{6+} in the upper two panels of Figure 3.1. We see that the matrix rate spectrum is centered properly around MR10 in the upper left panel. The Epq-spectrum can then be translated into a 1D speed spectrum using Eq. 2.1 which is shown in the lower left panel of Figure 3.1. As this spectrum still corresponds to the raw count rates measured with CTOF, it has to be corrected for the different phase space coverage at different speed bins. This is done simply by multiplying the obtained count rates $N_j(v)$ at every speed v_j with a relative factor $\propto 1/v_j^2$ that is derived in section 2.2, so that we end up with the phase-space corrected count rates

$$n(v_j) = \frac{v_0^2}{v_j^2} \cdot N(v_j) \,, \tag{3.1}$$

where v_0 is a normalization constant with the dimension of a speed that can be chosen arbitrarily[1] but fixed for the whole speed range v_j. The phase-space corrected count rates $n(v_j)$ represent the 1D-reduced velocity distribution function that is shown in the lower right panel of Figure 3.1 with the normalization speed $v_0 = v(N_{max})$, so that the maximum count rate of the distribution does not change due to the phase-space correction. From these VDFs we calculate the ion mean speed as the first moment of the distributions as

$$\langle v_{ion} \rangle = \frac{1}{C_n} \cdot \sum_{j=0}^{116} n_j \cdot v_j \,, \tag{3.2}$$

where $C_n = \sum_{j=0}^{116} n_j$ is the appropriate normalization[2]. The calculated mean ion speed $v_{ion} = 352\,\mathrm{km/s}$ for the analyzed cycle is shown in the lower right panel as the black vertical line that can be then compared to the mean proton speed $v_{ion} = 349\,\mathrm{km/s}$ that is measured simultaneously with the CELIAS/PM. This mean proton speed is calculated as the first moment of the proton 1D-reduced VDF as explained in section 2.3 and shown as the red vertical line. In an analogous way the ion thermal speed is calculated as the second moment of the VDF:

$$v_{ion,th} = \sqrt{\frac{1}{C_n - 1} \cdot \sum_{j=0}^{116} \left(\langle v_{ion} \rangle - n_j \cdot v_j \right)^2} \tag{3.3}$$

with the same normalization C_n as in Eq. 3.2.

[1] This is only true as long as one does not want to derive absolute particle densities from the VDFs.

[2] Note that the index can be always assumed to obtain values from 0 to 116 as the count rates of Epq-steps that are not reached by the ESA stepping in the given cycle are set automatically to 0.

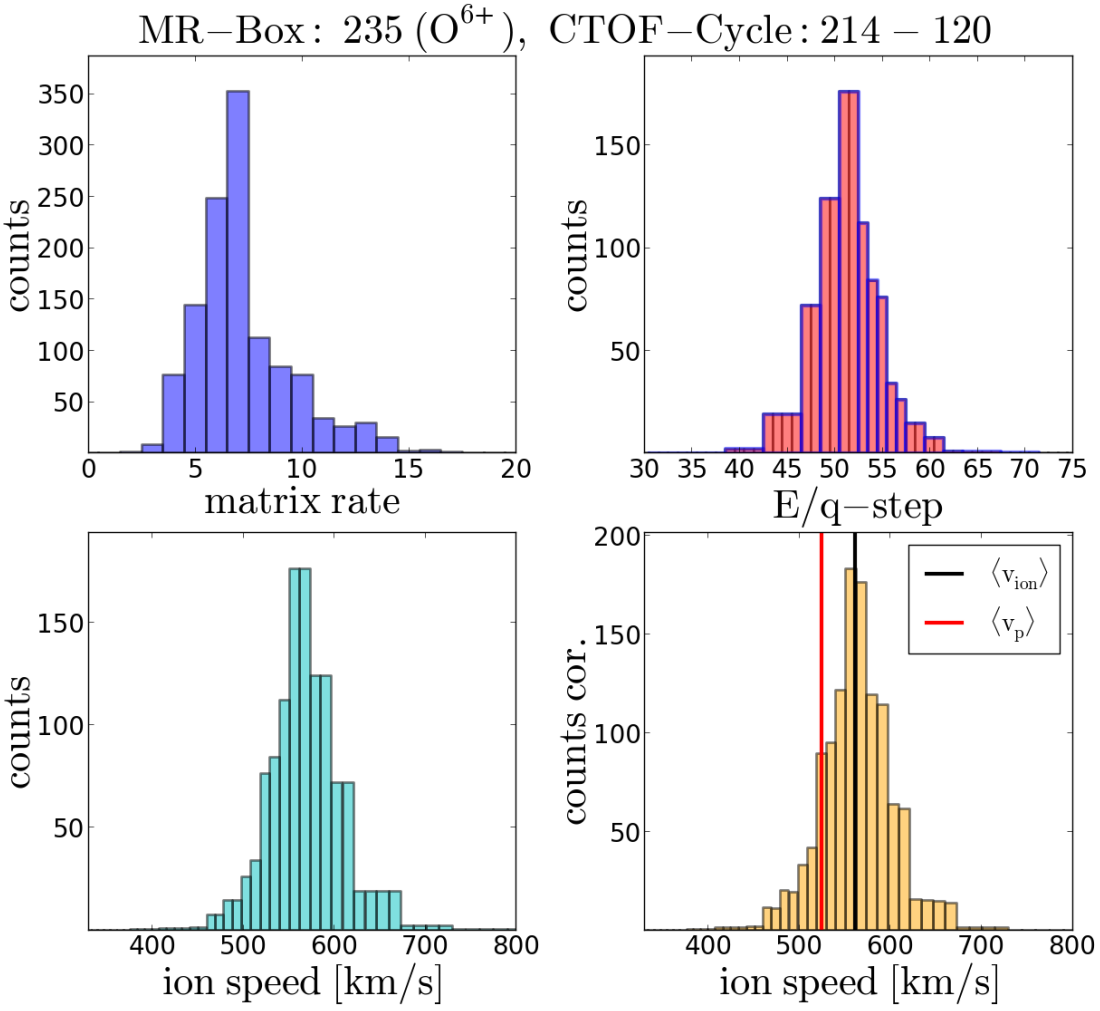

FIGURE 3.2: Translation from the matrix count rate spectrum (upper left panel) to the 1D-reduced VDF (lower right panel) for MR-box 235 in the same way as in Figure 3.1 but for cycle 120 on DOY 214, 1996, which is measured in the fast solar wind. We find for the given cycle a mean ion speed of $\langle v_{O^{6+}} \rangle = 561\,\mathrm{km/s}$ while the simultaneously measured mean proton speed is $\langle v_p \rangle = 525\,\mathrm{km/s}$.

In Figure 3.2 we derive the 1D-reduced O^{6+} VDF in the same way as in Figure 3.2, but for cycle 120 on DOY 214, 1996, which is an example of a VDF measured under fast wind conditions. We can see that the matrix rate spectrum is considerably wider than for the slow wind case, which agrees well with the expectation of higher kinetic temperatures in the fast solar wind as described in chapter 1. However, we also recognize in the upper left panel that the central matrix rate MR10 is not even close to be the matrix rate with the highest count rate. This mismatch indicates that the onboard estimation of the solar wind heavy ion speed does not work correctly in the fast wind. As a result, the calculated central Epq-step does not match well with the center of the VDF, but it is shifted to the low-speed flank as can be seen in the upper right panel. Although we can still obtain meaningful VDFs due to the moderate resolution loss in the VDF flanks, the

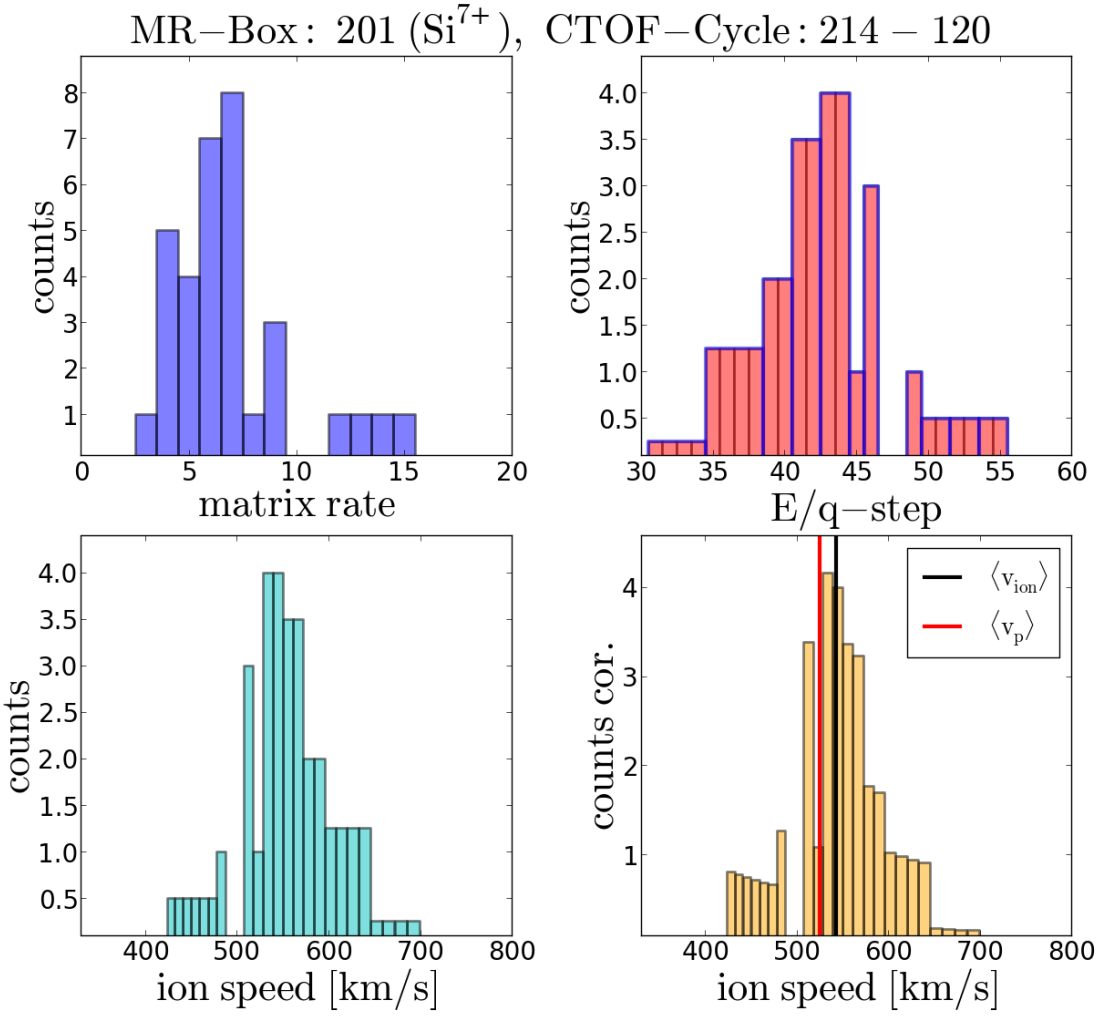

FIGURE 3.3: Translation from the matrix count rate spectrum (upper left panel) to the 1D-reduced VDF (lower right panel) for the same fast wind cycle 120 on DOY 214, 1996, as in Figure 3.2 but for MR-box 201. The selected MR-box is the same that was selected by [Hefti, 1998a] for the determination of the mean Si^{7+} speed. The calculated mean speed for Si^{7+} in the given cycle is $\langle v_{Si^{7+}} \rangle = 543\,km/s$ which has to be compared to the same proton speed $\langle v_p \rangle = 525\,km/s$ as in Figure 3.2.

miscalculation leads to differences in the count rate resolution between the low- and high-speed flanks of the VDFs. This effect already introduces a small systematic bias in the calculation of the ion mean speed, depending on the concrete form of the conversion from matrix count rates to Epq-spectrum count rates that is chosen.

As can be seen from the lower right panel in Figure 3.2 we find for the given cycle a mean ion speed of $\langle v_{O^{6+}} \rangle = 561\,km/s$ while the simultaneously measured mean proton speed is $\langle v_p \rangle = 525\,km/s$. Thus, for this fast wind cycle we measure a differential speed of $\Delta v_{ip} = 36\,km/s$, while in the slow case the differential speed was $\Delta v_{ip} = 3\,km/s$ which is on the order of the systematic measurement uncertainties as described in chapter 5.

In Figure 3.3 we show the VDF derivation for the same fast wind cycle DOY 214, 120 for Si^{7+} that is associated with MR box number 201 after the preflight calibration (see Figure 2.4). In comparison with Figure 3.2 we see that the count rates for Si^{7+} are about a factor of 40 lower than for O^{6+} which is roughly in agreement with the expected relative abundances (compare section 5.5). Similar to the O^{6+} case we also observe that the central matrix rate MR10 does not match the matrix rates with the highest count rates and the measured core of the matrix rate spectrum is shifted to lower matrix rates to an extent that at the nominal central matrix rate MR10 no counts are measured at all. Thus, the calculated energy-per-charge center step 47 lies in a gap between the core of the VDF and a subpopulation at higher Epq-steps as can be seen in the upper right panel. The calculated mean speed for Si^{7+} in the given cycle is $\langle v_{Si^{7+}} \rangle = 543\,km/s$ which has to be compared to the same proton speed $\langle v_p \rangle = 525\,km/s$ as in Figure 3.2.

In Figure 3.4 we show the VDF derivation for the same fast wind cycle DOY 214, 120 for the counts in matrix box 92. This MR-box is one of the three boxes that were selected by [Hefti, 1998a] for the determination of the mean Fe^{9+} speed. In comparison with Figure 3.3 we find comparable count rates for Fe^{9+} and Si^{7+} as one would expect from the similar elemental abundances of silicon and iron [Aschwanden, 2005]. Also for this MR-box we find that the measured VDF is shifted to lower matrix rates compared to the nominal central matrix rate MR10, so that no count rates are measured at MR10. We further observe a similar subpopulation of counts at lower Epq-steps as in the Si^{7+} case. However, for Fe^{9+} this apparent subpopulation is separated much more clearly from the core of the distribution, which means that these particles are measured at much lower speeds than the majority of Fe^{9+} counts. This raises the question whether these counts could be actually Fe^{9+} counts as they are statistically in contrast with approximately Maxwellian speed distributions. We also note that due to the relatively large speed difference of these low-speed counts to the VDF core, these counts are subject to a substantial phase space correction up to a factor of 3 as can be seen in the lower right panel of Figure 3.4.
As an overall result one obtains a very low ion mean speed of $\langle v_{Fe^{9+}} \rangle = 468\,km/s$ if one just calculates the mean speed routinely as the first moment of the whole count sample, which is obviously not a good statistical measure for the observed distribution. On the other hand, as such apparent low-speed subpopulations are seen in most measured Fe^{9+} (and many Si^{7+}) VDFs one cannot offhand exclude these particles without clearly identifying a physical effect that explains their occurrence in the respective ion MR-boxes.

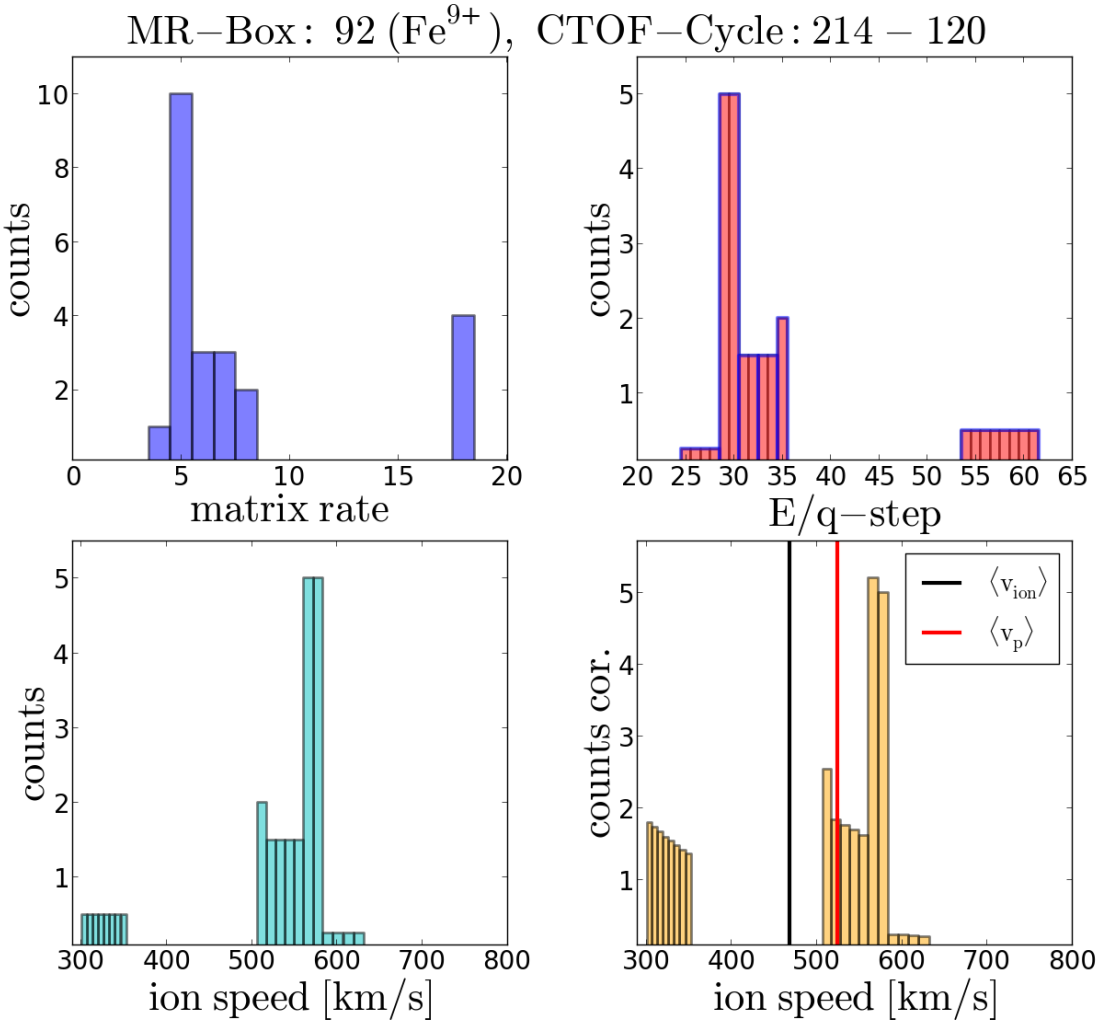

FIGURE 3.4: Translation from the matrix count rate spectrum (upper left panel) to the 1D-reduced VDF (lower right panel) for the same fast wind cycle 120 on DOY 214 1996 as in Figure 3.2 and 3.3 but for MR-box 92, which was identified by [Hefti, 1998a] to belong to Fe^{9+}. A clear subpopulation of particles is observed at very low speeds, so that the mean speed calculation is corrupted.

3.2 Statistical Analysis of Heavy Ion Differential Speeds

In the following we conduct a statistical study with the differential speeds calculated as described above from 5-minute cycle short-term VDFs that are derived from the CTOF matrix rate data over the period DOY 174-220 in 1996. In Figure 3.5 we show 2-dimensional histograms of the more than 12000 short-term ion-proton differential speeds

$$\Delta v_{ip} = \langle v_{ion} \rangle - \langle v_p \rangle \tag{3.4}$$

of O^{6+} (upper panels), Si^{7+} (middle panels), and Fe^{9+} (lower panels) versus the simultaneously measured proton mean speed v_p for the full time period DOY 174-220 in 1996. The left three panels show the absolute measured number of occurrences for a combination $(v_p, \Delta v_{ip})$ within a given (proton speed, differential speed)-bin, while in the right panels the number of occurrence is normalized to the maximum at each proton speed bin. At first glance the obtained statistical differential speed pattern depends on the proton speed and is quite different for the three ion species. The calculated mean differential speeds at each proton speed bin are given by the black dots that are connected by the solid black line to guide the eye. In the very slow wind below mean proton speeds of 380 km/s we find that O^{6+} streams at the same speed as the protons, while the differential speed gradually increases between 380 and 480 km/s before a plateau of the highest differential speeds is reached with mean differential speed values of around 35 km/s at proton mean speeds between 480 and 540 km/s. At the highest two proton speed bins the differential speed drops to values of about 25 km/s. Considering the underlying occurrence statistics, we see that the center of mass of the distribution lies between 320 and 400 km/s, so that we measure most of the time in the slow wind and only occasionally in the fast wind above $v_p \approx 500$ km/s. As discussed in section 1.1, this is the natural outcome of the SOHO measurement site in the ecliptic around solar minimum in 1996, where no speeds comparable to the polar wind speeds of about 800 km/s can be detected. However, the total measurement statistics of more than 12000 cycles are sufficiently high to ensure the significance of the observed trend also in the fast wind where we have several hundred VDFs measured. This is also confirmed by the (1σ-) standard errors of the calculated mean differential speeds that are given by the black error bars for each calculated mean differential speed $\langle \Delta v_{ip} \rangle$. For every proton speed bin this standard error is calculated as

$$\Delta(\langle \Delta v_{ip} \rangle) = \sqrt{\frac{1}{(N-1)N} \cdot \sum_{k=1}^{K} \left(\langle \Delta v_{ip} \rangle - n_k \cdot \Delta v_{ip,k} \right)^2} \tag{3.5}$$

where K is the number of $(v_p, \Delta v_{ip})$-bins in each proton speed bin that contain at least $n_k \geq 10$ occurrences and $N = \sum_{k=1}^{K} n_k$. The condition $n_k \geq 10$ is applied in order to exclude outliers of differential speed measurements that can be caused by an ion mean speed calculation from a VDF that contains an extremely low number of counts which is sometimes the case.

For Si^{7+} we find that in the slow wind below 400 km/s we observe small negative mean differential speeds around -10 km/s. Also at intermediate proton speeds between 400 km/s and 480 km/s the mean differential speed obtains mainly small negative values between 0 and -10 km/s. In the fast wind above 480 km/s we find a plateau

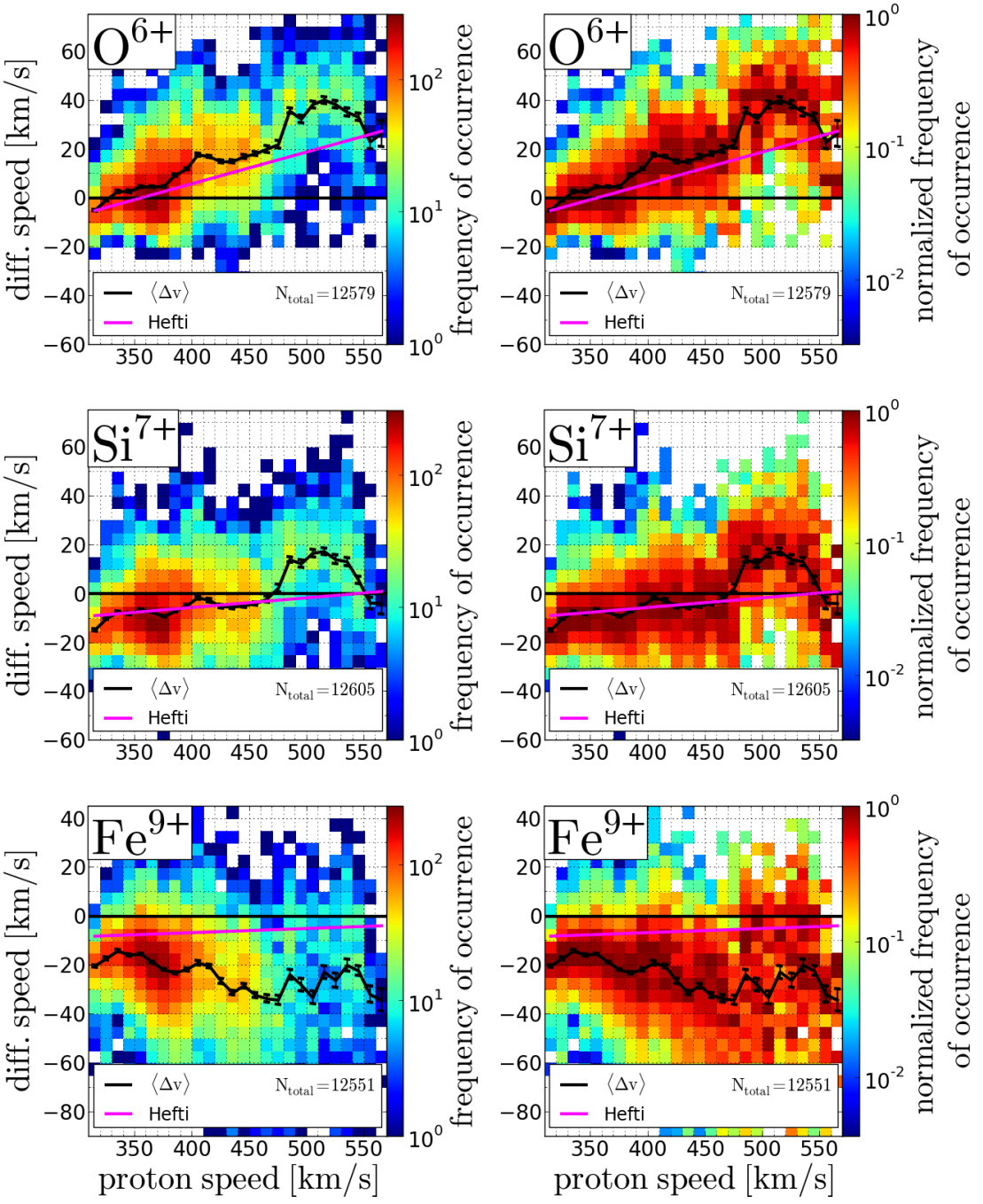

FIGURE 3.5: Two-dimensional histograms of the observed differential speeds between O^{6+}, Si^{7+}, Fe^{9+} and the solar wind protons, respectively, derived from the CTOF matrix rate data for the measurement period DOY 174-220 in 1996. The left three panels show the absolute measured frequency of occurrences within the given time period for a combination $(v_p, \Delta v_{ip})$ within a given (proton speed, differential speed)-bin. The black line represents the mean differential speed $\langle \Delta v_{ip} \rangle$ at a given proton speed bin, the error bars mark the 1σ standard error of $\langle \Delta v_{ip} \rangle$. The magenta lines show the linear best fit obtained by [Hefti, 1998a], for the time period DOY 93-229 in 1996. The three right panels show the frequency of occurrence for a combination $(v_p, \Delta v_{ip})$ normalized to the maximum within each proton speed, so that the mean and spread of the differential speed distribution is better visible for all solar wind proton speeds.

similar to the one observed for O^{6+} but at lower mean differential speeds of about 15 km/s before also a similar decrease to mean differential speeds values of around 0 km/s is observed at the highest proton speeds above 540 km/s.
As shown in Figure 3.5, for Fe^{9+} we only find negative differential speeds between -10 and -35 km/s, when we routinely calculate the mean speed as the first moment of all measured counts, regardless of the large spread in speed between the different sub-populations. While this is obviously problematic in itself it also leads to high negative differential speeds compared to the protons and the other heavy ion species. Thus, a deeper investigation has to be conducted to find out the physical origin of the two populations in particular for Fe^{9+} in order to ensure that we obtain physically meaningful and accurate differential speed measurements.
Still, in order to compare our findings with the results by [Hefti, 1998a] we plotted their obtained linear relations for the mean differential speed of O^{6+}, Si^{7+} and Fe^{9+} with respect to the mean proton speed as magenta line into the panels of Figure 3.5[3]. Although the time period of the earlier study is about a factor of 3 larger, we can see that for O^{6+} we find a good agreement between the observed trends in particular for the slow and intermediate speed range, where both studies find a similar gradient for the increase of differential speed with increasing proton speed and only a small absolute speed difference of about 5 km/s, which could easily be explained by the additional data in the earlier study but also by the different calculation method for the mean speed, as [Hefti, 1998a] applied a fit to the short-term VDFs to derive the ion mean speed. However, at high proton speeds above 480 km/s our differential speeds for O^{6+} deviate by a somewhat larger amount of 10-15 km/s compared to the earlier results for O^{6+}. Interestingly this difference is similar in magnitude to the difference that we observe in the fast wind for Si^{7+} between the two studies, while in the slow and intermediate wind the results of Si^{7+} between the two studies also agree well. To summarize, the differential speed analysis with the MR data shows a reasonable agreement for O^{6+} and Si^{7+} in the slow and intermediate wind, but show larger deviations in the fast wind. The analysis of Fe^{9+} is difficult without a deeper understanding of the underlying measurement data, but we mention, that if we could neglect the low-speed population completely, an overall mean differential speed of about zero would be found from the Fe^{9+} MR data, that is similar to the results by [Hefti, 1998a]. As we find now differential speeds in the fast wind for two of the three investigated ion species but also negative differential speeds in the slow wind for Si^{7+} and completely inconclusive results for Fe^{9+}, we have to state that the derived differential speeds from the CTOF matrix rate data yield an overall inconclusive picture. This might be partly caused by the utilization of the onboard

[3]Note that the mean proton speed utilized in the earlier study by [Hefti, 1998a] is exactly the same CELIAS/PM data product that we utilize for our study here. The linear ion-proton differential speed relations in dependence of the proton speed are obtained from the fitted ion speed gradients given in the lower part of each panel in Figure 1.13.

post-processed data products. These onboard products lead on one hand to reasonable agreement with the results obtained by [Hefti, 1998a] in particular for the probably best-resolved ion species O^{6+}, but on the other hand we see that they implicate certain inaccuracies and have to be mainly used as a black box relying on the preflight calibration and the resulting onboard algorithms.

To enable a more systematic investigation of a wider set of ion species, in the following we conduct a revised data analysis of the CTOF heavy ion data including a new characterization of the CTOF sensor response which is based purely on Pulse Height Analysis (PHA) data. This data product does not only have higher resolution in mass, mass-per-charge and ion speed but going back to this low-level data will also improve our general understanding of the CTOF measurements and make the results largely independent of the preflight calibration.

Chapter 4

Characterization of the CTOF Sensor Response

In this chapter we conduct a so-called *in-flight calibration* of the CTOF instrument based on the long-term PHA data in order to fully characterize the sensor response to solar wind ions. On the basis of this sensor response model, the (base-rate-corrected) PHA counts can be then probabilistically assigned to individual ion species, depending on the particles' signal in energy-per-charge (Epq), time-of-flight (TOF) and residual energy (ESSD). To achieve this goal, the CTOF response model has to predict the individual peak positions and shapes in the ET-matrices (see Figure 2.3) for each measurable solar wind heavy ion species at any given Epq-step. In the end of the calibration we also discuss the treatment of the so-called instrumental background, which are contributions to the measured count rate data that originate either from irregular solar wind ion signals such as random-coincidences or energy pile-ups or are signals from other particle populations than solar wind ions such as pick-up ions.

4.1 Probabilistic Ion Count Assignment

The simplest way of assigning measured PHA counts to certain ion species is to form two dimensional boxes in the ET-matrices that contain a fixed range of TOF and ESSD channels for each Epq-step and all counts measured in these channels are assigned to the same ion species. It is possible to follow such approach, but the only improvement to the MR-box scheme in chapter 2 would be that one defines the boxes on the basis of in-flight long-term data instead of the preflight-calibration measurements. However, these ET-boxes (or m-m/q-boxes) are a massive over-simplification of the actual problem because in the PHA data we can see the substantial overlap between the ion peaks

in the ET matrices. Thus, the majority of counts cannot be assigned deterministically to a certain species, but instead, we have to assign them in a probabilistic manner:

For every Epq-step the total count rate at each channel (or bin) in ET space can be modeled as the sum of the count rate for all detectable ion species $1 \leq i \leq N_{ion}$:

$$\widetilde{C}(\tau, \epsilon) = \sum_{i=1}^{N_{ion}} \widetilde{C}_i(\tau, \epsilon) \tag{4.1}$$

with the (unknown) step-dependent individual species count rate contributions $\widetilde{C}_i(\tau, \epsilon)$ for each ET-bin. For a sufficiently large number of measured counts the contributions $\widetilde{C}_i$ can be regarded as quasi-continuous distributions in ET space and the shape of these distributions i.e. the relative count rate at each channel compared to all other channel count rates does not change anymore with even increasing measured count rates, assuming that the detector itself does not change over time. One can then separate the distributions into a constant normalized part $R_i(\tau, \epsilon)$ that describes the shape of the species distribution and a variable scaling parameter N_i:

$$\widetilde{C}_i(\tau, \epsilon) = R_i(\tau, \epsilon) \cdot N_i =: \widetilde{C}(N_i, \tau, \epsilon) \, . \tag{4.2}$$

with the normalization of R_i:

$$\forall \, i : \, \sum_{\tau} \sum_{\epsilon} R_i(\tau, \epsilon) = \sum_{\tau, \epsilon} R_i(\tau, \epsilon) = 1 \, . \tag{4.3}$$

The function R_i can be considered as a probability density function that we call the sensor response for the respective ion species at the given Epq-step. The complimentary scaling parameter N_i is then the (total) count rate for the given ion species at this Epq-step, which is the quantity that we are ultimately interested in.
As the species responses are independent of the count rate it is clear that once they are known from the instrument calibration measurements with high counting statistics, they are constant at any given measurement time as long as no physical changes of the instrument occur. Instead, for any finite ion count rate N_i, the distribution of the actually measured count rates $C_i(T, E)$ in the ET-matrix can be considered as sampled from the model distribution $\widetilde{C}(N_i, \tau, \epsilon)$ and the deviations that occur are purely due to the statistical nature of the ion interaction in the carbon foil and the SSD. Thus, as each detected ion event is statistically independent from all others, the probability that a certain ion species is measured with the count rate C_i at a certain ET-bin is given by a Poisson distribution with the expectation value $\lambda_i = \widetilde{C}(N_i, \tau, \epsilon)$:

$$P_{\tau,\epsilon}(\lambda_i, C_i) = \frac{\lambda_i^{C_i}}{C_i!} e^{-\lambda_i} \, , \quad C_i \in \mathbb{N}, \quad \lambda_i \in \mathbb{R}_{>0}. \tag{4.4}$$

Consequently, the probability that the overall measured count rate in a certain ET-bin obtains a value C is given as

$$P_{\tau,\epsilon}(\lambda, C) = \frac{\lambda^C}{C!} e^{-\lambda}\,, \quad C \in \mathbb{N}, \quad \lambda \in \mathbb{R}_{>0}. \tag{4.5}$$

with the expectation value

$$\lambda = \sum_{i=1}^{N_{ion}} \widetilde{C}_i(\tau,\epsilon) =: \widetilde{C}(\underline{N}, \tau, \epsilon)\,, \tag{4.6}$$

where $\underline{N}$ denotes the vector containing all total ion count rates $1 \leq N_i \leq N_{ions}$. The vector-form is motivated by the fact that the count rate model is linear in the ion count rates and therefore can be expressed in a more compact way as

$$\widetilde{C}(\underline{N}, \tau, \epsilon) = \underline{N} \cdot \underline{R}(\tau, \epsilon) \tag{4.7}$$

where the response model of all ion species is expressed as the vector
$\underline{R}(\tau,\epsilon) = (R_1(\tau,\epsilon), ..., R_i(\tau,\epsilon), ..., R_{N_ions}(\tau,\epsilon))^T$.

In the given situation, where the probability to measure certain count rates $C(\tau,\epsilon)$ depends on the underlying ion count rate vector $\underline{\mathrm{N}}$, we can apply a maximum-likelihood estimation [Press, 1991] and derive the most probable values of $\underline{\mathrm{N}}$ as the ones which maximize simultaneously the probability of obtaining the *actually* measured count rates $C(\tau,\epsilon)$ at the given ET-bins. By multiplying the probabilities of the measured count rates $C(\tau,\epsilon)$ of all ET-bins we find the total probability of the measured count rate sample which has to be maximized as

$$P = \prod_{\tau,\epsilon} P_{\tau,\epsilon}(\widetilde{C}(\underline{N}), C) = \prod_{\tau,\epsilon} \left(\frac{\widetilde{C}(\underline{N})^C}{C!} e^{-\widetilde{C}(\underline{N})} \right) \tag{4.8}$$

Instead of maximizing Eq. 4.8 it is mathematically equivalent and numerically favorable to minimize the negative logarithm of the probability product:

$$\begin{aligned} -\ln(P) &= -\ln\left[\prod_{\tau,\epsilon} \left(\frac{\widetilde{C}(\underline{N})^C}{C!} e^{-\widetilde{C}(\underline{N})} \right) \right] \\ &= \sum_{\tau,\epsilon} \left[-\ln\left(\frac{\widetilde{C}(\underline{N})^C}{C!} \right) + \widetilde{C}(\underline{N}) \right] \\ &= \sum_{\tau,\epsilon} \left[-C \ln(\widetilde{C}(\underline{N})) + \ln(C!) + \widetilde{C}(\underline{N}) \right] \end{aligned} \tag{4.9}$$

Since the term $\ln(C!)$ is independent of the model $\widetilde{C}$ we can neglect it in the minimization so that we find the following merit function:

$$M(C, \widetilde{C}(\underline{N})) = \sum_{\tau,\epsilon} \left[\widetilde{C}(\underline{N}) - C \ln(\widetilde{C}(\underline{N})) \right] \tag{4.10}$$

which can be numerically minimized. As the count rate model $\widetilde{C}(\underline{N}, \tau, \epsilon)$ is essentially a parametrization of the response model with the free parameter vector $\underline{N}$, we call this numerical minimization a fit of the response model $\underline{R}(\tau, \epsilon)$ to the measured data $C(\tau, \epsilon)$. As fit- or minimization-algorithm we utilize the Levenberg-Marquardt algorithm [Levenberg, 1944, Marquardt, 1963] and the BFGS algorithm [Broyden, 1970, Fletcher, 1970, Goldfarb, 1970, Shanno, 1970] as they are implemented in the 'optimize' module as part of the scientific python ('scipy') library [1]. Further details about the concrete usage of these algorithms are given in the context of concrete fit results in the following sections and chapters.

Finally, we note that for the case of sufficiently high counting statistics within each relevant ET bin the measured count rates follow approximately a normal distribution

$$P_{\tau,\epsilon}(\mu, \sigma, C) = \frac{1}{\sqrt{2\pi}\sigma} \cdot \exp\left(-\frac{(C-\mu)^2}{2\sigma^2} \right) \quad C \in \mathbb{N}, \quad \lambda \in \mathbb{R}_{>0}. \tag{4.11}$$

with the same expectation value as the Poisson distribution $\mu := \lambda = \widetilde{C}(\underline{N})$ and standard deviation $\sigma := \sqrt{\lambda} = \sqrt{\widetilde{C}(\underline{N})}$. In analogy to Eq. 4.8 - 4.9 we can then derive a merit function for the normally distributed count rate approximation by calculating the total sample probability:

$$\begin{aligned} -\ln(P) &= -\ln\left[\prod_{\tau,\epsilon} \left(\frac{1}{\sqrt{2\pi}\sigma} \cdot \exp\left(-\frac{(C-\mu)^2}{2\sigma^2} \right) \right) \right] \\ &= \sum_{\tau,\epsilon} \left[-\ln\left(\frac{1}{\sqrt{2\pi}\sigma} \right) + \frac{(C-\mu)^2}{2\sigma^2} \right] \end{aligned} \tag{4.12}$$

Yet, if we used directly this expression as the merit function M, the σ-values would depend on $\underline{N}$ and thus would vary during the minimization. This turns out to be problematic for the numerical convergence of the fit as large deviations between modeled count rate $\widetilde{C}$ and measured count rate C are scaled down for large model values $\widetilde{C}$. To avoid this problem, we calculate the σ-values from the measured count rates in each ET-bin instead, so that they are constant during the minimization[2]. So when we approximate $\sigma = \sqrt{C}$ and then omit in Eq. 4.12 all terms and factors that are independent

[1] https://www.scipy.org/

[2] This way of defining the weights $w = 1/\sigma^2 = 1/C$ in the minimization function is known as Neymann's (weighted) χ^2 [Baker and Cousins, 1984] which is justified by the fact that as the fit converges, both σ-values become similar $\sigma_{\widetilde{C}} \to \sigma_C$.

of $\underline{N}$ we obtain as merit function

$$M(C, \widetilde{C}(\underline{N})) = \sum_{\tau,\epsilon} \left[\frac{(C - \widetilde{C}(\underline{N}))^2}{C} \right] = \sum_{\tau,\epsilon} \left[\frac{(C - \mu(\underline{N}, \underline{R}))^2}{\sigma^2} \right] = \chi^2(\underline{N}, \underline{R}) \,. \tag{4.13}$$

This is the regular χ^2-distribution that is used in the standard 'weighted least-square fitting' procedure with the weights $w = 1/\sigma^2$ and normally distributed statistical errors σ around the model value μ. The advantage of Eq. 4.13 over Eq. 4.10 is that Eq. 4.13 directly provides a standard goodness estimation of the fit, which we can use to compare the goodness of different proposed response models $\underline{R}$ (see sections 4.4 and 4.5 and in particular section 4.6).

4.2 Systematic Ion Selection for the CTOF Response Model

To derive the response model for the CTOF sensor we first need to select a physically meaningful set of ion species that we expect to be detectable in the CTOF data. In principle, the design of the CTOF entrance system as well as the TOF and ESSD measurement range allow a large number of different ion species to be measured with a valid signal in the CTOF PHA triple coincidence data at reasonable solar wind and suprathermal speeds. However, as every measurement has limited counting statistics it is not meaningful to include all these ion species in the response model as we have reliable upper estimates from other experiments and theoretical considerations that many of these species have very low abundances so that they cannot be resolved in the data. To allow for a systematic selection of physically meaningful solar wind ion species we use a comprehensive overview of elemental abundances in the solar corona [Aschwanden, 2005], as this is the source region of the solar wind, in combination with model calculations of ion charge state abundances [Arnaud and Rothenflug, 1985] in dependence of the coronal electron temperature.

Considering first the elemental abundances we include all elements that have a relative coronal abundance larger than 10^{-6} times the coronal hydrogen abundance which yields the elements helium, carbon, nitrogen, oxygen, neon, sodium, magnesium, aluminum, silicon, sulfur, argon, calcium, iron and nickel. Among the elements with low and intermediate masses ($m \leq 20$ amu) the most abundant elements are helium, carbon, oxygen and neon which compared to hydrogen have relative coronal abundances of 8.5%, 0.032%, 0.063% and 0.012%, respectively. Among those with high mass numbers ($m \geq 28$ amu), which can be well-separated in the CTOF measurements from the former elements, the most abundant elements are silicon and iron both with relative coronal abundances of 0.0040% compared to hydrogen. As nitrogen, magnesium

and sulfur show relative coronal abundances of 0.0079%, 0.0040% and 0.0016% with respect to hydrogen, their abundances are lower, but still comparable in order of magnitude with respect to some of their neighbor elements. We thus include them in the response model not only because they potentially influence the speed spectra of their adjacent more abundant ion species but also their own most abundant charge states can be resolved at least in the CTOF long-term data matrices for the slow wind case. In contrast the elements sodium, aluminum, argon, calcium and nickel have relative coronal abundances between 0.0002% and 0.00025% with respect to hydrogen which makes them even one order of magnitude less abundant than magnesium and sulfur. Yet, as the charge state distribution is quite different for each element and can even vary considerably with the solar wind type we include these elements as well, as they could still influence the count rates of certain other ion species. This is in particular true, as we have to take into account that in the ET-matrices we compare adjacent ion species at slightly different speeds which virtually enhances the measured count rate of the ion species that is just sampled at the maximum of its speed distribution at a given Epq-step. The next abundant elements are phosphorous, chlorine, and cobalt which have relative coronal abundances below 0.0001% with respect to hydrogen, and are more than one order of magnitude less abundant than their adjacent elements, so that we do not include these elements in the response model.

We assess now the relative charge state abundances utilizing the zero-density model calculations by [Arnaud and Rothenflug, 1985] and the coronal freeze-in (electron) temperatures that were derived by [Aellig, 1998a] from the CTOF iron charge state abundances of Fe^{8+} - Fe^{12+} for the time interval DOY 185-220, 1996, that covers a large part of the analysis period in this work. The study yields freeze-in temperatures in the range between $T_{C,el} = 10^{5.9}$ K and $T_{C,el} = 10^{6.2}$ K which is in very good agreement with many other studies on the coronal electron temperature (e.g. [Geiss and Gloeckler, 1995, Landi, 2007]). At these typical coronal electron temperatures a large fraction ($\geq$ 80%) of the solar wind helium, oxygen and neon particles is expected to occur as He^{2+}, O^{6+}, and Ne^{8+} as these charge states are strongly favored due to the complete vacancy of their respective outermost atomic electron shell. For carbon the situation is more complicated because the relative carbon charge state abundances, that result from the typical coronal temperature range, are highly sensitive to small deviations in $T_{C,el}$ due to the comparable ionization potentials of C^{4+}, C^{5+} and C^{6+}. The same applies for silicon and iron for which a wide range of charge states is expected to occur that is centered around the species Si^{8+} - Si^{9+} and Fe^{9+} - Fe^{11+} for an average value of $T_{C,el} = 10^{6.1}$ K. In general, the expected relative abundances of the most abundant solar wind ions by [Arnaud and Rothenflug, 1985] are in good agreement with the observed solar wind charge states over longer time periods (e.g. [von Steiger et al., 2000]).

For the CTOF response model we include for each of the selected elements all charge states with expected relative abundances larger than 10^{-3} at least for one of the listed electron temperature values $T_{C,el} \in \{10^{5.9}\ \mathrm{K}, 10^{6.0}\ \mathrm{K}, 10^{6.1}\ \mathrm{K}, 10^{6.2}\ \mathrm{K}\}$ in [Arnaud and Rothenflug, 1985]. Hence, even in the case of underestimated ion count rates due to inaccuracies in the charge state abundance modeling by a factor of 10 we include all relevant charge states down to a few percent relative count rate contribution. In this manner, the largest ion set that is currently included in the CTOF response model, i.e. for which we calculated individual ion response functions R_i contains 91 ion species of the 14 aforementioned elements helium - nickel.
Yet, in many cases in which we deal with subsamples of the CTOF data, the response model ion set has to be systematically reduced due to low counting statistics. This is done in order to allow a numerically stable fit of the most relevant ion species over all relevant Epq-steps. In fact, the largest ion set which we apply in the heavy ion velocity distribution analysis consists of 71 ion species belonging to 11 elements: helium, carbon, nitrogen, oxygen, neon, magnesium, silicon, sulfur, calcium, iron, and nickel. In section 4.6 we give an overview of the included ion species in Table 4.1 and also explain the systematic reduction of the response model ion set for low counting statistics in detail. This approach finally yields the *Full Calibrated (FC)*, *Full Stable (FS)* and *Reduced Stable (RS)* response models for the CTOF sensor.

4.3 Derivation of the CTOF Response Model

So far we described in section 4.1 how we can derive the ion count rates $\underline{N}$ from the measured count rates in the ET-matrix $C(\tau, \epsilon)$ based on an instrumental response model $\underline{R}(\tau, \epsilon)$ for a given set of ion species that we obtained in section 4.2. Once we know, which ion species to include in the response model, one could in principle determine the individual responses $R_{ij}(\tau, \epsilon)$ at each Epq-step $0 \leq j \leq 116$ for each of these species separately in a preflight calibration by exposing the CTOF sensor to the respective ion beam and adjusting the particle energy. However, in the available ion sources at the time of the CTOF preflight-calibration there were only a limited number of elements available that are relatively easy to vaporize in pure form (mainly light ions and noble gases). Furthermore, these limited preflight calibration runs were not even conducted for the assembled instrument but only for each of the three measurement sections (E/q, TOF, ESSD) separately [Oetliker, 1993a, Hovestadt et al., 1995, Hefti, 1998b, Aellig, 1998b]. As much as this information is helpful for plausibility checks, on the whole it is not enough to derive a systematic response model from it. Instead, it could be shown for similar time-of-flight mass spectrometers such as

Ulysses/SWICS and ACE/SWICS, that given the in-flight measured PHA data accumulated over longer time periods one can derive a sophisticated response model of these sensors [von Steiger et al., 2000], [Berger, 2008] that is even superior to preflight-data based models in the aspect that some instrument components are subject to small changes during the launch and cruise phase (i.e. due to outgassing in space and mechanical stress from launch vibrations and temperature changes).

In the following we describe the derivation of the response model on the basis of such an in-flight calibration. As mentioned before, we can assume that the response model $\underline{R}(\tau, \epsilon)$ is independent of the measured plasma samples for all times and so we can use at each given Epq-step j the total accumulated count rate $C_j(\tau, \epsilon)$ to determine $\underline{R}_j(\tau, \epsilon)$. Still, in the in-flight calibration $C(\tau, \epsilon)$ is in general the sum of the count rate of several ion species within each ET-bin and thus the individual ion responses have to be obtained from a similar minimization as described in section 4.1. As the measurement principle is universal for all ion species, we can assume that all species responses can be represented by a general peak model R so that the individual ion peak at each Epq-step is a parametrization of this universal model:

$$R_{ij}(\tau, \epsilon) := R(\underline{P}_{ij}, \tau, \epsilon) \tag{4.14}$$

with the individual parameter vector $\underline{P}_{ij}$ that fully describes the observed ion peak. Mathematically, the minimization function can still be exactly expressed as in Eq. 4.10 but as we deal with high counting statistics we approximate this function as in 4.13:

$$M(C, \widetilde{C}(N_{ij}, \{\underline{P}_{ij}\})) = \sum_{\tau,\epsilon} \left[\frac{(C - \widetilde{C}(N_{ij}, \underline{P}_{ij}))^2}{C} \right] . \tag{4.15}$$

Compared to Eq 4.13 we now have in addition to the accumulated long-term count rates N_{ij}[3] an additional number of free parameters in the fit given by the set of parameter vectors $\{\underline{P}_{ij}\}$ for all ion species at all Epq-steps. This set has the dimension $N_{steps} \times N_{ions} \times N_{params}$, where $N_{params} = dim(\underline{P}_i)$ depends on how many parameters we need to parametrize each of the ion response functions R_i at a given Epq-step j.

[3]Note that these long-term count rates here are recorded over all arbitrary solar wind conditions to maximize the counting statistics for the in-flight calibration. Thus, in contrast to the long-term count rates in chapter 5, that are recorded for a well-defined proton speed, these cont rates cannot be used for any determination of the heavy ion kinetic properties as we would arbitrarily mix different wind regimes.

When we just assume a 2-dimensional Gaussian as the simplest realization of the general peak model:

$$\begin{aligned} R(\underline{P}_{i,j},\tau,\epsilon) &= R_\tau(\underline{P}^{ij}_\tau,\tau)\cdot R_\epsilon(\underline{P}^{ij}_\epsilon,\epsilon) \\ &= G(\tau^{ij}_0,\sigma^{ij}_\tau,\tau)\cdot G(\epsilon^{ij}_0,\sigma^{ij}_\epsilon,\epsilon) \\ &= \frac{1}{\sqrt{2\pi}\sigma^{ij}_\tau}\cdot\exp\left(-\frac{1}{2}\cdot\left(\frac{(\tau-\tau^{ij}_0)}{\sigma^{ij}_\tau}\right)^2\right)\cdot\frac{1}{\sqrt{2\pi}\sigma^{ij}_\epsilon}\cdot\exp\left(-\frac{1}{2}\cdot\left(\frac{(\epsilon-\epsilon^{ij}_0)}{\sigma^{ij}_\epsilon}\right)^2\right) \\ &=: G_{2D}(\underline{P}_{G,ij},\tau,\epsilon) \end{aligned} \tag{4.16}$$

the individual parameter vector for each species is given as $\underline{P}_{i,j} = (\tau^{ij}_0,\epsilon^{ij}_0,\sigma^{ij}_\tau,\sigma^{ij}_\epsilon)^T$ and thus contains four parameters per Epq-step. Including the free peak heights, we therefore would have to deal with 459(!) free parameters at a given Epq-step if we tried to fit the responses of all 91 selected relevant ion species simultaneously. As theoretically required, this number is still lower than the number of information-containing data points which is given by about 10^3-10^4 filled ET-bins for the approximately 50 most relevant Epq-steps for the solar wind energy range. Yet, due to the large overlap of the ion peaks in the ET-matrices it is in practice impossible to obtain a stable and physically meaningful fit with such a large set of free parameters.
Yet, the parameters $\underline{P}_{i,j}$ are not random, but follow a measurement systematic, depending on the ion species properties mass m, charge q and atomic number Z as well as their speed v_{pacc} with which they enter the TOF section and which can be calculated from Eq. 2.9 for every Epq-step. Therefore, the $\underline{P}_{i,j}$ are related to each other both between the ion species and among all Epq-steps, so that we can massively reduce the number of free parameters in the response model fit if we can describe their relations in a proper physical way based on the known instrument characteristics described in chapter 2. In order to understand and finally predict the behavior of the parameters $\underline{P}_{i,j}$ we build-up the full CTOF response model subsequently as it is described in the following sections of this chapter: First, we determine the ion positions in the ET-matrices for all ion peaks at each Epq-step (section 4.4). Second, we determine the peak shapes of all ion species with their already fixed positions (section 4.5). Third, we assess the overall goodness and consistency of the response model (section 4.6).

4.4 Characterization of Ion Peak Positions

As the starting point of the CTOF in-flight calibration we show in Figure 4.1 as an example the long-term data ET matrix for Epq-step 55. By combining our knowledge of the CTOF measurement principle from section 2.2 with our expectation of elemental

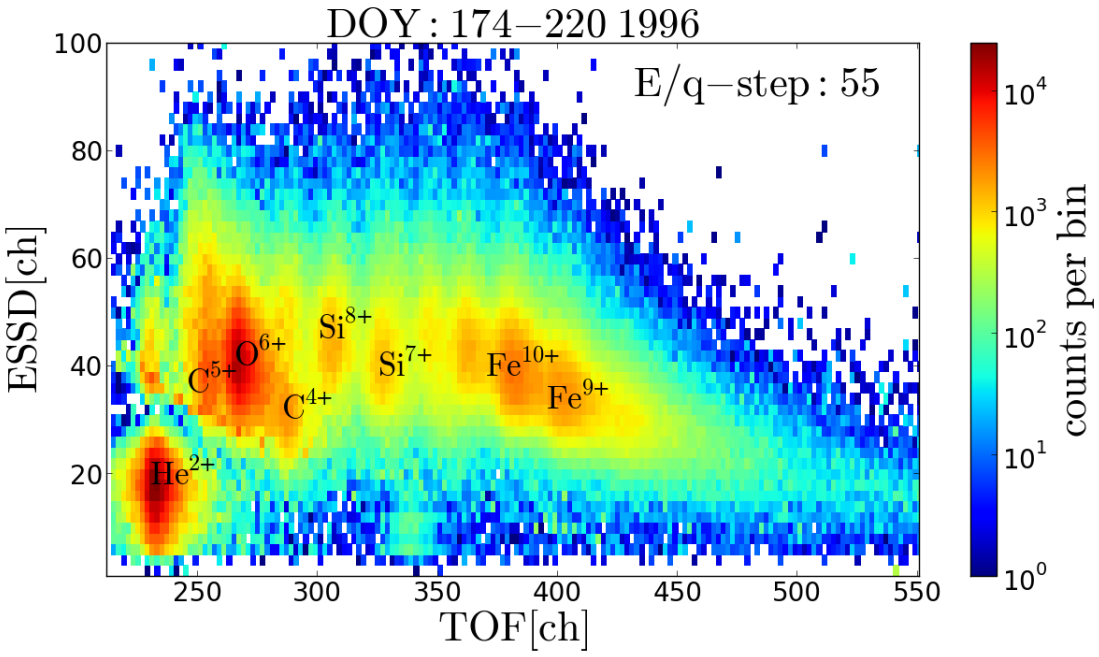

FIGURE 4.1: CTOF ET-matrix at Epq-step 55 for the base-rate corrected long-term PHA data with the accumulated count rate for DOY 174-220 in 1996. We can clearly identify the peaks of several more abundant ion species such as He^{2+}, C^{4+}, C^{5+}, O^{6+}, Si^{7+}, Si^{8+}, Fe^{8+} - Fe^{11+}, of which are used in the inflight-calibration of the CTOF sensor. We can also identify the peak of the only dominant pick-up ion species He^{+} at the position ($\tau \approx 340$ ch, $\epsilon \approx 10$ ch).

and charge state abundances from section 4.2 we can identify several ion species of the most abundant solar wind elements such as He^{2+}, C^{5+}, Si^{7+} - Si^{9+}, Fe^{8+} - Fe^{11+} which have clear peak signals at this Epq-step. We can also identify the He^{+} peak which is the only dominant pick-up ion peak in the triple coincidence data. On a large scale the identified ions seem to be well-ordered with increasing mass-per-charge from low to high TOF channels, following the simplified relation $\tau \propto \sqrt{m/q}$ that we derived in Eq. 2.6. Yet, we already see from the comparison of He^{+} and Si^{7+} that the peaks of ion species with the same m/q-value but larger difference in mass are not centered at the same TOF channel. Similarly, when we compare C^{4+} and Si^{9+} (at ($\tau \approx 290$ ch, $\epsilon \approx 50$ ch)) we find that the ESSD signal is not proportional to the incident energy at the SSD. Instead the central Si^{9+} ESSD channel is only about 1.6 times higher than the respective ESSD channel of C^{4+}, while one would expect an energy ratio of $m_{Si}/m_C = 2.3$ as both peaks are located at about the same TOF channel. Both observations show the non-negligible presence of the ions' speed- and element-specific energy loss in the carbon foil (related to α_τ) and their pulse height defect in the SSD (related to α_ϵ), which we discussed theoretically in Eq. 2.8 and 2.9.

For a limited range of Epq-steps we can directly determine the position of several predominant ion species by applying 2-dimensional Gaussians as given by Eq. 4.16 as fit-function to these ion peaks. However, due to the unknown dependence of α_τ and α_ϵ on v and Z it is difficult to extrapolate all ion species positions from the few identified species at a relatively small number of Epq-steps in a consistent way to a much wider set of ion species over the whole Epq-step range. Therefore, we simulated the passage of the ions through the foil and their stopping in the SSD with the TRIM (Transport of Ions in Matter) Monte-Carlo simulation code [Ziegler et al., 2008] to obtain a consistent set of ion peak position predictions of the most relevant species for all Epq steps.
By using the TRIM simulation tool, a first CTOF ET-matrix position calibration was conducted already by [Janitzek, 2014] for a small set of solar wind ions, following a similar approach by [Taut, 2014] that was developed for the CTOF double coincidence data in the pick-up ion energy range. In the initial attempt we used seven reference ion species He^{2+}, O^{6+}, Si^{7+}, Si^{8+}, Fe^{8+}, Fe^{9+}, and Fe^{10+} to derive a limited response model that allowed first estimates for the differential speeds of O^{6+}, Si^{7+} and Fe^{8+} - Fe^{10+} which could be then compared to the derived values by [Hefti, 1998a]. The following position calibration builds on the former calibration by generalizing the approach to the more comprehensive ion set described in the previous section 4.2 and taking into account the deviations in the ET-matrices due to the base-rate correction of the PHA data that was not considered in the former calibration. For completeness, we first briefly summarize in the next subsection the conducted simulations to derive the ET-positions for the solar wind reference ions, before we apply a correction to the obtained positions that follows from the base rate correction and then describe the generalization to the full response model. For further details concerning the conducted TRIM simulations we refer the reader to the original work [Janitzek, 2014].

Simulated Ion Peak Positions

For the TRIM simulation we took as incident particles the seven aforementioned reference ions He^{2+} - Fe^{10+} at incident energies that correspond to the nominal kinetic energies of the ions at Epq-steps $27 \leq j \leq 73$ after the post-acceleration (see Table B.2)

$$E_{acc}(q_i, j) = \left[\left(\frac{E}{q} \right)_j + U_{acc} \right] \cdot q_i \tag{4.17}$$

where we used $U_{acc} = 23.85$ kV as the post-acceleration voltage [Taut, 2014]. As the detector geometry is limited in the TRIM simulation package, the carbon foil was represented by a 24 nm thick carbon layer [Taut, 2014] while the SSD consisted of a 75 nm thick SiO2 dead-layer [Oetliker, 1993a, Janitzek, 2014] stacked on a several micrometer

thick sensitive silicon layer in which the ions fully stop. In the latter, only the energy deposit that is transferred to the target electrons and thus can excite these electrons to the conduction band is taken into account as electronic energy loss that can be measured by the SSD.

It turns out that when we consider the simulated *residual kinetic energy fraction* after the carbon foil α_τ in dependence of the incident energy E_{acc}, that it can be approximated for all elements[4] with the empirical relation

$$\alpha_\tau^{ij} = \alpha_\tau(E_{acc}(q_i, j)) = \frac{A_i}{B_i \cdot E_{acc}(q_i, j)} + C_i \tag{4.18}$$

where A_i, B_i and C_i are element-specific constants that we obtain from a fit to the simulated values α^{ij} and which are given in Table B.3 in appendix B. In Figure 4.2 we depict the simulated remaining energy fraction α_τ after the carbon foil for the most abundant solar wind elements helium - iron as a function of their kinetic energy after the post-acceleration E_{acc}. The simulated TOF values are then given by

$$\tau_{ij}[\text{ns}] = \sqrt{\frac{m_i \cdot L_\tau^2}{2 \cdot \alpha_\tau^{ij} \cdot E_{acc}(q_i, j)}} \tag{4.19}$$

where $L_\tau = 70.5$ mm is the length of the TOF section as described in section 2.2. From the comparison of the simulated TOF values τ[ns] with the observed ET-matrix TOF positions τ[ch] of the reference ion species we could confirm with a good accuracy of $\Delta\tau = \pm 1$ ch the linear conversion from instrumental channel to the physical time-of-flight that was found by [Taut, 2014] from the pick-up ion energy range as:

$$\tau[\text{ns}] = A_\tau \cdot \tau[\text{ch}] + B_\tau \tag{4.20}$$

with universal conversion constants $A_\tau = 0.200723$ ns/ch and $B_\tau = -1.46909$ ns that are valid for all reference ion species over all their simulated Epq-steps, respectively. When we now assume that the instrumental dependencies in Eq. 4.18 and Eq. 4.20 hold for all ion species i and all Epq-steps $0 \leq j \leq 116$, we can predict the ion positions in all 117 ET-matrices with the general expression:

$$\tau_{i,j}[\text{ch}] = A_\tau^{-1} \cdot \left(\sqrt{\frac{m_i \cdot L^2}{2 \cdot \alpha_{i,j} \cdot \left[(E/q)_j + U_{acc} \right] \cdot q_i}} - B_\tau \right) \tag{4.21}$$

where m_i and q_i are the ion species' mass and charge.

[4] Note that the charge state of the ion species is only relevant for calculating the incident energy of the particles but does not influence the energy loss in the carbon foil as the ions lose their initial charge state information already within the first layers of the foil [Ziegler et al., 2008].

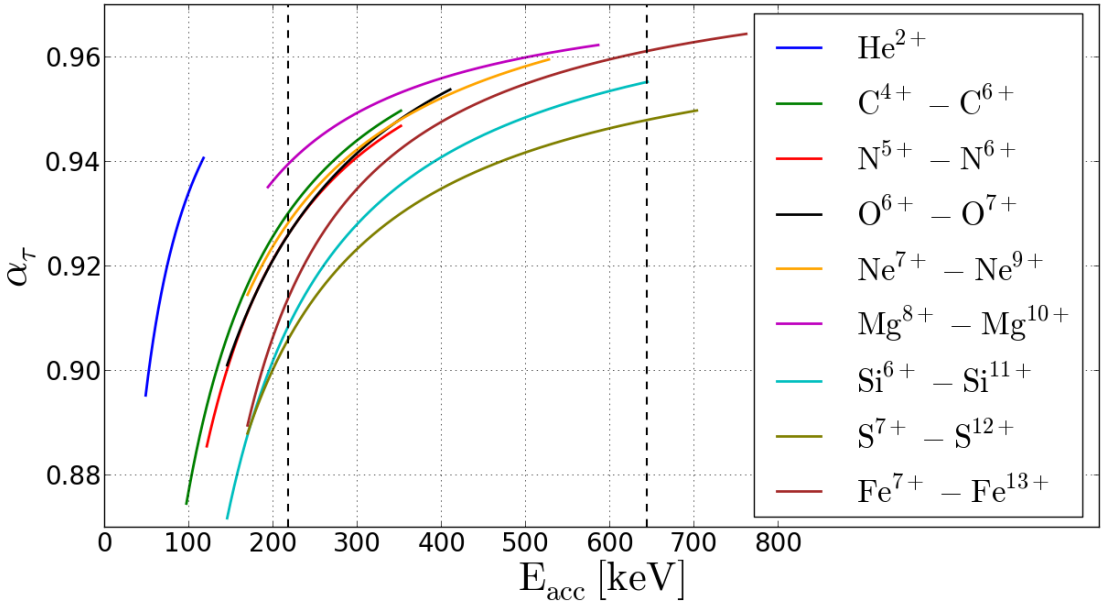

FIGURE 4.2: Simulated remaining energy fraction α_τ after the carbon foil for the most abundant solar wind elements helium - iron as a function of their kinetic energy after the post-acceleration E_{acc}. The lower (higher) energy range limit correspond to Epq-step 116 (0) of the lowest (highest) clearly observed charge state in the CTOF data within this work which e.g. for iron is Fe^{7+} (Fe^{13+}). As an example, we also marked with the dashed black vertical lines the energy range for the most abundant calcium species Ca^{9+} - Ca^{11+} for Epq-steps 0-116, as calcium is one of the low-abundance elements for which we approximated α_τ with the iron value $\alpha_{\tau,Fe}$. Note that, the energy ranges are already quite a conservative estimation as the Epq-steps in which the bulk of the solar wind species is measured lies between Epq-step 15 and 90 depending on the m/q-value of the ion species and the solar wind speeds.

For the full ion set we simulated the relative energy loss for the remaining more abundant elements carbon, nitrogen, neon, magnesium and sulfur so that their constants A_i, B_i, and C_i can also be found in Table B.3. For carbon, neon and magnesium we also compared the observed position of their most abundant charge states C^{4+} - C^{6+} and Ne^{8+}, Mg^{10+} at several Epq-steps in the ET matrices with the simulated ion positions and found only small deviations of $|\Delta\tau| \leq 2$ ch. Finally, for the remaining least abundant elements sodium, aluminum, argon, calcium, and nickel we approximate the TOF positions as follows: From Figure 4.2 we find that there is no clear systematic in the remaining energy fraction, α_τ, after the carbon foil with the element atomic number. On the other hand the maximum difference between the minor elements ($Z > 2$) at equal energies is about $\Delta\alpha_\tau$ =2%. Therefore, we approximate the value α_τ for the remaining elements with the energy loss that we obtained from the simulation of iron which is over the whole range of incident energies close to the mean relative loss of all calibrated elements. Consequently we calculate the TOF position of sodium - nickel for all Epq-steps with Eq. 4.21.

Similar to the derivation of the TOF positions we obtained from the comparison of the simulated electronic energy deposit ϵ[eV] in the SSD and the measured residual energy positions ϵ[ch] the pulse height fractions α_ϵ of the reference ion species, together with the linear conversion from ESSD channel to the physical electronic energy loss in the SSD [Janitzek, 2014]:

$$\epsilon[\text{keV}] = A_\epsilon \cdot \epsilon[\text{ch}] \tag{4.22}$$

with the universal conversion constant $A_\epsilon = 1.9616$ keV/ch. By including the additional species C^{5+} in the comparison we found that for all elements heavier than helium the obtained PHF is speed-independent and thus scales only with the atomic number Z, which is in agreement with the SSD preflight calibration by [Hefti, 1998b]. We then interpolated the PHF values of neon and magnesium linearly in Z and found good agreement ($|\Delta\epsilon| \leq 2$ ch) with the observed positions for Ne^{8+} and Mg^{10+}, so that we interpolated the pulse height fractions of the remaining elements (with $2 < Z < 26$) nitrogen, oxygen, sodium, aluminum, sulfur, argon, and calcium in the same way. For nickel ($Z = 28$) we ran an additional simulation that confirmed the extrapolated value of its pulse height fraction which leads to slightly lower(!) predicted ESSD peak positions than iron. In Figure 4.3 we show the derived pulse height fractions α_ϵ for all calibrated minor elements ($Z > 2$) in dependence of their atomic number Z. All obtained pulse height fractions $\alpha_\epsilon(Z_i)$ are also given in Table B.5 in appendix B. With the given pulse height fractions $\alpha_\epsilon^i = \alpha_\epsilon(Z_i)$ and by combining Eq. 2.9 , Eq. 4.20, and Eq. 4.22 we can finally express the ESSD peak position for each ion species i at each Epq-step j in dependence of the previously calculated TOF peak position:

$$\epsilon(\tau_{ij})[\text{ch}] = A_\epsilon^{-1} \cdot \alpha_\epsilon^i \frac{m_i \cdot L_\tau^2}{(A_\tau \cdot \tau_{ij} + B_\tau)^2} \,. \tag{4.23}$$

Ion Position Corrections

So far, the calculated values for the TOF and ESSD positions were derived from the PHA data before the base rate correction was conducted. This has the effect that in particular the ESSD position of most ion species is actually over-estimated due to the fact that nearly all species peaks are distributed over at least two priority ranges and thus the respective low-priority range part of the peaks (that lies at lower ESSD channels) is under-represented in count rate in the uncorrected data. We find that this effect is negligible for iron as the base-rate factors are relatively low in PR1 and PR2, but can be substantial for e.g. carbon, oxygen, neon, magnesium, silicon (e.g. compare Figure 2.6 in chapter 2). As the peak position deviations are still relatively small (~ 2 ch) compared to the overall measurement range in residual energy the base rate correction does not

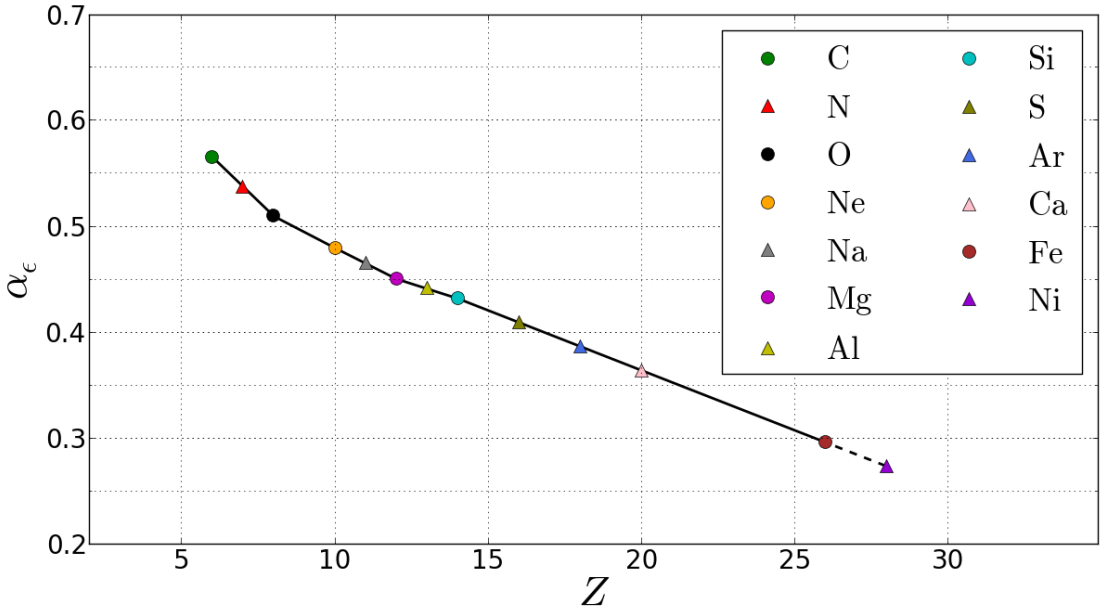

FIGURE 4.3: Derived pulse height fractions α_ϵ for all calibrated minor elements ($Z > 2$) in dependence of their atomic number Z. The ESSD position corrections are already included in the pulse height fraction (PHF) values (see text for details). For all elements with well-observable ion species peaks (marked with a circle) we find a TOF-independent pulse height defect over the observed TOF range. For all other elements (marked with a triangle), we assumed the same TOF-independence and interpolated α_ϵ as a linear function of its atomic number. For nickel, we extrapolated α_ϵ as its atomic number is still relatively close to iron. For helium we found a TOF-dependent pulse height defect. The corresponding values $\alpha_\epsilon(\tau)$ can be calculated from Eq. B.1 and Table B.4 in the appendix and yield $0.66 < \alpha_\epsilon < 0.91$ for He^{2+} for Epq-steps $0 \leq j \leq 116$.

change fundamentally the observed measurement systematics in the ESSD positions. Thus, we do not conduct a new calibration from scratch, but apply systematic corrections to the calculated positions: For the aforementioned well-observable elements carbon - silicon we shift the former calculated peak ESSD positions to lower channels until we reach a minimum in the χ^2-value that we derive from a fit of the now corrected response model to the count rate data after Eq. 4.15[5]. We apply this procedure consecutively for each element carbon - silicon in the order of decreasing elemental abundance. As the ESSD position after Eq. 4.23 does not explicitly depend on the ion charge q_i or the Epq-step j this correction is automatically applied to all charge states of a given element and at all Epq-steps simultaneously. For helium and iron no correction had to be applied, for all other elements for which the ESSD peak position cannot be observed well with the necessary accuracy (nitrogen, sodium, aluminum, sulfur, argon and nickel) we interpolated the corrections linearly. The correction for carbon might be

[5]For this fit we initially use a 2D-Gaussian peak shape as given in Eq. 4.16 with estimated peak widths as in Eq. 4.26 and 4.27 and later the improved peak shape model as in Eq. 4.41, but it turns out that the optimal ion position calibration is hardly sensitive to the peak shape.

biased, because the border region of PR5 to PR4 could not be reconstructed properly as discussed in the previous chapter. The final equation for the calculation of the ESSD positions after the base-rate correction is then given by

$$\epsilon(\tau_{ij})[ch] = A_{\epsilon}^{-1} \cdot \alpha_{\epsilon,cor}^{i} \cdot \alpha_{\epsilon}^{i} \frac{m_i \cdot L_{\tau}^{2}}{(A_{\tau} \cdot \tau_{ij} + B_{\tau})^{2}} \tag{4.24}$$

where the obtained correction factors $\alpha_{\epsilon,cor}^{i}$ are listed for all mentioned elements in the last column of Table B.5 in the appendix and all remaining quantities are the same as in Eq. 4.23.

We also observed small shifts in the TOF position ($\sim$ 2 ch) towards lower TOF channels after the base rate correction which is due to the same former count rate underrepresentation of the low-priority range part of each peak that lies at lower TOF channels. We corrected this effect in the same way as for the ESSD channels, by shifting all ion charge states of a given element towards the new observed positions of its dominant charge states. However, further improvement could be achieved here, as each ion species could be adjusted individually after Eq. 4.21 as long as these shifts are still small compared to the distances among the charge states of each element so that the overall systematical approach is kept. The final equation for the calculation of the TOF positions after the base-rate correction reads then

$$\tau_{i,j}[\mathrm{ch}] = A_{\tau}^{-1} \cdot \left(\sqrt{\frac{m_i \cdot L^{2}}{2 \cdot \alpha_{i,j} \cdot \left[(E/q)_j + U_{acc} \right] \cdot q_i}} - B_{\tau} \right) + \tau_{cor}^{i} \tag{4.25}$$

where the obtained channel corrections τ_{cor}^{i} are listed for all mentioned elements in the last column of Table B.3 in the appendix and all remaining quantities are the same as in Eq. 4.21. In Figure 4.4 we show an example of the calibrated ion positions for the full ion-set response for Epq-step 55 at which a large number of ion species peaks can be directly observed. A comprehensive overview of the calibrated ET-matrices at a wider range of Epq-steps is given in appendix C.

4.5 Characterization of Ion Peak Shapes

In order to assign the measured ion counts to certain ion species, we need in addition to the most probable ion species peak position at any given Epq-step also an estimation for the extension of the characteristic peaks in ET space. In a first step, we approximate the ion species peak shapes as 2-dimensional Gaussians $G_{2D}(\underline{P}_{G,ij}, \tau, \epsilon)$ after Eq. 4.16.

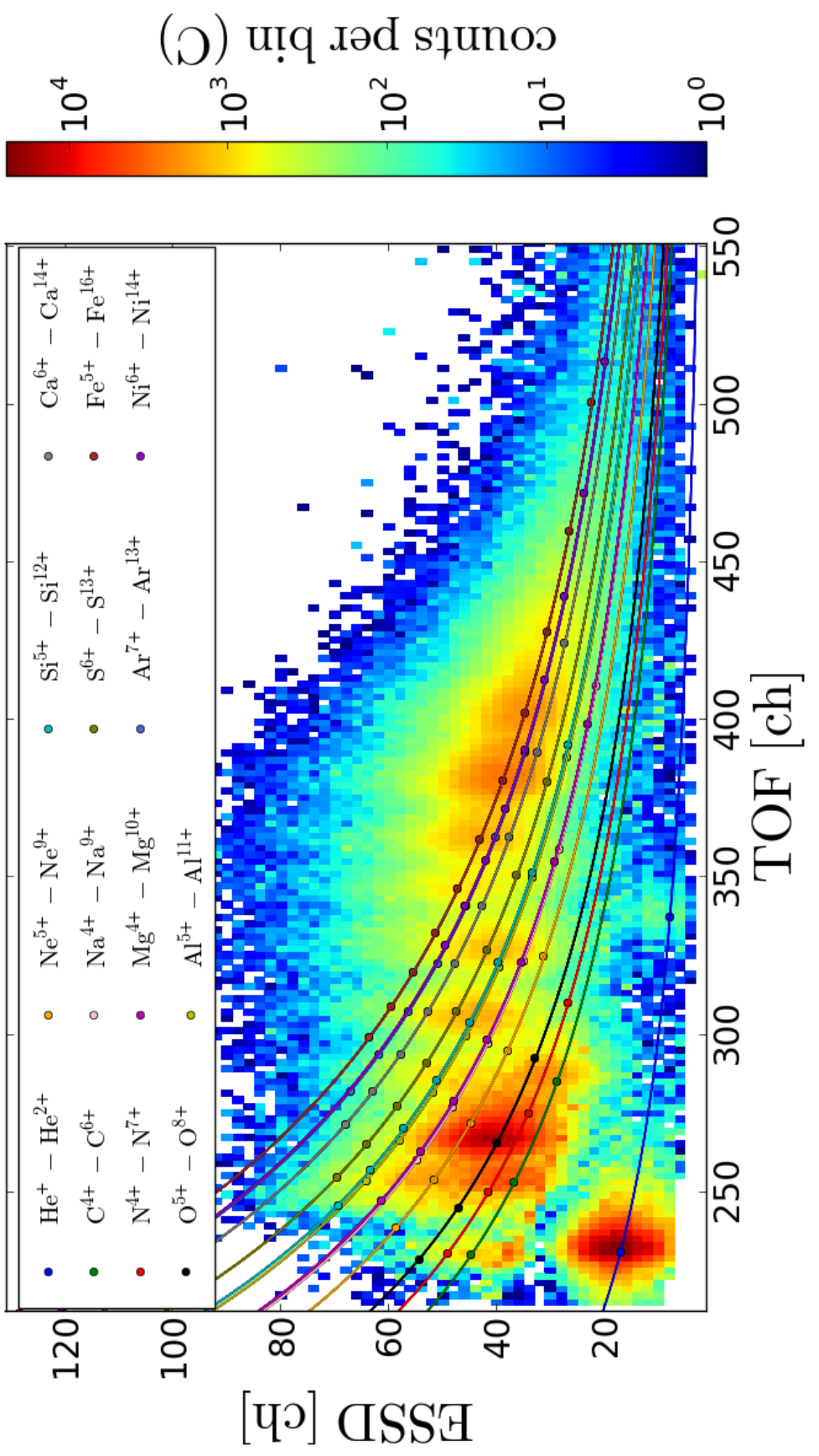

FIGURE 4.4: Calibrated peak positions at Epq-step 55 for the 91 ion species that are included in the CTOF *Full calibrated (FC)* response model after section 4.2. As we can see, the calibrated (step-independent) elemental hyperbola $\epsilon_i(\tau_i)$ yield very similar ESSD positions in particular for the ion peaks of sodium and aluminum in comparison with their more abundant adjacent elements magnesium and silicon, respectively. Similarly the argon peak positions are very close to nickel due to the increasing pulse height defect with increasing Z. Therefore, sodium, aluminum and argon had to be excluded in the speed spectra analysis in chapters 5 and 6 to obtain stable fit results as it is explained in section 4.6.

The Gaussian Peak Model for CTOF

The Gaussian peak approximation has been used for most solar wind heavy ion studies with time-of-flight mass spectrometers, in particular for all studies that used the full triple coincidence information to conduct a systematic investigation of a larger solar wind heavy ion set such as [von Steiger et al., 2000, von Steiger and Zurbuchen, 2006, Berger et al., 2011]. To fully parametrize the Gaussian peak model, one needs to determine the standard deviations of the peaks in time-of-flight and residual energy, σ_τ and σ_ϵ, which for convenience we denote in the following also as the *peak widths*. For the CTOF response model, we obtained a first estimate of the peak widths from the fit of the reference ion species in the previous section 4.4, in which all ion peak parameters $\underline{P}_{G,ij} = (\tau_0^{ij}, \epsilon_0^{ij}, \sigma_\tau^{ij}, \sigma_\epsilon^{ij})$ were treated as free parameters for each ion and each Epq-step, so that we obtained σ_τ and σ_ϵ consistently with the ion positions for a number of Epq-steps. As we investigated in [Janitzek, 2014], the determined TOF and ESSD signal widths unfortunately do not fit well the estimated widths by the TRIM simulation. Instead, the simulation rather underestimates the widths by relative values up to about 50% e.g. for iron ions, even if we took into account potential broadening effects such as the velocity acceptance of the CTOF entrance system. Therefore, we cannot make further use of the TRIM simulations for the quantitative description of the peak shapes. On the other hand, we know that the ion species lose their initial charge state information already in the first atomic layers of the carbon foil [Ziegler et al., 2008] from whereon they obtain a (low) equilibrium charge state which only depends on their initial energy E_{acc} and atomic number Z. Thus, in a first approximation all ion species of a given element do not only have the same most probable TOF and ESSD position when they enter with the same energy into the foil but also behave identical in their statistical scattering process, so that we can assume that for each element the widths σ_τ and σ_ϵ for all charge states can be expressed as a universal function of their entrance speed v_{acc} given in Eq. 2.3, or equivalently as a function of their measured TOF and ESSD position at any given Epq-step.

In fact, the conducted 2D-Gaussian fits yield that the TOF widths scale in good approximation linearly with the entrance speed of the ion species into the carbon foil at the respective Epq-step [Janitzek, 2014] even regardless of the atomic number Z:

$$\sigma_\tau^{ij} = A_{\sigma_\tau} \cdot v_{acc}^{ij} + B_{\sigma_\tau} \tag{4.26}$$

where $A_{\sigma_\tau} = (0.0040 \pm 0.0002)\ \mathrm{ch}/(\mathrm{km\ s^{-1}})$ and $B_{\sigma_\tau} = (10.3 \pm 0.2)\ \mathrm{ch}$ are in a good approximation universal parameters that are valid for all reference ion species. A similar relation was found by [Berger, 2008] for the Gaussian peak widths of the very similar SWICS instrument onboard the ACE spacecraft, who found a linear relation between

the observed TOF positions and TOF widths of the measured ion species for all Epq-steps. The increasing TOF width with decreasing entrance speed (or increasing time-of-flight) can be understood qualitatively due to the increasing cross-section for elastic scattering due to collisions with the carbon nuclei in the foil for slower ions. For CTOF it turns out that Eq. 4.26 is also a reasonable approximation for the remaining well-observable ion peaks of carbon, neon, and magnesium so that we use it as the general TOF width parametrization for the Gaussian response model.

For the residual energy measurement, we found from the initial 2-dimensional Gaussian fits of He^{2+}, O^{6+} and Fe^{8+} - Fe^{10+} a similar linear relation between the ESSD ion peak position ϵ_{ij} and the ESSD peak width σ_ϵ^{ij} for each ion species over the respective Epq-steps:

$$\sigma_\epsilon^{ij} = A_{\sigma_\epsilon} \cdot \epsilon_{i,j} + B_{\sigma_\epsilon} \tag{4.27}$$

where $A_{\sigma_\epsilon} = (0.102 \pm 0.003)$ and $B_{\sigma_\epsilon} = (2.368 \pm 0.097)$ ch are again universal parameters that are valid for most reference ion species simultaneously. Yet, for some ion species such as Si^{7+} and Si^{8+} we obtained from the Gaussian fits considerably larger values for the energy widths. This can be explained by the fact that these ions have a strong overlap in ESSD with the adjacent ion species of S^{8+} and S^{9+}, that have the same or very similar mass-per-charge ratios but slightly higher mass. In addition, the respective sulfur charge states are lower but comparable in order of magnitude to the fitted silicon charge states. Furthermore, also other elements such as magnesium and calcium can contribute with their non-negligible charge states such as Mg^{6+}, Mg^{7+} or Ca^{10+} to the apparent silicon peaks. In general, we have to state that although the absolute values of the TOF and ESSD standard deviations are comparable, the overall peak resolution is much higher in the TOF measurement as here all ion species are distributed over about 400 channels, while in the ESSD measurement these species are distributed over only 80 channels.

A Critical Revision of the Gaussian Peak Shape Model

While the 2D Gaussian peak shape model is a convenient choice for its analytic simplicity, there is no physical reason that the time-of-flight or residual energy signal should follow this shape in detail. To assess the goodness of the model in detail we take a look at several dominant ion species peaks in order to compare the measured peak shape with the fitted 2D Gaussian model. For the comparison we choose He^{2+} and the

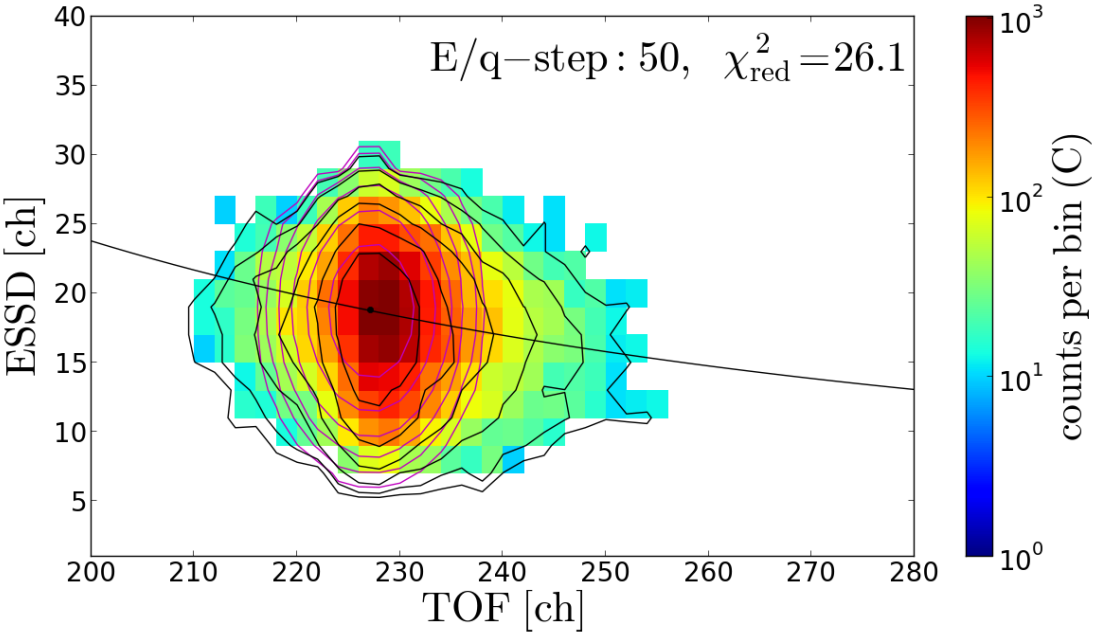

FIGURE 4.5: Fit of the 2D-Gaussian peak model to the measured He^{2+} long-term data peak. The position and width parameters are taken from the calibrated CTOF standard response model as described in the previous sections and only the count rate is fitted as described in Eq. 4.28. The black data contour lines correspond to $10^{-1/3}$, $10^{-2/3}$, 10^{-1}, $10^{-4/3}$, $10^{-5/3}$, 10^{-2} times the maximum data count rate C_{max}. The magenta contour lines show the corresponding count rate levels of the fitted count rate model $\widetilde{C}(\underline{N}, \underline{R})$.

Only ET-bins with at least 10 actually transmitted PHA counts are considered.

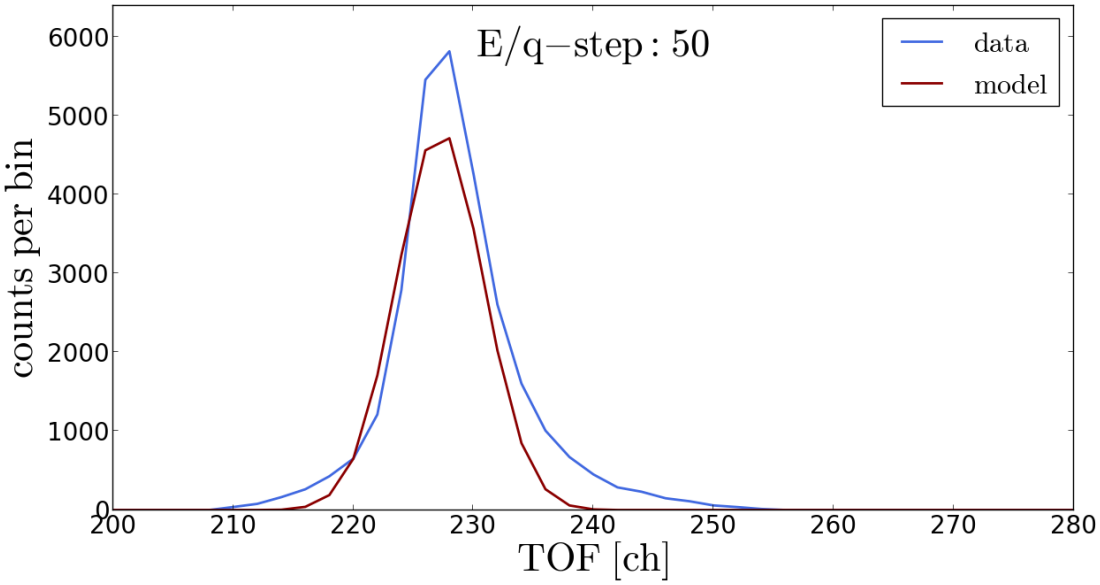

FIGURE 4.6: Comparison of the measured TOF histogram with the same 2D-Gaussian peak model fit as in Figure 4.5 (dark red line), but integrated over all ESSD bins at each given TOF bin.

iron sequence Fe^{7+} - Fe^{11+} which lie at the lower and upper boundary of the measurement range in mass and mass-per-charge. While He^{2+} is well separated from all other ions due to its low mass and mass-per-charge value, the selected iron species have by an order of magnitude higher abundances than the nearby elements calcium and nickel with comparable mass and mass-per-charge, so that the contamination of the main iron peaks due to the latter should be relatively small. Figures 4.5 - 4.8 show the fit of the Gaussian response model to the observed He^{2+} peak in the long-term data[6] accumulated over the full period DOY 174-220, 1996 at Epq-step 50. In the fit, the position and widths of the peak are calculated from the response model after equations 4.21, 4.23, 4.26, and 4.40, and only the count rate N is fitted as a free parameter, which is bijectively related to the height of the modeled peak. In Figure 4.5 the measured long-term data counts are visualized in the ET-matrix cut-out by the black contour lines while the fit is represented by the magenta contour lines. The black data contour lines correspond to $10^{-1/3}$, $10^{-2/3}$, 10^{-1}, $10^{-4/3}$, $10^{-5/3}$, 10^{-2} times the maximum data count rate C_{max} and the magenta contour lines show the corresponding count rate levels of the fitted count rate model $\widetilde{C}(\underline{N}, \underline{R})$.

In Figure 4.6, the solid blue line is the measured reduced count rate histogram for the time-of-flight measurement which is the count rate integral over all ESSD bins for each TOF bin. It can be compared to the reduced response model which is the integral over the fitted response model over all ESSD bins for each TOF bin. Note that the shown fit (dark red line) is *not* equal to a (reduced) fit of the TOF measurement alone, since the applied fit-model is the same as in Figure 4.5, defined on the full 2-dimensional ET space, and thus contains the full residual energy information.

In the fit we only include ET-bins $1 \leq k \leq n$ with sufficiently high measured count rate $C_k(\tau, \epsilon) \geq 10$ and each bin contains 2×2 channels in the ET-matrix as described in section 2.2. Due to the high counting statistics within the peak in general, the lower count rate limit is only a minor restriction for the determination of the peak shape, but it allows us to assume that the count rate uncertainty in each bin is approximately normally distributed around the measured value. Thus, the merit function to be minimized in the fit has the standard form of Eq. 4.13:

$$\chi^2 = \sum_{k=1}^{n} \left(\frac{(C_k - \widetilde{C}_k(N))^2}{\sigma_k^2} \right) \tag{4.28}$$

[6] In the case of He^{2+} the measured peak is almost entirely located in priority range PR5 so that no significant change of the peak shape due to the base rate correction occurs. Instead, due to the problematic reconstruction of the whole priority range PR5, the attempt to correct the count rate is more likely to introduce artificial bias. Therefore, we conduct the peak shape analysis for He^{2+} with the uncorrected count rate data as the accumulated count rate in the long-term PHA data is more than sufficient to assess the shape of the peak adequately.

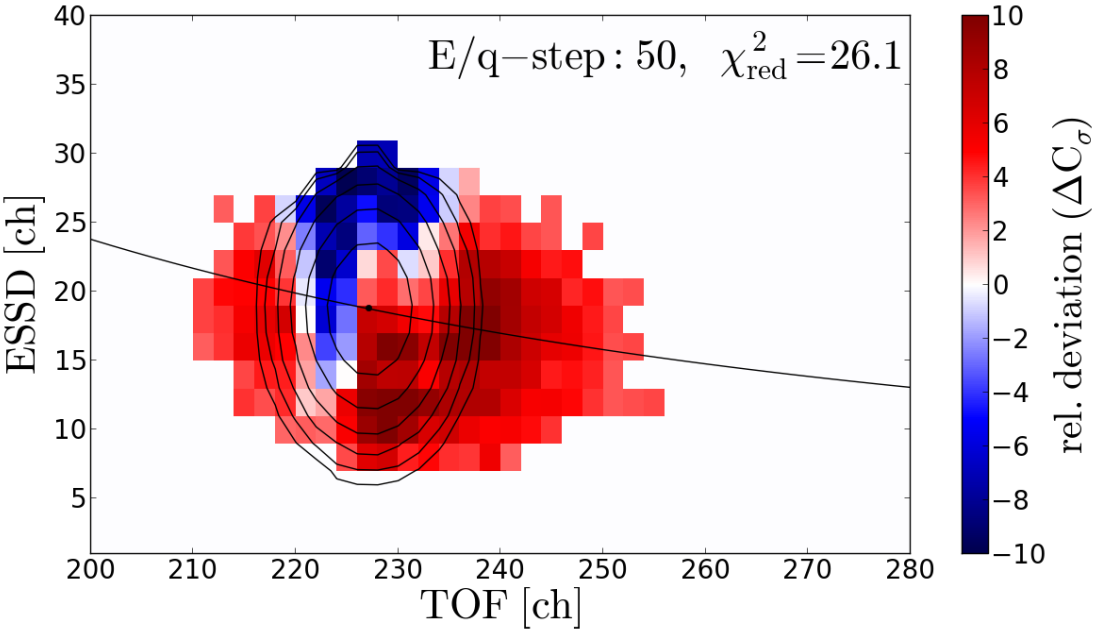

FIGURE 4.7: Relative deviation between long-term count rate data and model for the same 2D-Gaussian peak model fit as in Figure 4.5. The overlaid contour lines are the same model count rate levels as in Figure 4.5. See text for further explanations.

where n is the number of bins with sufficient count statistics and $\sigma_k = \sqrt{C_k}$[7] is the statistical count rate uncertainty derived from the measured count rate. The goodness-of-fit is then given by the reduced χ^2 which includes the number of contributing ET-bins and free parameters:

$$\chi^2_{red} = \frac{\chi^2}{n - n_p} \,. \tag{4.29}$$

where n_p is in general equal to the number of fitted ion species and therefore in the isolated He^{2+} case we have $n_p = 1$ and $n \approx 200$.

From Figure 4.5 and 4.6 we can see that the measured peak shape shows major deviations compared to the modeled peak shape. To quantify the deviations, in Figure 4.7 we show the fit residuals $\Delta C = C - \widetilde{C}$ in units of the count rate standard deviation, which we call the *relative deviation*

$$\Delta C_\sigma := \Delta C / \sigma \tag{4.30}$$

[7]Note, that when the fits are applied to the base-rate corrected PHA count rate, as it is the case for all minor heavy ions ($Z > 2$), the value σ_k has to be calculated as the square-root of the uncorrected count rate scaled with the base rate factor: $\sigma_k = \sqrt{C_{uncor} \cdot f_{br}} \geq \sqrt{C_{cor}} = \sqrt{C_{uncor} \cdot f_{br}}$ where f_{br} are the base rate factors calculated in appendix A.

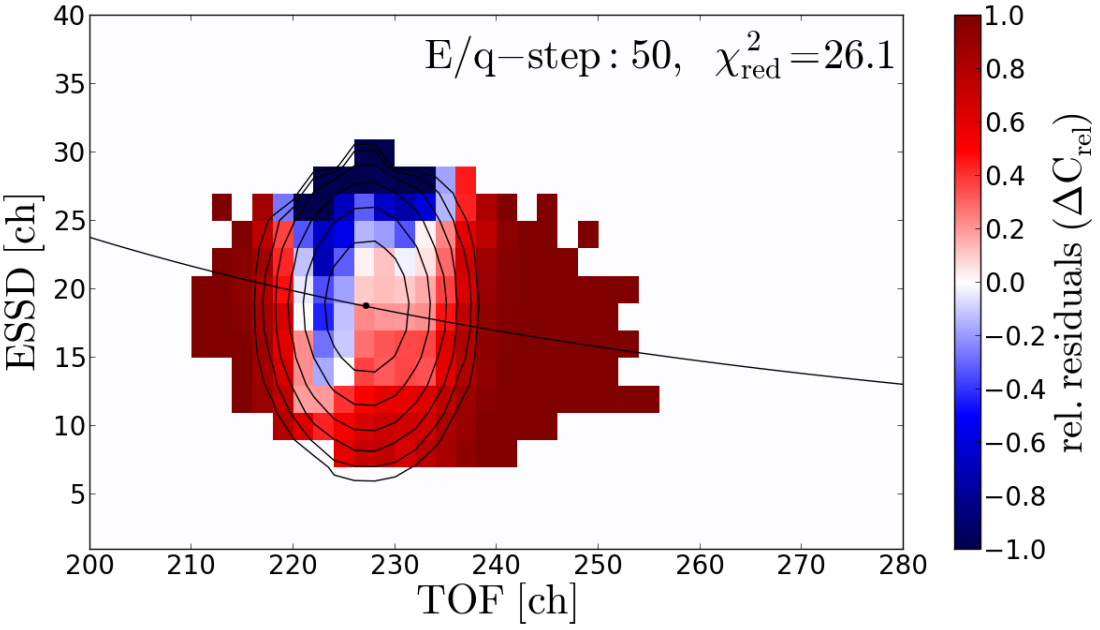

FIGURE 4.8: Relative residuals between long-term count rate data and model for the same 2D-Gaussian peak model fit as in Figure 4.5. The overlaid contour lines are the same model count rate levels as in Figure 4.5. See text for further explanations.

and in Figure 4.8 we show the residuals scaled by the measured count rate which we denote as the *relative residuals*

$$\Delta C_{rel} := \Delta C / C \,. \tag{4.31}$$

Both quantities ΔC_σ and ΔC_{rel} give us complimentary information and together with the absolute measured count rates C we can identify crucial systematic deviations between data and model that can lead to significant systematic errors in the resulting velocity distribution functions:

As ΔC_σ represents the contributions to the calculated χ^2-value per bin, it allows to estimate how likely it is that the actual measured count rates in a given area of the ET-matrix were sampled from the model. If the count rates are too unlikely to be statistical deviations, we can identify them as local systematic deviations from the model. On the other hand these systematic deviations do not need to cause large systematical errors in the resulting VDFs that we obtain from the total ion count rates N_{ij} over the whole E/q-range (see Eq. 3.2) as the count rates enter in the speed weights both in the enumerator and denominator: $w_{ij} = N_{ij} / \sum_j N_{ij}$. Thus, a large systematic error in the VDF can only occur if at a given Epq-step the measured absolute value N_{ij} is high but also the relative count rate error $\Delta N^{ij}_{rel} = \Delta N_{ij} / N_{ij}$ is large. For the latter the local sum

of the relative deviations $\sum_k \Delta C_{k,rel}$ is an upper estimate[8] of ΔN_{rel}^{ij} for the dominant ion species in a given area of the ET-matrix.

Hence, the analysis of all three quantities C, ΔC_σ and ΔC_{rel} together as shown in Figures 4.5, 4.7 and 4.8 can be used to identify systematic errors in the ion speed determination that arise from systematic errors in the response model. This can be achieved by spotting systematic count rate deviations (large ΔC_σ) in the high-count rate areas of the ET-matrix (large C) that are also large compared to the measured count rate (large ΔC_{rel}) and therefore might eventually sum up to large deviations $\Delta N_{ij}/N_{ij}$ of the measured ion species of interest. Yet, neither ΔC_σ nor ΔC_{rel} alone is sufficient for a crucial error identification under the given count rates C. This is because the observed deviations (ΔC) can be systematic but negligible for the VDF determination (happens frequently for high count rates per bin). On the other hand, the observed deviations can be significant for the VDF determination but not systematic (happens frequently for low count rates per bin), so that they cannot be improved by a better response model.

Analyzing Figures 4.5 - 4.8 in the explained way, we find large systematic deviations between the data and the Gaussian model both in the core and at the flanks of the He^{2+} peak. From the residual plots we find relative deviations up to $\Delta C_\sigma = 10(!)$ σ even at the highest count rates within the 10% model count level. These differences between data and model also yield large relative residuals of the average order of $\Delta C_{rel} = 40\%$ and up to $\Delta C_{rel} = 80\%$ of the count rate in the core. In the flanks of the peak we find that the largest relative deviations occur along the time-of-flight axis where the data peak shows tails which cannot be modeled adequately with the Gaussian model. In particular the pronounced tail at the high-TOF flank is largely underestimated for all energy channels which contributes to a large part to the overall underestimation of the count rate as we can see from Figure 4.6. On the whole, the assumed Gaussian peak shape model fails to reproduce the actual data resulting in a poor goodness-of-fit estimation of $\chi^2_{red} = 26(!)$ with an overall underestimation in count rate of about $\Delta N_{rel} \approx 25\%$ when we sum over the whole peak. As these differences are of comparable order in magnitude to the count rate itself, the observed systematic differences in the model can play a role in the calculation of the corresponding VDFs and the accurate determination of the VDF moments if they show a systematic pattern over the Epq-step range. This would be even more the case if the considered ion peak had an adjacent ion species in

[8] Note that there can be still systematic errors in the model without major deviations between C and $\widetilde{C}$, if one just mixes up the positions of species or adds species to the model that can a priori not occur in the solar wind. To avoid or at least minimize these misassignments it is important to apply a systematical calibration approach. Also for ion species that have small count rates N_{ij} compared to the dominant species at the given Epq-step, j, the relative error can be much larger if e.g. the whole count rate difference $\sum_k \Delta C_{k,rel}$ is assigned to the low-count rate species i. Therefore, naturally the dominant ion species with the highest abundances are the most reliable ones as only for these species major systematic deviations between model and data can be spotted reliably.

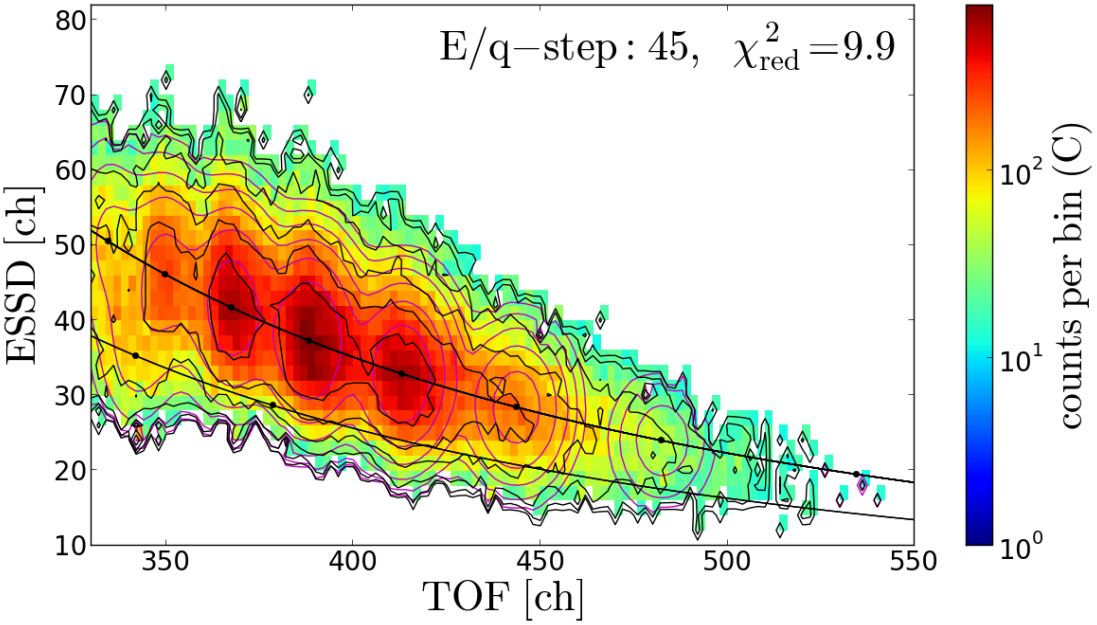

FIGURE 4.9: Fit of the 2D-Gaussian peak model to the measured main iron long-term data peaks Fe^{7+} - Fe^{11+}. In the fit we also include the adjacent species Si^{5+}, Si^{6+}, and Fe^{6+}, Fe^{12+}. The position and width parameters are taken from the calibrated CTOF standard response model as described in the previous sections and only the nine species count rates are fitted as described in Eq. 4.28. The black data contour lines correspond to $10^{-1/3}$, $10^{-2/3}$, 10^{-1}, $10^{-4/3}$, $10^{-5/3}$, 10^{-2} times the maximum data count rate C_{max}. The magenta contour lines show the corresponding count rate levels of the fitted count rate model $\widetilde{C}(\underline{N}, \underline{R})$. Only ET-bins with at least 10 actually transmitted PHA counts are considered.

its high-TOF flank with lower abundance. For this minor species a small percentage of non-assigned counts of the main peak could easily exceed its own absolute count rate and change completely the measured VDF as a pure effect of the response model accuracy. Yet, while the isolated He^{2+} is the best example to study the pure differences between model and data as no other ion species can compensate the observed deviations, it misses the essential point of overlapping peaks that we study in the following example of the iron ion sequence.

In contrast, the peaks of the aforementioned iron species ions Fe^{7+} - Fe^{11+} have strong overlap among each other and partially also with a few non-negligible silicon charge states. In Figures 4.9 - 4.12 we analyze the applied fit of the Gaussian response model in the same way as for the He^{2+} case. We fit only ET-matrix excerpts which contain in their center the well-resolved ion species Fe^{7+} - Fe^{11+} and include in addition the adjacent species Si^{5+}, Si^{6+}, and Fe^{6+}, Fe^{12+}. The figures clearly show that the two-dimensional Gaussian model is oversimplified as the asymmetric data contours barely match the model count contours. From the relative deviations in Figure 4.11 we see that

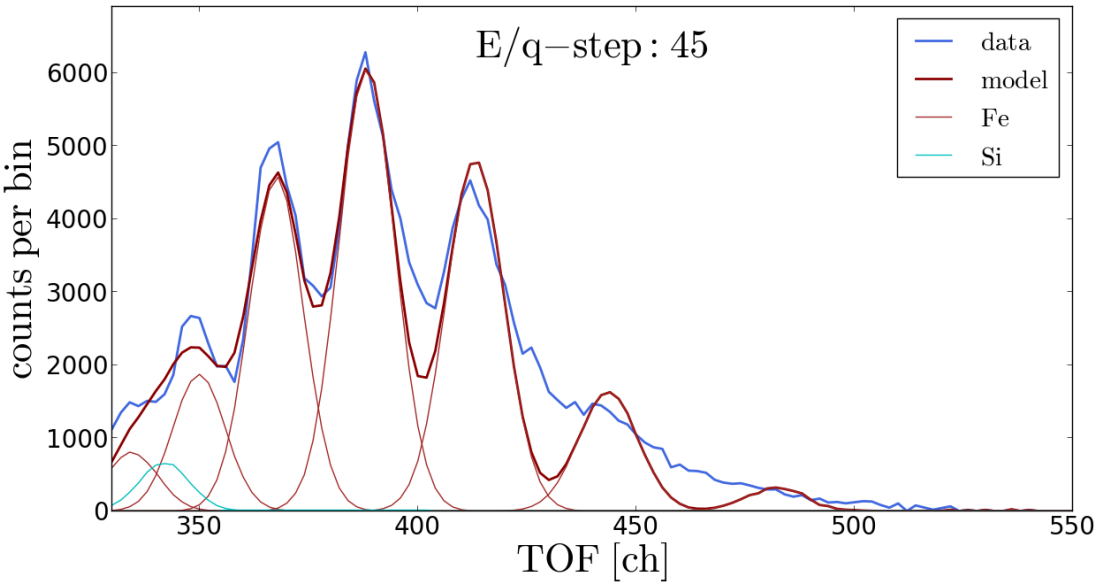

FIGURE 4.10: Comparison of the measured TOF histogram with the same 2D-Gaussian peak model fit as in Figure 4.9 (dark red line), but integrated over all ESSD bins at each given TOF bin. Also the individual species peaks are the energy-integrated peaks of their corresponding 2D-peaks which contribute to the overall model. Thus, the area of each individual peak equals the overall count rate of the peak and can be used for count rate comparison between the species at the given Epq-step. The red peaks are Fe^{12+} - Fe^{6+}, and the cyan peaks are Si^{6+} and Si^{5+} (from left to right, respectively).

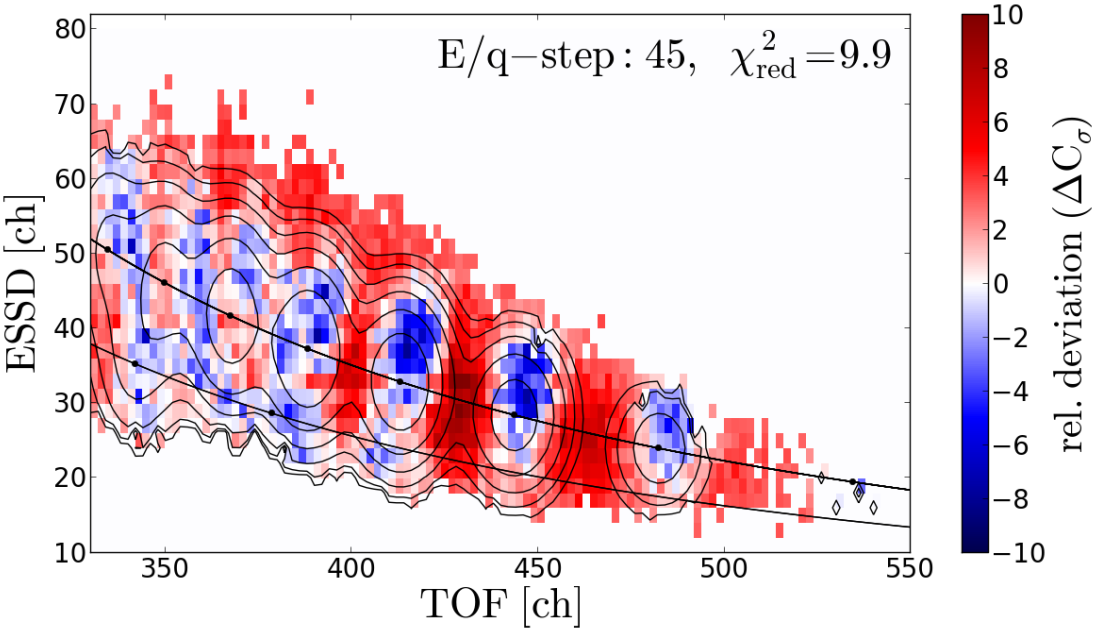

FIGURE 4.11: Relative deviation between long-term count rate data and model for the same 2D-Gaussian peak model fit as in Figure 4.9. The overlaid contour lines are the same model count rate levels as in Figure 4.9. See text for further explanations.

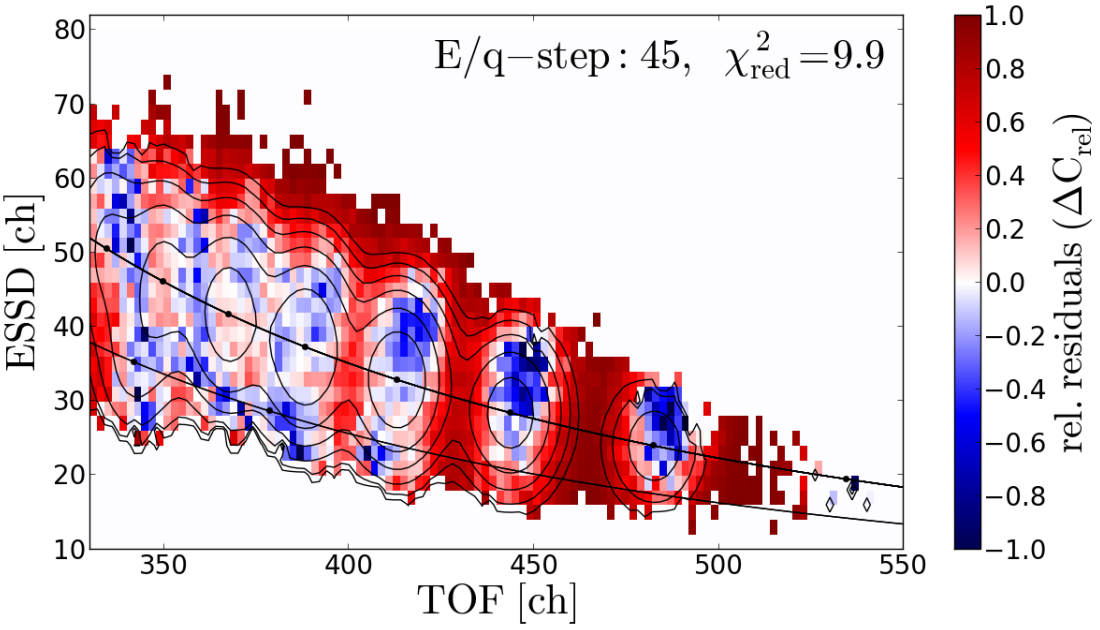

FIGURE 4.12: Relative residuals between long-term count rate data and model for the same 2D-Gaussian peak model fit as in Figure 4.9. The overlaid contour lines are the same model count rate levels as in Figure 4.9. See text for further explanations.

the model systematically underestimates the count rate of the time-of-flight channels between the iron peaks while at the peak centers the fit tries to compensate this effect with an overshoot in count rate. These large deviations up to values of $|\Delta C_\sigma| \approx 9$ lead to a poor goodness-of-fit value $\chi^2_{red} \approx 10$. Figure 4.12 shows that the observed systematic deviations are also large compared to the measured count rate and reach values up to $\Delta C_{rel} = 80\%$. Since also the absolute measured count rates are high in the described areas of massive model under- and over-estimation as can be seen from Figure 4.9, the deviations in count rate can in principle cause substantial errors in the resulting velocity distribution functions.

In Figure 4.13 we see that the long-term data fit of the iron sequence cannot be improved substantially by including additional minor ion species from the response model. In fact, the extended model yields relative abundances for Ni^{8+} and Ni^{9+} compared to the most abundant iron charge states Fe^{9+} - Fe^{11+} that are about an order of magnitude larger than expected from remote-sensing studies [Aschwanden, 2005] of the photosphere and corona. The counts that are thus (most probably) falsely assigned to nickel and other species are missing in the iron VDFs. From the detailed analysis of Figures 4.5 - 4.13, we could observe at least one major systematic deviation between model and data that occurred for all investigated ion peaks, which is the presence of pronounced tails at the high-TOF flank of the peaks. This feature can be seen already for He^{2+} but even more pronounced for all heavy minor ions (compare also O^{6+} in Figure 4.1)

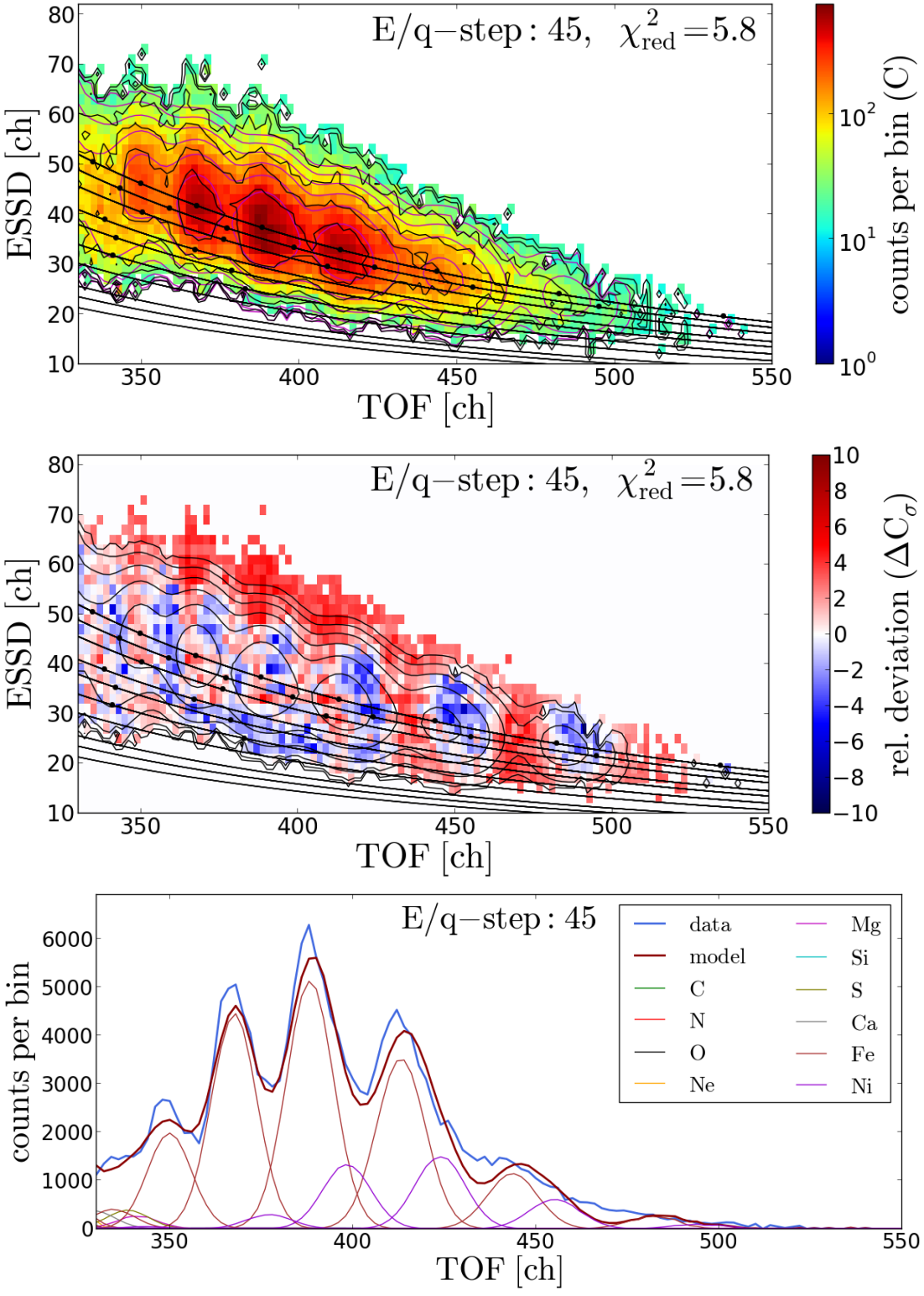

FIGURE 4.13: Fit of the 2D-Gaussian peak model to the measured main iron long-term data peaks Fe^{7+} - Fe^{11+}. In the fit we include all ion species of the listed elements carbon - nickel that lie in the wider vicinity of the iron peaks. The position and width parameters are taken from the calibrated CTOF standard response model as described in the previous sections and only the species count rates are fitted as described in Eq. 4.28. The three panels are analogous to Figures 4.9, 4.11 and 4.10. We omitted the relative residuals here for brevity, but a similar comparison is given in Figure 4.24 for the whole ET-matrix at Epq-step 55.

and in particular for the investigated iron ions. The formation of high-TOF (or equivalently low-energy) tails can be well-understood in a qualitative manner as the result of multiple effects that are inherent to the measurement principle of time-of-flight mass spectrometers based on the carbon-foil technique:

1. The electronic energy loss of an ion event in a thin target such as the foil cannot be described by a Gaussian, but more accurately by a Landau-distribution [Landau, 1944] that already shows an asymmetrical tail towards low energies.

2. In addition to the electronic energy loss, the ions also lose energy to the target nuclei via elastic collisions. Since the nuclear interactions are more effective for heavier ions at lower energies [Ziegler et al., 2008] this effect is not negligible at solar wind energies (even after the post-acceleration) and leads to an increased low energy tail for many species.

3. The transformation from the residual energy distribution (after the carbon foil) to time-of-flight is not symmetrical, but equally wide energy bins translate into TOF bins with increasing width with decreasing energy[9]. This leads automatically to more pronounced high-TOF flanks even for the case of a symmetrical residual kinetic energy distribution of the ions after the foil.

4. In addition to the energy loss, even the pure scattering in the carbon foil leads to an asymmetrical time-of-flight distribution. This can be easily recognized by the fact that at each Epq-step there is a well-defined minimum time-of-flight for those ions that pass the foil without any scattering, but in principle no upper limit for the time-of-flight exists.

On a quantitative level the situation is complicated and therefore, simulations such as TRIM are commonly used to assess the first, second and fourth point simultaneously. Unfortunately, for our case of very low ion speeds compared to most other applications, already the widths of the time-of-flight peaks could not be estimated accurately by TRIM [Janitzek, 2014] so we cannot assume that the simulation is an accurate quantitative prediction of the peak shape.
Yet, we need to include the observed tails into the response model as we showed that the fraction of potentially assigned counts is not negligible compared to the number of overall counts assigned for certain species. In the past, a few empirical approaches were made to describe the observed peak shape of certain ion species more accurately.

[9] This can be seen by expressing the time-of-flight as a function of the residual kinetic energy after the foil: $\tau(E_{res}) = \sqrt{mL_\tau^2/(2E_{res})}$ and then simply calculating the absolute value of the derivative which leads to $|dT| = \sqrt{mL_\tau^2/8} \cdot E^{-3/2}|dE|$.

As an example [Koeten, 2009] parametrized the He^{2+} peak shape measured with the ACE/SWICS instrument very accurately with a larger set of empirical parameters in order to use this parametrization for the characterization of the much less abundant C^{4+}_{13} isotope signal. In the case of CTOF [Aellig, 1998b] analyzed the iron data for the period DOY 185-220, 1996 by applying an asymmetric Gaussian fit to the TOF measurement with two different σ_τ-values for the low-TOF and high-TOF flank, respectively. While the approach by [Koeten, 2009] is not feasible for a response model with a large number of ion species due to the high number of parameters per peak, the asymmetric Gaussian peak shape applied by [Aellig, 1998a] still yields relatively large deviations from the actual observed peak shape, in particular when a larger part of the iron sequence is fitted simultaneously and the full 2-dimensional ET-information is used. Therefore, we develop in the following section an alternative analytical peak shape model which allows a more accurate description of the observed peak-tails based on a small set of parameters that can be scaled easily for all solar wind ion species.

An Improved Peak Shape Model for CTOF

As the starting point for our model we choose a parametrization of the Moyal function [Moyal, 1955] to model the high-TOF flank of the observed ion peaks:

$$R^{ij}_{\tau\geq\tau_0} = M^1(\tau_0^{ij}, \sigma_\tau^{ij}, c_\tau^{ij}, \tau) = N \cdot \exp\left[-\frac{1}{2}\left(\frac{(\tau-\tau_0^{ij})}{c_\tau^{ij}\cdot\sigma_\tau^{ij}} + \exp\left(-\frac{(\tau-\tau_0^{ij})}{c_\tau^{ij}\cdot\sigma_\tau^{ij}}\right)\right)\right] \quad (4.32)$$

where τ_0^{ij} and σ_τ^{ij} are the TOF position and width-parameter for ion species i at Epq-step j obtained from Eq. 4.25 and 4.26, respectively. To adapt the high-TOF flank of the model to the observed peak tails, R^{ij} includes the additional scaling parameter ${c_\tau}^{ij}$ that still has to be determined empirically. The normalization $N = e^{-1/2}$ is chosen so that M^1 reaches its maximum at a value of 1.

For most heavy elements the low TOF-flanks of their well-observable ion peaks show no significant deviations from a Gaussian peak shape (and in fact were even better modeled than with a Moyal function) as we find from the fits of the reference ions O^{6+}, Si^{7+}, Si^{8+} and Fe^{8+} - Fe^{10+}. The only exceptions are the two lightest calibrated elements helium and carbon for which we find small low-TOF flanks. These can be well-observed for He^{2+} (as seen in Figure 4.6) and C^{6+}, but not particularly well for He^{+}, C^{4+} and C^{5+} as the pick-up ion species has lower count rates and is disturbed by the SSD energy threshold and the carbon species have major adjacent ion peaks O^{6+} and O^{7+} at their low-TOF flank, respectively. Therefore, we model the low TOF-flank

with the general approach of a Kappa-function:

$$R^{ij}_{\tau\leq\tau_0} = K^1(\tau_0^{ij}, \sigma_\tau^{ij}, \kappa_\tau^{ij}, \tau) = \left[1 + \frac{1}{2\kappa_\tau^{ij}}\left(\frac{\tau_0^{ij} - \tau}{\sigma_\tau^{ij}}\right)^2\right]^{-\kappa_\tau^{ij}} \tag{4.33}$$

which becomes a regular Gaussian in the limit of infinitely high κ_τ^{ij}-values:

$$\forall\ \tau_0^{ij}, \sigma_0^{ij}, \tau \in \mathbb{R} : \lim_{\kappa_\tau^{ij}\to\infty} K^1((\tau_0^{ij}, \sigma_\tau^{ij}, \kappa_\tau^{ij}, \tau)) = G^1(\tau_0^{ij}, \sigma_\tau^{ij}, \tau) \tag{4.34}$$

where the index 1 just denotes that both functions are already normalized to a maximum value of 1. We find that both for the helium and C^{6+} peaks the observed low-TOF flanks do not change systematically over the observed Epq-steps and can therefore be described with an element-specific constant

$$\kappa_\tau^{ij} = \kappa_\tau^{i} = \begin{cases} 1.5 & \text{if } Z = 2 \\ 1.8 & \text{if } Z = 6 \\ 10 & \text{if } Z > 6 \end{cases} \tag{4.35}$$

where the value $\kappa_\tau = 10$ is just chosen high enough so that we cannot find any difference between a Gaussian and a Kappa-flank within the given TOF measurement resolution. We admit that in contrast to the well-justified high-TOF flanks we have no secured theory of the instrumental origin of the small low-TOF (or high energy) flanks, but the low-TOF flanks are much less pronounced than the high-TOF tails and do not play a role for the vast majority of measured ion species. So we do not investigate this point further and also approximated nitrogen with the Gaussian flank as no clear low-TOF flank observations are possible for this element.

With the described functions K^1 and M^1 the new peak shape function in time-of-flight can be written as

$$R_\tau(\tau_0^{ij}, \sigma_\tau^{ij}, \kappa_\tau^{ij}, c_\tau^{ij}, \tau) = \begin{cases} K^1(\tau_0^{ij}, \sigma_\tau^{ij}, \kappa_\tau^{ij}, \tau) & \text{if } \tau \leq \tau_0 \\ M^1(\tau_0^{ij}, \sigma_\tau^{ij}, c_\tau^{ij}, \tau) & \text{if } \tau \geq \tau_0 \end{cases} \tag{4.36}$$

As can be seen from Figures 4.5 and 4.9 the He^{2+} and iron peaks also show a small asymmetry along the residual energy axis but they are skewed in the opposite direction so that we neglect this point for the general model. What we see in both cases is that the tails are not exactly pointing along the TOF axis but the counts are smeared out

along the elemental hyperbolae, causing part of the asymmetry along the ESSD axis. This effect can be explained by the fact that both TOF and ESSD measurement are not independent of each other but those particles which lose a larger amount of energy in the carbon foil are measured on average both at higher TOF channels and lower ESSD channels. We can take this effect into account by keeping in principle the Gaussian shape along the energy-axis

$$R_\epsilon(\epsilon_0^{ij}, \sigma_\epsilon^{ij}, \epsilon) = G^1(\epsilon_0^{ij}, \sigma_\epsilon^{ij}, \epsilon) \,, \tag{4.37}$$

but substituting the fixed energy position ϵ_0^{ij} at each TOF-bin τ with a τ-dependent value by generalizing Eq. 4.24 to[10]

$$\epsilon_0(\tau) = A_\epsilon \cdot \alpha_\epsilon^i \frac{m_i \cdot L_\tau^2}{(A_\tau \cdot \tau + B_\tau)^2} \,. \tag{4.38}$$

By expressing the ESSD position as a function of the TOF-bin, the energy signal is always normally distributed around the most probable ESSD bin for each TOF bin

$$R_\epsilon(\sigma_\epsilon^{ij}, \tau, \epsilon) = G^1(\epsilon_0(\tau), \sigma_\epsilon^{ij}, \epsilon) \,, \tag{4.39}$$

and the tails of the peak follow the curvature of the elemental hyperbolae given by Eq. 4.24. Finally, due to the new peak shape we need to refine the energy peak widths σ_ϵ^{ij} in Eq. 4.39. For this reason we vary all ion widths simultaneously with a linear factor $\sigma_{\epsilon,rel}$ for a wide range of Epq-steps and find the optimal scaling factor $\sigma_{\epsilon,rel} = 0.85$ for the Kappa-Moyal model compared to the Gaussian model. Thus, the final energy width calibration for the Kappa-Moyal model for all ion species i at all Epq-steps j reads

$$\sigma_\epsilon^{ij} = \sigma_{\epsilon,rel} \cdot \left(A_{\sigma_\epsilon} \cdot \epsilon_{i,j} + B_{\sigma_\epsilon}\right) \,. \tag{4.40}$$

where $A_{\sigma_\epsilon} = 0.102$ and $B_{\sigma_\epsilon} = 2.368$ ch are the same constants as in Eq. 4.27.
Thus, the new 2-dimensional *Kappa-Moyal* peak shape model reads:

$$R(\underline{P}_{ij}, \tau, \epsilon) = N \cdot R_\tau(\tau_0^{ij}, \sigma_\tau^{ij}, \kappa_\tau^{ij}, c_\tau^{ij}, \tau) \cdot R_\epsilon(\sigma_\epsilon^{ij}, \tau, \epsilon) =: R_{KM}(\underline{P}_{ij}, \tau, \epsilon) \,. \tag{4.41}$$

where $\underline{P}_{ij} = [\tau_0^{ij}, \sigma_\tau^{ij}, \kappa_\tau^{ij}, c_\tau^{ij}, \sigma_\epsilon^{ij}]$ is the individual parameter vector for each ion species i at a given Epq-step j that fully determines the individual response function R_{ij}, and N is a normalization that has to be chosen adequately for each combination (i, j) so that $\sum_{\tau,\epsilon} R_i(\tau, \epsilon) = 1$ holds.

As κ_τ^{ij} is defined in Eq. 4.35 for all species and all other parameters of the new peak

[10] Note that this generalization is only possible because in Eq. 4.24 the ESSD position ϵ_{ij} does not depend explicitly on the Epq-step but is completely defined by the TOF position τ_{ij}.

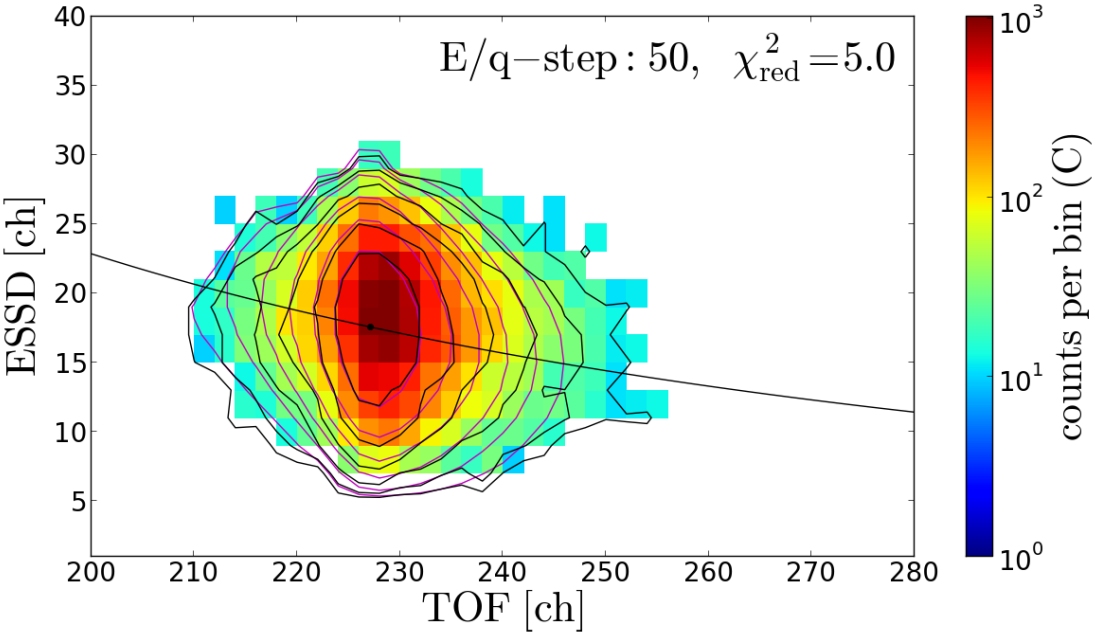

FIGURE 4.14: Fit of the Kappa-Moyal peak model to the measured He^{2+} long-term data peak. The black data contour lines correspond to $10^{-1/3}$, $10^{-2/3}$, 10^{-1}, $10^{-4/3}$, $10^{-5/3}$, 10^{-2} times the maximum data count rate C_{max}. The magenta contour lines show the corresponding count rate levels of the fitted count rate model $\widetilde{C}(\underline{N}, \underline{R})$. Only ET-bins with at least 10 actually transmitted PHA counts are considered.

shape model are well determined from the standard Gaussian peak shape model, the only remaining problem is to find an adequate parametrization of the tail parameter c_τ. Similar to the peak width parametrization of the Gaussian peak model, we can assume that for a given element all charge states should show the same peak shape when their peak is measured at the same position in the ET matrix. So that we can express c_τ as a function of the TOF position and this function should increase monotonically with increasing TOF position because the tails become more pronounced with decreasing particle energies. As a simple ansatz we choose a linear parametrization over the whole TOF-range of interest:

$$c_\tau(\tau) = A_C \cdot \tau \tag{4.42}$$

with a fixed constant $A_C > 0$ which can be different for each element.
To obtain the optimal tail parametrization for iron we scan the one-dimensional parameter space for A_c by fitting the iron peak sequence with a set of Kappa-Moyal response models $\underline{R}_{KM}(A_C)$ with increasing values A_C and select the A_C value that gives the lowest χ^2_{red} in the minimization after Eq. 4.15. As an additional condition we require that the selected A_c value has to stay relatively constant over the whole range of Epq-step

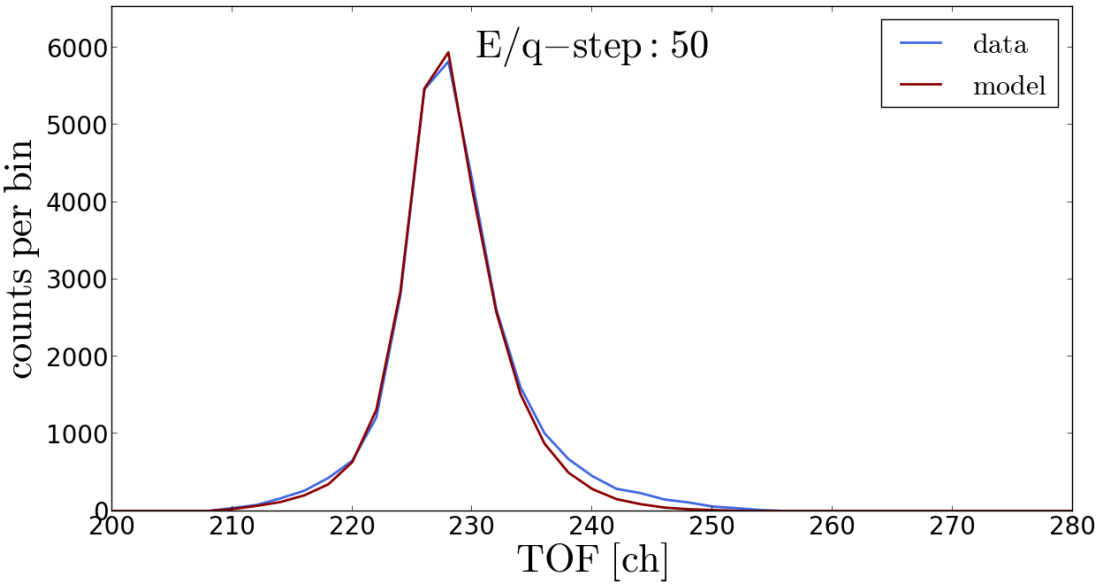

FIGURE 4.15: Comparison of the measured TOF histogram with the same Kappa-Moyal peak model fit as in Figure 4.14 (dark red line), but integrated over all ESSD bins at each given TOF bin.

39 to 60 which is the most relevant Epq-range for the iron species at solar wind speeds. In order to neglect contributions from most other ion species we only fitted at each Epq-step excerpts of the ET-matrices which contain in their center the well-resolved ion species Fe^{7+} - Fe^{11+} and include in addition the adjacent species Si^{5+}, Si^{6+}, and Fe^{6+}, Fe^{12+} in the same way as in Figure 4.9. For iron we find an optimal value of $A_c = (0.0040 \pm 0.0010)\ \mathrm{ch}^{-1}$ where we consider the fluctuation of the value over the Epq-step range as the uncertainty. This uncertainty is sufficiently small as it translates into a difference in peak volume of less than 10%, if we consider the change of the iron TOF response function R_τ given in Eq. 4.36 with typical iron peak TOF parameters $\tau_0 = 380\,\mathrm{ch}$ and $\sigma_\tau = 6\,\mathrm{ch}$. As a lower estimation for the lighter ion species we applied the same approach to the well-separated He^{2+} peak for the Epq-step 40 to 80 which yields the optimal value of $A_c = 0.0035 \pm 0.0005\ \mathrm{ch}^{-1}$ with a deviation that is even lower than for iron because the flanks of the He^{2+} peak are not contaminated by other species. Unfortunately, the He^{+} peak could not be used for a meaningful estimation of A_c because it shows major irregularities in its peak shape (in particular a double peak structure along the ESSD axis for many Epq-steps) as it lies very close to the energy threshold of the SSD. For most other elements such as neon, magnesium or silicon a direct estimation of the peak parameter is also problematic as they have less visible tails than iron and significant overlap with their adjacent ion species. The only exception is the O^{6+} peak which due to its very high relative abundance allows at least an estimation of the upper limit of the scaling parameter as $A_c \leq 0.0035$, even if there is a contribution of N^{5+} in its high-TOF flank. From these estimations we find

that the observed deviation between the A_c-values for different elements is within the uncertainty of the scaling parameter. Hence, we conclude that within the limitations of this strongly simplified model there is actually no significant evidence for an elemental dependence of the scaling parameter so that we obtain the universal value of $A_c = 0.0035\,\mathrm{ch}^{-1}$ for all elements and thus the high-TOF tails scale only with the TOF position of the peak. This observation is not obvious as one would rather expect an explicit mass dependence of the tails. However, it is phenomenologically similar to the observed behavior of the TOF widths in the Gaussian peak model parametrization that do not show any major dependence on ion mass, either. One way to explain this finding is that the most abundant ion species that dominate the estimation of both parameters σ_τ and A_c are ordered approximately on a diagonal in the ET-matrices, so that it is hard to disentangle the dependencies on mass or atomic number (that scale with ESSD) and time-of-flight with our simple parametrizations. Deeper insights could be achieved here by a detailed analysis of the peak shapes of Mg^{10+} and (if the SSD threshold effects can be understood) He^+, as these species are relatively abundant and are the ones which lie most off of this diagonal. Yet, in this work we use the tail scaling parameter A_C for all ion species since He^{2+} and the analyzed iron ions mark the lower and upper limits of the measurement range both in TOF and ESSD and thus the generalization can be considered as interpolation.

As the Kappa-Moyal peak shape model is now completely parametrized we can evaluate it in the same way as the Gaussian model. In Figures 4.14 - 4.17 we show the fit of the new peak shape model to the long-term data He^{2+} peak at the same Epq-step 50 as in Figure 4.5. We see from Figure 4.14 that over all the peak is modeled significantly better compared to the Gaussian model in Figure 4.9 as the contour lines match well for all flanks down to the 10% count rate level and partially beyond. We also find that the observed deviations are on average more than a factor of 2 lower for almost all parts of the peak so that we find a goodness-of-fit value $\chi^2_{red} = 5$ that is about five times lower than for the Gaussian model. On the other hand this value is still much larger than a value for a truly good model $\chi^2_{red} \gtrapprox 1$ and we (still) observe in Figure 4.16 several areas of the data peak that show significant systematic deviations from the model, e.g. at the low-ESSD flank around channels ($\tau = 227\,\mathrm{ch}$, $\epsilon = 10\,\mathrm{ch}$), at the low-ESSD/high-TOF flank around ($\tau = 233\,\mathrm{ch}$, $\epsilon = 14\,\mathrm{ch}$), or further out at the high-TOF flank for all ET-bins with $\tau > 240\,\mathrm{ch}$. Hence, the measured count rate data on the whole is still very unlikely to be sampled from the exact model peak shape. This is not so surprising as we cannot really model the peak shape from first principles as discussed in the previous subsection, but rather made the approach of a simple and scalable model that should just catch the main systematic deviations. Therefore, following our analysis in

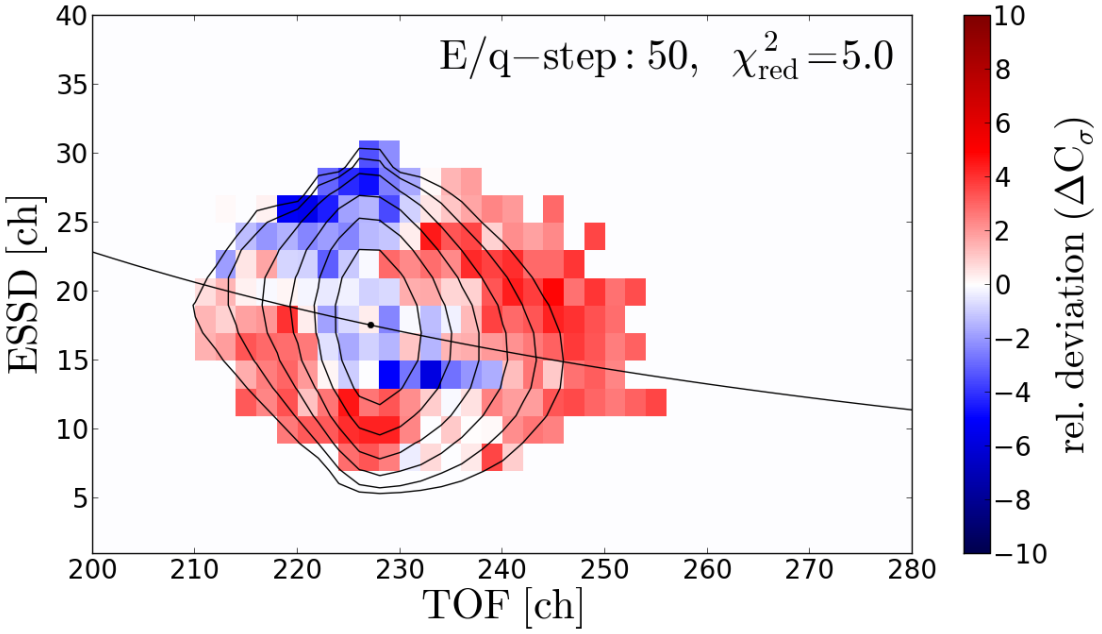

FIGURE 4.16: Relative deviation between long-term count rate data and model for the same Kappa-Moyal peak model fit as in Figure 4.14. The overlaid contour lines are the same model count rate levels as in Figure 4.14. See text for further explanations.

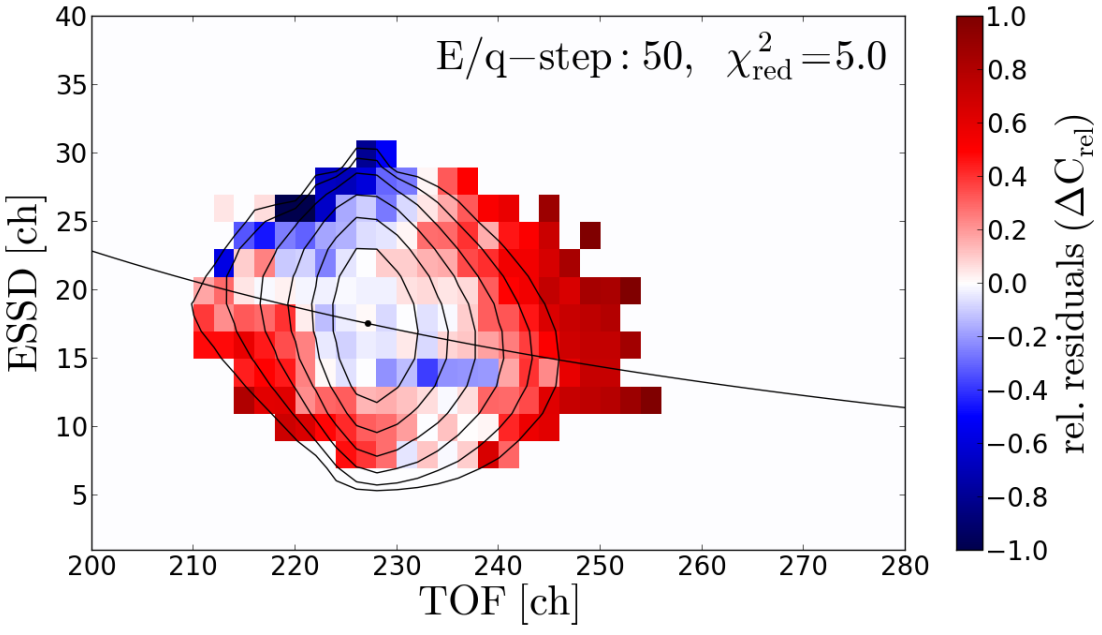

FIGURE 4.17: Relative residuals between long-term count rate data and model for the same Kappa-Moyal peak model fit as in Figure 4.14. The overlaid contour lines are the same model count rate levels as in Figure 4.14. See text for further explanations.

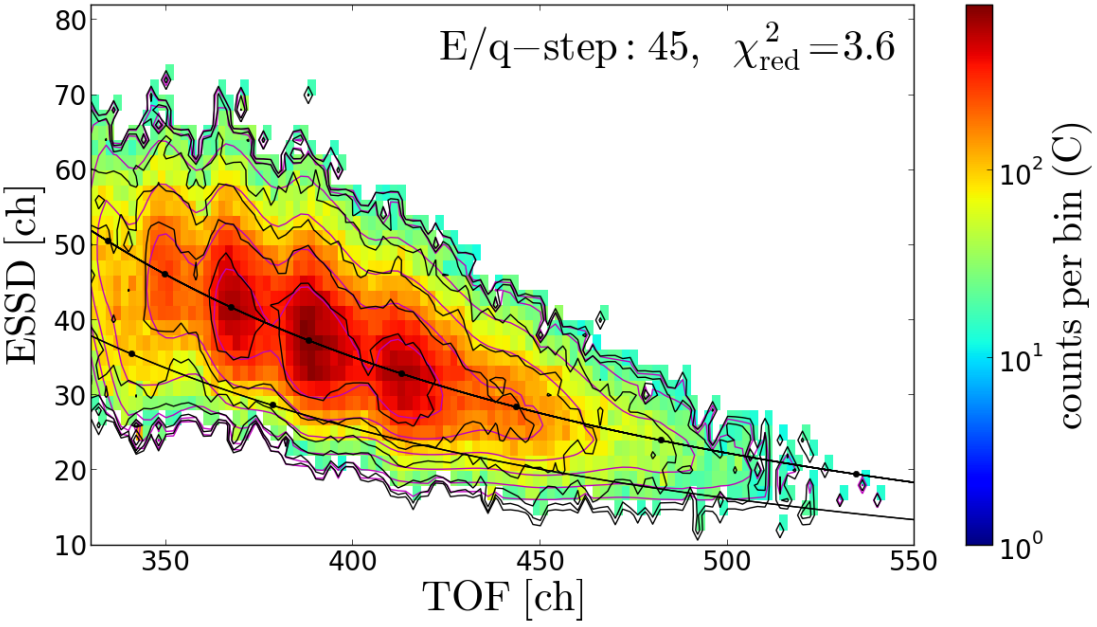

FIGURE 4.18: Fit of the Kappa-Moyal peak model to the measured main iron long-term data peaks Fe^{7+} - Fe^{11+}. In the fit we also include the adjacent species Si^{5+}, Si^{6+}, and Fe^{6+}, Fe^{12+}. The black data contour lines correspond to $10^{-1/3}$, $10^{-2/3}$, 10^{-1}, $10^{-4/3}$, $10^{-5/3}$, 10^{-2} times the maximum data count rate C_{max}. The magenta contour lines show the corresponding count rate levels of the fitted count rate model $\widetilde{C}(\underline{N}, \underline{R})$. Only ET-bins with at least 10 actually transmitted PHA counts are considered.

the previous subsection we now have a look at the relative count rate differences in Figure 4.17 in order to estimate how strongly the observed systematic deviations can affect the overall count rate. We find that in the area within the 10% count rate contour level which contains about 90% of the total peak count rate, there is only one ET-bin that is more than 30% off the model value and the average deviation is now about 10% of the count rate for all of these ET-bins. Large deviations on the order of the count rate $\gtrapprox$ 50% can be found only around and beyond the 1% model count rate contour level. This yields that the possible count rate deviations are on the maximum order of a 10% effect. If these deviations show a systematic increase or decrease with the Epq-step (which is the worst case scenario) their impact is comparable to the (small) effect that speed dependent detection efficiencies can have on the measured VDFs and their moments (see section 4.8).

We continue the Kappa-Moyal peak model evaluation with the iron sequence Fe^{7+} - Fe^{11+}. In Figures 4.18 - 4.22 the individual ion response functions have the form of the new peak shape model with the only exception that along the energy axis we used a

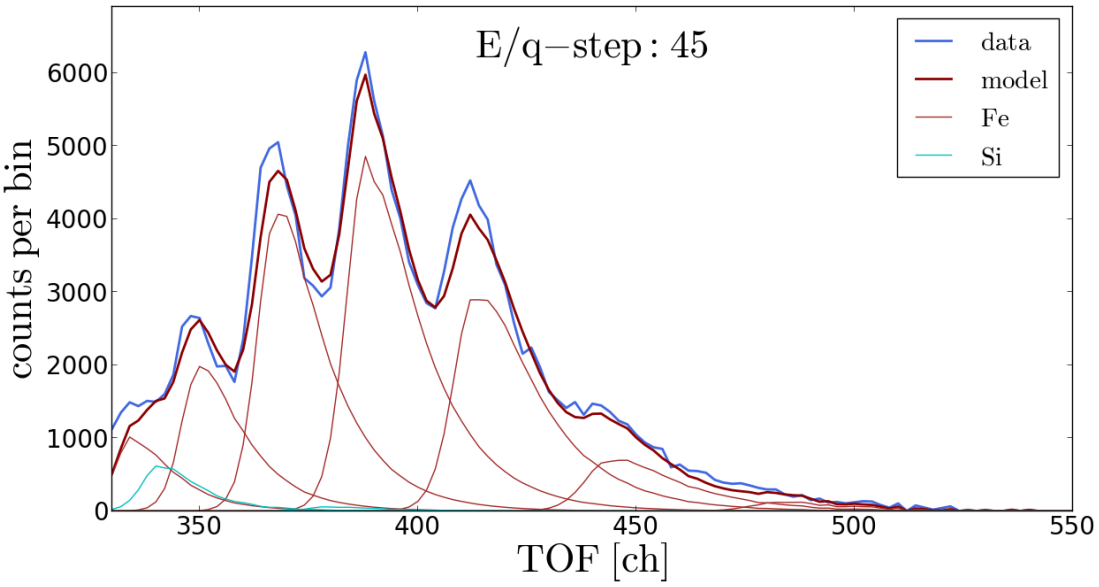

FIGURE 4.19: Comparison of the measured TOF histogram with the same Kappa-Moyal peak model fit as in Figure 4.18 (dark red line), but integrated over all ESSD bins at each given TOF bin. Also the individual species peaks are the energy-integrated peaks of their corresponding 2D-peaks which contribute to the overall model. Thus, the area of each individual peak equals the overall count rate of the peak and can be used for count rate comparison between the species at the given Epq-step. The red peaks are Fe^{12+} - Fe^{6+}, and the cyan peaks are Si^{6+} and Si^{5+} (from left to right, respectively).

Gaussian with two different width parameters $\sigma_{\epsilon,up}$, $\sigma_{\epsilon,low}$[11] for R_ϵ instead of the regular Gaussian G_ϵ to model better the high energy flank of iron. The exact modeling of the upper energy flank is possible since there are no elements of comparable abundance expected that lie at higher energy channels than iron. For R_τ we use the same expression as in Eq. 4.36 with the universal tail scaling parameter $A_c = 0.035$ ch^{-1}. In the fit we included the same ET matrix excerpt as for the Gaussian peak model with the same ion species Si^{5+}, Si^{6+} and Fe^{5+} - Fe^{12+}.

Similar to the He^{2+} case, we find that the Kappa-Moyal peak model reflects better the observed shape of the iron ion peaks, so that the observed gaps and overshoots of the model along the TOF axis are not present anymore and the vast majority of ET-bins within the 10% count-level area shows a relative deviation of less than 3σ. As can be seen from Figure 4.21 also the relative count rate difference within this area shows little fluctuation so that it rarely exceeds a value of 0.2 and has an average value even below 0.1. It is a good indicator that also the count contributions among the iron ion species are modeled consistently. The only part of the fitted ET-matrix excerpt where the model

[11] The ESSD-position dependent scaling for $\sigma_{\epsilon,up}$, $\sigma_{\epsilon,low}$ is given in Eq. B.3 - B.5 in the appendix.

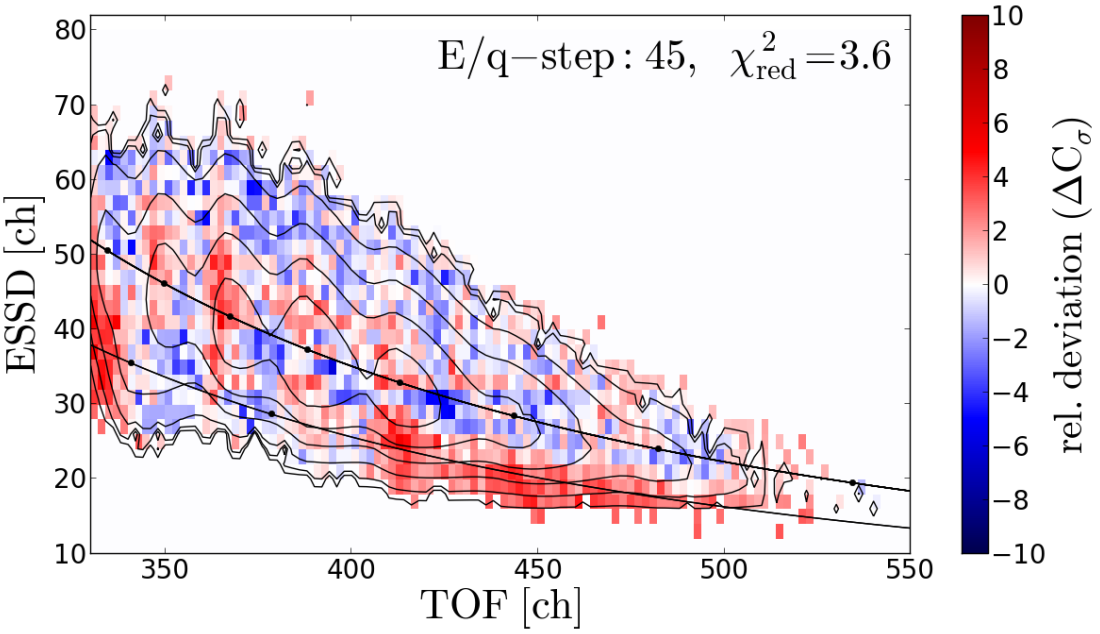

FIGURE 4.20: Relative deviation between long-term count rate data and model for the same Kappa-Moyal peak model fit as in Figure 4.18. The overlaid contour lines are the same model count rate levels as in Figure 4.18. See text for further explanations.

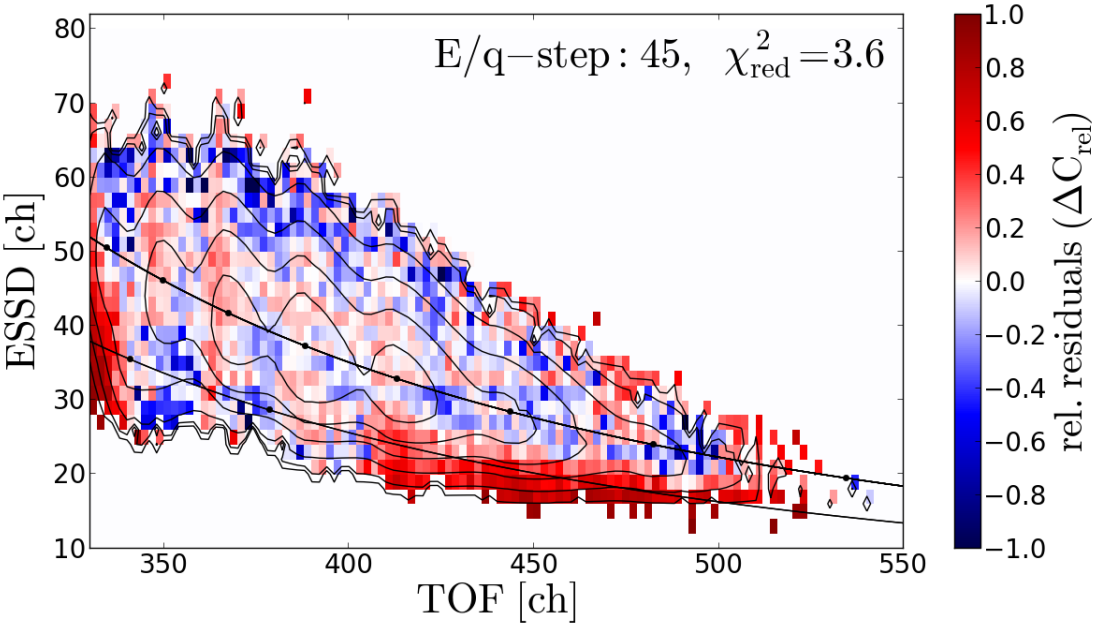

FIGURE 4.21: Relative residuals between long-term count rate data and model for the same Kappa-Moyal peak model fit as in Figure 4.18. The overlaid contour lines are the same model count rate levels as in Figure 4.18. See text for further explanations.

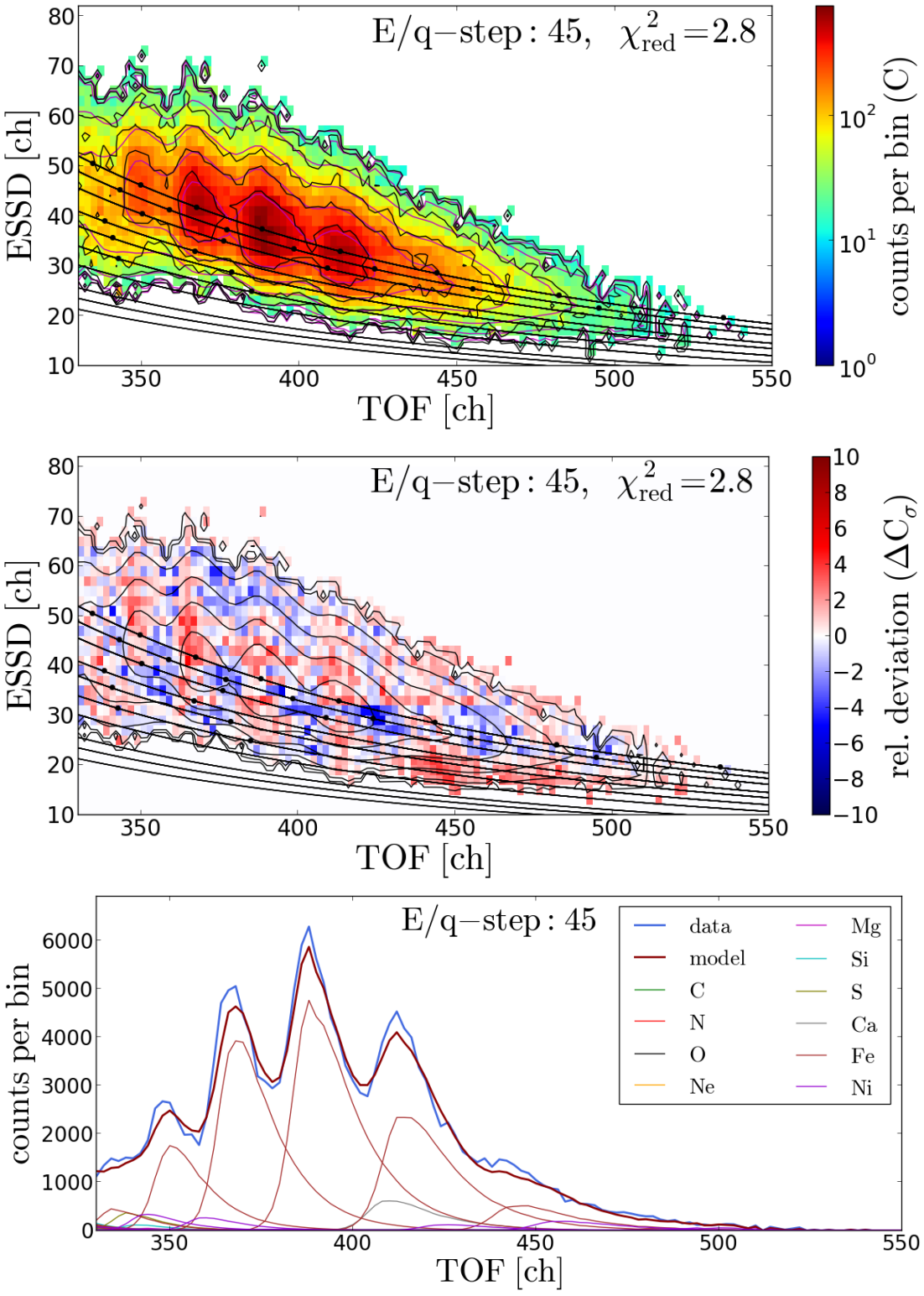

FIGURE 4.22: Fit of the Kappa-Moyal peak model to the measured main iron long-term data peaks Fe^{7+} - Fe^{11+}. In the fit we include all ion species of the listed elements carbon - nickel that lie in the wider vicinity of the iron peaks. The three panels are analogous to Figures 4.18, 4.20 and 4.19. We omitted the relative residuals here for brevity, but a similar comparison is given in Figure 4.23 for the whole ET-matrix at Epq-step 55.

deviates stronger from the data is in the area $\tau \geq 410$ ch and $\epsilon \approx 20$ ch where the model underestimates the lower energy flanks of Fe^{7+} and Fe^{8+}. However, this part of the ET matrix is also contaminated by helium random coincidences that we discuss in section 4.7, so that this is not necessarily a problem of the peak shape model itself. The overall goodness-of-fit value is calculated as $\chi^2 = 3.6$ and is therefore about 3 times lower than for the Gaussian peak shape model.

When we compare Figure 4.19 with Figure 4.10 we find that the iron ions' count rate contributions to each of the observed peaks are modified due to the asymmetric tails. Each ion peak gives a substantial contribution to the peak at its high-TOF flank, so that the formerly observed gaps between the peaks are closed and a smooth tail at very high-TOF channels is formed with contributions from several ion species. This also means that the count rate of the ion species that are on the high-TOF flank of a larger peak tend to lose systematically in count rate while those at the low-TOF flank tend to gain counts in comparison to the Gaussian fit. In the demonstrated case in the given Epq-step this is seen best for Fe^{12+} which was most under-estimated by the Gaussian model while Fe^{7+} was most over-estimated. Furthermore, we can see from Figure 4.22 where we included the same additional ion species as in Figure 4.13 that the count rates of Ni^{8+} and Ni^{9+} have decreased dramatically compared to the Gaussian model fit and all nickel charge states are now on the order of 1-10% compared to the most abundant iron charge states. This is in good agreement with the coronal abundance ratio of 5% [Aschwanden, 2005] between iron and nickel that is found from remote-sensing data. Yet, we also would expect the shown calcium peaks have count rates comparable to nickel, but Ca^{6+} still shows a higher count rate even if it is considerably lower than those of nickel in Figure 4.13. This shows that also the improved peak model has its limitations, but we recall that nickel and calcium are among the elements with the lowest relative abundances in the model so that naturally we have to regard their count rates with caution. Before we present the measured speed distributions in the next chapters we give a short summary of the full improved response model, discuss the overall model sensitivity to small deviations in the calibration and have a look at the instrumental background that mainly consists of random coincidences of the most abundant ion species.

4.6 The Full CTOF Response Model

Summarizing the previous sections of this chapter, the full CTOF response model contains the individual ion responses of 91 ion species of the 14 most abundant heavy solar wind elements helium, carbon, nitrogen, oxygen, neon, sodium, magnesium,

aluminum, silicon, sulfur, argon, calcium, iron and nickel. All included ion species are given in the second column of Table 4.1. For the individual response functions $R_{i,j}(\tau, \epsilon)$ that model the observed ion peaks in the ET-matrices for every calibrated species $i \in \{1, 2, ..., 91\}$ at every Epq-step $0 \leq j \leq 116$, two general models R are available: The standard 2D-Gaussian peak model R_G and the improved Kappa-Moyal peak model R_{KM}. The 2D-Gaussian peak model is defined in analogy to the existing response models of e.g. ACE/SWICS [Berger, 2008, Koeten, 2009] in Eq. 4.16 with the individual peak model parameter vector for each species $\underline{P}_G^{i,j} = (\tau_0^{ij}, \epsilon_0^{ij}, \sigma_\tau^{ij}, \sigma_\epsilon^{ij})^T$ where the peak TOF τ_0^{ij} and ESSD positions ϵ_0^{ij} can be obtained from Eq. 4.25 and Eq. 4.24, respectively, and the width parameters σ_τ^{ij} and σ_ϵ^{ij} are given by Eq. 4.26 and Eq. 4.27, respectively. The new Kappa-Moyal peak model is defined in Eq. 4.41 with the peak model parameter vector for each species $\underline{P}_{KM}^{i,j} = (\tau_0^{ij}, \epsilon_0^{ij}, \sigma_\tau^{ij}, \kappa_\tau^{ij}, c_\tau^{ij}, \sigma_\epsilon^{ij})^T$ where the additional peak parameters κ_τ^{ij} and c_τ^{ij} can be obtained from Eq. 4.35 and Eq. 4.42, respectively. The parameter σ_ϵ^{ij} has been refined for the Kappa-Moyal model in Eq. 4.40. For iron an even more accurate parametrization of the ESSD peak shape could be obtained and is included in the Kappa-Moyal model that contains separate parametrizations of the lower and upper ESSD peak flank as given in Eq. B.3 with two width parameters $\sigma_{\epsilon,up}$ and $\sigma_{\epsilon,low}$ that can be calculated from Eq. B.4 and Eq. B.5 in the appendix. In the following we call this full response model with the maximum number of calibrated ion species the *Full Calibrated (FC)* response model[12], to distinguish it from the *Full Stable (FS)* and the *Reduced Stable (RS)* CTOF response models (see below) that include smaller ion species sets, but could be directly applied to the PHA data to obtain the ion speed distributions in chapter 5 and 6.

The Full and Reduced Stable Response Models

In order to derive the most consistent velocity distribution functions from the data it would be ideal to fit the Full Calibrated response model $\underline{R}_{ij}(\tau, \epsilon)$ to the respective ET-matrix count rates $C_j(\tau, \epsilon)$ after Eq. 4.10. However, when including all calibrated ion species it turns out that frequently the fit does not converge numerically with any of the applied minimization algorithms. The reason is that some ion species have very similar positions in the ET-matrices due to their very similar mass and mass-per-charge values as can be seen from Figure 4.4. In combination with the limited counting statistics of the investigated data subsamples (i.e. restricted solar wind proton speed or restricted time periods) this causes the fit to be under-determined in parts of the ET-matrix due to

[12]Note, that we cannot make explicit use of the CTOF Full Calibrated response model in this work to derive the kinetic properties of the ion species, as explained below. Yet, this full model is still useful to obtain e.g. estimates of elemental abundances of the minor elements sodium, aluminum and argon from certain Epq-steps at which their major charge states have the highest count rate, or to estimate the influence of these ion species on the speed spectra of the adjacent ions at these Epq-steps.

the large overlap of such peaks. This problem even occurs in the long-term data speed spectra analysis where we investigate the accumulated counts over the whole measurement period DOY 174-220, 1996, but filtered for a very narrow proton speed interval. Therefore, we systematically exclude those elements from the fitted response model that have the lowest abundances and their ion species have very similar ion positions to their adjacent more abundant ion species. We thus exclude for the systematic speed measurements all ion species of the elements sodium, aluminum, and argon, for which it would be anyway hard to resolve their speed distributions due to their expected low count rates. It is clear that this artificial change of the response model might influence the count rates of adjacent ion species that have higher but still comparable abundances as the excluded species. Yet, for the most relevant species that have at least one order of magnitude higher count rates, this effect is negligible because the resulting local count rate deviations are below the typical response model accuracy that we have discussed in the previous section.

Finally, we also have to exclude the priority range PR5 from our analysis as we cannot reconstruct properly the count rates in this area of the ET-matrix. This is necessary, as we can see e.g. from Figure 4.1 that the border region of PR5 to PR4 is systematically over-estimated in count rate after the base-rate correction and this could cause systematic bias of certain ion species such as the carbon species that partly lie in this area. Since He^{2+} cannot be included in the analysis anyways due to the PID onboard suppression (see section 2.2) and practically all He^{+} counts can be considered as pick-up ions [Arnaud and Rothenflug, 1985] the exclusion of PR5 is not a major restriction for the overall systematic speed analysis. After the response model reduction, the largest set of ion species that allows a numerically stable fit for all Epq-steps in the long-term data contains 69 ion species which are given in the third column of Table 4.1. Thus, the corresponding response model that we call in the following the *Full Stable* (FS) response model for CTOF includes the ten remaining elements carbon, nitrogen, oxygen, neon, magnesium, silicon, sulfur, calcium, iron and nickel with all their charge states that we selected in section 4.2.

While the FS response model leads to an overall fit convergence for the analysis of the long-term CTOF data both in the slow and in the fast wind, it turns out that for the fast wind case where we have a much lower number of measurement cycles available, many ion species even among the most abundant ones show large count rate fluctuations in their count rate spectra over all Epq-steps due to the (already) low counting statistics and their (still) large peak overlap with adjacent ion species (see section 5.5). Therefore, we conduct complimentary fits with a Reduced Stable (RS) response model to further analyze the count rate spectra of the most abundant ion species under the

Included Element:	Full Calibrated Model	Full Stable Model	Red. Stable Model
Criterion: $A_{Z,rel} > 10^{-6} \cdot A_H$	Criterion: $A_{q,rel} > 10^{-3}$	Criterion: Overall Fit Convergence	Criterion: 5 Best-Resolved Elements & $A_{q,rel} > 10^{-2}$
Helium*	He^{+}, He^{2+}	-	-
Carbon	C^{4+} - C^{6+}	C^{4+} - C^{6+}	C^{4+} - C^{6+}
Nitrogen	N^{4+} - N^{7+}	N^{4+} - N^{7+}	-
Oxygen	O^{5+} - O^{8+}	O^{5+} - O^{8+}	O^{6+}, O^{7+}
Neon	Ne^{5+} - Ne^{9+}	Ne^{5+} - Ne^{9+}	Ne^{6+} - Ne^{8+}
Sodium	Na^{4+} - Na^{9+}	-	-
Magnesium	Mg^{4+} - Mg^{10+}	Mg^{4+} - Mg^{10+}	-
Aluminum	Al^{5+} - Al^{11+}	-	-
Silicon	Si^{5+} - Si^{12+}	Si^{5+} - Si^{12+}	Si^{5+} - Si^{12+}
Sulfur	S^{6+} - S^{13+}	S^{6+} - S^{13+}	-
Argon	Ar^{7+} - Ar^{13+}	-	-
Calcium	Ca^{6+} - Ca^{14+}	Ca^{6+} - Ca^{14+}	-
Iron	Fe^{5+} - Fe^{16+}	Fe^{5+} - Fe^{16+}	Fe^{5+} - Fe^{16+}
Nickel	Ni^{6+} - Ni^{14+}	Ni^{6+} - Ni^{14+}	-

TABLE 4.1: Overview of the included ion species in the *Full Calibrated* (FC), *Full Stable* (FS), and *Reduced Stable* (RS) CTOF response model. The selection criteria for the FC model are described in section 4.2 while the additional selection criteria for the FS and RS response models are explained in detail in the text of the current section 4.6.
* Also note that the helium ions are not in the applied models (even if they fulfill all selection criteria), as we have to exclude priority range PR5 because of the onboard PID suppression that does not allow a base rate reconstruction for PR5.

assumption that their less abundant neighbor species can be neglected. In the RS response model we only include the five best-resolved elements (except for helium): carbon, oxygen, neon, silicon and iron with their most abundant ion species that have an expected relative charge state abundance of at least 10^{-2}. In this way we obtain 28 ion species for the RS model which are given in the last column of Table 4.1. We also use the RS model for the CTOF short term-data analysis in chapter 6 both in the slow wind and fast wind case as for the short term data analysis we naturally have to deal with very low counting statistics for all kind of solar wind regimes. In the following we assess the goodness of both the FS and RS response models over the whole ET-matrix both for the Kappa-Moyal peak model and the 2D-Gaussian peak model.

Goodness and Sensitivity of the Response Models

In Figure 4.23 we analyze the FS response model with the Kappa-Moyal peak shape model for Epq-step 55 for the full relevant ET-matrix (PR1-PR4) in the same way as we did with He^{2+} and the iron species Fe^{7+} - Fe^{11+} in section 4.5 with the only difference that we omit the reduced TOF histograms for brevity. As before, we fit the model to

the base rate corrected PHA count rates and only include ET-bins in the fit with more than ten transmitted PHA counts per bin to allow a meaningful approximation of the χ^2_{red} value. We also exclude priority range PR5, as explained above, as the failed base rate reconstruction in this area would strongly bias the overall χ^2_{red} value. Thus, the shown fit of the FS Kappa-Moyal response model to the data in Figure 4.23 includes 69 free count rate parameters N_i that are bijectively related to the modeled peak heights of each ion species, respectively, while all other parameters of the model are fixed as explained in sections 4.4 and 4.5. The same conditions apply for the shown case of the FS response model with the Gaussian peak shape in Figure 4.24. Finally, we have 28 free parameters for the fits of the RS response model to the same PHA data in Figures 4.25 and 4.26 again with the Kappa-Moyal and Gaussian peak shape model, respectively. From the contour plot in the upper panel of Figure 4.23 we see that the model and the data contour levels match well at almost all parts of the ET matrix with a few deviations for the Si^{9+} and C^{4+} peaks at ET-channels ($\tau \approx 280$ ch, $\epsilon \approx 50$ ch) and ($\tau \approx 280$ ch, $\epsilon \approx 30$ ch) where we can see that the model is able to catch the presence of these peaks in the vicinity of the much larger O^{6+} peak, but it does not reflect their shape very accurately. On the other hand some other features are modeled quite precisely such as the C^{5+} and Ne^{8+} peak at ET-channels ($\tau \approx 260$ ch, $\epsilon \approx 35$ ch) and ($\tau \approx 260$ ch, $\epsilon \approx 50$ ch), respectively, or even the Fe^{12+} peak at ET-channels ($\tau \approx 350$ ch, $\epsilon \approx 55$ ch). Also the low-charge iron peak shapes are modeled accurately as one would expect from the previous analysis with the only exception that the Fe^{8+} peak at ET-channels ($\tau \approx 430$ ch, $\epsilon \approx 30$ ch) is slightly over-estimated, although the count rate maximum close to the position of Fe^{8+} can be modeled precisely. In the middle panel of Figure 4.23 we can see that for the vast majority of ET bins the measured count rates show moderate deviations from the modeled count rate below 3σ although we find several small areas where the deviation is larger and reaches up to 6σ. On the other hand when we consider the relative residuals in the lower panel of Figure 4.23, we find small values $\Delta C_{rel} < 0.2$ for the whole relevant ET-matrix where we find high count rates, so that the observed systematic deviations in the middle panel are not crucial for the count rate determination of the major ion species. While this is the case for the whole central ET-matrix from C^{5+} at the lowest TOF and ESSD channels to the iron ions at the high TOF and ESSD channels, we find large deviations for the boundaries. Yet there, the count rate is negligibly low, except for the C^{6+} peak at ET-channels ($\tau \approx 240$ ch, $\epsilon \approx 45$ ch), where we can see the influence of He^{2+} pile-up counts (see section 4.7). When we compare the , FS Kappa-Moyal model fit with the FS Gaussian model fit in Figure 4.24, we see that several features are modeled worse, such as the C^{4+} and Si^{9+} peaks that are not

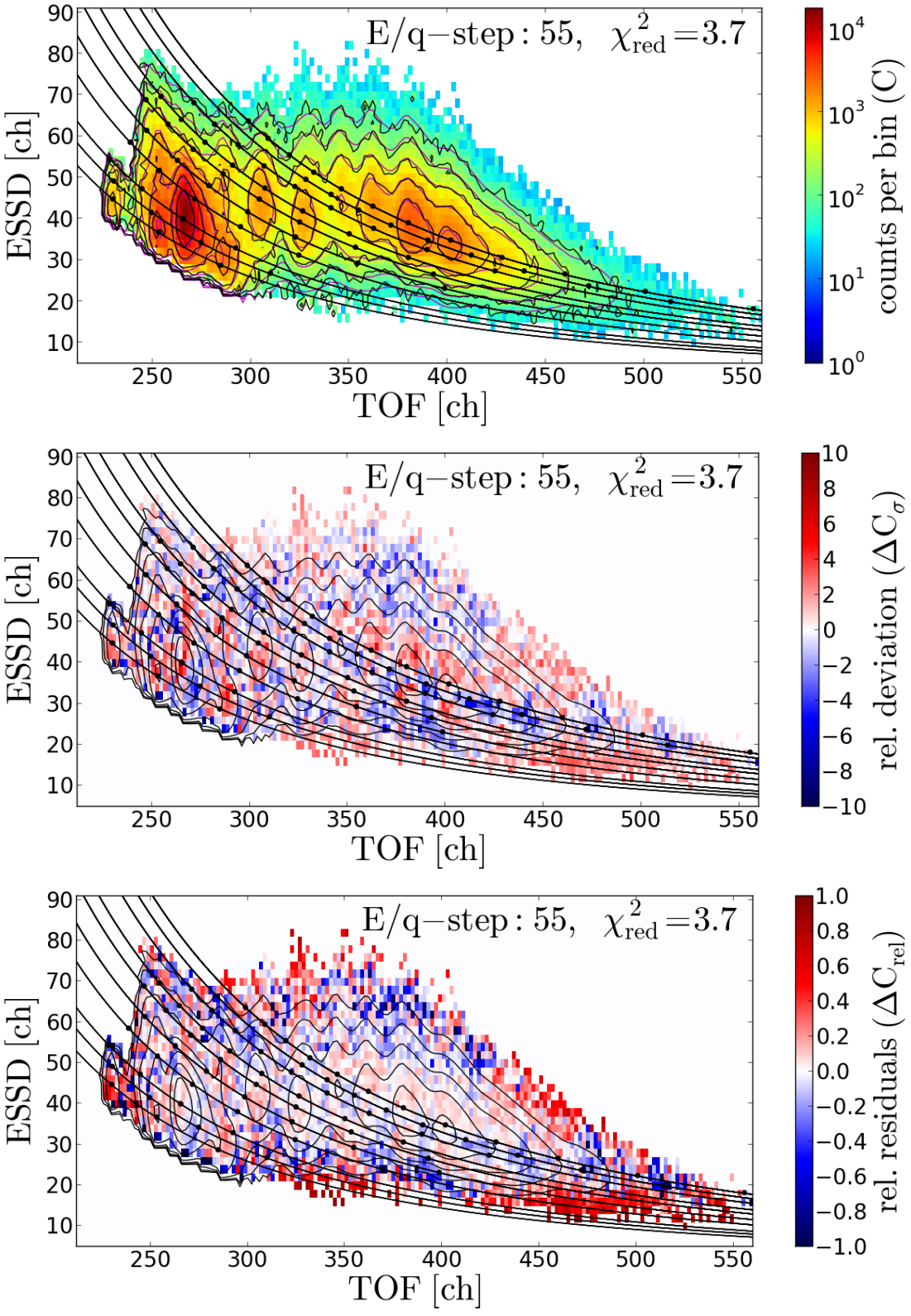

FIGURE 4.23: Two-dimensional contour plot of the CTOF *Kappa-Moyal Full Stable* response model fitted to the whole relevant ET-histogram (within the priority ranges PR1-PR4) at Epq-step 55 (upper panel) and the corresponding relative deviations (middle panel) and relative residuals (lower panel). The model contains 69 ion species (black dots) that lie on the 10 elemental hyperbolae. In all plots the black data contour lines correspond to $10^{-1/3}$, $10^{-2/3}$, 10^{-1}, $10^{-4/3}$, $10^{-5/3}$, 10^{-2}, $10^{-7/3}$ times the maximum data count rate C_{max}, which is located within the O^{6+} peak. The magenta contour lines show the corresponding count rate levels of the fitted count rate model $\widetilde{C}(\underline{N}, \underline{R})$ also scaled by the maximum data count rate C_{max}.

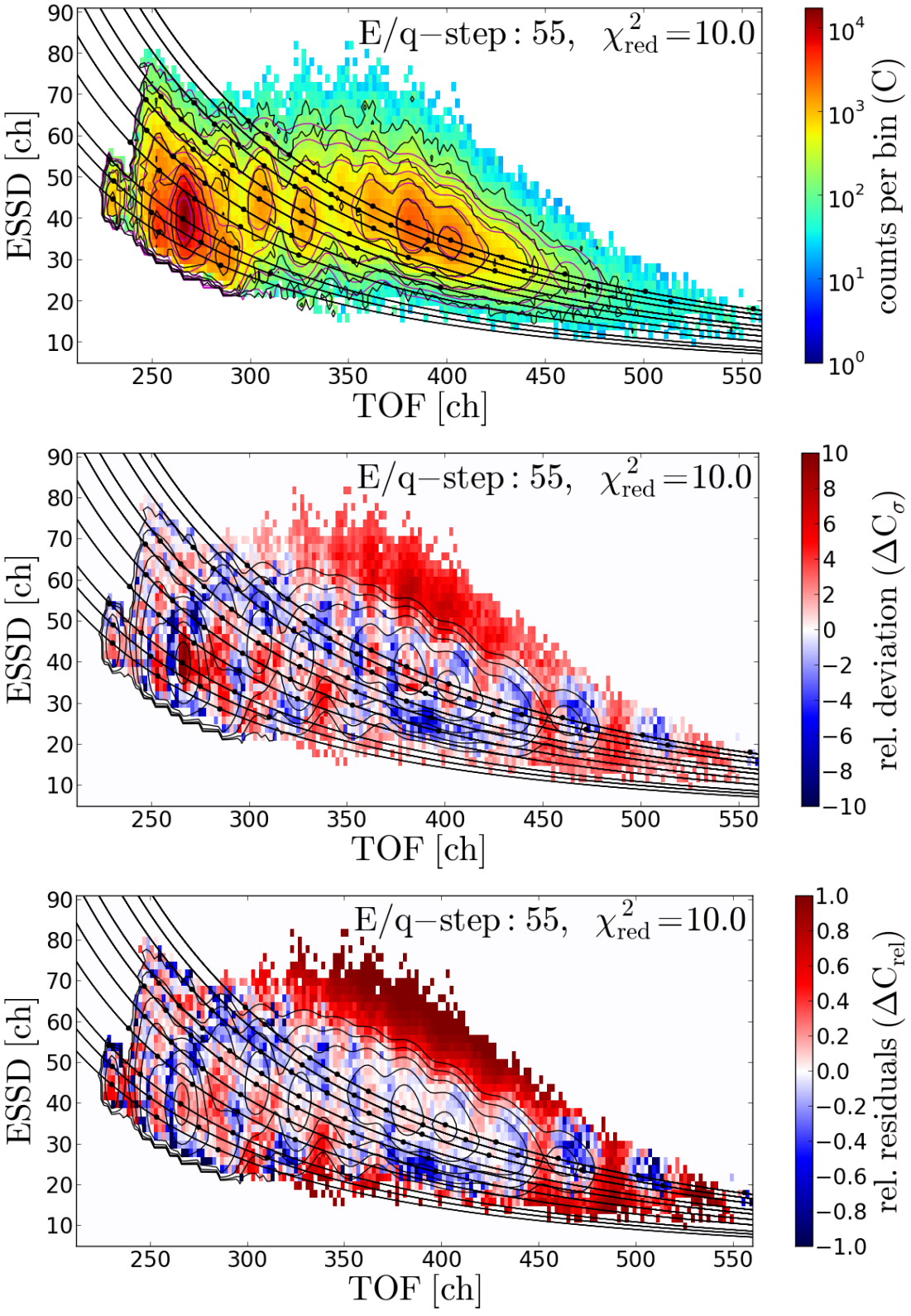

FIGURE 4.24: Two-dimensional contour plot of the CTOF *Gaussian Full Stable* response model fitted to the whole relevant ET-histogram (within the priority ranges PR1-PR4) at Epq-step 55. and the corresponding relative deviations (middle panel) and relative residuals (lower panel). The model contains 69 ion species (black dots) that lie on the 10 elemental hyperbolae. In all plots the black data contour lines correspond to $10^{-1/3}$, $10^{-2/3}$, 10^{-1}, $10^{-4/3}$, $10^{-5/3}$, 10^{-2},, $10^{-7/3}$ times the maximum data count rate C_{max}, which is located within the O^{6+} peak. The magenta contour lines show the corresponding count rate levels of the fitted count rate model $\widetilde{C}(\underline{N}, \underline{R})$ also scaled by the maximum data count rate C_{max}.

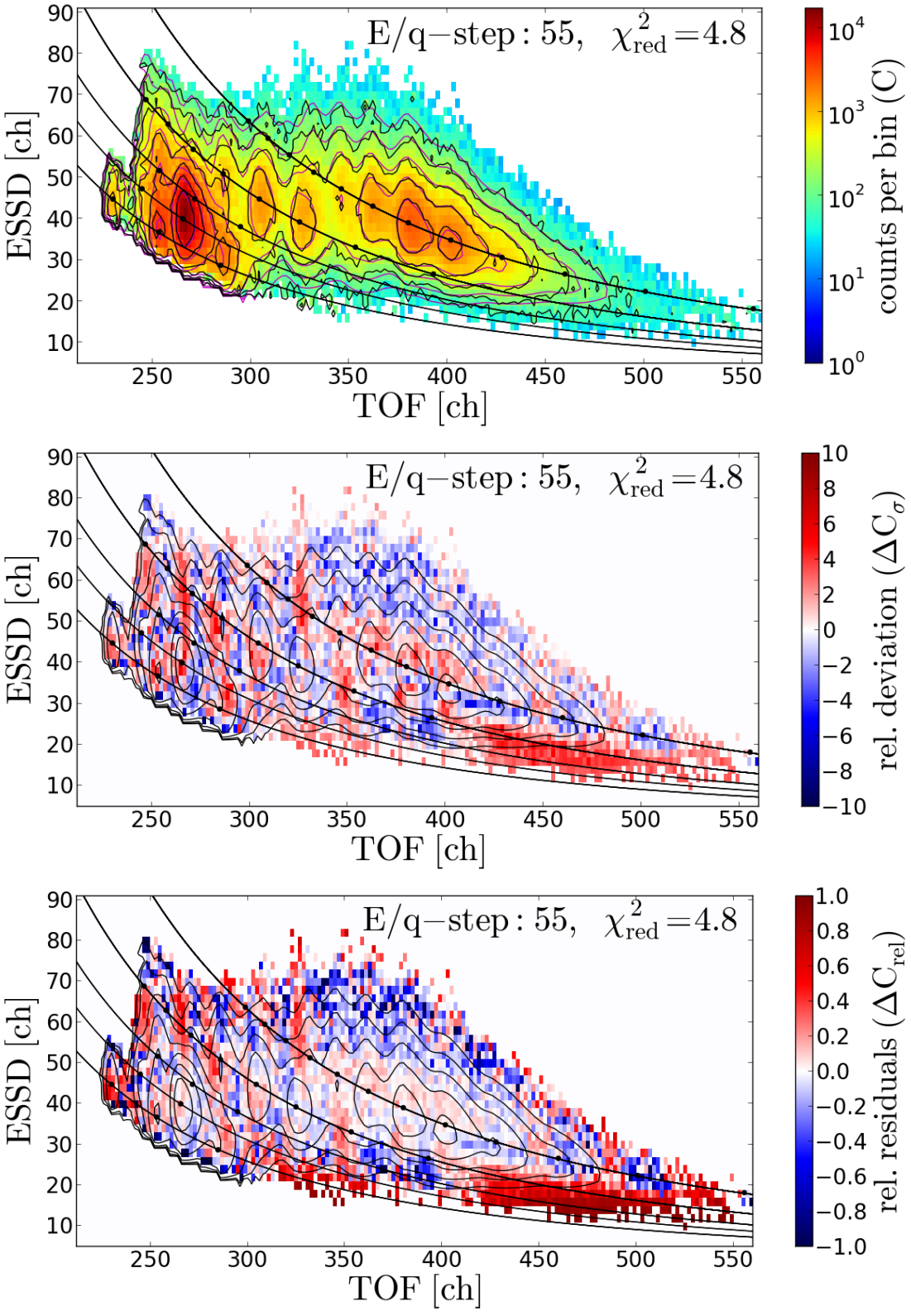

FIGURE 4.25: Two-dimensional contour plot of the CTOF *Kappa-Moyal Reduced Stable* response model fitted to the whole relevant ET-histogram (within the priority ranges PR1-PR4) at Epq-step 55 (upper panel) and the corresponding relative deviations (middle panel) and relative residuals (lower panel). The model contains 28 ion species (black dots) that lie on the 5 elemental hyperbolae. In all plots the black data contour lines correspond to $10^{-1/3}$, $10^{-2/3}$, 10^{-1}, $10^{-4/3}$, $10^{-5/3}$, 10^{-2}, $10^{-7/3}$ times the maximum data count rate C_{max}, which is located within the O^{6+} peak. The magenta contour lines show the corresponding count rate levels of the fitted count rate model $\widetilde{C}(\underline{N}, \underline{R})$ also scaled by the maximum data count rate C_{max}.

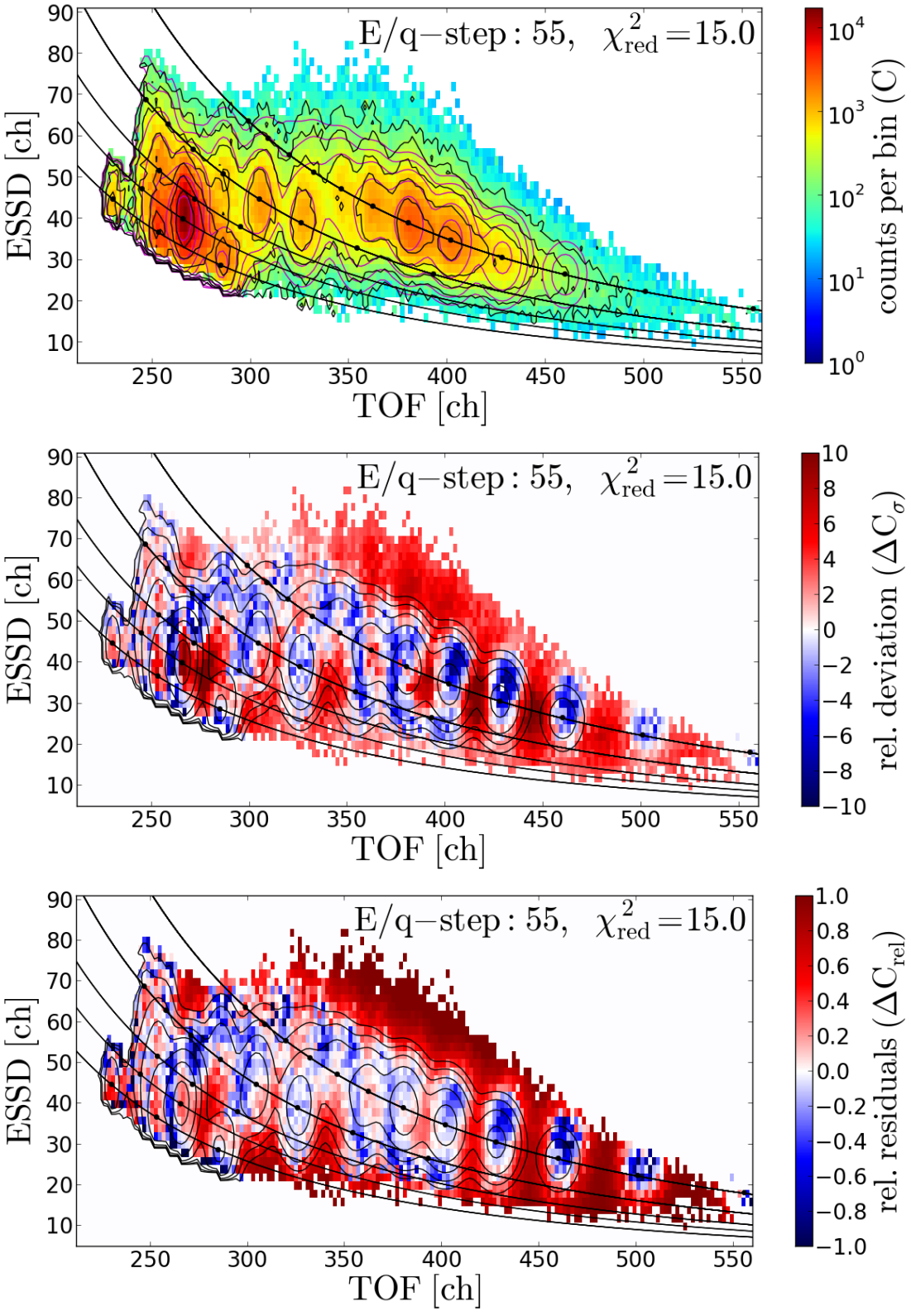

FIGURE 4.26: Two-dimensional contour plot of the CTOF *Gaussian Reduced Stable* response model fitted to the whole relevant ET-histogram (within the priority ranges PR1-PR4) at Epq-step 55 (upper panel) and the corresponding relative deviations (middle panel) and relative residuals (lower panel). The model contains 28 ion species (black dots) that lie on the 5 elemental hyperbolae. In all plots the black data contour lines correspond to $10^{-1/3}$, $10^{-2/3}$, 10^{-1}, $10^{-4/3}$, $10^{-5/3}$, 10^{-2}, $10^{-7/3}$ times the maximum data count rate C_{max}, which is located within the O^{6+} peak. The magenta contour lines show the corresponding count rate levels of the fitted count rate model $\widetilde{C}(\underline{N}, \underline{R})$ also scaled by the maximum data count rate C_{max}.

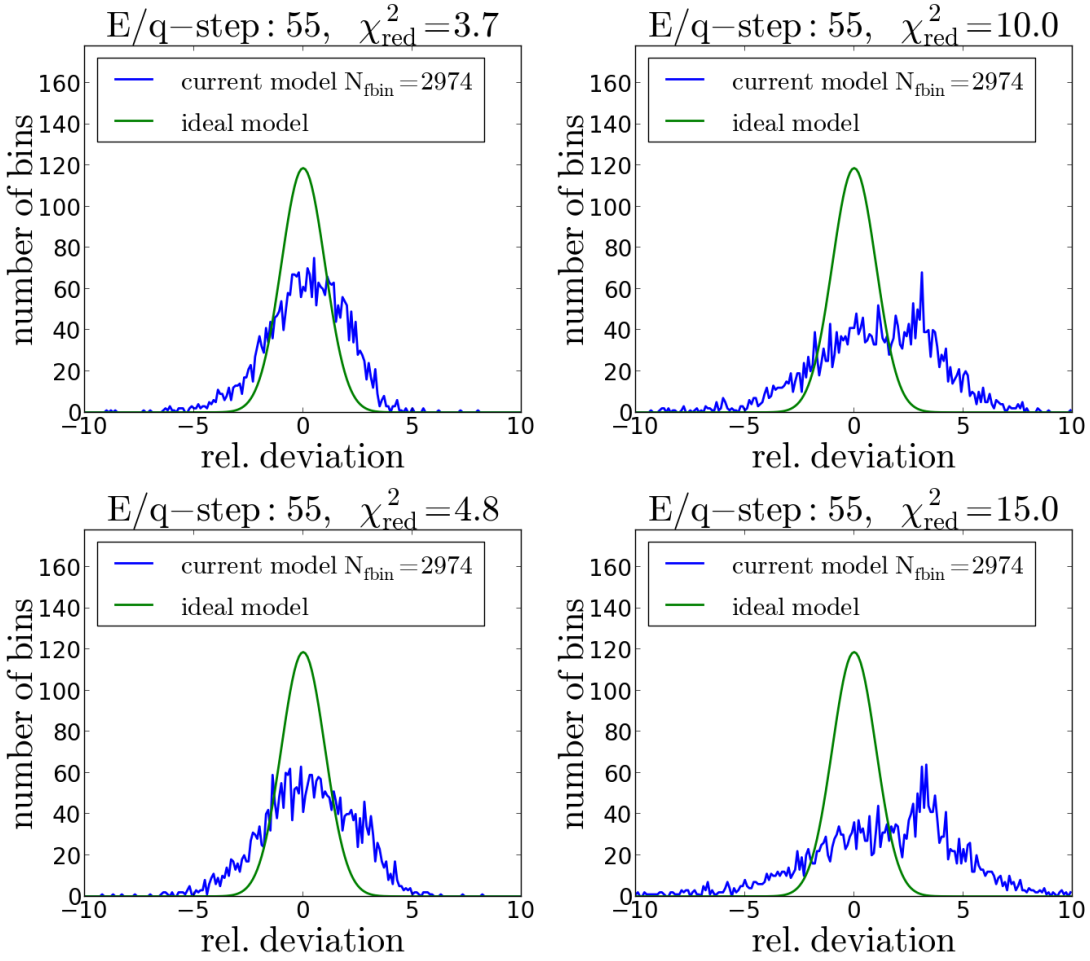

FIGURE 4.27: Histograms of the relative deviations (blue) depicted in the middle panels of Figures 4.23 - 4.26 in comparison to a relative deviation distribution that would arise from a perfect model $\chi^2_{red} = 1$ purely due to statistical deviations (green).

caught well by the Gaussian model besides the clear deviations in the iron tails. Consequently, we observe on average higher relative deviations that reach up to $\Delta C_\sigma = 10$ in the vicinity of the O^{6+} peak and the overall goodness of fit is almost, a factor of 3 worse than for the FS Kappa-Moyal response model fit. We also see that some areas with large relative deviations show also higher relative residuals, in particular between C^{5+}, O^{6+}, C^{4+} and Si^{9+} with $\Delta C_{rel} \gtrsim 0.4$. This applies even more for the high-TOF flank of Fe^{8+} and Fe^{7+}.

As we discussed in Figure 4.22 and 4.13, we have to consider that due to the large number of ion species in the fit, a part of the actual deviations between data and model can be compensated by nonphysically high count rates for certain minor species which we did not take into account in the evaluation, yet. To evaluate such effects, the analysis of the count rates with the Reduced Stable response model is an important complimentary approach (both here and in the speed spectra analysis itself in chapter 6). We thus,

also compare the Reduced Stable response model fits for the Kappa-Moyal and Gaussian peak shapes. In Figure 4.25 we can see that the reduction does not have dramatic effects neither on the relative deviations nor on the relative residuals for most parts of the ET-matrix and also the model goodness is still by a factor of 2 better than the model goodness for the Full Stable Gaussian model. On the other hand, we can see from the comparison of Figures 4.24 and 4.26, that the Gaussian model becomes much worse in certain areas of the ET-matrix in particular for the low-charge iron species Fe^{8+} and Fe^{7+}, but also in the vicinity of C^{4+}. Thus, when comparing Figures 4.25 and 4.26, we see that with the same (reduced number) of ion species the model goodness of the RS Kappa-Moyal model is again by a factor of 3 better than for the RS Gaussian model.
In appendix C we show this comparison between the different response models fitted to the PHA long-term data for a representative set of Epq-steps $j \in \{39, 50, 60, 70, 80, 86\}$ where Epq-step 39 is the lowest step for which we had enough statistics to fit the full model in a numerically stable way in the normal count rate approximation and Epq-step 86 is the highest step where the statistics allowed this fit. When we compare the goodness of fit for the reduced and full model over all Epq-steps given in the appendix, we find that both show decreasing χ^2_{red} values with decreasing Epq-step, down to very similar values of $\chi^2_{red} \approx 2$ for Epq-step 39. This however, does not automatically mean that the model gets actually better for low Epq-steps but this is mainly explained with the decreasing number of total counts with decreasing Epq-step as most ions with low and intermediate m/q values do not occur at these steps yet. With lower statistics it becomes just less visible how good (or bad) the peak shape is determined in detail and we just cannot compare the goodness of the models between different steps with the calculated χ^2_{red} due to the massive changes in count rates over the whole Epq-step range. However, we can compare the goodness of the long-term data fit for each given Epq-step among the response models and we find that for all Epq-steps the calculated χ^2_{red}-values for the Kappa-Moyal models are significantly lower than the corresponding values for the Gaussian models, so that the Kappa-Moyal peak shape model is a real improvement. As expected, the Kappa-Moyal Full Stable response model yields the lowest χ^2_{red}-values among all four compared cases (as seen in Figures 4.23 - 4.26), but as mentioned above, with lower counting statistics the difference between the reduced and full models becomes small. We will make use of this observation for the investigation of the short term data in chapter 6, where we have very low counting statistics and will thus apply the Reduced Stable response model to obtain lower count rate fluctuations among the fit results without losing substantial quality in the model.

We finally investigate the sensitivity of the response model to small systematic deviations to check whether the calibrated configuration of peak parameters yields actually

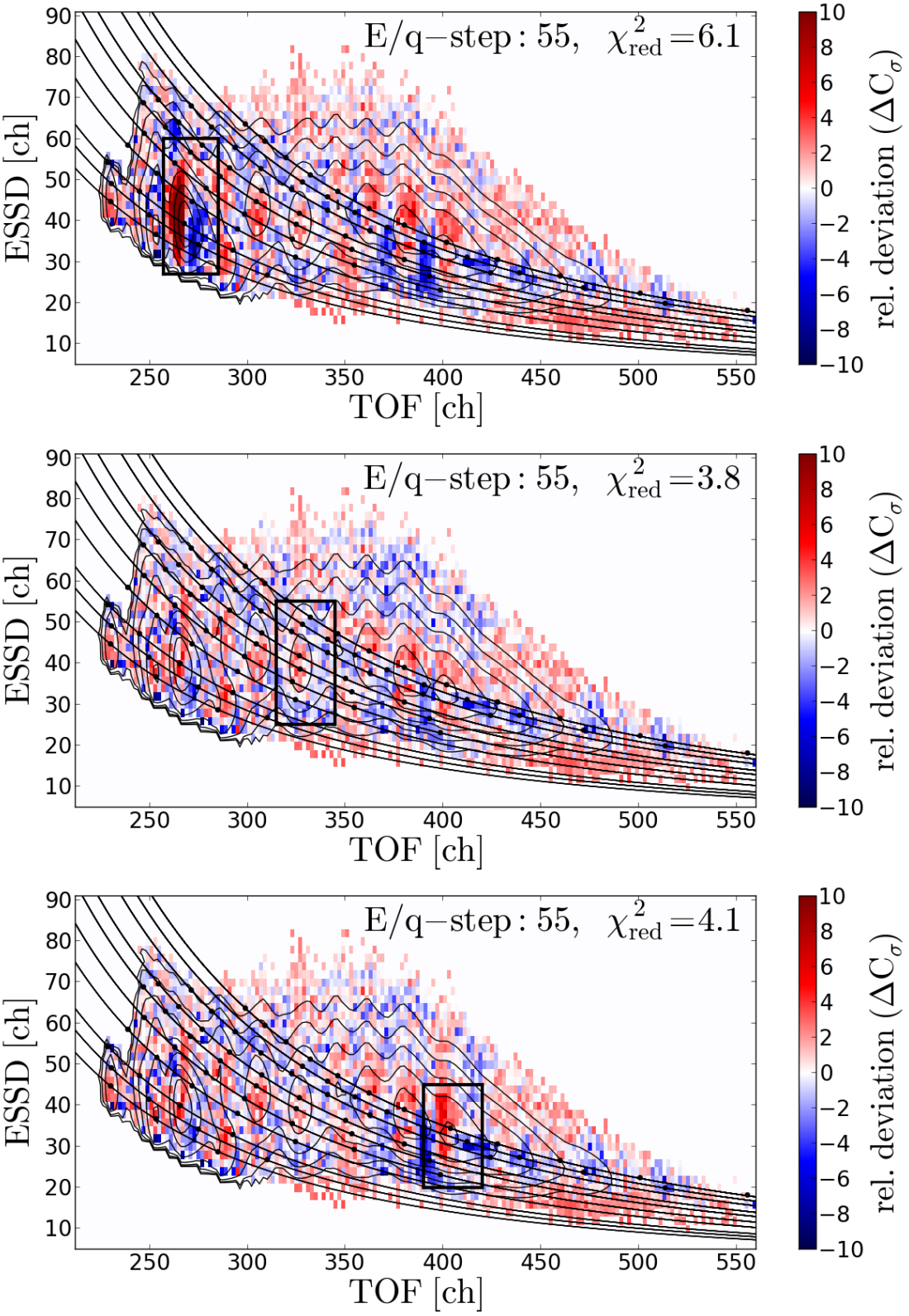

FIGURE 4.28: Check of the response model sensitivity to small shifts in the determined ion positions for O^{6+} (upper panel), Si^{7+} (middle panel) and Fe^{9+} (lower panel). The respective ion positions are shifted in the response model by +2 ch in Time-of-Flight compared to the calibrated ion position in the shown Epq-step 55. The respective relative deviations between model and data that occur in an area around the nominal peak position (marked by the black frame) can be directly compared to the relative deviations in Figure 4.23.

a significant minimum in parameter space and the observed low deviations are not just a random result due to the superposition of many ion species. In order to check in particular the ET environment of the best resolved and therefore presumably most reliable ion species we change in Figure 4.23 artificially the optimized position of O^{6+}, Si^{7+} and Fe^{9+} by (only) +2 channels in TOF in order to observe the corresponding change in the relative deviations and relative count residuals as well as in χ^2_{red}. As we can see from Figure 4.28 the biggest change is observed for the position shift of O^{6+} (in the upper panel), as one would expect due the high abundance of this species. We can clearly see that after the shift the model significantly underestimates the count rates at the low-TOF flank of the O^{6+} peak while it over-estimates the high TOF flank. The corresponding χ^2_{red}-value nearly doubles due to the arranged change. A smaller but still clearly visible effect can be seen if we shift the TOF position of Fe^{9+} (in the lowest panel of Figure 4.28) analogously by +2 channels which causes pronounced deviations along the TOF axis among the iron sequence while the global χ^2_{red} value is increased by about 0.4. Finally, for Si^{7+} we do not see any significant change at all in the relative deviation and the χ^2_{red} value only changes by 0.1 compared to the optimized model in Figure 4.23. This means that the TOF position of Si^{7+} is not that well defined compared to the other two major ion species and could be easily shifted by a few channels in TOF. A similar behavior of the selected ion species is found for shifts in the ESSD channels. This illustrates well the kind of under-determination of the peak parameters within parts of the ET-matrix with many adjacent ions where as a consequence also the resulting speed spectra are subject to higher systematic uncertainties. Naturally, for ion species with low abundances this effect can be even larger and it therefore illustrates the necessity of a systematical ion peak position calibration that reduces these uncertainties.

4.7 Instrumental Background

As another source of systematic errors we have to discuss the instrumental background which can be defined for this study as all count signals that do not represent a valid measurement of a heavy solar wind ion. This means either the measurement of other particles (solar wind protons, pick-up ions, high energy particles/cosmic rays, photons) or the measurement of solar wind ions at clearly unphysical TOF or ESSD channels. In the following we discuss the observed background from these different particle populations:

Solar Wind Protons: In the analyzed CTOF triple coincidence data we do not observe any proton signal at the nominal peak position due to the suppression by the interruption of the Epq-stepping and in addition to the onboard fast analog identification

system (PID) that filters further out ion counts at the nominal position of the protons and (partly) alpha particles in the ET-matrices at a given Epq-step. During the CTOF prefligth tests a suppression of 100% of the proton counts and 90% of the helium counts [Hovestadt et al., 1995] was found.
Pick-Up Ions: As we described above, the CTOF instrument is also designed to detect pick-up ions. Yet, the only dominant pick-up ion species that occurs in the CTOF PHA triple coincidence data at similar Epq-steps as the solar wind heavy ions is He^{+} which is well-separated from all relevant solar wind ion species. All other pick-up ion species, if detected at all in the TC data, are measured with relatively low count rates at very low Epq-steps because they have typically very high mass-per-charge values as they are mostly single- or twofold-charged ions (compare [Taut, 2014]).
High Energy Particles / Cosmic Rays: During the whole measurement period DOY 174-220, 1996, we found only a few (< 100) counts that we identify as higher energetic/cosmic ray particle as these were measured at clearly higher energy channels in the SSD probably while a regular solar wind ion triggered a start condition at the carbon foil. Therefore, it seems that the anti-coincidence worked reliably during the whole measurement time and any background from high energetic particles is negligible.
Secondary UV Photons: We also find that the suppression of UV photo electrons in the CTOF entrance system [Hovestadt et al., 1995] worked well as otherwise these electrons would have constantly triggered start pulses in the carbon foil. In this case the energy signal of many ions would not be related to its TOF measurement anymore and the ion peaks would be much less visible in a uniform back ground. In other words, we would observe a much lower signal-to-noise ratio.
Solar Wind Ion Energy Pile-Ups: In Figure 2.3 we recognize that the energy shape of the C^{6+} peak is actually a double-peak structure. As this figure still shows the base-rate uncorrected data and the lower peak is situated at about twice the ESSD position of the He^{2+} peak, we conclude that this peak is caused by He^{2+} pile-up events. These are events where in the case of high particle fluxes two He^{2+} ions are measured simultaneously at the SSD surface and are assigned to only one time-of-flight measurement, virtually doubling the energy of the detected particle. Anyway, the C^{6+} measurement cannot be analyzed properly in many cases as it has the same m/q value as He^{2+} and is therefore also cut-off in its speed distribution due to the interrupted Epq-stepping. Consequently, we do not make any efforts to correct the pile-ups. There is no significant pile-up observed for any other heavy ion species.

We finally turn to the most significant background contribution that results from so-called *random coincidences* (RCs) of the most abundant solar wind ions, in particular He^{2+}. Random coincidences occur, when the start and the stop pulse in the time-of-flight measurement is not triggered by the same particle as nominally anticipated by

the instrument design, but instead by two different particles in a way that the first particle triggers the start pulse of the TOF measurement at the carbon foil and opens up the sensitive time-window for a stop pulse at the SSD, and the second particle then triggers a stop pulse at the SSD surface without having triggered a start pulse at the carbon foil. This is possible as none of the pulse triggers works with 100% efficiency and the sensitive time window has some tolerance as it should allow for the measurements of particles with different speeds (and mass) at the same Epq-step. In absolute numbers these random coincidences happen more often for species with high abundance simply because their flux is higher. Furthermore, there is no well-defined relation in time between the RC start and stop pulse so that the apparent TOF signal of these events is smeared out. For these reasons, the majority of the random coincidences measured in CTOF are caused by alpha particles, as these are 1) not completely cut-off by the Epq-stepping 2) much more abundant than the other heavy ion species 3) not sorted out effectively by the PID when they appear at higher TOF values than anticipated for a regular alpha particle count and 4) when they appear at these higher TOF levels they have the same base rate weight as low-abundant ion species and are even transmitted as PHA words.

In Figure 4.29 we show the long-term PHA data for Epq-step 73 (as always integrated over all cycles in the time period DOY 174-220, 1996). At this Epq-step He^{2+} is measured at a speed of 422 km/s calculated after Eq. 2.1. This is a relatively frequent solar wind speed in the respective measurement period and thus the He^{2+} random coincidences are extremely pronounced in the ET matrix at this Epq-step. As one would expect, the RC counts can be found at the same energies as the He^{2+} peak and they reach out with nearly constant intensity to very high TOF channels. But even if the He^{2+} RC count rates are high, due to their well defined location only ions measured at low ESSD channels are contaminated. Because of the given relation between ESSD, TOF and mass-per-charge expressed in Eq. 4.25 and 4.24 these ions are measured at high TOF channels and have relatively high m/q-values such as Mg^{5+}, $Si^{6+}$and in particular the low iron charge states Fe^{7+} - Fe^{9+}. On the other hand, He^{2+} has a very low m/q value which causes that the critical ion species are measured at much lower speeds than He^{2+} for the same Epq-step and thus the core of their speed distribution is already completely scanned before those Epq-steps are reached in which the He^{2+} random coincidences start to appear. Therefore, we do not observe any regular count rate distributions for these ions at the shown Epq-step 73 as for instance Fe^{9+} is measured at a speed of 239 km/s at Epq-step 73 and even Si^{6+} is measured at a very low speed of 276 km/s. To illustrate that the observed background counts identified as random coincidences are really associated with He^{2+} and to illustrate how narrow the

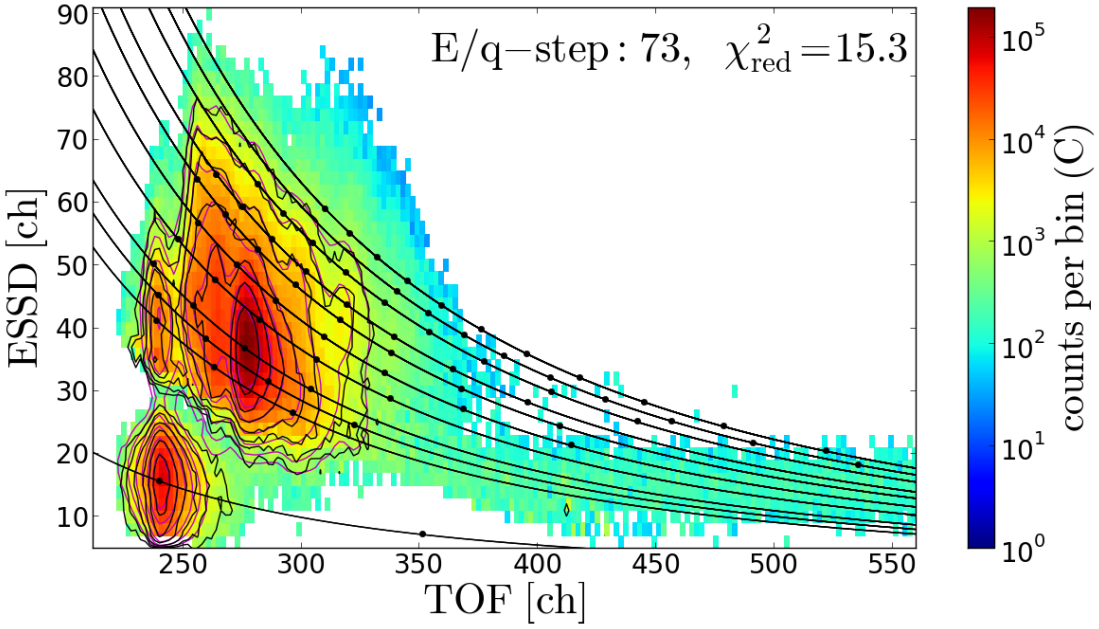

FIGURE 4.29: Long-term ET-matrix for Epq-step 73 showing the integrated (base-rate corrected) PHA count rates for DOY 174-220. We can clearly recognize the He^{2+} random coincidences measured at the same ESSD channels as the He^{2+} peak, but smeared out over the TOF channels. The reason for the start of the signature around TOF channels 350-400 is that they are only picked in the transmitted PHA sample, when they are not in the priority range of He^{2+} (PR5), as they are still very unlikely to occur compared to a nominal He^{2+} count, but not unlikely occur compared to e.g. a count of Fe^{7+} (e.g. in PR1).

speed band is in which the random coincidences appear, we make use of the fact that in any case the heavy ion speeds are still relatively close to the proton speed, and filter the PHA data for time intervals in which the proton speed is below 380 km/s which is about 2-3 thermal speeds lower than the He^{2+} speed in Epq-step 73. Thus, in this case He^{2+} is strongly suppressed even if we assume some reasonable amount of differential speed, while all species with higher mass-per-charge are nearly unaffected by the proton speed filter. As a result, it can be seen in Figure 4.30 that the RC background has vanished completely.

With the given understanding of the CTOF response function, including the crucial background component of the He^{2+} random coincidences, we can now also understand the origin of the apparent subpopulation at very low speeds (high Epq-steps) in particular for Fe^{9+} in the matrix rate analysis in chapter 3. From the lower right panel in Figure 3.2 we see that the O^{6+} speed is measured roughly at 560 km/s in the given cycle in the fast wind. When we now assume that He^{2+} is streaming with a similar speed, then it should be measured around Epq-step 59 after Eq. 2.1. As we can see from the upper right panel in Figure 3.4 this matches very well with the center of the Epq-steps at which the low-speed subpopulation in the Fe^{9+} measurements is measured. When

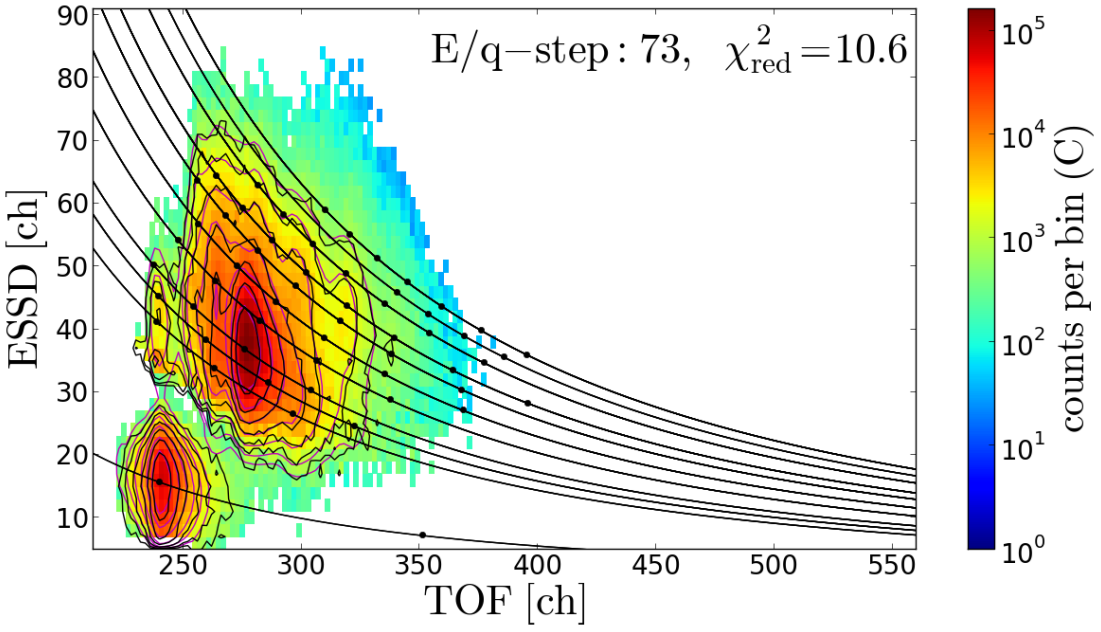

FIGURE 4.30: Long-term ET-matrix for Epq-step 73 showing the integrated (base-rate corrected) PHA count rates for DOY 174-220, but this time under the filter condition, that we only include cycles in which the simultaneously measured proton speed is below 380 km/s. As in this case He^{2+} is suppressed, the He^{2+} random coincidences also vanish.

we now have a look at the less obvious subpopulation in the silicon case in Figure 3.3, we find that here these particles are not measured at an Epq-step close to 59 so they cannot be He^{2+} random coincidences. Instead, when we calculate again after Eq. 2.1 the Epq-step of O^{6+} measured under the observed mean speed of around 560 we find a corresponding Epq-step of 52 which matches very well with the Epq-steps of the observed small subpopulation in the upper right panel of Figure 3.3, so that in this case it is likely that at least a part of these counts are O^{6+} random coincidences. This makes complete sense as O^{6+} is the most abundant minor heavy ion species and in contrast to He^{2+} it is measured at ESSD channels much more similar to Si^{7+}.

After understanding the influence of the random coincidences on the VDF measurements, we have to get rid of this bias as well as possible. From a quantitative comparison we find that the He^{2+} random coincidences never appear at the same Epq-step in which the VDF core of the relevant high m/q-ion species is measured (defined by the 2σ interval around the most probable ion speed). This is the case both for the slow and the fast wind as can be seen from the long-term spectra in the next chapter, even if the speed distributions in the fast wind are considerably wider. Therefore, in the long-term speed spectra analysis in chapter 5, our mean speed calculation is not strongly affected by the He^{2+} random coincidences. In the short-term VDF analysis in chapter 6 we take advantage of basically the same proton speed filter technique so that we cut-out all

counts in the short-term VDFs that are measured at speeds below

$$v_{cut}^{\alpha-RC} = \langle v_p \rangle - 0.2 \cdot \langle v_p \rangle \tag{4.43}$$

where 20% of the mean proton speed corresponds to more than 3 proton thermal speeds in the slow wind and 2 proton thermal speeds in the fastest measured wind. In order not to bias the ion mean speed calculation by this cut-off we then calculate the mean speed from a symmetrized interval around the most probable mean speed as explained in section 6.2. A bit more problematic are the O^{6+} RC counts as these lie at higher energies so that they can also contaminate Si^{7+}, Fe^{9+} or Fe^{10+} for instance, and appear also at lower Epq-steps, so that they have some overlap with these ions in particular in the fast wind. However, as O^{6+} is much less abundant than He^{2+}, these events occur much less frequently and thus have limited statistical impact on the calculated mean speeds of the most abundant silicon and iron ions. This can be seen statistically by the fact that, in contrast to Fe^{9+}, we do see a similar increase to O^{6+} in the Si^{7+} data in Figure 3.5 despite this O^{6+} RC bias.

4.8 Instrumental Detection Efficiencies

For time-of-flight mass spectrometers such as CELIAS/CTOF there exist speed-dependent instrumental detection efficiencies that can cause similar over-representations of measured particle speeds as the different phase space coverage of the CTOF entrance system described in Chapter 2. For instance to trigger a double coincidence (DC) event, particles must

- pass through the carbon foil and release enough secondary electrons from the carbon foil that trigger a start signal in the first MCP
- reach the SSD (after being scattered in the carbon foil) and release again enough secondary electrons from the SSD surface that trigger a stop signal in the second MCP.

To even trigger a triple coincidence (TC), the particle must in addition penetrate the SSD dead-layer and create enough electron-hole pairs to create an electronic signal that exceeds the SSD energy threshold. All these processes are not only element specific but depend also on the energy of the incident particles.

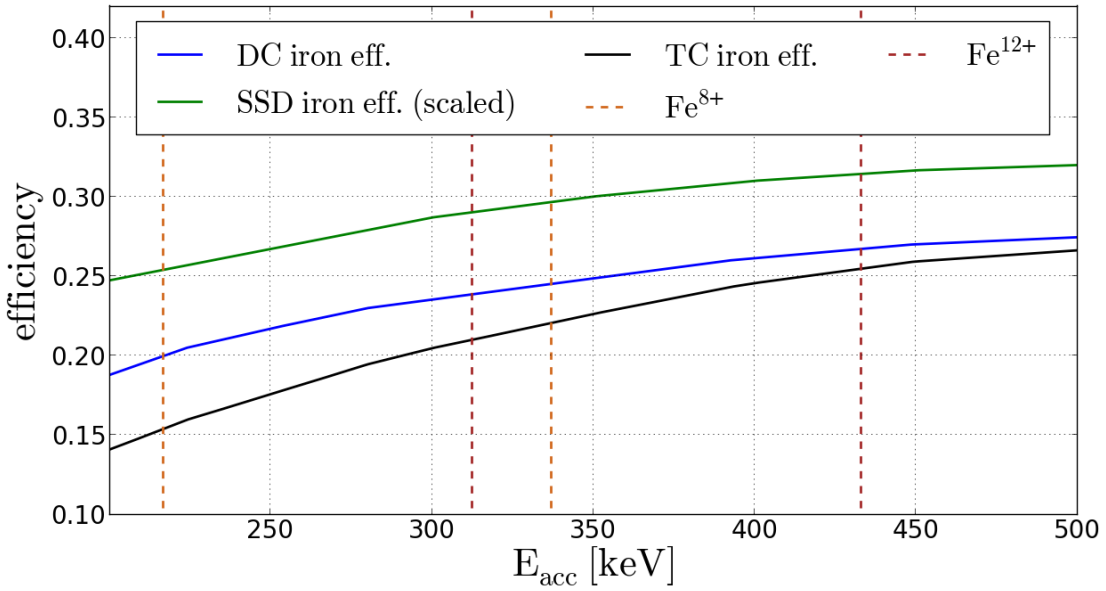

FIGURE 4.31: Estimated triple coincidence (TC) efficiency for iron ions (black) together with the double coincidence efficiency (blue) and the SSD efficiency (green) which we scaled with a factor of 0.33. The DC efficiency was modeled by [Aellig, 1998b] after measurements by H. Grünwaldt with the CTOF flight spare model and has an uncertainty of less than 10%. The SSD efficiency is modeled by[Aellig, 1998b] after measurements of the ACE/SWICS SSD, which is similar to the CTOF SSD. For the SSD efficiency no uncertainty was given. Overlaid are the E_{acc}-ranges for Fe^{8+} and Fe^{12+} that correspond to measured speeds (before post-acceleration) between 300 and 700 km/s. The DC and SSD efficiency values are given in Table B.6 and Table B.7 in the appendix.

Given a certain species of incident particles all mentioned effects favor the detection of fast particles over slow particles as

- the mean number of secondary electrons both in the foil and SSD surface increases with higher kinetic energies of the projectile
- the mean (Rutherford) scattering angle of the particles after the foil decreases with higher speed
- the mean number of created energy-hole pairs increases with higher kinetic energy of the incident particle

This means that in the measured VDF for any given ion species we over-estimate the faster particles compared to the slower ones and we have to estimate this systematic effect in order to quantify its influence on the calculated mean speed. With precise simulations of each contributing sensor component also including the focusing of the incident ion populations in the CTOF entrance system as well as the response of the MCPs one could in principle derive the detection efficiencies for all relevant ion species

as it was accomplished by [Koeten, 2009] for the ACE/SWICS sensor. Yet, these models can have large uncertainties if several of the instrument parameters are not well-known so that a large set of possible parameter combinations arises. This is in particular the case for CTOF, where after more than 20 years after the instrument failure we only have limited documentation of the sensor so that e.g. we have no detailed information of the quadrupole lens in the entrance system or of the MCP response. Therefore, we rely for our estimations on an efficiency model for iron ions that was developed by [Aellig, 1998b] on the basis of calibration measurements with the CTOF flight spare model and the ACE/SWICS solid state detector which is similar to the CTOF SSD. In Table B.6 in the appendix we list the estimated DC efficiencies η_{DC} that we extracted from Figure 4.10 in [Aellig, 1998b] for iron. These values are extrapolated from oxygen and argon measurements with the TOF section of the CTOF sensor by H. Grünwaldt at the Max-Planck-Institute for Aeronomy in Katlenburg-Lindau. The measurements were performed over the energy-per-nucleon range 1-20 keV/nuc which fully covers the energy range of all relevant solar wind ion species after the post-acceleration. The obtained DC efficiency dependence on the particles' energy after the post-acceleration is shown as the blue curve in Figure 4.31. The SSD efficiencies η_{SSD} are modeled by [Aellig, 1998b] on the basis of measurements of the ACE/SWICS solid state detector which is similar to the CTOF SSD, which were performed by the University of Bern at the ion beam facility of the University of Giessen. The SSD efficiency values are given in Table B.7 and are extracted from Figure 4.14 in [Aellig, 1998b]. They are represented by the green curve in Figure 4.31 which we scaled by a factor of 0.33 to allow for a better visual comparison of the shown curves. As a particle has to trigger both a double coincidence and a valid SSD signal to contribute to the triple coincidence count rate, we obtain the speed dependent TC efficiency for iron by a simple multiplication

$$\eta_{TC} = \eta_{DC} \cdot \eta_{SSD} \,. \tag{4.44}$$

The TC efficiency is shown as the black curve in Figure 4.31 where we also overlaid the E_{acc}-range that corresponds to the relevant solar wind speed range between 300 and 700 km/s for the iron species Fe^{8+} and Fe^{12+}. In contrast to other studies that focus on elemental or charge state abundances, we are not interested in the absolute efficiencies of a certain ion species compared to a different one, but we only need an estimation of the detection efficiency gradient over the solar wind speed range for a given species. From Figure 4.31 we find an absolute efficiency increase from about 15% to 22% for Fe^{8+} and from about 21% to 25% for Fe^{12+}. While this corresponds to a relative change of almost 50% and 20%, respectively, over their whole relevant solar wind speed range, we have to keep in mind that the core of a typical solar wind VDF is

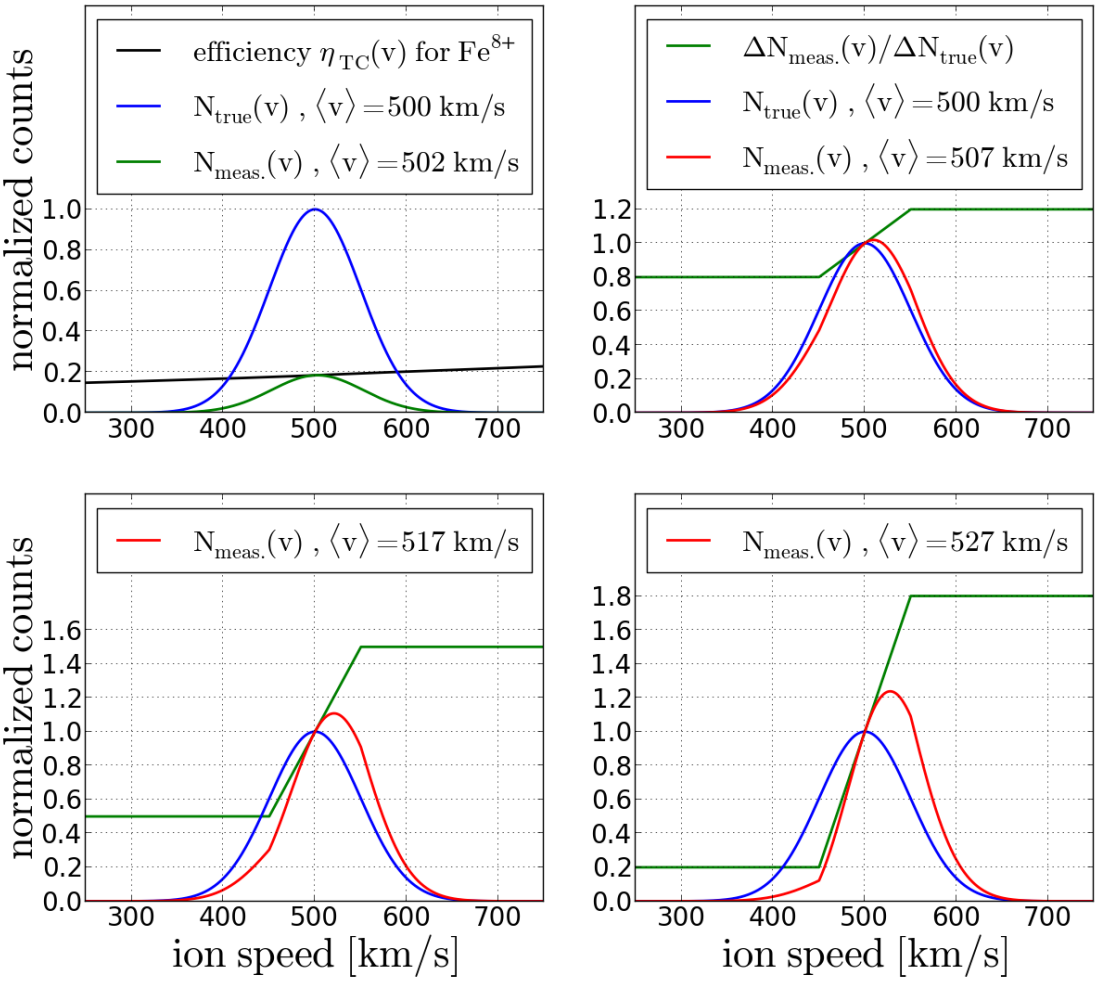

FIGURE 4.32: Upper left panel: Systematic deviation of the measured VDF (green) from an assumed true VDF (blue) due to the speed-dependent CTOF instrumental triple coincidence detection efficiency $\eta(v)$ (black), that we estimated from the CTOF preflight calibration data after [Aellig, 1998b]. We see that although η is low neither the VDF shape nor the mean speed changes significantly due to the small gradient of $\eta(v)$, while the calculated change for Fe^{8+} can be even assumed as an upper estimate for other heavy ion species as explained in the text. The true VDF is assumed as approximately Maxwellian with a thermal speed of 50 km/s as it is typically observed in the fastest wind measured with CTOF in the period DOY 174-220, 1996. The other panels illustrate by the artificial function $\Delta N_{meas}/\Delta N_{true}$ (green) how dramatic systematic errors in the response model have to be over the course of the Epq-steps (in the VDF core) in order to change significantly the obtained mean speed of the VDF. As all efficiency effects are more pronounced for wider (hotter) VDFs, they are even smaller in the slow wind with typically colder VDFs.

measured over a much smaller fraction of this speed range. In the upper left panel of Figure 4.32, we therefore show the effect that the estimated iron detection efficiency has on an ideal Maxwellian VDF that has a mean speed of 500 km/s and a thermal speed of 50 km/s which are typical values for the fast wind that we measure with CTOF in the time period DOY 174-220, 1996. We see that while most counts that enter CTOF are not detected as TC events due to the low value of the efficiency $\eta(v)$, the shape of the measured VDF N_{meas} shows only small deviations from the assumed fast wind VDF. This is due to the still moderate change of $\eta(v)$ that modifies the assumed true distribution after

$$N_{meas}(v) = \eta(v) \cdot N_{true}(v) \tag{4.45}$$

by only a few percent over the given speed range of the VDF core. Compared to other discussed measurement uncertainties, this results in an insignificant change of the obtained mean speed of $\Delta_\eta \langle v \rangle = 2\,\mathrm{km/s}$ and is well below the differential speeds $\Delta v \gtrsim 10\,\mathrm{km/s}$ that we aim to resolve. We can see from Figure 4.31 that the efficiency gradient is larger for Fe^{8+} than for Fe^{12+} which is a typical behavior of the detection efficiency with the given detection principle where the overall detection probability is very sensitive close to the detection energy threshold and then saturates to an almost constant value for higher kinetic energies. Unfortunately, from the limited laboratory calibration measurements we can only estimate the TC efficiency for iron ions as the SSD efficiency is given for iron only by [Aellig, 1998b]. However, the low charge states of iron have the lowest speeds of all relevant ion species after passing the post-acceleration and are therefore also expected to have the largest efficiency gradients of all these ion species. Thus, Fe^{8+} as the lowest dominant charge state of the well-resolvable iron species, can serve as an upper estimate of the efficiency gradient for all relevant ion species. This means that the instrumental efficiencies can be completely neglected for our studies mainly due to the fact that the solar wind speed distributions are relatively narrow (even in the fast wind) compared to e.g. pick-up ion distributions where the instrumental detection efficiencies can play a crucial role for the speed estimation. In the other panels of Figure 4.32 we just illustrate that the mean speeds could also be overestimated due to systematical over- and underestimations of the VDF flanks by an inaccurate response model for a certain ion species. However, this systematic under/over-representation in the model must be dramatic to create differential speeds on the order of $\Delta v_{ip} > 10\,\mathrm{km/s}$ that one expects at 1 AU. Such model inaccuracies as shown in the two lower panels can be excluded for the major ion species as we showed in the detailed response model description.

Chapter 5

Heavy Ion Long-Term Speed Spectra at 1 AU

In this chapter we present the first results of our CTOF studies in the form of long-term integrated velocity distribution functions that we call *long-term speed spectra*. To derive these distributions functions, in a first step we integrate the base-rate corrected PHA short-term count rates $C_k(\tau, \epsilon)$ over all valid[1] CTOF cycles k in the measurement period DOY 174-220 in which the simultaneously measured proton speed, obtained from the CELIAS Proton Monitor, lies within a narrow well-defined speed range $v_p \in [v_{p,min}, v_{p,max}]$. This is equivalent to filtering the long-term data count rates $C(\tau, \epsilon)$ that we used for the response model characterization in the previous chapter 4 for the respective time periods with $v_p \in [v_{p,min}, v_{p,max}]$. In a second step we then fit the CTOF response model to these filtered long-term count rates $C_{v_p}(\tau, \epsilon)$ as described in Eq. 4.10 for each Epq-step $0 \leq j \leq 116$. From these fits we obtain directly the long-term ion count rates $N_{ij}^{v_p} = N_i^{v_p}(v_j)$ for all included ion species i of a given CTOF response model. These count rates represent the resulting long-term speed spectra that are measured in a well-defined proton speed regime.
Since the long-term speed spectra $N_i^{v_p}(v_j)$ contain a relatively high number of ion counts they allow in a first instance for systematic sanity checks of the derived speed spectra by a systematic comparison of the measured relative ion species abundances and spectral shapes. However, in the main instance we aim to analyze the long-term speed spectra for signatures of differential streaming which we identify by calculating the mean speeds of the obtained long-term speed distributions and see whether they deviate significantly from the well-defined mean proton speeds $\langle v_p \rangle \in [v_{p,min}, v_{p,max}]$.

[1] See section 5.1 for details of the cycle selection.

In this long-term spectra analysis one has to be aware of the fact that besides the restricted proton speed the other solar wind plasma parameters such as the proton density and kinetic temperature vary in general over the extended time period and might thus influence the occurrence and size of non-thermal plasma features. Furthermore, as described in chapters 1 and 2 also the in-situ magnetic field can influence present differential speeds in two ways: First in the case of an actual dependence of the ion (differential) speed magnitude on the local Alfvén speed and second by the in-situ field direction that determines the projection of the present differential speed on the instrument measurement axis and thus determines the measurable amount of occurring differential speeds. From these considerations it is clear that one has to be careful with the interpretation of the derived long-term speed spectra, as they represent a long-time average over different solar wind plasma and magnetic field conditions that are present in the given solar wind speed range. For this reason we choose to call the long-term integrated speed distributions presented in this chapter long-term *speed spectra* in contrast to the short-term *velocity distribution functions* that we derive in the next chapter 6 from the CTOF short-term PHA data, as the latter are only integrated over the intrinsic CTOF 5-minute cycle duration and thus can provide a direct link to the local plasma and magnetic field conditions at each given measurement cycle.
On the other hand, the overall measurement period DOY 174 - 220, 1996, is short compared to a solar cycle and as we measure at solar minimum conditions the solar wind outflow is relatively well-structured by the large-scale magnetic dipole field of the Sun which reduces the variability of the measured solar wind regimes. In fact as the full investigated period only includes about 1.7 Carrington rotations, it is comparable to typical time scales of larger changes in the coronal hole structure. Therefore, as already stated in chapter 3 it is likely that we observe fast wind from the same coronal hole that extends down to low latitudes in the two periods after DOY 188 and DOY 215, so that the primary acceleration conditions of this wind might be comparable. From this perspective the long-term averaging could be less problematic, although we still have the super-imposed effects of the varying local magnetic field.
Finally, the precise evaluation of the thermal speeds from the long-term spectra is more complicated as even small changes of the mean speed on the order of 10 km/s which corresponds to the proton speed filter intervals that we use for our analysis are comparable to the thermal speeds of the VDFs in the slow and intermediate wind regimes. We therefore can only get a rough estimation of the thermal speeds from the long-term measurements and consequently we investigate the thermal speeds almost exclusively in the short-term data in chapter 6.

5.1 Data Selection and Sample Sizes

In the following we analyze the derived speed spectra integrated over all CTOF measurement cycles within the full measurement period DOY 174-220, 1996, under the condition that the simultaneously measured proton bulk speed falls within a well-defined narrow speed range. To give an overview of the number of cycles that we can include for the long-term analysis, we show in Figure 5.1 the histogram of the maximum reached Epq-steps[2] for all measurement cycles in which a 5-minute average proton speed was measured within the intervals [330 km/s, 340 km/s], [490 km/s, 500 km/s], [500 km/s, 510 km/s], and [510 km/s, 520 km/s] and where the condition of more than 500 transmitted PHA words is met. We find that in principle we have more available cycles in the slow wind interval than in each of the fast wind intervals. This is mainly due to the low number of fast wind streams that could be measured at the SOHO site during solar minimum in 1996 and partly due to the unfortunate CTOF telemetry scheme that yields an over-proportional number of cycles with an extremely low number of transmitted PHA counts in the fast wind periods. We further see that the distributions of the ESA stop-steps consist of two different populations for solar wind (proton) speed intervals. This is because the ESA stops either in the rising high-speed flank of He^{2+} (lower Epq-steps) or in the high-speed flank of H^{+} (higher Epq-steps) depending on the solar wind density and temperature. In general, for any given solar wind speed the ESA is stopped already in the He^{2+} flank when the wind is dense and/or cold as then the threshold in the SSR rate is more easily reached at a given Epq-step .
For the goal of a comparative analysis of long-term speed spectra recorded over a relatively large speed range it is crucial to only take into account those cycles that cover a sufficiently large span in Epq-steps. This is necessary in order not to artificially cut-off the low-speed flank of the spectra for certain ion species, as the speed spectra shall be derived from the same set of cycles for all species simultaneously, which means from one series of up to 117 response model fits to the long-term data. In order to find a compromise between the highest possible number of included cycles and a reasonably wide speed range for a high number of ion species it is a natural choice to set the minimum stop-step filter in the gap of the bimodal stop-step distribution. In this way, we lose a fraction of the cycles and might also introduce a small bias as we implicitly select low density/high temperature cycles. Yet, this is not a major problem as in this first analysis, we only aim to evaluate whether there can be found any signature of differential speeds in the long-term data at all, even when this is only the case under certain solar wind conditions. On the other hand, the selected ESA stop-step filter allows for

[2]We call the maximum reached Epq-step for each cycle in the following the *ESA stop-step*, corresponding to the lowest measured energy-per-charge value in the electrostatic analyzer for the given cycle.

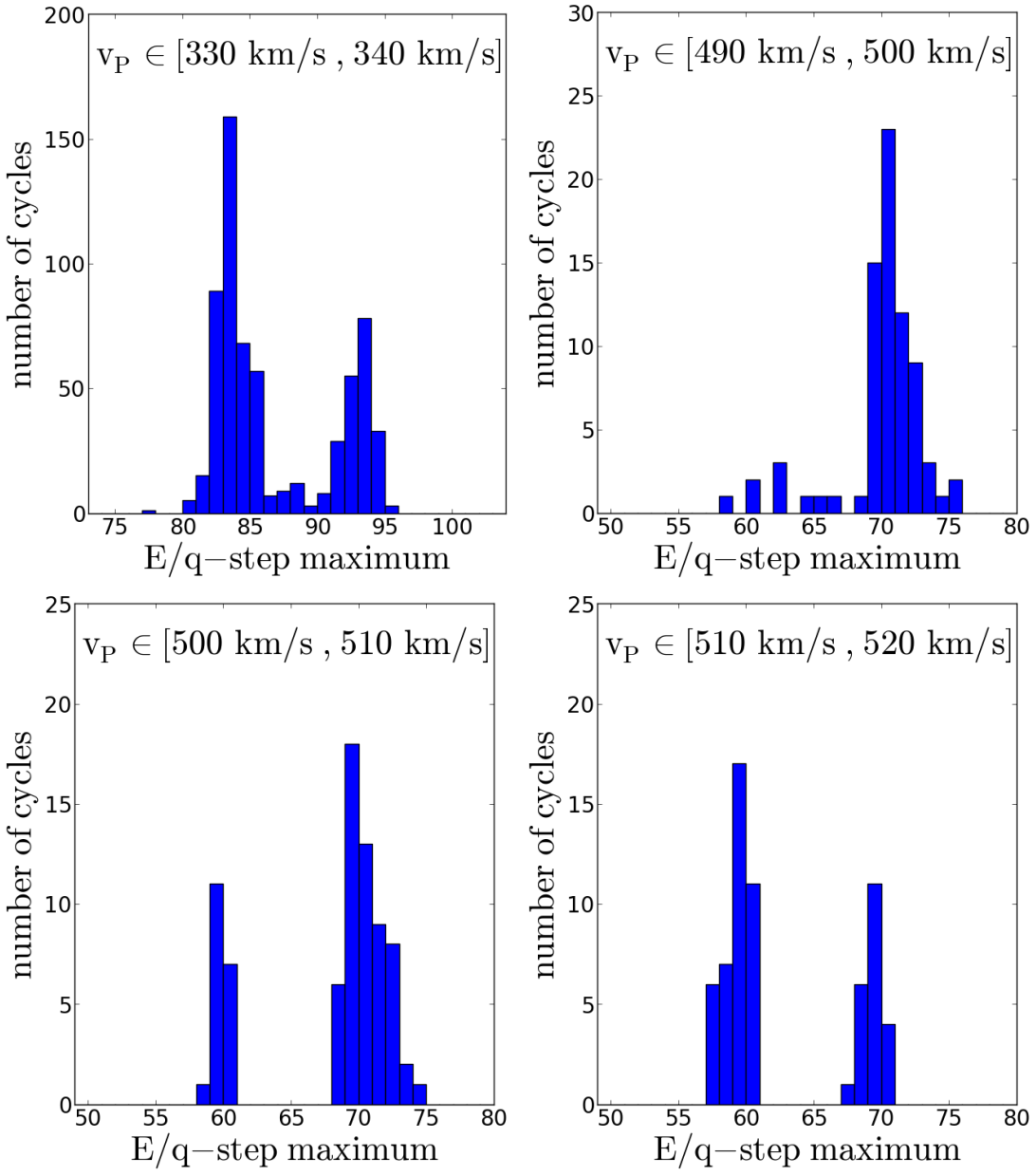

FIGURE 5.1: Histogram of the maximum reached Epq-step (*stop-step*) by the CTOF electrostatic analyzer (ESA) for measurement cycles in the slow solar wind with simultaneously measured proton speed $v_p \in [330\,\mathrm{km/s}, 340\,\mathrm{km/s}]$ (upper left panel) and in the fast wind with proton speed $v_p \in [490\,\mathrm{km/s}, 500\,\mathrm{km/s}]$, $v_p \in [500\,\mathrm{km/s}, 510\,\mathrm{km/s}]$, and $v_p \in [510\,\mathrm{km/s}, 520\,\mathrm{km/s}]$ (upper right panel and both lower panels, respectively). Due to the ESA stop-step condition explained in the text, we only utilize cycles in the long-term speed analysis for $v_p \in [330\,\mathrm{km/s}, 340\,\mathrm{km/s}]$ that have maximum reached Epq-steps $j \geq 90$ and for $v_p \in [500\,\mathrm{km/s}, 510\,\mathrm{km/s}]$ that have maximum reached steps $j \geq 68$. We thus have about 3.5 times more cycles included in the slow wind analysis than in the fast wind analysis.

a speed scan of ion species with mass-per-charge values as low as m/q =2.3 down to about 2 thermal speeds below their speed distribution maximum as we show below. For the following comparison of speed spectra in the slow and fast wind, we choose the proton speed ranges of [330 km/s, 340 km/s] and [500 km/s, 510 km/s], respectively. While for the slow wind case the choice of the proton speed bin is not critical in terms of cycle statistics and we just choose a bin close to the minimum speed that can be reliably measured by the CELIAS proton monitor, for the fast wind case we see from Figure 5.1 that when we switch from the [500 km/s, 510 km/s] to the [510 km/s, 520 km/s] proton speed interval, we find a relatively large drop in cycle numbers in particular in the population of high stop-steps (57 compared to 22 valid cycles). We therefore use for this first analysis the proton speed interval [500 km/s, 510 km/s] and set the minimum ESA stop-step filter condition inclusively on Epq-step 68 to utilize the full cycle statistics of the higher stop-step population. Analogously, we set this condition inclusively at Epq-step 90 for the slow wind case. This leaves us with a sample size of about 190 cycles in the slow wind bin [330 km/s, 340 km/s] and 55 cycles in the fast wind bin [500 km/s, 510 km/s] which corresponds to a total measurement period of approximately 16 hours in the slow wind and about five hours in the fast wind. While the slow wind sample is measured over several periods over the whole measurement period, the fast wind is measured on 5 days only: DOY 185, 186, and 213, 214, 215 containing measurement periods of a few minutes to hours. Due to the time difference of about 27 days between the two observed fast periods it is likely that both originate from the same recurrent coronal hole that extended to low latitudes over the consecutive Carrington rotations 1911 and 1912 [Hefti, 1998a].

5.2 Derivation of Heavy Ion Long-Term Speed Spectra

In order to derive speed spectra for individual ion species we finally apply the CTOF response model to the PHA count data to conduct the probabilistic ion count assignment as described in section 4.1. Note that for these fits we have to use the Poisson χ^2-minimization function in Eq. 4.10 as even in the long-term data for the lowest Epq-steps (corresponding to highest Epq-values) the low count rates cannot be approximated with normal statistics anymore. However, this is not a problem as we already estimated the goodness of the response model in the previous section and, as discussed there, the instrument response itself can be assumed as constant for all times and does not depend on the counting statistics nor on the solar wind conditions. To conduct the fits we use the Broyden-Fletcher-Goldman-Shanno (BFGS) minimization algorithm [Broyden, 1970, Fletcher, 1970, Goldfarb, 1970, Shanno, 1970] which is also a conjugate-gradient

method similar to the Levenberg-Marquardt (LM) algorithm [Levenberg, 1944, Marquardt, 1963][3], that we used in chapter 4.
As a last check we also compared the overall estimated count rates by the fit with the overall number of actually measured counts in the ET-matrix at any relevant Epq-step j and find differences up to the order of a few percent for the fits with the Kappa-Moyal response model in the long-term term data. As in total we have to assign the exact number of counts to the ion species that are actually measured we renormalize the fitted count rate contribution at each ET-bin within any given ET-matrix j by assuming that

$$\forall \tau, \epsilon : \widetilde{C}(\tau, \epsilon) \stackrel{!}{=} C(\tau, \epsilon) \tag{5.1}$$

after having performed the fit. Thus, for each ion species its $\widetilde{C}_i$ contribution that adds up to the model total count rate $\widetilde{C}$ is normalized as

$$\widetilde{C}_{i,norm}(\tau, \epsilon) = \frac{C(\tau, \epsilon)}{\widetilde{C}(\tau, \epsilon)} \cdot \widetilde{C}_i(\tau, \epsilon) \tag{5.2}$$

so that the final ion count rate for a given ion species at a given Epq-step $0 \leq j \leq 116$ reads

$$N(v_{ij}) = N_{ij,norm} = \sum_{\tau,\epsilon} \widetilde{C}_{i,norm}(\tau, \epsilon) \tag{5.3}$$

where v_{ij} is again the nominal ion speed that corresponds to the given Epq-step after Eq. 2.1. The explained normalization procedure follows the applied procedure in [Berger, 2008].

5.3 Analysis of Speed Spectra

We illustrate the analysis of the long-term speed spectra with the measured spectra of O^{6+} and O^{7+} that are shown in Figure 5.2 for the described slow wind case ($v_p \in [330\,\mathrm{km/s}, 340\,\mathrm{km/s}]$). When fitting a 1D-Maxwellian (or Gaussian) to the measured reduced speed spectra we can see that both ion spectra consist of a thermal core which

[3]The reason for the application of the BFGS algorithm instead of the LM algorithm is purely a practical one, as the BFGS algorithm is implemented in the *fmin* method of the *python scipy optimize* library that can be used with a user-defined minimization function, while the standard *scipy optimze leastsq* routine that works with the Levenberg-Marquardt algorithm expects the standard χ^2-minimization function given in Eq. 4.13. For the model calibration fits we used the latter method as it calculates automatically the covariance matrix from which one can directly calculate the estimated errors of the fitted ET positions and widths in section 4.4 and 4.5. We compared the obtained ion count rates for both minimization algorithms and found differences far below the deviations between data and response model regardless of the count statistics.

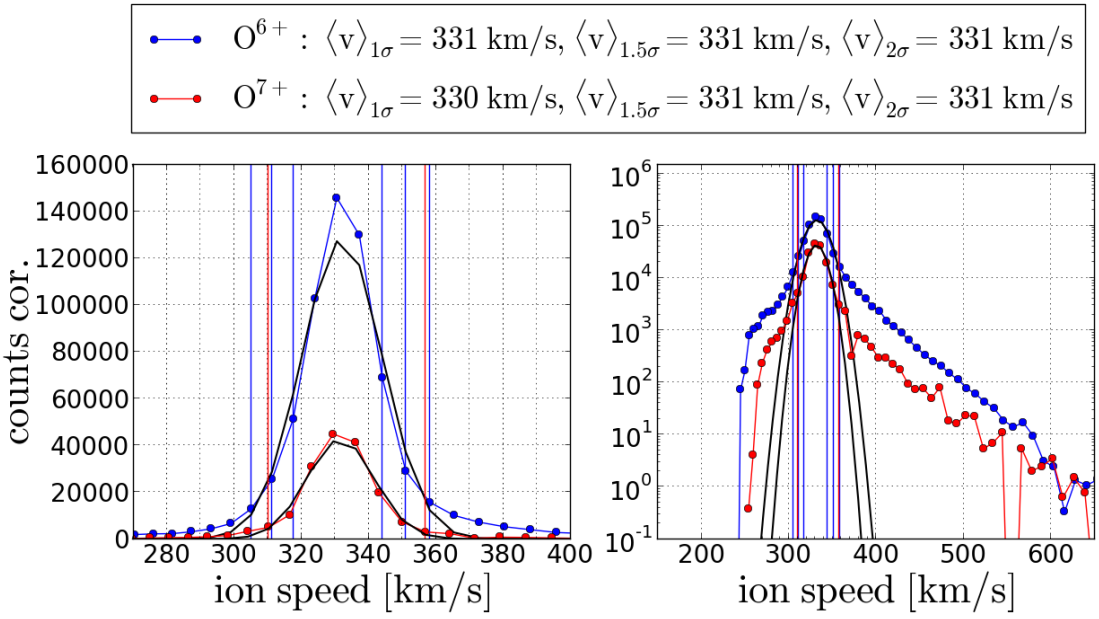

FIGURE 5.2: Long-term accumulated speed spectra for O^{6+} and O^{7+} under the condition $v_p \in [330\,\mathrm{km/s}, 340\,\mathrm{km/s}]$ for DOY 174-220, 1996. The spectra are shown in linear (left) and logarithmic (right) count rate scale and are phase-space corrected as described in chapter 3. Estimated mean speeds from the Gaussian fit for the ion species: O^{6+} : $\langle v_i \rangle = 332\,\mathrm{km/s}$, O^{7+} : $\langle v_i \rangle = 332\,\mathrm{km/s}$.

is well-described by the fit and a supra- (and sub-) thermal tail at very high (low) speeds that show in first approximation an exponential decrease (increase). One can now either obtain the core mean speed $\langle v_i \rangle$ of a given ion species from the applied fit or derive it from a moment calculation that we define in analogy to chapter 3:

$$\langle v_i \rangle = \frac{1}{\sum_{j=s_{min}}^{s_{max}} n_{ij}} \cdot \sum_{j=s_{min}}^{s_{max}} n_{ij} \cdot v_{ij} \tag{5.4}$$

where $n_{ij} = n(v_{ij})$ is the (phase space corrected[4]) count rate measured at the speed v_j that is calculated for the given ion species from the respective Epq-step j after Eq. 2.1. As discussed in the previous section we cannot simply calculate the mean speed over the full Epq-step range $0 \leq j \leq 116$ as we have to take into account the interruption of Epq-stepping, but on the other hand we have to ensure that the selected speed range is symmetrical with respect to the core of the distribution in order not to bias the calculated mean speeds. Making again use of the Gaussian approximation for the distribution, we determine 1σ-, 1.5σ-, and 2σ- intervals for the calculation of the mean speed that are centered around the most probable speed v_{max} with count rate n_{max}. These intervals are illustrated in Figure 5.2 as vertical blue lines for O^{6+}. The most narrow 1σ

[4] As discussed in 4.8 any further instrumental efficiency corrections are negligible for this study of solar wind spectra as long as we are only interested in the kinetic properties of the thermal core of the spectra.

interval is limited by the speed values on both flanks of the spectrum where a running average of the count rate drops (the first time) below a value which is 0.61 times lower than n_{max}. Accordingly, we limit the 1.5σ and 2σ environments at the speed bins where the distribution drops below values of $0.32 \cdot n_{max}$ and $0.14 \cdot n_{max}$, respectively. The 2σ-environment is also marked for O^{7+} as a red vertical line in Figure 5.2. We use the running average to ensure a higher stability in the presence of non-monotonic flanks of the spectra. In the slow wind the running average is calculated over 3 adjacent speed values only, to be applicable for the relatively cold ion distributions, while in the fast wind we use a running average of 5 adjacent speed values.
The three different intervals used for the calculation of the mean speed are needed in order to ensure the independence of the mean speed on the selected calculation interval. When we compare the mean speeds obtained from the moment calculation in Figure 5.2 among each other, we find a very good agreement with differences below 1 km/s for O^{6+} and 1 km/s for O^{7+}. Also the comparison of the fitted mean values with the calculated moments yields a very good agreement for both species with a maximum speed difference of 2 km/s, which is about one order of magnitude lower than the differential speeds we aim to resolve.
The main advantage of the moment calculation method compared to the fit is the higher stability in the presence of larger count rate jumps in the spectrum. This can be illustrated with a comparison of the two methods for the same ion species O^{6+} and O^{7+} in the fast wind case ($v_p \in [500\,\text{km/s}, 510\,\text{km/s}]$) that is shown in Figure 5.3. For the case of O^{6+} we find a similar picture as in the slow wind, with zero difference between the mean speeds obtained from the moment calculation and a slightly higher maximum difference of 3 km/s compared to the fitted mean speed. However, for O^{7+} where we have much lower count rates the fit yields a much lower speed value of 522 km/s because it most likely underestimates the high speed flank. On the other hand, the presumed 1σ-interval moment yields a very high speed value of 549 km/s because it is centered around the most frequent speed which shows a large jump in count rate. This jump is most likely not physical but introduced by occasional inaccuracies of our count assignment (fit) method in the presence of closely adjacent ion species of similar or larger order in abundance magnitude (see section 5.5).

We finally check that the artificial cut-off of the ion spectra at the ESA stop-step does not influence the calculation of the mean speeds from the given σ-intervals. As can be seen in Figures 5.2 and 5.3 the spectra reach different minimum speeds as a result of the ions' different m/q values with the O^{7+} scan finishing at a higher minimum speed. However, we note that the observed minimum speed corresponds to the absolute maximum Epq-step reached within all valid cycles which belongs to Epq-step 95 in the selected

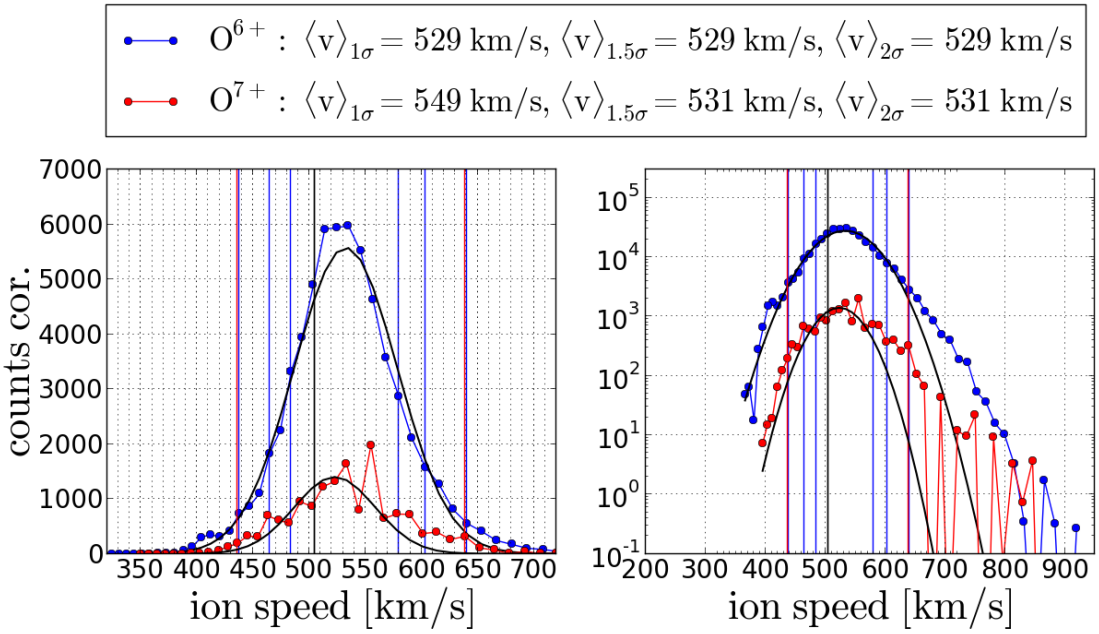

FIGURE 5.3: Long-term accumulated speed spectra for O^{6+} and O^{7+} under the condition $v_p \in [500\,\text{km/s}, 510\,\text{km/s}]$ for DOY 174-220, 1996. The spectra are shown in linear (left) and logarithmic (right) count rate scale and are phase-space corrected as described in chapter 3. In the linear scaling the count rates of O^{6+} are scaled down by a factor of 0.2. Estimated mean speeds from the Gaussian fit for the ion species: $O^{6+}: \langle v_i \rangle = 532\,\text{km/s}$, $O^{7+}: \langle v_i \rangle = 522\,\text{km/s}$.

slow wind range and to step 74 in the fast wind range as can be seen in Figure 5.1. The important speed for O^{7+} in the slow wind is $v_{stop,slow} = 281$ km/s which belongs to our selected minimum stop-step 90, and $v_{stop,fast} = 436$ km/s belonging to stop-step 68 in the fast wind. While in the slow wind due to the cold plasma the lower boundary of the 2σ-environment ($v_{2\sigma} \approx 310$ km/s) is far away from $v_{stop,slow}$, the boundary in the hotter fast wind ($v_{2\sigma,fast} = 436$) just equals the critical value $v_{stop,fast}$. Finally, we find a drop of the count rate starting for both ions shortly after the respective stop-speed is reached, which is not physical but just the end of the Epq-scan for a rapidly increasing number of cycles between Epq-step 90 and 95 in the slow wind and 68 and 74 in the fast wind. For O^{6+} the same thing happens at lower speeds and is thus less critical. In fact O^{7+} is the ion with the lowest mass-per-charge ($m/q = 2.29$ amu/e) that we include in the analysis and is therefore supposed to be the most critical case, but we also applied the same check to all analyzed physically meaningful ion spectra to exclude that ion species with slightly higher mass-per-charge values are affected in case they show considerably hotter distributions than O^{7+}.

5.4 Slow Wind Speed Spectra

In Figure 5.4 we show the accumulated long-term spectra for the best-resolved[5] charge states of the elements carbon, oxygen, neon, magnesium, silicon, sulfur, and iron in linear (left) and logarithmic (right) count rate scale. Note that in the linear representation we scaled for better comparison of the spectral shape the count rate of O^{6+} with a factor of 0.2 and the count rates of C^{5+}, Ne^{8+} and Mg^{10+} with a factor of 0.5. We find for all depicted ions a very similar spectral shape as they all consist of an approximately Maxwellian core and an extended suprathermal tail as described in the previous section 5.3. For most ions we can also find the signature of a subthermal tail, although one has to be careful with the spectral comparison at low speeds as the different species are cut-off at different speeds due to the interruption of the Epq-stepping as explained above, as well as due to the occurrence of He^{2+} random coincidences in particular for several silicon and iron charge states.

We note that the suprathermal tail can be measured to about 500-600 km/s for the presented ion species and follows in good approximation an exponential decrease which has a slightly steeper slope for the very heavy ions Mg^{10+} - Fe^{10+} compared to the lighter heavy ions C^{5+} - Ne^{8+}. In general the observed exponential tails are a signature of stochastic acceleration that is happening most likely at shocks in the inner heliosphere, which during periods of low solar activity are formed mainly at Corotating Interaction Regions (CIRs). Due to this difference in the underlying acceleration mechanism that can energize a small fraction of the ions up to several tens of MeV/nuc [Mewaldt, 2001], these tails are not further analyzed in this work but will be investigated in the future within the context of particle shock acceleration from solar wind energies to suptrathermal energies and beyond e.g. in a combined study with the SOHO/STOF sensor.
In the spectral cores, the calculated mean speeds from the 1σ-, 1.5σ- and 2σ-intervals of a given species centered around their most frequently measured speeds, show very little variation for each of the selected ion species with a maximum difference of 2 km/s. Thus, we find fairly symmetrical cores for all of these ion species which yields a well-defined mean speed calculated with the given method over these extended core intervals which ensures a meaningful comparison between the different ion species. For all shown ion species in Figure 5.4 we calculate mean speeds between 330 and 333 km/s which is clearly comparable to the mentioned differences in mean speed calculated

[5] In most cases the best-resolved charge state of a given element is the one with the highest relative abundance in the given solar wind speed regime (such as O^{6+}, Ne^{8+},Mg^{10+}, or Fe^{10+}), but in some cases a slightly less abundant charge state is even better resolved due to its dominant count rate compared to the ion species in its close environment in the ET-matrices while the more abundant species is located close to an even more abundant species (as it is the case for Si^{8+} and Si^{9+}).

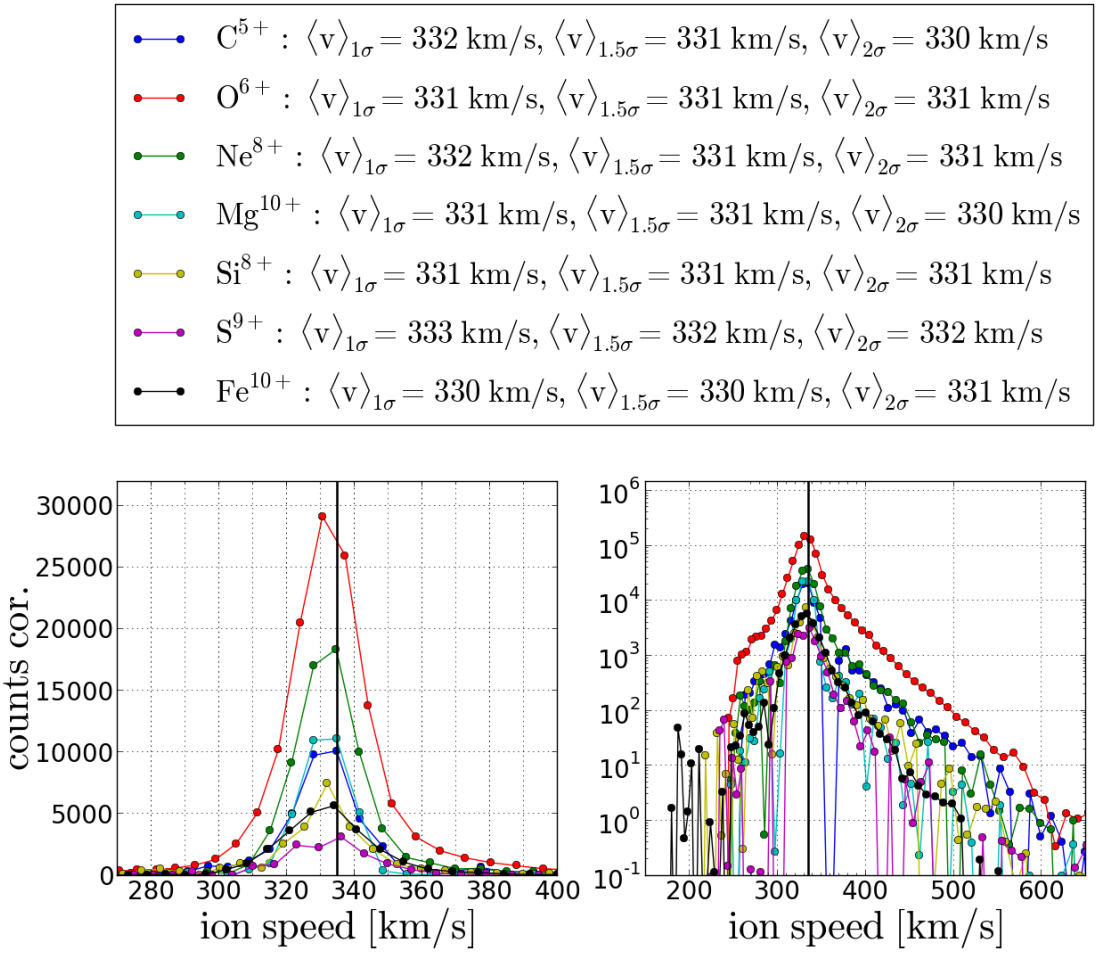

FIGURE 5.4: Long-term accumulated speed spectra for C^{5+} - Fe^{10+} under the condition $v_p \in [330\,\text{km/s}, 340\,\text{km/s}]$ for DOY 174-220, 1996. The spectra are shown in linear (left) and logarithmic (right) count rate scale. In the linear scaling the count rates of C^{5+}, O^{6+}, Ne^{8+}, and Mg^{10+} are scaled down by a factor of 0.5, 0.2, 0.5, and 0.5, respectively.

from the different σ-intervals and we can thus conclude that within the measurement accuracy the measurements are consistent with the hypothesis that all these species stream at the same speed in the analyzed slow wind case $v_p \in [330\,\text{km/s}, 340\,\text{km/s}]$. On the other hand, when we calculate the mean speed of the protons for all cycles in this given speed range (both density-weighted and not density-weighted) we find a mean speed of 335 km/s as one would expect for a large number of cycles. The proton mean speed is marked by the black vertical line in Figure 5.4. Thus, if one only considers the small statistical spread between the calculated ion species mean speeds[6] one could conclude that the heavy ion species are streaming even a bit slower than the protons in the slow solar wind. Yet, the observed difference of maximum 5 km/s between

[6]The 1-sigma standard error of the mean speed for all shown speed spectra is on the order of ≤ 1 km/s for all shown species in Figure 5.4 due to the high counting statistics and thus even below the spread between the calculated σ-interval mean speeds for all these species.

the mean heavy ion and proton speeds is on the order of the estimated systematic measurement accuracies both in the CTOF and PM measurements as we discuss below.

Before continuing with the comparison of the individual charge states of each element, we conduct a plausibility check of the observed relative abundances, not only to ensure one last time the correct assignment also of the less abundant elements in the ET-matrix, but also to prove that the base-rate correction yields reasonable ratios between the strongly corrected low-mass ions and only weakly corrected high-mass ions and thus works properly. In the last column of Table 5.1 we show the long-term slow-wind abundances measured with CTOF for the ion species C^{5+} - Ni^{9+} relative to O^{6+} over the period DOY 174-220 in 1996. As before, these charge states are selected as a sample of the best resolved ion charge states for each of the 9 analyzed elements other than oxygen. We compare these measured relative abundances with the predictions that we derive from the semi-empirical approach of observed elemental abundances in the corona [Aschwanden, 2005] and theoretically calculated charge state abundances for an estimated coronal temperature of $10^{6.1}$ K and $10^{6.2}$ K [Arnaud and Rothenflug, 1985]. Thus, the predicted relative ion abundances in the second and third column of Table 5.1 are calculated as

$$\left(\frac{N_{ion}}{N_{O^{6+}}}\right)_{pred} = \frac{N_{el,ion} \cdot N_{q,ion}(T_{C,el})}{N_O \cdot N_{q=6}(T_{C,el})} \tag{5.5}$$

where $N_{el,ion}$ and N_O are typical elemental abundances obtained from remote sensing measurements in the corona after [Aschwanden, 2005] while $T_{C,el} = 10^{6.1}$ K and $T_{C,el} = 10^{6.2}$ K represent approximately the lower and upper limit of observed coronal (electron) temperatures range during subperiods of slow solar wind at the time of our measurements. These are calculated as the iron freeze-in temperatures derived from the in-situ iron charge state abundances by [Aellig, 1998a] who used for their study the SOHO/CELIAS/CTOF iron PHA count data during a large subperiod DOY 185-220 of our study. We see that except for the sulfur charge state S^{8+} all selected ion species are observed with a relative abundance compared to O^{6+} that is within the expected range determined by the obtained coronal temperatures during the same measurement period. When strictly following the predictions we should observe about 20 % less S^{8+} and thus we might overestimate sulfur compared to its adjacent elements silicon and magnesium. Yet, we consider the overall relative charge state abundance comparison as acceptable because 1) the CTOF abundances are derived without elemental efficiency corrections due to the scarce preflight-calibration data and 2) the observed differences are comparable to the deviations and uncertainties of typical heavy minor measurements both in the corona and solar wind [Aschwanden, 2005, Bochsler, 2007].

Ratio: N_{O6+}/	Prediction		CTOF
	$\log(T_{C,el}/K) = 6.1$	$\log(T_{C,el}/K) = 6.2$	
$N_{C^{5+}}$	4	7	7
$N_{N^{6+}}$	18	12	17
$N_{Ne^{8+}}$	5	4	4
$N_{Mg^{10+}}$	7-22*	5-14*	7
$N_{Si^{8+}}$	14-41*	40-120*	21
$N_{S^{9+}}$	76	78	60
$N_{Ca^{10+}}$	124-372*	171-513*	250
$N_{Fe^{10+}}$	17-52*	28-85*	30
$N_{Ni^{9+}}$	210-631*	349-1047*	500

TABLE 5.1: Ion species abundances relative to O^{6+}: predicted vs. measured with CTOF in this work. The predictions are derived from the combination of the observed elemental abundances in the solar corona [Aschwanden, 2005] and the Arnaud and Rothenflug model [Arnaud and Rothenflug, 1985] for ionization and recombination rates at a given plasma electron temperature $T_{C,el}$. The predictions denoted with * have a large uncertainty range due to the observed discrepancies between coronal and solar wind abundances which are commonly explained with the FIP effect which might enrich the listed low-FIP elements up to a factor of 3 in the solar wind [Aschwanden, 2005]. The estimates of the electron temperature $T_{C,el}$ in the coronal source region of the slow solar wind are the calculated freeze-in temperatures obtained from an earlier CTOF study during the time interval DOY 185-220, 1996 by [Aellig, 1998a]. The relative CTOF abundances are measured without any correction for the elemental instrumental efficiency and have an accuracy of about 10 % for all species other than $N_{Ni^{9+}}$.

In the following, we compare for a given analyzed element the measured speed spectra of its best-resolved charge states among each other. We discuss explicitly the charge states of carbon, oxygen, silicon and iron that alone cover a wide range in mass and mass per charge. A larger, representative sample of measured long-term speed spectra of ion species belonging to all ten analyzed elements carbon - nickel are shown in appendix D.

As expected, we can see for the case of *carbon* in Figure 5.5 that C^{4+} is much less abundant in the measured slow wind than C^{5+}. Despite the small asymmetry in the core, we find for C^{4+} very similar mean speeds between 330 km/s and 334 km/s calculated from all three different σ-intervals. As we can see, these speeds are also very close to the calculated mean speeds of C^{5+} that lie between 330 and 332 km/s. When we have a look in the logarithmic representation, we find that the spectra of C^{4+} and C^{5+} also resemble each other over a wider speed range. The spectrum of C^{6+} is not analyzed here, due to the strong influence of the Epq-stepping interruption on it as well as due to the contamination with He^{2+} pile-up counts (see section 4.7).

As discussed already in the method description, for *oxygen* we find very similar mean speeds for O^{6+} and O^{7+}. The spectrum of O^{8+} is not analyzed here as it has again

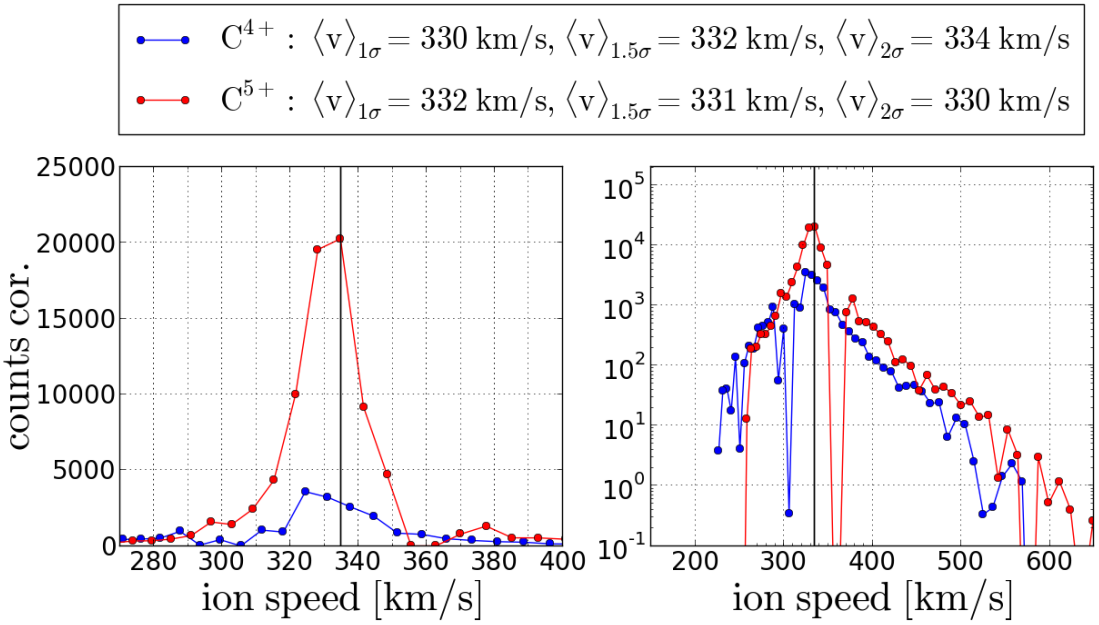

FIGURE 5.5: Long-term accumulated speed spectra for C^{4+} - C^{5+} under the condition $v_p \in [330\,\mathrm{km/s}, 340\,\mathrm{km/s}]$ for DOY 174-220, 1996. The spectra are shown in linear (left) and logarithmic (right) count rate scale.

the same mass-per-charge as He^{2+} and thus is biased by the ESA cut-off as well, while O^{5+} [Wimmer-Schweingruber et al., 1998] has a relatively low abundance and cannot be separated well from the more abundant C^{4+} peak.

For *silicon* we show in Figure 5.6 the best-resolved charge states Si^{7+} - Si^{11+}. Si^{6+} has a low abundance in the slow wind while the spectrum of Si^{12+} shows large count rate jumps in its core. This is due to the interference with other adjacent more abundant ion species such as Mg^{10+}. We see that the depicted silicon species show a reasonable charge state distribution centered around the most abundant species Si^{9+}, except for Si^{11+}, that is slightly over-represented compared to Si^{10+}. Interestingly, this ion species is also the only one that shows a significantly higher mean speed of 337 km/s compared to the other silicon charge states that are all measured at 330 ± 1 km/s, which fits well into the mean speeds of most other major charge states of the other discussed elements. As the Si^{11+} spectrum does not show any major signatures of irregularities or interference with other adjacent species its speed difference is remarkable and could be investigated closer in the future.

In the case of *iron*, we show in Figure 5.7 the spectra of the most abundant charge states Fe^{7+} - Fe^{13+}. In the left panel we can see a very similar spectral core shape for Fe^{8+} - Fe^{13+} while for Fe^{7+} we find a wider distribution, which however might be influenced by the adjacent species at the flanks as the respective Fe^{7+} count rates are relatively

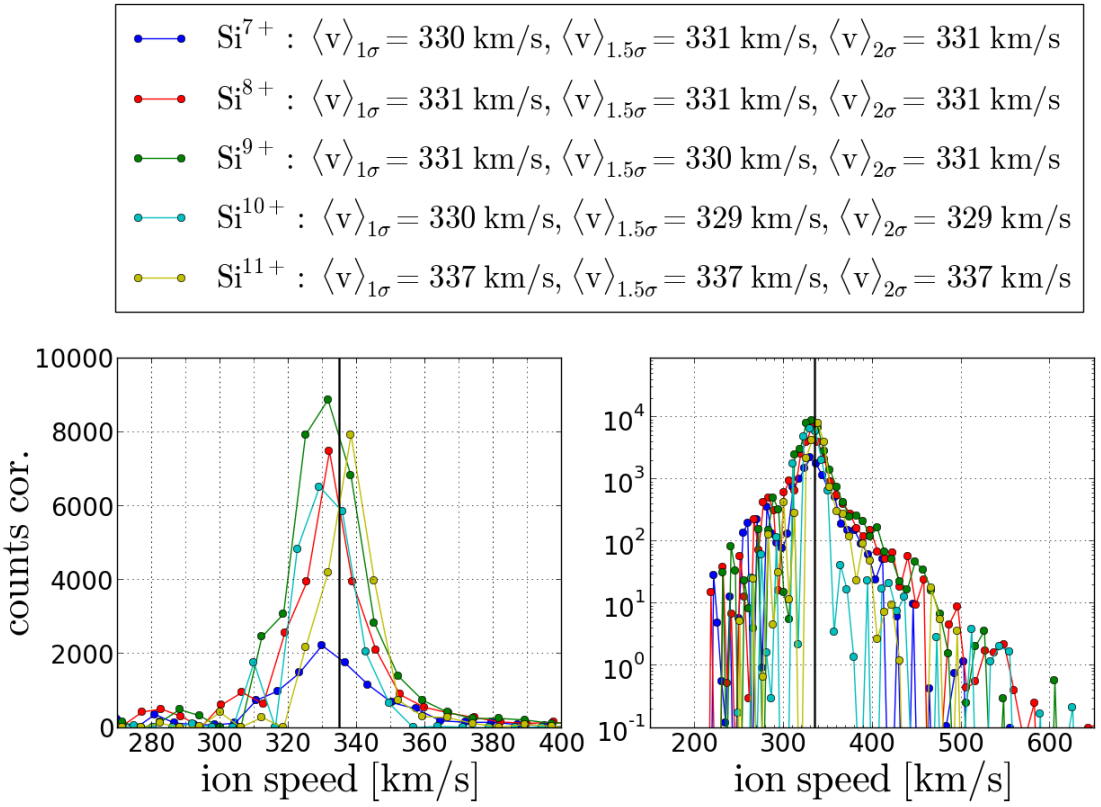

FIGURE 5.6: Long-term accumulated speed spectra for Si^{7+} - Si^{11+} under the condition $v_p \in [330\,\text{km/s}, 340\,\text{km/s}]$ for DOY 174-220, 1996. The spectra are shown in linear (left) and logarithmic (right) count rate scale.

low. Nonetheless, all spectra show very similar mean speeds both considering the different calculation intervals for each of the species as well as the mean speeds among the different charge states which very between 328 and 333 km/s.

We now aim to systematically compare the mean speeds of the different heavy ion species among each other and with the solar wind mean proton speed. In the comparison we only include ion species that 1) have sufficient counting statistics to identify an approximately Maxwellian core (e.g. unlike N^{5+} in appendix D), 2) do not have frequent jumps of their own count rate magnitude in the distribution core (e.g. unlike S^{9+} in the fast wind case discussed below), and 3) have a reasonable relative abundance compared to the discussed best-resolved ion species and among the elemental charge states (e.g. unlike the nickel ion species in appendix D). In Figure 5.8 we show the mean speeds that we calculated just as the arithmetic mean[7] of the derived 1σ-, 1.5σ-, and 2σ-interval mean speeds for all species that fulfilled the above criteria, which results in the shown 28 species for the elements carbon - iron. We can see that out of the resulting

[7]With the exception, that if one of the three mean speed values is off more than 15 km/s from both of the others, the mean speed is calculated from the remaining two values.

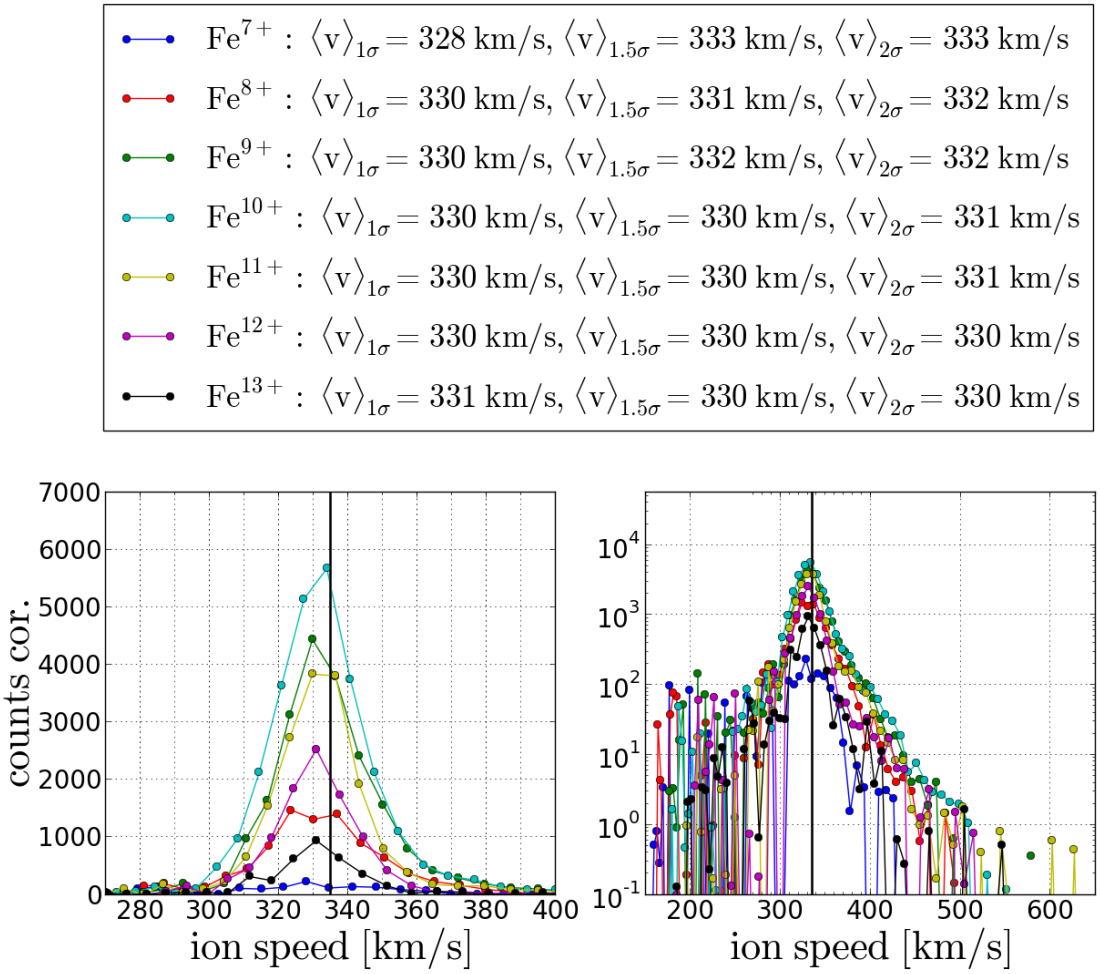

FIGURE 5.7: Long-term accumulated speed spectra for Fe^{7+} - Fe^{13+} under the condition $v_p \in [330\,\text{km/s}, 340\,\text{km/s}]$ for DOY 174-220, 1996. The spectra are shown in linear (left) and logarithmic (right) count rate scale.

28 ion species only Ne^{7+} is outside a 5 km/s tolerance interval, that also represents the range of filtered proton speeds. We find for the whole sample that the most frequently measured mean speed is 331 km/s and the average mean speed is 332 km/s. As already observed for the best resolved ion species, this might statistically indicate that the heavy minor ions stream on average a few km/s slower than the solar wind protons. Yet, this effect can be also easily created by a small mismatch of the inter-calibration between the SOHO/CELIAS CTOF sensor and the Proton Monitor as a difference of less than 5 km/s in the slow wind is well within the 1σ-standard deviation (2% of the proton mean speed) of the measured relative SOHO/CELIAS/PM speed compared to the WIND/SWE proton speeds shown in Figure 2.8. As explained in section s 2.4 and 4.8 there are also other uncertainties in the proton and heavy ion measurements that are on the order of a few km/s such as the ion-specific instrumental detection efficiencies and small geometry effects that we cannot take into account. Therefore, we do not

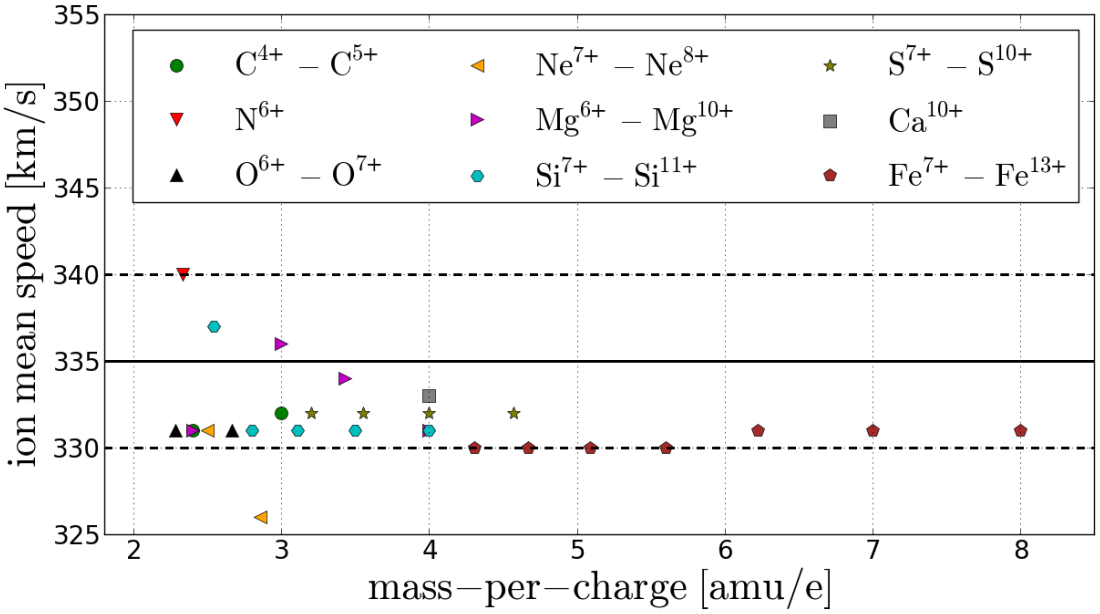

FIGURE 5.8: Long-term heavy ion mean speeds as a function of the ions' mass-per-charge derived from the CTOF Kappa-Moyal Full Stable response model for DOY 174-220, 1996 under the condition $v_p \in [330\,\mathrm{km/s}, 340\,\mathrm{km/s}]$. Note , that Mg^{9+} is not included because of too high count rate jumps in its speed spectrum core. The black solid line marks the mean proton speed and the dashed black lines mark the filtered proton speed interval.

consider these measured differential speeds as significant.

As extensively discussed in the last chapter 4, a potentially important source of systematic uncertainty within the analysis of the CTOF data is the utilized response model. In a first instance we investigate to which extent the measured speeds of the analyzed charge states of carbon, oxygen, neon, silicon and iron vary when we conduct the exact same analysis as described above with the Kappa-Moyal Reduced Stable (RS) response model that we introduced in the previous chapter and which contains 28 ion species in the applied fits belonging to the five aforementioned elements only. We analyzed the obtained (RS) long-term speed spectra in the same way as for the Full Stable response model and in appendix D we show a representative sample of these derived long-term speed spectra measured under the same slow-wind filter condition $v_p \in [330\mathrm{km/s}, 340\mathrm{km/s}]$ and integrated over the same measurement cycles. When we apply the same criteria to these speed spectra as above for the full model, and again calculate the mean ion speed as the arithmetic mean of the 1σ-, 1.5σ- and 2σ-interval mean speeds we obtain the minor ion mean speeds depicted in Figure 5.9.

On the whole we find very similar speeds compared to Figure 5.8 so that the most frequently measured mean speed is still 331 km/s, the overall average heavy ion speed of the sample has only changed by about 1 km/s to 331 km/s and for all shown ion

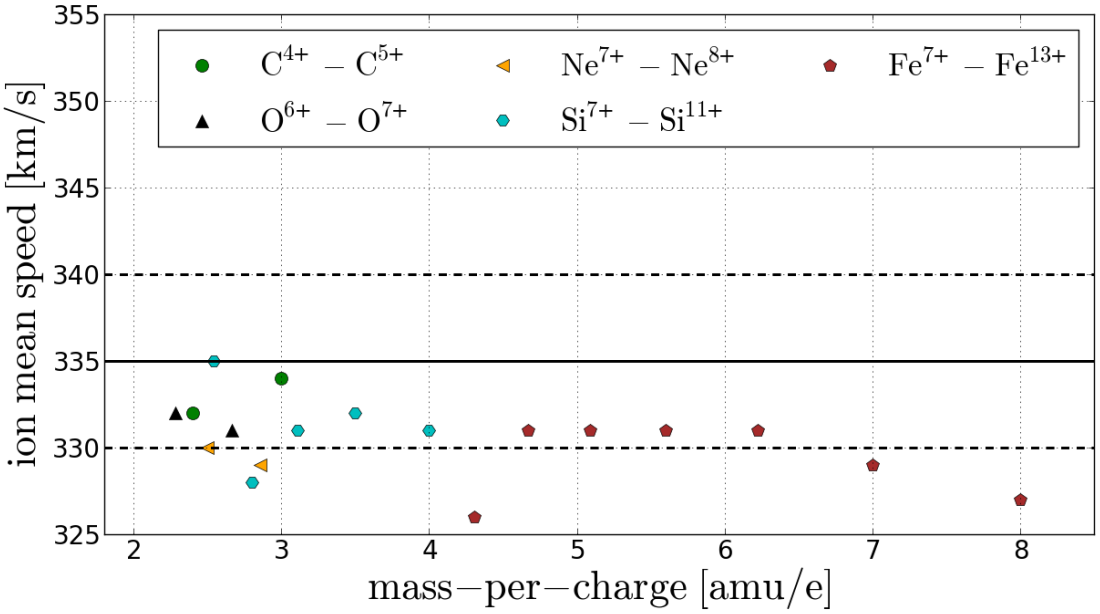

FIGURE 5.9: Long-term heavy ion mean speeds as a function of the ions' mass-per-charge derived from the CTOF Kappa-Moyal Reduced Stable response model for DOY 174-220, 1996 under the condition $v_p \in [330\,\mathrm{km/s}, 340\,\mathrm{km/s}]$.

species the change in their individual mean speeds is below 5 km/s. However, for certain ion species the shift in the measured ion mean speed due to the response model change is larger than for others. The biggest shifts can be observed for Fe^{7+} (-4 km/s), Fe^{13+} (-4 km/s), Ne^{7+} (+3km/s) and Si^{10+} (-3 km/s). As expected, these ion species have relatively low abundances compared to at least one of their adjacent ion species which can be a charge state of the same element such as for Fe^{7+} (mainly Fe^{8+}) and/or another prominent ion species of a different element such as for Fe^{13+} (mainly Si^{7+} besides Fe^{12+}), Ne^{7+} (primarily O^{6+}), and Si^{10+} (primarily O^{6+}). On the other hand, for the dominant ion species such as e.g. O^{6+}, C^{5+}, Si^{8+} or Fe^{10+} the magnitude of the observed change in ion speed due to the response model reduction is below 2 km/s in the analyzed slow wind case, so that they yield indeed the most reliable speed measurements.

5.5 Fast Wind Speed Spectra

In an analogous manner to the slow wind measurements we present in the following the long-term speed spectra for the fast wind case that is given by the filter condition $v_p \in [500\mathrm{km/s}, 510\mathrm{km/s}]$. In Figure 5.10 we show the fast-wind long-term speed spectra for the same charge states as in Figure 5.4. The spectra are shown in linear (left) and logarithmic (right) count rate scale and in the linear representation the count rates

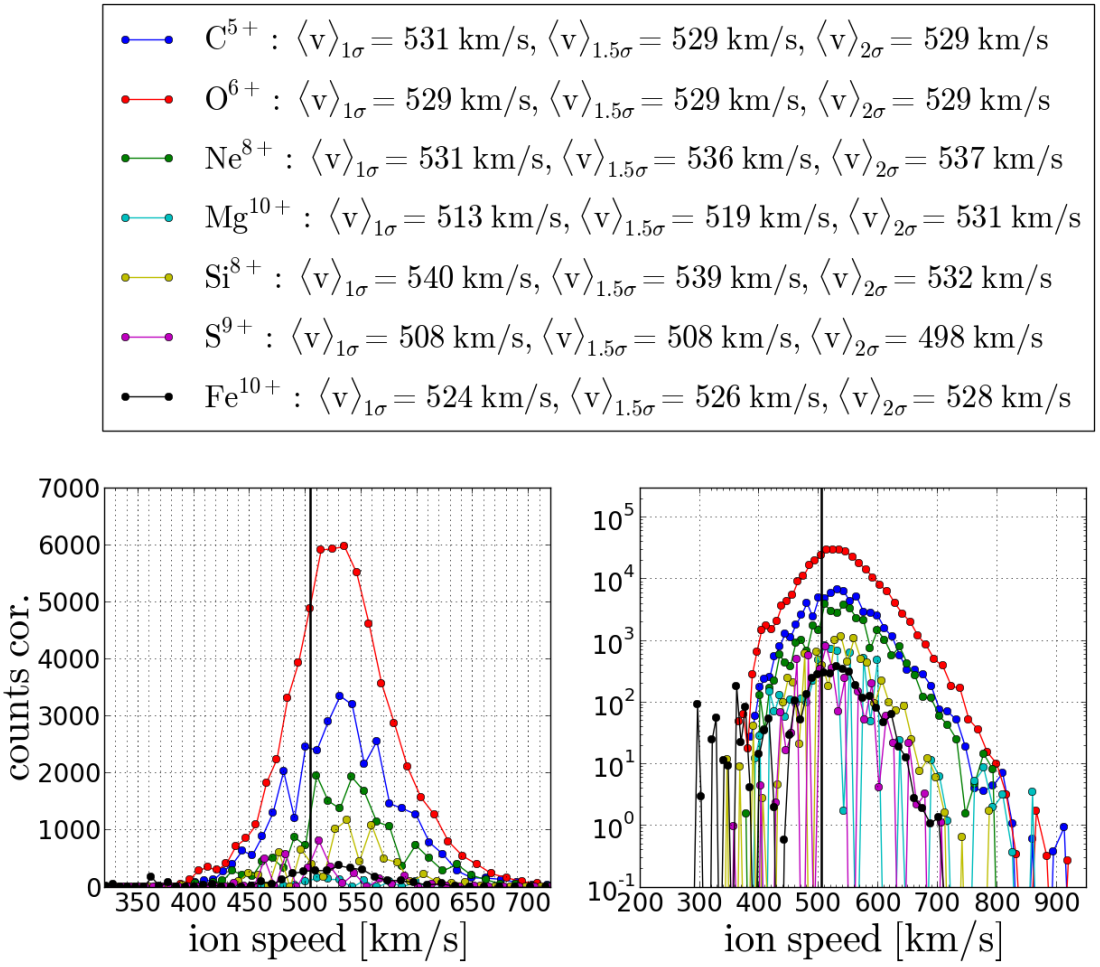

FIGURE 5.10: Long-term accumulated speed spectra for C^{5+} - Fe^{10+} under the condition $v_p \in [500\,\text{km/s}, 510\,\text{km/s}]$ for DOY 174-220, 1996. The spectra are shown in linear (left) and logarithmic (right) count rate scale. In the linear scaling the count rates of C^{5+}, O^{6+}, Ne^{8+}, and Mg^{10+} are scaled down by a factor of 0.5, 0.2, 0.5, and 0.2, respectively.

of C^{5+}, O^{6+}, Ne^{8+}, and Mg^{10+} are scaled down with a factor of 0.5, 0.2, 0.5, and 0.2, respectively. As can be seen, the measured count rates are up to one order of magnitude lower in the fast wind spectra compared to Figure 5.4 which is mainly to the fact that we have a much lower number of measurement cycles in the fast wind during the whole measurement period, but also due to lower particle densities in the fast wind. The lower count rates, (that are already the base-rate corrected count rates and thus in reality are derived from even fewer statistically independent transmitted PHA counts) lead to stronger jumps in the count rate spectra even among the more prominent ion species as can be recognized in Figure 5.10. For the less abundant elements such as sulfur, calcium or nickel these count rate jumps reach the magnitude of the actual count rate even in the core of their distribution as can be seen for S^{9+}.

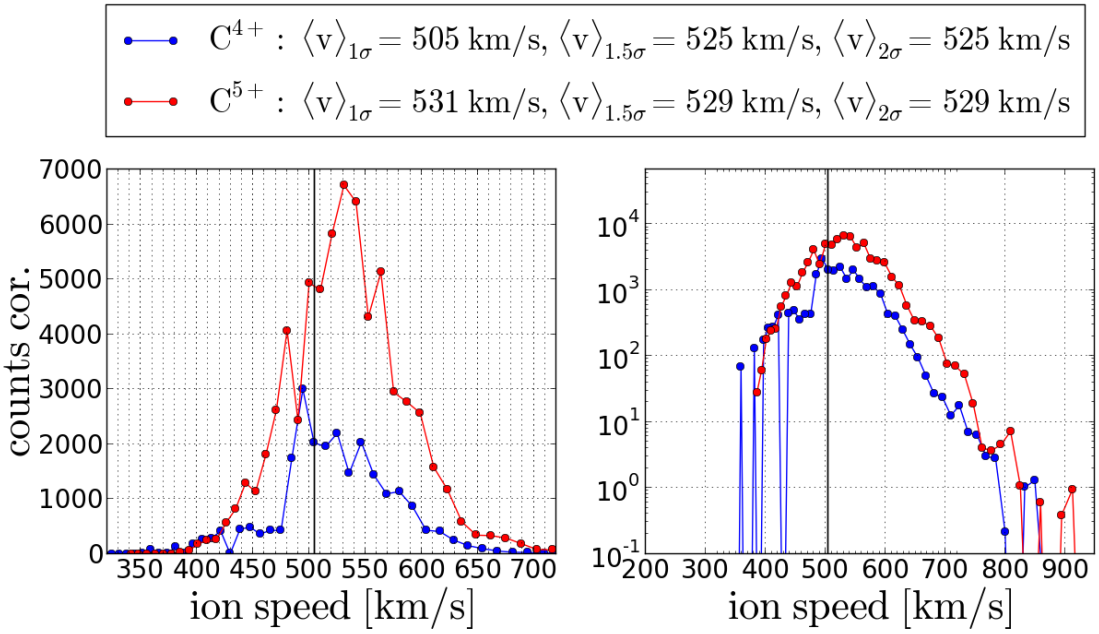

FIGURE 5.11: Long-term accumulated speed spectra for C^{4+} - C^{5+} under the condition $v_p \in [500\,\text{km/s}, 510\,\text{km/s}]$ for DOY 174-220, 1996. The spectra are shown in linear (left) and logarithmic (right) count rate scale.

In principle, we find two main differences for the measured fast wind heavy ion speed spectra compared to the slow wind case, which are 1) the larger widths of the distributions that correspond to higher kinetic temperatures and 2) the higher mean speeds for the minor ion species compared to the mean proton speed ($\langle v_p \rangle = 505\,\text{km/s}$) marked again as the black vertical line. In the following the mean speeds are again calculated as the first moment of the $1\sigma, 1.5\sigma$ and 2σ- intervals as explained in section 5.3.

In general, we observe that the differences between the derived mean speeds of the three different σ-intervals are higher in the fast wind which can be explained by the lower count rates in combination with the wider speed distributions. However, in detail we can see from Figure 5.10 that the calculated speeds deviate less for certain ion species such as for C^{5+}, O^{6+}, and Fe^{10+} ($<$ 5 km/s) than for others such as Ne^{8+}, Mg^{10+}, Si^{8+}, S^{9+} (5-10 km/s) with the largest differences calculated for S^{9+} which coincides with the highest relative count rate jumps in the core of the S^{9+} speed spectrum. When we have a look at the differential speeds in Figure 5.10 we find that the species with the most robust mean speeds show differential speeds of about 20 to 25 km/s, while the group with less stable speeds show a wider spread of -7 to 35 km/s with only S^{9+} showing partly negative differential speeds. To study these differential speeds in the fast wind case in greater detail we analyze in the following the long-term speed spectra of the most abundant carbon, oxygen, silicon and iron charge states in greater

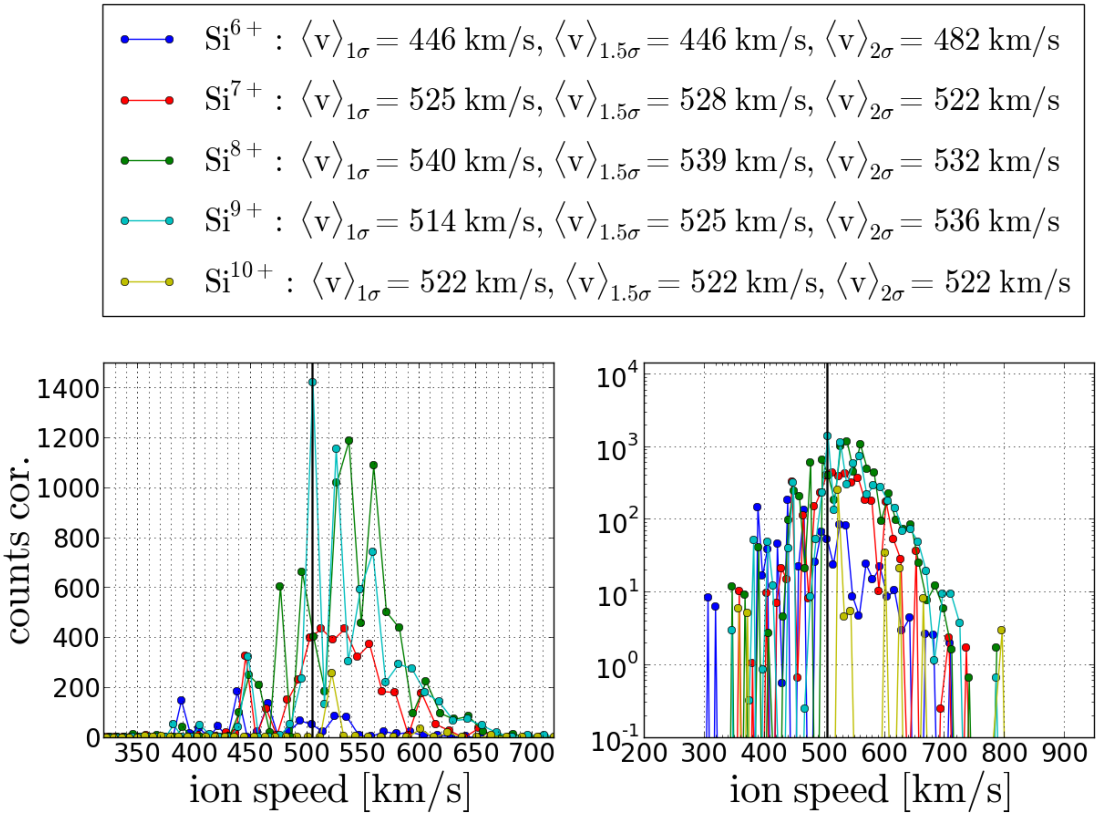

FIGURE 5.12: Long-term accumulated speed spectra for Si^{6+} - Si^{10+} under the condition $v_p \in [500\,\text{km/s}, 510\,\text{km/s}]$ for DOY 174-220, 1996. The spectra are shown in linear (left) and logarithmic (right) count rate scale.

detail in analogy to the slow wind case. Again, a bigger sample of ion speed spectra is shown in appendix D also including the spectra of less abundant elements such as sulfur and calcium.

In Figure 5.11 we show the long-term integrated speed spectra of the *carbon* charge states C^{4+} and C^{5+} for the time period 174-220 1996. We see that C^{5+} is still more abundant in the given fast wind $v_p \in [500\,\text{km/s}, 510\,\text{km/s}]$ than C^{4+} by a factor of ≈ 3 which indicates after [Arnaud and Rothenflug, 1985] a kinetic temperature of around $T_{C,el} \approx 10^{6.0}\,\text{K}$, that is in reasonable agreement with most other observed elemental charge state distributions in this fast wind case. Also in the fast wind the spectrum for C^{4+} and C^{5+} consist of approximately Maxwellian distributions in the core of the VDF, but from 650 km/s (which corresponds to about 2.5σ) on the suprathermal tail is clearly observed. In the core C^{4+} looks more asymmetric than C^{5+} with the maximum count rate at 490 km/s. Yet, the observed asymmetry is mainly due to an exceptionally high count rate at this single speed bin, which causes also the (apparent) low mean speed for the 1σ-interval, as by definition the reference speed for the calculation is the highest (phase-space corrected) count rate. As the number of included speed bins increases

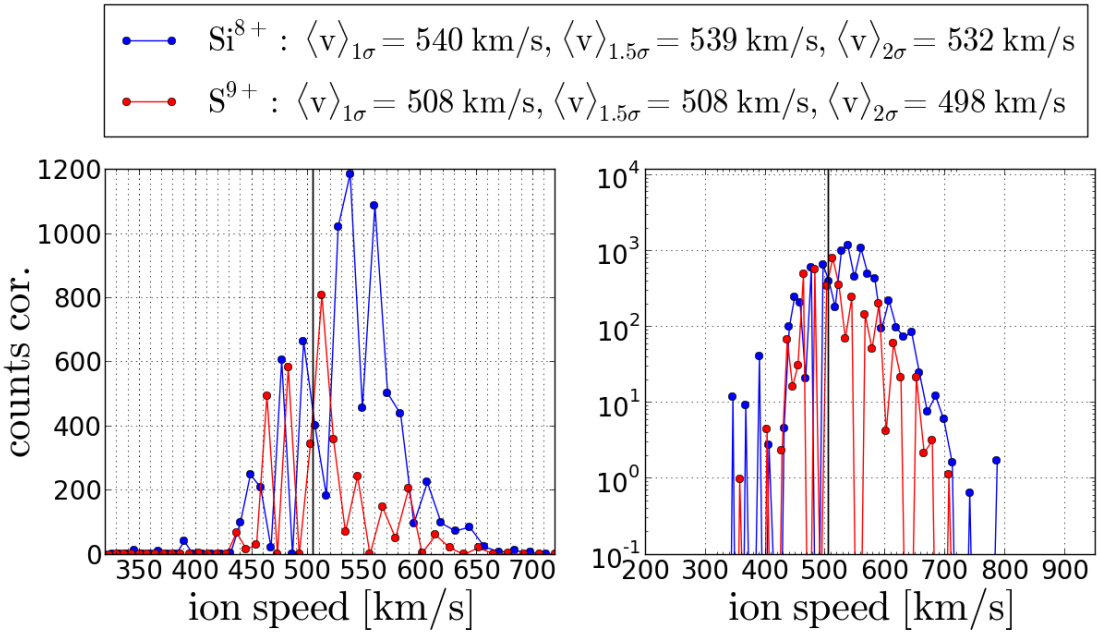

FIGURE 5.13: Long-term accumulated speed spectra for Si^{8+} and S^{9+} under the condition $v_p \in [500\,\text{km/s}, 510\,\text{km/s}]$ for DOY 174-220, 1996. The spectra are shown in linear (left) and logarithmic (right) count rate scale.

for the 1.5σ- and 2σ-interval respectively, we see that the calculated mean speeds for C^{4+} of 525 km/s are much closer to the average calculated mean speed of C^{5+} of about 530 km/s. This is very similar to the measurement of the *oxygen* ions O^{6+} and O^{7+} in Figure 5.3 with the only difference that in the case of C^{4+} the most frequently measured speed that dominates the calculation within the 1σ-interval lies at the low-speed flank of the distribution.

In the case of *silicon* we see that for the given proton speed interval only Si^{7+}, Si^{8+} and Si^{9+} are measured with sufficient count statistics to calculate the mean speeds from an applicable Maxwellian approximation of their distribution cores. We further recognize that as expected the relative abundances of the lower charge states are higher compared to the slow solar wind case, so that e.g. Si^{8+} and Si^{9+} are now measured with comparable count rates and already Si^{10+} has a very low count rate, so that we show here Si^{6+} instead of Si^{11+}. While Si^{7+} shows relatively small count rate jumps in the core and we therefore measure relatively consistent mean speeds for the 1σ-, 1.5σ- and 2σ-interval, the spectra of Si^{8+} and Si^{9+} show larger jumps and thus we also find a larger spread in their mean speeds between 514 and 540 km/s.

The origin of the count rate jumps can be better understood from the comparison of adjacent ion species with comparable abundance and large overlap such as Si^{8+} and S^{9+} that are depicted in Figure 5.13 and show pronounced jumps in their obtained spectra.

We can see in particular from the linear plot in the left panel that the count rates of Si^{8+} and S^{9+} alternate in an anti-correlated pattern from one speed-bin to the next which can be observed best at their lower speed flank. As both species have very similar mass-per-charge, the same speed bin relates to the same Epq-step so that the overall existing counts in the ET-matrix environment of both species are assigned (almost) entirely to one species in one Epq-step and then (almost) entirely in the subsequent Epq-step to the other species, which is not likely to be a true physical feature of the distributions. Thus, in this Epq-step range the two species cannot be resolved well enough under the given count statistics in the fast wind, despite the systematic calibration approach. While on the low-speed flank it is likely that the nominally less abundant S^{9+} ion is assigned with a too high count rate due to the described pattern, on the high speed flank it is possible that Si^{8+} is over-represented in count rate which would explain the asymmetry of both observed distributions simultaneously. In general, the observation of the bad separation between silicon and sulfur charge states might explain the finding in the previous section 5.4 that sulfur is probably overestimated by a small factor in the CTOF data. A small refinement of the model in this range might lead to less asymmetric spectra for silicon and sulfur in the fast wind and simultaneously to even more similar speeds among the ion species. Ion species with lower counting statistics in the vicinity of more or equally abundant species are naturally more affected by this effect than the dominant ion species and therefore show a wider spread in the observed mean speeds.

Finally, we have a look on the *iron* ions in the fast wind. These cover a wide span in the higher mass-per-charge range and are therefore crucial for the understanding of the heavy ion speeds on the whole. From Figure 5.14 we can see that the most abundant iron charge states in the measured fast wind are Fe^{9+} and Fe^{10+} with almost the same relative abundance and which show only little count rate jumps so that they are calculated with relatively consistent mean speeds between 519 and 524 km/s and 524 and 528 km/s, respectively for their 1σ - 2σ environments. For Fe^{8+} we calculate somewhat lower mean speeds between 511 and 520 km/s, where the 1σ-interval measurement of 511 km/s can be again denoted to an exceptionally high count rate in the low speed of the distribution while the two larger intervals give a consistent value of 520 km/s. For Fe^{11+} we find the highest iron mean speeds between 529 and 533 km/s. On the other hand, Fe^{7+} and Fe^{12+} yield quite asymmetrical spectral shapes with higher count rates at the low-speed flank, which lead to low but consistent mean speeds between 508 and 516 km/s and 502 and 509 km/s, respectively. The count rates assigned to Fe^{13+} in this fast wind case are for most speed bins extremely low, so that no meaningful distribution can be recognized and the nominal mean speed is falsely calculated from the He^{2+} random coincidences , which yield higher count rates than the regular Fe^{13+} spectrum.

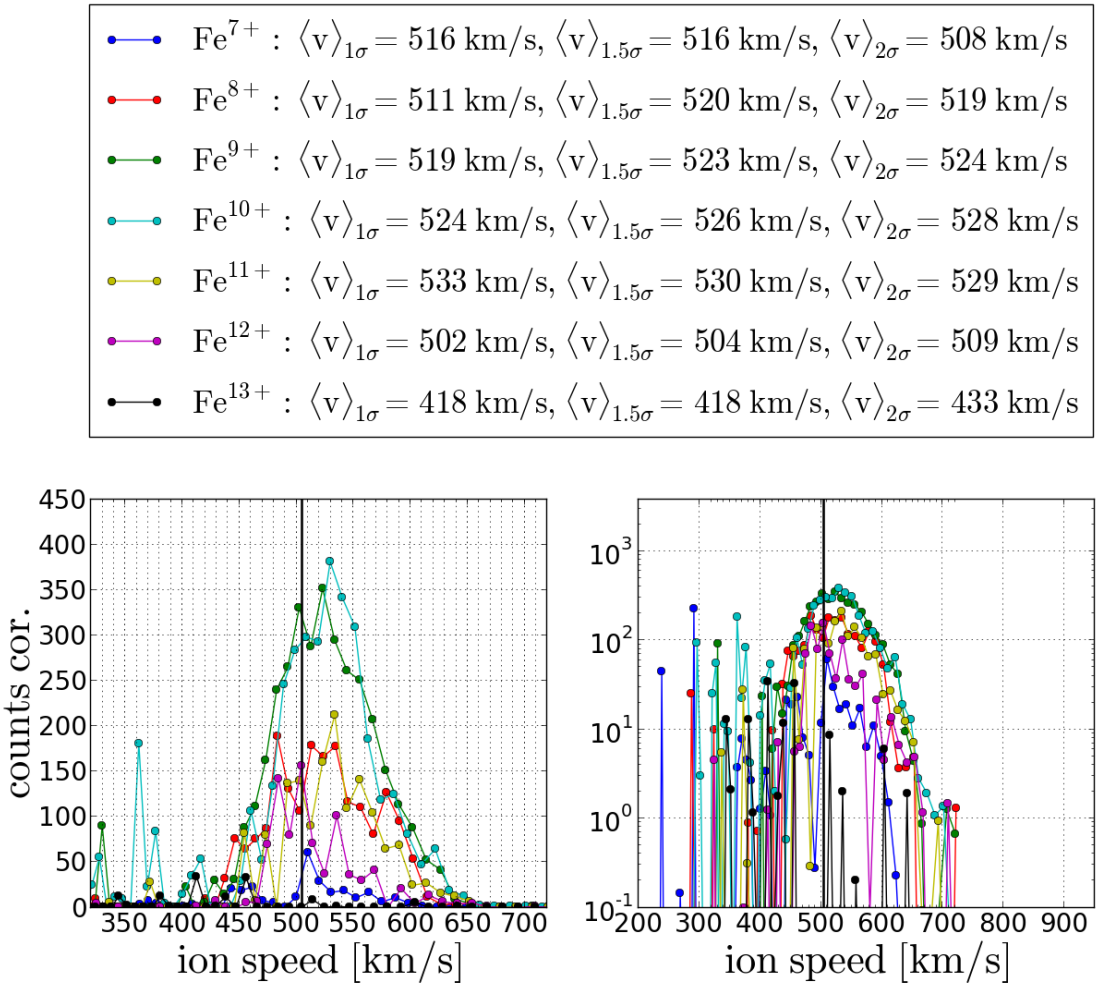

FIGURE 5.14: Long-term accumulated speed spectra for Fe^{7+} - Fe^{13+} under the condition $v_p \in [500\,\text{km/s}, 510\,\text{km/s}]$ for DOY 174-220, 1996. The spectra are shown in linear (left) and logarithmic (right) count rate scale.

Similar to the other elements the observed iron charge state distribution yields a lower mean charge state than for the slow wind, where the highest count rates were clearly observed for Fe^{10+}.

In order to gain an overview over the heavy ion mean speeds measured by CTOF under the fast wind condition $v_p \in [500\,\text{km/s}, 510\,\text{km/s}]$ we finally calculate from the derived mean speeds of the 1σ, 1.5σ and 2σ-intervals an overall consistent mean speed for a given species by calculating the arithmetic mean speed of the three speed values[8]. For the mean speed comparison we only included ion species that fulfill the same three count spectra criteria as defined for the slow wind case in the previous section 5.4. These are an approximately Maxwellian VDF core with little count rate jumps and consistent relative abundance with respect to the best resolved ion species and among

[8] Again, with the exception, that if one of the three mean speed values is off more than 15 km/s from both of the others, the mean speed is calculated from the remaining two values (see e.g. C^{4+} and O^{7+}).

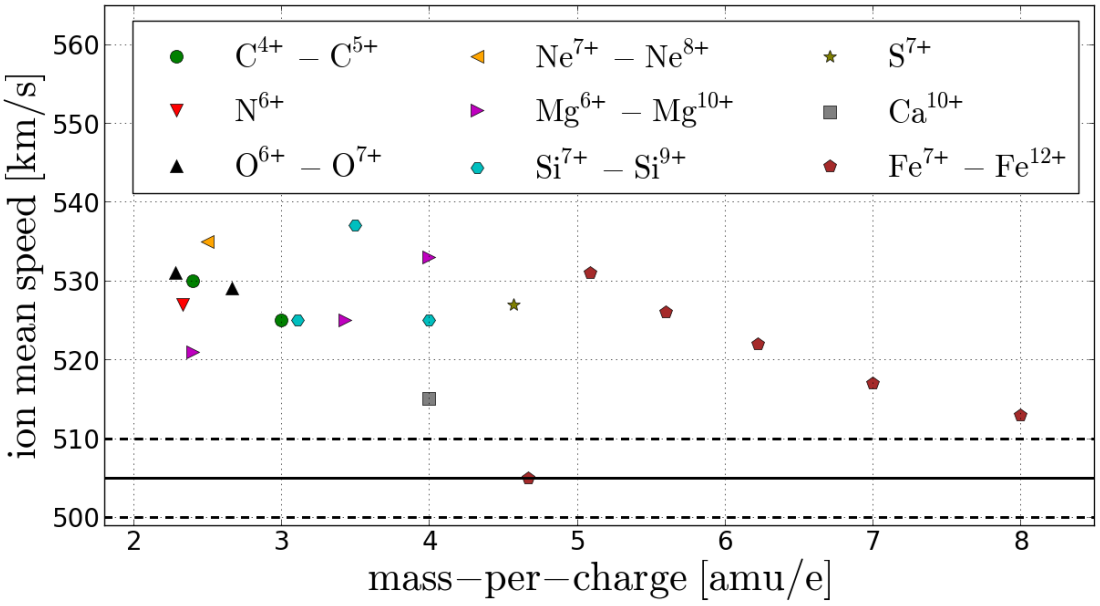

FIGURE 5.15: Long-term heavy Ion mean speeds as a function of the ions' mass-per-charge derived from the CTOF Kappa-Moyal Full Stable response model for DOY 174-220, 1996 under the condition $v_p \in [500\,\mathrm{km/s}, 510\,\mathrm{km/s}]$. Note , that Mg^{8+} and Mg^{9+} are not included because of too high count rate jumps in their respective speed spectrum core. Ne^{7+} is overlaid by the legend as it is measured with an outlying differential speed of $\Delta v_{ip} = 560\,\mathrm{km/s}$ (compare appendix D). The black solid line marks the mean proton speed and the dashed black lines mark the filtered proton speed interval.

the major charge states of the same element. From this procedure, we obtain for the given fast wind case the mean speeds of 21 ion species (out of the 69 species included in the applied ET-matrix fits with the Kappa-Moyal Full Stable response model) that are depicted in Figure 5.15.

We can see that most ion species that fulfill the above criteria are measured at speeds between 520 and 535 km/s and no species is measured at speeds below the mean proton speed. Thus, when taking the measured differences between the different sigma-interval speeds as an estimation of the statistical uncertainties[9] of the derived mean speeds, we see a statistically highly significant signature of differential streaming in the investigated fast wind speed interval with the majority of differential speeds observed between 15 and 30 km/s. This corresponds to spectral mean speeds that are measured at Epq-steps that are more than 1 and up to 3 Epq-steps away from the Epq-step corresponding to the nominal proton speed for the given species, respectively.

In general, we cannot identify any significant trend in the measured differential speeds in dependence of the ion species up to a mass-per-charge value of $m/q \approx 5\,\mathrm{amu/e}$. In

[9] As already mentioned before, the 1σ standard errors of the spectral mean speeds for the presented ion species are even lower than the observed deviations between the σ-interval mean speeds, even if we use for the error calculation the raw underlying count statistics of the measured PHA counts.

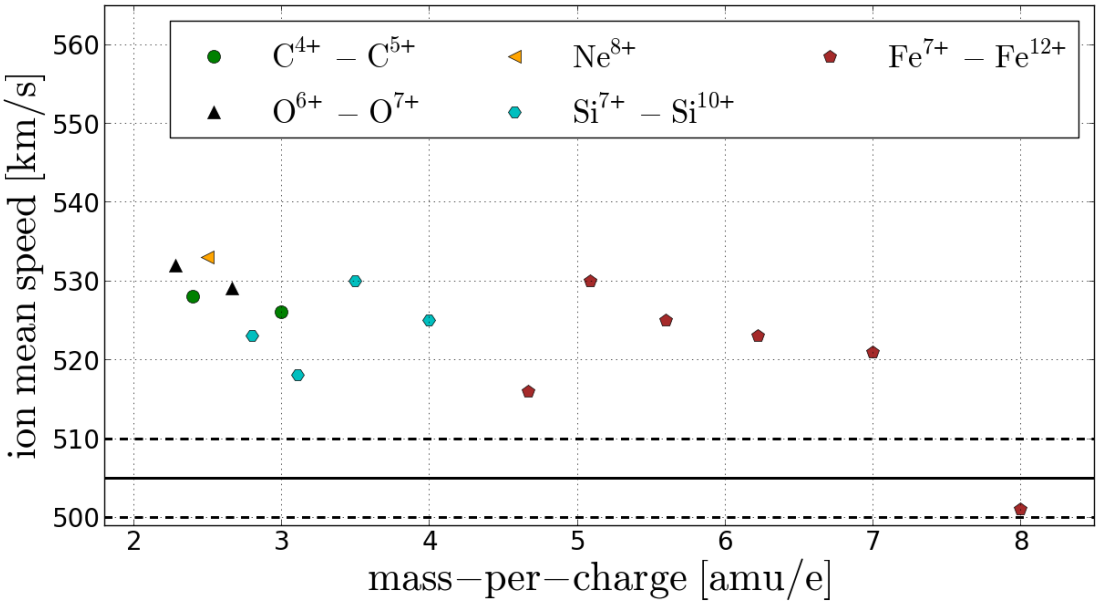

FIGURE 5.16: Long-term heavy ion mean speeds as a function of the ions' mass-per-charge derived from the CTOF Kappa-Moyal Reduced Stable response model for DOY 174-220, 1996 under the condition $v_p \in [500\,\mathrm{km/s}, 510\,\mathrm{km/s}]$.

the mass-per-charge range above $m/q \approx 5\,\mathrm{amu/e}$, we find a decreasing trend of differential speeds with increasing mass-per-charge on the order of $\Delta(\langle \Delta v_{ip} \rangle)/(m/q) \approx -5\,(\mathrm{km\ e})/(\mathrm{amu\ s})$.

However, before we make any further attempts to quantify any observed trend, we compare again the differential speeds obtained from the Full Stable response model with the differential speeds that we derive from the Reduced Stable response model to get an estimation of the stability of the measured speed values. In Figure 5.16 we depict the 15 ion mean speeds that we obtain from the CTOF Kappa-Moyal RS response model with the same calculation procedure and under the same spectral criteria as for the CTOF Kappa-Moyal FS response model. We see that the main result is the same, i.e., that the vast majority of ion species are measured at positive differential speeds between 15 and 30 km/s compared to the main proton speed. Yet, we do observe for few ion species major shifts in differential speed when comparing Figure 5.15 and 5.16 that are (almost) comparable in magnitude with the observed differential speeds compared to the protons. The largest changes are observed for Fe^{12+} (-14 km/s), Fe^{7+} (-11 km/s), Si^{8+} (-7 km/s), Si^{9+} (-7 km/s), while all other observed shifts are below 5 km/s. These relatively large changes can be again explained by the relatively low abundances of Fe^{12+} and Fe^{7+} compared to their adjacent dominant charge states (Si^{7+}, Fe^{11+} and Fe^{8+}, respectively) while for Si^{8+} and Si^{9+}, probably the pure number of adjacent ion species (in particular sulfur and magnesium ion species) makes it hard for the fit to

assign a more consistent count rate to the silicon species in the fast wind case. As we could see before, with the higher counting statistics in the slow wind the speed of the silicon species could be determined more reliably. Yet, as in the slow wind case the overall agreement between the two models means that no significant overall systematic bias on the order of any significant differential speed magnitude can be introduced for the major ion species in the fast wind case by a systematic reduction of the ion set. This observation will be used in the next chapter for the analysis of the short-term data samples that often do not contain enough counts to evaluate them with the Full Stable response model.

When comparing Figures 5.15 and 5.16 we also see that the decreasing trend in differential speed with increasing mass-per-charge observed for the iron ions has to be questioned now as in Figure 5.16 Fe^{8+} and Fe^{7+} do not line up anymore to an approximately linear decrease and in particular the speed measurement of Fe^{7+} could be identified as one of the most unreliable measurements. While so far we investigated the influence of the systematic reduction of the response model ion set on the obtained heavy ion speeds, we still have to investigate the systematic influence of the ion peak shape on these speeds. This is accomplished in the following last section of this chapter, which can be considered as the main systematic uncertainty analysis for the CTOF response model(s), as we have seen from the model sensitivity analysis in the previous chapter that no significant changes in the peak positions of the major ion species could have occurred in the calibration.

5.6 Estimation of the Systematic Ion Speed Uncertainties

In the following we want to investigate how the measured mean speeds of both the low-m/q and high-m/q ion species behave when we apply a systematical transition of the peak shape from a Gaussian peak model to the Kappa-Moyal peak model. As the observed changes are better visible when we include less ions in the fit, this systematic uncertainty analysis is illustrated for the Reduced Stable (RS) Response model but is qualitatively also valid for the Full Response model. In Figure 5.17 we show in blue the resulting model goodness χ^2_{red} when fitting the CTOF Kappa-Moyal Reduced Stable (hereafter KM-RS) model to the base-rate-corrected PHA long-term data as in chapter 4, but with different tail-scaling parameters A_C (see Eq. 4.42) that are shown on the x-axis. The three blue lines show the obtained χ^2_{red}-values as a function of A_C for the fit at Epq-step 40 (dotted line), 60 (solid line) and 80 (dashed line) to represent the wide range of typical Epq-steps for nearly all solar wind minor ion species The χ^2_{red}-values are calculated for (relatively coarse) discrete values of the tail scaling parameter $A_C \in \{0.5 \cdot 10^{-3}\,\mathrm{ch}^{-1},\ 1.5 \cdot 10^{-3}\,\mathrm{ch}^{-1},\ 2.5 \cdot 10^{-3}\,\mathrm{ch}^{-1},\ \ldots,\ 9.5 \cdot 10^{-3}\,\mathrm{ch}^{-1},\ 10.5 \cdot$

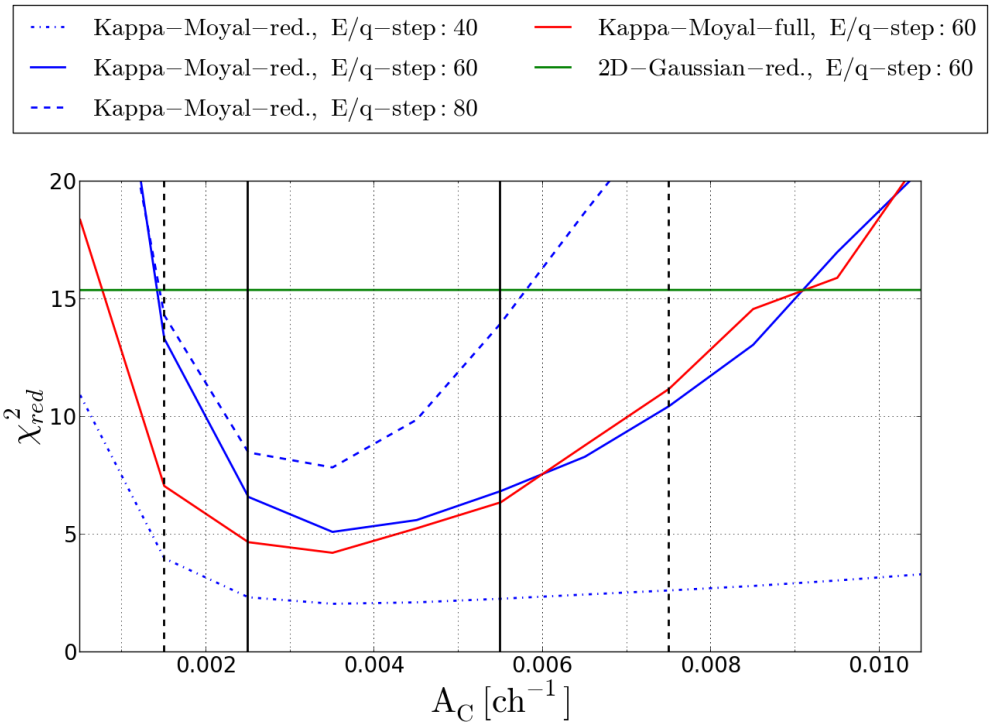

FIGURE 5.17: Response model goodness (χ^2_{red}) as a function of the universal tail-scaling parameter A_C (see Eq. 4.42) for the CTOF Kappa-Moyal Reduced Stable response model (KM-RS) in blue for Epq-step 40 (dotted line), 60 (solid line) and 80 (dashed line). The systematic 1σ-uncertainty interval is calculated from the (KM-RS) model for Epq-step 60 as described in the text and marked by the vertical black solid lines. To investigate the systematic change of the heavy ion mean speeds in dependence of the adjusted tail parameter in the applied (KM-RS) model, we evaluated the mean speeds for a sample of ion species with model tail-scaling parameters in the interval [$A_C = 0.0005\,\mathrm{ch}^{-1}$,$A_C = 0.0075\,\mathrm{ch}^{-1}$] (see text and the following Figures 5.18 - 5.20). The case $A_C = 0.0015\,\mathrm{ch}$ describes the case of an approximately Gaussian peak shape as can be also seen from the comparison with the Gaussian Reduced Stable response model (G-RS) at Epq-step 60 represented by the green solid line. The red solid line shows the model goodness for the CTOF Kappa-Moyal Full Stable (KM-FS) response model for Epq-step 60.

$10^{-3}\,\mathrm{ch}^{-1}$} covering a wider range of values around the optimal tail-scaling parameter $A_C = 0.0035\,\mathrm{ch}^{-1}$ that we found in chapter 4. By the red solid line we also show the calculated model goodness in dependence of A_C for the CTOF Kappa-Moyal Full Stable (KM-FS) response model at Epq-step 60, that shows naturally smaller χ^2_{red}-values at the low-tail flank as more included ions can better compensate a too low tail-scaling parameter, but as the KM-RS model, it also has its minimum at $A_C = 0.0035\,\mathrm{ch}^{-1}$. Finally, we plotted the χ^2_{red}-values of the Gaussian Reduced Stable response model (G-RS) for comparison as the green solid line, which is by definition independent of any tail scaling parameter. As we can see, for all three Epq-steps the selected optimal peak scaling parameter A_C yields the lowest χ^2_{red}-value as it is supposed to be for a response model

that should be valid for all Epq-steps[10]. Note that the KM-RS model curve for Epq-step 40 shows naturally a weak dependency on the tail parameter as the low counting statistics in this step does not allow a very good distinction between the different models. The curve at Epq-step 80 would in principle allow for the best distinction between the models due to the high count rates, if not at this Epq-step only ions species with low mass-per-charge and thus with relatively low TOF values and small peak tails would be measured. Therefore, probably the best overall model evaluation can be done at an intermediate Epq-step 60, where still several iron and silicon ion species are present in the data and the count rates are sufficient to observe the goodness of the model in dependence on the tail scaling parameter A_C. Thus, following the standard uncertainty estimation method for approximately normal counting statistics after [Press, 1991] we obtain the boundaries of the 1σ confidence interval for the tail-parameter at those values A_C where the solid blue line $\chi^2_{red,KMRS-60}(A_C)$ exceeds the minimum value $\chi^2_{red,KMRS-60}(A_C = 0.0035\,\mathrm{ch}^{-1})$ by an absolute difference of $\Delta\chi^2_{red} = 1$. This is the case approximately at $A_C = 0.0025\,\mathrm{ch}^{-1}$ and $A_C = 0.0055\,\mathrm{ch}^{-1}$ and these values are marked by the black solid vertical lines in Figure 5.17[11].

As in the previous sections of this chapter, we can now derive the ion mean speeds in a certain solar wind speed regime by fitting the proton-speed-filtered long-term data with the KM-RS response models with different tail parameter A_C to investigate the dependence of these ion speeds on the model peak shape. Except for the change of A_C the fits are exactly conducted as described previously in this chapter and the corresponding spectra from which we calculate the mean speeds are shown at the end of Appendix D. We show the variation of the ion mean speeds here for the best resolved ion species of carbon - silicon (compare Figure 5.10) and the most reliable iron charge states Fe^{8+}- Fe^{11+} for the discussed fast wind case $v_p \in [500\,\mathrm{km/s}, 510\,\mathrm{km/s}]$. In Figure 5.18 we show the derived mean speeds for the ion species C^{4+} - Fe^{11+} as a function of mass-per-charge for the case of the optimal tail-scaling parameter $A_C = 0.0035\,\mathrm{ch}^{-1}$ that are thus equivalent to the values in Figure 5.16. Yet, we plotted in addition as the gray shaded area the calculated 1σ confidence interval that we obtain from the mean speed values of the ion species, that are derived from the RS model fit with tail-scaling parameter $A_C = 0.0025\,\mathrm{ch}^{-1}$ (lower speed confidence interval boundary) and $A_C = 0.0055\,\mathrm{ch}^{-1}$ (upper speed confidence interval boundary). We see that the systematic uncertainty due to the peak tail scaling is small for ions with low mass-per-charge

[10] The shown χ^2_{red}-values for the optimal value $A_C = 0.0035\,\mathrm{ch}^{-1}$ can be directly read out from the response model plots for a wide range of Epq-steps in appendix C, both for the Reduced Stable and Full Stable CTOF response model.

[11] The fact, that we would obtain slightly different confidence interval boundaries for Epq-step 80, shows that the ansatz of a universal tail-scaling parameter is only an approximation while in fact this value is probably a bit lower for the low-m/q ions and a bit higher for the high-m/q ions.

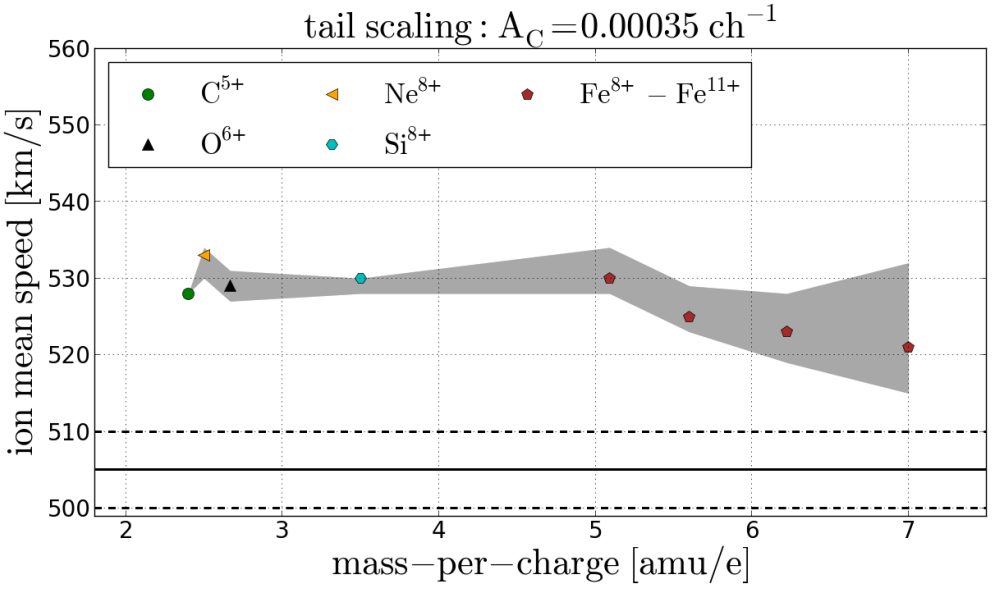

FIGURE 5.18: Mean speeds for the heavy ion species C^{5+} - Fe^{11+} derived from the Kappa-Moyal Reduced Response Model with tail-scaling parameter $A_C = 0.0035\,\mathrm{ch}^{-1}$ that represents the optimal tail scaling parameter. The 1σ-confidence interval that is represented by the gray-shaded area is given by the mean speeds derived for the shown ion species with the KM-RS model with $A_C = 0.0025\,\mathrm{ch}^{-1}$ (lower speed boundary) and $A_C = 0.0055\,\mathrm{ch}^{-1}$ (upper speed boundary) as can be seen in Figure 5.17.

as these lie on average at lower TOF values and have naturally small tails that do not alter much when the tail-scaling parameter changes. On the other hand for the iron ions the uncertainty is much larger and reaches up to almost 20 km/s for Fe^{8+} which is comparable to the observed differential speeds.

We examine next the case of a very low tail-scaling parameter $A_C = 0.0015\,\mathrm{ch}^{-1}$ that virtually equals the Gaussian case as can be also seen from Figure 5.17 where the χ^2_{red}-values of the reduced Gaussian and Kappa-Moyal response model intersect approximately at this value. We see from Figure 5.19 that for this quasi-Gaussian model, the calculated mean speeds are clearly below the lower boundary of the confidence interval. On the other hand, for very large tail scaling parameters such as ($A_C = 0.0075\,\mathrm{ch}^{-1}$), we find mean speeds above the upper speed confidence interval boundary as can be seen in Figure 5.20. In this way it becomes clear that the observed mean speeds (and thus differential speeds) for the high-m/q ion species (in particular the major iron charge states) are a sensitive quantity that depends crucially on the applied peak shape model, while for the low and intermediate m/q-values this effect is small. We discuss the consequences of this error estimation in chapter 7.

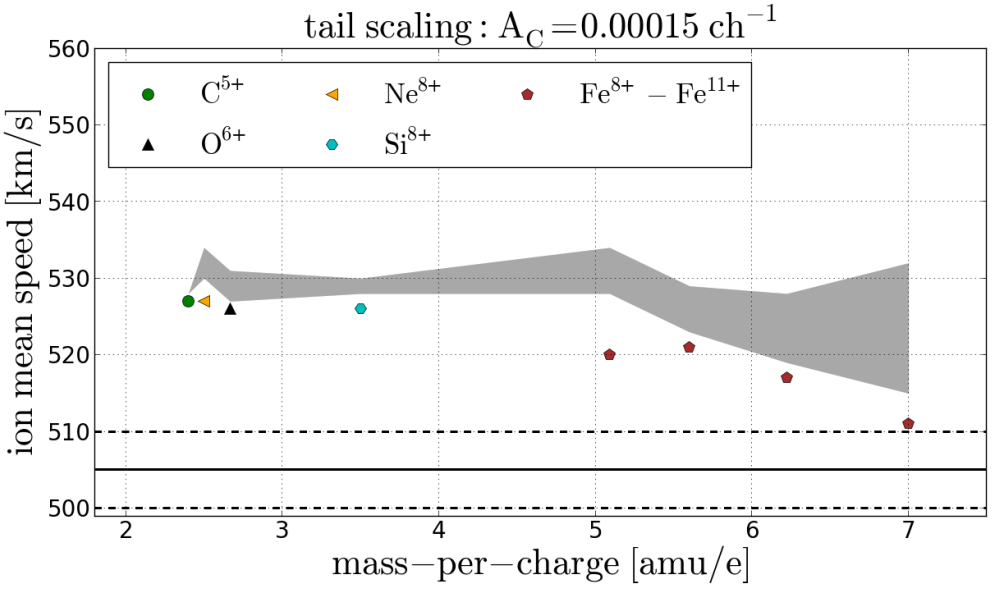

FIGURE 5.19: Mean speeds for the heavy ion species C^{5+} - Fe^{11+} derived from the Kappa-Moyal Reduced response model with tail-scaling parameter $A_C = 0.0015\,\mathrm{ch}^{-1}$ that represents approximately the case of a Gaussian peak shape. The 1σ-confidence interval that is represented by the gray-shaded area is given by the mean speeds derived for the shown ion species with the KM-RS model with $A_C = 0.0025\,\mathrm{ch}^{-1}$ (lower speed boundary) and $A_C = 0.0055\,\mathrm{ch}^{-1}$ (upper speed boundary) as can be seen seen in Figure 5.17.

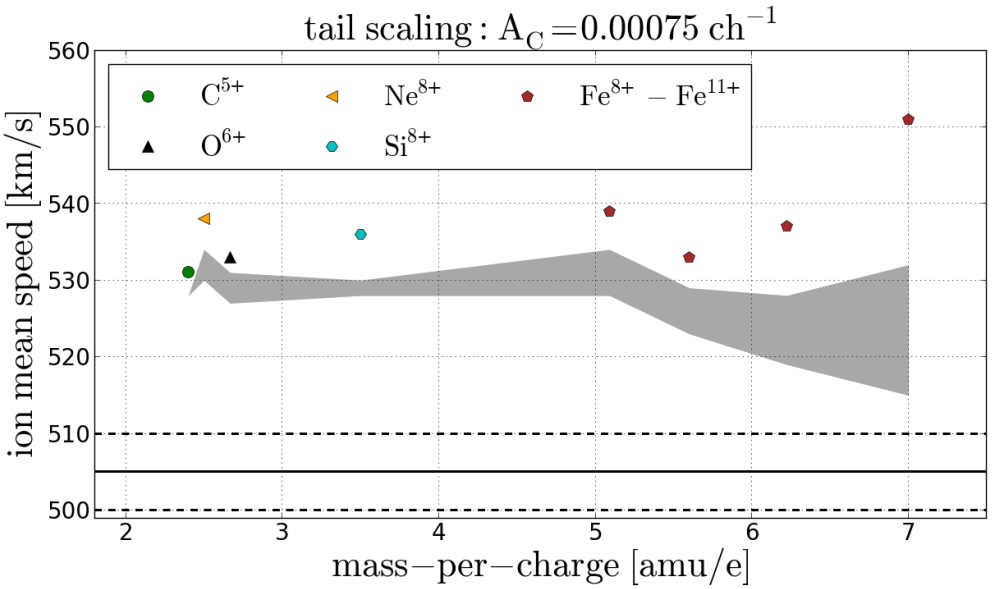

FIGURE 5.20: Mean speeds for the heavy ion species C^{5+} - Fe^{11+} derived from the Kappa-Moyal Reduced response model with tail-scaling parameter $A_C = 0.0075\,\mathrm{ch}^{-1}$ that represents overestimated peak tails. The 1σ-confidence interval that is represented by the gray-shaded area is given by the mean speeds derived for the shown ion species with the KM-RS model with $A_C = 0.0025\,\mathrm{ch}^{-1}$ (lower speed boundary) and $A_C = 0.0055\,\mathrm{ch}^{-1}$ (upper speed boundary) as can be seen in Figure 5.17.

Chapter 6

Heavy Ion Kinetic Properties Derived from Short-Term Velocity Distribution Functions at 1 AU

In this chapter we analyze the heavy ion *short-term velocity distribution functions*. These are derived from *short-term* count rates that are analyzed for each CTOF cycle separately, and thus are routinely obtained with the intrinsic CTOF cycle cadence of 5 minutes. Notably, the solar wind VDFs are relatively narrow compared to the speed range defined by the whole instrument cycle. Thus, for each species the core of the VDF is scanned in about 10-20 Epq-steps, depending on the solar wind type, so that we can calculate the heavy minor ion mean and thermal speeds with a typical integration time of 30-60 seconds. This duration is on the order of 10 gyroperiods for heavy ion species at typical B-field magnitudes of a few nanotesla at 1 AU.

Typical substantial changes in the solar wind plasma parameters such as density or temperature occur on timescales of a few minutes to hours and the same is observed for the magnitude of the convected magnetic background field. Therefore, the moments that we derive from the short-term VDFs can be regarded as a true in-situ description of the local plasma sample at the time of the measurement as all particles within the VDF are measured under comparable plasma conditions. This is in general not the case for the density-weighted mean speeds that are derived from the long-term speed spectra in chapter 5 even if all ions are measured under the condition of very similar proton speeds. Another important feature of the short-term VDF analysis is that one automatically obtains a time series for the moments of the distributions from which one can investigate similarities and differences *between* the different ion species measured

under identical plasma and B-field conditions[1] at a given time.
Yet, a quantity that routinely changes on comparable (and even shorter) timescales than those of the CTOF measurement cadence and integration times is the magnetic field direction that fluctuates e.g. due to intermediate- and high-frequency Alfvén waves ($f \gtrsim 10^{-2}$ Hz). Therefore, the *measured* differential speed magnitude even in the short-term data is always subject to the projection effect discussed in section 2.4 that results on average in a systematic under-estimation of the differential speeds. Although the study by [Berger et al., 2011] showed that this effect can be largely corrected when taking the simultaneously measured in-situ magnetic field data into account, this requires in most cases B-field measurements at the exact site of the particle measurement[2] which are not available for SOHO. However, for occasional time periods of constant magnetic field direction over several hours at L1, [Nemecek et al., 2020] were able to relate the differential speeds measured onboard SOHO in this work with the magnetometer data of the Wind spacecraft to find experimental support for their kinetic model of the multi-species solar wind plasma.
The natural downside of the short-term data are the very low counting statistics for heavy minor ions with atomic number $Z > 2$. However, due to the instrument's large geometry factor [Hovestadt et al., 1995] we obtain higher counting statistics with CTOF within a cadence of 5 minutes than with the comparable ACE/SWICS experiment within a longer cadence of 12 minutes. This advantage makes the CTOF measurements highly valuable despite the short operation period of the sensor. Yet, as the high geometry factor is enabled by the adaptive stopping of the Epq-stepping in the electrostatic analyzer (see sections 2.2 and 5.3), it comes with the disadvantage of only partially scanned VDFs for low-m/q ion species in a number of instrument cycles. This has to be taken into account in the following analysis in order to derive accurate mean and thermal speeds.

6.1 Derivation of Heavy Ion Short-Term Velocity Distribution Functions

In order to derive short-term velocity distribution functions with the intrinsic 5-minute measurement cadence of the CTOF instrument, we need to fit the PHA count data for each instrument cycle separately. Due to the low count rates, we use for these fits the Reduced Stable (RS) response model and we emphasize that so far these short-term

[1] This might even allow some conclusions on the ambient magnetic field direction even if the local B-field is not measured in-situ, because all ion species are subject to the same projection effect of the measured differential speeds as explained in section 2.4.
[2] This is because such small scale B-field fluctuations cannot be extrapolated with the necessary accuracy from other spacecraft sites.

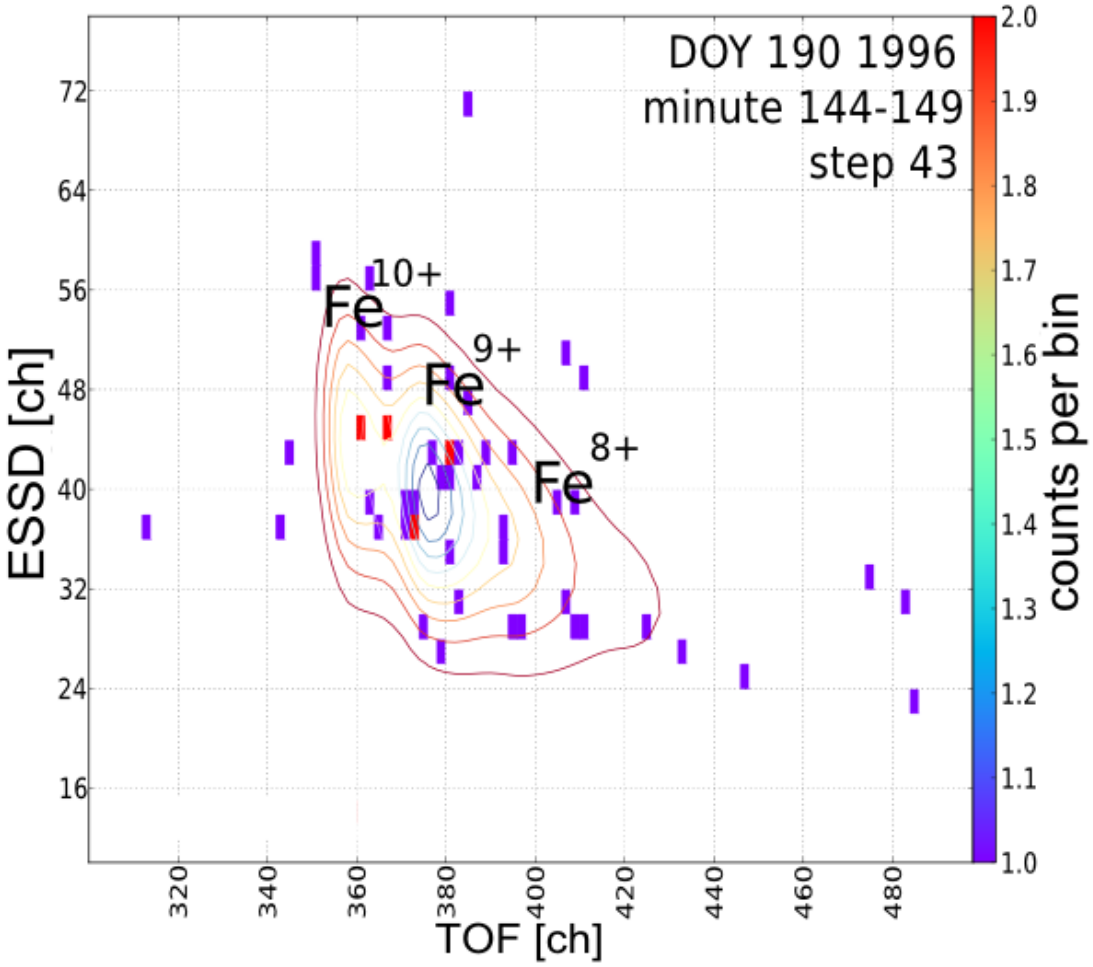

FIGURE 6.1: Close-up of the measured iron sequence of cycle 29 on DOY 190, 1996, with the applied short-term fits as contour lines. For better recognition, we marked the peaks belonging to the dominant iron species Fe^{8+} - Fe^{10+} at this Epq-step. Note that the measured counts to which the fit is applied are not corrected with the base rate factors prior to the fit, as explained in the text. Yet, for iron the correction factor is usually negligible since the base rate factor for the priority range PR1 is typically close to 1. As in the long-term fits the peak shape is fixed and only the peak heights of the included ion species are fitted simultaneously, so that the integral of each fitted peak corresponds approximately to the number of counts for each ion species and thus the fit yields the relative count rate contribution of every species for each bin $\widetilde{c}_{tr,i}(\tau, \epsilon)$. So far, the short-term data is only evaluated with the Reduced Stable Gaussian response model. Adapted after [Janitzek et al., 2016].

data fits have only been conducted with the Gaussian peak model[3]. As in chapter 5 we use for the fits the Poissonian minimization function given in Eq. 4.10 and utilize as solver the BFGS algorithm. In Figure 6.1 we show an example of the short-term data fits for Epq-step 43 in cycle 29 on DOY 190, 1996. Yet, in contrast to the long-term

[3]This is due to the fact that first we analyzed the CTOF short-term PHA data with the Gaussian peak model and only then developed the Kappa-Moyal peak model in order to evaluate systematic uncertainties of the response model with the CTOF long-term data.

analysis the short-term fits cannot be conducted after the PHA base rate correction is applied. This is because the low number of counts on the order of $C(\tau,\epsilon) \gtrsim 1$ multiplied with partially very high base rate factors $f_{br} \gtrsim 10$ lead to count rate distributions in the ET-matrices 'seen' by the fit algorithm, that are very unlikely to result from the response model and thus frequently the algorithm cannot find a meaningful minimum and yields unphysical results.
Therefore, for each CTOF cycle and Epq-step we fit first the response model to the transmitted, i.e. uncorrected short-term PHA data to obtain the uncorrected count rate contributions $\widetilde{C}_{tr,i}(\tau,\epsilon)$ for each ion species in each ET-bin. After the fit, these count rate contributions are normalized as in Eq. 5.2 to ensure that we distribute the exact number of PHA counts as actually transmitted. Only then we multiply, similar to Eq. 2.13, the base rate factors $F_{br}(\tau,\epsilon)$ from Eq. A.1 with the uncorrected count rate contributions to obtain for each ion species the base-rate corrected short-term count rates within each ET-bin as [4]

$$\widetilde{C}_i(\tau,\epsilon) = F_{br}(\tau,\epsilon) \cdot \widetilde{C}_{tr,i}(\tau,\epsilon) \tag{6.1}$$

where the priority scheme information is implicitly included via the TOF and ESSD bin positions in the ET-matrix. The rest of the analysis follows then the same scheme as described in chapters 3 and 5: For each CTOF cycle and Epq-step j the normalized and base-rate corrected count rate contributions are summed up over all ET-bins to obtain the total short-term count rates for each species i as in Eq. 5.3. By relating the Epq-step for each species to the corresponding speed after Eq. 2.1 and applying the standard phase space correction from Eq. 3.1, we finally obtain the short-term ion speed spectra or the (reduced) ion velocity distribution functions (VDF), given as $N(v_{ij})$, for each CTOF 5-minute cycle.

In Figure 6.2 we show the 1D-reduced short-term VDF for Fe^{9+} that we obtain for the same measurement cycle for which we showed the short-term data fit at Epq-step 43 in Figure 6.1. As the applied corrections for iron are small, the VDF total number of about 18 counts at a speed of 437 km/s is comparable to the number of counts that are measured in the vicinity of the Fe^{9+} peak in the ET-matrix at Epq-step 43 in Figure 6.1. We see that these are sufficient to determine statistically accurate mean and thermal speeds from the measured VDF. In this case the ion mean speed is estimated as $\langle v_{ion} \rangle = 428\,\mathrm{km/s}$ and the ion thermal speed as $v_{th,ion} = 31\,\mathrm{km/s}$. For the simultaneously measured protons we (only) obtain the mean and thermal speed from the

[4] Note that due to the necessary change in order between base-rate correction and count rate fit compared to the long-term data analysis, the count rate contributions at the border between the priority ranges can be biased. Yet, with the given short-term counting statistics, this approach is the only feasible one, because of the mentioned extremely unstable fits after applying first the base-rate correction to the short-term PHA data.

CELIAS Proton Monitor data so that their (thus simplified) distribution is visualized in red as a 1D-Maxwellian with proton mean speed $v_p = 403\,\mathrm{km/s}$ and thermal speed $v_{th,p} = 35\,\mathrm{km/s}$.

6.2 Derivation of Mean and Thermal Speeds from Short-Term Velocity Distribution Functions

As discussed in the long-term analysis in the previous chapter, also in the short-term analysis we only include cycles with a sufficient number of total PHA words ($N_{PHA,min} \geq 500$) and we have to ensure that these moments are not biased by the instrumental cut-off due to the interruption of the electrostatic analyzer (ESA) E/q-stepping. In contrast to the long-term analysis we have to ensure now for each cycle individually that the moments that we derive from the VDF are not influenced due to this artificial cut-off. This is done by looking up the maximum reached Epq-step corresponding to the lowest measured speed at each cycle and then mirroring this speed to the upper flank of the VDF to obtain the maximum included speed for a symmetrical moment calculation. Thus, we calculate the mean speed for a given species as

$$\langle v \rangle = \frac{1}{\sum_{j=s_{min}}^{s_{max}} n_j} \cdot \sum_{j=s_{min}}^{s_{max}} n_j \cdot v_j \tag{6.2}$$

where the lowest speed is the ESA cut-off speed $v_{s,low} := v_{s,cut} \leq v_{s,max}$ and the highest included speed $v_{s,up}$ is the highest speed v_s that fulfills

$$v_s \leq v_{s,cmax} + (v_{s,cmax} - v_{s,cut})\,, \tag{6.3}$$

so that we obtain a symmetric speed range around the most frequently measured speed $v_{s,max}$ with the highest (phase-space-corrected) count rate C_{max}. Naturally, this approach only ensures an unbiased calculation of the mean speed, when a sufficiently large part of the VDF is scanned to ensure that the actual most probable speed (that one would calculate if the VDF was not cut) is not even below the cut-off speed. For all (major) ions with mass-per-charge equal or larger than the mass per-charge of O^{6+} ($m/q \gtrsim 2.7$) we find that the average speed difference $\Delta v = v_{s,cmax} - v_{s,cut}$ observed in the roughly 10^4 short term data VDFs is at least $\Delta v \gtrsim \sigma_v$ for all proton speed regimes, where σ_v is the standard deviation of the measured long-term speed spectra which is about 15 km/s in the slow wind and 50 km/s in the fast wind. This corresponds to a difference of 2 and 5 Epq-steps, respectively. Assuming again approximately 1D-Maxwellian/Gaussian distributions, we can conclude with the given counting statistics

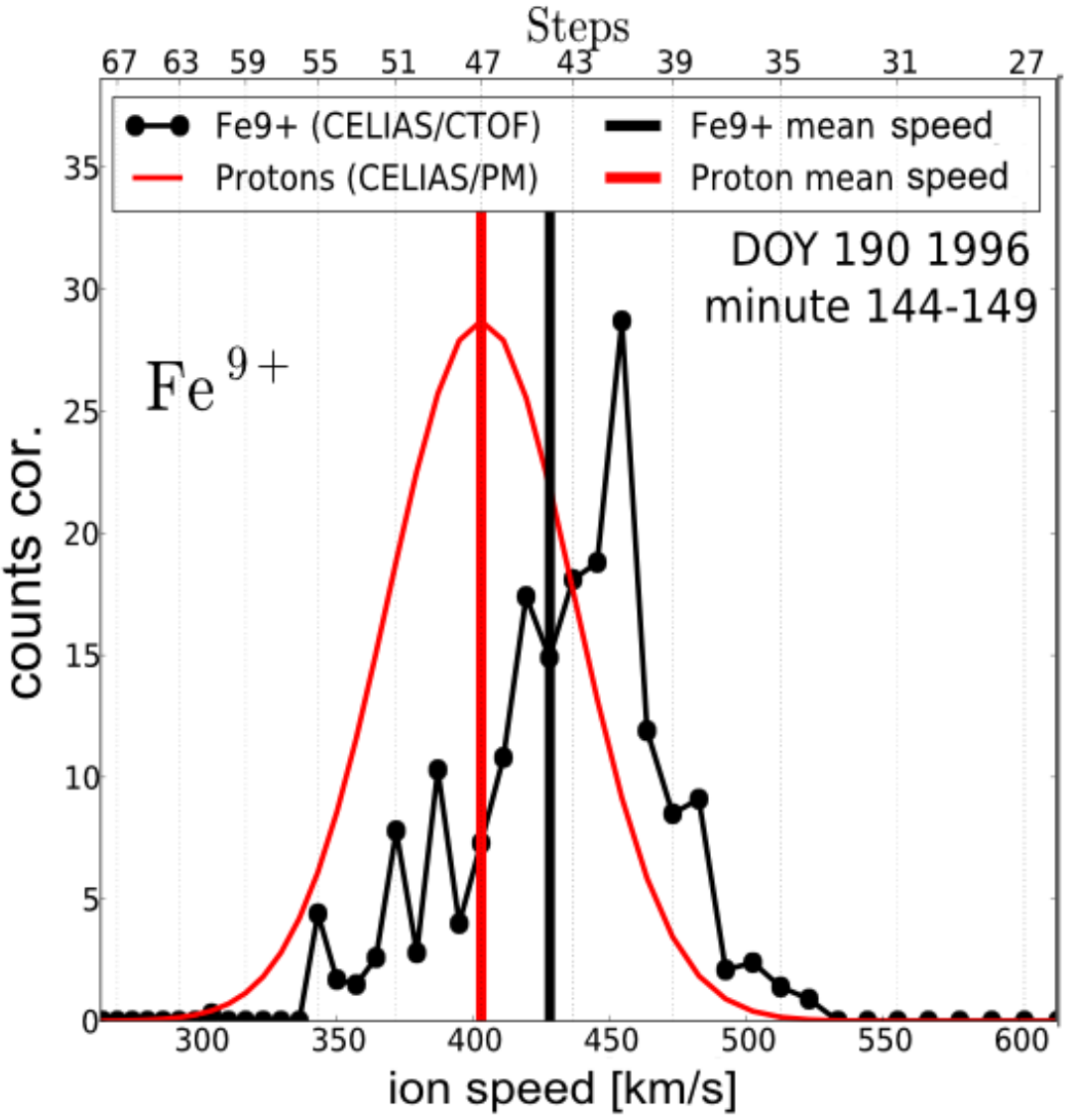

FIGURE 6.2: 1D-reduced velocity distribution function for Fe^{9+} (shown in black) obtained for measurement cycle 29 on DOY 190, 1996. As this is the exact same cycle as in Figure 6.1 and the applied corrections for iron are small, the VDF count rate of about 18 counts at a speed of 437 km/s is comparable to the number of counts that are measured in the vicinity of the Fe^{9+} peak in the ET-matrix at Epq-step 43 in Figure 6.1. To visualize the conversion from a given Epq-step to the corresponding Fe^{9+} speed, we also included the Epq-step axis on the top of the Figure. For the given ion VDF the mean speed is calculated as $\langle v_{ion} \rangle = 428\,\mathrm{km/s}$ and marked by the fat black vertical line. For the simultaneously measured protons we obtain as mean speed $v_p = 403\,\mathrm{km/s}$ which is marked by the fat red vertical line, and as thermal speed $v_{th,p} = 35\,\mathrm{km/s}$. A 1D-Maxwellian VDF calculated from the given proton moments is shown in red for comparison. Adapted after [Janitzek et al., 2016].

that the mean speeds of these ion species calculated with the described symmetrized speed-range method are statistically very unlikely to be biased, as the probability that the actual most probable speed lies below the ESA cut-off speed for a significant number of VDFs is very low. We finally note, that for the high-m/q ion species (in particular the iron species), the Epq-stepping is not a crucial limitation as the stopping occurs at very low speeds for these species. However, as they are measured at same ESSD channels as He^{2+}, they are affected by He^{2+} random coincidences and we therefore cut-off their speed spectrum as described in Eq. 4.43. Thus, for these species we apply exactly the same symmetrized mean speed calculation method, but just with $v_{cut}^{\alpha-RC}$ instead of the ESA stepping cut-off $v_{s,cut}$.

Derivation of Thermal Speeds

For the derivation of the thermal speed we only select well-resolved ion species for which a large part of the VDF, down to more than 1 typical thermal speed is measured, with the thermal speed again approximated from the long-term speed spectra. Thus, we restrict the analysis to six species: Si^{7+}, Si^{8+}, Fe^{8+}, Fe^{9+}, Fe^{10+}, Fe^{11+}. We note for later studies that in principal one could relax the minimum thermal speed requirement, if one calculates the thermal speed only from the high speed VDF flank assuming complete symmetry around the most probable speed. The thermal speeds are calculated for a given ion species as the second moment of the 1D-reduced VDFs after

$$v_{th} = \sqrt{\frac{1}{\sum_{j=s_{min}}^{s_{max}} n_j} \cdot \sum_{j=s_{min}}^{s_{max}} \left(\langle v \rangle - n_j \cdot v_j\right)^2}\,. \tag{6.4}$$

6.3 Heavy Ion Differential Speeds

Differential Speed Time-Series

For all major species that are included in the CTOF Reduced Stable response model and $m/q > 2.6\,\mathrm{amu/e}$ we calculated approximately 10000 mean ion speeds for the measurement period DOY 174-220 in 1996 as described in the previous section. in Figures 6.3 and 6.4 the mean speeds are visualized as a time series for O^{6+} (black), Si^{8+} (cyan) and Fe^{10+} (brown), together with the solar wind mean proton speed (green), measured by the CELIAS PM. In the upper panel of Figure 6.3 we show an overview over the whole measurement period, that consists of only two subperiods DOY 185 - 186 and DOY 213 - 216, 1996 where we measure speeds that are typically classified

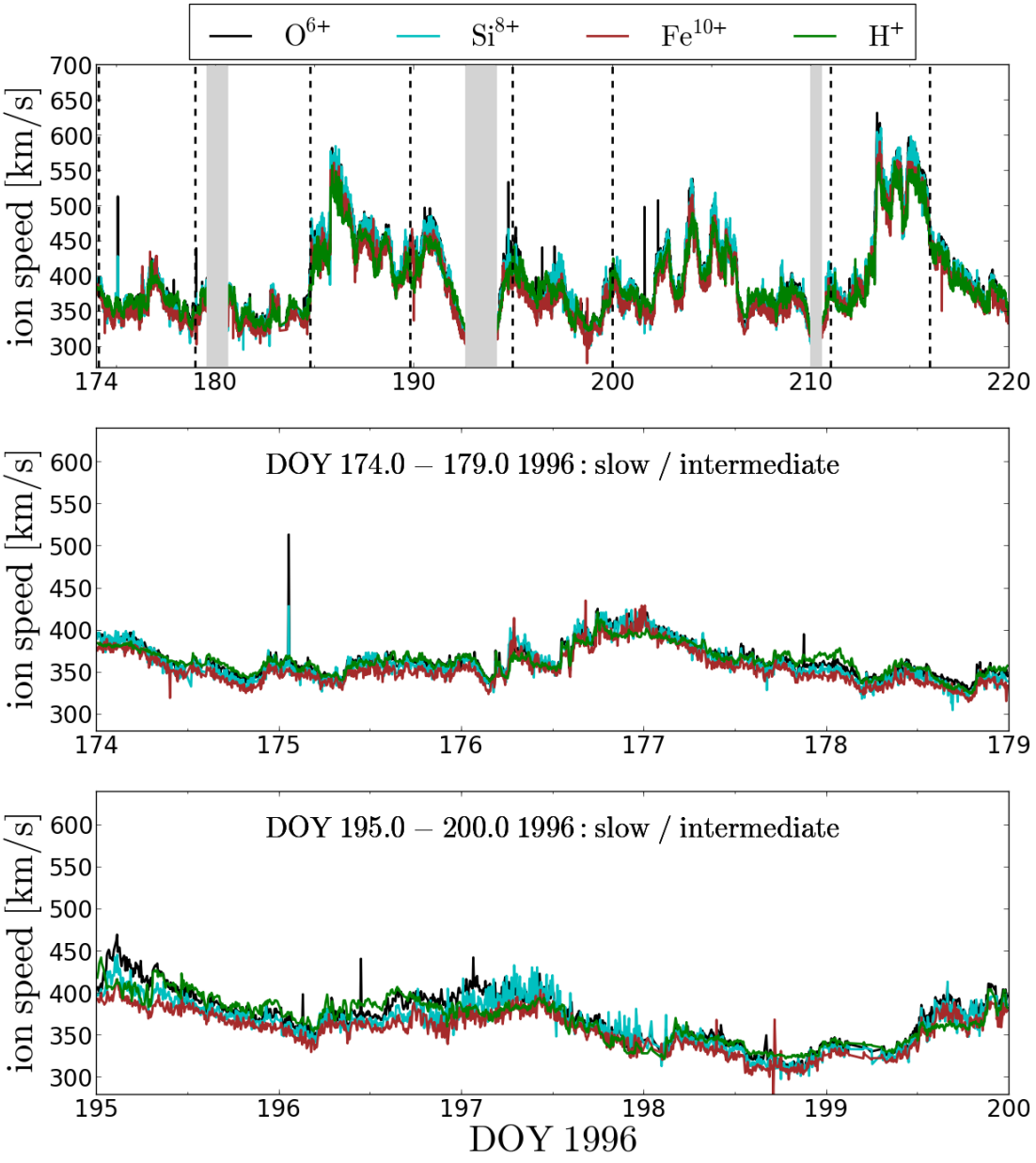

FIGURE 6.3: Time series of the mean ion speeds obtained from the CTOF short-term data analysis for O^{6+} (black), Si^{8+} (cyan) and Fe^{10+} (brown), that can be compared to the mean proton speeds (green) which are measured simultaneously with the CELIAS Proton Monitor (PM). In the upper panel the full measurement period is shown for DOY 174-220, that contains almost 10^4 valid measurement cycles. The four time intervals between the vertical dashed lines (with the first interval starting on DOY 174) are described in greater details in the text. The gray shaded time intervals mark data gaps in the CTOF data (DOY 179-180) and time intervals with excluded PM measurements in the very slow wind as described in section 2.3. In the two lower panels we show two of the discussed subperiods in the slow and slow/intermediate speed range between DOY 174 - 179 and DOY 195 - 200 in 1996, respectively, in larger resolution. Note that in the time series we rarely see extreme fluctuations in the derived mean speed which is a good indication for the quality of the applied fits which are conducted generally on very low counting statistics.

as fast wind ($v_p \gtrsim 500\,\mathrm{km/s}$). We further observe several subperiods of intermediate speeds between 400 km/s and 500 km/s and two longer periods of slow wind below 400 km/s at DOY 174 - 184 and DOY 206 - 209, 1996. Several time intervals with very low proton speeds are excluded from the study as these occur together with low proton thermal speeds that show an artificial distribution pattern below $v_{th} = 21\,\mathrm{km/s}$ as described in section 2.3. The excluded time intervals during DOY 193-194 and DOY 210 are marked by the gray shaded areas in the upper panel of Figure 6.3. During DOY 179-180 we have a data gap in the CTOF PHA data which is also shaded in gray.
In the middle panel of Figure 6.3 we show with a higher time and speed resolution the subperiod between DOY 174 and 179 in the slow solar wind while in the lower panel the subperiod 195 - 200 is shown, where we measure slow and intermediate wind speeds. Note that this distinction between slow, fast and intermediate speeds corresponds roughly to the identified speed regimes in Figure 3.5 of chapter 3 and we will further justify it in the next subsection. For the slow solar wind period we see that there are no continuous periods of clear positive differential speeds $\Delta v_{ip} \gg 10\,\mathrm{km/s}$ between the heavy ions and the protons recognizable, but only one shorter period of small negative differential speeds during a few hours at the end of DOY 177 and the beginning of DOY 178. In the time interval DOY 195-200 we can observe for certain periods some speed differences between the protons and ions up to a maximum of 20 km/s, but these differential speeds alternate in their sign, as sometimes the heavy ions are faster than the protons (e.g. beginning of DOY 195, end of DOY 199) and at other times it is the opposite (e.g. mid of DOY 196, end of DOY 198) and no clear correlation with the proton speed is observed. The only general feature that one might already recognize in the slow and intermediate wind is that among the heavy ions, the Fe^{10+} speed tends to be the lowest in most cases.

When we now focus on the fast wind streams in the upper two panels of Figure 6.4 (which for direct comparison are depicted with the same scaling on the y-axis as the two lower panels of Figure 6.3) we do observe clear signatures of differential speeds over extended time periods. In the upper panel one can recognize that all heavy ions stream faster than the protons with differential speeds between about 20 km/s (mainly for Fe^{10+}) and 30-40 km/s (mainly for Si^{8+} and O^{6+}) over a continuous period of about one day (end of DOY 185 - end of DOY 187). This period coincides with the highest proton speeds in the shown subperiod that contains the full first fast stream. At somewhat lower proton speeds of around 450 km/s or between the beginning of DOY 187 and the mid of DOY 188 the pattern is again more complex with O^{6+} and Si^{8+} streaming mostly faster than the protons while Fe^{10+} streams partly faster and partly slower than the protons.

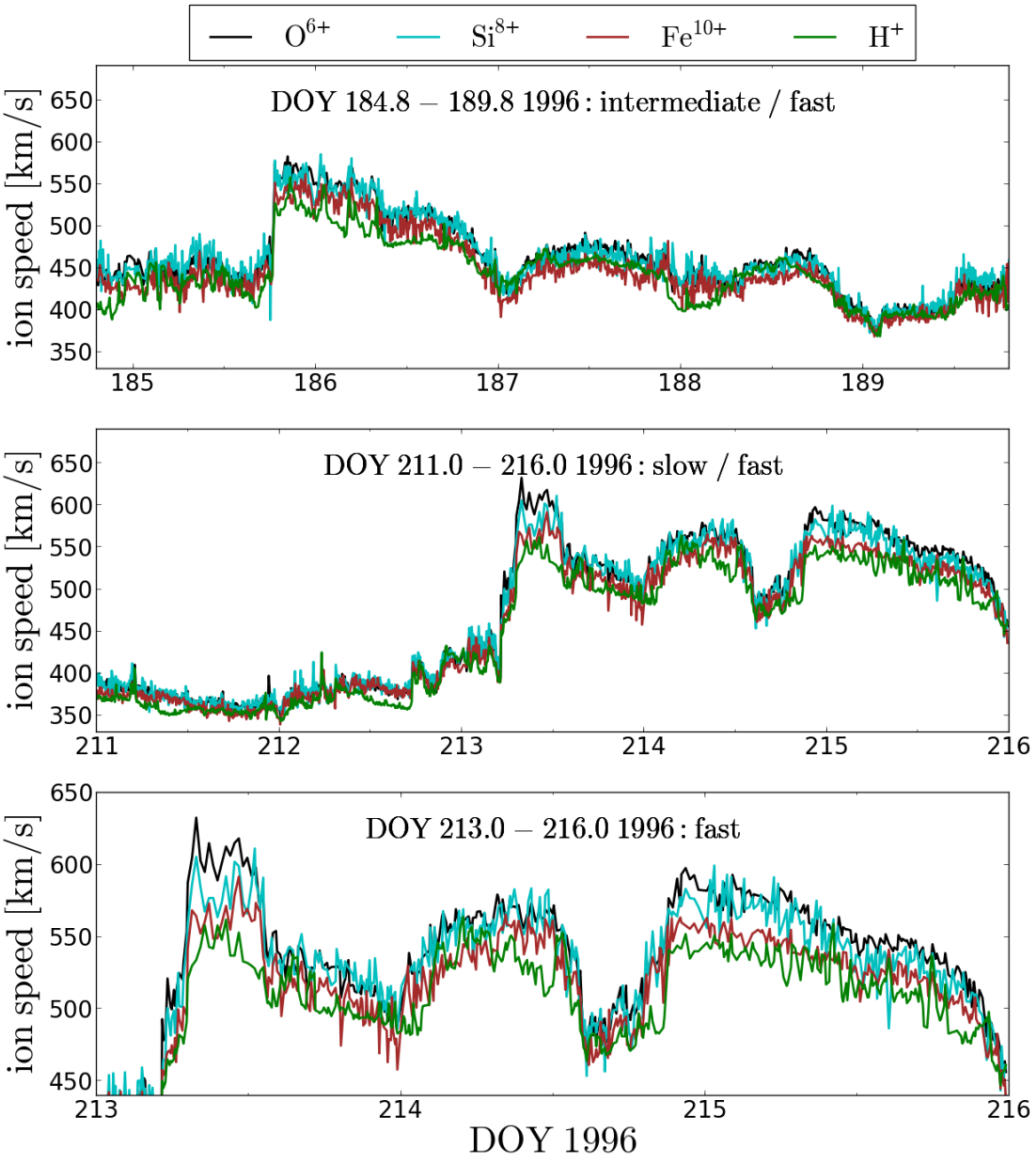

FIGURE 6.4: Time series of the mean ion speeds obtained from the CTOF short-term data analysis for O^{6+} (black), Si^{8+} (cyan) and Fe^{10+} (brown), that can be compared to the mean proton speeds (green) which are measured simultaneously with the CELIAS Proton Monitor (PM). In the two upper panels we show the two remaining subperiods marked by vertical dashed lines in the upper panel of Figure 6.3 between DOY 184.8 - 189.8 and DOY 211 - 216 in 1996, respectively. The upper panel shows the transitions between intermediate and fast wind speeds for the first observed fast stream. The middle panel shows the transition from slow to fast wind for the second observed fast wind stream. The speed scale on the y-axis in these two panels is the same as in the two lower panels of Figure 6.3, so that the speed differences can be compared by eye. The lowest panel is a zoom of the second fast stream between DOY 213 and 216, 1996 with increased resolution both on the time and speed axis.

In the middle panel of Figure 6.4 we see a rapid transition from a slow to a fast wind structure on DOY 213, 1996. These pattern typically occurs when the fast wind runs into the slow wind at corotating interaction regions in the inner heliosphere [Prölss, 2004]. Thus, between midday on DOY 213 until the end of DOY 215 we find the second observed fast stream with proton speeds of more than 500 km/s almost over the entire period of 3 days. Yet, in detail we observe a finer structure of three short substreams with the highest observed proton speeds of the whole sample up to about 550 km/s. A zoom of this fast wind period between DOY 213 and 216 is shown in the lower panel of Figure 6.4, from which we can see that in particular for O^{6+} differential speeds of about 50 km/s are reached within the first substream while in the second substream the differential speeds are (only) on the order of 20-30 km/s. In the third substream they increase again in the beginning where they again reach up to 40-50 km/s before they slowly reduce to about 20 km/s by the end of the stream. The observed differential speed difference between the three streams is interesting as the proton speed is about equal over large parts of the substreams, but the differential speed behaves differently. If we only had measurements of one heavy ion species one could explain this observation with an ambient magnetic field that is more co-aligned with the measurement axis in the first and the third case but more perpendicular aligned in the second case (see section 2.4). However, we observe that both in the first and the third stream the heavy ion speeds are well-ordered by mass-per-charge (with the highest speed observed for O^{6+} as the ion species with the lowest m/q) while in the second substream all ion speeds are very similar with average differential speeds among each other of less then 10 km/s and in particular Fe^{10+} has even higher differential speeds in the second stream than in the third stream. Such subtle features could in general be a signature of different acceleration / speed regulation mechanism dominating in the different streams and should be investigated in detail in the future. As the discussed signatures are stable over a few hours, they are not only statistically significant but might also be investigated with extrapolated magnetic field measurements from the Wind spacecraft that is in the given time-period in the vicinity of L1. Yet, as the CTOF measurement period is limited such a study can only have the character of a case study, while a complimentary analysis with e.g. ACE/SWICS measurement data would allow a search of such features over long time periods (see the discussion in section 7.2 both for the B-field extrapolation and the comparison with ACE/SWICS measurements). In the following, we focus on a statistical analysis of the differential speeds observed over the full analyzed measurement period DOY 174-220 that can be compared to the results obtained from the CTOF matrix rate data in chapter 3.

Statistical Analysis of Differential Speeds

In the following we present a statistical study of the differential speeds calculated as described above from 5-minute cycle short-term PHA data over the period DOY 174-220 in 1996. We analyze the measured differential speeds for their dependence on the simultaneously measured mean proton speeds as well as for their dependence on the measured (proton-proton and ion-proton) collisional age.

Differential Speed Dependence on the Solar Wind Proton Speed

In Figure 6.5 and Figure 6.6 we present the 2-dimensional histograms of the ion-proton differential speeds Δv_{ip} of the ion species C^{4+}, O^{6+}, Si^{7+} - Si^{10+}, Fe^{8+} - Fe^{11+} versus the simultaneously measured proton mean speed for the full time period DOY 174-220 in 1996. In these figures we show the absolute measured number of occurrences for a combination $(v_p, \Delta v_{ip})$ within a given (proton speed, differential speed)-bin, while in Figure 6.7 and 6.8 we depict the corresponding 2D-histograms for the same ion species with the respective frequency of occurrence for every $\Delta v_{ip} - v_p$ bin normalized to 1 within each proton speed bin, so that the maximum and spread of the differential speed distribution is better visible for all solar wind proton speeds. The shown results can be directly compared for the three ion species O^{6+}, Si^{7+}, Fe^{9+} that were analyzed with the matrix rate data in chapter 3. However, note that the overall number of occurrences in each panel are about 20% smaller than for the analyzed matrix rate data, which is due to the fact that we filter out all cycles with very low proton thermal speeds $v_{th} < 21\,\mathrm{km/s}$ and in addition we had to exclude from the PHA data analysis all time intervals with too small counting statistics caused by the limited CTOF telemetry budget. Again, in all figures the calculated mean differential speeds at each proton speed bin are given by the black dots, that are connected by the solid black line to guide the eye. In Figure 6.5 and 6.6 the (1σ) standard error of the mean differential speed $\langle \Delta v_{ip} \rangle$ for each proton speed bin is calculated in the exact same way as in Eq. 3.5. In addition we plot in Figures 6.7 and 6.8 as dashed lines the standard deviation of the distributions for every proton speed, which can be regarded as a measure for the variability of the measured differential speed under well-defined proton speed conditions (but under the projection effects of the varying B-field direction).

In general we find for all analyzed ion species a step-like differential speed pattern that can be described within the aforementioned three different speed regimes of slow, intermediate and fast wind: In the slow wind below proton speeds of 380 km/s we observe ion speeds that are similar or lower than the proton speed, yielding relatively constant

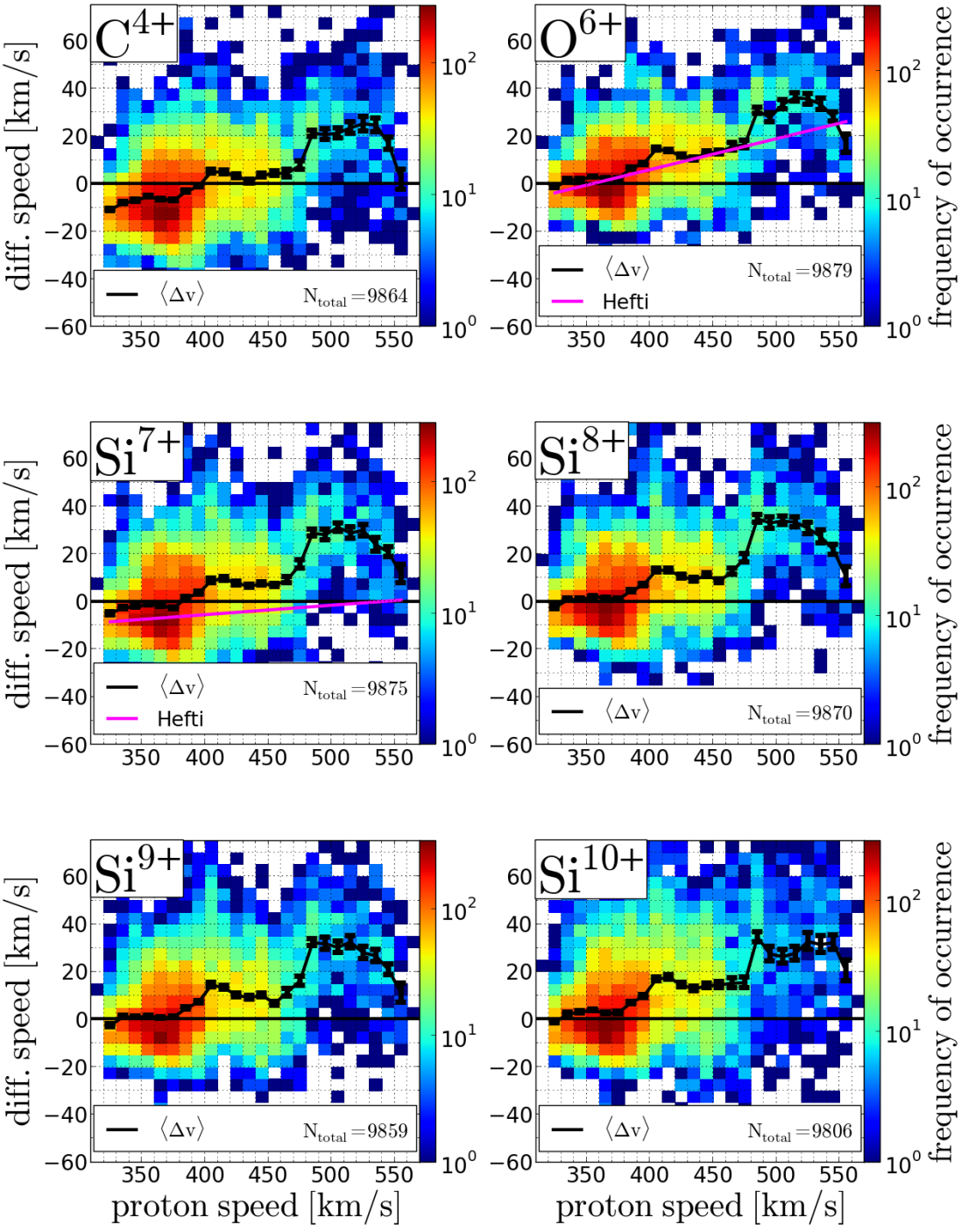

FIGURE 6.5: Two-dimensional histograms of the observed differential speeds between C^{4+}, O^{6+}, Si^{7+}, Si^{8+}, Si^{9+}, Si^{10+} and the solar wind protons, respectively, derived from the (base-rate-corrected) CTOF PHA data for the measurement period DOY 174-220 in 1996. The panels show the absolute measured frequency of occurrence within the given time period for a combination $(v_p, \Delta v_{ip})$ within a given (proton speed, differential speed)-bin. The black line represents the mean differential speed $\langle \Delta v_{ip} \rangle$ at a given proton speed bin, the error bars mark the 1σ standard error of $\langle \Delta v_{ip} \rangle$. The magenta lines in the panels belonging to O^{6+} and Si^{7+} show the linear best fit obtained for the mean differential speed by [Hefti, 1998a], for the time period DOY 93-229 in 1996.

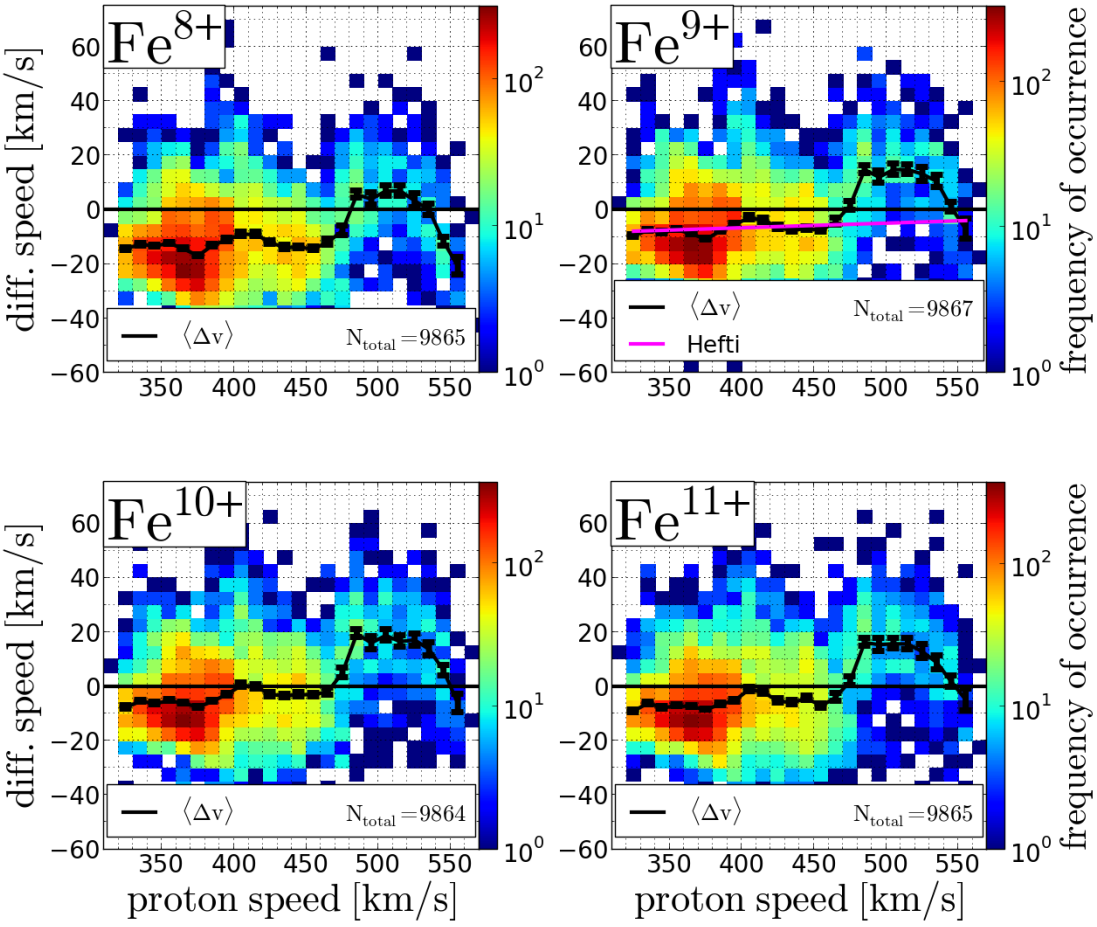

FIGURE 6.6: Two-dimensional histograms of the observed differential speeds between Fe^{8+}, Fe^{9+}, Fe^{10+}, Fe^{11+} and the solar wind protons, respectively, derived from the (base-rate-corrected) CTOF PHA data for the measurement period DOY 174-220 in 1996. The panels show the absolute measured frequency of occurrence within the given time period for a combination $(v_p, \Delta v_{ip})$ within a given (proton speed, differential speed)-bin. The black line represents the mean differential speed $\langle \Delta v_{ip} \rangle$ at a given proton speed bin, the error bars mark the 1σ standard error of $\langle \Delta v_{ip} \rangle$. The magenta line in the panel belonging to Fe^{9+} shows the linear best fit obtained for the mean differential speed by [Hefti, 1998a], for the time period DOY 93-229 in 1996.

differential speeds for any given ion species between about -15 km/s (for Fe^{8+}) and a bit less than 5 km/s (for O^{6+}) in this speed regime. The transition to intermediate proton speeds between 380 and 400 km/s leads to a small increase of the differential speeds: We find small positive differential speeds on the order of 10 km/s for O^{6+} and the analyzed silicon ions, while for C^{4+} we observe only a slight positive differential speed of less than 5 km/s. For the iron ions we measure still mostly negative differential speeds. These differential iron speeds lie in the range between 0 and -5 km/s for Fe^{10+} while for Fe^{8+} they cover again a lower range between -10 km/s and -15 km/s,

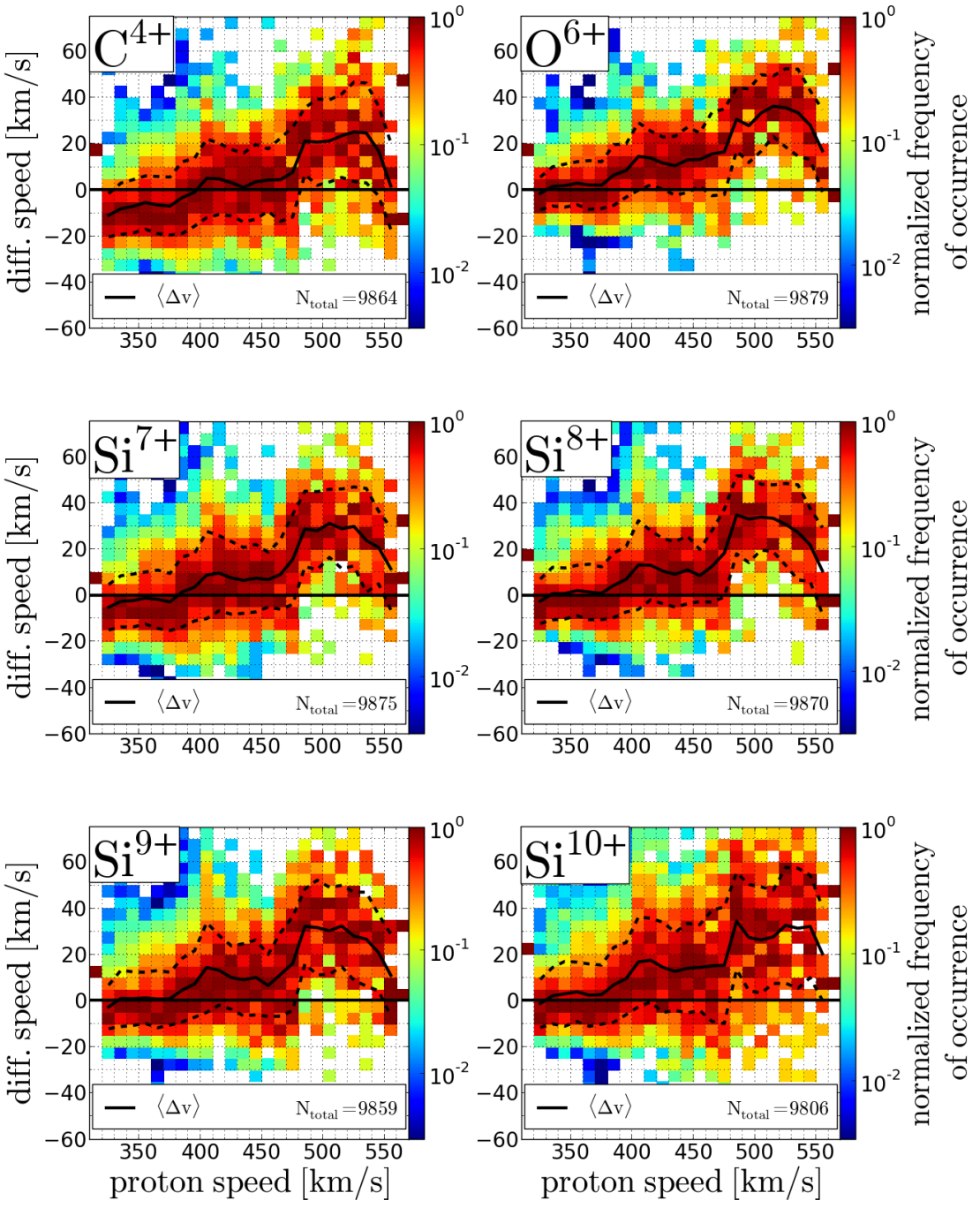

FIGURE 6.7: Two-dimensional histograms of the observed differential speeds between C^{4+}, O^{6+}, Si^{7+}, Si^{8+}, Si^{9+}, Si^{10+} and the solar wind protons, respectively, derived from the (base-rate-corrected) CTOF PHA data for the measurement period DOY 174-220 in 1996. The panels show the measured frequency of occurrences normalized to the maximum of a each proton speed bin, respectively. As in Figure 6.5 the black line represents the mean differential speed $\langle \Delta v_{ip} \rangle$ at a given proton speed bin, while the additional dashed lines represent the standard deviation of the differential speed distribution at each proton speed bin.

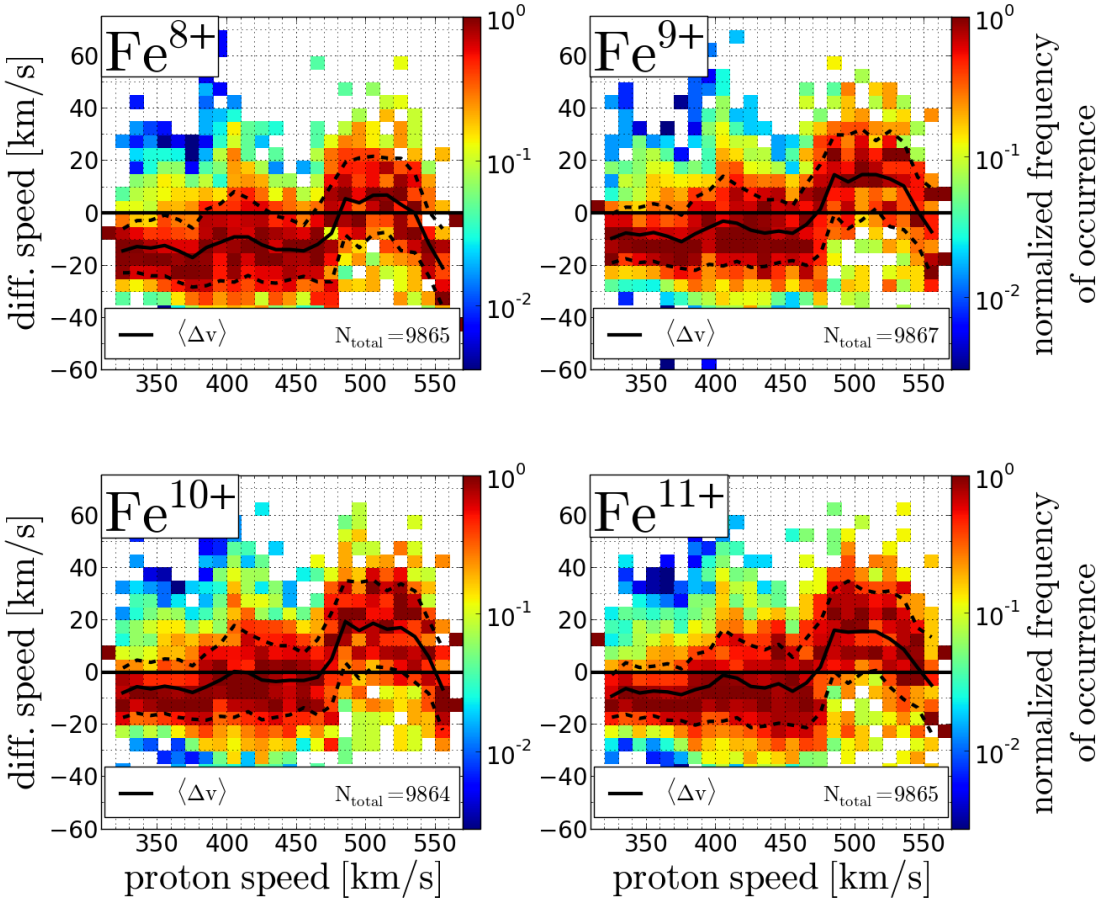

FIGURE 6.8: Two-dimensional histograms of the observed differential speeds between Fe^{8+}, Fe^{9+}, Fe^{10+}, Fe^{11+} and the solar wind protons, respectively, derived from the (base-rate-corrected) CTOF PHA data for the measurement period DOY 174-220 in 1996. The panels show the measured frequency of occurrences normalized to the maximum of a each proton speed bin, respectively. As in Figure 6.5 the black line represents the mean differential speed $\langle \Delta v_{ip} \rangle$ at a given proton speed bin, while the additional dashed lines represent the standard deviation of the differential speed distribution at each proton speed bin.

which is only slightly higher than in the slow wind regime. At a relatively sharp border of 480 km/s we find for all ion species a significant increase in differential speed of about 20 km/s regardless of their differential speed magnitude at intermediate speeds which is followed for all ion species by a plateau of nearly constant differential speed in the fast wind at proton speeds above 480 km/s up to proton speeds of 540-550 km/s. Therefore, the differential speeds reached at these plateaus are different, so that we find for O^{6+} and the silicon ion species the highest differential speeds of around 30-35 km/s while for C^{4+}, we find a differential speed in the fast wind between 20 and 25 km/s. For iron the observed magnitude of high-speed differential speed is lower on average and depends once more on the charge state. While we measure differential speeds between 15 and 20 km/s for Fe^{9+} - Fe^{11+}, we find for Fe^{8+} differential speeds of only

about 5 km/s. The observed differences in differential speed between the ion species in the fast wind are in their maximum 25-30 km/s (between O^{6+} and Fe^{8+}). Yet, we note that the ion species with smaller differential speeds in the fast wind have at the same time also larger negative differential speeds in the slow wind. This can be seen from the comparison of O^{6+} and Si^{7+} - Si^{10+} with C^{4+}, Fe^{9+}-Fe^{11+} and in particular Fe^{8+}, for which the absolute value of negative differential speeds in the slow wind is even larger than the observed differential speed in the fast wind. We discuss this result in chapter 7 in the context of mass and charge dependence of the observed differential speeds (see next section 6.3) and in particular in the light of the systematic measurement uncertainties that we derived from the long-term data in the previous chapter.

On the whole the observations from the statistical analysis of the short-term differential speeds derived from the (base-rate-corrected) CTOF PHA data yield a different picture than the results found by [Hefti, 1998a] for the (wider extended) time period DOY 93-229 in 1996. For comparison the earlier results that were derived by [Hefti, 1998a] from the CTOF matrix rate data for O^{6+}, Si^{7+} and Fe^{9+} are again plotted as the magenta lines for the respective ion species in Figures 6.5 and 6.6. Although we observe a good agreement in the slow wind regime, the earlier results yield significantly lower mean ion speeds in the fast wind with differences between the two studies of 10-15 km/s for O^{6+}, about 30 km/s for Si^{7+} and about 20 km/s for Fe^{9+}. Thus, our result of both significant differential speeds in the fast wind for almost all analyzed ion species (both concerning the statistical and systematic uncertainties) is in clear contrast to the conclusions of the earlier SOHO/CELIAS study, that only found clear positive differential speeds for O^{6+} in the fast wind while Si^{7+} and Fe^{9+} were found to stream with about the same mean speed as the solar wind protons.

Differential Speed Dependence on the Solar Wind Collisional Age

As discussed in section 1.4 the differential speed in the solar wind can be reduced by Coulomb collisions between the solar wind ions and protons. At a given measurement location such as the SOHO site at L1 one can estimate the impact of Coulomb collisions on the measured plasma sample by the collisional age A_C (see e.g. [Kasper et al., 2017, Maruca et al., 2013]). Therefore, apart from the proton speed the collisional age A_C is another possible parameter to order the differential speed of the measured solar wind. We note that with the CELIAS CTOF sensor and Proton Monitor we can measure all parameters that are necessary to calculate both the proton-proton ($A_{C,pp}$) and ion-proton collisional age ($A_{C,ip}$) of the in-situ measured plasma samples after Eq. 1.42 - Eq. 1.48 in chapter 1. In the left panels of Figure 6.9 we show the 2-dimensional histograms of the

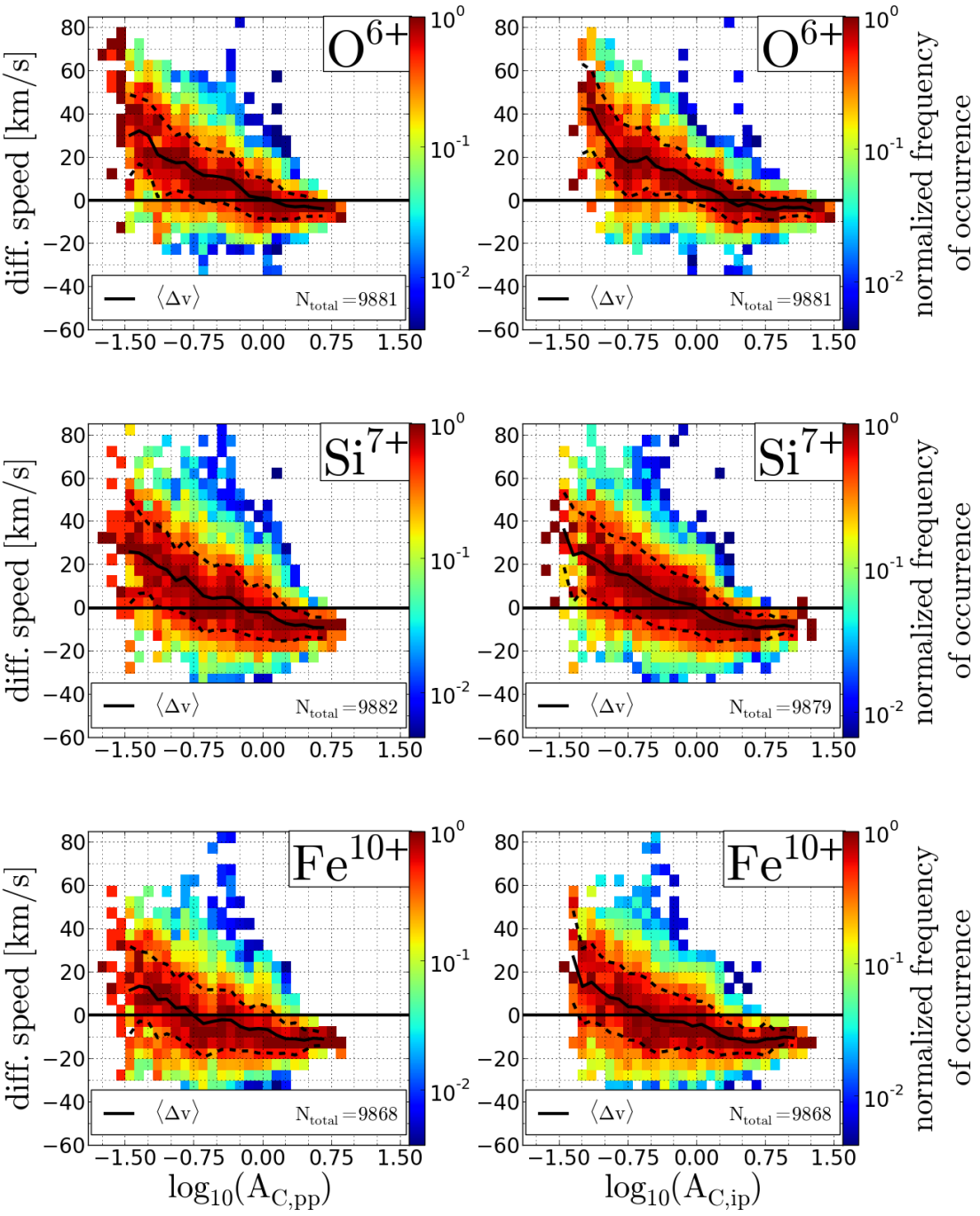

FIGURE 6.9: Two-dimensional histograms of the observed differential speeds between O^{6+}, Si^{7+}, Fe^{10+} and the solar wind protons versus the decadic logarithm of the simultaneously measured proton-proton collisional age (left panels) and the ion-proton collisional age (right panels) for the measurement period DOY 174-220 in 1996. The panels show the measured frequency of occurrence within the given time period normalized to the maximum of a each collisional age bin, respectively. As in Figure 6.5 the black line represents the mean differential speed $\langle \Delta v_{ip} \rangle$ at a given collisional age bin, while the additional dashed lines represent the standard deviation of the differential speed distribution at each proton speed bin.

ion-proton differential speeds Δv_{ip} for the ion species O^{6+}, Si^{7+} and Fe^{10+} versus the simultaneously measured decadic logarithm of the proton-proton collisional age for the analyzed time period DOY 174-220 in 1996. In the right panels of Figure 6.9 we depict the differential speed histograms for the same species versus the decadic logarithm of their individual ion-proton collisional age, which is calculated with the respective ion parameters from Eq. 1.42 - Eq. 1.48. In analogy to Figure 6.7 and 6.8 all panels show directly the normalized frequency of occurence i.e. the number of occurences during the measurement period DOY 174-220, 1996, normalized to a maximum value of 1 for each collisional age bin[5]. The calculated mean differential speed for each collisional age bin with at least 10 occurrences is connected by the black solid line, while the dashed line marks the (1σ-) standard deviation calculated in each bin. The (1σ-) standard error bars are even smaller than for the proton-speed-dependence analysis in Figure 6.7 and 6.8 for all statistically relevant bins and therefore not shown here. We only show in detail the results for O^{6+}, Si^{7+} and Fe^{10+} as our measurements showed that the differences between the ion species are small compared to the overall observed trend.

As can be seen from all six panels, we find a clear trend of decreasing differential speeds with increasing collision age for all ion species as one would expect it for any real nonthermal signature. Naturally, the ion-proton collisional age is higher than the proton-proton collisional age as the age scales in a first approximation proportional to q^2/m which can be seen from Eq. 1.44. At the lowest collisional age we find for each ion species differential speeds that are comparable in magnitude not only between the $A_{C,pp}$ and $A_{C,ip}$ case but also compared to the maximum differential speeds reached at high proton speeds between 480 and 540 km/s. Interestingly, at the highest collisional ages we find now for *all* ion species small negative differential speeds of less than -5 km/s for O^{6+} and about -10 km/s for Fe^{10+}. However, on the whole the difference in spanned $\langle \Delta v \rangle$ is not significantly smaller for any analyzed order parameter v_p, $A_{C,pp}$ and $A_{C,ip}$ (also compared to the average standard deviation of the differential speed distributions of about 20 km/s that is given by the mean difference between the solid and dashed line over all x-axis bins). Thus, we cannot conclude from Figures 6.7 - 6.9 that any potential order parameter v_p, $A_{C,pp}$, $A_{C,ip}$ of the differential speed is superior to the other two. Therefore, a strong role of collisions in the regulation of the ion-proton differential speed in the analyzed solar wind plasma is compatible with the observed trends but cannot be proven from the shown measurements alone.

[5] We still note that the absolute frequencies of occurrence are much higher at low collisional age values just because SOHO measured mainly slow wind during the measurement period.

Mass- and Charge-Dependency of Differential Speeds

We finally analyze the differential speeds that we obtained from the short-term VDFs for their dependence on the ion species' mass and charge. In Figure 6.10 we show the differential speeds of the ion species C^{4+}, O^{6+}, Si^{7+} - Si^{9+} and Fe^{8+} - Fe^{11+} as a function of their mass-per-charge value since we have seen in chapter 1 that the magnitude of differential speed might be sensitive to the ions-mass-per charge if local resonant ion-cyclotron resonance plays a crucial role in the determination of the differential speeds.
.

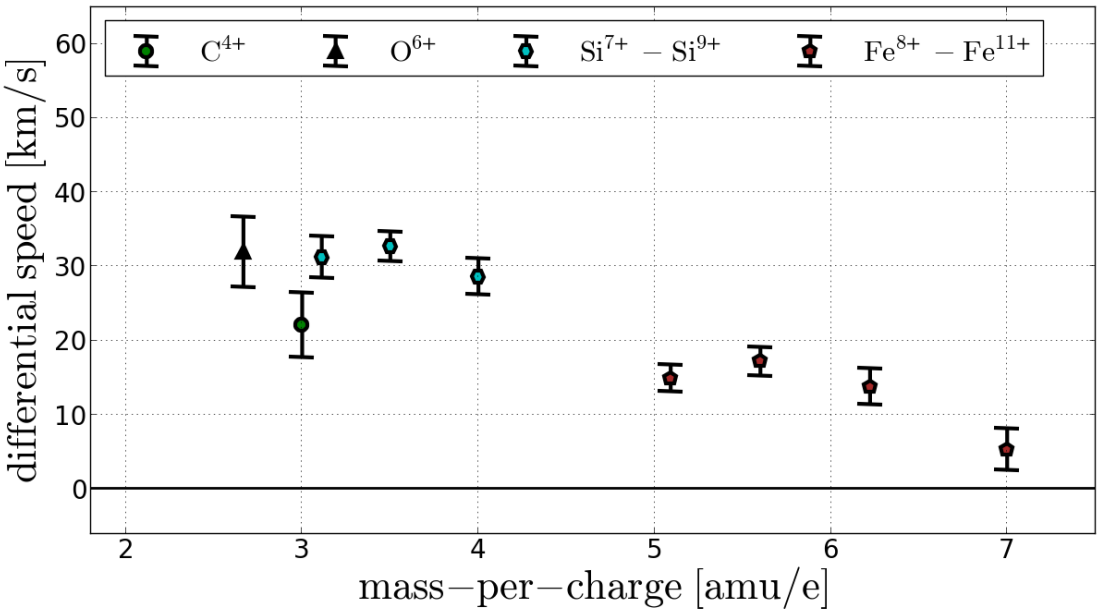

FIGURE 6.10: Mean differential speeds for the ion species C^{4+} - Fe^{11+} as a function of the ions' mass-per-charge. The differential speeds are derived with the Gaussian Reduced Stable (G-RS) response model from the CTOF (base-rate-corrected) short-term PHA data and the CELIAS/PM proton mean speeds.

The mean differential speeds that are shown in Figure 6.10 are calculated as the mean of all 6 mean differential speeds in the fast wind regime proton speed bins $v_p \in [480 - 540]$ km/s and the error bars are calculated as the 1σ-standard error of these 6 values. We can see in Figure 6.10 that among the ion species with lower mass-per-charge $m/q \leq 4$ amu/e, O^{6+} and Si^{7+} - Si^{9+} are measured with mean differential speeds of about 30 km/s without any statistically significant differences as can be seen from the overlapping error bars for this group. Within this group C^{4+} is measured at a somewhat lower mean differential speed of 22 ± 4 km/s with only very small overlap of the error bar with Si^{7+} and no overlap with the other species. The analyzed ion species at higher mass-per-charge values are the four central iron charge states. The gap between the two groups is given by the fact that neither Si^{6+} nor any of the higher

iron charge states yields very stable differential speeds as could be already observed in the long-term data. As discussed above, the iron ion species on the whole show lower differential speeds in particular in the short-term data with mean values of less than 20 km/s, but in particular Fe^{8+} is measured with a very small speed difference of about 5 km/s. Thus, on the whole we find from this analysis of the short-term VDFs a trend of decreasing differential speed with increasing mass-per-charge among the investigated heavy minor ion species. Assuming for simplicity an approximately linear relation with mass-per-charge, the gradient of this trend can be calculated as $\Delta(\langle \Delta v_{ip} \rangle)/(\Delta m/q) \approx -5$ (e km)/(amu s). However, one has to discuss this result in the light of the systematic uncertainty estimation obtained from the long-term data which is done in chapter 7.

6.4 Heavy Ion Thermal Speeds

Statistical Analysis of Thermal Speed Ratios

As described in section 6.2, we also analyzed the thermal speeds for the well-resolved ion species Si^{7+}, Si^{8+}, Fe^{8+}, Fe^{9+}, Fe^{10+}, and Fe^{11+}. Due to their relatively high mass-per-charge values, $4 \leq m/q \leq 7$, their velocity distribution functions are scanned down to more than 1 typical thermal speed for all CTOF cycles and therefore they can be analyzed for the whole measured time period DOY 174-220 without any bias caused by the CTOF Epq-analyzer at all occurred solar wind conditions. In the following we conduct a statistical analysis of the ions' thermal speeds relative to the simultaneously measured proton thermal speeds in an analogous way as it was done for the mean speeds of the heavy ions. As already described in chapter 1 the thermal speed of an ion species is linked to the kinetic temperature via its mass m. If one determines the thermal speed from a cut along a certain axis x of the VDF, the corresponding temperature along this cut is given by [Hefti, 1998a, Tracy et al., 2015, Hernandez and Marsch, 1985]:

$$T_x = \frac{m v_{th,x}^2}{2 k_B} , \tag{6.5}$$

where k_B is the Boltzmann constant.[6] To allow for better comparability with recent studies with ACE/SWICS data, [Tracy et al., 2015] and Ulysses/SWICS data [von Steiger and Zurbuchen, 2006] we work here directly with the thermal speeds of the heavy ions and compare them to the thermal speed of the protons.

[6] In our case, the 1D-reduced VDFs are not a well-defined cut through the VDFs but rather an integration over a range of ion speeds that depend on the variable ambient magnetic field direction (see Figure 2.9). Yet, we cannot correct for these subtle effects as we have no in-situ B-field measurements onboard SOHO.

In Figure 6.11 we show the 2-dimensional histograms of the ion-proton thermal speed ratio $v_{i,th}/v_{p,th}$ for the aforementioned ion species Si^{7+} - Fe^{10+} versus the decadic logarithm of simultaneously measured ion-proton collisional age for the analyzed time period DOY 174-220 in 1996. Again, we only show the histograms of the normalized frequency of occurrence within each collisional age-bin, but mention that the center-of-mass of the distribution is in the collisional solar wind around $\log_{10}(A_{C,ip}) \approx 0$. As the distribution of the thermal speed ratio is not symmetrical it makes a difference whether one calculates the mean ratio or the most frequently observed ratio for a given collisional age bin. In each panel of Figure 6.11 we approximated the latter by calculating the mean ratio only within those bins that reach at least 0.6 in their frequency of occurrence which corresponds approximately to the standard deviation of the distribution. This approximation of the most frequently observed speed ratio, denoted as $\langle v_{i,th}/v_{p,th} \rangle$ is shown as the black solid line in the panels and the standard deviation as the dashed black lines. The standard error of $\langle v_{i,th}/v_{p,th} \rangle \lesssim 0.01$ for all statistically relevant collisional age bins is negligible and not depicted here.

We can see that at low collisional age values ($\log_{10}(A_{C,ip}) \lesssim 0$) the most frequent measured thermal speed ratios are centered for each species around a relatively constant value that lies between 0.85 and 1.0 with small differences depending on the species. Thus, in the collisionless solar wind we clearly observe nonthermal kinetic temperatures between the ion species with slightly lower than mass-proportional temperatures as the thermal speed ratios are close to unity but not exactly 1. Around a collisional age of $\log_{10}(A_{C,ip}) \approx 0$ we see that all speed ratios start to decrease to values clearly below one. This can be interpreted as the beginning of a thermalization between the ion species temperatures. However, a complete thermalization cannot be observed even at the highest observed collisional age values of about $\log_{10}(A_{C,ip}) \approx 1$ which can be seen from the fact that neither the silicon nor the iron ions reach the thermal equilibrium ratio of 0.19 and 0.13 respectively, that can be calculated from Eq. 6.5 as $\langle v_{i,th}/v_{p,th} \rangle = \sqrt{m_i/m_p}$. Yet, we note that the minimum measurable thermal speed ratio is limited by the combination of speed bin width, given by the distance between two Epq-steps in the relevant solar wind speed range, and the finite counting statistics. Thus, even if thermal equilibrium were reached between the species we could probably not resolve that for the very heavy ions with the still limited counting statistics of CTOF . The same effect applies to all other time-of-flight mass spectrometers with similar Epq-resolution and counting statistics (compare e.g. [Tracy et al., 2015]).

From a theoretical point of view it is quite appealing that a significant thermalization can be observed above a collisional age on the order of 1, where on average the ions

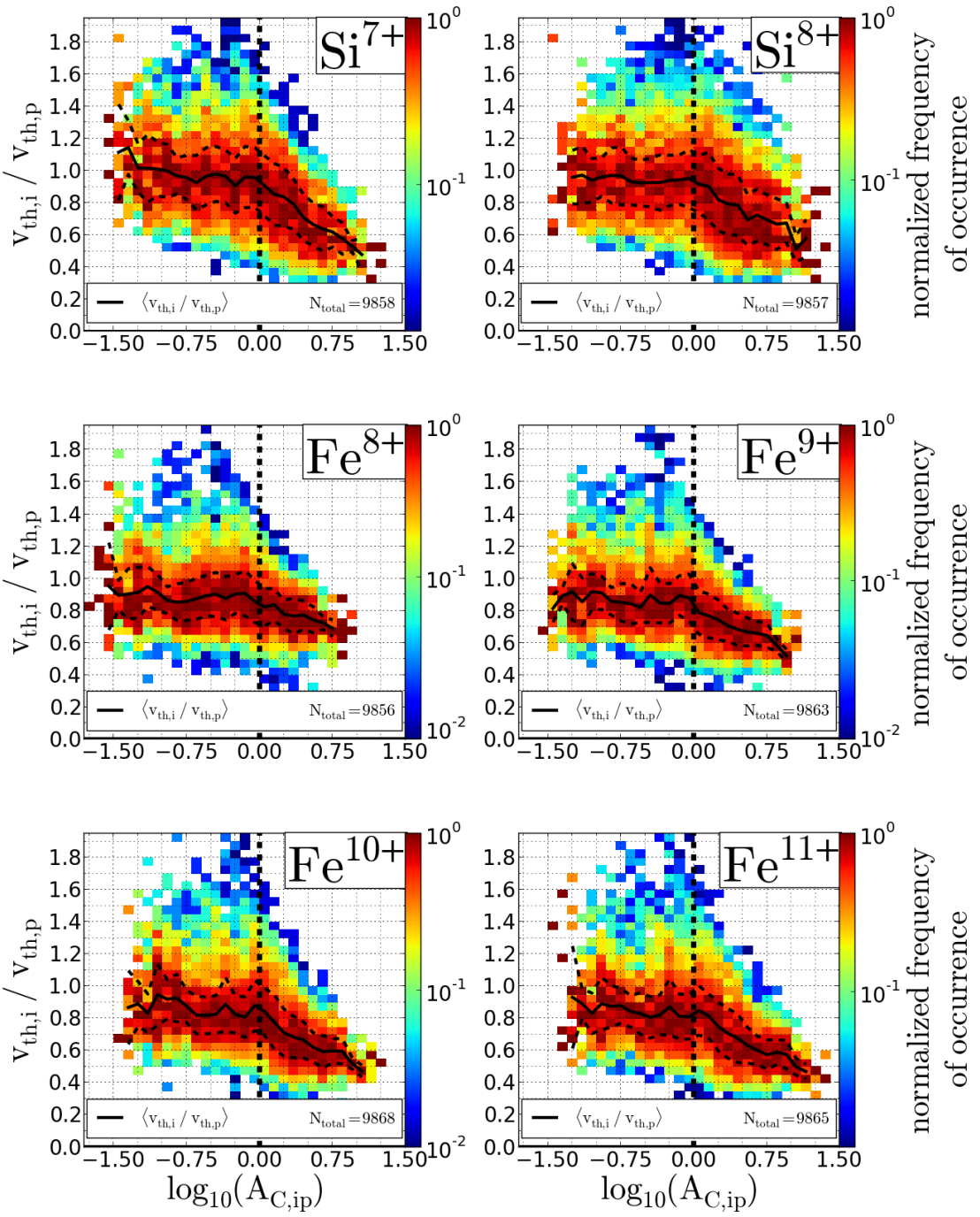

FIGURE 6.11: Two-dimensional histograms of the observed thermal speed ratios between Si^{7+}, Si^{8+}, Fe^{8+}, Fe^{9+}, Fe^{10+}, Fe^{11+} and the solar wind protons, respectively, derived from the (base-rate-corrected) CTOF PHA data for the measurement period DOY 174-220 in 1996. The panels show the measured frequency of occurrence within the given time period normalized to the maximum of a each proton speed bin, respectively. As in Figure 6.5 the black line represents an approximation of the most probable thermal speed ratio as described in the text and denoted as $\langle v_{th,i}/v_{th,p}\rangle$ at a given proton speed bin, while the additional dashed lines represent the standard deviation of the thermal speed distribution at each proton speed bin.

have undergone already a significant amount of small-angle deflections on their trajectory due to the collisions. Furthermore, this result is also in good agreement with the findings of [Livi et al., 1986] and [Kasper et al., 2017], among others. However, one has to have in mind that the calculated collisional age is a very rough approximation that does not take into account explicitly the collision history of the sample but is purely calculated from the values measured at 1 AU. We mention that the measured thermal speeds are in reasonable agreement with the earlier SOHO/CELIAS study by [Hefti, 1998a] who found mass-proportional kinetic temperatures in the fast wind and significant deviations from this relation in the slow wind. The study by [Tracy et al., 2015] shows a similar transition from nonthermal speed ratios $\langle v_{i,th}/v_{p,th}\rangle \gtrsim 1$ in the collisionless wind ($\log_{10}(A_{C,ip}) \lesssim 0$) to ratios $\langle v_{i,th}/v_{p,th}\rangle < 1$ in the collisional wind ($\log_{10}(A_{C,ip}) > 0$.), but the transition is smoother and the exact speed ratios in the fast wind yield over-mass-proportional heating with $\langle v_{i,th}/v_{p,th}\rangle \approx 1.3$ at $\log_{10}(A_{C,ip}) = -1.5$. Ultimately, also the study by [von Steiger and Zurbuchen, 2006] yields about equal thermal speeds in the fast wind measured by Ulysses. Thus, all observations agree in the findings of mass-proportional kinetic temperatures to first order but the open remaining question is whether signatures of deviations towards under- or over-mass-proportional heating dominate.

Finally, we compare the relaxation of the two investigated nonthermal features of *differential speed* in Figure 6.9 and of *nonthermal kinetic temperatures* in Figure 6.11. First we see that the decrease of differential speed with increasing collisional age is relatively smooth, while one can recognize for all ion species a clear break point at $(A_{C,ip}) \approx 1$ where the decrease of the thermal speed ratio starts. Second, the nonthermal kinetic temperatures are maintained in the solar wind plasma up to much higher collisional age values than the differential speeds that have been dropped to about zero or below already at $(A_{C,ip}) \approx 1$. Qualitatively, this observation is in agreement with theoretical expectations as the thermalization time scale for speed equalization is shorter than for temperature equalization. However, a quantitative comparison of the two time scales from the analytical model by [Hernandez and Marsch, 1985] yields smaller differences in collisional age. On the other hand, a comparable delay between thermal speed and differential speed relaxation is observed also for alpha particles with measurements onboard the Wind spacecraft [Kasper et al., 2017] and for minor ion species with ACE/SWICS[7]. The comparison of both features on the same collisional time scale might yield the additional information that is needed to determine the quantitative role of collisions in the thermalization of the solar wind.

[7] Private communication with L. Berger (2019).

Chapter 7

Discussion

In this final chapter we focus on discussing, as a particular result, the mass-per-charge dependency of the derived differential speeds and compare the new SOHO/CELIAS results with the ACE/SWICS measurements by [Berger et al., 2011].

7.1 Mass-per-Charge Dependence of the Heavy Ion Differential Speeds

Both the long-term speed spectra and the short-term VDFs show significant differential speeds of the solar wind heavy ions compared to the protons in the fast wind. Comparing the magnitude of Δv_{ip} for different ion species, both measurements also show higher differential speeds for ion species with lower mass-per-charge, but the difference between low-m/q and high-m/q ion species is less than 10 km/s in the long-term data (see Figure 5.15 and 5.16) while it is about 20 km/s in the short-term data as we see in Figure 6.10. This means that we observe a stronger dependence of differential speed on mass-per-charge in the short-term data than in the long-term averaged data. The observed difference between the two results is a substantial fraction ($\gtrsim$ 30%) of the overall differential speeds observed at 1 AU. We note that this difference exists mainly due to the measured speeds of the four iron ions Fe^{8+} - Fe^{11+} which alone cover a relatively large range of about 40% of the measured m/q-range. These four iron species are measured with $5\,\mathrm{km/s} \leq \Delta v_{ip} \leq 15\,\mathrm{km/s}$ in the short-term data while they are measured with $15\,\mathrm{km/s} \leq \Delta v_{ip} \leq 30\,\mathrm{km/s}$ in the long-term data as can be seen from the same Figures 5.15, 5.16, and 6.10. From the systematic uncertainty analysis in chapter 5 we infer that the difference between the two results can be most likely explained by the fact that the short-term data is analyzed still with the Gaussian response model while the

shown long-term data in chapter 5 is already analyzed with the more accurate Kappa-Moyal peak model. To illustrate this point we show in Figure 7.1 for several major heavy ion species the comparison between the observed mean short-term differential speeds[1] (filled symbols) and the measured long-term differential speeds for the proton speed range $v_p \in [500, 510]$ (empty symbols) but this time derived with the Gaussian peak shape model for direct comparison. We see that in this case the long-term differential speeds match exactly with the short-term differential speeds for iron when they are derived with the same response model. The gray-shaded area shows the estimated range of systematic uncertainty that we derived from the long-term mean speed error estimation of the Kappa-Moyal model in chapter 5 for the different peak tail parameters, with the best tail parameter $A_C = 0.0035\,\mathrm{ch}^{-1}$ lying roughly in the middle of this area. Ideally, the short-term data should be also evaluated with the more accurate Kappa-Moyal peak model in the future. Yet, the improvement of the response model is a systematic effect independent of the measurement statistics, so that we expect a similar correction for the differential speeds derived from the short-term data when the improved model is applied in the respective short-term data fits. As can be seen from the extension of the gray area this correction is larger for ions with high mass-per-charge, such as the iron ions, so that the strong decreasing trend of differential speeds with increasing mass observed in the short-term data is expected to be reduced.

We further note that the improved peak shape model also reduces the negative differential speeds for iron in the slow wind that we observe for instance in Figure 6.6. This can be seen from Figures 5.8 and 5.9, where we only observe small negative differential speeds for the iron ions of about -5 km/s which is comparable to the other ion species and can be easily explained by the uncertainties of the CELIAS Proton Monitor.
A second, minor reason for the stronger trend in the short-term data is the difference in average differential speed that is observed for the low-m/q ions, that are measured with differential speeds around 25 km/s in the long-term data in Figures 5.15 and 5.16 while we find differential speeds around 30 km/s in the short-term data in Figure 6.10. As can be seen from the gray-shaded area in Figure 7.1, this difference cannot be explained by the difference in the response model. It is in general plausible that nonthermal features in the short-term data are more pronounced as they are less likely to be averaged out over shorter integration periods. However, it is not clear why this should only apply to the heavy ion species with lower mass-per-charge, but not to iron as can be seen from Figure 7.1. One explanation might be that we have an instrumental effect here that is related to the high base rate factors for low-m/q ion species that cannot be

[1] These differential speeds are calculated for each species as the mean differential speed in the proton speed range between 480 km/s and 540 km/s analog to Figure 6.10.

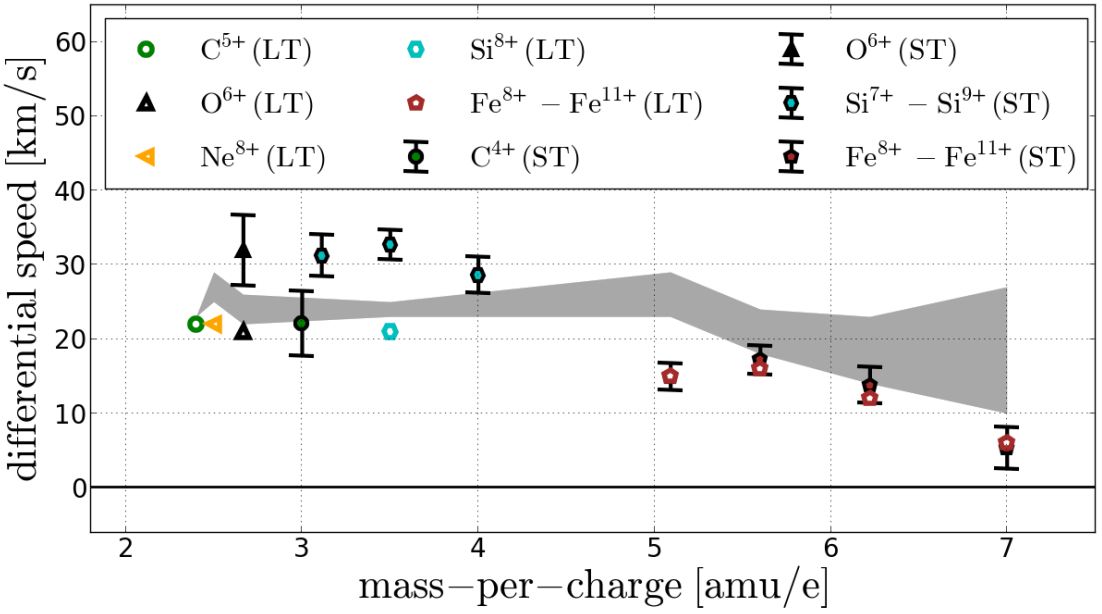

FIGURE 7.1: Long-term (LT) and short-term (ST) differential speeds obtained for several major ion species derived with the Gaussian Stable Reduced response model as a function of the ions' mass-per-charge. The gray-shaded area is the systematic uncertainty interval that we obtained from the long-term speed analysis with the Kappa-Moyal Reduced Stable response model.

included properly in the short-term fits as explained in section 6.1. Under the two discussed circumstances, the observed trend in the short-term data in Figure 6.10, might to a large part be an instrumental effect. In fact, the systematic speed uncertainty interval, derived from the long-term data analysis with the Kappa-Moyal response model, allows even a complete absence of any trend with mass-per-charge within the statistical (1σ-) standard error bars of the analyzed species in Figure 7.1. Therefore, our results can be considered to be also compatible with all species streaming at the same differential speed of about 25 km/s in the measured fast wind. Yet, what is statistically very unlikely from the measured long-term and short-term data and the systematic error analysis is that the ion species follow the opposite trend of increasing differential speed with increasing mass-per-charge. This is particularly interesting as such a trend could be expected, if the ions were accelerated locally to their differential speed cut-off that results from the resonance condition in chapter 1. We note that the mass-per-charge dependent differential cut-off speeds from Eq. 1.28, that follow from the ion-cyclotron resonance condition and the waves' dispersion relation, can be modified e.g. when one assumes that further ion species carry the waves (see Eq. 1.29 and Figure 1.9). Yet, it is difficult to see how the trend of Eq. 1.28 could be completely inverted theoretically to make the model work. In this context it does not help if we assume a harder power spectrum of the ambient waves (with a lower exponent γ in Eq. 1.40) as we do not only need to prevent the theoretical preferential acceleration of the high-m/q ions to fit the

measured trend but also have to allow the low-m/q ions such as O^{6+} and C^{5+} to overcome significantly the cut-offs in Eq. 1.28 which cannot be achieved by just providing more power. Instead, one probably has to look for a second-stage acceleration process that builds upon the initial acceleration provided by the ion-cyclotron resonance and acts then more efficiently on the low-m/q ion species to overcome the differential cut-off speeds. Close to the Sun, one can assume that such an additional acceleration mechanisms exists based on the mirror force that converts the energy stored in the high kinetic temperatures of the ions into kinetic energy to efficiently accelerate the solar wind [Hollweg and Isenberg, 2002]. Yet, this mechanism is based on large expansion factors of the magnetic field in the coronal holes that do not exist at 1 AU. We conclude that at least an isolated ion-cyclotron resonance process as it is described in a simplified analytical manner in [Isenberg and Hollweg, 1983] can hardly act as the dominant local source of ion-proton differential speeds that show a decreasing (or even constant) trend with increasing mass-per-charge in combination with differential speeds magnitudes of the observed order $\Delta v_{ip} \lesssim v_A$.

7.2 Heavy Ion Differential Speeds at 1 AU

We finally aim to compare the SOHO/CELIAS results with the differential speeds that [Berger et al., 2011] obtained from the ACE/SWICS data. This comparison is in particular interesting as both measurements were conducted in fast wind streams measured at L1 around solar minimum (but not at the same time as the ACE/SWICS observations are from early 2008). For this purpose we corrected our short-term differential speeds with the geometrical correction factor of $f_{geo} \approx 1.4$ explained in section 2.4 and converted the corrected differential speeds into units of the Alfv́en speed v_A^{Wind}, which we extrapolated from the Wind spacecraft. This should not be too problematic as, in contrast to the B-field direction, the B-field magnitude and solar wind density can be expected to be relatively stable for the small distances between the spacecraft (on heliospheric scales). The results are shown in the lower panel of Figure 7.2 and can be compared to the upper panel of Figure 7.2 which are the results by [Berger et al., 2011] that we already showed in chapter 1. When we compare the upper and lower panel of Figure 7.2, we find that in general there is a good agreement between the results as in both cases the obtained results are on the order of a substantial fraction of the Alfvén speed with the most reliable low-m/q species lying approximately around half the Alfvén speed in both studies. Although, there are some differences, e.g., for the iron ions that are measured at differential speeds that are about 0.1 - 0.3 v_A larger in the ACE measurements, depending on which species we compare and whether we

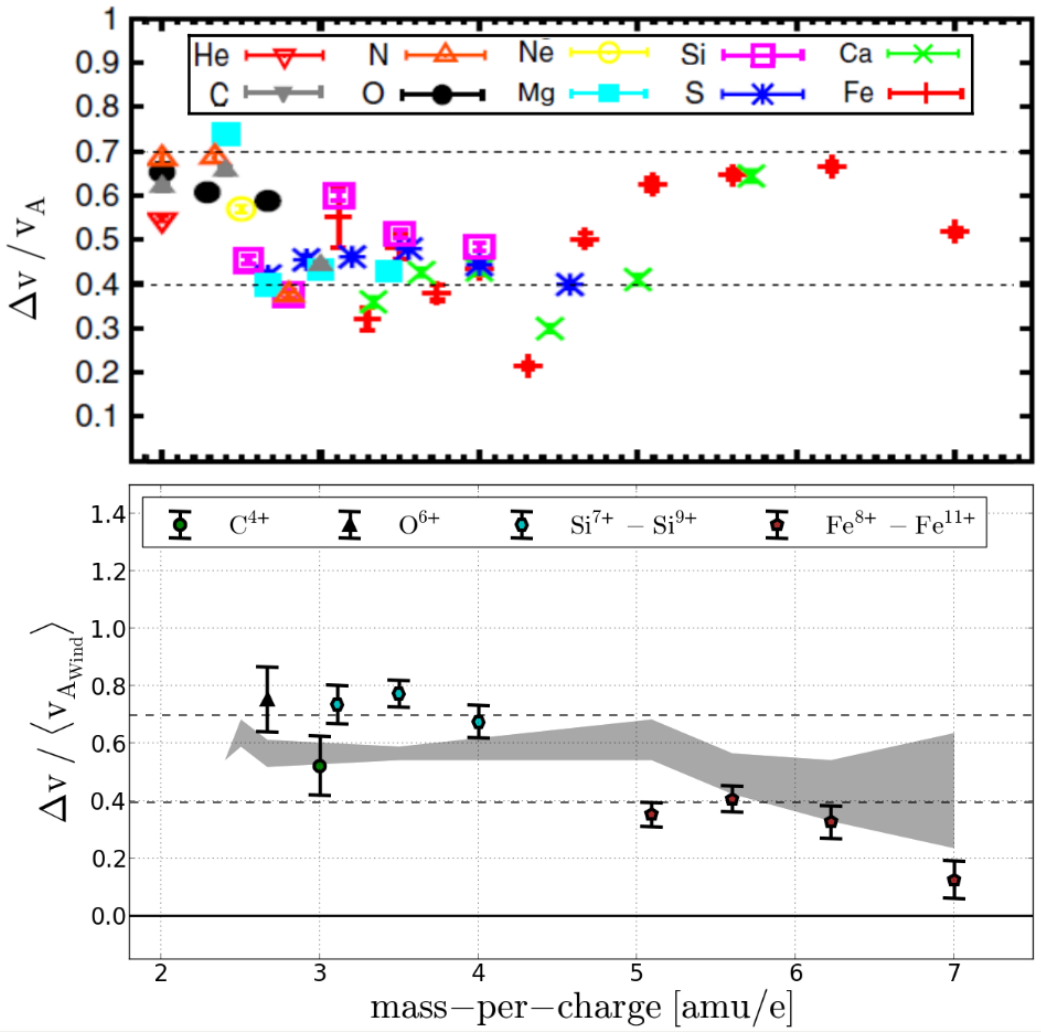

FIGURE 7.2: Upper panel: Mean B-field-corrected differential speeds $\langle \Delta v_{ip} \rangle$ derived by [Berger et al., 2011] for two fast wind streams in 2008 as described in chapter 1. Lower panel: mean average-B-field-corrected differential speeds $\langle \Delta \widetilde{v}_{ip} \rangle$ obtained from the short-term data for the major ion species C^{4+} - Fe^{11+}, in units of the average Alfv én speed that we extrapolated from the Wind spacecraft for the fast wind stream between DOY 213 and 216, 1996. The gray-shaded area corresponds to the systematic uncertainty interval that we obtained from the long-term speed measurements in chapter 5. The upper panel is adapted from [Berger et al., 2011].

compare with the short or long-term results for CTOF. On the other hand, we see that these differences between the two measurements even for the most different differential speeds are still comparable to the spread of the observed differential speeds among ion species (with similar mass-per-charge) within each of the two studies and also to the systematic uncertainty for iron. Therefore, we conclude that the new differential speed results obtained from SOHO/CELIAS and the ACE/SWICS results at L1 are consistent within their measurement uncertainties and yield an overall (B-field-corrected) differential speed between the heavy ions and solar wind protons of $\langle \Delta v_{ip} \rangle \approx (0.5 \pm 0.2)\, v_A$ with the heavy ions streaming faster than the protons.

In summary, the analysis of the SOHO/CELIAS data has shown the clear presence of differential streaming between heavy ions and protons in the fast, collisionless solar wind at 1 AU. Under the given conditions, we consider this differential streaming as a universal feature of solar wind heavy ions as the vast majority of measured ion species are significantly faster than the solar wind bulk protons. The measured differential speeds show a decreasing trend with increasing mass-per-charge. From these findings we conclude that a local acceleration process, based entirely on ion-cyclotron resonance as the dominant source of the differential speeds, is rather unlikely. This is because such a process would lead to the opposite trend of increasing differential speeds with increasing mass-per-charge as described in chapter 1. Instead, the observations are compatible with a scenario in which the differential speeds observed at 1 AU are remnants from initial preferential acceleration processes close to the Sun. Here, the speed differences are mediated and regulated primarily by Coulomb collisions and/or plasma instabilities while the particles travel away from the Sun. Such a scenario is also in agreement with the observed differential speed decrease with increasing collisional age of the solar wind. In order to distinguish whether Coulomb collisions, specific instabilities or other kinetic processes dominate the evolution of the solar wind on its way out to 1 AU and beyond (compare e.g. [Verscharen et al., 2015]), it seems promising to combine the measurements of different non-thermal features, e.g., by the differential speed and the thermal speed ratios as discussed in chapter 6. By investigating the ion kinetic temperatures with the SOHO/CELIAS data, we find clear signatures of preferential heavy ion heating in the fast, collisionless wind that is slightly less than mass-proportional.

In the near future, the ESA/NASA Solar Orbiter mission will enable us to address these questions on the basis of measured 3-dimensional solar wind heavy ion velocity distributions in combination with magnetic field measurements at the spacecraft site and other in-situ and remote sensing measurements. These observations will be made at distances between 1 and 0.3 AU from the Sun. Particularly, at the closest distances, we expect to measure pronounced non-thermal features for the solar wind heavy ions in the fast wind similar to the ones observed in the earlier Helios mission for protons and alpha particles. Yet, the measurements at 1 AU always serve as a reference and can be compared to these new measurements. With the derived SOHO/CELIAS results in this work, that are in good agreement with ACE/SWICS measurements, we have now a solid baseline for the observations of heavy ion differential streaming and preferential heating at 1 AU.

Appendix A

Supplementary Documentation of the CTOF PHA Base-Rate Correction

A.1 PHA Base-Rate Correction

In this appendix we briefly describe the derivation of the base-rate factors that are necessary to apply the base rate correction of the transmitted CTOF PHA data. For reproducibility we give explicitly the utilized functions and show examples of the accomplished base rate correction for several Epq-steps in the CTOF long-term PHA data.

With the conversion functions in A.1 and A.1 from Epq, TOF and ESSD to mass and mass-per charge channel, and the known conversion from Epq-step to matrix rate that is given in Eq. 2.12 we can for every given cycle directly relate the transmitted PHA data count rate within a given part of the ET-matrix at a given Epq-step to the actually measured count rate of the corresponding MR data within the corresponding MR-Box. This comparison is shown in Figures A.2 and A.1 for the first measured cycle on DOY 174. We now do not have to compare the count rate of every MR box with the corresponding area in ET-space individually, but instead have to sum up the count rates of all MR boxes and all corresponding ET-areas in the same priority range to derive one single base-rate factor for each priority range at each Epq-step for each cycle[1]. The definition of the priority ranges in ET-space and m-m/q space is shown in Figure A.3.

[1]Note, that for all matrix rates other than MR8-MR12, the matrix count rates are binned together from several Epq-steps as explained in chapter 2. As there are less matrix rates than Epq-steps at this point the calculation of the base-rate factors is not exact but the same approximation for the conversion from the MR-spectrum to the Epq-spectrum have to be applied as for the evaluation of the matrix rate data which is described in detail in chapter 3.

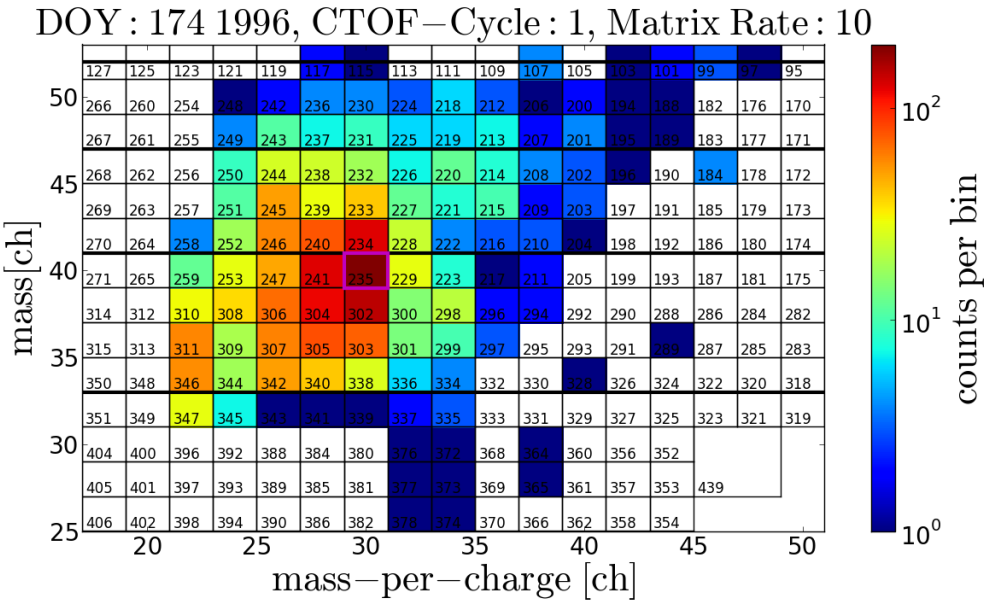

FIGURE A.1: Close-up of the matrix rate box scheme filled with the measured (and onboard assigned) counts during the first 5-minute CTOF cycle measured on DOY 174, 1996 for matrix rate MR10. The magenta framed box is the nominal box for O^{6+} after [Hefti, 1998b].

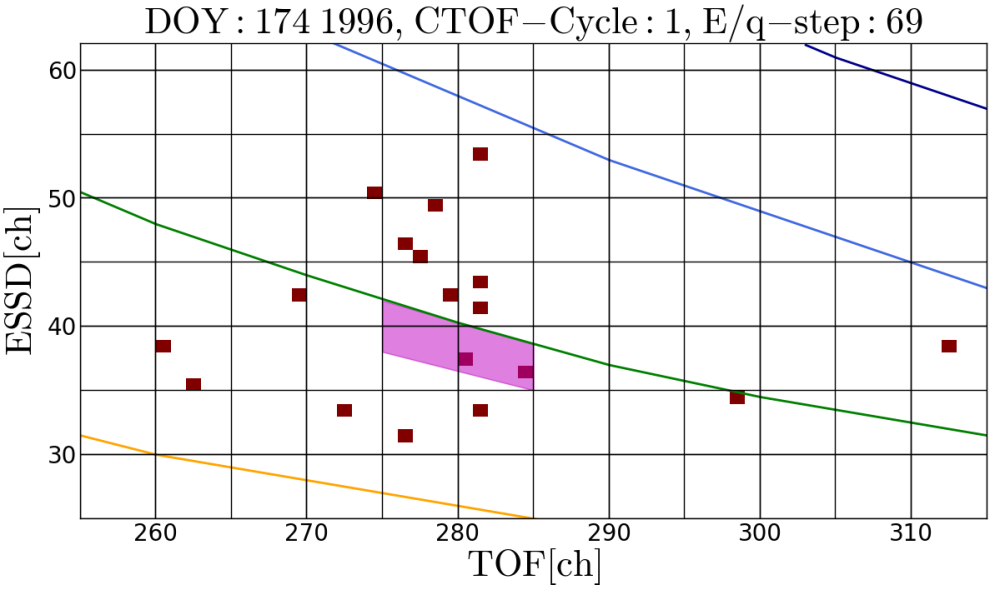

FIGURE A.2: Close-up of the ET-matrix filled with the transmitted PHA counts during the first 5-minute CTOF cycle measured on DOY 174, 1996 for Epq-step 69. This step corresponds to matrix rate MR10 for MR-box 235 at the onboard estimated heavy ion speed of 395.4 km/s at the given cycle, which is the same as in Figure A.1. The MR-box 235 corresponds to the magenta-shaded area in the ET-matrix which at the Epq-step 69 only contains two transmitted PHA words while e.g. for the whole priority range PR4 (limited by the orange and green lines) 9 PHA counts were transmitted. In this case the same number of 9 PHA counts is also transmitted for PR3 (limited by the green and light blue lines) at the given Epq-step.

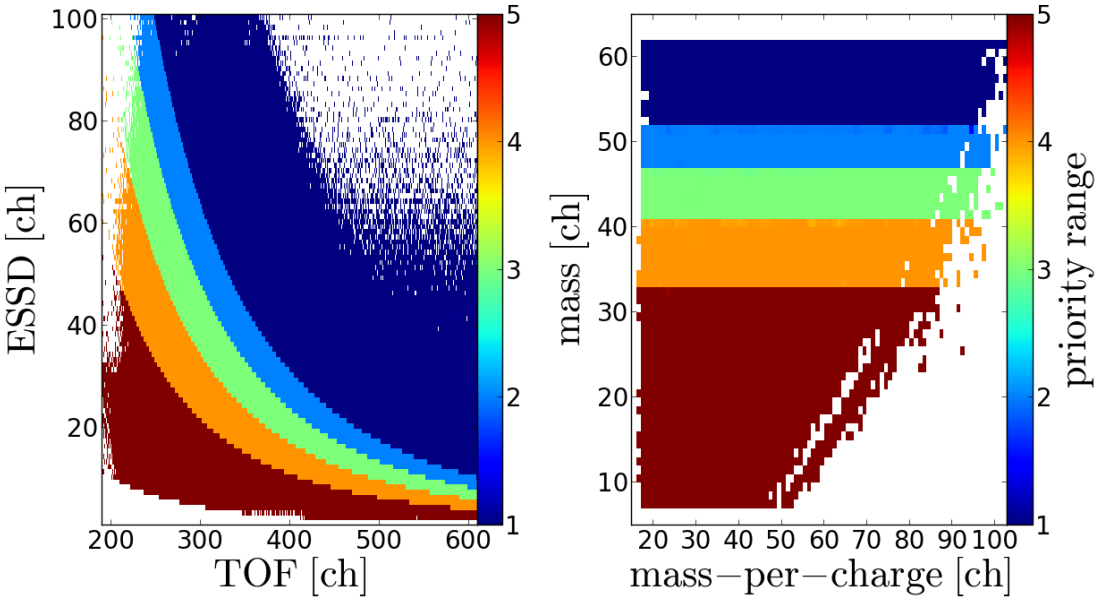

FIGURE A.3: The left panel shows the definition of the Priority Ranges 1-5 (from top to bottom) in the ET-matrix as we obtain it from the *Range* data product in the CTOF PHA data. The assignment of the priority range for each PHA count depends only on its detected TOF and ESSD channel but not on the Epq-step, indicating that the ranges are defined in mass only. This can be confirmed by the right panel which shows the range of the PHA counts after their TOF and ESSD channels have been translated into mass and mass-per-charge after A.1 and A.1. In both panels the counts of all Epq-steps $0 \leq j \leq 116$ are included. As can be seen the borders in mass in the right panel are very sharp, so that the nominal conversion algorithm from Epq, TOF, ESSD to m, mpq, MR (after [Hefti, 1998b]) can be proofed valid. The only exceptions are a few bins in PR2 and PR4 at the border to PR1 and PR3 respectively, which are probably due to unreconstructable rounding/truncation errors.

Finally, the base-rate factors are obtained from the division of the integrated priority range MR count rates by the integrated priority range PHA count rates

$$F_{br}(\tau, \epsilon) = F_{br}(PR) = \frac{N_{MR}(PR)}{N_{PHA}(PR)} \,. \tag{A.1}$$

In Figure A.4 we show a comparison of $N_{MR}(PR)$ and $N_{PHA}(PR)$ for the first cycle of DOY 174, 1996, and priority ranges PR1 and PR4. When the transmitted PHA count rates are finally multiplied with these base-rate factors we obtain the base-rate-corrected PHA count rates (see Eq. 2.13). These base-rate corrected long-term PHA counts are shown in Figures A.5 - A.9 for Epq-steps 40 to 80. Unfortunately, the described base rate factor reconstruction does not work for the helium priority range PR5 because He^{2+} is additionally onboard suppressed by the PID.

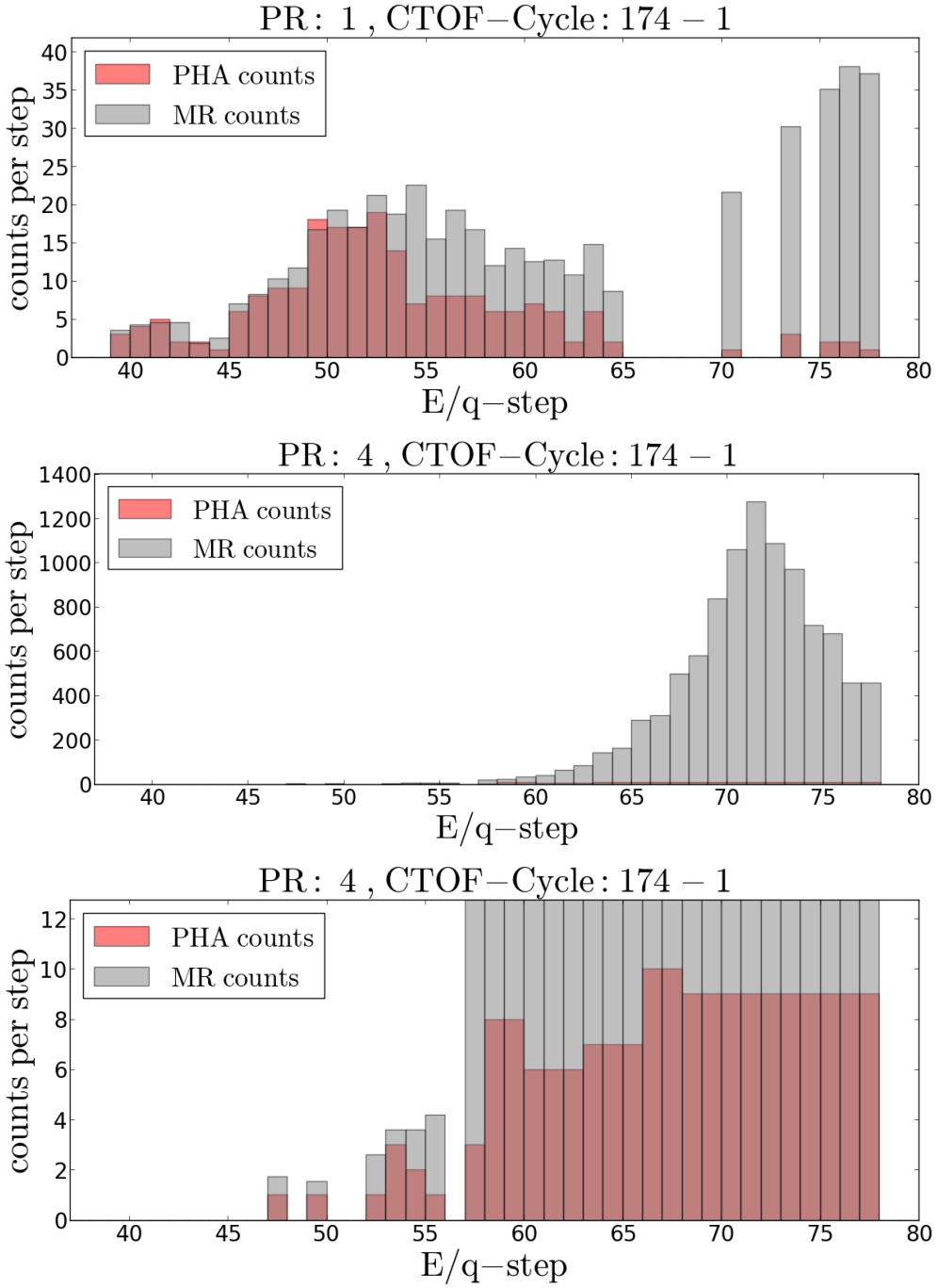

FIGURE A.4: Comparison of the measured integrated MR counts (gray) and the transmitted integrated PHA counts (red) in priority ranges PR1 (upper panel) and PR4 (middle and lower panel) for the first cycle on DOY 174 for all relevant Epq-steps with at least one detected count. The ratio of the two quantities at each cycle and each step yields the base rate factors with which the PHA counts have to be multiplied to represent the true number of measured counts. While for PR1 the measured MR and transmitted PHA counts are of comparable order, the difference between the two quantities reaches up to two orders of magnitude in PR4 so that the lower panel is a close-up of the middle panel that allows a better recognition of the transmitted PHA words. At Epq-step 69 we find $N_{PHA} = 9$ and $N_{MR} = 845$ yielding a base-rate weight of $w_{br}^{PR4} = N_{MR}/N_{PHA} \approx 93.89$ for priority range PR4 at the given cycle and Epq-step.

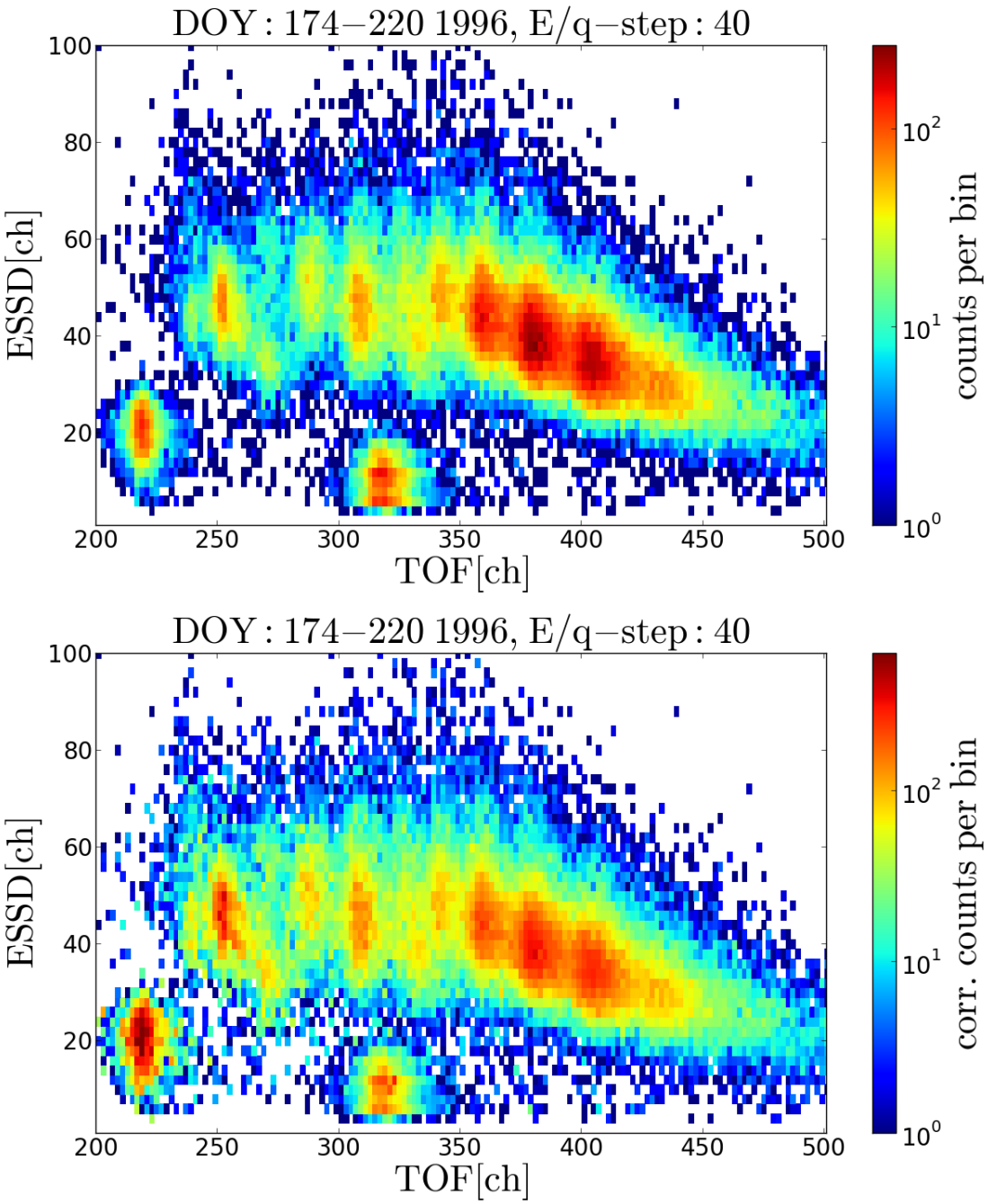

FIGURE A.5: Comparison of the uncorrected (upper panel) and corrected (lower panel) count rates for the accumulated long-term PHA data (DOY 174-220) for Epq-step 40.

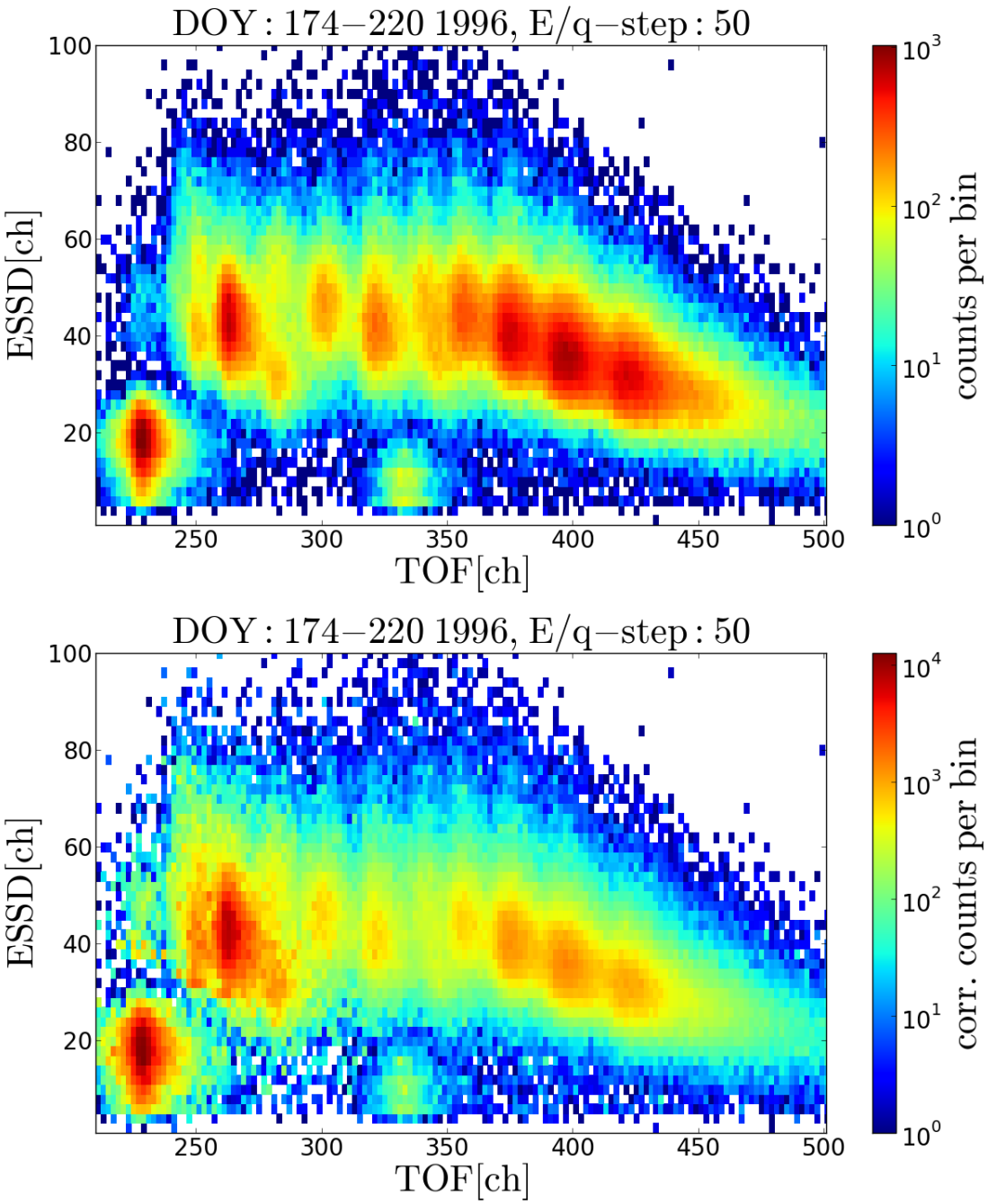

FIGURE A.6: Comparison of the uncorrected (upper panel) and corrected (lower panel) count rates for the accumulated long-term PHA data (DOY 174-220) for Epq-step 50.

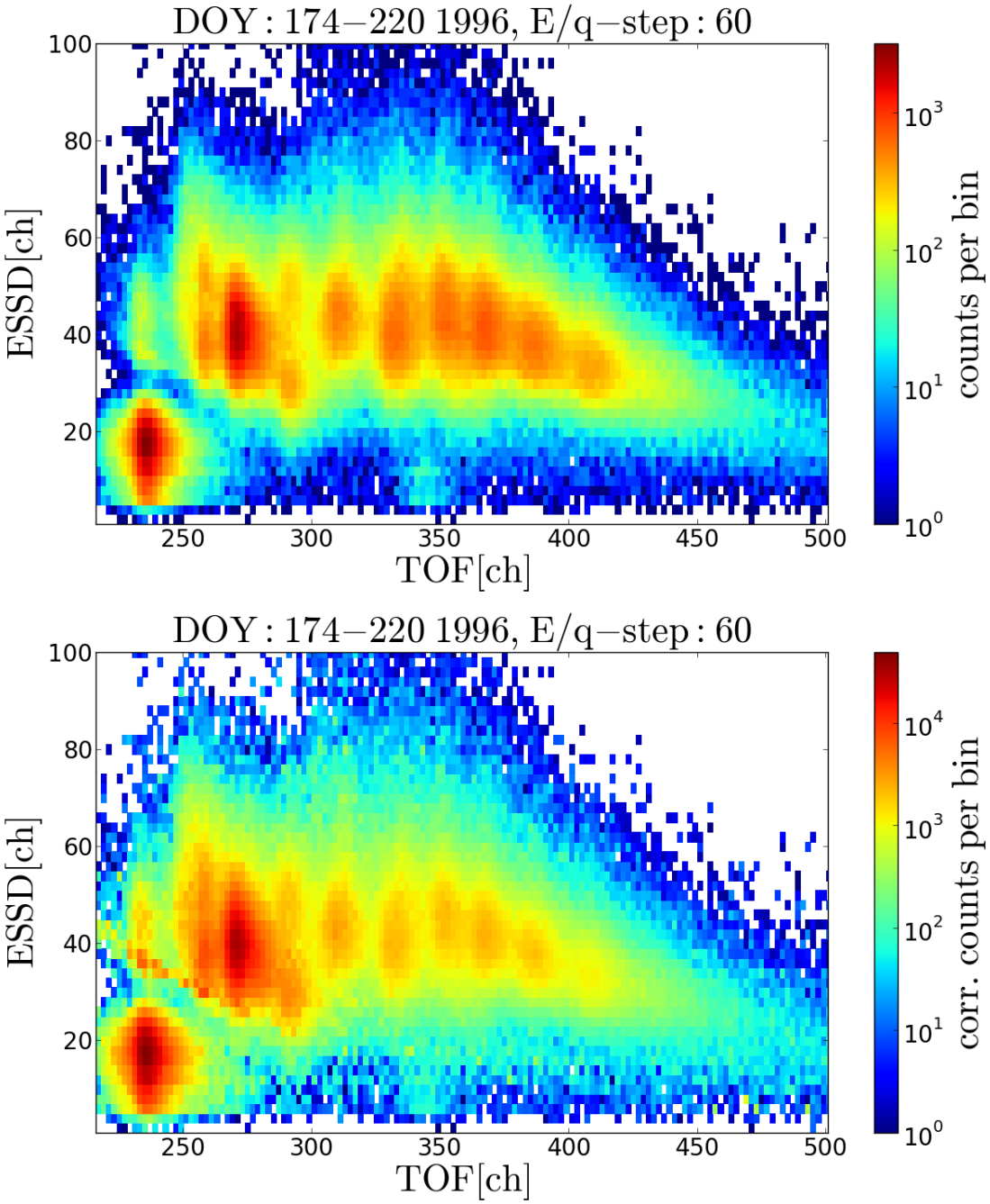

FIGURE A.7: Comparison of the uncorrected (upper panel) and corrected (lower panel) count rates for the accumulated long-term PHA data (DOY 174-220) for Epq-step 60.

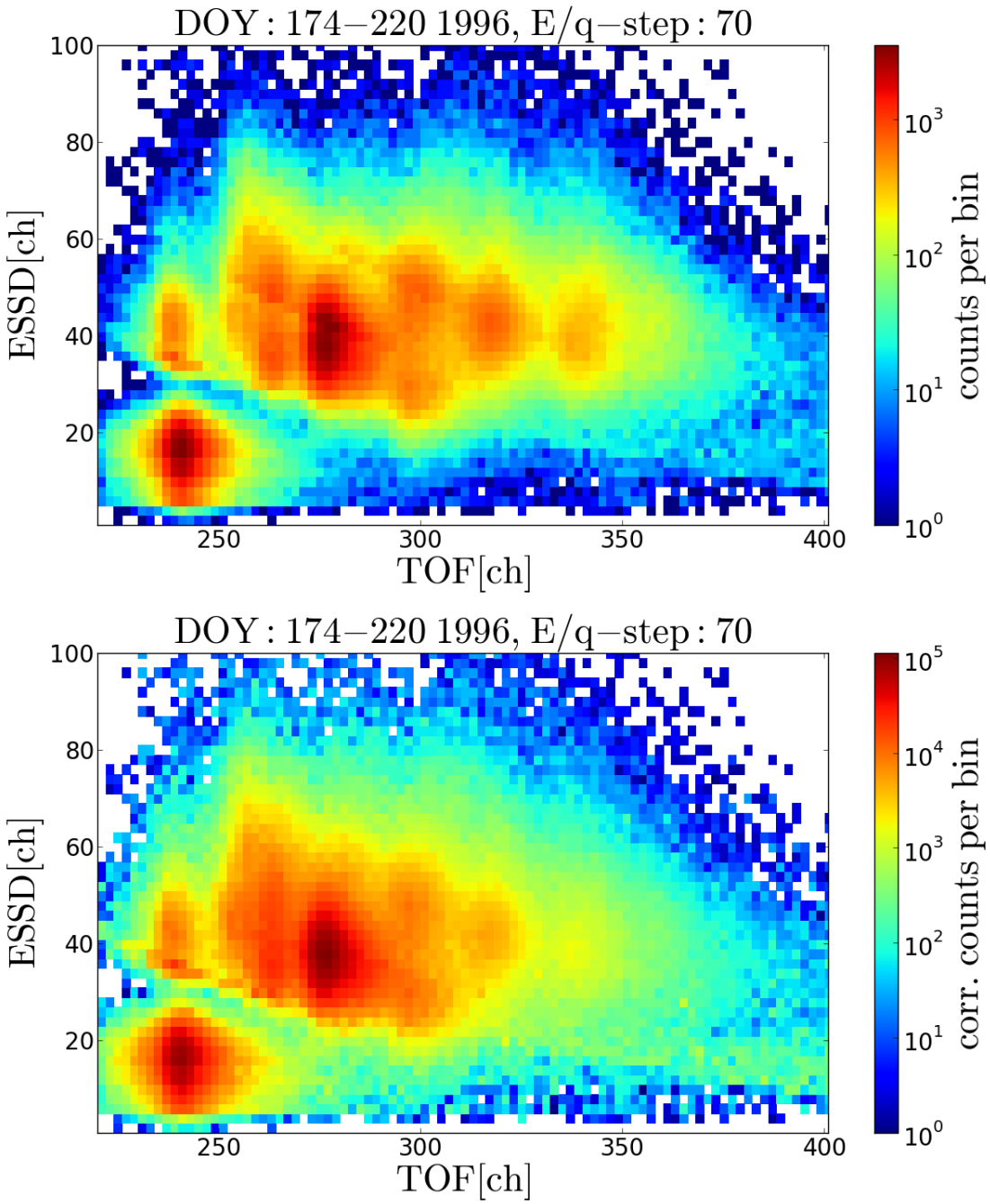

FIGURE A.8: Comparison of the uncorrected (upper panel) and corrected (lower panel) count rates for the accumulated long-term PHA data (DOY 174-220) for Epq-step 70.

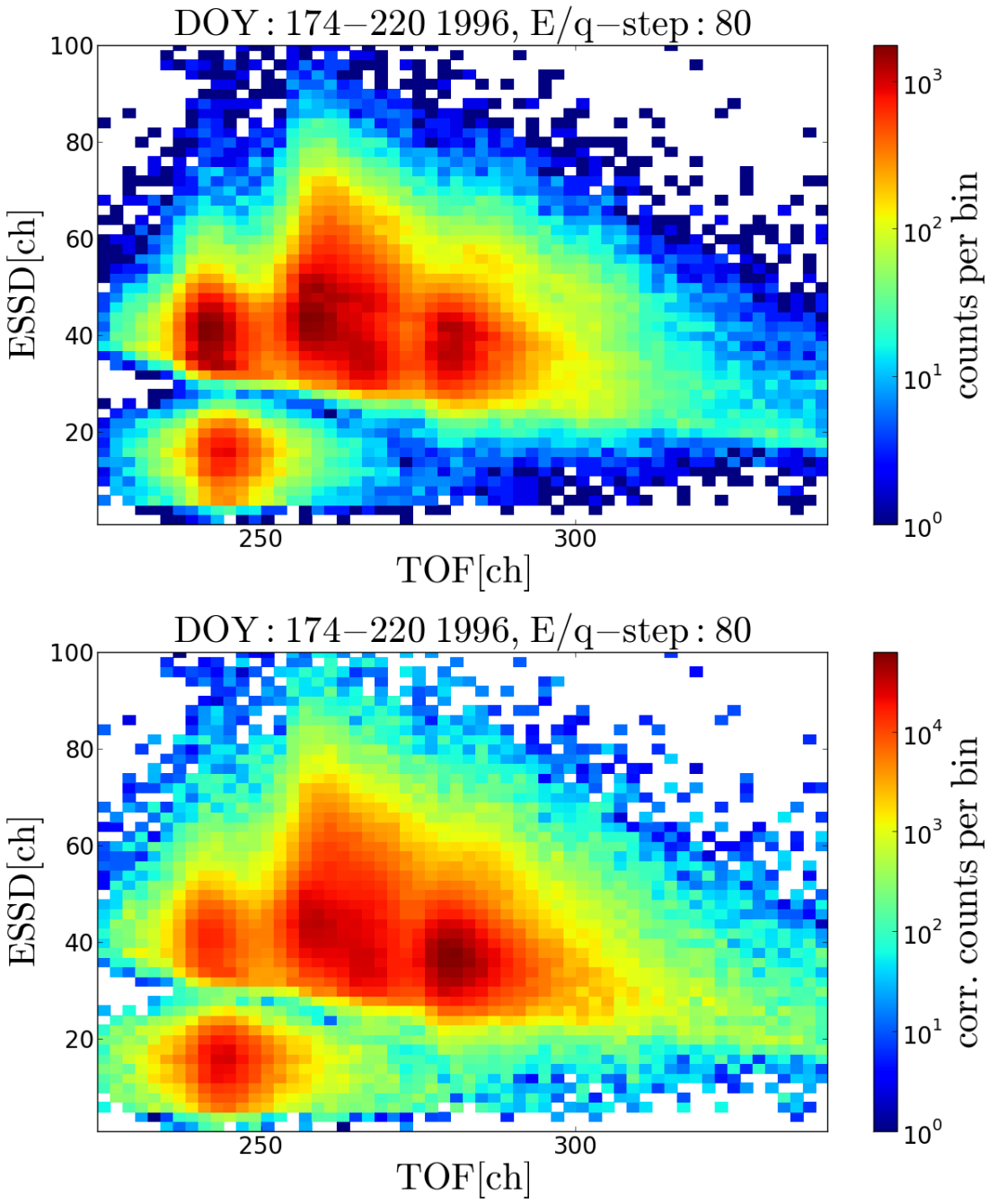

FIGURE A.9: Comparison of the uncorrected (upper panel) and corrected (lower panel) count rates for the accumulated long-term PHA data (DOY 174-220) for Epq-step 80.

CTOF onbord Mass-per-Charge Classification

After [Hefti, 1998b] the conversion from a measured combination of Epq-step j and TOF channel τ to mass-per-charge channel m/q is given by:

$$m/q = A_0 + A_1 u + A_2 u^4 \tag{A.2}$$

where

$$A_0 = A_{00} + A_{01} w + A_{02} w^2 \tag{A.3}$$

$$A_1 = A_{10} + A_{11} w + A_{12} w^2 \tag{A.4}$$

$$A_2 = A_{20} + A_{21} w + A_{22} w^2 \tag{A.5}$$

and

$$u = \ln(\tau) + \text{lnTADC} \tag{A.6}$$

$$w = \ln(U_0 \cdot r^j + U_{acc}) \tag{A.7}$$

with U_0, r and U_{acc} given as in Table B.1 and lnTADC$= -1.632172$.
The remaining parameters are given by

$A_{00} = -294.5961$	$A_{01} = 31.4464$	$A_{02} = -0.2448$
$A_{10} = 60.1287$	$A_{11} = -1.3393$	$A_{12} = 0.1219$
$A_{20} = -0.026322$	$A_{21} = 0.002940$	$A_{22} = 0.000599$

TABLE A.1: Parameter settings for the onboard mass-per-charge classification algorithm.

CTOF onbord Mass-Classification

After [Hefti, 1998b] the conversion from a measured combination of TOF channel τ and ESSD channel ϵ to mass channel m is given by:

$$m = B_0 + B_1 v + B_2 v^2 + B_3 u + B_5 u^3 + B_6 v u \tag{A.8}$$

where

$$v = \ln(\epsilon) + \text{lnEADC} \tag{A.9}$$

with lnEADC= 0.855, u as given in Eq. A.6 and the remaining parameters

$B_0 = -20.755203$	$B_1 = -2.605667$	$B_2 = 0.529373$
$B_3 = -14.045425$	$B_5 = 0.790695$	$B_6 = 3.744827$

TABLE A.2: Parameter settings for the onboard mass-per-charge classification algorithm.

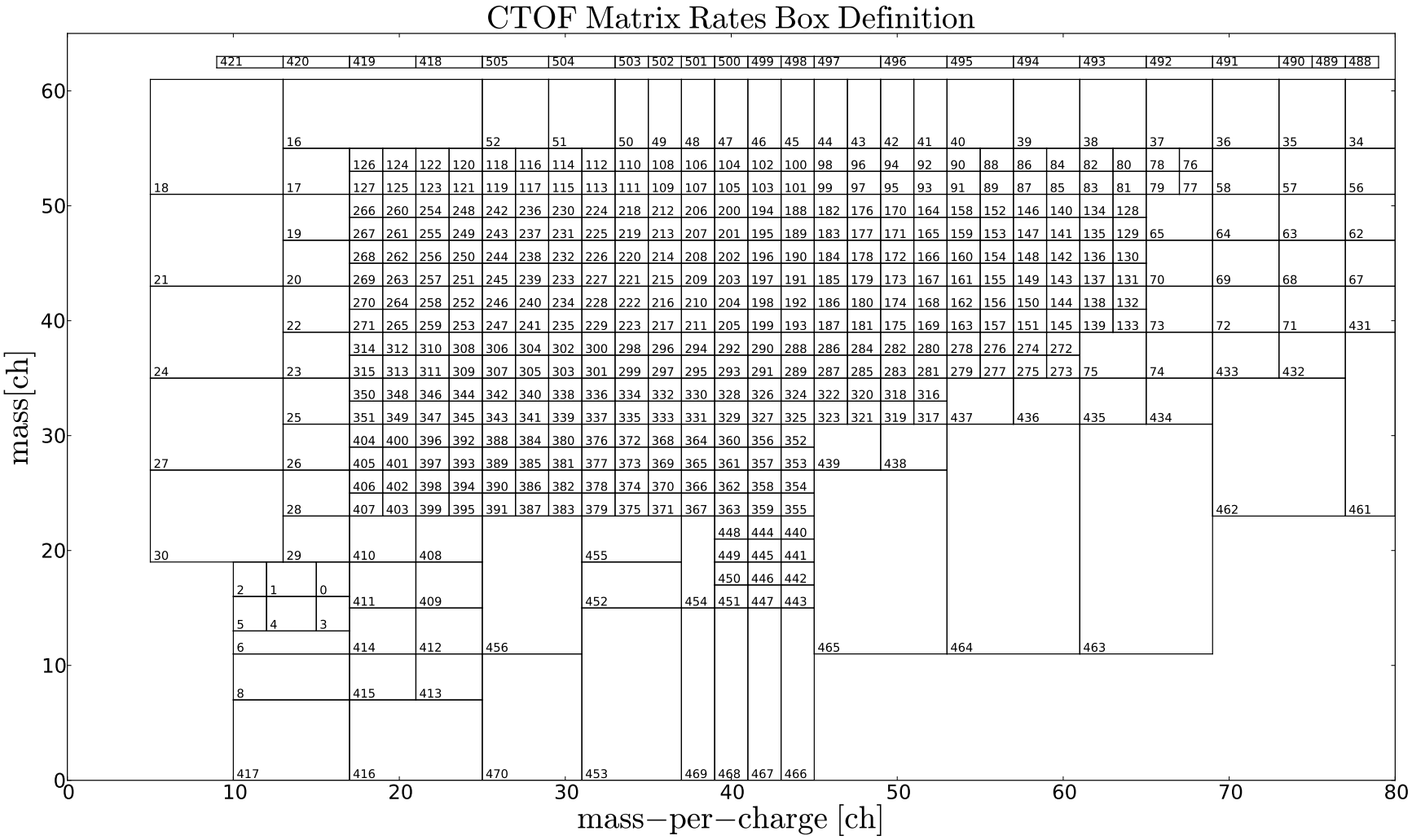

FIGURE A.10: CTOF Matrix Rates Box Definition as explained in section 2.2.

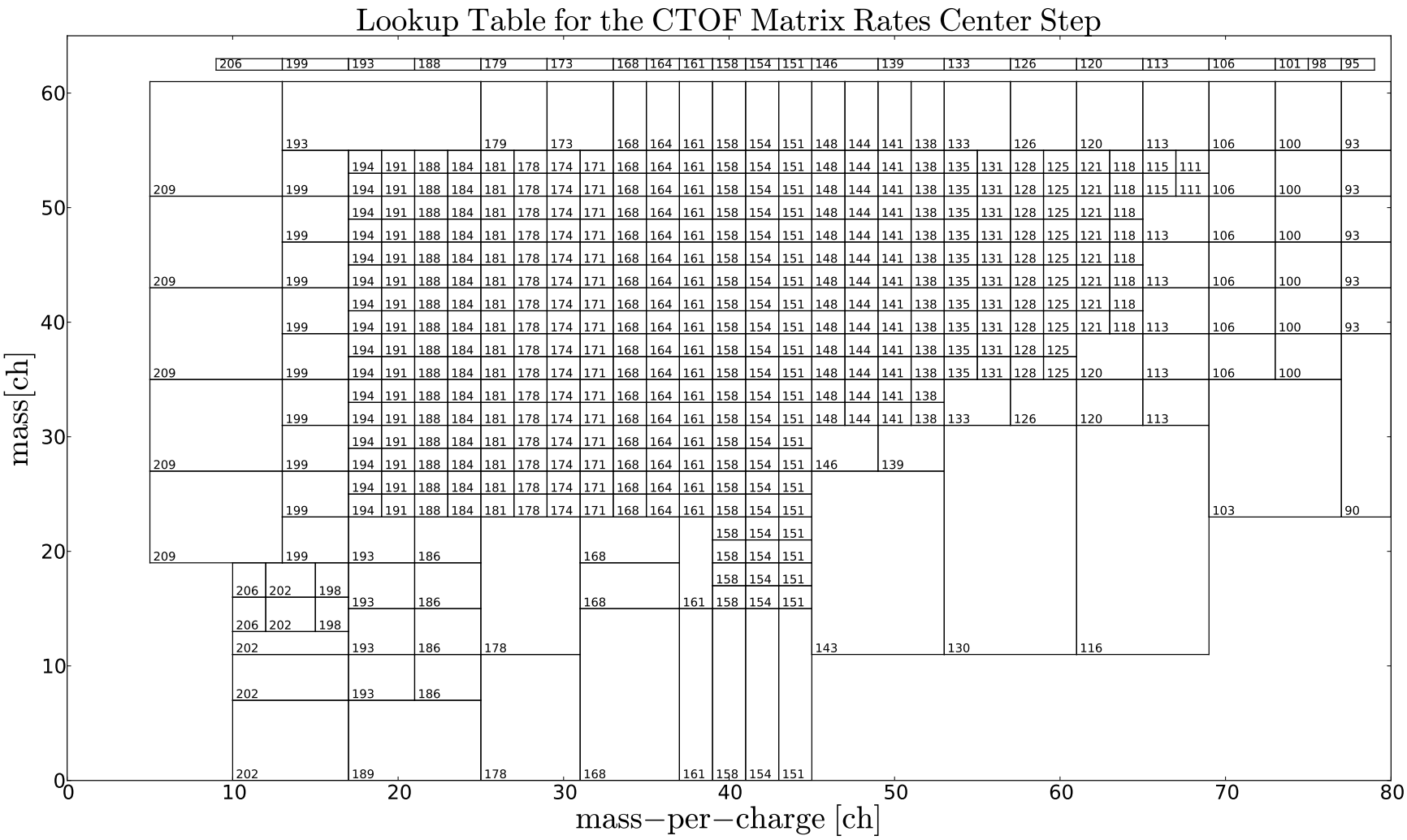

FIGURE A.11: Look-up Table for the CTOF Matrix Rates Center Step as explained in section 2.2.

Appendix B

Supplementary Documentation of the CTOF Response Model

B.1 Fundamental CTOF Instrument Parameters

Instrument Parameter	Value	Unit	Reference
L_τ	70.5	mm	[Hefti, 1998b, Aellig, 1998b]
U_0	0.331095	kV	[Hefti, 1998b, Aellig, 1998b]
r	1.040926	1	[Hefti, 1998b, Aellig, 1998b]
U_{acc}	23.85	kV	[Taut, 2014]
d_{C-foil}	24	nm	[Taut, 2014]
$d_{SSD-SiO2}$	75	nm	[Oetliker, 1993a, Janitzek, 2014]
$\delta v_{E/q}$	0.0121	1	[Aellig, 1998b]

TABLE B.1: Summary of fundamental CTOF instrument parameters for the in-flight calibration and derivation of the velocity distribution functions.

B.2 TRIM Simulation Input-Spectra

Ion	min. step	max. step	min. E_{acc} [keV]	max. E_{acc} [keV]
He^{2+}	30	73	**52**	**69**
O^{6+}	40	70	**156**	**185**
Si^{7+}	38	58	**191**	220
Si^{8+}	38	58	218	**251**
Fe^{8+}	27	57	**219**	285
Fe^{9+}	25	60	242	329
Fe^{10+}	27	60	270	**356**

TABLE B.2: Simulation input energies calculated as reference ion energy range after post-acceleration. The table is adapted from Janitzek(Master,2014).

B.3 TOF-Position Calibration

Element	A	B	C	TOFCOR ($= \tau_{cor}$) [ch]
He	5.889321	17.70091	0.015628	0
C	13.08489	21.96882	0.015237	-2
N	13.19550	14.60739	0.017141	-1
O	17.35453	45.98613	0.008159	-2
Ne	13.62666	26.34092	0.015860	-3
Na*	12.28412	-35.53477	0.018663	-2
Mg	8.235615	6.927236	0.023816	-2
Al*	12.28412	-35.53477	0.018663	-2
Si	14.71547	-7.057364	0.021663	-1
S	13.89511	1.125358	0.030509	-1
Ar*	12.28412	-35.53477	0.018663	0
Ca*	12.28412	-35.53477	0.018663	0
Fe	12.28412	-35.53477	0.018663	0
Ni*	12.28412	-35.53477	0.018663	0

TABLE B.3: Look-up Table for the calculation of the TOF positions in the CTOF base-rate corrected PHA ET-matrices. The constants A,B,C are for the calculation of the relative energy loss in the carbon foil α_τ according to Eq. 4.18 in section 4.4. The asterisk * marks the elements, for which we did not obtain α_τ from a TRIM simulation but approximated it with the iron value $\alpha_{\tau,Fe}$ as an approximation of the mean relative energy loss (see section 4.4). The value TOFCOR is the correction of the TOF channels for all ion species of the given element and for all E/q-steps $0 \leq j \leq 116$. The correction is applied in Eq. 4.25.

B.4 ESSD-Position Calibration

Helium is the only element for which we observe a TOF-dependent pulse height defect (in agreement with [Hefti,1997,PhD]). The corresponding PHF-value is calculated from a polynomial fit $\alpha_{\epsilon}^{He}(\widetilde{E}_{nuc}(\tau_{ij}))$ to the TRIM simulation that is in good agreement with the measured ESSD position of He^{2+} (see section 4.4 and Janitzek(Master,2014)):

$$\alpha_{\epsilon}^{He}(\widetilde{E}_{nuc}) = C0_{\alpha_{\epsilon},He} \cdot \widetilde{E}_{nuc}^{3} + C1_{\alpha_{\epsilon},He} \cdot \widetilde{E}_{nuc}^{2} + C2_{\alpha_{\epsilon},He} \cdot \widetilde{E}_{nuc} + C3_{\alpha_{\epsilon},He} \tag{B.1}$$

with the constants $C0_{\alpha_{\epsilon},He}$ - $C3_{\alpha_{\epsilon},He}$ given in Table B.4 and the energy/nucleon-proportional term:

$$\widetilde{E}_{nuc} = \frac{L_{\tau}^{2}}{2} \cdot (A_{\tau} \cdot \tau_{ij} + B_{\tau})^{-2} \cdot \frac{\text{amu}}{\text{keV}} \tag{B.2}$$

where τ_{ij} is the calibrated TOF peak position at Epq-step $0 \leq j \leq 116$ for He^{2+} or He^{+}, respectively, and the remaining constants L_{τ}^{2} as given in Table B.1, A_{τ}, B_{τ} as given in Eq. 4.20 and amu$= 1.66 \cdot 10^{-27}$ kg and keV$= 1.602 \cdot 10^{-16}$ C.
For all other calibrated elements carbon - nickel for which we obtained a TOF-independent pulse height defect the constant PHF-value is given in Table B.5 and can be directly used in Eq. 4.23.

Element	$C0_{\alpha_{\epsilon},He}$	$C1_{\alpha_{\epsilon},He}$	$C2_{\alpha_{\epsilon},He}$	$C3_{\alpha_{\epsilon},He}$
He	5.117329e-05	-2.923190e-03	6.387425e-02	2.480608e-01

TABLE B.4: Look-up Table for the calculation of the ESSD positions in the CTOF (base-rate corrected) PHA ET-matrices for helium (He^{2+}, He^{+}).

Element	PHF ($= \alpha_\epsilon$)	PHFCOR ($= \alpha_{\epsilon,cor}$)
C	0.609	39.0/42
N*	0.575	39.2/42
O	0.542	39.5/42
Ne	0.510	39.5/42
Na*	0.495	39.5/42
Mg	0.479	39.5/42
Al*	0.464	40.0/42
Si	0.448	40.5/42
S*	0.423	40.7/42
Ar*	0.397	40.9/42
Ca*	0.372	41.1/42
Fe	0.296	42.0/42
Ni*	0.273	42.0/42

TABLE B.5: Look-up Table for the calculation of the ESSD positions in the CTOF (base-rate corrected) PHA ET-matrices as described in section 4.4 for all calibrated elements with atomic number $Z > 2$ for which we obtain a pulse height defect that is independent of the ions TOF position. The PHF-value is derived for the uncorrected PHA count rate data. The PHF-value for the base-rate corrected PHA count rate data is calculated by $\alpha_{\epsilon,brcor} = \alpha_\epsilon \cdot \alpha_{\epsilon,cor}$ as described by Eq. 4.24. The elements that are marked with * are linearly interpolated as described in section 4.4.

B.5 ESSD-Width Calibration for Iron

As the dominant iron species Fe^{8+} - Fe^{11+} are well separated from other ion species of comparable abundance, their ESSD peak shape can be modeled more accurately from the CTOF long-term data. We use an asymmetrical Gaussian for this purpose:

$$\begin{aligned} R_{\epsilon,Fe}(\sigma_{\epsilon,up}, \sigma_{\epsilon,low}, \tau, \epsilon) =& G^1_{asym}(\epsilon_0(\tau), \sigma_{\epsilon,up}, \sigma_{\epsilon,low}, \epsilon) \\ =& \begin{cases} \exp\left(-\dfrac{(\epsilon_0 - \epsilon(\tau))^2}{2\sigma^2_{\epsilon,low}}\right) & \text{if } \epsilon \leq \epsilon_0(\tau) \\ \exp\left(-\dfrac{(\epsilon_0 - \epsilon(\tau))^2}{2\sigma^2_{\epsilon,up}}\right) & \text{if } \epsilon \geq \epsilon_0(\tau) \end{cases} \end{aligned} \tag{B.3}$$

where $\sigma_{\epsilon,up}$ and $\sigma_{\epsilon,low}$ are the width parameters for the upper and lower ESSD flanks, respectively and $\epsilon_0(\tau)$ is the calibrated most probable ESSD channel at each given TOF channel after Eq. 4.24. Assuming a linear scaling of both width-parameters with $\epsilon_0(\tau)$:

$$\sigma_{\epsilon,up}(\epsilon_0(\tau)) = A_{\sigma_{\epsilon,up}} \cdot \epsilon_0(\tau) + B_{\sigma_{\epsilon,up}} \tag{B.4}$$

and

$$\sigma_{\epsilon,low}(\epsilon_0(\tau)) = A_{\sigma_{\epsilon,low}} \cdot \epsilon_0(\tau) + B_{\sigma_{\epsilon,low}} \tag{B.5}$$

we find from fits to the iron data peaks at Epq-steps 39 - 55 the optimal scaling parameters $A_{\sigma_{\epsilon,up}} = 0.167$, $B_{\sigma_{\epsilon,up}} = 0.5\,\text{ch}$ and $A_{\sigma_{\epsilon,low}} = 0.139$, $B_{\sigma_{\epsilon,low}} = -1.0\,\text{ch}$. We recognize that the upper ESSD-flank in the data is more pronounced than the lower ESSD flank, which is in agreement with [Aellig,PHD], although one would expect it the other way around if the energy loss in the SiO_2 dead-layer was the main reason for the peak asymmetry along the ESSD axis (see the TRIM simulations in [Janitzek(2014)]). Clearly, a deeper understanding of the ESSD signal formation for very heavy ions i.e. from laboratory calibration measurements is necessary here to improve the peak shape models for time-of-flight mass spectrometers in current or future missions.

B.6 CTOF Detection Efficiencies

E_{acc}/nuc [keV/amu]	DC-Efficiency, Iron
1	0.035
1.5	0.080
2	0.110
2.5	0.140
3	0.165
3.5	0.185
4	0.205
4.5	0.218
5	0.230
6	0.245
7	0.260
8	0.270
9	0.275
10	0.280
12	0.290
14	0.295
16	0.298
18	0.300
20	0.300

TABLE B.6: Double Coincidence efficiencies for iron modeled after measurements of oxygen and argon with CTOF flight spare model at MPAe Katlenburg-Lindau. The values are extracted from Figure 4.11 in [Aellig, 1998b]. The model uncertainties are 10% in the typical energy range for the main charge states of iron (estimated by [Aellig, 1998b]).

E_{acc} [keV]	SSD-Efficiency, Iron
200	0.75
250	0.81
300	0.87
350	0.91
400	0.94
450	0.96
500	0.97

TABLE B.7: SSD efficiencies estimated by [Aellig, 1998b] after measurements of the ACE/SWICS SSD at the Ion Beam Facility at the University of Giessen. The values are obtained from Figure 4.14 in [Aellig, 1998b].

Appendix C

CTOF Response Model Overview

In the following appendix we present the derived CTOF response models by showing the 2D-contour plots, relative deviation plots, relative residual plots, reduced TOF plots (both in logarithmic and linear count rate scaling), reduced ESSD plots, and finally the relative deviation histograms of the developed models. The plots are created for Epq-steps 39, 50, 60, 70, 80, and 86 for the Gaussian Full Stable (G-FS) response Model, the Kappa-Moyal Full Stable (KM-FS) response Model, the Gaussian Reduced Stable (G-RS) response model, and the Kappa-Moyal Reduced (KM-RS) response model. All plots can be interpreted as described in detail in chapter 4 and in particular in section 4.6.

C.1 The Gaussian Full Stable Response Model

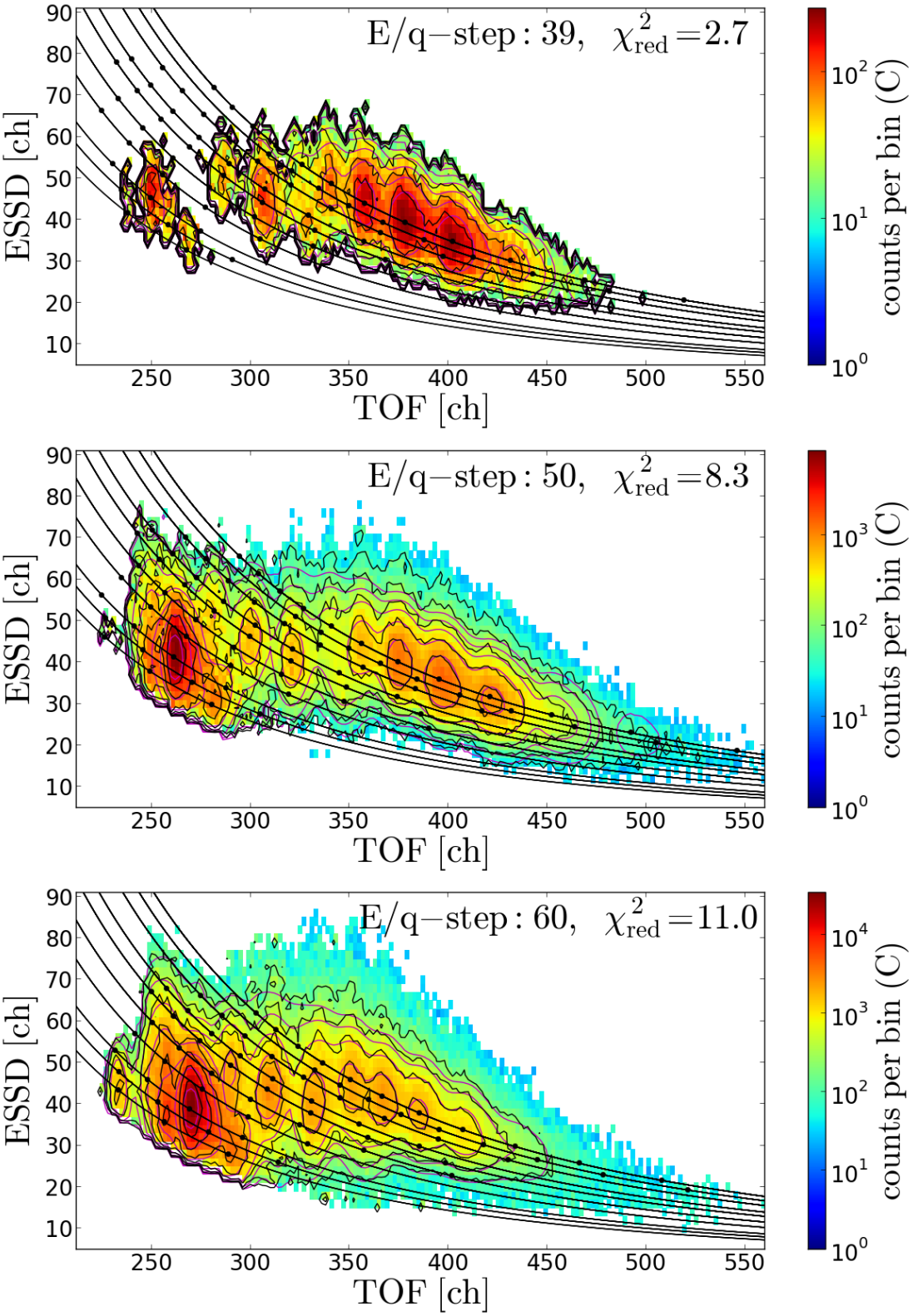

FIGURE C.1: 2D-contour plot of the CTOF *Gaussian Full Stable* response model (magenta contour lines) fitted to the accumulated long-term ET-matrix count rates (black contour lines) for Epq-steps 39, 50 and 60.

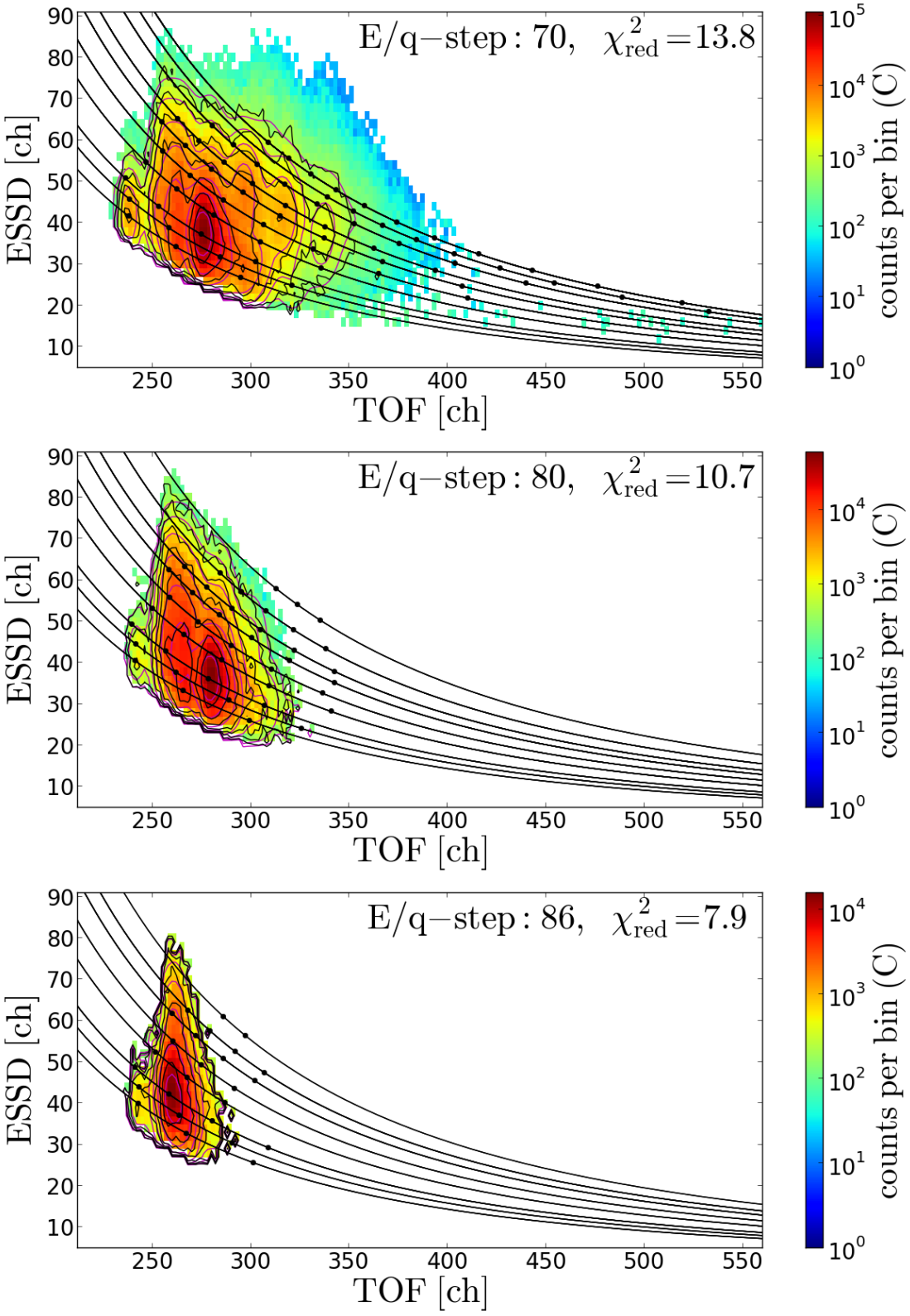

FIGURE C.2: 2D-contour plot of the CTOF *Gaussian Full Stable* response model (magenta contour lines) fitted to the accumulated long-term ET-matrix count rates (black contour lines) for Epq-steps 70, 80 and 86. Note that in these steps we filter the data for He^{2+} random coincidences via the proton speed as explained in chapter 4. The proton-speed filter conditions for Epq-steps 70, 80, and 86 are $v_p \in [0, 420\,\mathrm{km/s}]$, $v_p \in [0, 345\,\mathrm{km/s}]$, and $v_p \in [0, 320\,\mathrm{km/s}]$, respectively.

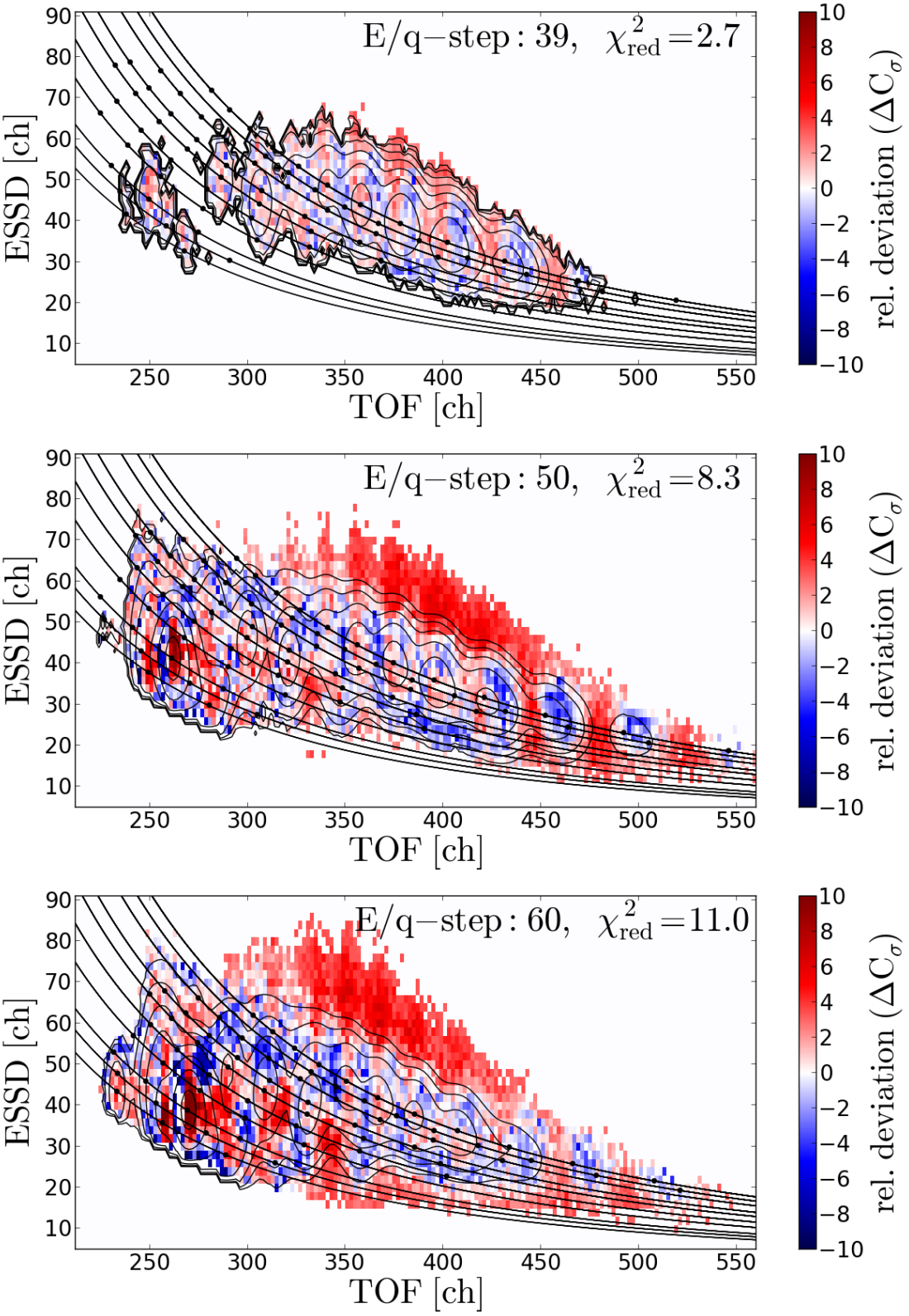

FIGURE C.3: Relative fit deviations for the Gaussian Full Stable response model for Epq-steps 39, 50 and 60.

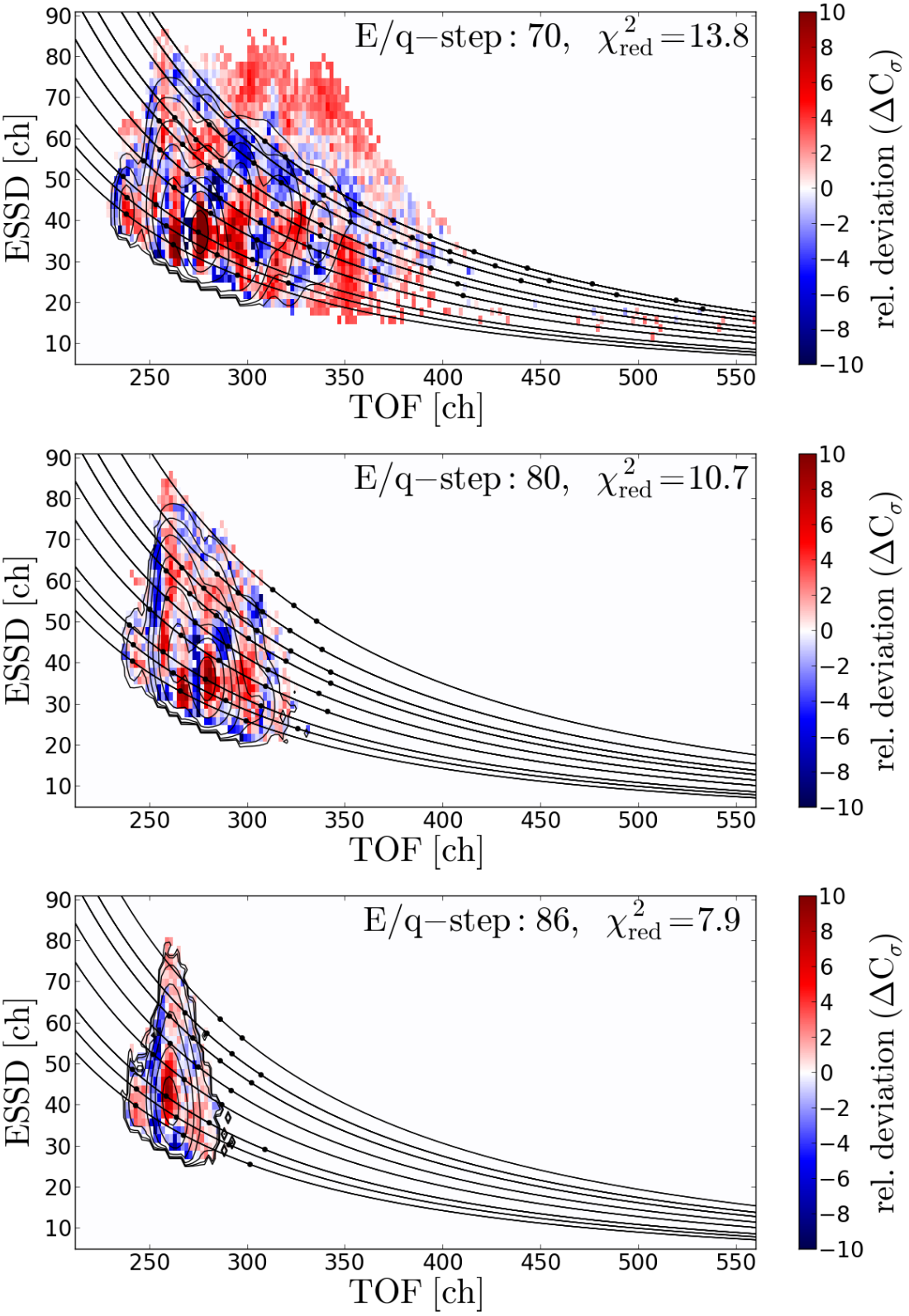

FIGURE C.4: Relative fit deviations for the Gaussian Full Stable response model for Epq-steps 70, 80 and 86.

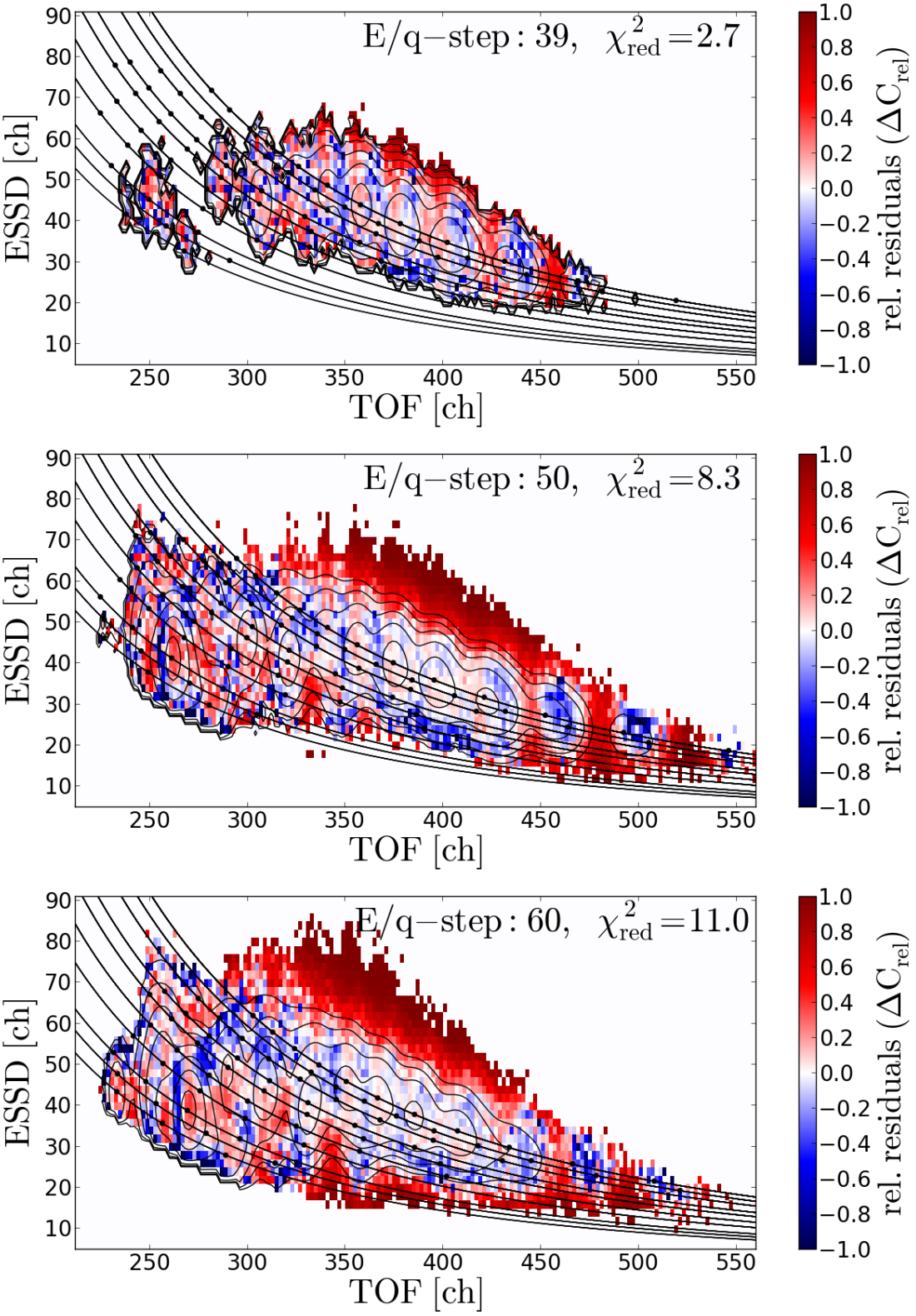

FIGURE C.5: Relative fit residuals for the Gaussian Full Stable response model for Epq-steps 39, 50 and 60.

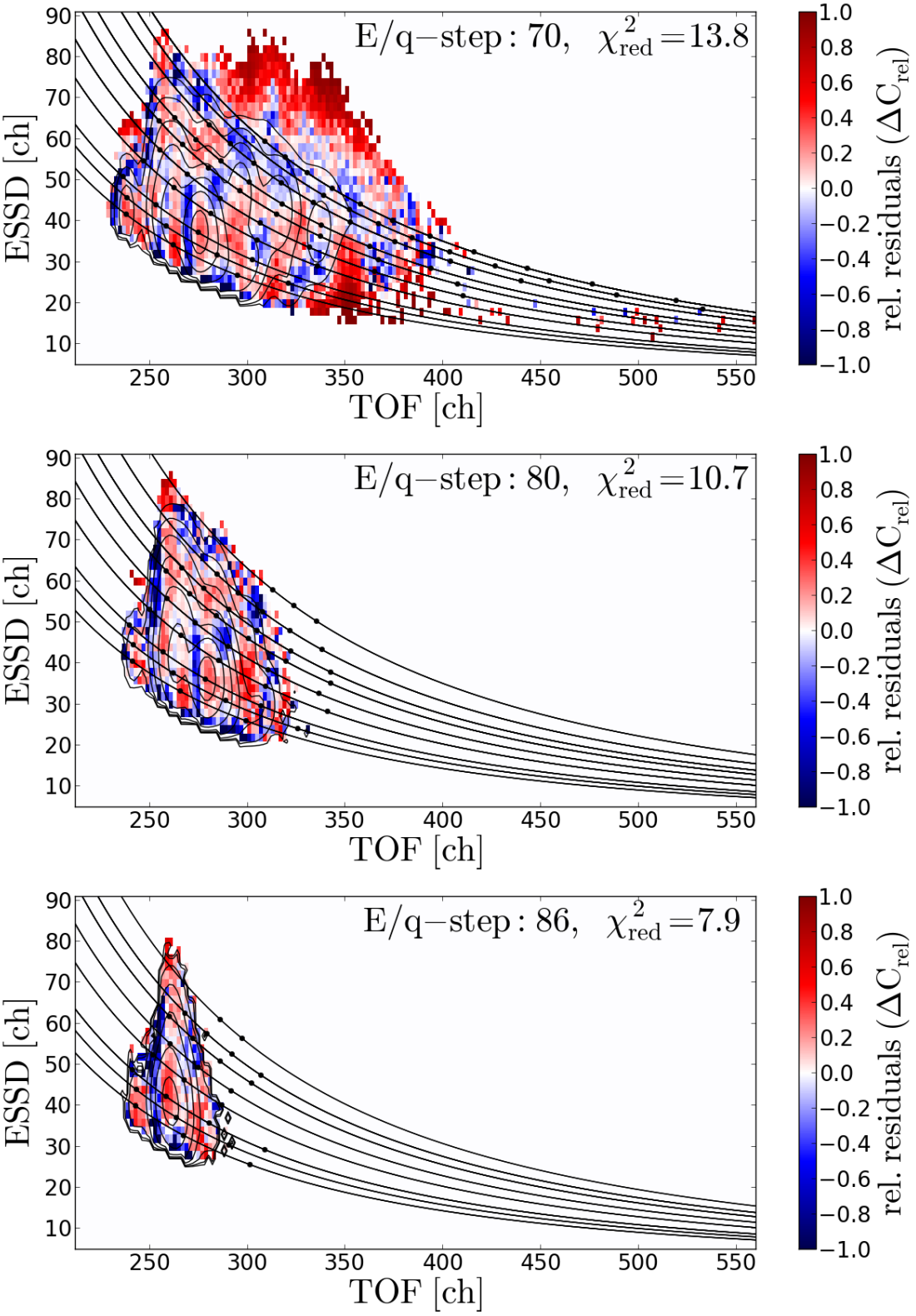

FIGURE C.6: Relative fit residuals for the Gaussian Full Stable response model for Epq-steps 60, 70 and 86.

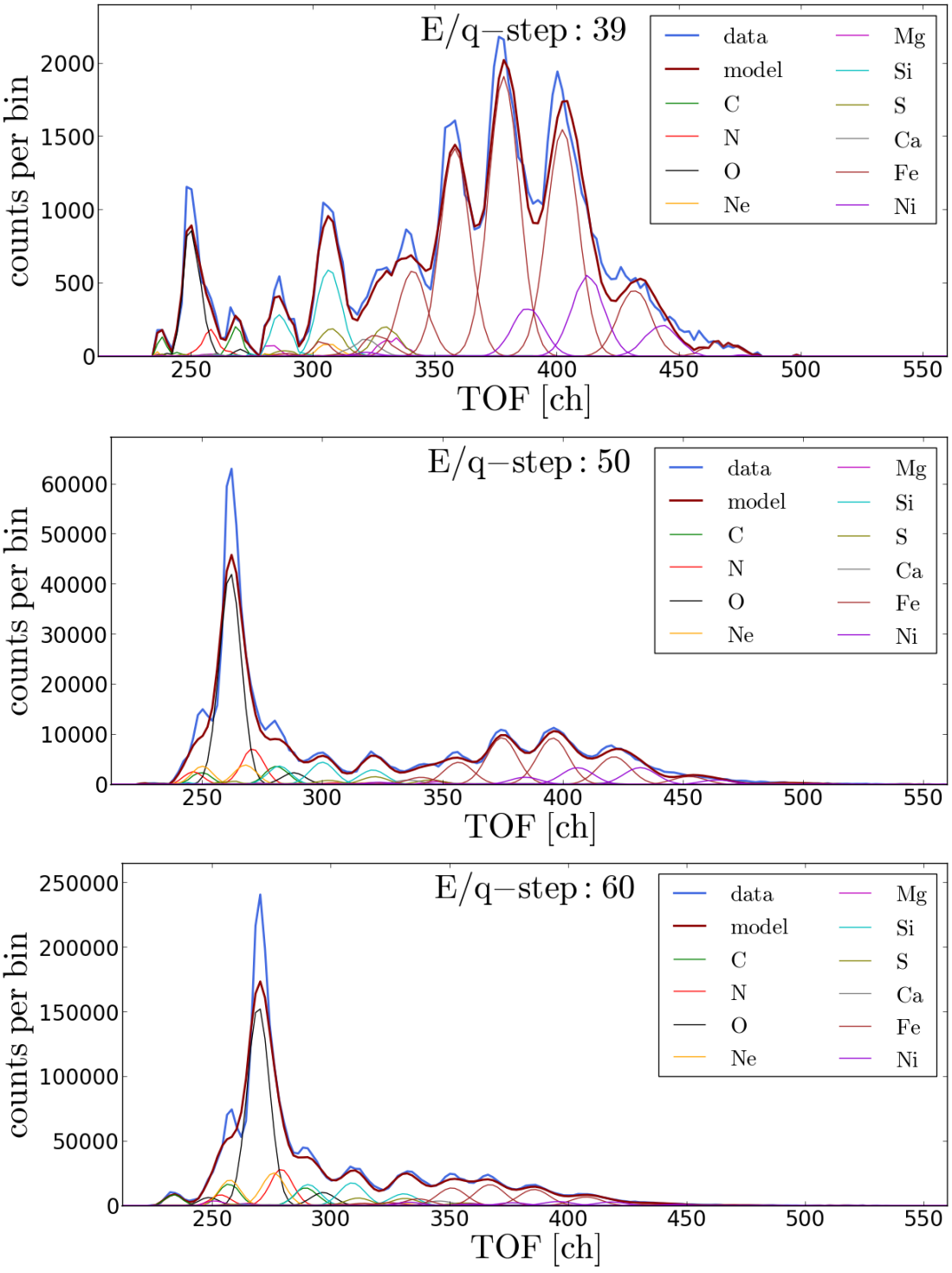

FIGURE C.7: ESSD-integrated count rates of the long-term measurements and the fitted Gaussian Full Stable response model for Epq-steps 39, 50 and 60.

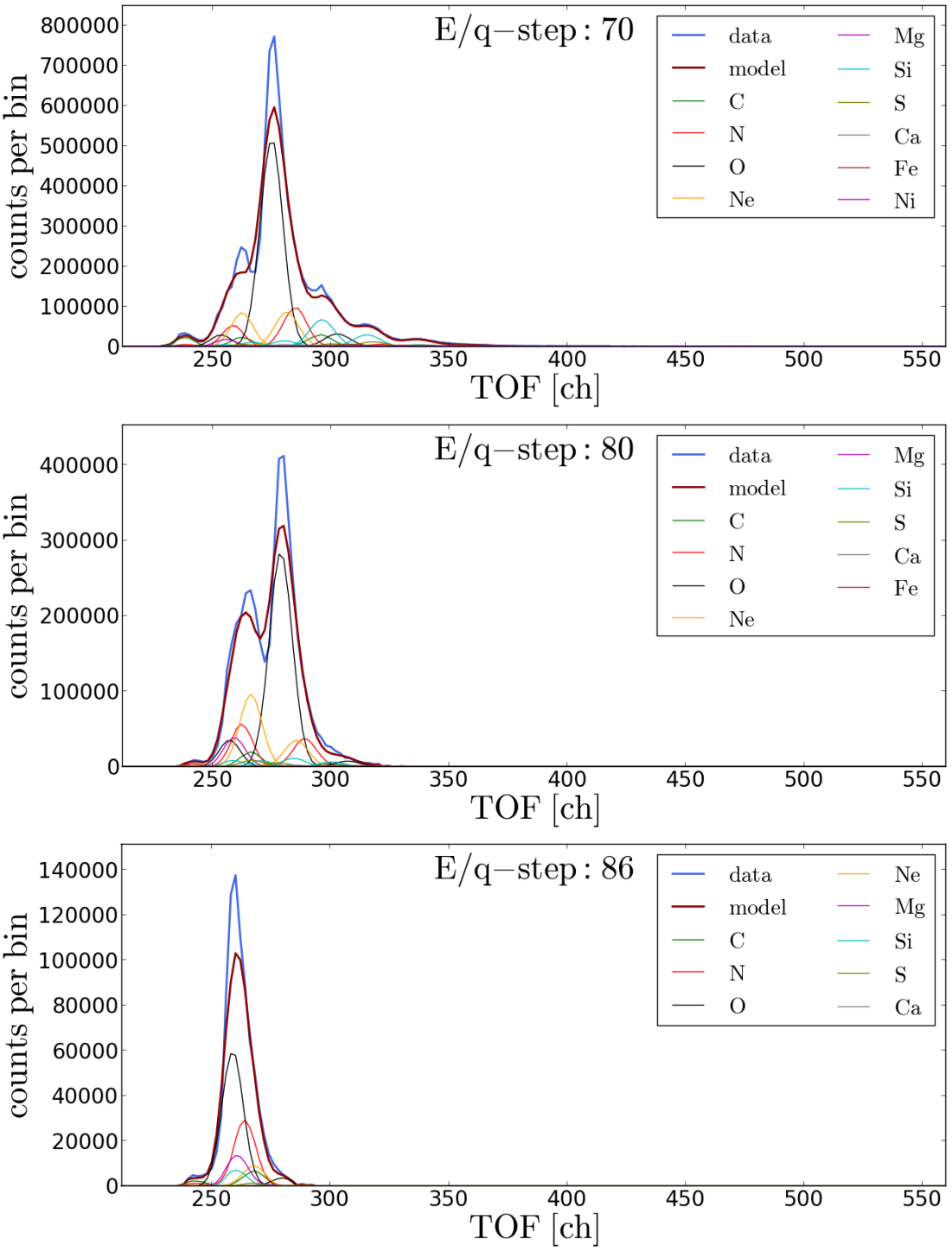

FIGURE C.8: ESSD-integrated count rates of the long-term measurements and the fitted Gaussian Full Stable response model for Epq-steps 70, 80 and 86.

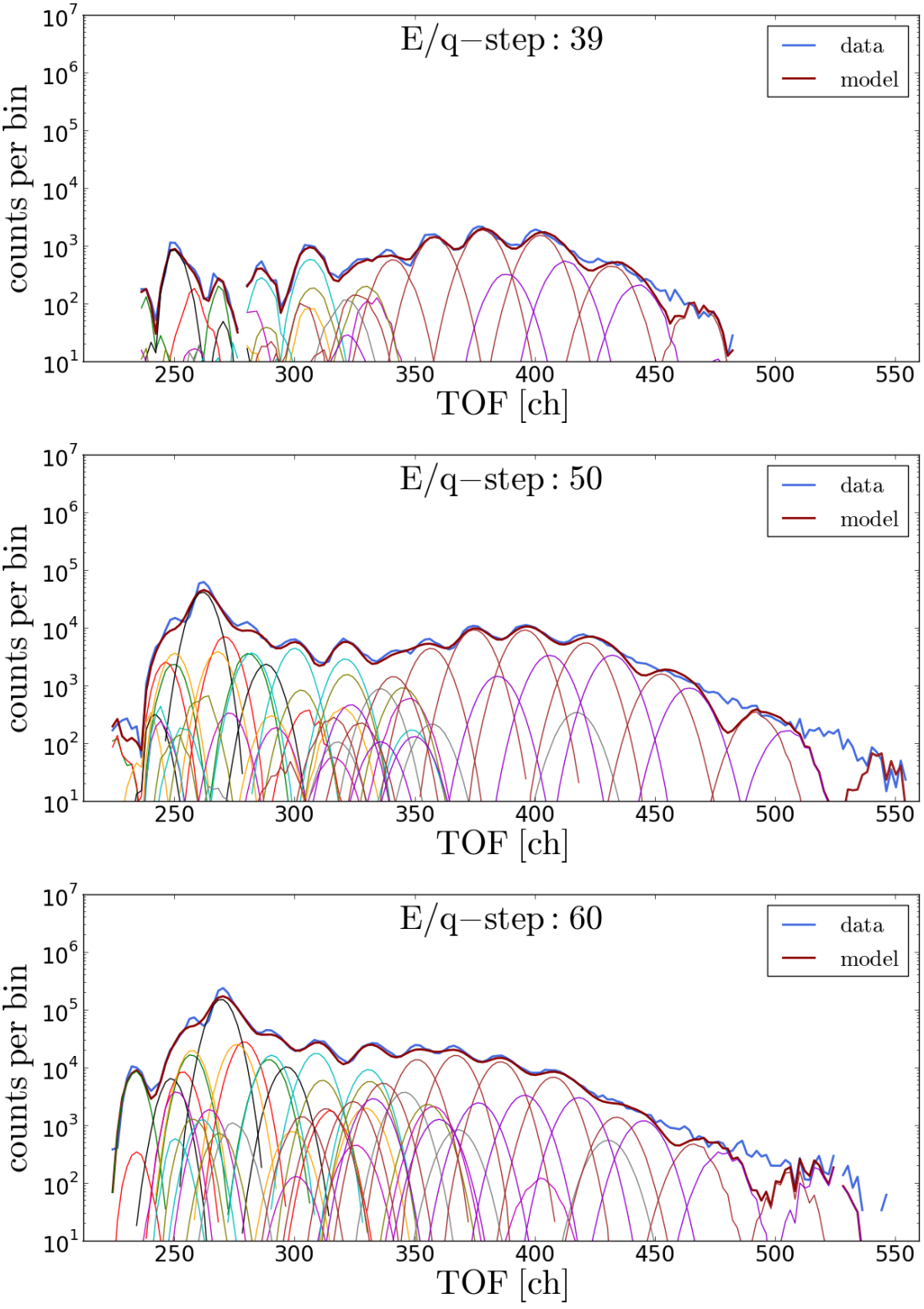

FIGURE C.9: ESSD-integrated logarithmic count rates of the long-term measurements and the fitted Gaussian Full Stable response model for Epq-steps 39, 50 and 60.

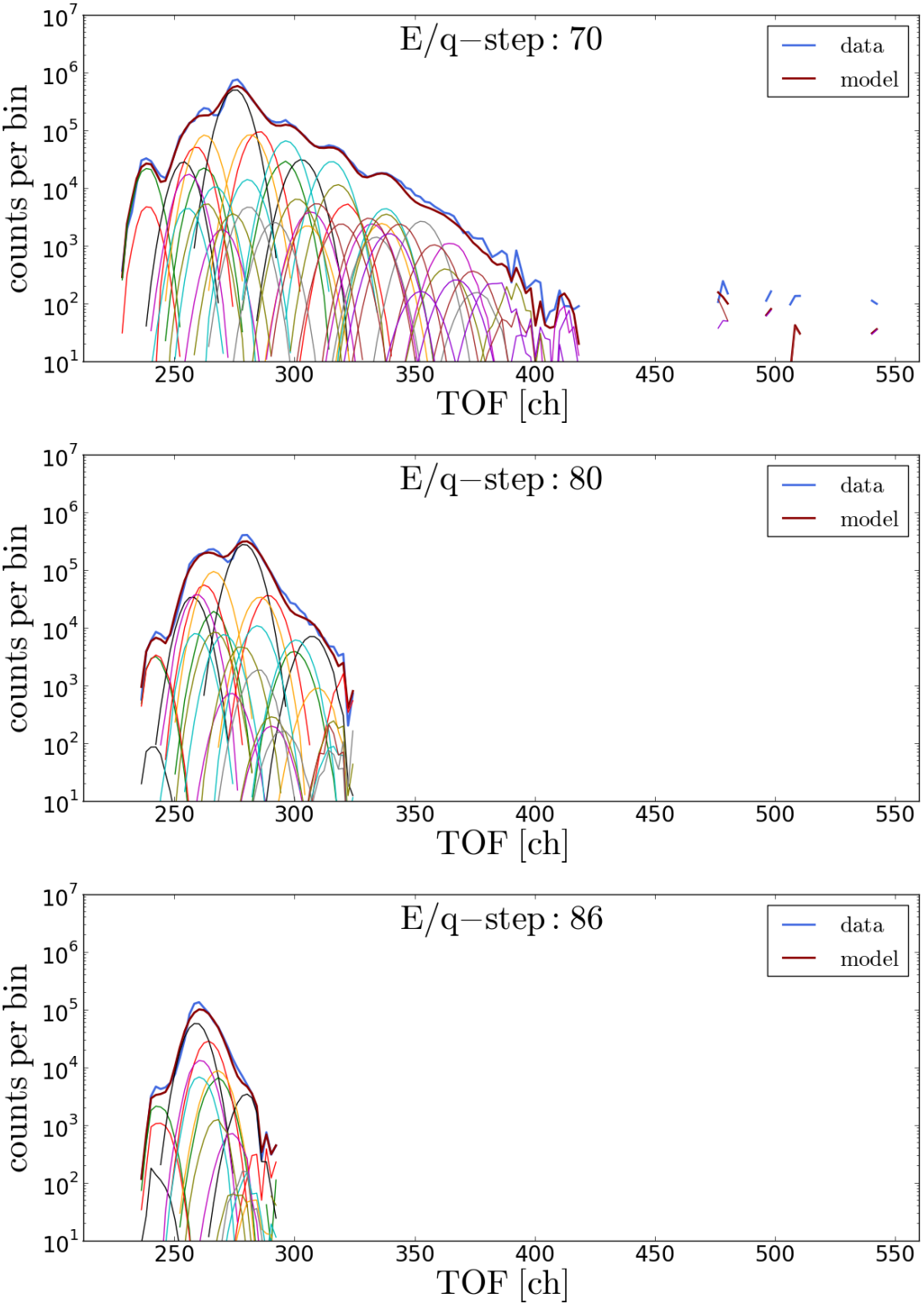

FIGURE C.10: ESSD-integrated logarithmic count rates of the long-term measurements and the fitted Gaussian Full Stable response model for Epq-steps 70, 80 and 86.

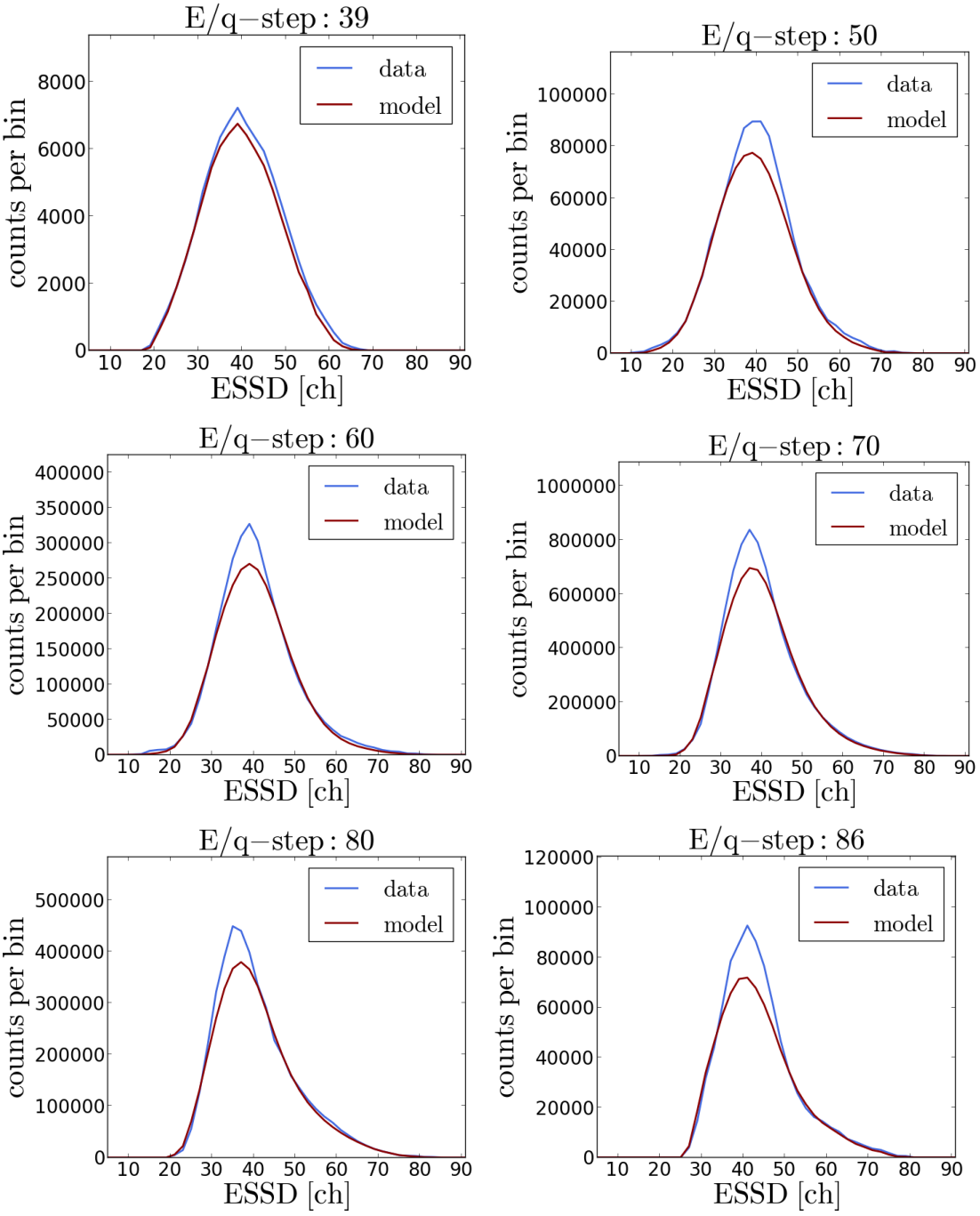

FIGURE C.11: TOF-integrated count rates of the long-term measurements and the fitted Gaussian Full Stable response model for Epq-steps 39 - 86.

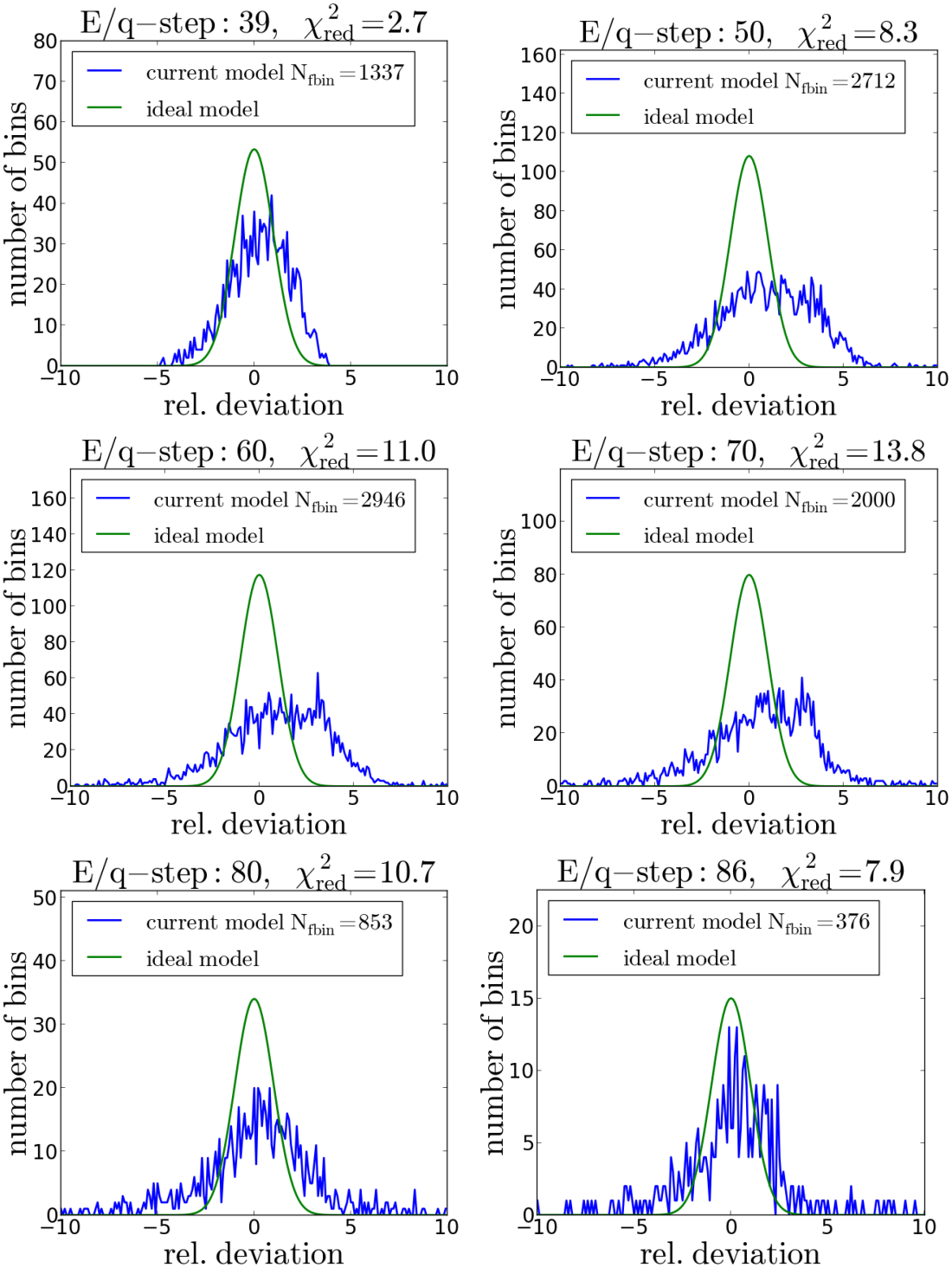

FIGURE C.12: Histograms of the relative deviations (blue) between the measured long-term data and the fitted Gaussian Full Stable response model for Epq-steps 39-86 in comparison to a relative deviation distribution that would arise from a perfect model $\chi^2_{red} = 1$ purely due to statistical deviations (green).

C.2 The Kappa-Moyal Full Stable Response Model

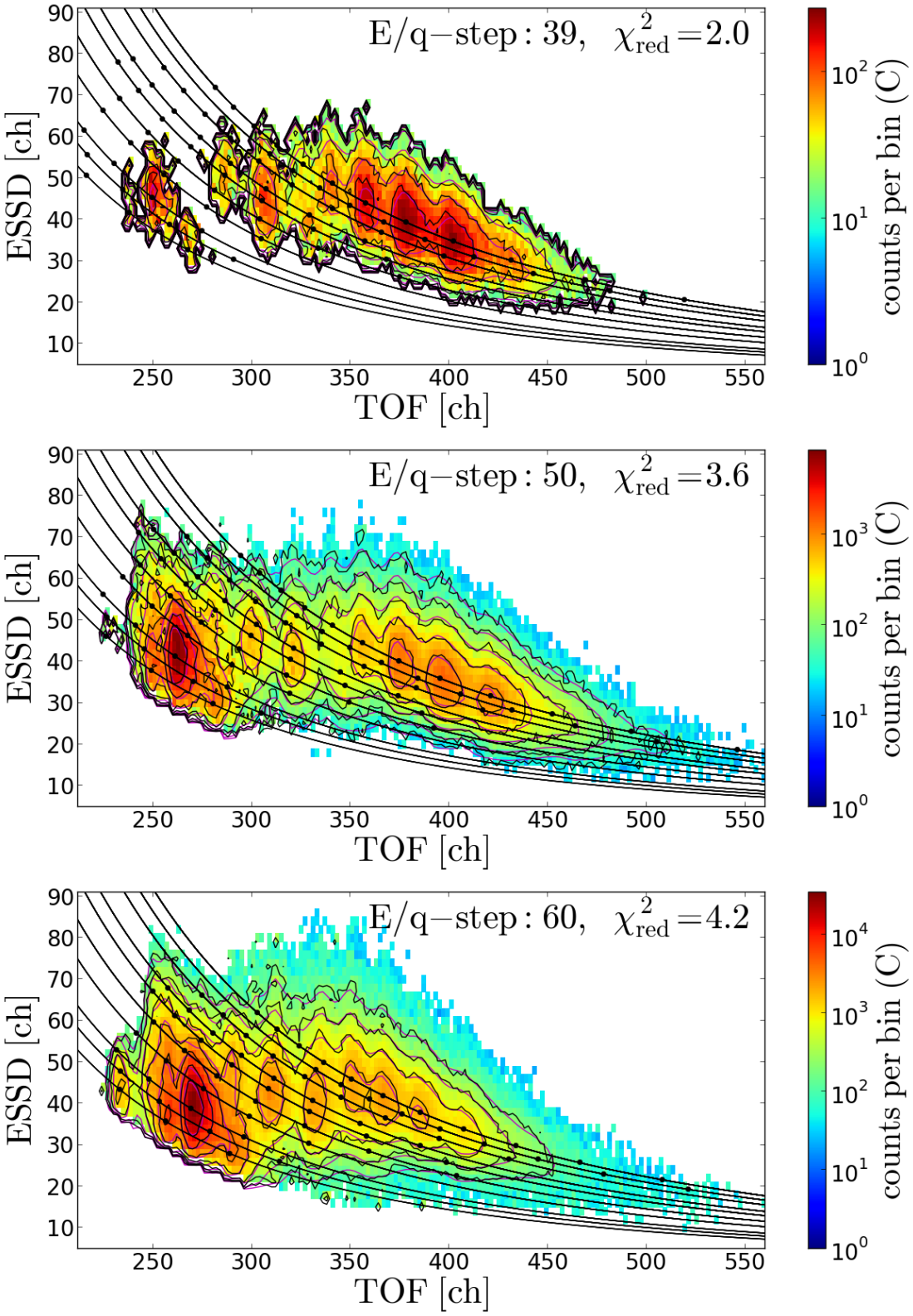

FIGURE C.13: 2D-contour plot of the CTOF *Kappa-Moyal Full Stable* response model (magenta contour lines) fitted to the accumulated long-term ET-matrix count rates (black contour lines) for Epq-steps 39, 50 and 60.

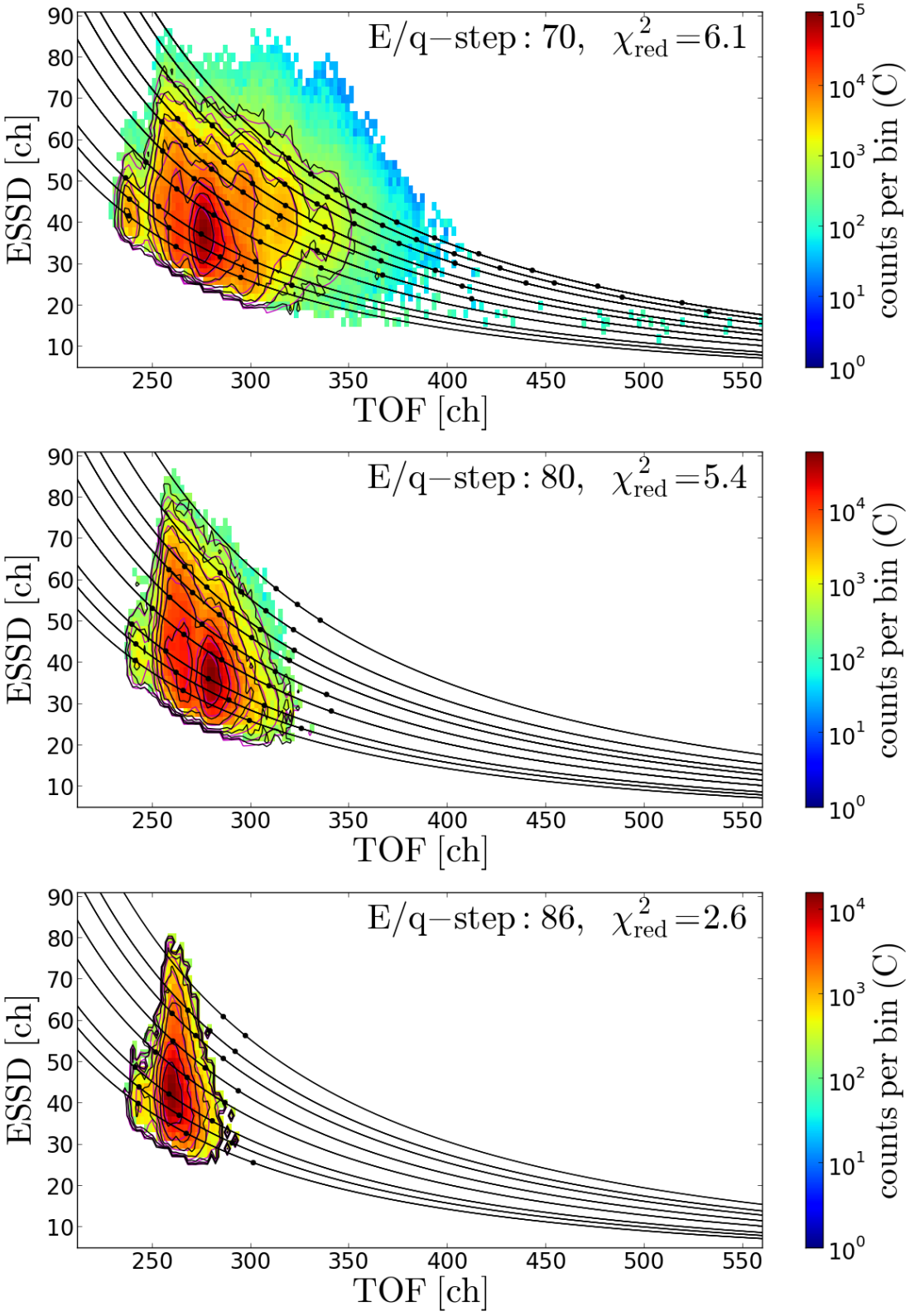

FIGURE C.14: 2D-contour plot of the CTOF *Kappa-Moyal Full Stable* response model (magenta contour lines) fitted to the accumulated long-term ET-matrix count rates (black contour lines) for Epq-steps 70, 80 and 86. Note that in these steps we filter the data for He^{2+} random coincidences via the proton speed as explained in chapter 4. The proton-speed filter conditions for Epq-steps 70, 80, and 86 are $v_p \in [0, 420\,\mathrm{km/s}]$, $v_p \in [0, 345\,\mathrm{km/s}]$, and $v_p \in [0, 320\,\mathrm{km/s}]$, respectively.

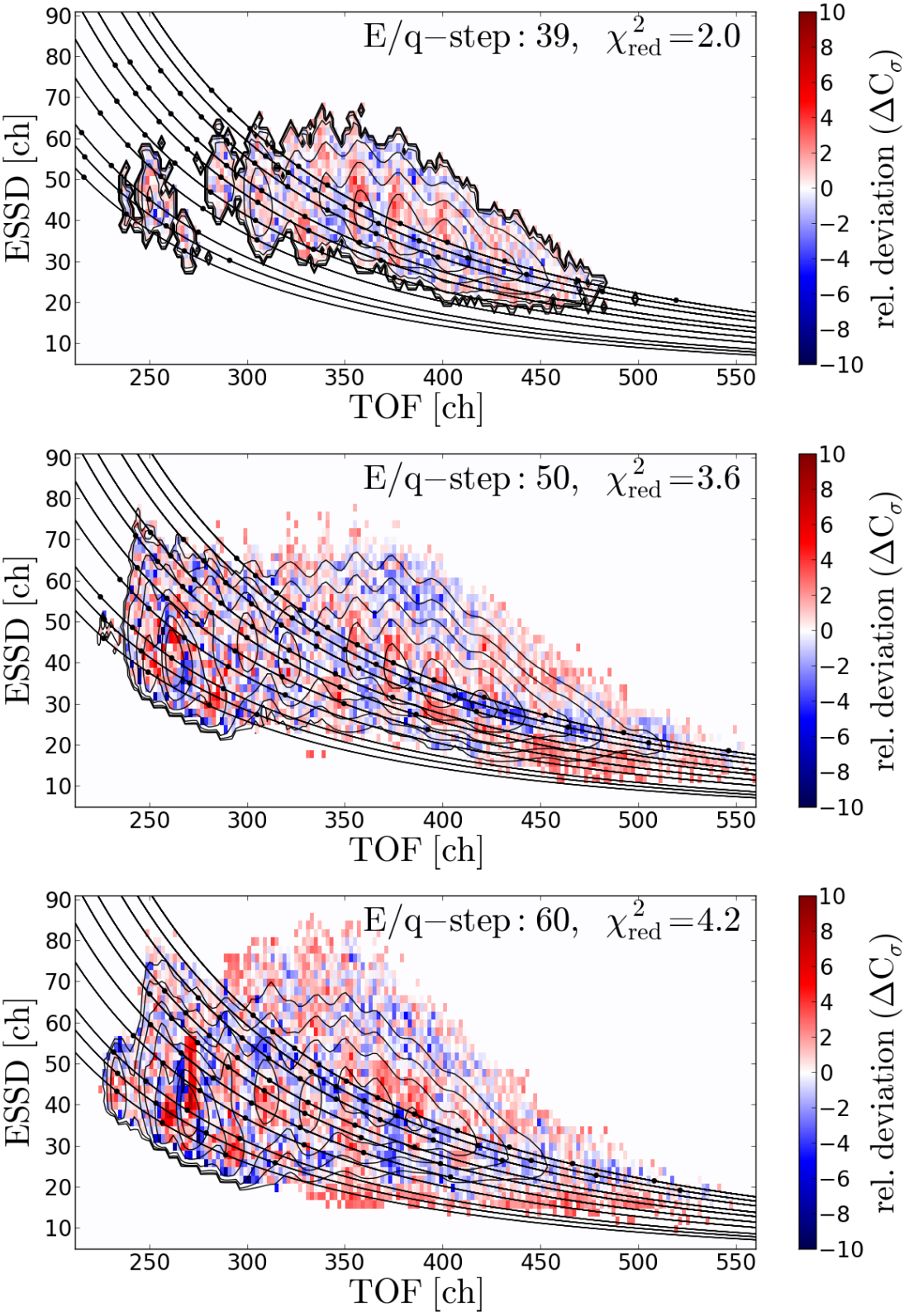

FIGURE C.15: Relative fit deviations for the Kappa-Moyal Full Stable response model for Epq-steps 39, 50 and 60.

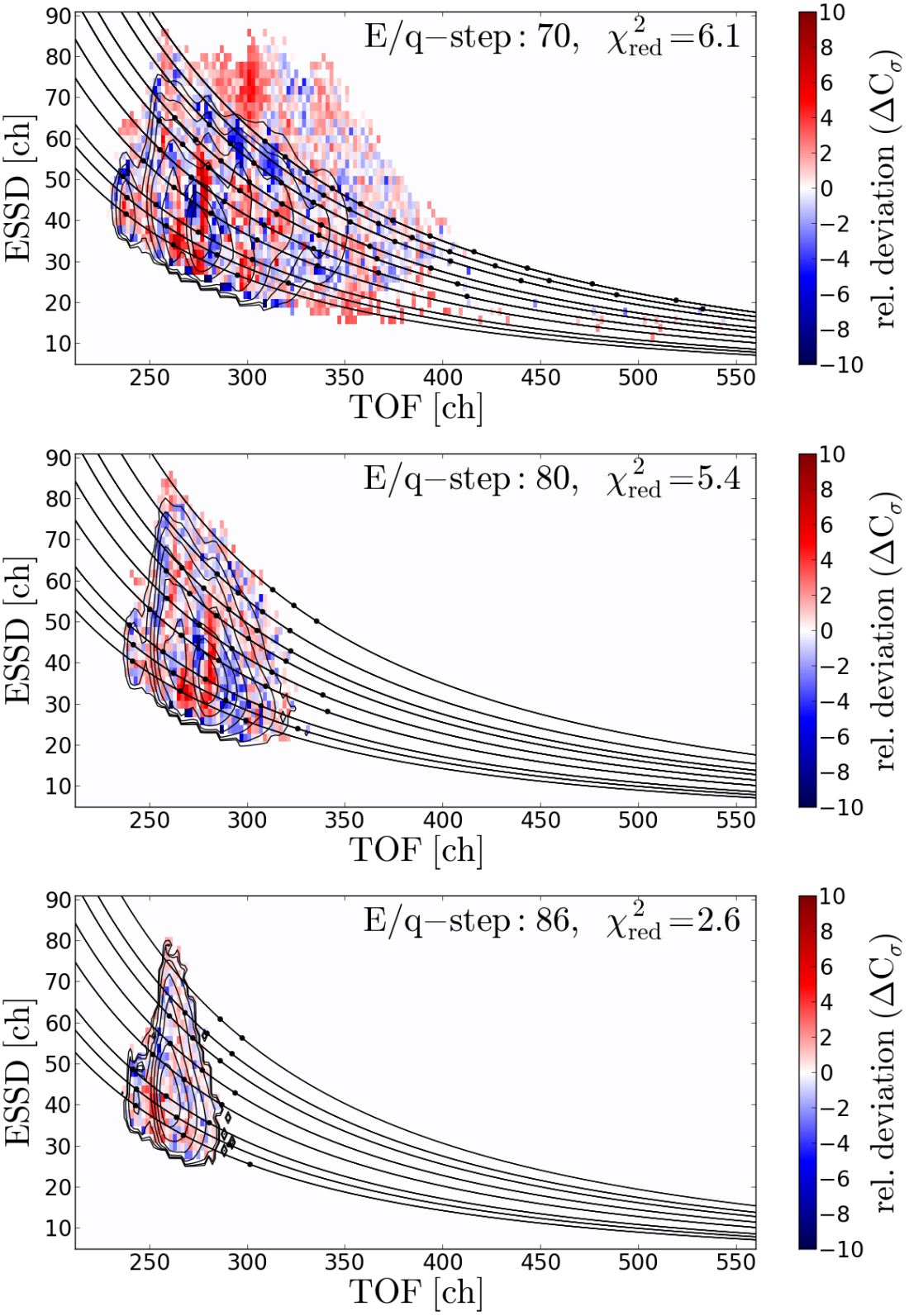

FIGURE C.16: Relative fit deviations for the Kappa-Moyal Full Stable response model for Epq-steps 70, 80 and 86.

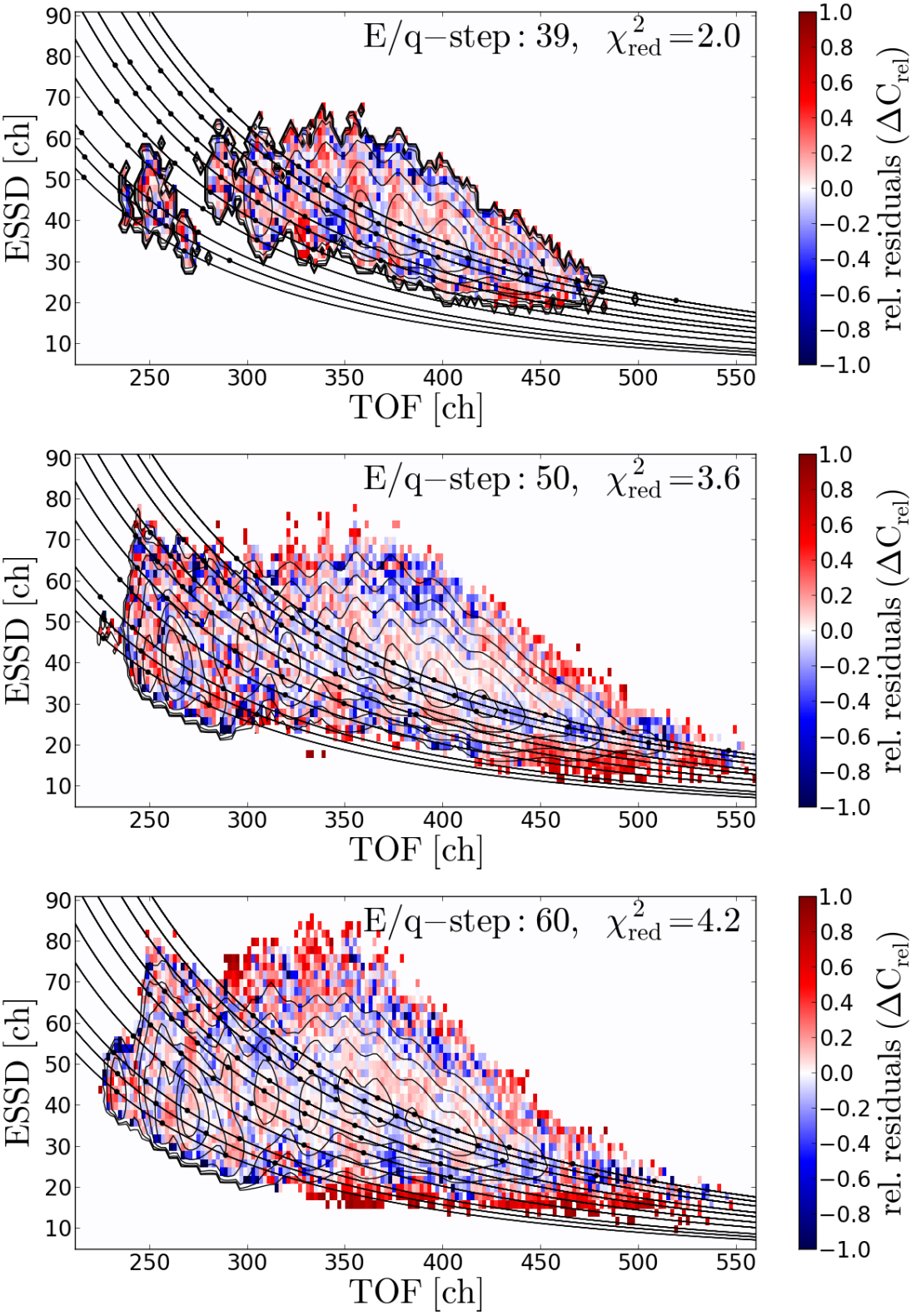

FIGURE C.17: Relative fit residuals for the Kappa-Moyal Full Stable response model for Epq-steps 39, 50 and 60.

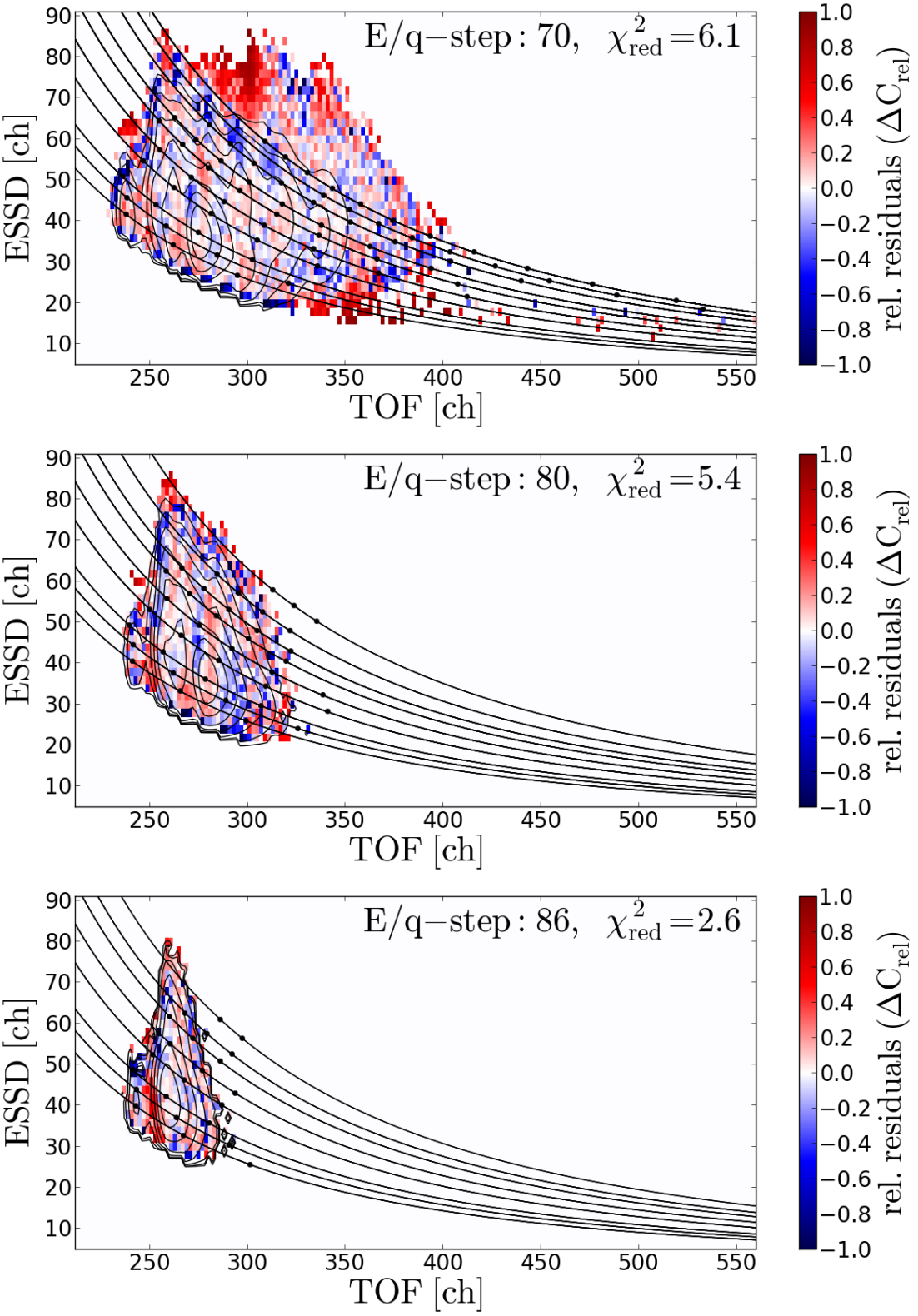

FIGURE C.18: Relative fit residuals for the Kappa-Moyal Full Stable response model for Epq-steps 70, 80 and 86.

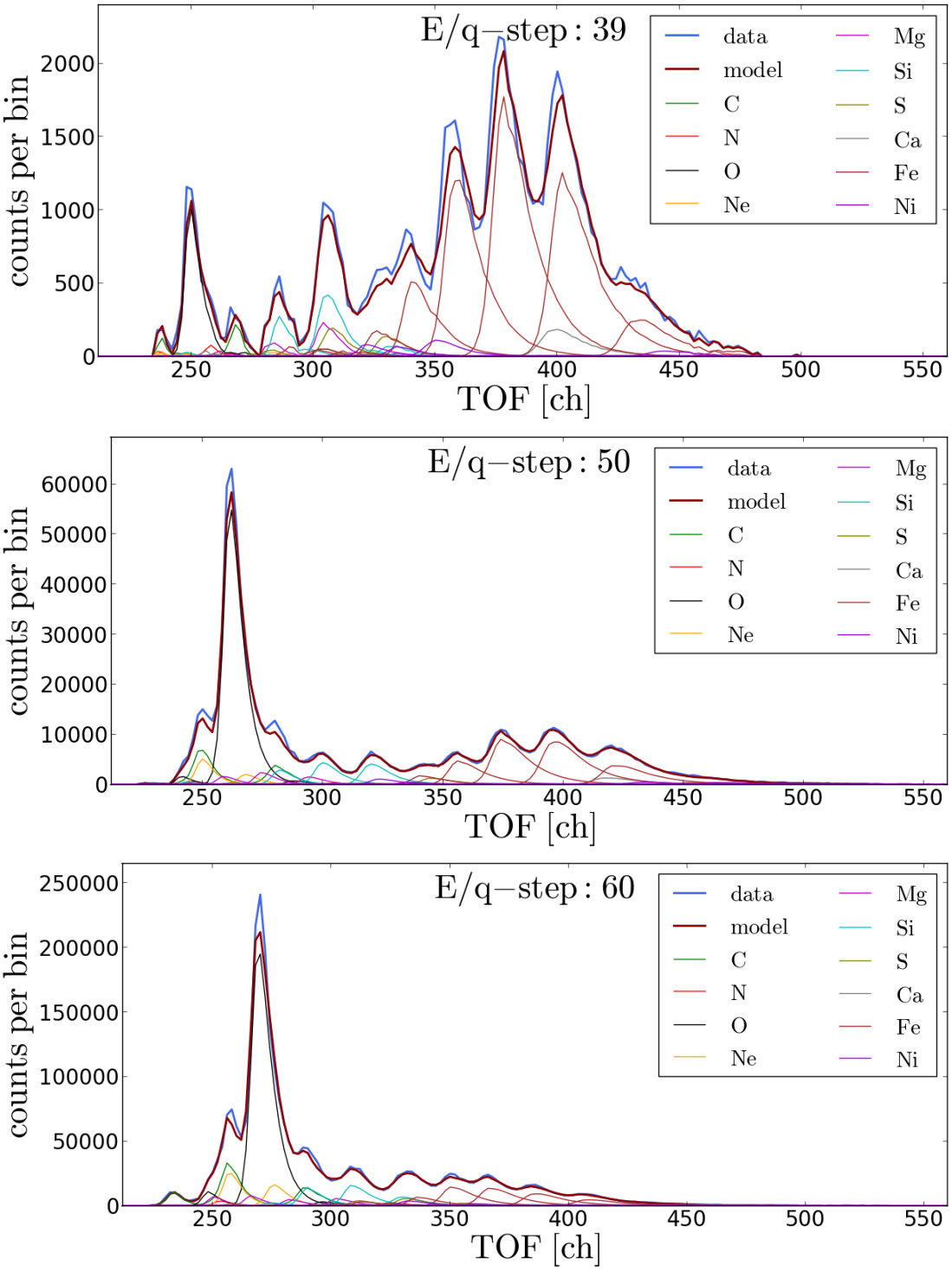

FIGURE C.19: ESSD-integrated count rates of the long-term measurements and the fitted Kappa-Moyal Full Stable response model for Epq-steps 39, 50 and 60.

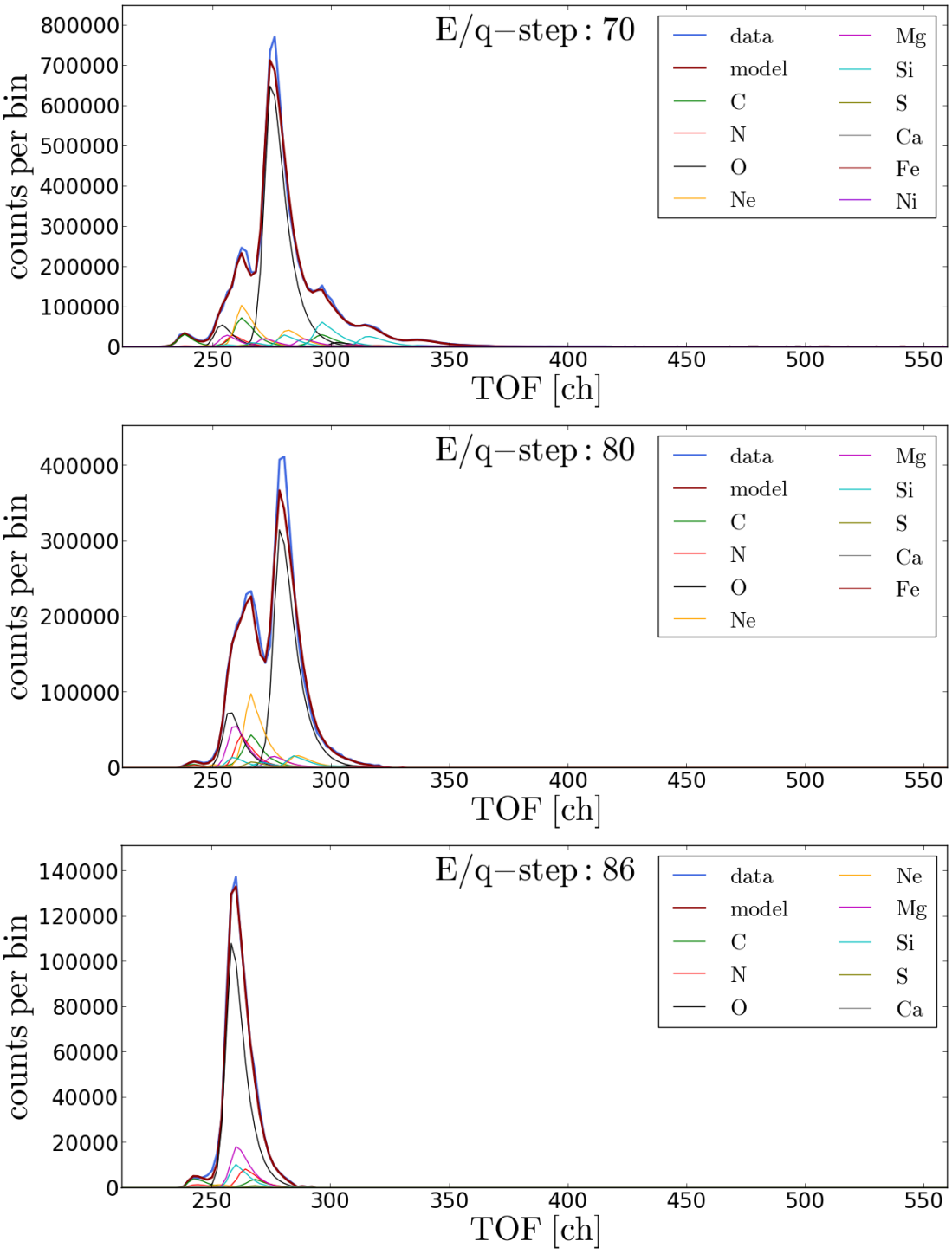

FIGURE C.20: ESSD-integrated count rates of the long-term measurements and the fitted Kappa-Moyal Full Stable response model for Epq-steps 70, 80 and 86.

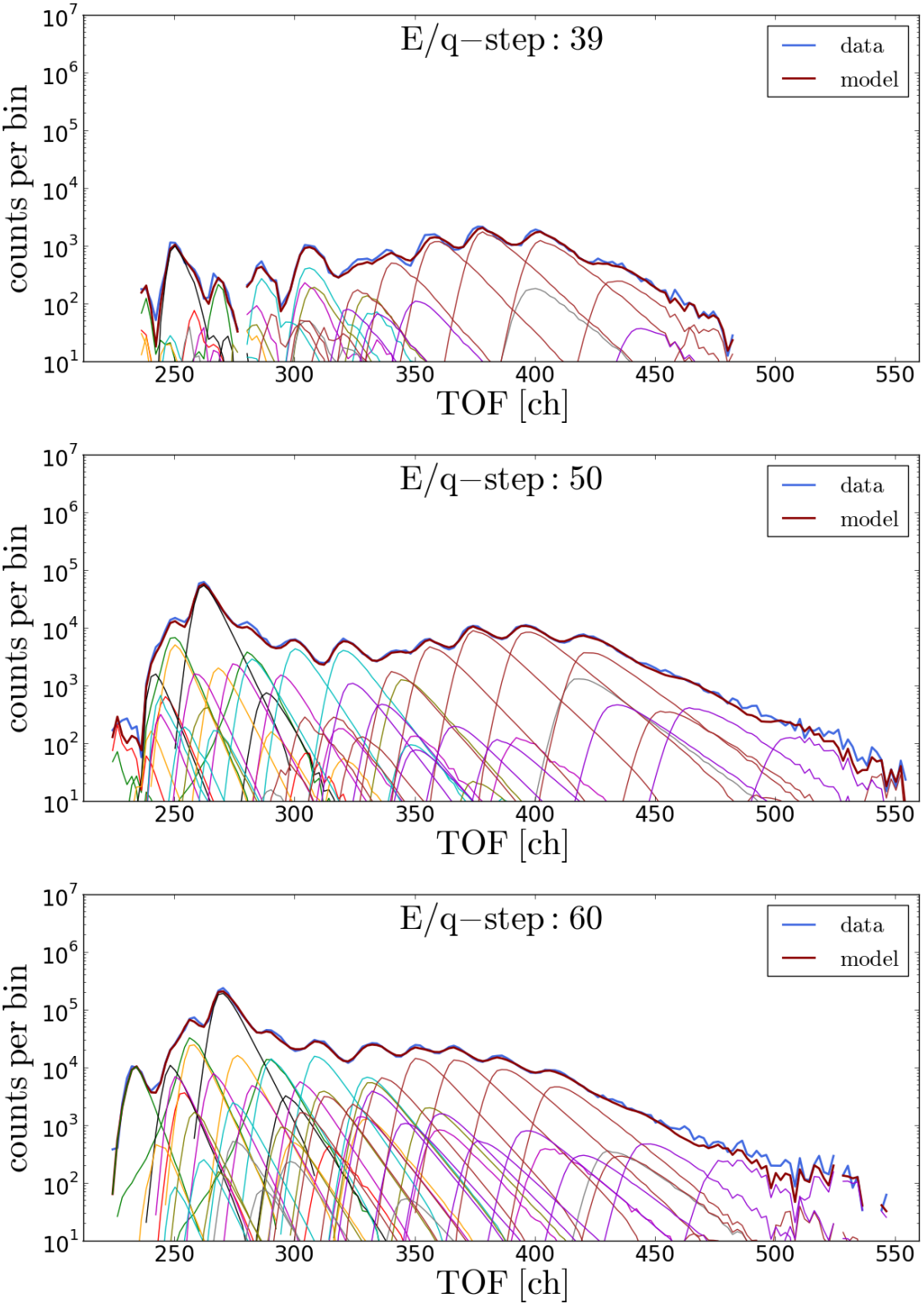

FIGURE C.21: ESSD-integrated logarithmic count rates of the long-term measurements and the fitted Kappa-Moyal Full Stable response model for Epq-steps 39, 50 and 60.

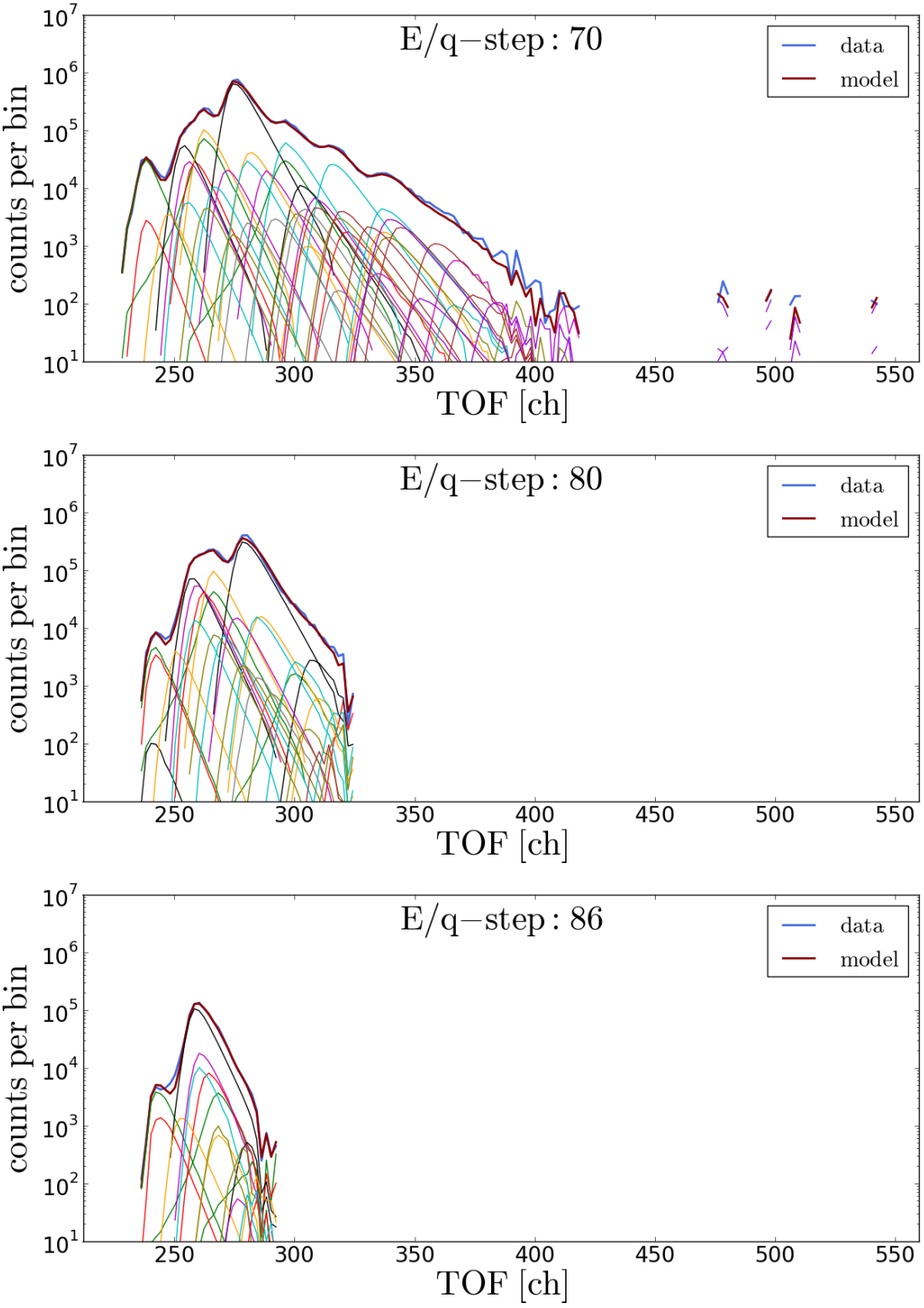

FIGURE C.22: ESSD-integrated logarithmic count rates of the long-term measurements and the fitted Kappa-Moyal Full Stable response model for Epq-steps 70, 80 and 86.

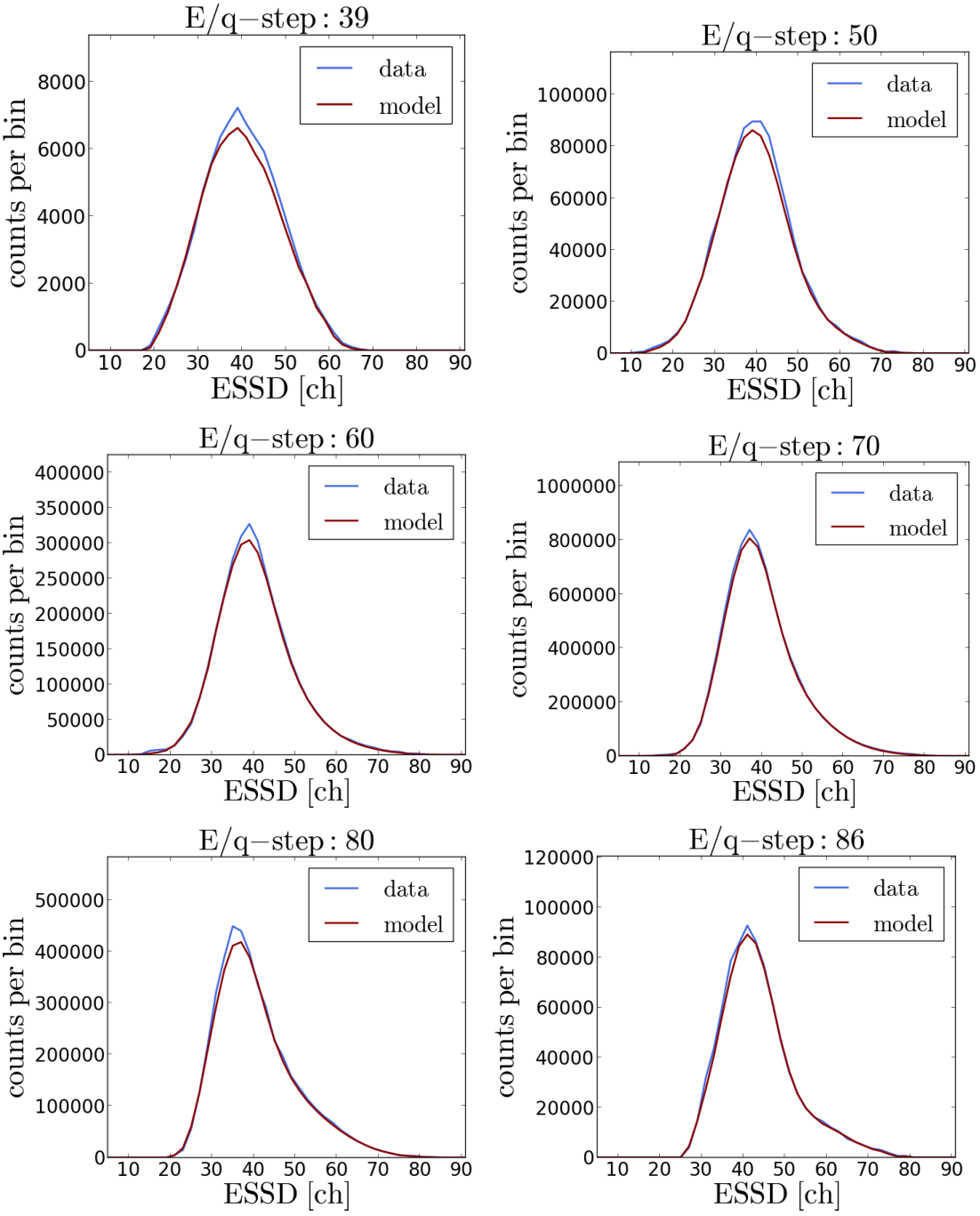

FIGURE C.23: TOF-integrated count rates of the long-term measurements and the fitted Kappa-Moyal Full Stable response model for Epq-steps 39 - 86.

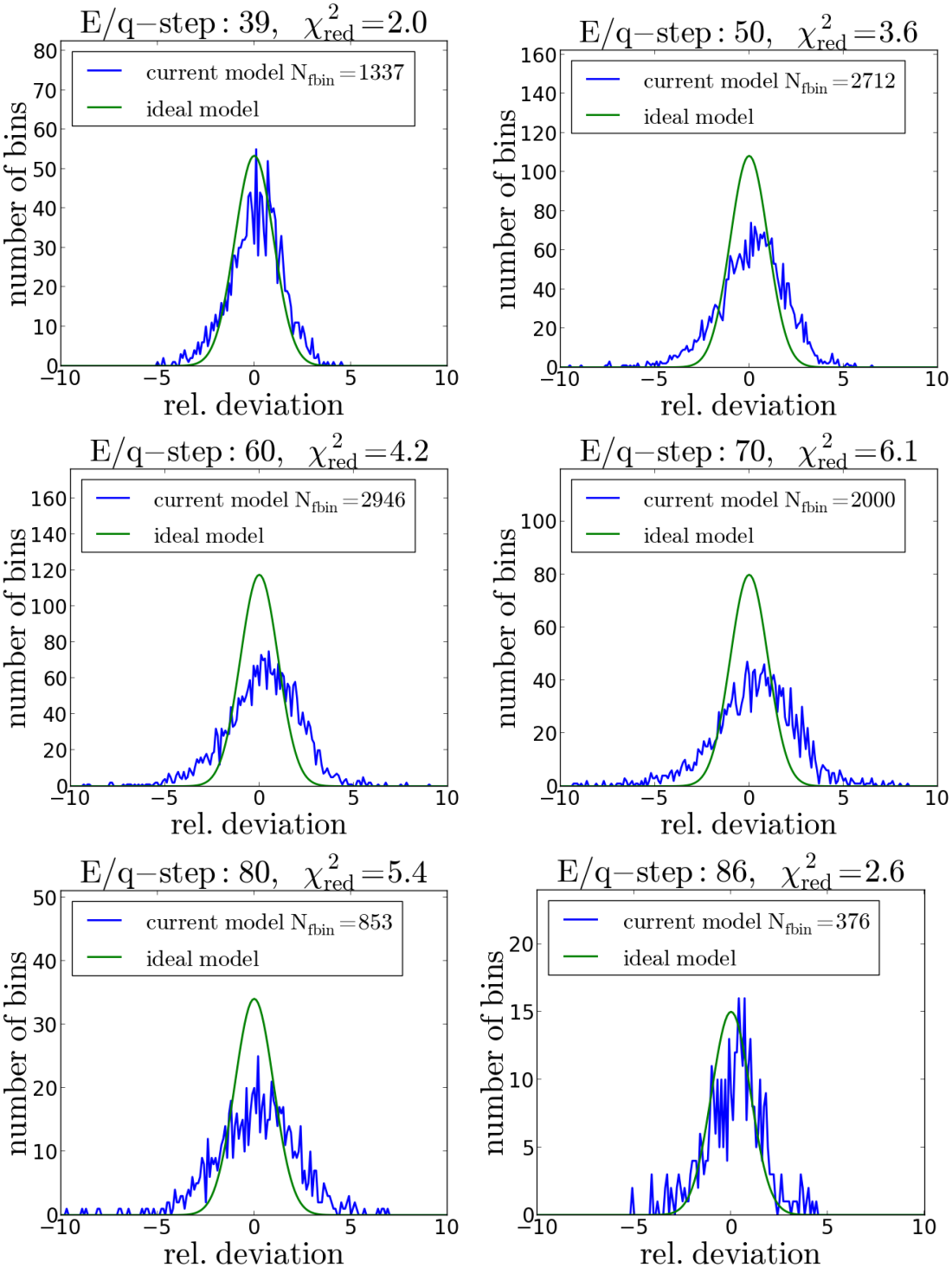

FIGURE C.24: Histograms of the relative deviations (blue) between the measured long-term data and the fitted Kappa-Moyal Full Stable response model for Epq-steps 39-86 in comparison to a relative deviation distribution that would arise from a perfect model $\chi^2_{red} = 1$ purely due to statistical deviations (green).

C.3 The Gaussian Reduced Stable Response Model

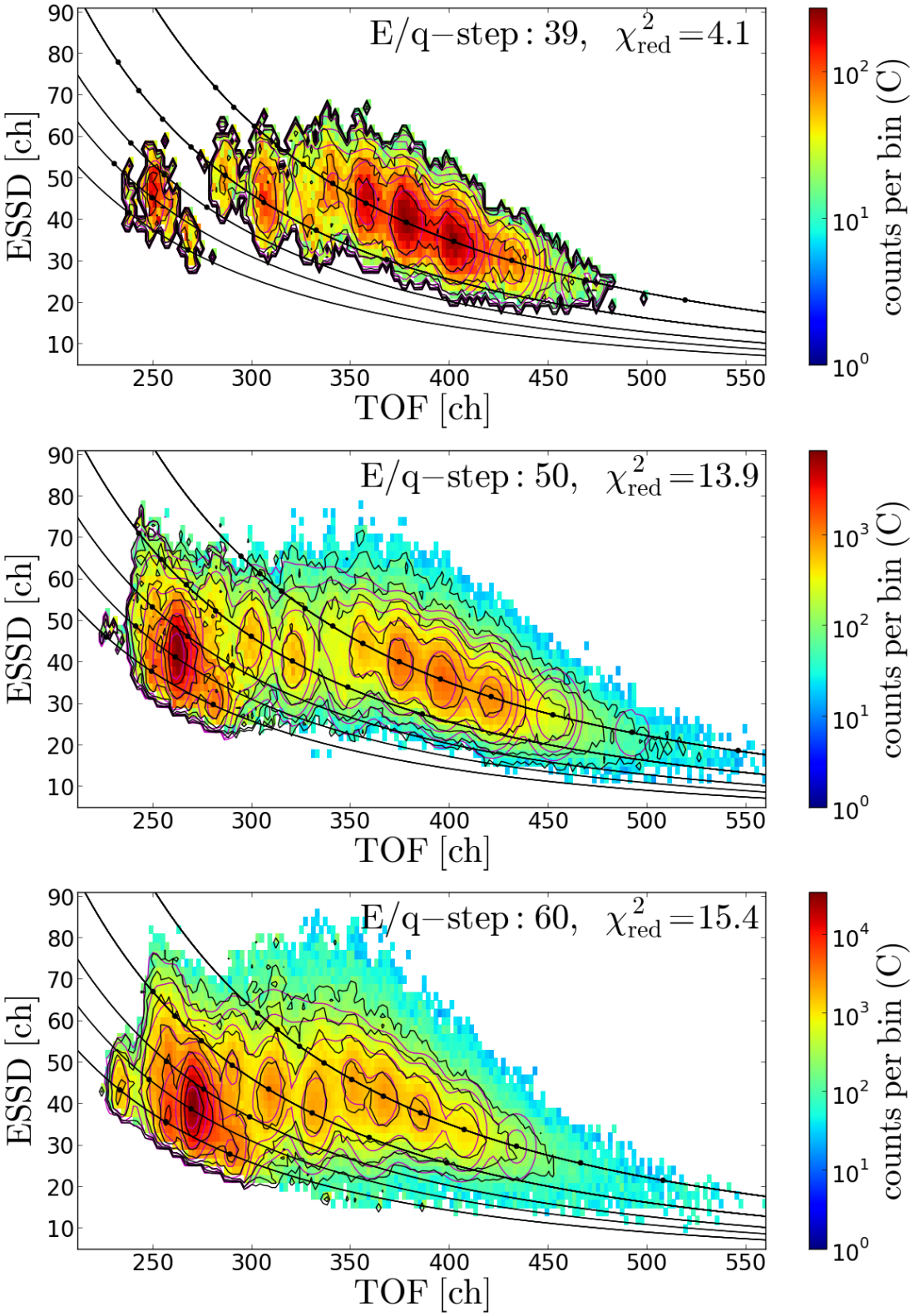

FIGURE C.25: 2D-contour plot of the CTOF *Gaussian Reduced Stable* response model (magenta contour lines) fitted to the accumulated long-term ET-matrix count rates (black contour lines) for Epq-steps 39, 50 and 60.

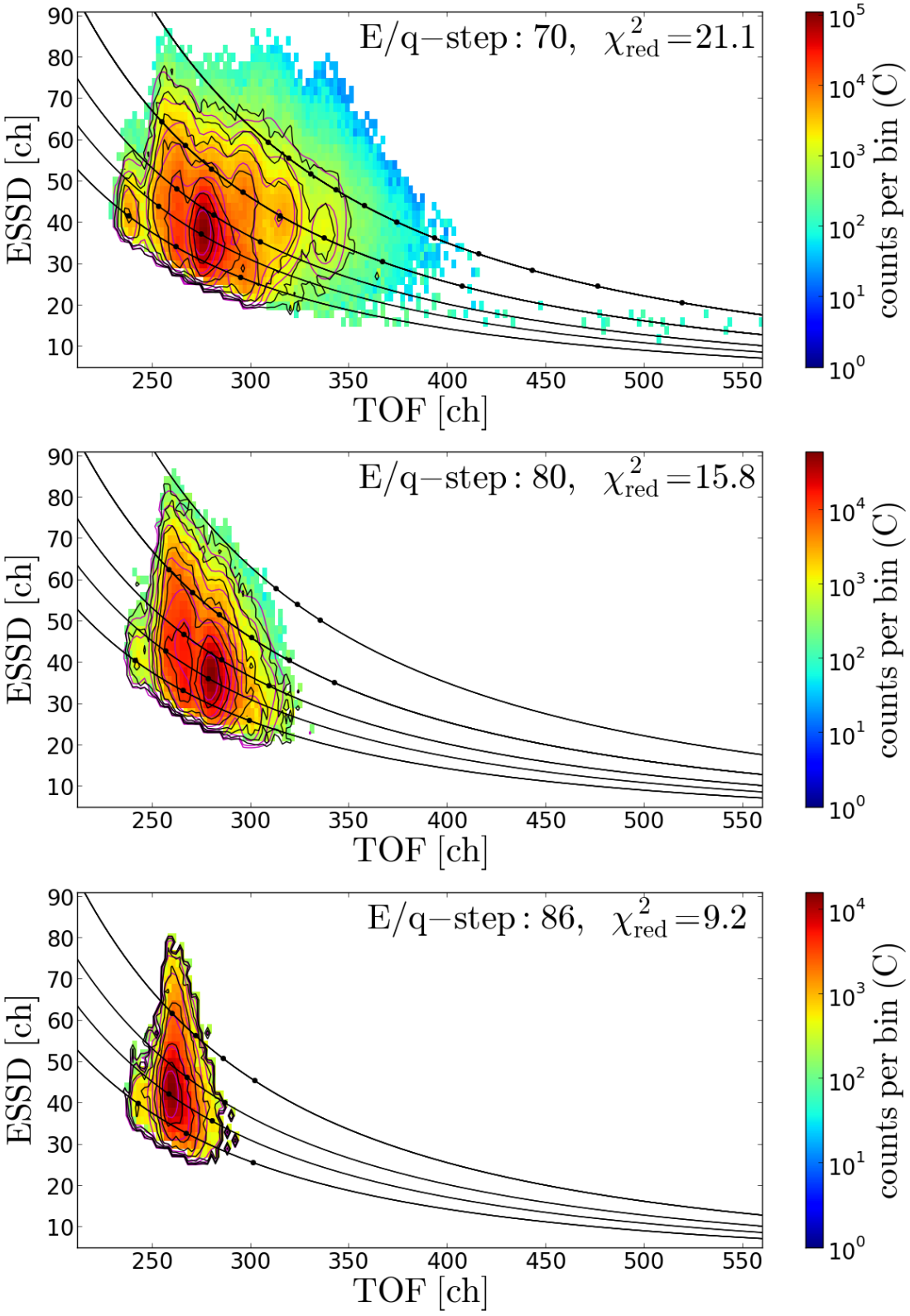

FIGURE C.26: 2D-contour plot of the CTOF *Gaussian Reduced Stable* response model (magenta contour lines) fitted to the accumulated long-term ET-matrix count rates (black contour lines) for Epq-steps 70, 80 and 86. Note that in these steps we filter the data for He^{2+} random coincidences via the proton speed as explained in chapter 4. The proton-speed filter conditions for Epq-steps 70, 80, and 86 are $v_p \in [0, 420\,\mathrm{km/s}]$, $v_p \in [0, 345\,\mathrm{km/s}]$, and $v_p \in [0, 320\,\mathrm{km/s}]$, respectively.

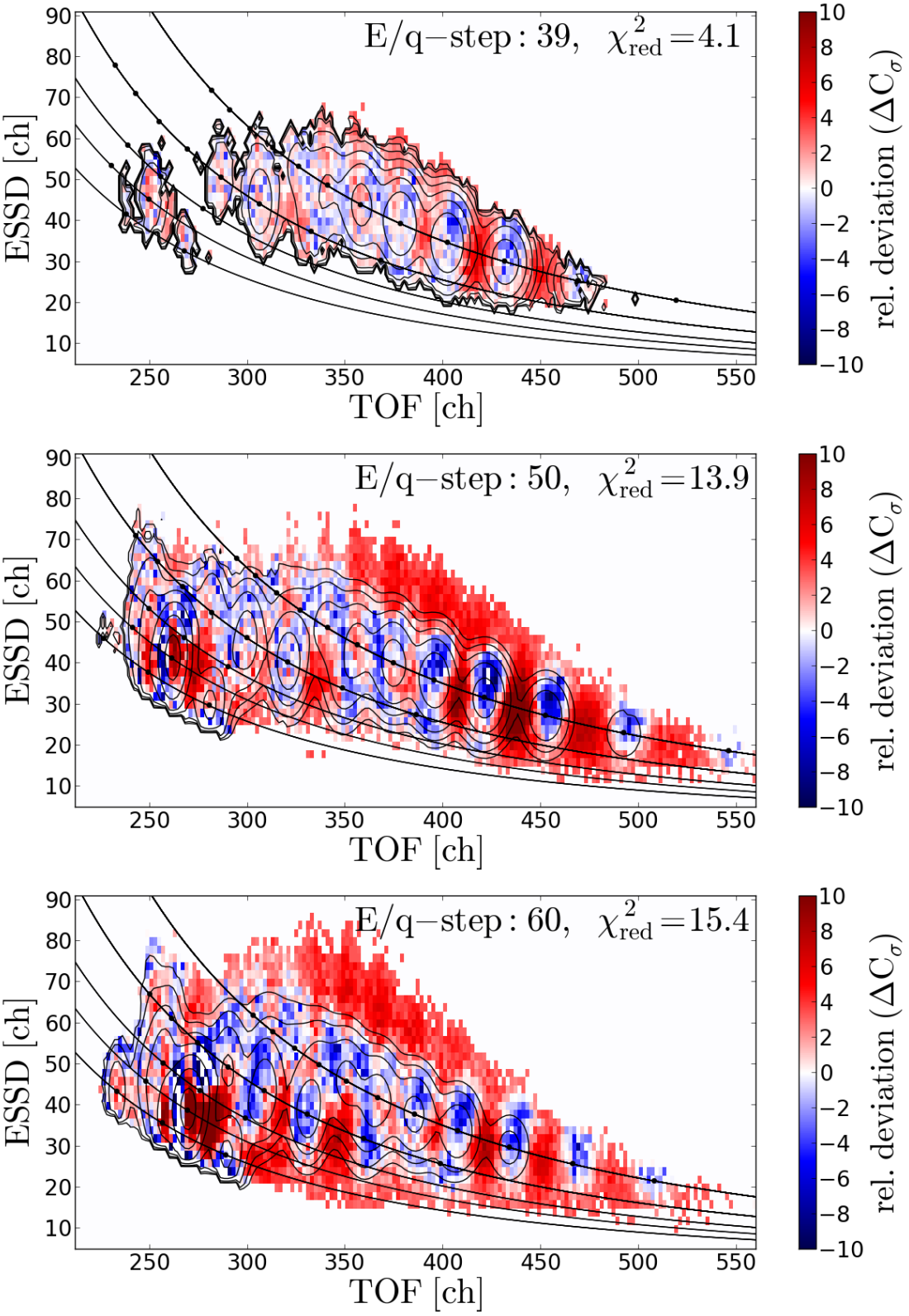

FIGURE C.27: Relative fit deviations for the Gaussian Reduced Stable response model for Epq-steps 39, 50 and 60.

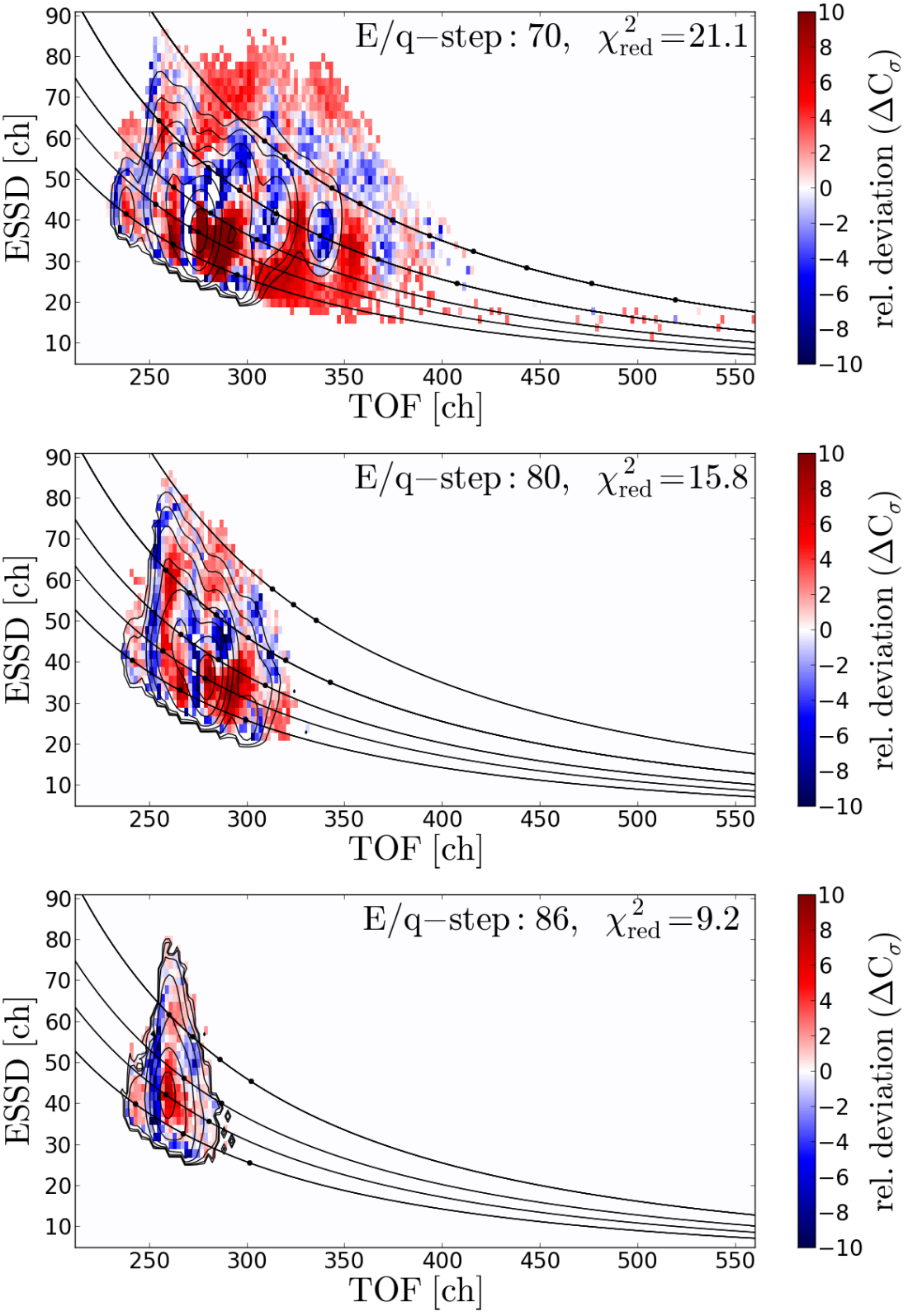

FIGURE C.28: Relative fit deviations for the Gaussian Reduced Stable response model for Epq-steps 70, 80 and 86.

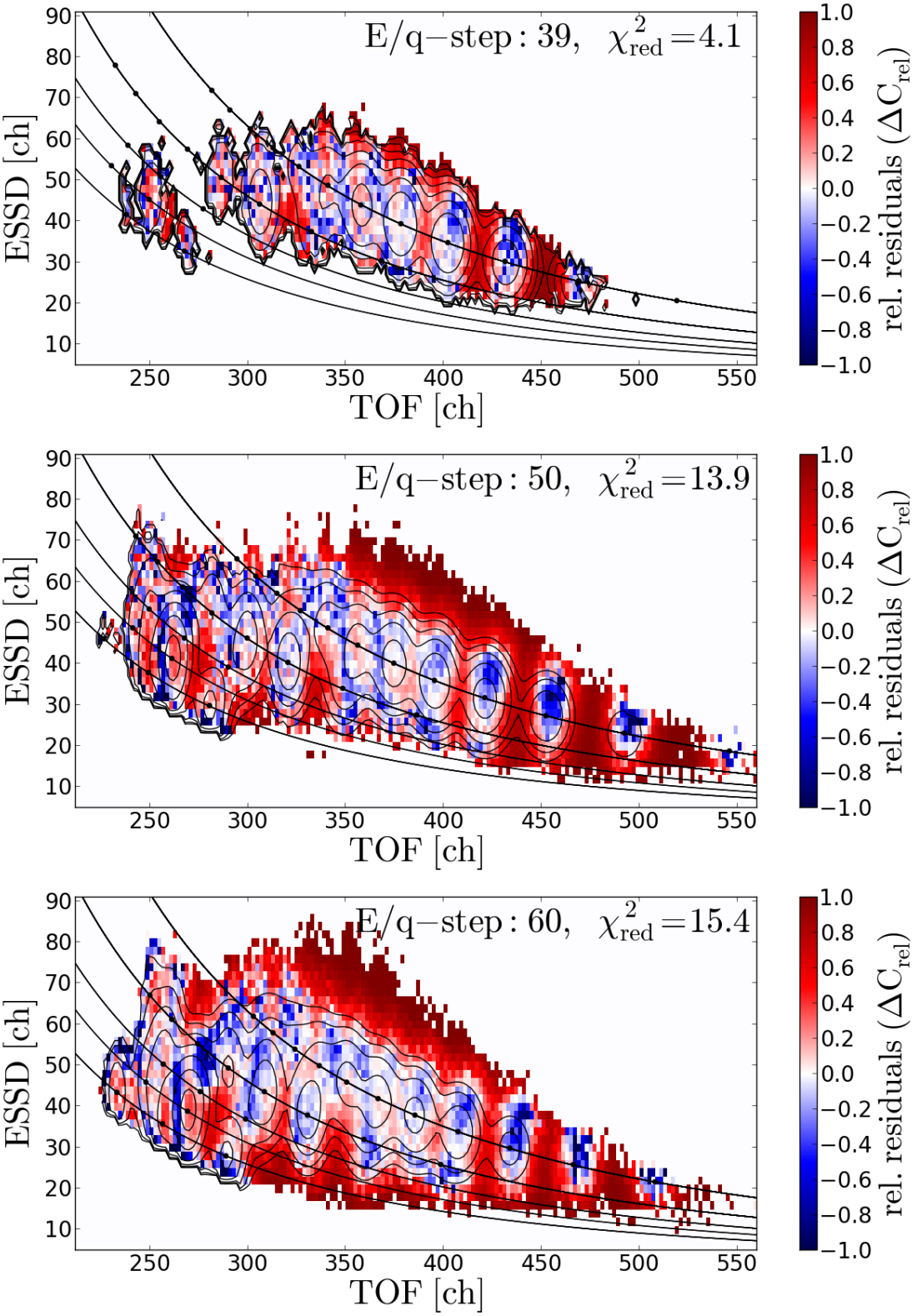

FIGURE C.29: Relative fit residuals for the Gaussian Reduced Stable response model for Epq-steps 39, 50 and 60.

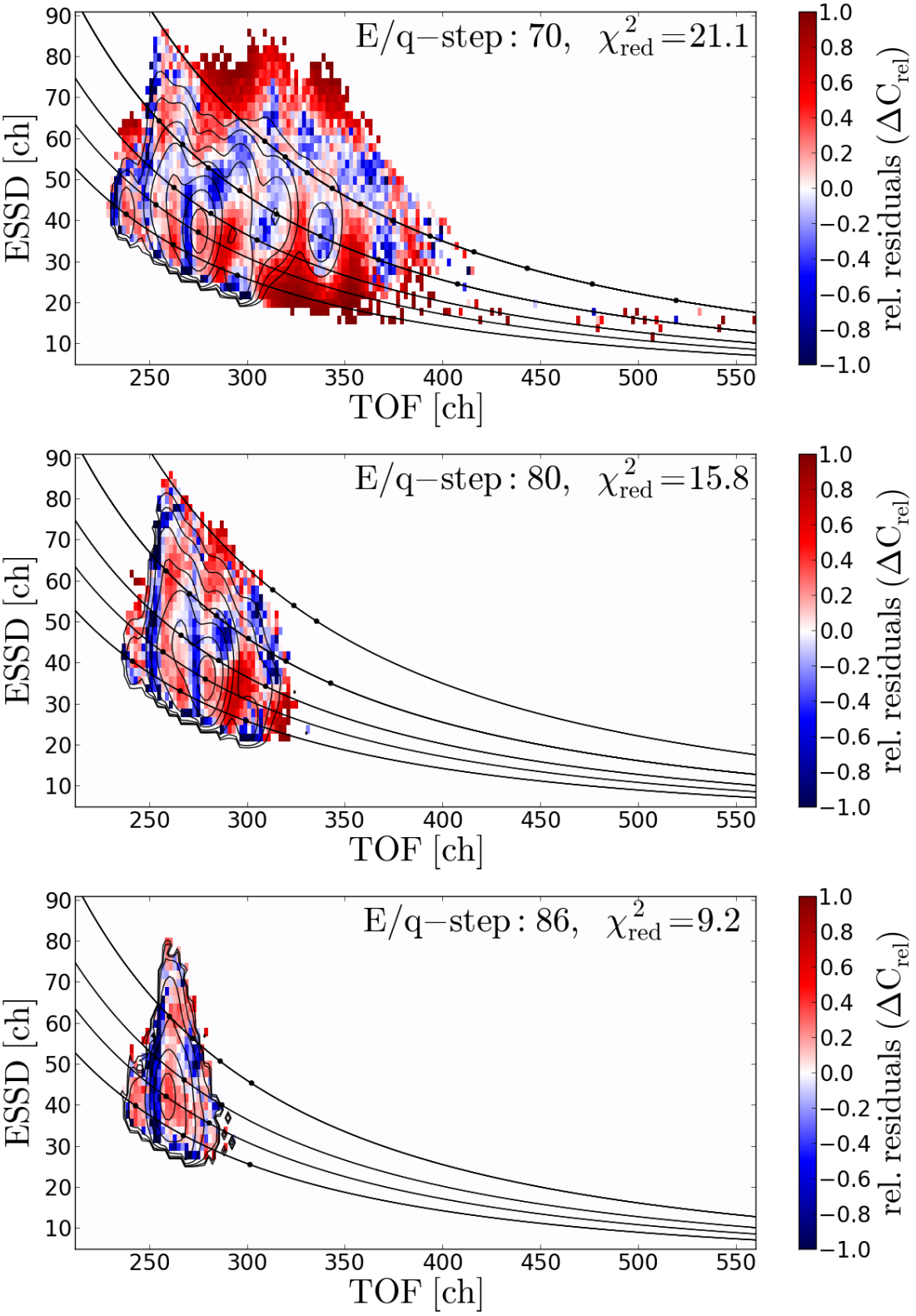

FIGURE C.30: Relative fit residuals for the Gaussian Reduced Stable response model for Epq-steps 70, 80 and 86.

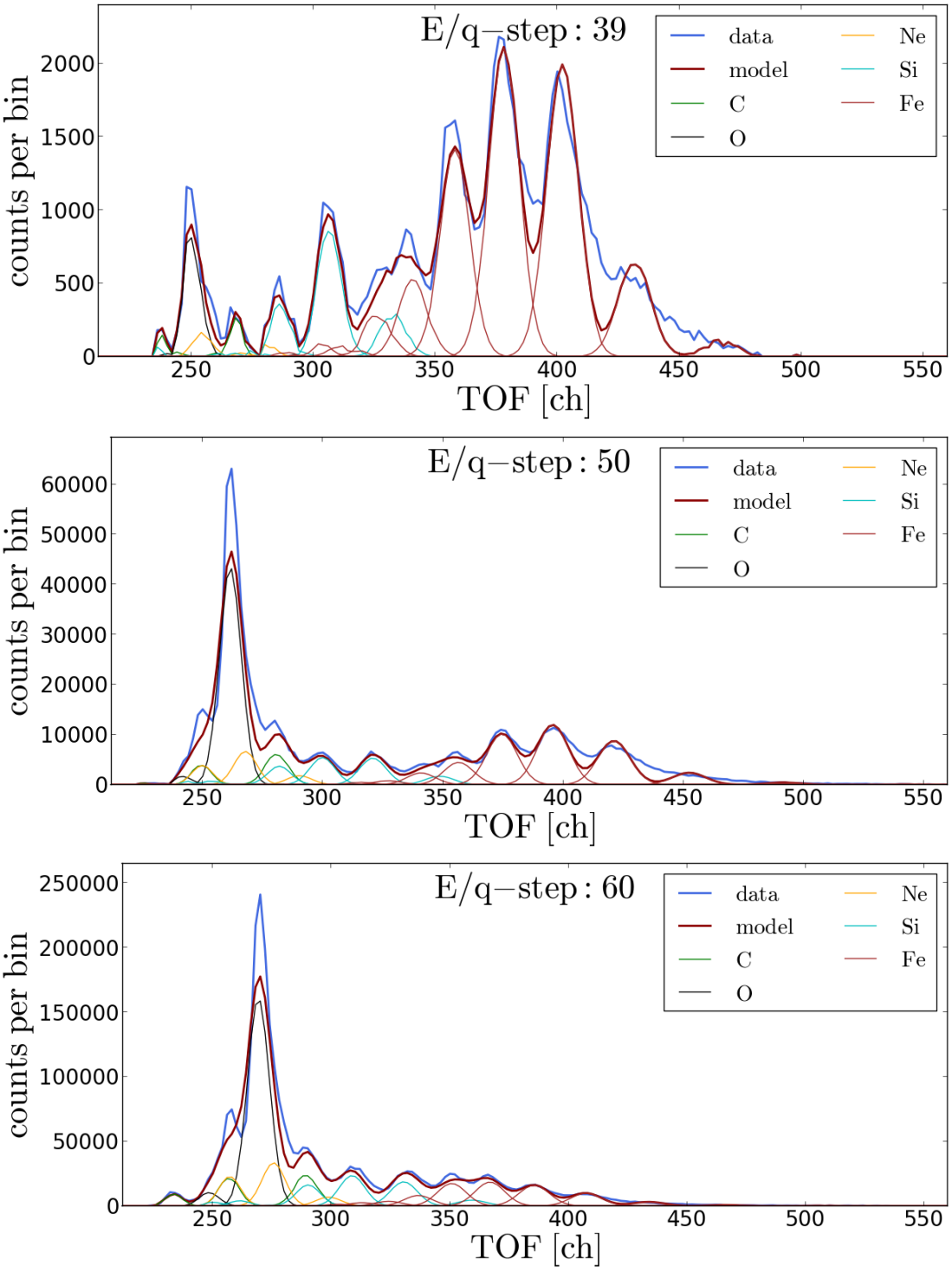

FIGURE C.31: ESSD-integrated count rates of the long-term measurements and the fitted Gaussian Reduced Stable response model for Epq-steps 39, 50 and 60.

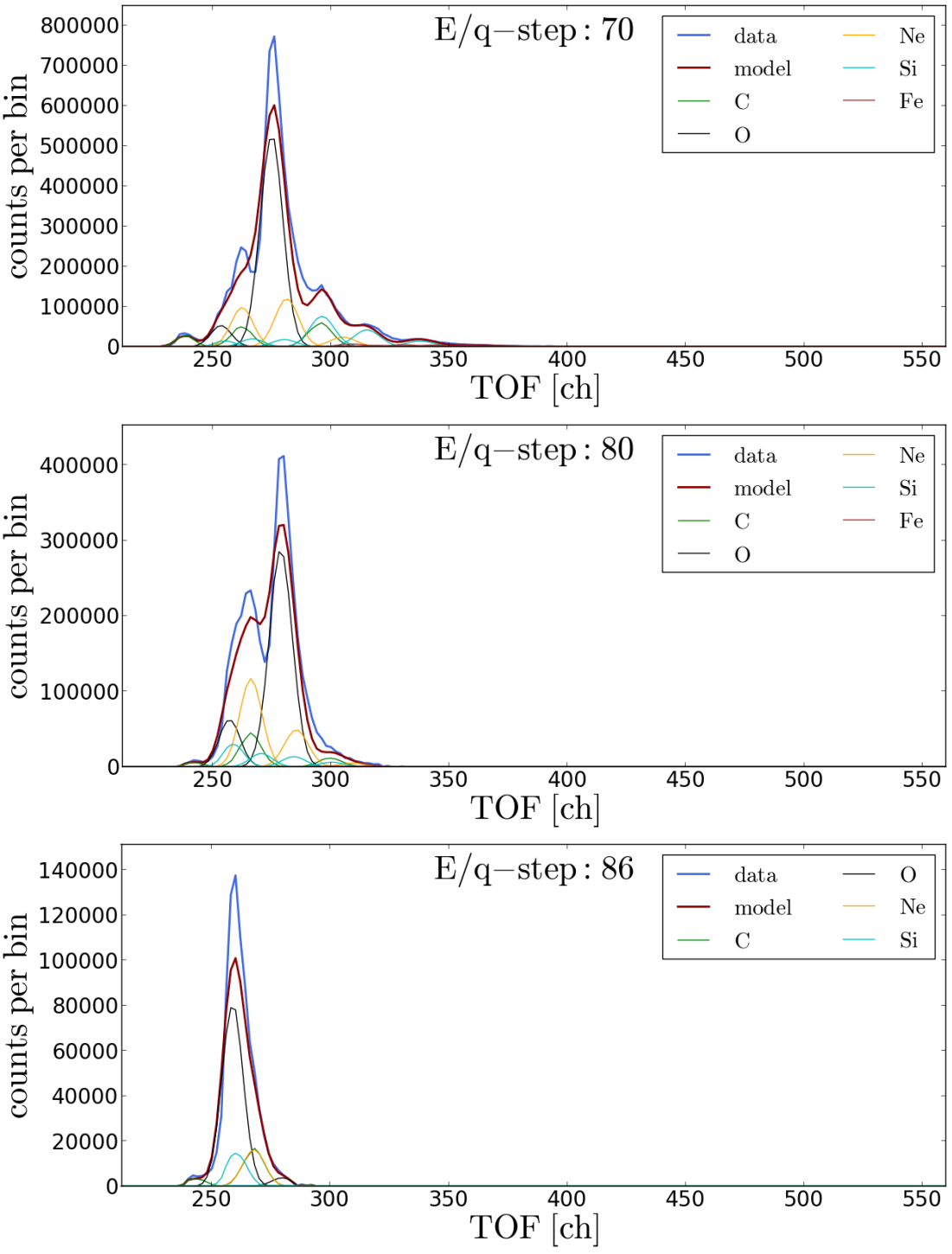

FIGURE C.32: ESSD-integrated count rates of the long-term measurements and the fitted Gaussian Reduced Stable response model for Epq-steps 70, 80 and 86.

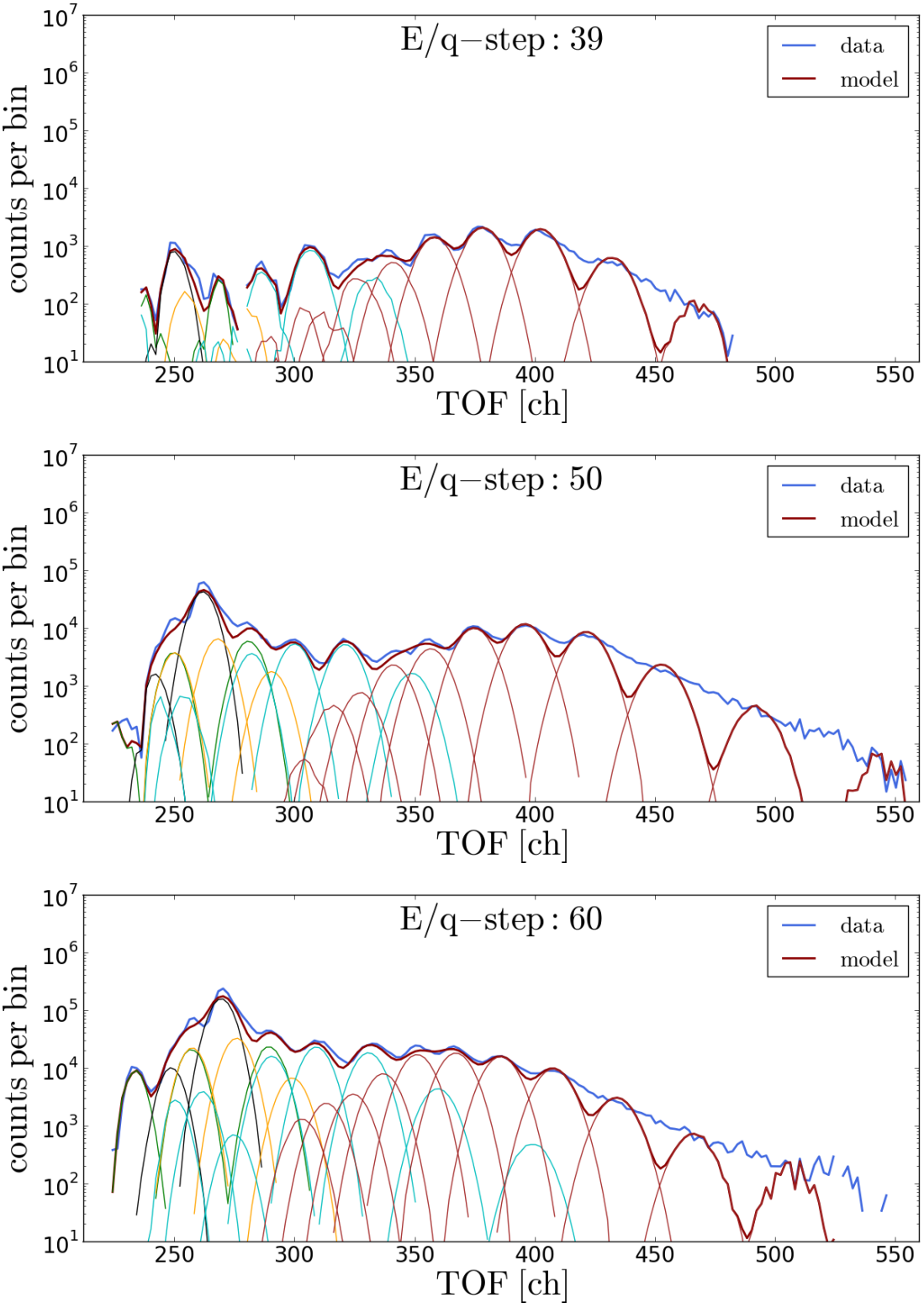

FIGURE C.33: ESSD-integrated logarithmic count rates of the long-term measurements and the fitted Gaussian Reduced Stable response model for Epq-steps 39, 50 and 60.

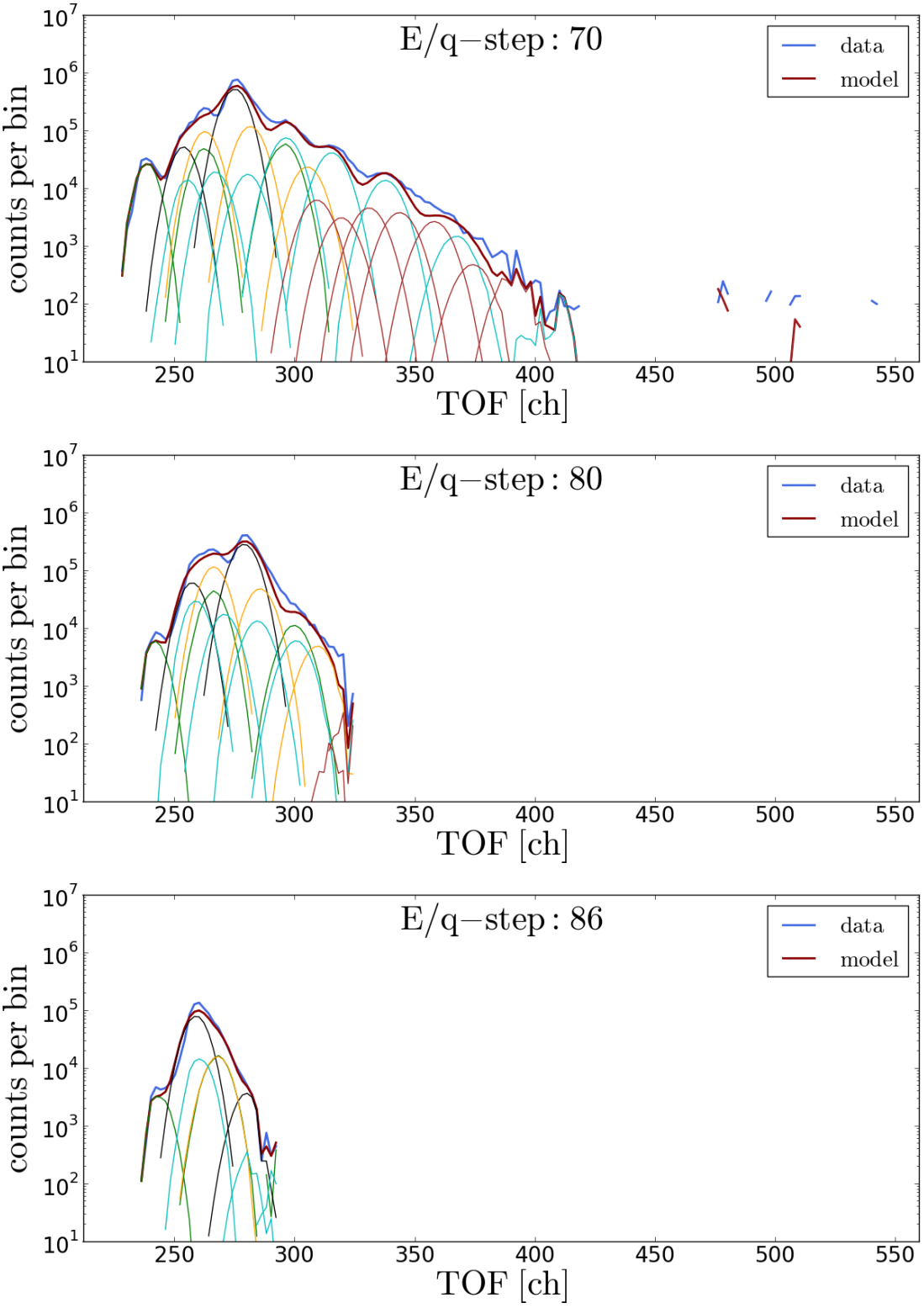

FIGURE C.34: ESSD-integrated logarithmic count rates of the long-term measurements and the fitted Gaussian Reduced Stable response model for Epq-steps 70, 80 and 86.

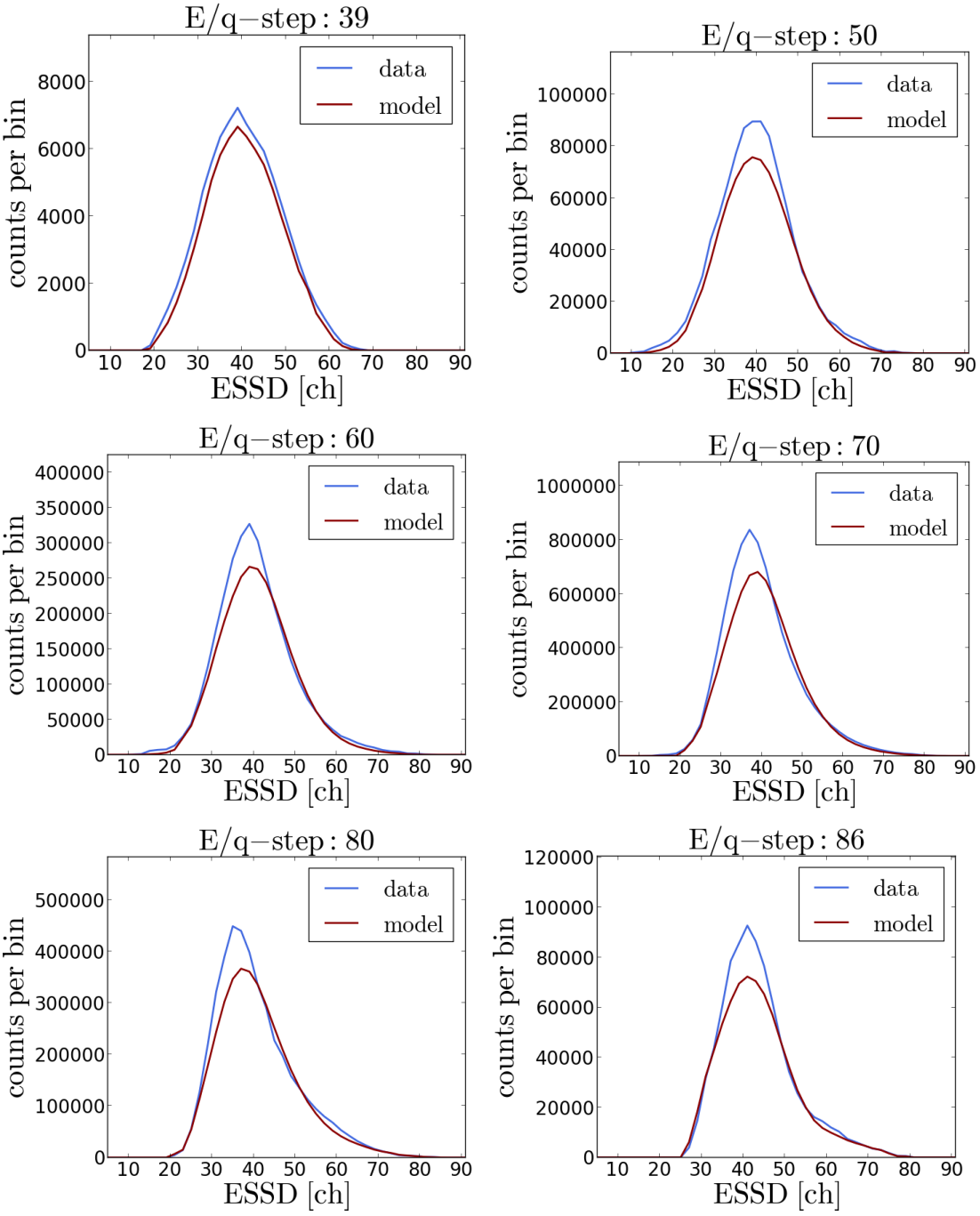

FIGURE C.35: TOF-integrated count rates of the long-term measurements and the fitted Gaussian Reduced Stable response model for Epq-steps 39 - 86.

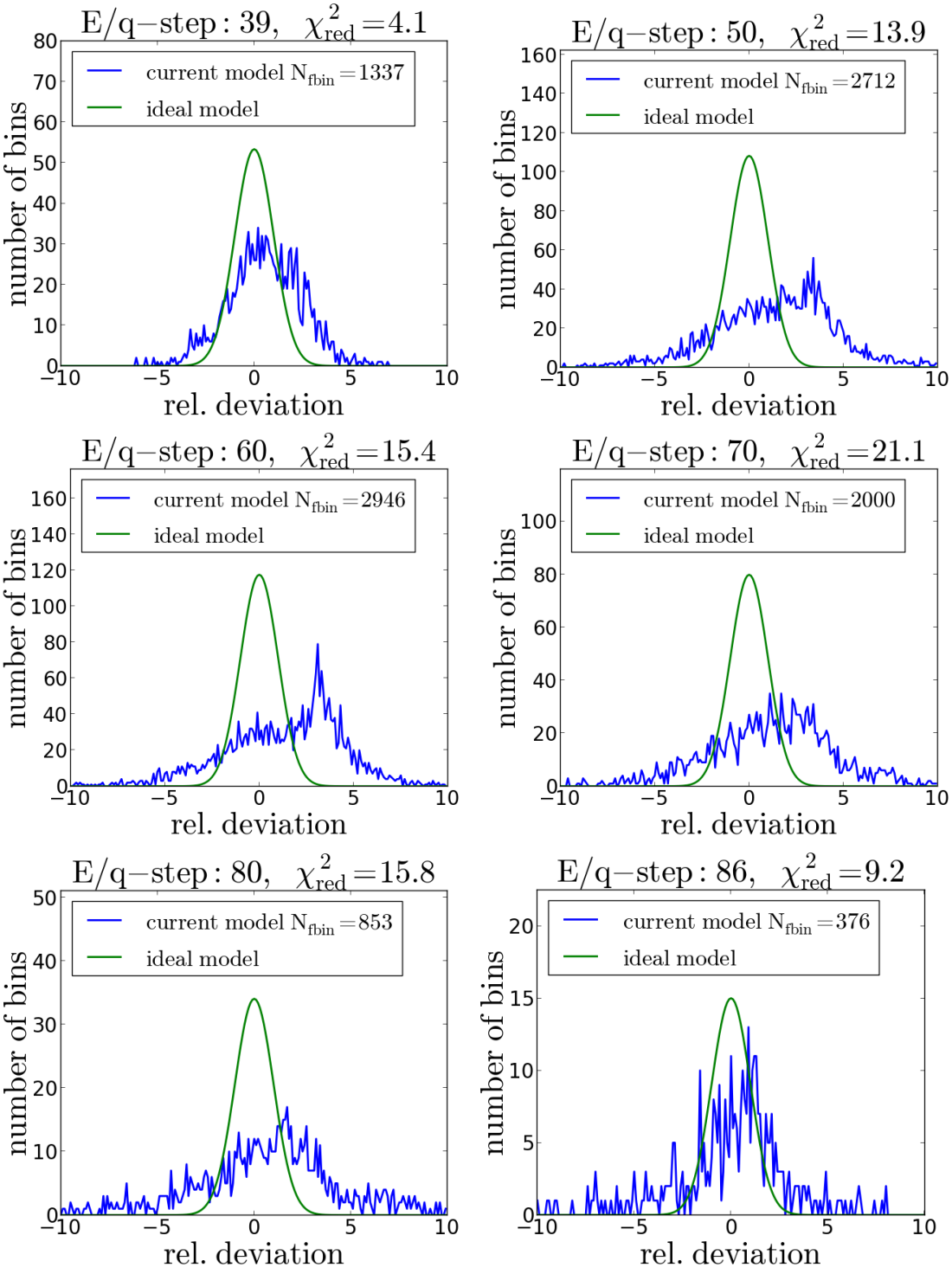

FIGURE C.36: Histograms of the relative deviations (blue) between the measured long-term data and the fitted Gaussian Reduced Stable response model for Epq-steps 39-86 in comparison to a relative deviation distribution that would arise from a perfect model $\chi^2_{red} = 1$ purely due to statistical deviations (green).

C.4 The Kappa-Moyal Reduced Stable Response Model

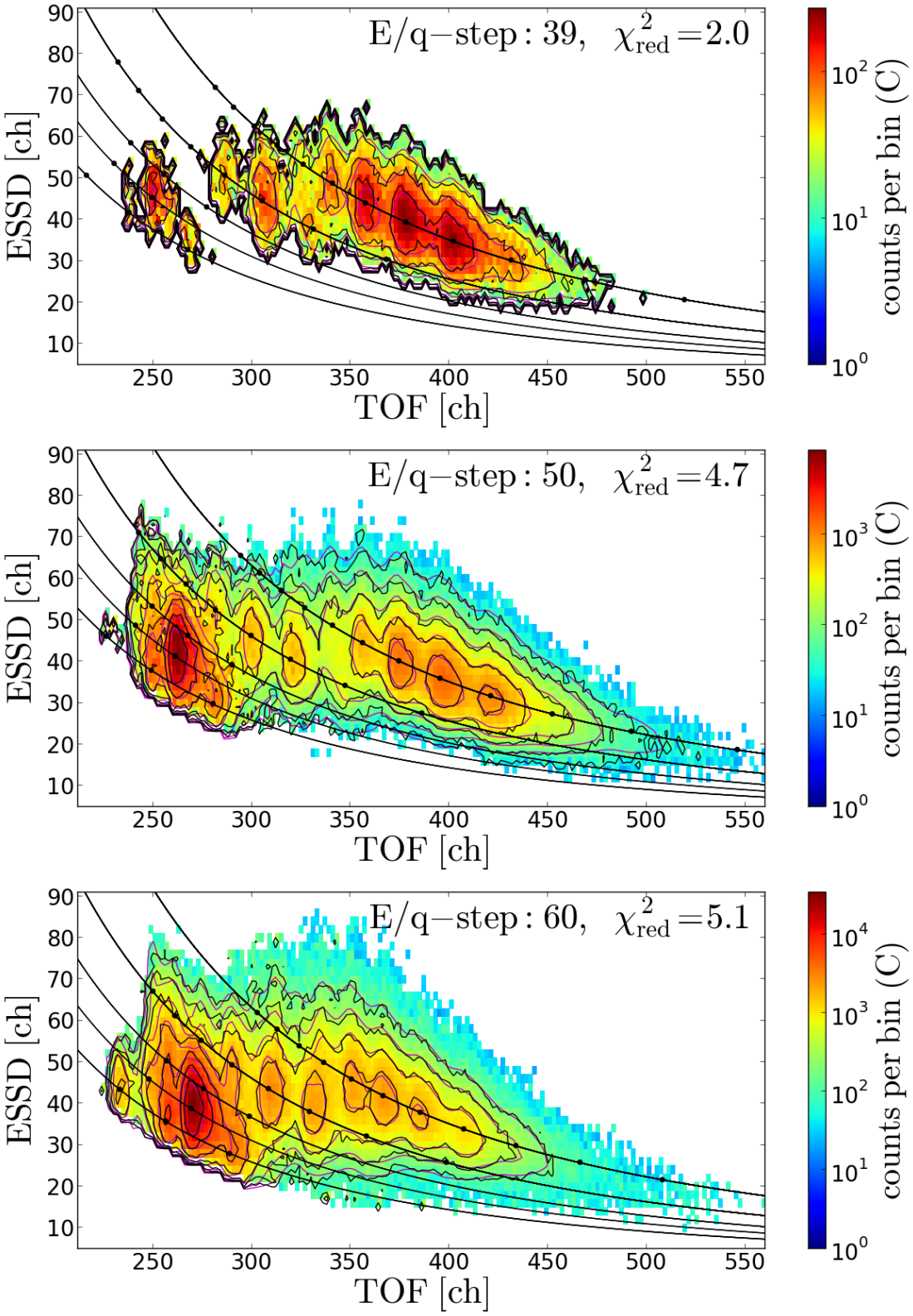

FIGURE C.37: 2D-contour plot of the CTOF *Kappa-Moyal Reduced Stable* response model (magenta contour lines) fitted to the accumulated long-term ET-matrix count rates (black contour lines) for Epq-steps 39, 50 and 60.

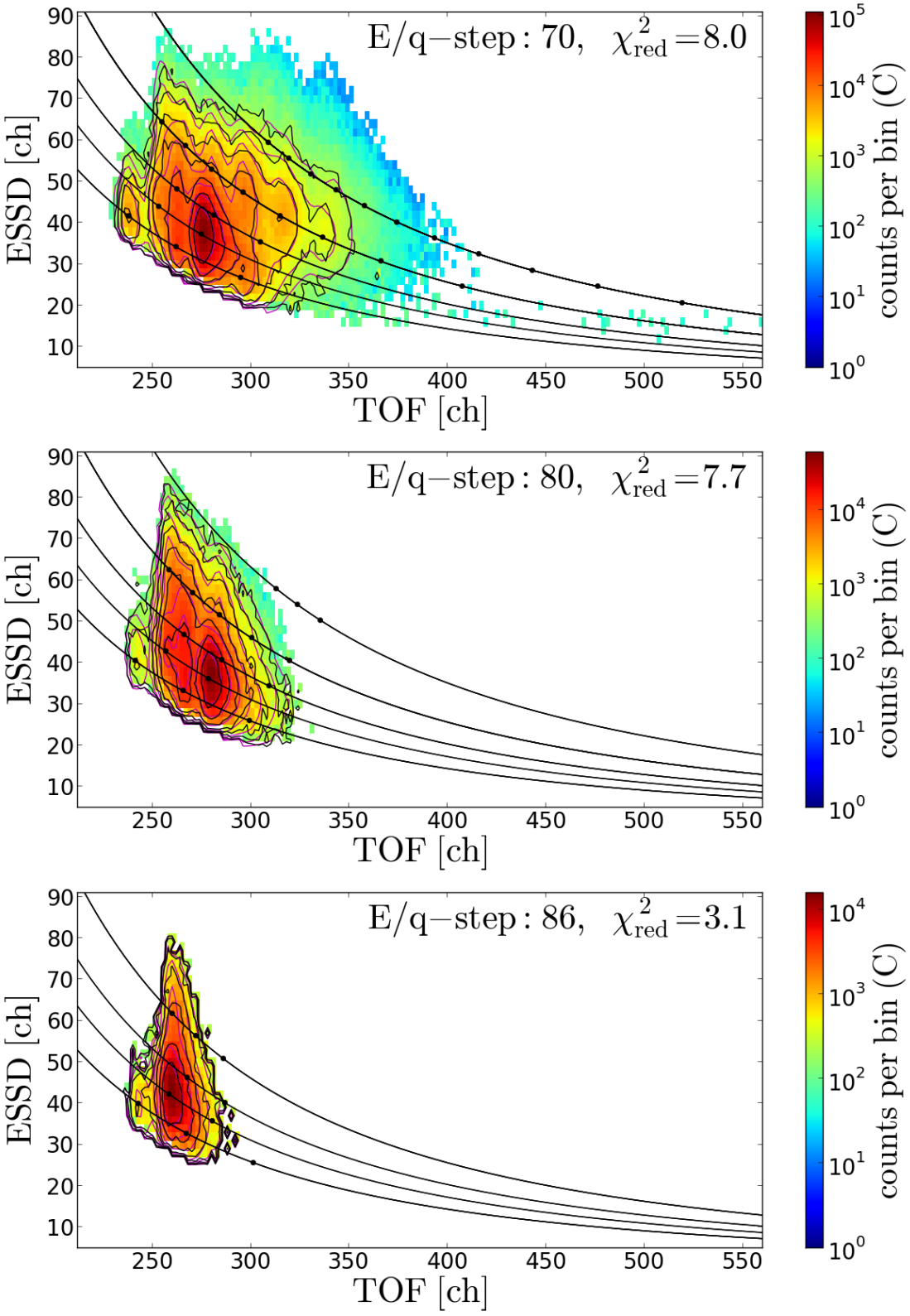

FIGURE C.38: 2D-contour plot of the CTOF *Kappa-Moyal Reduced Stable* response model (magenta contour lines) fitted to the accumulated long-term ET-matrix count rates (black contour lines) for Epq-steps 70, 80 and 86. Note that in these steps we filter the data for He^{2+} random coincidences via the proton speed as explained in chapter 4. The proton-speed filter conditions for Epq-steps 70, 80, and 86 are $v_p \in [0, 420\,\mathrm{km/s}]$, $v_p \in [0, 345\,\mathrm{km/s}]$, and $v_p \in [0, 320\,\mathrm{km/s}]$, respectively.

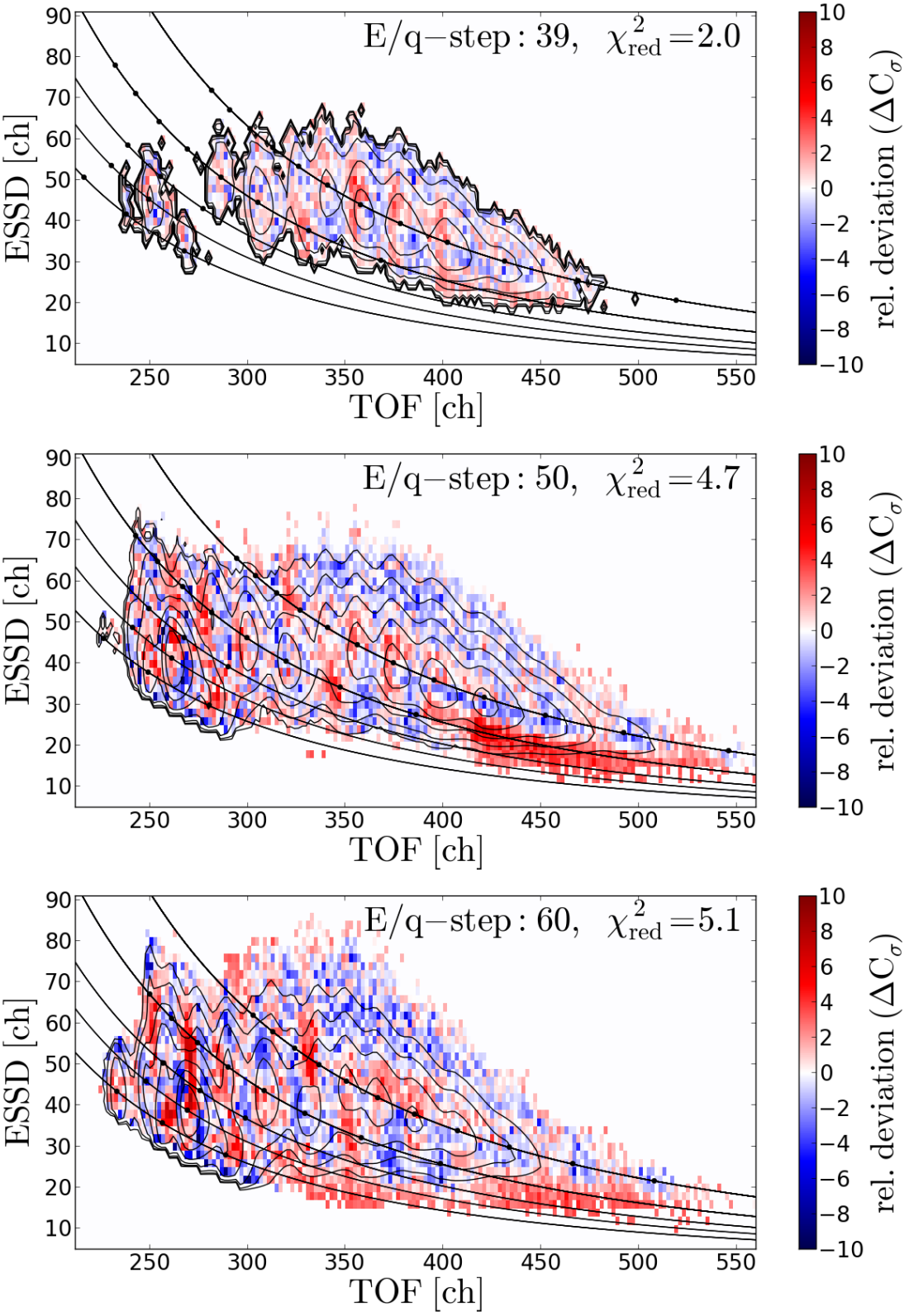

FIGURE C.39: Relative fit deviations for the Kappa-Moyal Reduced Stable response model for Epq-steps 39, 50 and 60.

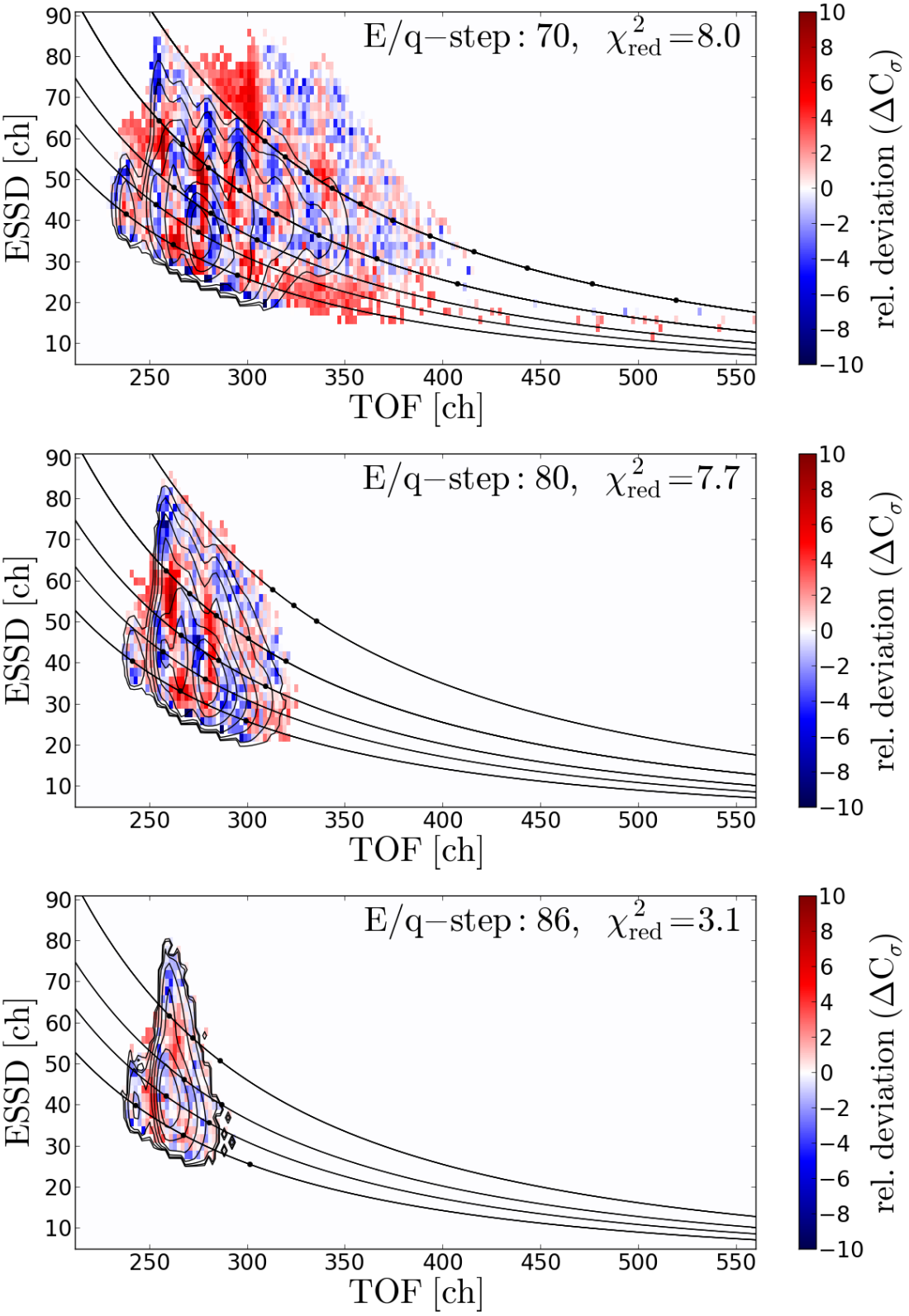

FIGURE C.40: Relative fit deviations for the Kappa-Moyal Reduced Stable response model for Epq-steps 70, 80 and 86.

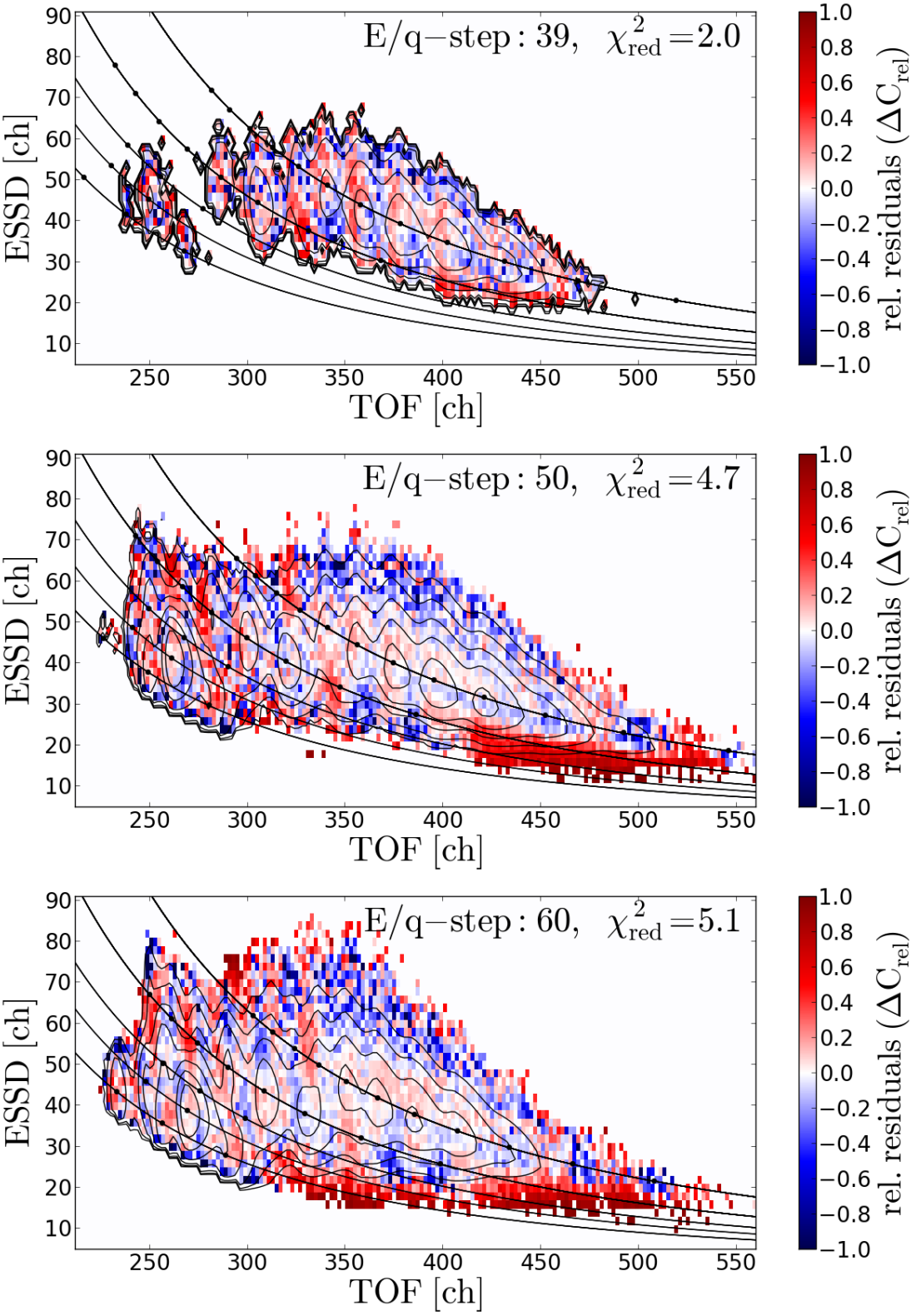

FIGURE C.41: Relative fit residuals for the Kappa-Moyal Reduced Stable response model for Epq-steps 39, 50 and 60.

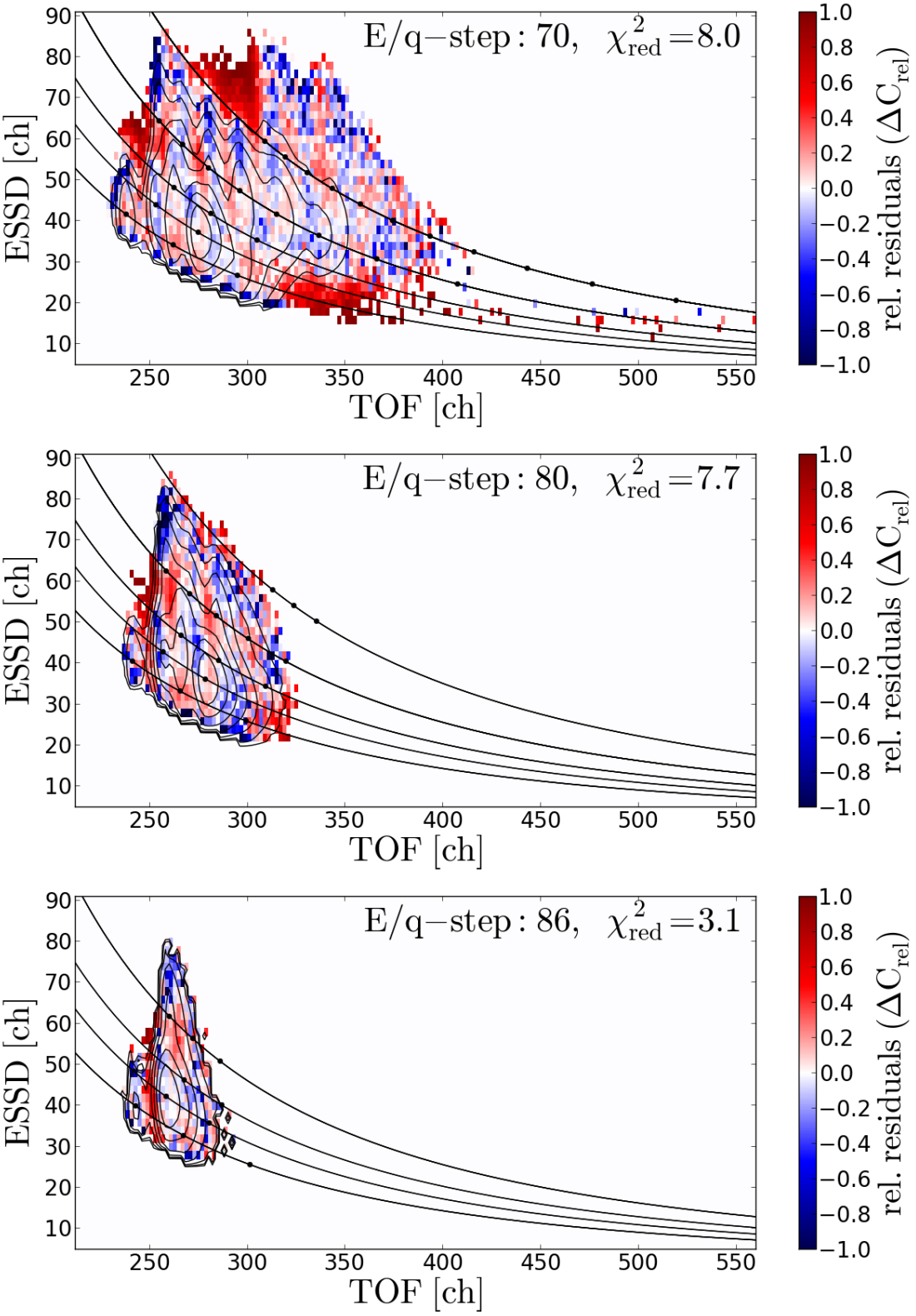

FIGURE C.42: Relative fit residuals for the Kappa-Moyal Reduced Stable response model for Epq-steps 70, 80 and 86.

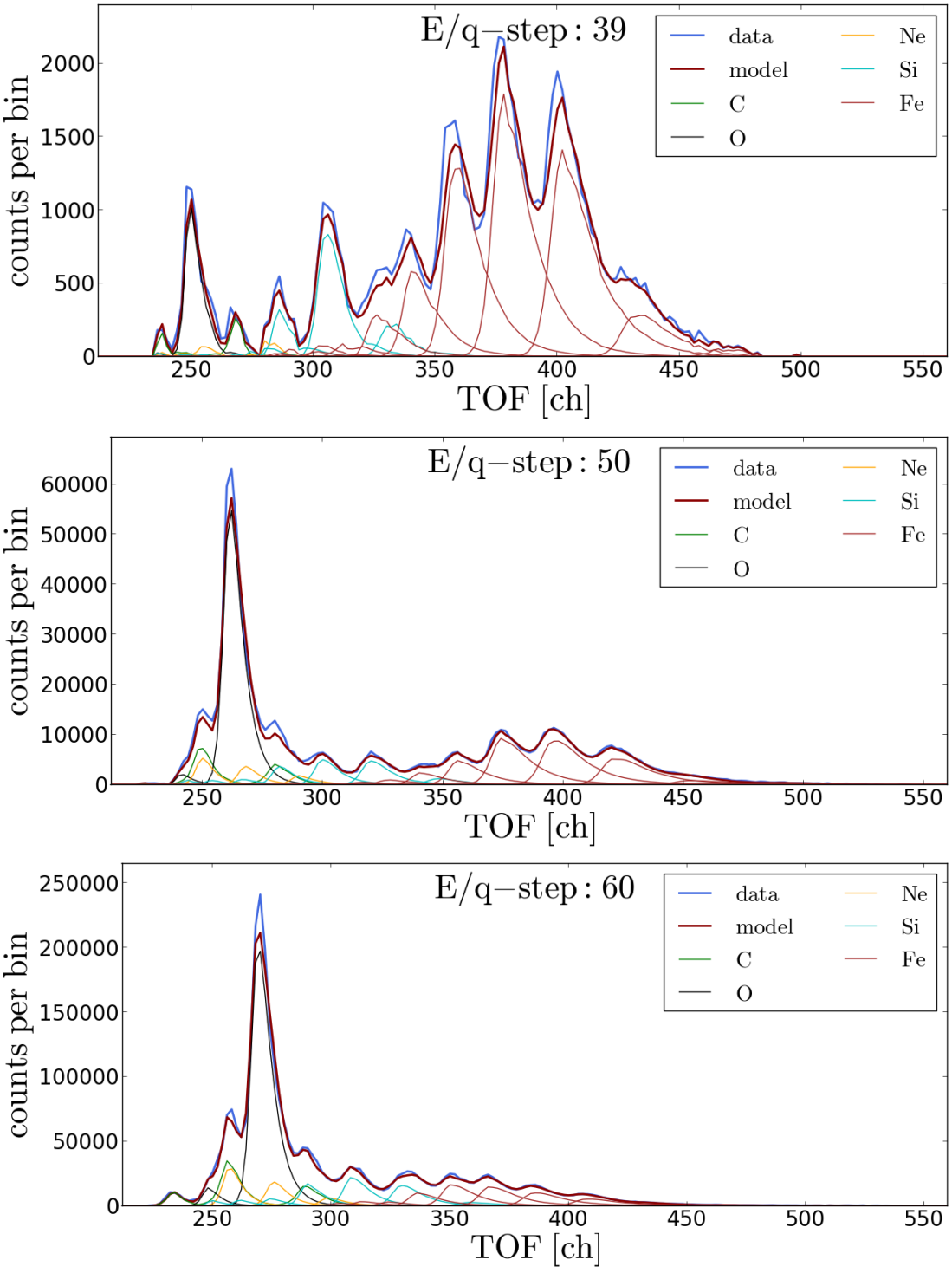

FIGURE C.43: ESSD-integrated count rates of the long-term measurements and the fitted Kappa-Moyal Reduced Stable response model for Epq-steps 39, 50 and 60.

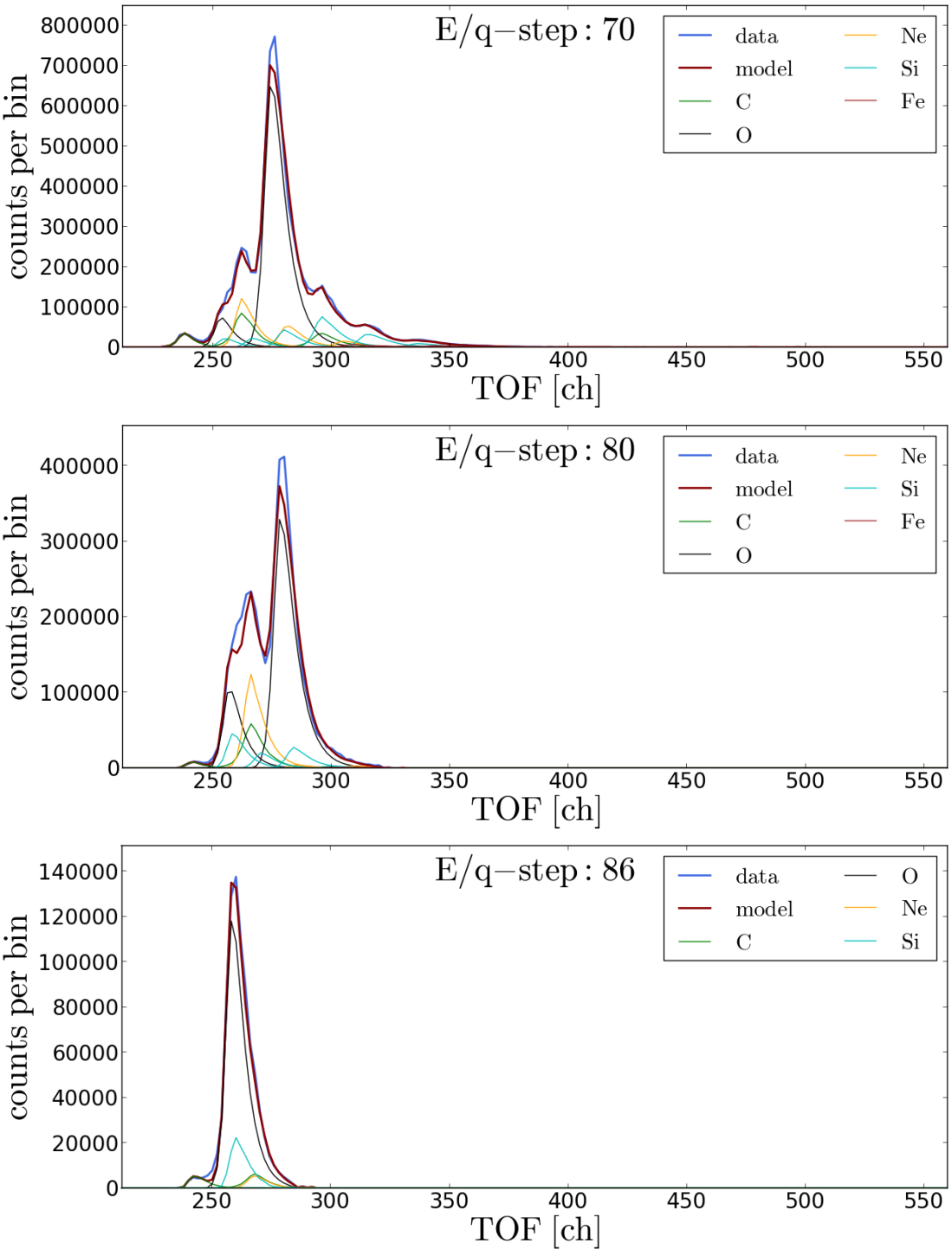

FIGURE C.44: ESSD-integrated count rates of the long-term measurements and the fitted Kappa-Moyal Reduced Stable response model for Epq-steps 70, 80 and 86.

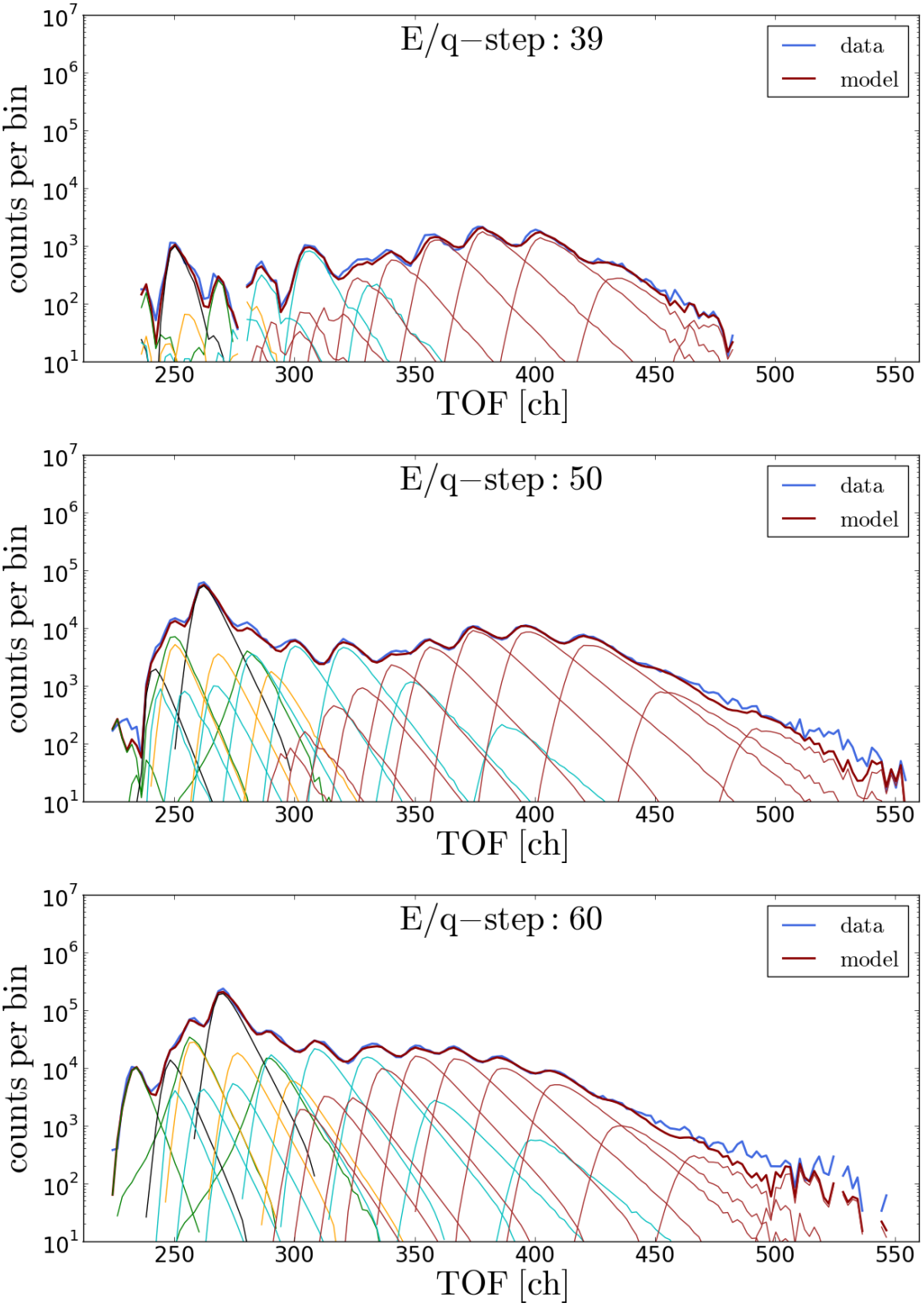

FIGURE C.45: ESSD-integrated logarithmic count rates of the long-term measurements and the fitted Kappa-Moyal Reduced Stable response model for Epq-steps 39, 50 and 60.

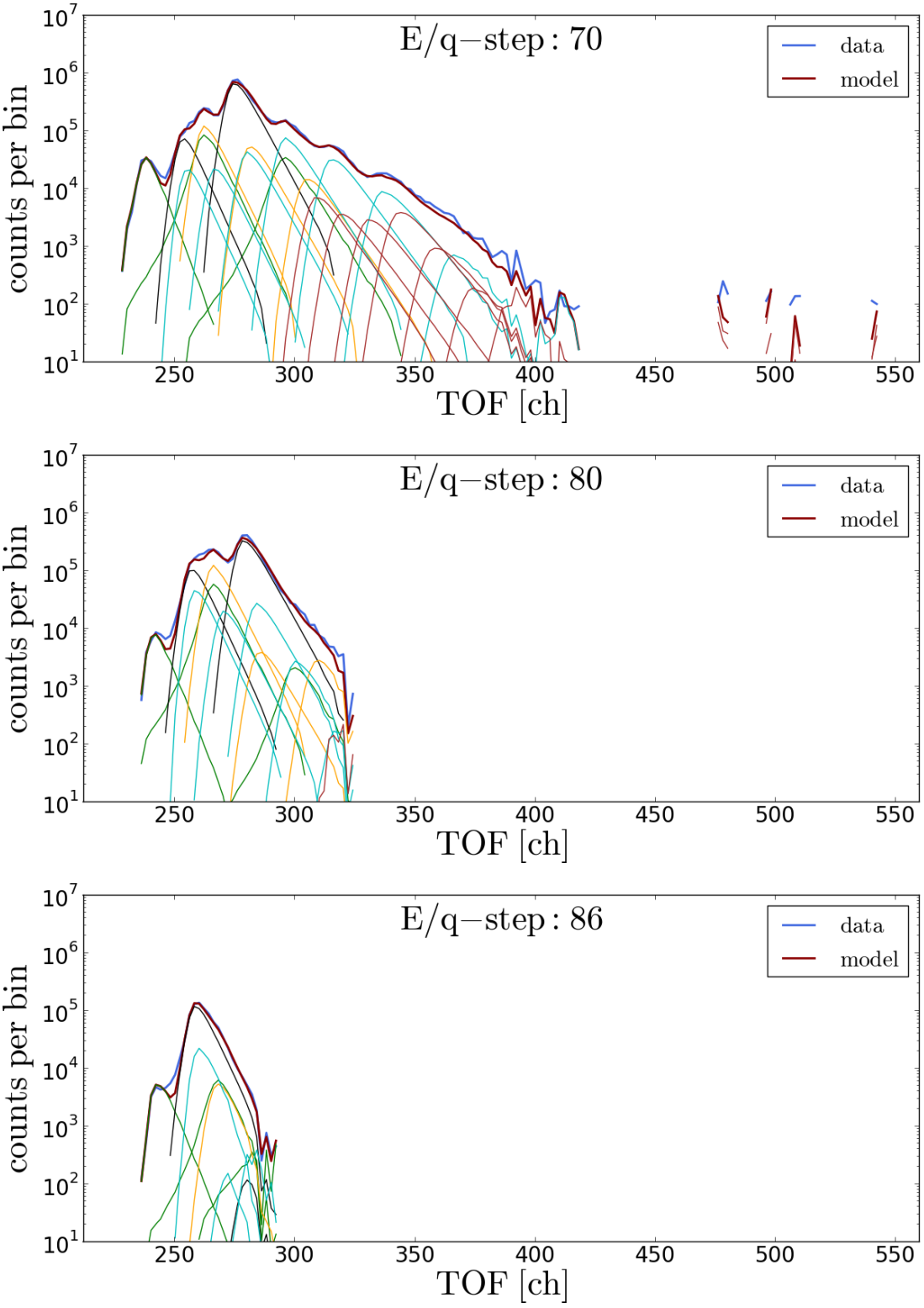

FIGURE C.46: ESSD-integrated logarithmic count rates of the long-term measurements and the fitted Kappa-Moyal Reduced Stable response model for Epq-steps 70, 80 and 86.

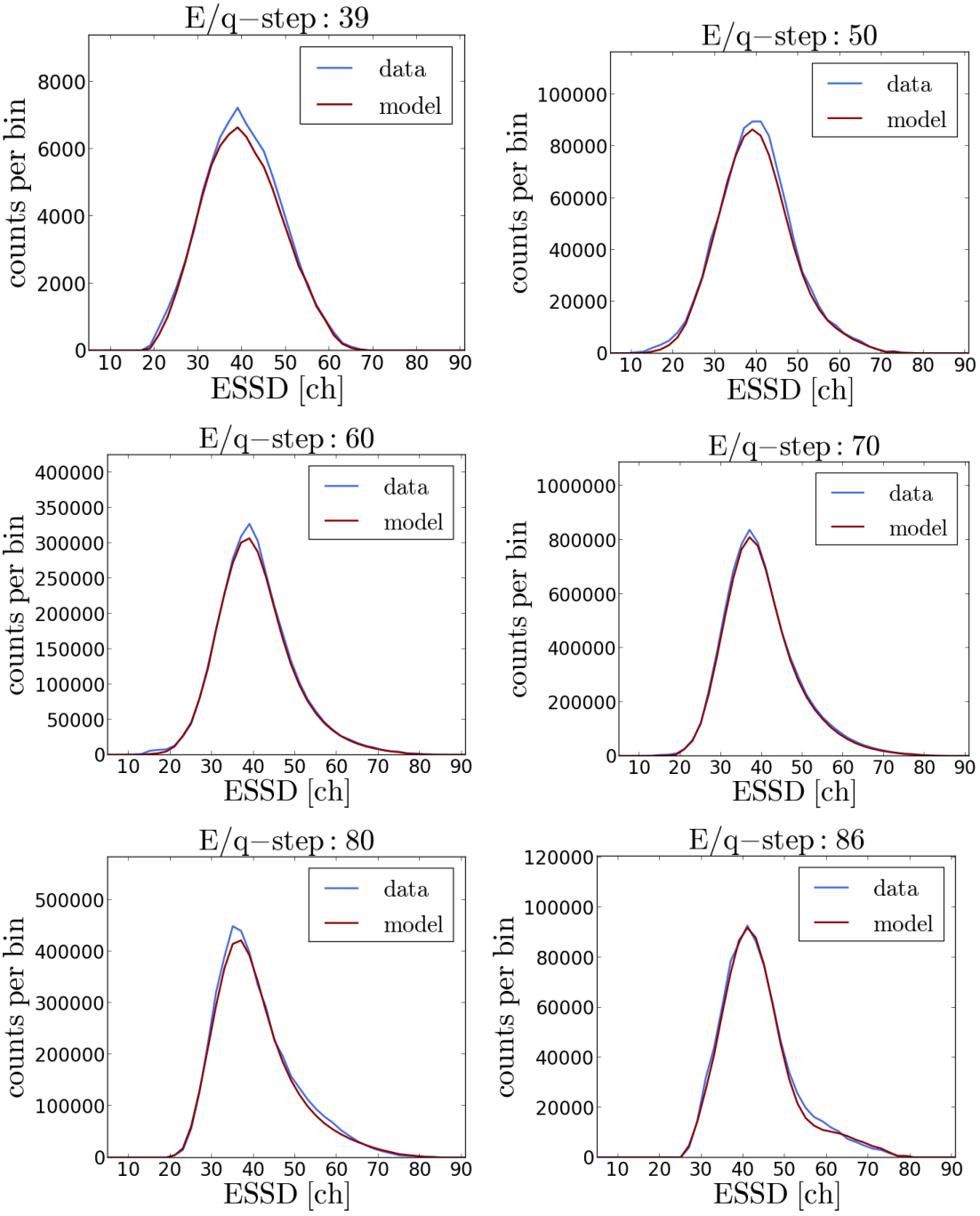

FIGURE C.47: TOF-integrated count rates of the long-term measurements and the fitted Kappa-Moyal Reduced Stable response model for Epq-steps 39 - 86.

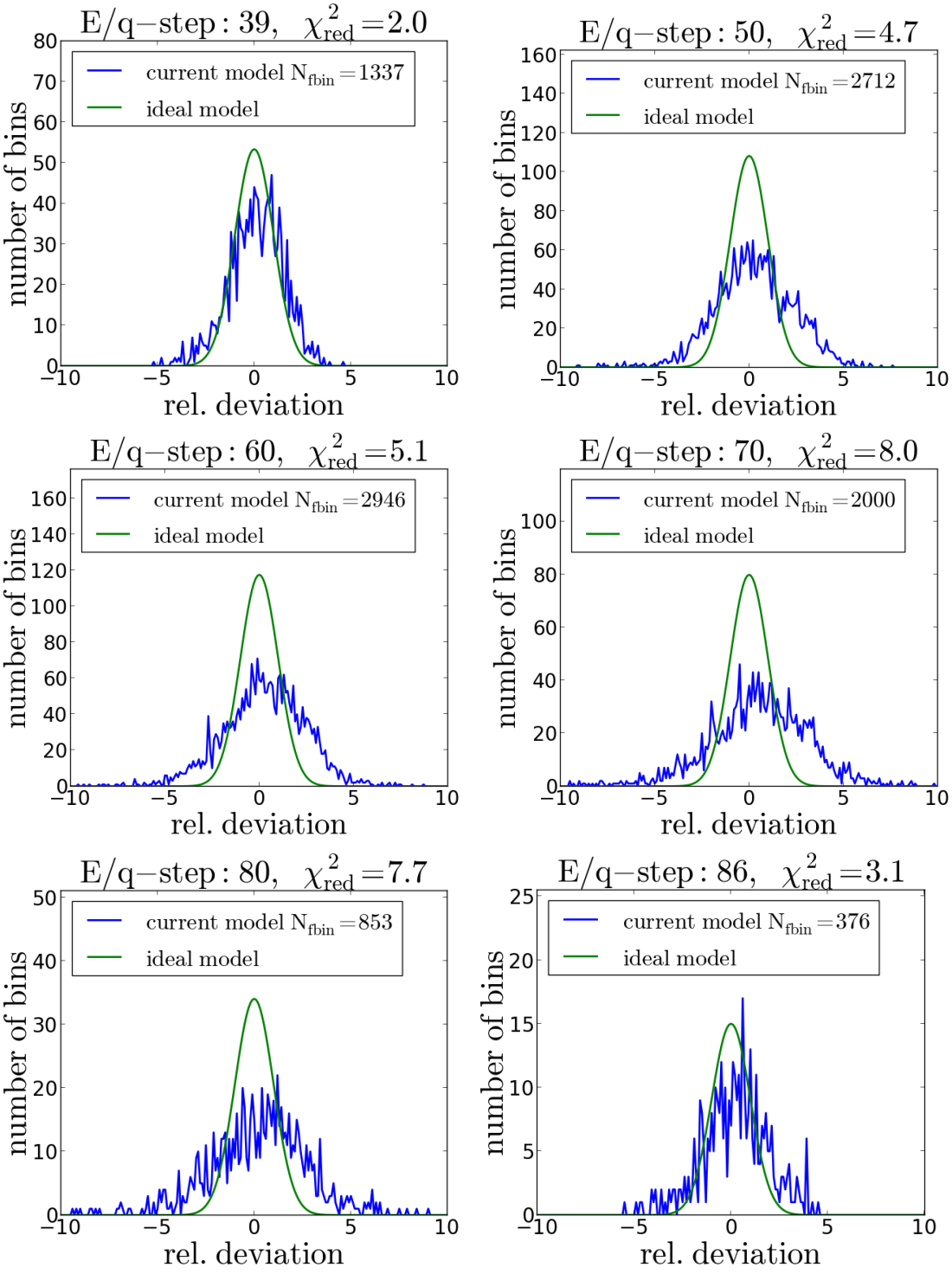

FIGURE C.48: Histograms of the relative deviations (blue) between the measured long-term data and the fitted Kappa-Moyal Reduced Stable response model for Epq-steps 39-86 in comparison to a relative deviation distribution that would arise from a perfect model $\chi^2_{red} = 1$ purely due to statistical deviations (green).

Appendix D

Heavy Ion Long-Term Speed Spectra Measured with CELIAS/CTOF

In this appendix we present a more comprehensive overview of long-term heavy ion speed spectra (recorded over the measurement period DOY 174-220, 1996) than we could discuss in detail in chapter 5. In total we show spectra of 43 ion species belonging to ten elements: carbon, nitrogen, oxygen, neon, magnesium, silicon, sulfur, calcium, iron and nickel. Among these elements we focus on those charge states that are expected to occur with the highest abundances after [Arnaud and Rothenflug, 1985]. The observed charge state distributions are in good agreement with these expectations for all elements, except for nickel, where one expects the most probable charge state between Ni^{8+} and Ni^{10+} for the estimated coronal temperature range. In fact the nickel spectra are probably to a large part contaminated by the much more abundant iron ions and cannot be regarded as reliable, so that nickel ions are not included in the differential speed analysis in chapter 5 and we only show them for completeness in Figure D.11, where some nickel charge state speed spectra might be true signatures due to the higher counting statistics in the slow wind case. Calcium has a comparably low elemental abundance as nickel but due to the fact that at coronal temperatures of $T \approx 10^6$ K the species Ca^{10+} is by far the most dominant charge state, we are able to resolve the core of the speed spectrum for Ca^{10+} reasonably well as can be seen from Figures D.9 and D.26.

As described in sections 5.4 and 5.5 we derived the ion speed spectra with the CTOF Full and Reduced Stable response model (defined in section 4.6) both for the slow wind case ($v_p \in [330\,\mathrm{km/s}, 340\,\mathrm{km/s}]$) and the fast wind case ($v_p \in [500\,\mathrm{km/s}, 510\,\mathrm{km/s}]$). We thus present in the following the corresponding 2×2 sets of speed spectra that lead to the mean differential speeds shown in Figures 5.8, 5.9 and 5.15, 5.16, respectively.

D.1 Long-Term Slow Wind Speed Spectra Obtained from the Kappa-Moyal Full Stable Response Model

As described in section 4.6 in the CTOF Full Stable Response Model we included 69 ion species in the fit of which we show here 42 ion species for the analyzed slow wind case ($v_p \in [330\,\mathrm{km/s}, 340\,\mathrm{km/s}]$). As further described in section 4.5 we used as optimal (TOF-position-dependent) tail scaling parameter $A_C = 0.0035\,\mathrm{ch}^{-1}$ to model the Kappa-Moyal peak shape for all ion species.

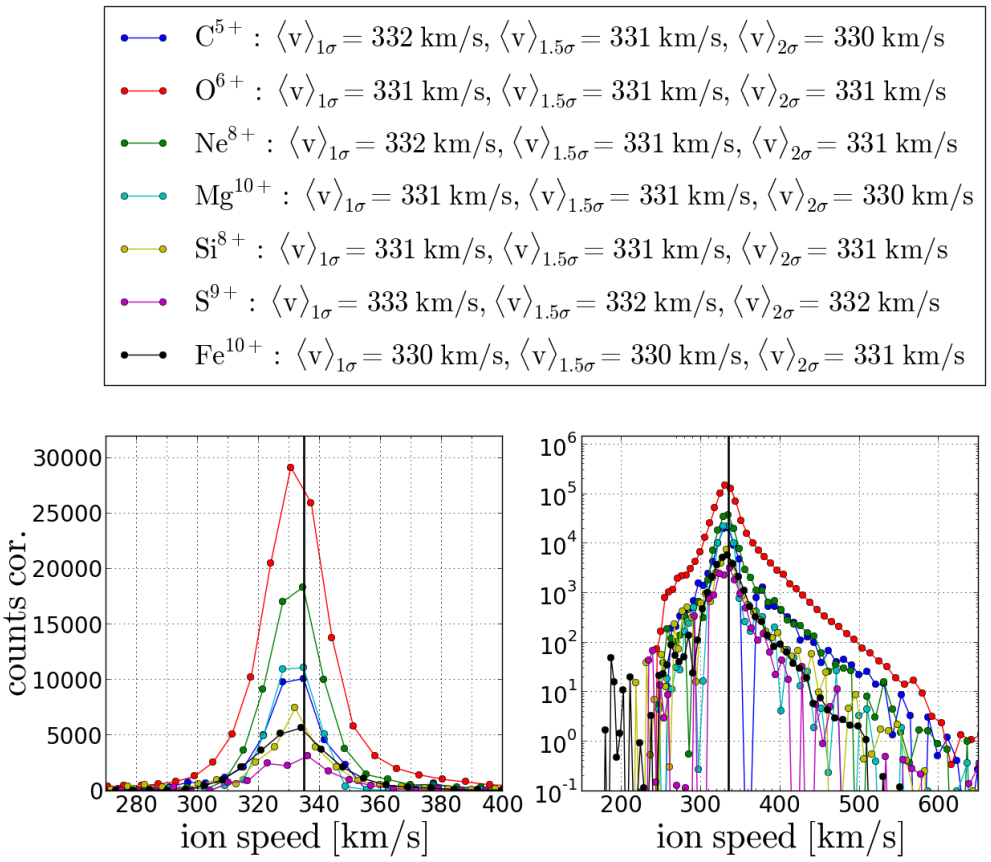

FIGURE D.1: Long-term accumulated speed spectra for C^{5+} - Fe^{10+} under the condition $v_p \in [330\,\mathrm{km/s}, 340\,\mathrm{km/s}]$ for the measurement period DOY 174-220, 1996. The spectra are shown in phase-space-corrected linear (left) and logarithmic (right) count rate scale. In the linear scaling the count rates of C^{5+}, O^{6+}, Ne^{8+} and Mg^{10+} are scaled down with a factor of 0.5., 0.2, 0.5, and 0.5, respectively. The black vertical line marks the mean proton speed.

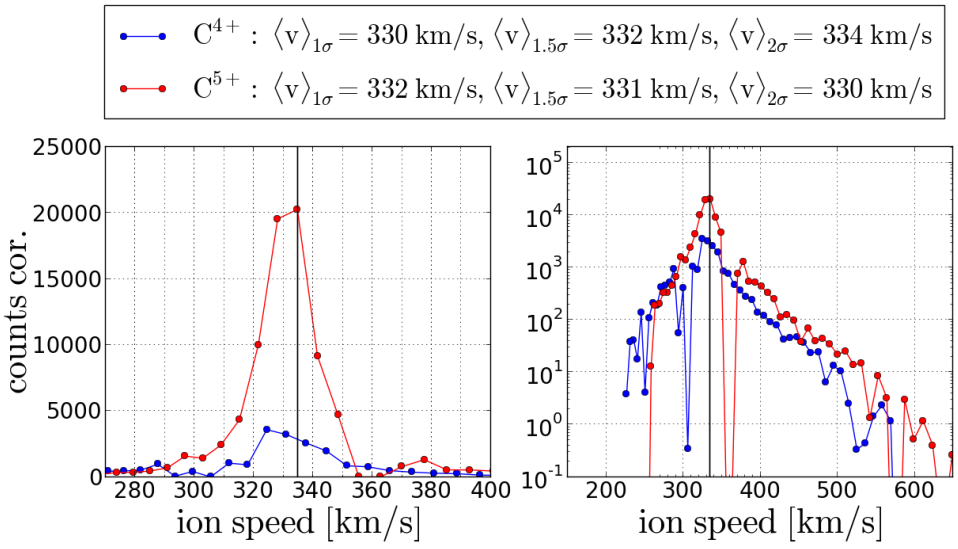

FIGURE D.2: Long-term accumulated speed spectra for C^{4+} - C^{5+} under the condition $v_p \in [330\,\text{km/s}, 340\,\text{km/s}]$ for the measurement period DOY 174-220, 1996. The spectra are shown in phase-space-corrected linear (left) and logarithmic (right) count rate scale. The black vertical line marks the mean proton speed.

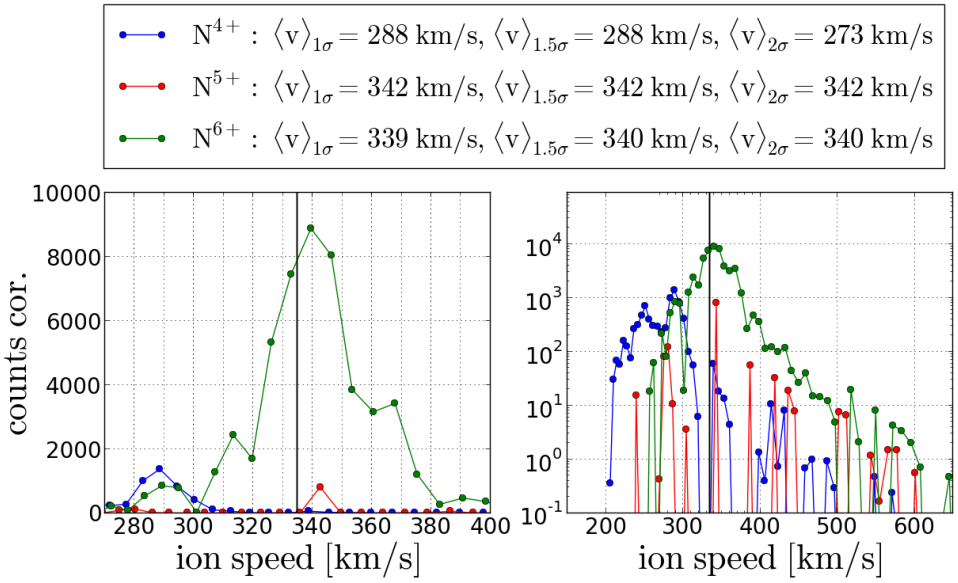

FIGURE D.3: Long-term accumulated speed spectra for N^{4+} - N^{6+} under the condition $v_p \in [330\,\text{km/s}, 340\,\text{km/s}]$ for the measurement period DOY 174-220, 1996. The spectra are shown in phase-space-corrected linear (left) and logarithmic (right) count rate scale. The black vertical line marks the mean proton speed.

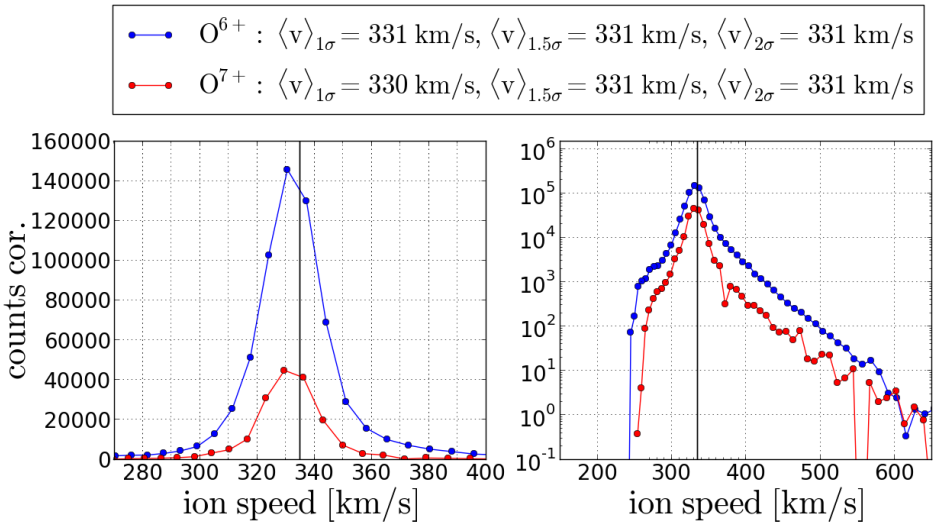

FIGURE D.4: Long-term accumulated speed spectra for O^{6+} - O^{7+} under the condition $v_p \in [330\,\mathrm{km/s}, 340\,\mathrm{km/s}]$ for the measurement period DOY 174-220, 1996. The spectra are shown in phase-space-corrected linear (left) and logarithmic (right) count rate scale. The black vertical line marks the mean proton speed.

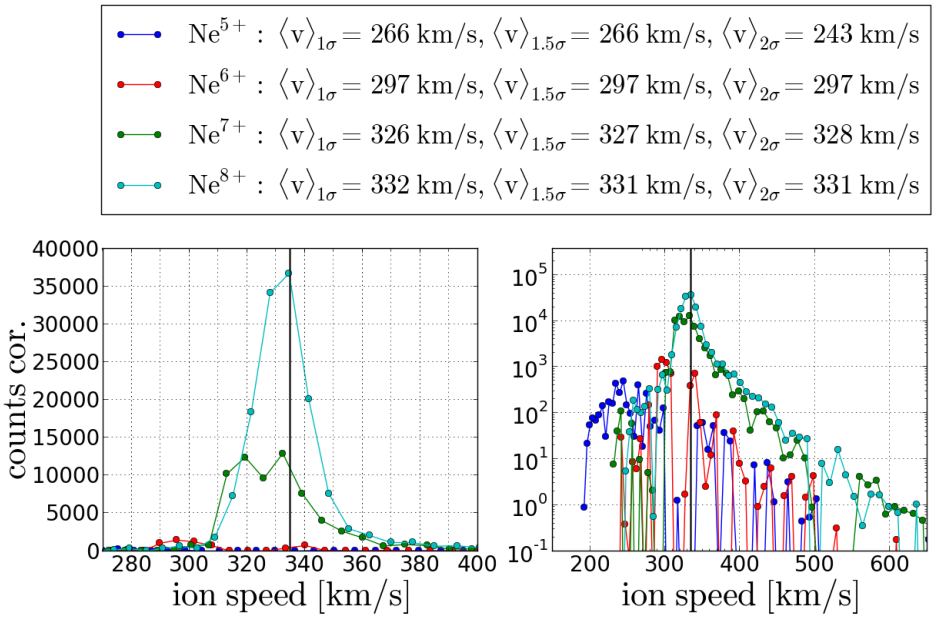

FIGURE D.5: Long-term accumulated speed spectra for Ne^{5+} - Ne^{8+} under the condition $v_p \in [330\,\mathrm{km/s}, 340\,\mathrm{km/s}]$ for the measurement period DOY 174-220, 1996. The spectra are shown in phase-space-corrected linear (left) and logarithmic (right) count rate scale. The black vertical line marks the mean proton speed.

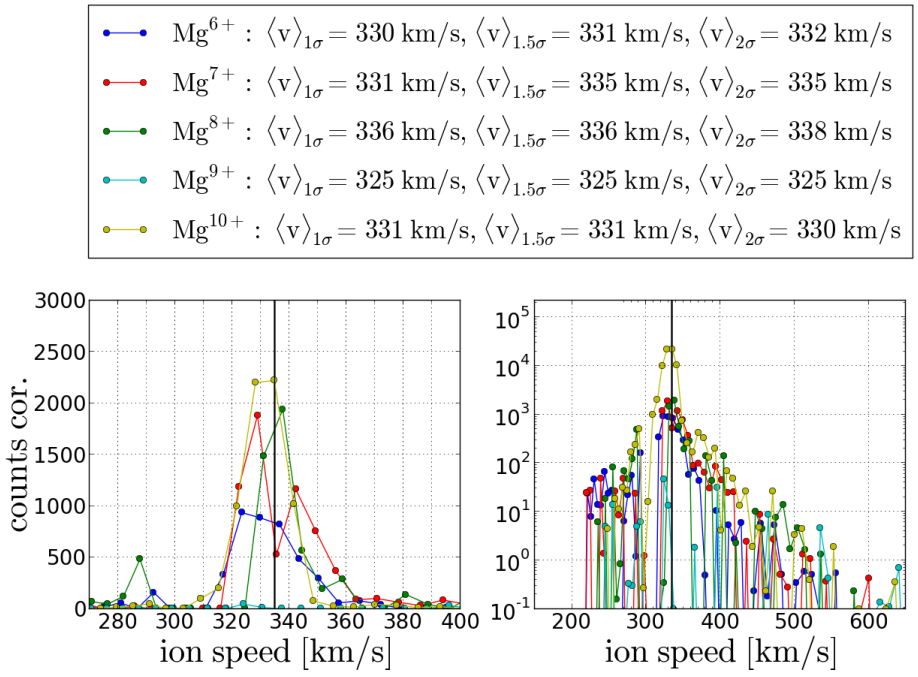

FIGURE D.6: Long-term accumulated speed spectra for Mg^{6+} - Mg^{10+} under the condition $v_p \in [330\,\text{km/s}, 340\,\text{km/s}]$ for the measurement period DOY 174-220, 1996. The spectra are shown in phase-space-corrected linear (left) and logarithmic (right) count rate scale. In the linear scaling the count rates of Mg^{10+} are scaled down with a factor of 0.1. The black vertical line marks the mean proton speed.

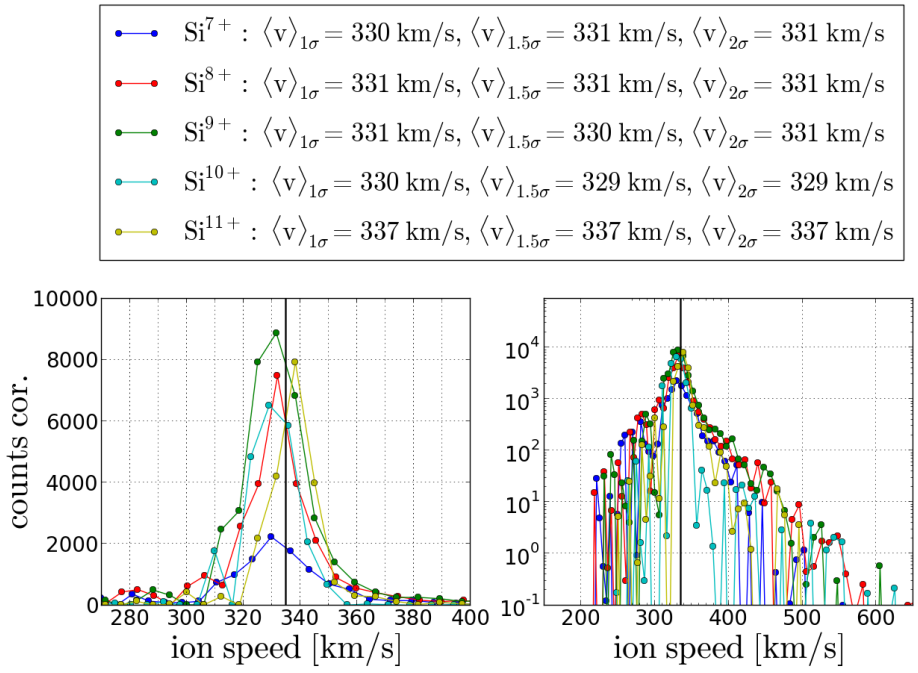

FIGURE D.7: Long-term accumulated speed spectra for Si^{7+} - Si^{11+} under the condition $v_p \in [330\,\text{km/s}, 340\,\text{km/s}]$ for the measurement period DOY 174-220, 1996. The spectra are shown in phase-space-corrected linear (left) and logarithmic (right) count rate scale. The black vertical line marks the mean proton speed.

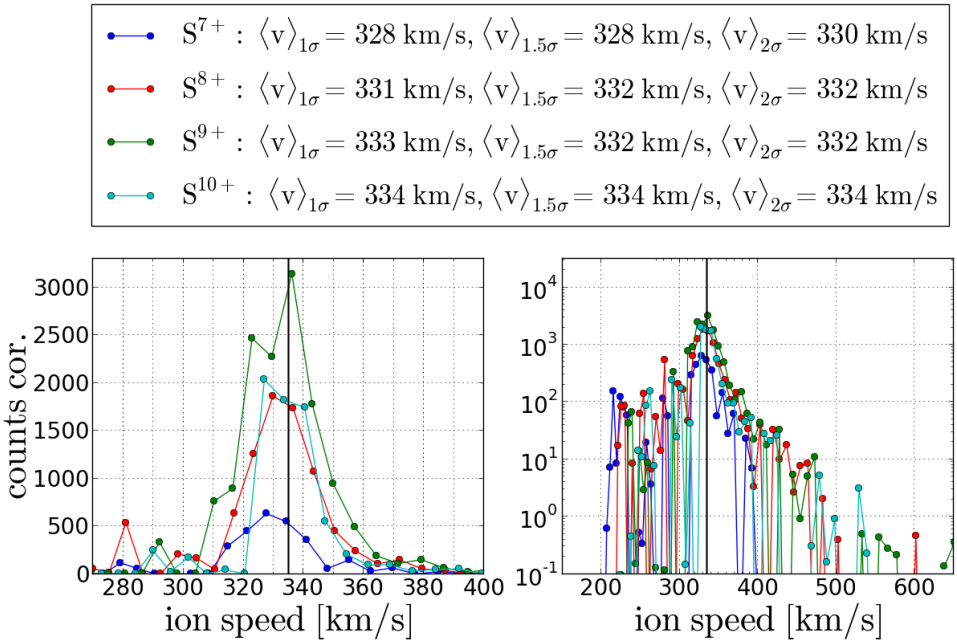

FIGURE D.8: Long-term accumulated speed spectra for S^{7+} - S^{10+} under the condition $v_p \in [330\,\mathrm{km/s}, 340\,\mathrm{km/s}]$ for the measurement period DOY 174-220, 1996. The spectra are shown in phase-space-corrected linear (left) and logarithmic (right) count rate scale. The black vertical line marks the mean proton speed.

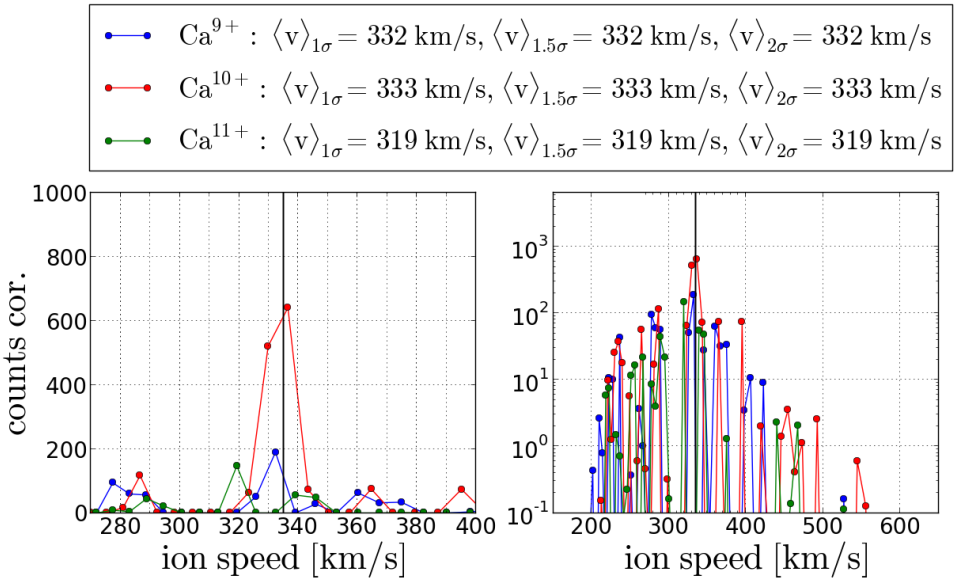

FIGURE D.9: Long-term accumulated speed spectra for Ca^{9+} - Ca^{11+} under the condition $v_p \in [330\,\mathrm{km/s}, 340\,\mathrm{km/s}]$ for the measurement period DOY 174-220, 1996. The spectra are shown in phase-space-corrected linear (left) and logarithmic (right) count rate scale. The black vertical line marks the mean proton speed.

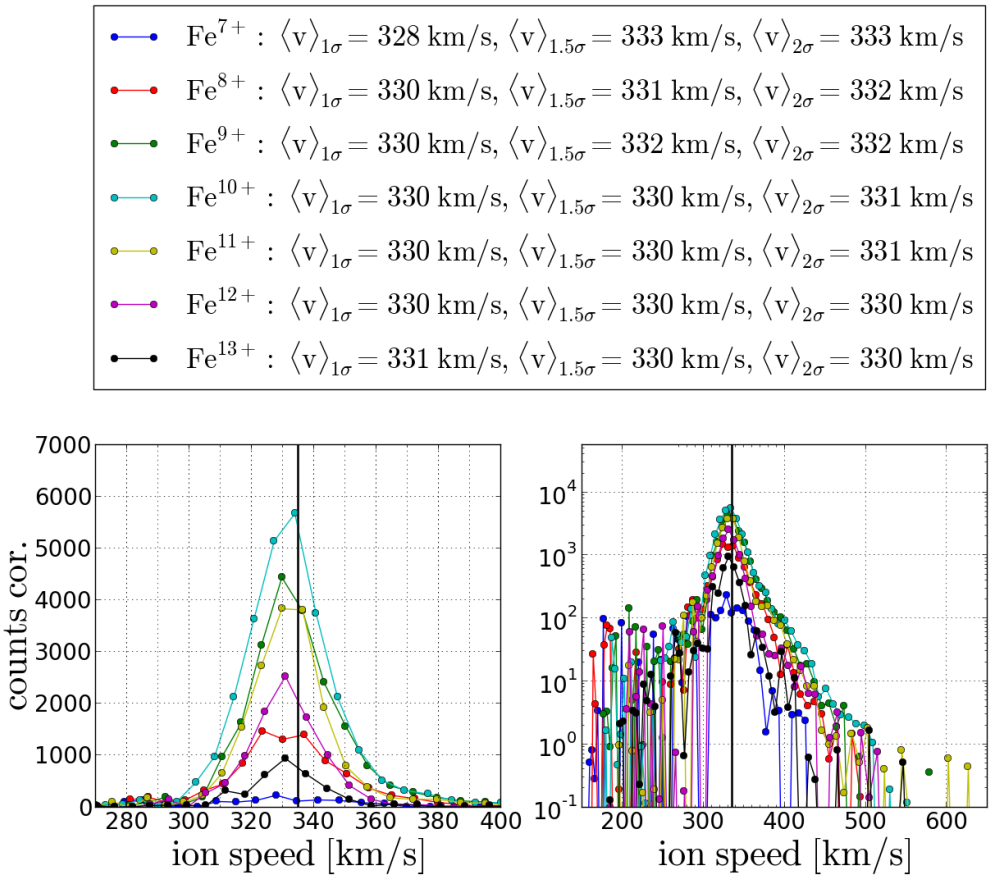

FIGURE D.10: Long-term accumulated speed spectra for Fe^{7+} - Fe^{13+} under the condition $v_p \in [330\,\mathrm{km/s}, 340\,\mathrm{km/s}]$ for the measurement period DOY 174-220, 1996. The spectra are shown in phase-space-corrected linear (left) and logarithmic (right) count rate scale. The black vertical line marks the mean proton speed.

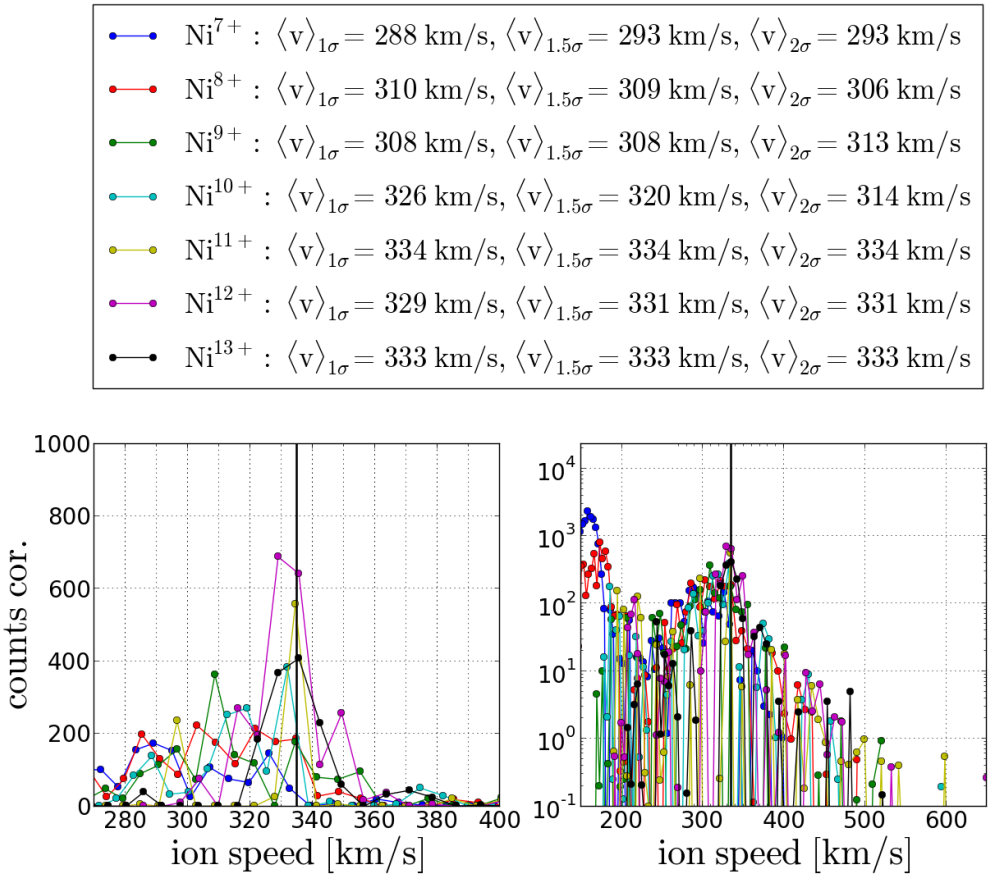

FIGURE D.11: Long-term accumulated speed spectra for Ni^{7+} - Ni^{13+} under the condition $v_p \in [330\,\mathrm{km/s}, 340\,\mathrm{km/s}]$ for the measurement period DOY 174-220, 1996. The spectra are shown in phase-space-corrected linear (left) and logarithmic (right) count rate scale. The increased count rates at $v_{ion} < 200\,\mathrm{km/s}$ (mainly) for Ni^{7+} - Ni^{8+} are almost entirely He^{2+} random coincidences. The black vertical line marks the mean proton speed.

D.2 Long-Term Slow Wind Speed Spectra Obtained from the Kappa-Moyal Reduced Stable Response Model

As described in section 4.6 in the CTOF Reduced Stable Response Model we included 28 ion species in the fit, belonging to the five elements carbon, oxygen, neon, silicon and iron, of which we show here 19 ion species for the analyzed slow wind case ($v_p \in [330\,\mathrm{km/s}, 340\,\mathrm{km/s}]$). As further described in section 4.5 we used as optimal (TOF-position-dependent) tail scaling parameter $A_C = 0.0035\,\mathrm{ch}^{-1}$ to model the Kappa-Moyal peak shape for all ion species.

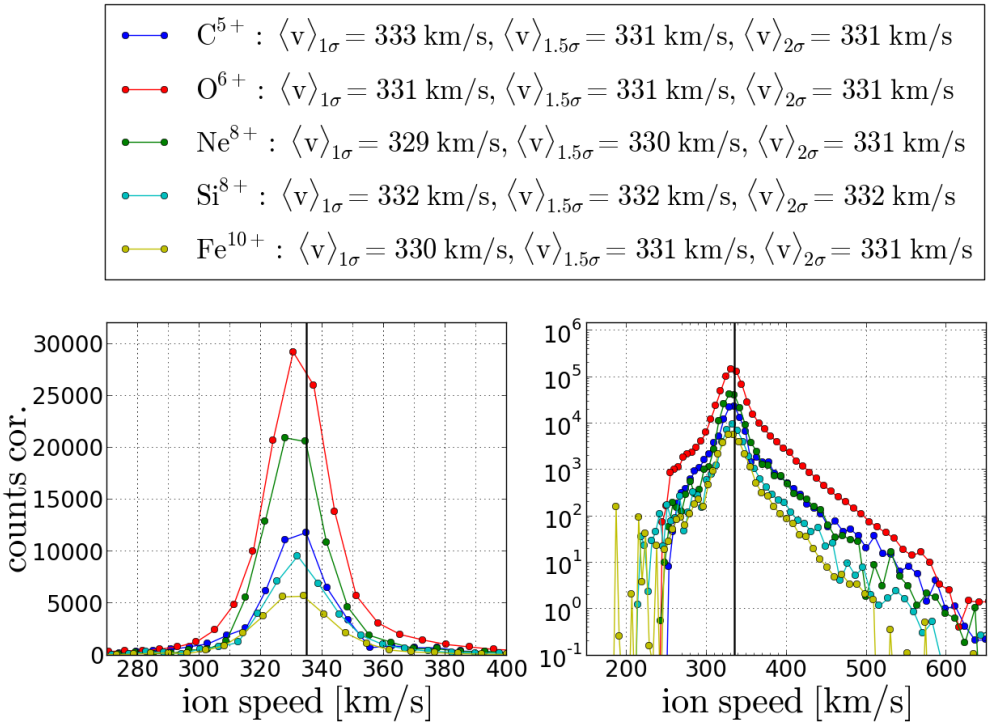

FIGURE D.12: Long-term accumulated speed spectra for C^{5+} - Fe^{10+} under the condition $v_p \in [330\,\mathrm{km/s}, 340\,\mathrm{km/s}]$ for the measurement period DOY 174-220, 1996. The spectra are shown in phase-space-corrected linear (left) and logarithmic (right) count rate scale. In the linear scaling the count rates of C^{5+}, O^{6+} and Ne^{8+} are scaled down with a factor of 0.5., 0.2 and 0.5, respectively. The black vertical line marks the mean proton speed.

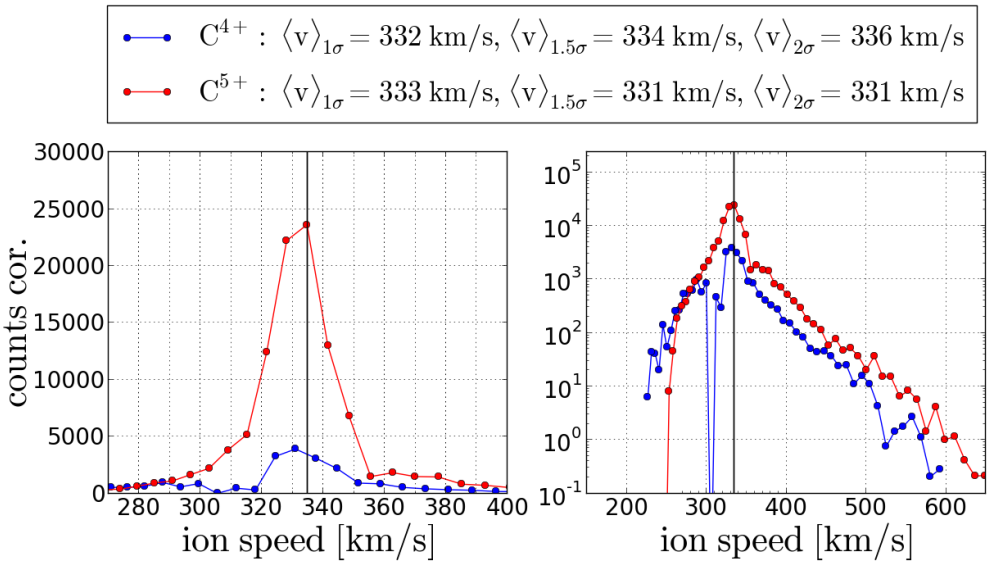

FIGURE D.13: Long-term accumulated speed spectra for C^{4+} - C^{5+} under the condition $v_p \in [330\,\mathrm{km/s}, 340\,\mathrm{km/s}]$ for the measurement period DOY 174-220, 1996. The spectra are shown in phase-space-corrected linear (left) and logarithmic (right) count rate scale. The black vertical line marks the mean proton speed.

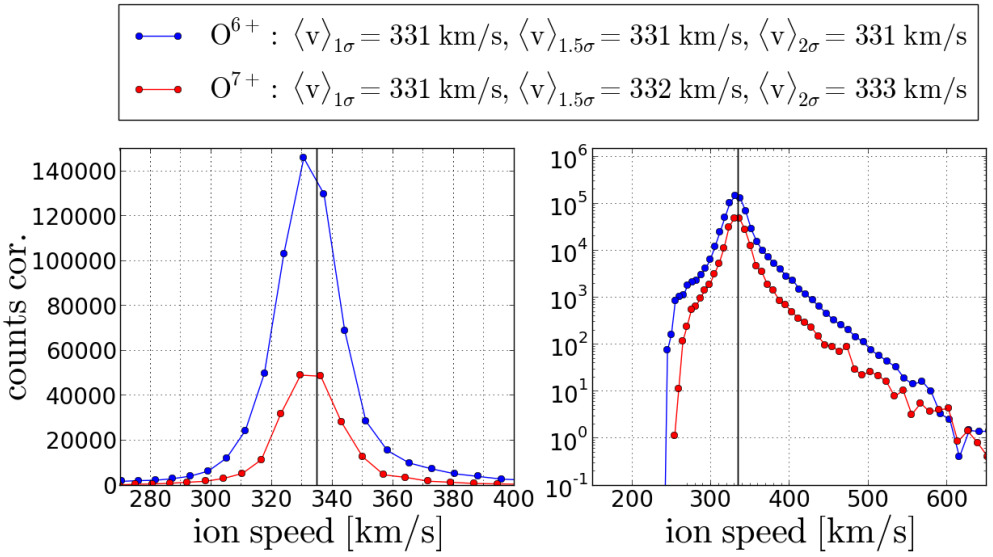

FIGURE D.14: Long-term accumulated speed spectra for O^{6+} - O^{7+} under the condition $v_p \in [330\,\mathrm{km/s}, 340\,\mathrm{km/s}]$ for the measurement period DOY 174-220, 1996. The spectra are shown in phase-space-corrected linear (left) and logarithmic (right) count rate scale. The black vertical line marks the mean proton speed.

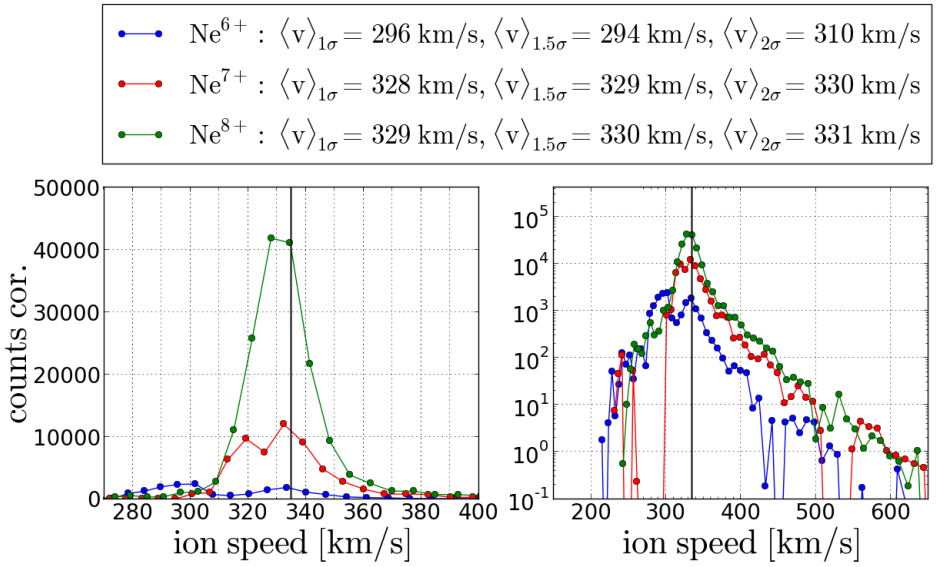

FIGURE D.15: Long-term accumulated speed spectra for Ne^{6+} - Ne^{8+} under the condition $v_p \in [330\,\text{km/s}, 340\,\text{km/s}]$ for the measurement period DOY 174-220, 1996. The spectra are shown in phase-space-corrected linear (left) and logarithmic (right) count rate scale. The black vertical line marks the mean proton speed.

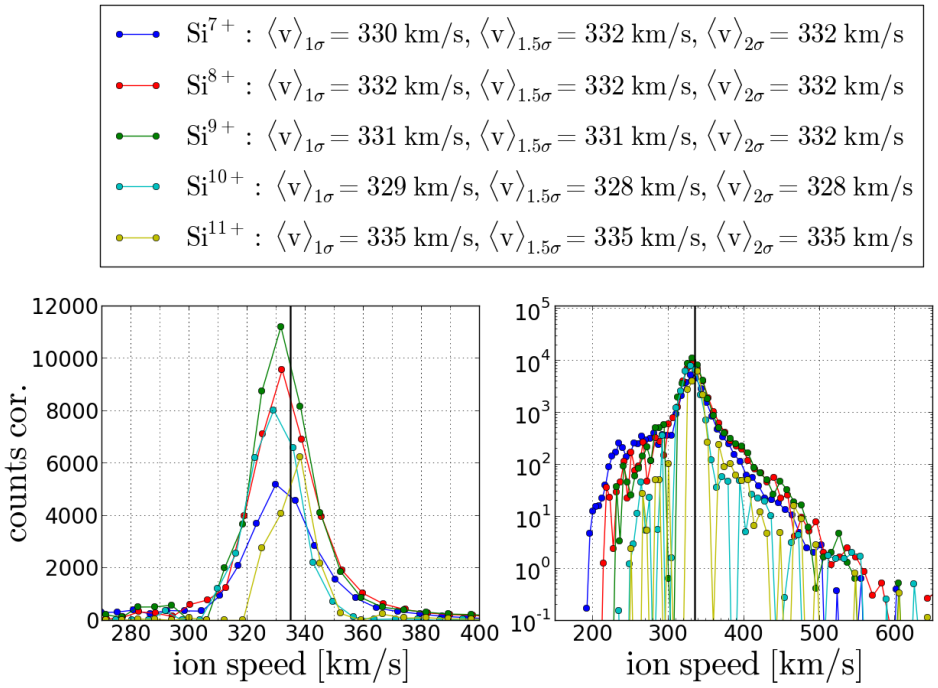

FIGURE D.16: Long-term accumulated speed spectra for Si^{7+} - Si^{11+} under the condition $v_p \in [330\,\text{km/s}, 340\,\text{km/s}]$ for the measurement period DOY 174-220, 1996. The spectra are shown in phase-space-corrected linear (left) and logarithmic (right) count rate scale. The black vertical line marks the mean proton speed.

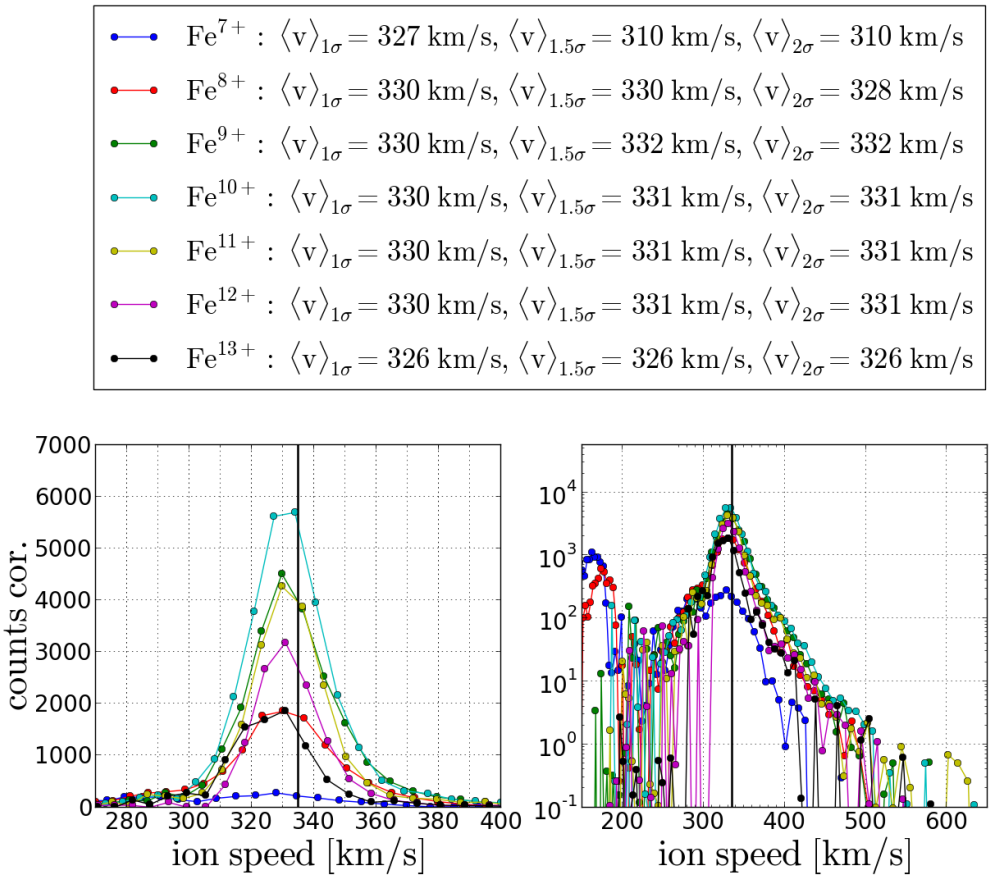

FIGURE D.17: Long-term accumulated speed spectra for Fe^{7+} - Fe^{13+} under the condition $v_p \in [330\,\mathrm{km/s}, 340\,\mathrm{km/s}]$ for the measurement period DOY 174-220, 1996. The spectra are shown in phase-space-corrected linear (left) and logarithmic (right) count rate scale. The black vertical line marks the mean proton speed.

D.3 Long-Term Fast Wind Speed Spectra Obtained from the Kappa-Moyal Full Stable Response Model

As described in section 4.6 in the CTOF Full Stable Response Model we included 69 ion species in the fit of which we show here 35 ion species for the analyzed fast wind case ($v_p \in [500\,\mathrm{km/s}, 510\,\mathrm{km/s}]$). As further described in section 4.5 we used as optimal (TOF-position-dependent) tail scaling parameter $A_C = 0.0035\,\mathrm{ch}^{-1}$ to model the Kappa-Moyal peak shape for all ion species.

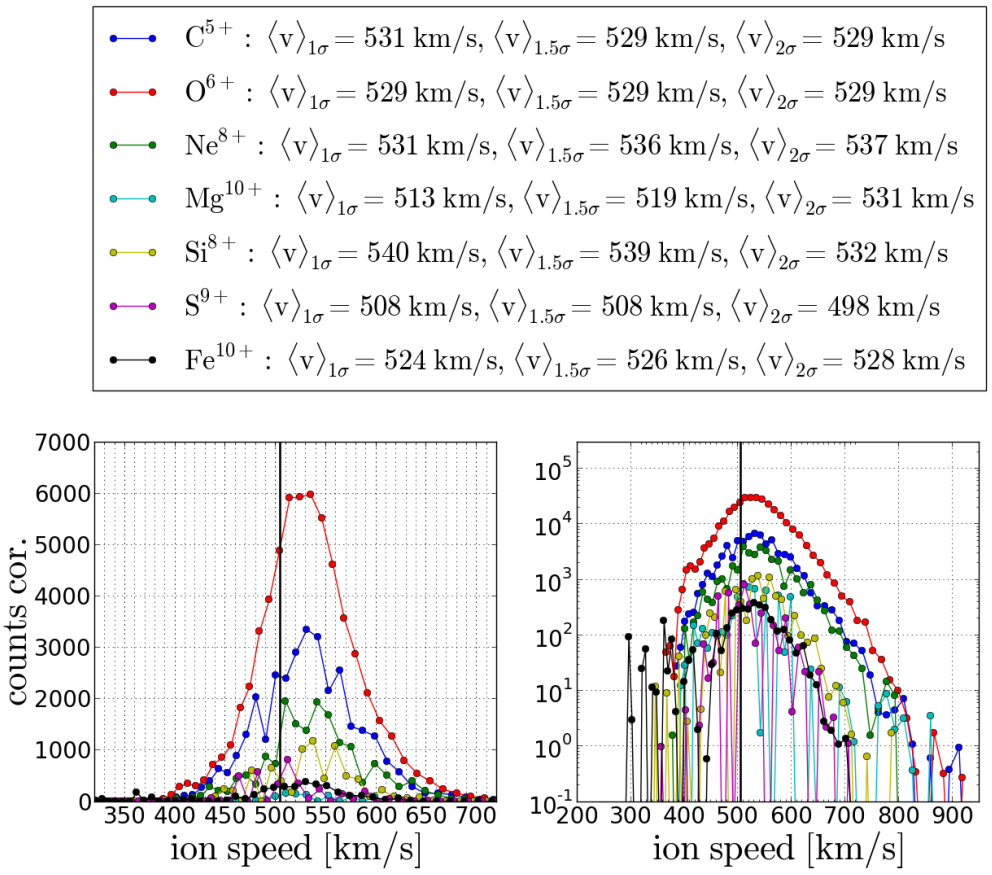

FIGURE D.18: Long-term accumulated speed spectra for C^{5+} - Fe^{10+} under the condition $v_p \in [500\,\mathrm{km/s}, 510\,\mathrm{km/s}]$ for the measurement period DOY 174-220, 1996. The spectra are shown in phase-space-corrected linear (left) and logarithmic (right) count rate scale. In the linear scaling the count rates of C^{5+}, O^{6+}, Ne^{8+} and Mg^{10+} are scaled down with a factor of 0.5., 0.2, 0.5, and 0.2 respectively. The black vertical line marks the mean proton speed.

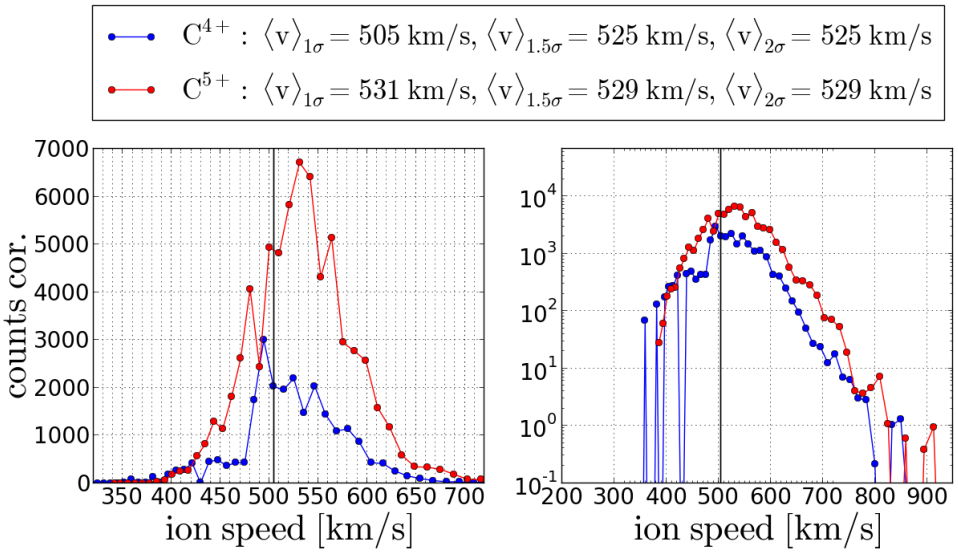

FIGURE D.19: Long-term accumulated speed spectra for C^{4+} - C^{5+} under the condition $v_p \in [500\,\mathrm{km/s}, 510\,\mathrm{km/s}]$ for the measurement period DOY 174-220, 1996. The spectra are shown in phase-space-corrected linear (left) and logarithmic (right) count rate scale. The black vertical line marks the mean proton speed.

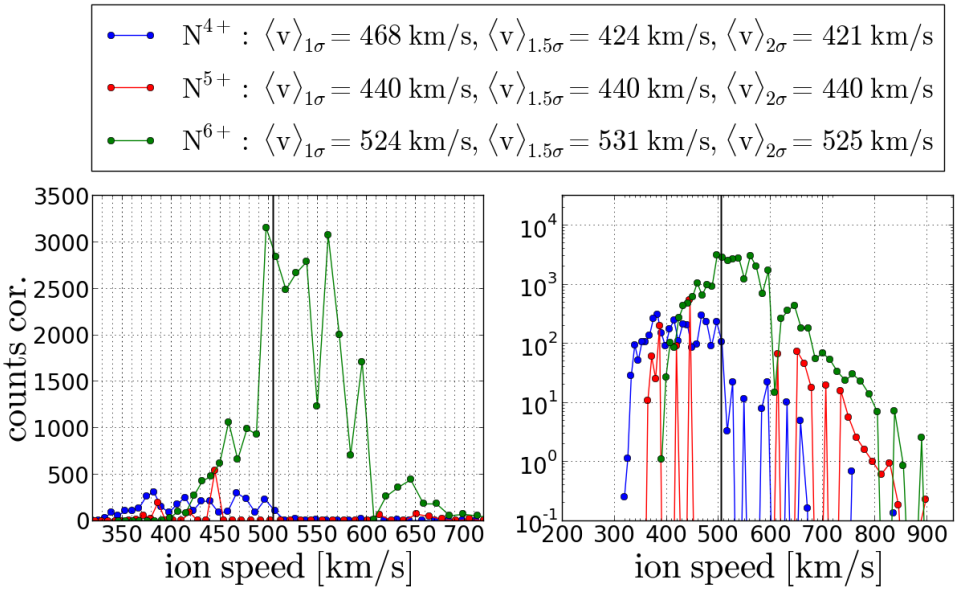

FIGURE D.20: Long-term accumulated speed spectra for N^{4+} - N^{6+} under the condition $v_p \in [500\,\mathrm{km/s}, 510\,\mathrm{km/s}]$ for the measurement period DOY 174-220, 1996. The spectra are shown in phase-space-corrected linear (left) and logarithmic (right) count rate scale. The black vertical line marks the mean proton speed.

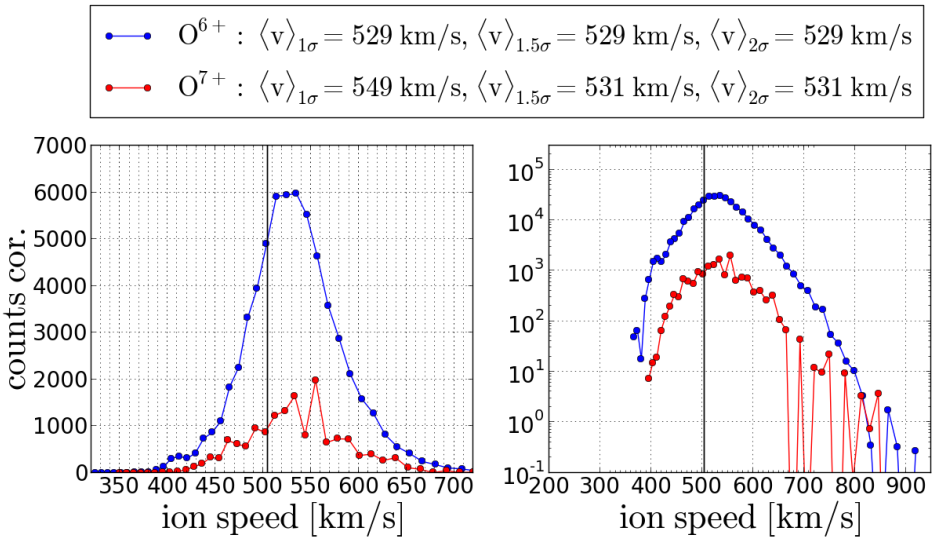

FIGURE D.21: Long-term accumulated speed spectra for O^{6+} - O^{7+} under the condition $v_p \in [500\,\mathrm{km/s}, 510\,\mathrm{km/s}]$ for the measurement period DOY 174-220, 1996. The spectra are shown in phase-space-corrected linear (left) and logarithmic (right) count rate scale. In the linear scaling the count rates of O^{6+} are scaled down with a factor of 0.2. The black vertical line marks the mean proton speed.

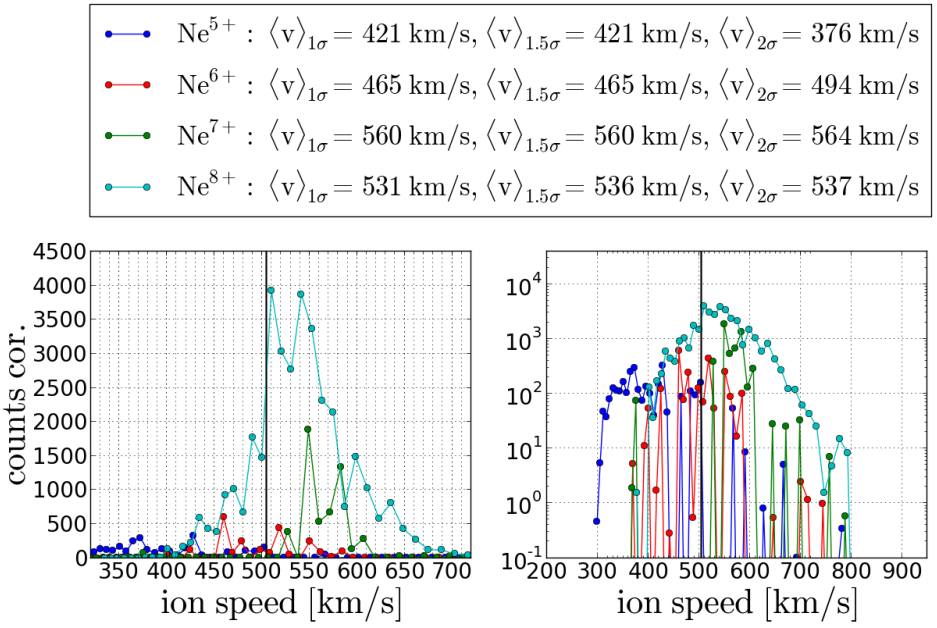

FIGURE D.22: Long-term accumulated speed spectra for Ne^{5+} - Ne^{8+} under the condition $v_p \in [500\,\mathrm{km/s}, 510\,\mathrm{km/s}]$ for the measurement period DOY 174-220, 1996. The spectra are shown in phase-space-corrected linear (left) and logarithmic (right) count rate scale. The black vertical line marks the mean proton speed.

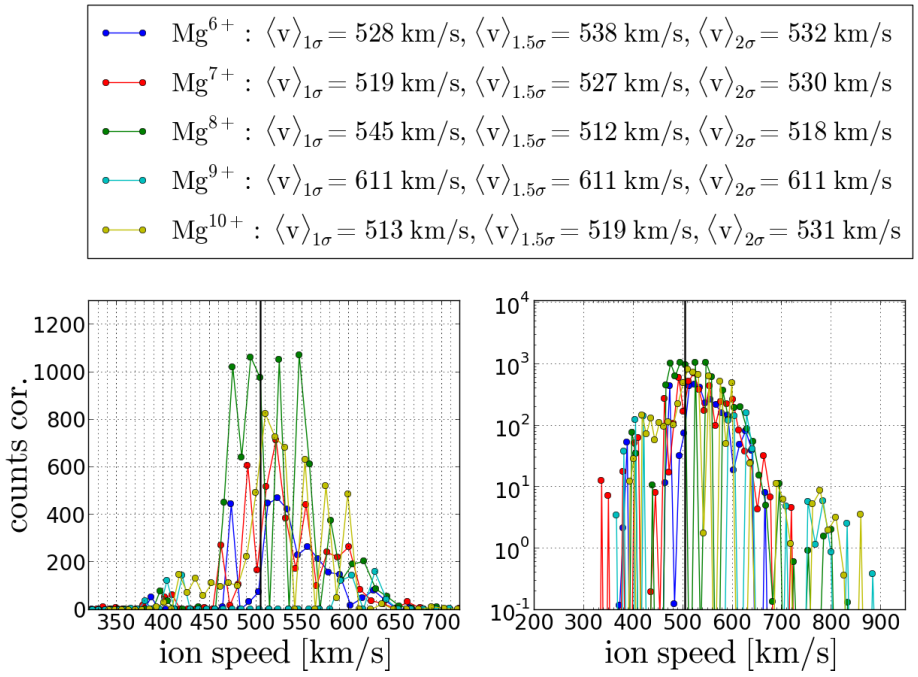

FIGURE D.23: Long-term accumulated speed spectra for Mg^{6+} - Mg^{10+} under the condition $v_p \in [500\,\mathrm{km/s}, 510\,\mathrm{km/s}]$ for the measurement period DOY 174-220, 1996. The spectra are shown in phase-space-corrected linear (left) and logarithmic (right) count rate scale. The black vertical line marks the mean proton speed.

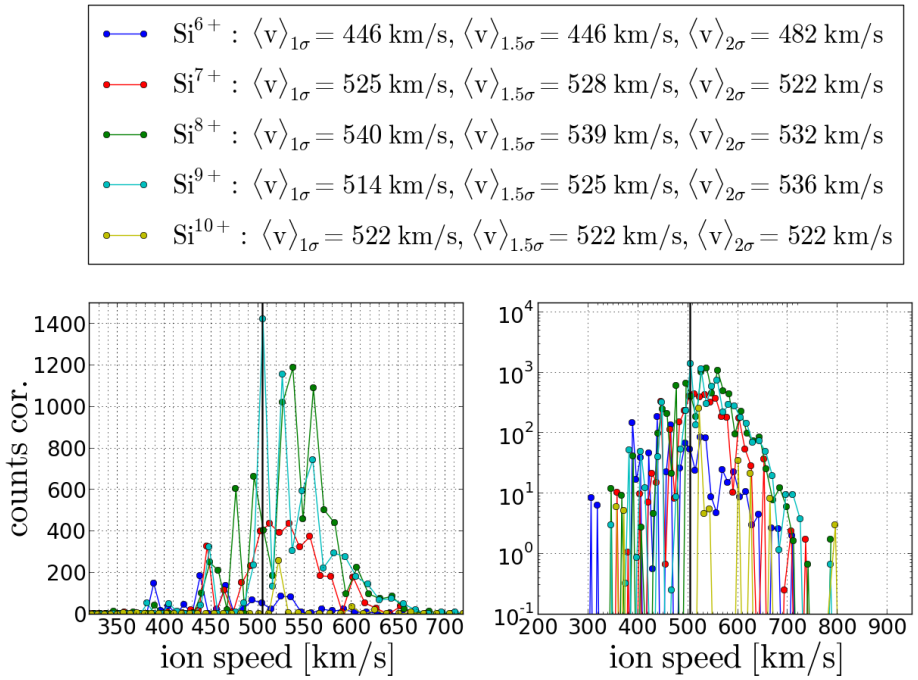

FIGURE D.24: Long-term accumulated speed spectra for Si^{6+} - Si^{10+} under the condition $v_p \in [500\,\mathrm{km/s}, 510\,\mathrm{km/s}]$ for the measurement period DOY 174-220, 1996. The spectra are shown in phase-space-corrected linear (left) and logarithmic (right) count rate scale. The black vertical line marks the mean proton speed.

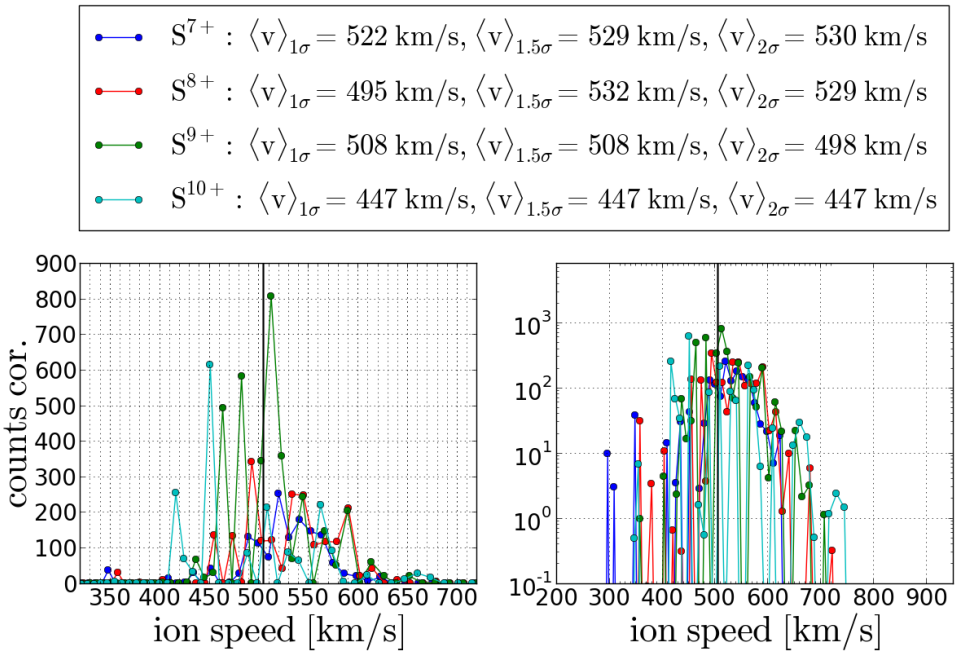

FIGURE D.25: Long-term accumulated speed spectra for S^{7+} - S^{10+} under the condition $v_p \in [500\,\text{km/s}, 510\,\text{km/s}]$ for the measurement period DOY 174-220, 1996. The spectra are shown in phase-space-corrected linear (left) and logarithmic (right) count rate scale. The black vertical line marks the mean proton speed.

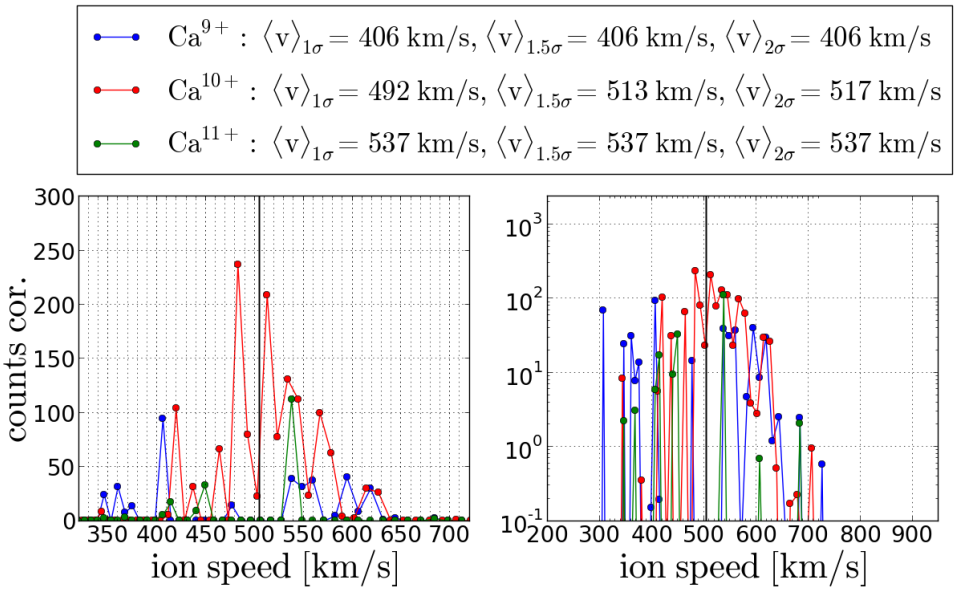

FIGURE D.26: Long-term accumulated speed spectra for Ca^{9+} - Ca^{11+} under the condition $v_p \in [500\,\text{km/s}, 510\,\text{km/s}]$ for the measurement period DOY 174-220, 1996. The spectra are shown in phase-space-corrected linear (left) and logarithmic (right) count rate scale. The black vertical line marks the mean proton speed.

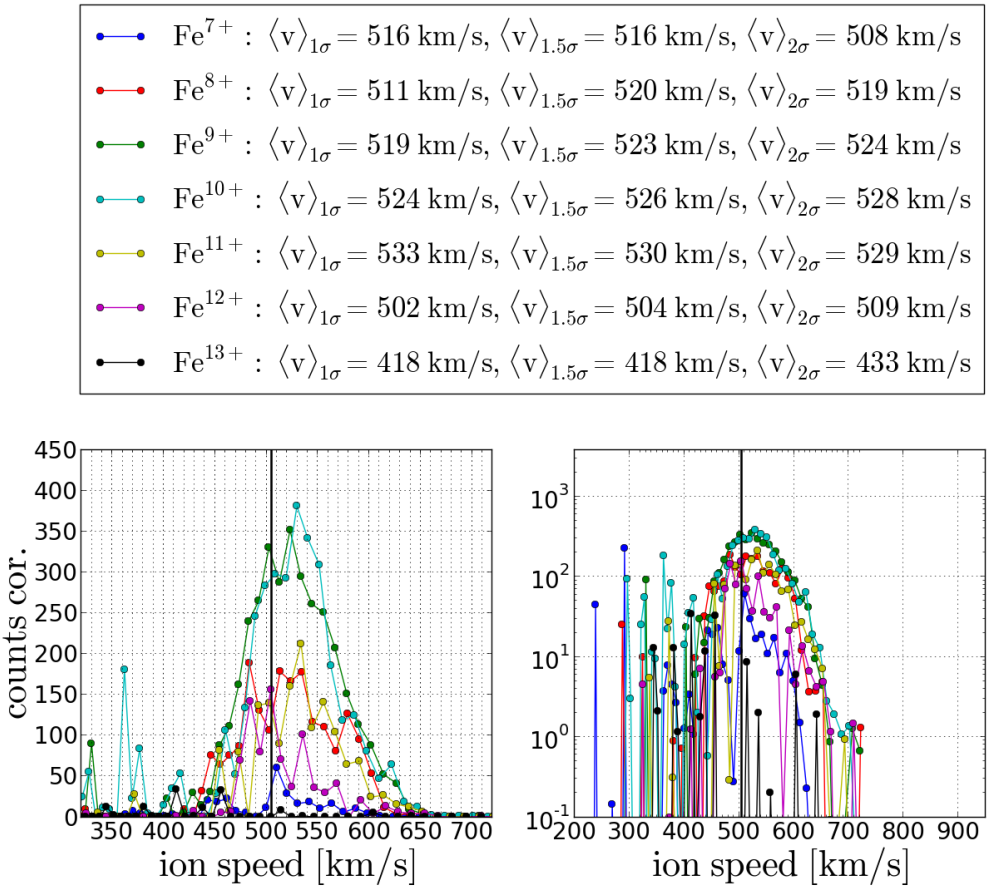

FIGURE D.27: Long-term accumulated speed spectra for Fe^{7+} - Fe^{13+} under the condition $v_p \in [500\,\mathrm{km/s}, 510\,\mathrm{km/s}]$ for the measurement period DOY 174-220, 1996. The spectra are shown in phase-space-corrected linear (left) and logarithmic (right) count rate scale. The black vertical line marks the mean proton speed.

D.4 Long-Term Fast Wind Speed Spectra Obtained from the Kappa-Moyal Reduced Stable Response Model

As described in section 4.6 in the CTOF Reduced Stable Response Model we included 28 ion species in the fit, belonging to the five elements carbon, oxygen, neon, silicon and iron, of which we show here 19 ion species for the analyzed slow wind case ($v_p \in [500\,\mathrm{km/s}, 510\,\mathrm{km/s}]$). As further described in section 4.5 we used as optimal (TOF-position-dependent) tail scaling parameter $A_C = 0.0035\,\mathrm{ch}^{-1}$ to model the Kappa-Moyal peak shape for all ion species.

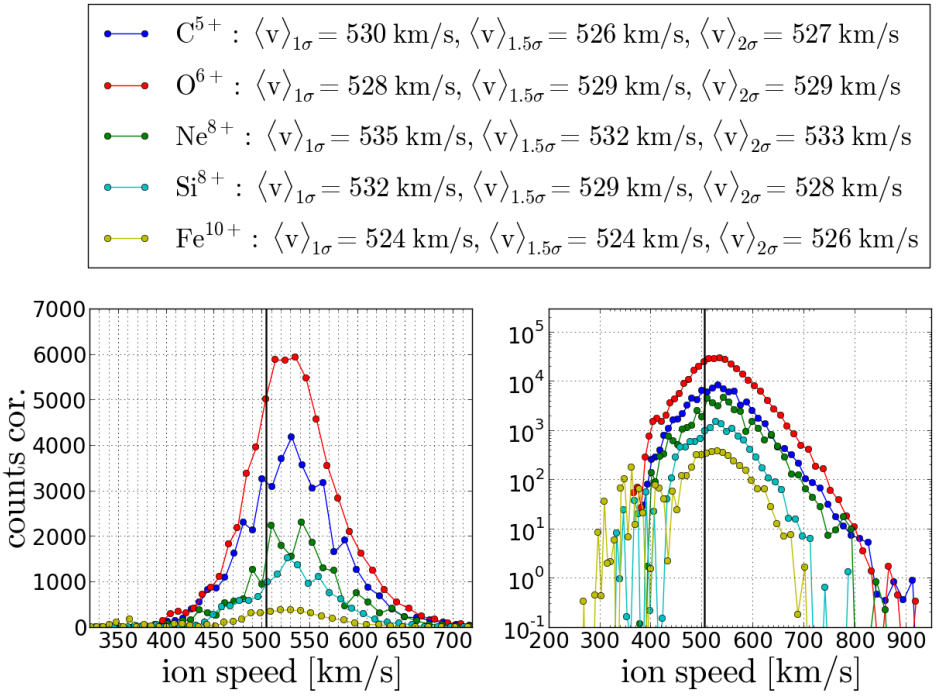

FIGURE D.28: Long-term accumulated speed spectra for C^{5+} - Fe^{10+} under the condition $v_p \in [500\,\mathrm{km/s}, 510\,\mathrm{km/s}]$ for DOY 174-220, 1996. The spectra are shown in phase-space-corrected linear (left) and logarithmic (right) count rate scale. In the linear scaling the count rates of C^{5+}, O^{6+} and Ne^{8+} are scaled down with a factor of 0.5., 0.2 and 0.5, respectively. The black vertical line marks the mean proton speed.

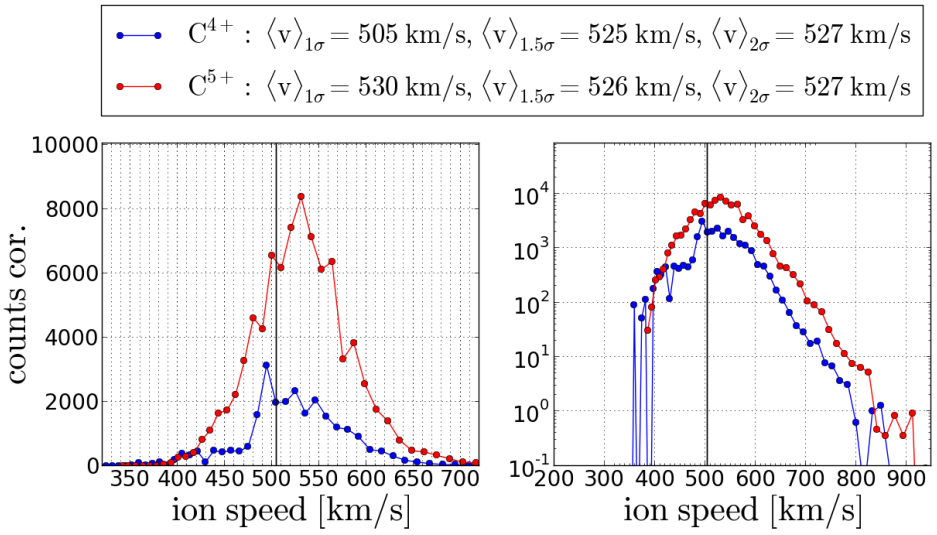

FIGURE D.29: Long-term accumulated speed spectra for C^{4+} - C^{5+} under the condition $v_p \in [500\,\mathrm{km/s}, 510\,\mathrm{km/s}]$ for the measurement period DOY 174-220, 1996. The spectra are shown in phase-space-corrected linear (left) and logarithmic (right) count rate scale. The black vertical line marks the mean proton speed.

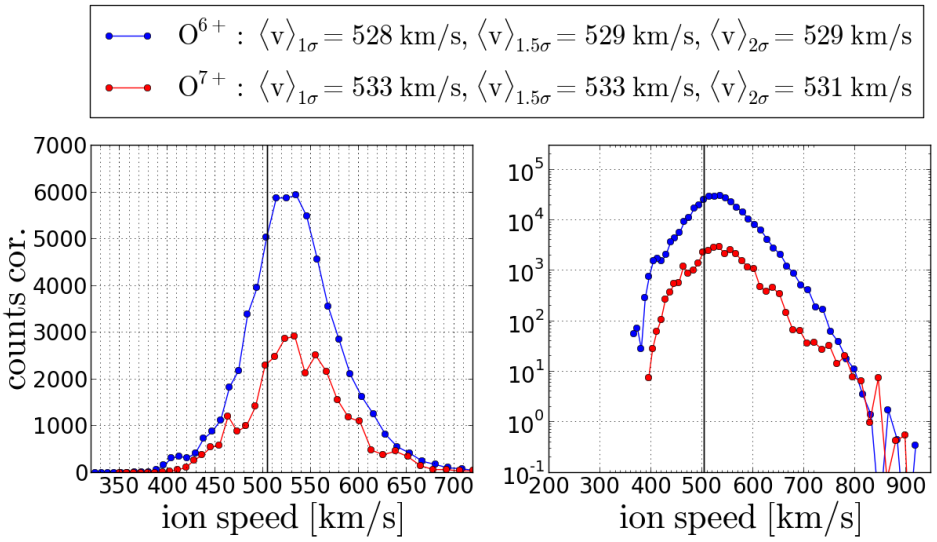

FIGURE D.30: Long-term accumulated speed spectra for O^{6+} - O^{7+} under the condition $v_p \in [500\,\mathrm{km/s}, 510\,\mathrm{km/s}]$ for the measurement period DOY 174-220, 1996. The spectra are shown in phase-space-corrected linear (left) and logarithmic (right) count rate scale. In the linear scaling the count rates of O^{6+} are scaled down with a factor of 0.2. The black vertical line marks the mean proton speed.

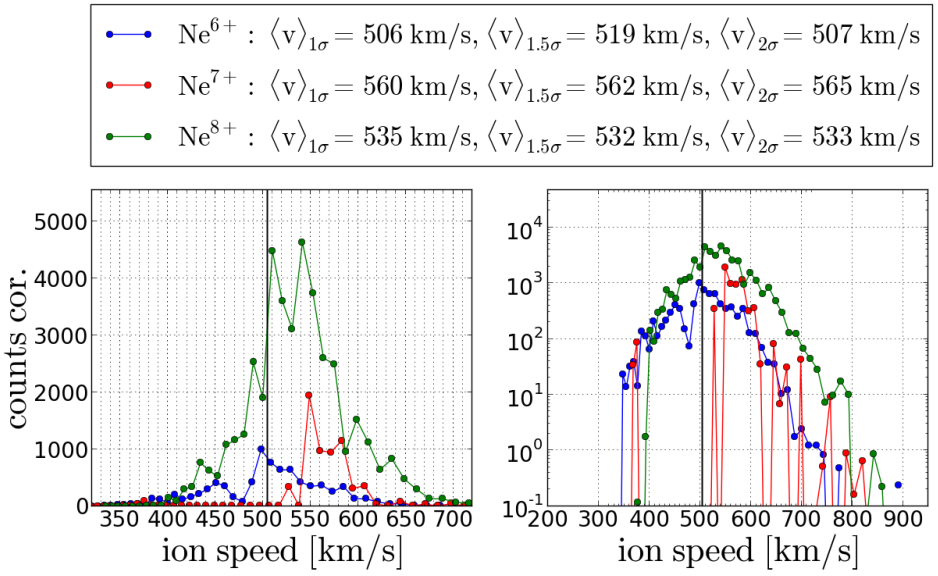

FIGURE D.31: Long-term accumulated speed spectra for Ne^{6+} - Ne^{8+} under the condition $v_p \in [500\,\text{km/s}, 510\,\text{km/s}]$ for the measurement period DOY 174-220, 1996. The spectra are shown in phase-space-corrected linear (left) and logarithmic (right) count rate scale. The black vertical line marks the mean proton speed.

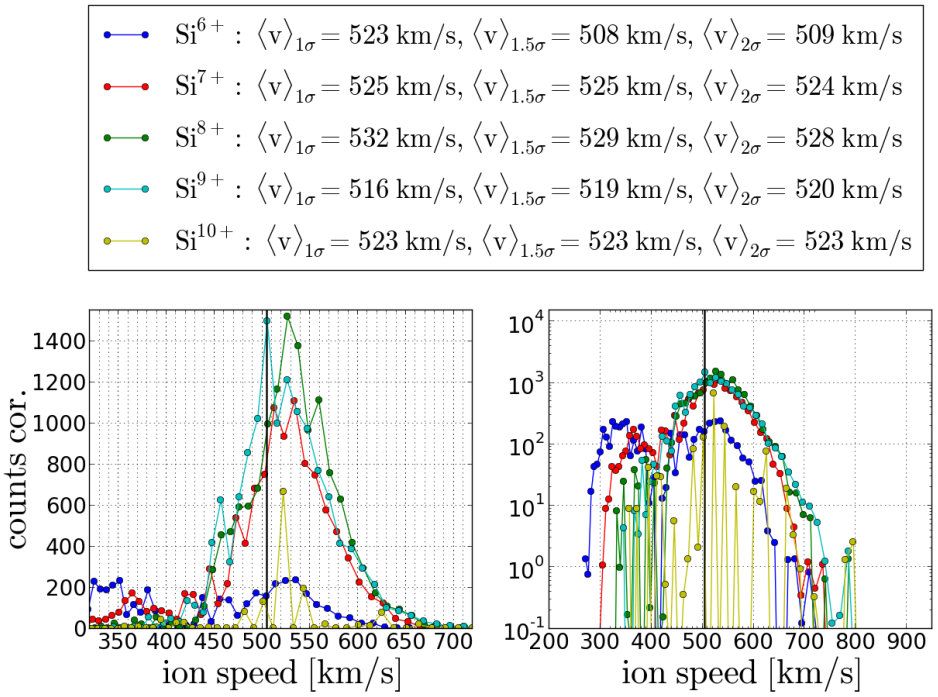

FIGURE D.32: Long-term accumulated speed spectra for Si^{6+} - Si^{10+} under the condition $v_p \in [500\,\text{km/s}, 510\,\text{km/s}]$ for the measurement period DOY 174-220, 1996. The spectra are shown in phase-space-corrected linear (left) and logarithmic (right) count rate scale. The black vertical line marks the mean proton speed.

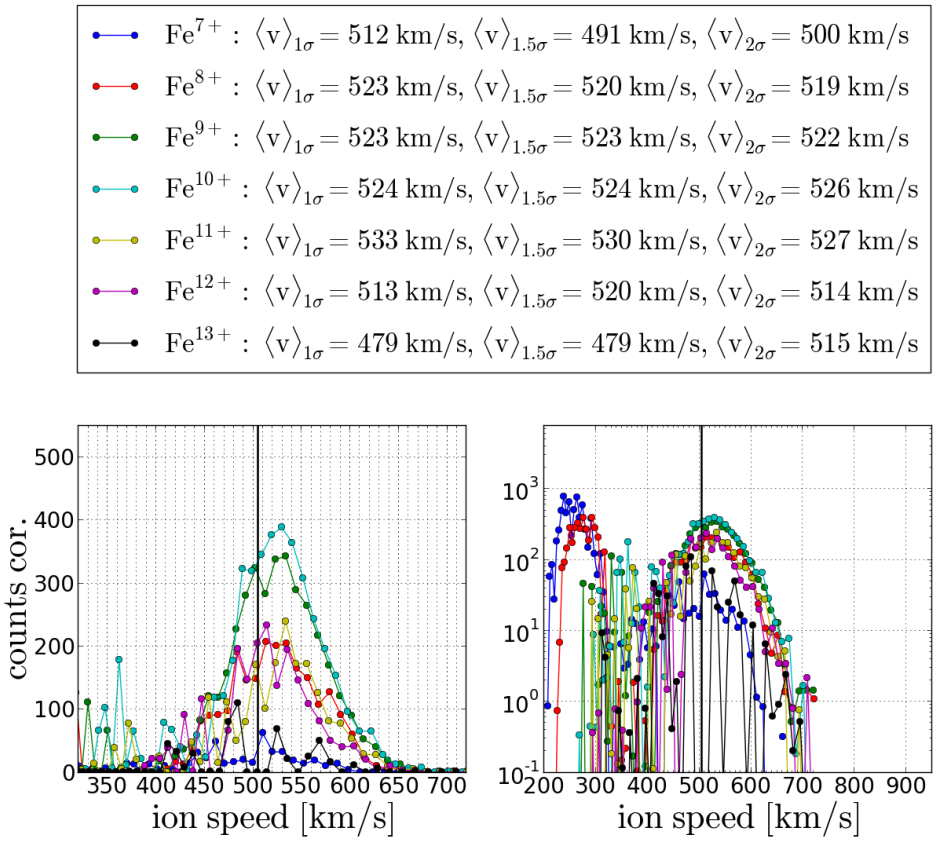

FIGURE D.33: Long-term accumulated speed spectra for Fe^{7+} - Fe^{13+} under the condition $v_p \in [500\,\text{km/s}, 510\,\text{km/s}]$ for the measurement period DOY 174-220, 1996. The spectra are shown in phase-space-corrected linear (left) and logarithmic (right) count rate scale. The increased count rates at $v_{ion} \lesssim 300\,\text{km/s}$ (mainly) for Fe^{7+} - Fe^{8+} are almost entirely He^{2+} random coincidences. The black vertical line marks the mean proton speed.

D.5 Long-Term Fast Wind Spectra Utilized for the Systematic Uncertainty Estimation

As explained in section 5.6, for the estimation of the systematic uncertainty related to the tail scaling parameter A_C we utilized the CTOF Reduced Stable Kappa-Moyal response model, which contains the same 28 ion species as in the previous sections of appendix D, but we varied A_C discretely within the interval $[0.0005\,\mathrm{ch}^{-1}, 0.0105\,\mathrm{ch}^{-1}]$ as can be seen in Figure 5.17. In the following we show the resulting long-term speed spectra for C^{5+}, O^{6+}, Ne^{8+}, Si^{8+} and Fe^{7+} - Fe^{13+} for a selection of tail scaling parameters $A_C \in \{0.0015\,\mathrm{ch}^{-1},\ 0.0025\,\mathrm{ch}^{-1},\ 0.0035\,\mathrm{ch}^{-1},\ 0.0055\,\mathrm{ch}^{-1},\ 0.0075\,\mathrm{ch}^{-1}\}$ which lie in the vicinity of the optimal value $A_C = 0.0035$ that was utilized in all previous sections of this appendix. As explained in section 5.6, the arithmetic mean of the ion mean speeds of Figures D.35 and D.37 result in the systematic uncertainty estimation that is represented by the shaded gray area in Figures 5.19 - 5.20 and 7.1 and 7.2, while the arithmetic mean of the obtained ion mean speeds from Figures D.34, D.36 and D.38 result in the ion mean speed values summarized in Figures 5.19 - 5.20. The long-term speed spectra of the upper and lower panel in Figure 5.18 are already shown in Figure D.28 and D.33, respectively, and only summarized here in one figure for better comparison.

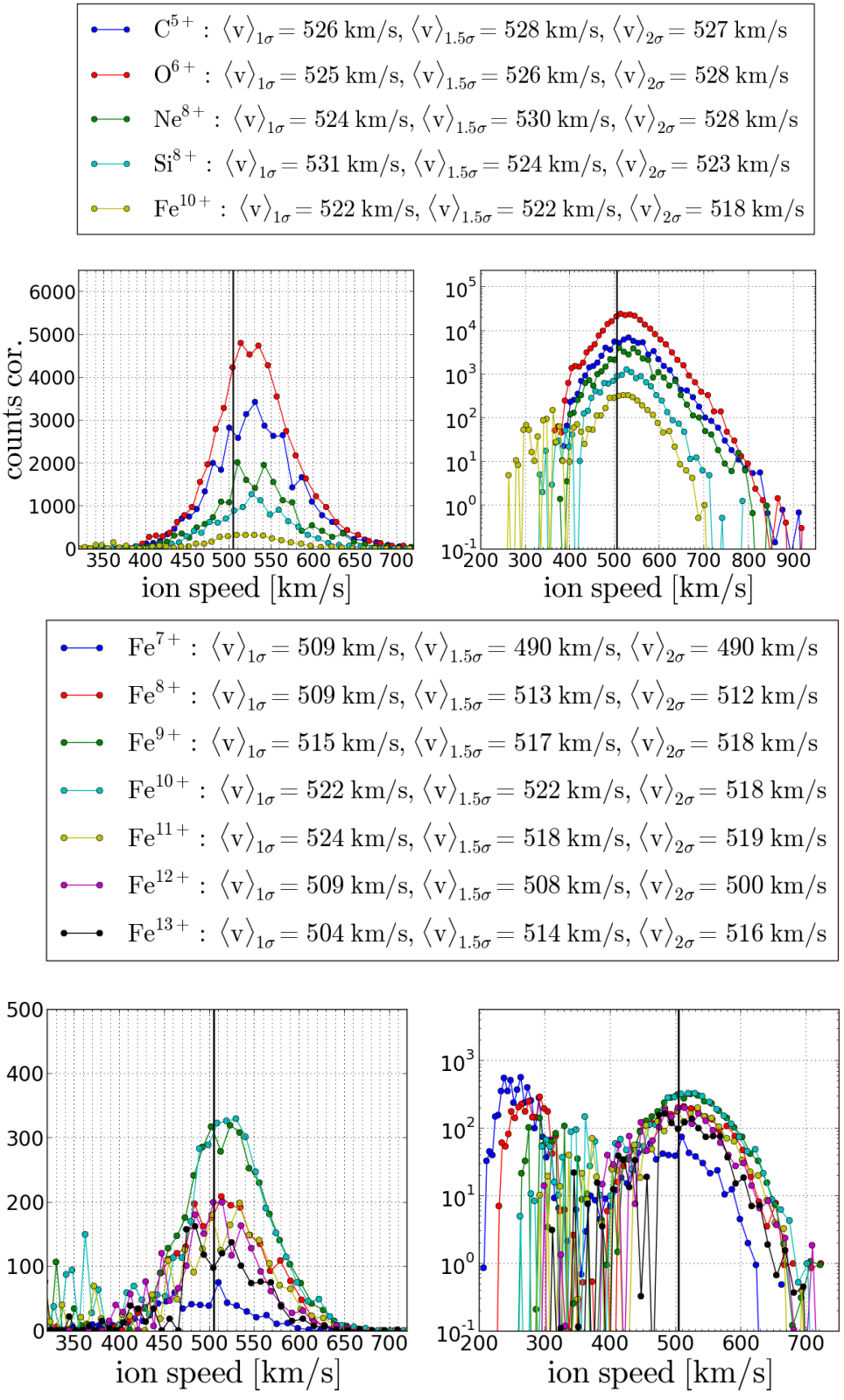

FIGURE D.34: Long-term accumulated speed spectra obtained from the Kappa-Moyal Stable Reduced response model with *tail scaling parameter* $A_C = 0.0015\,\mathrm{ch}^{-1}$ for the same ion species selection C^{5+} - Fe^{10+} as in Figure D.28 (upper panels) and Fe^{7+} - Fe^{13+} (lower panels) under the same fast wind condition $v_p \in [500\,\mathrm{km/s}, 510\,\mathrm{km/s}]$ and for the same measurement period DOY 174-220, 1996. In the linear scaling the count rates of C^{5+}, O^{6+} and Ne^{8+} (upper left panel) are scaled down with a factor of 0.5., 0.2 and 0.5, respectively. The black vertical line marks the mean proton speed.

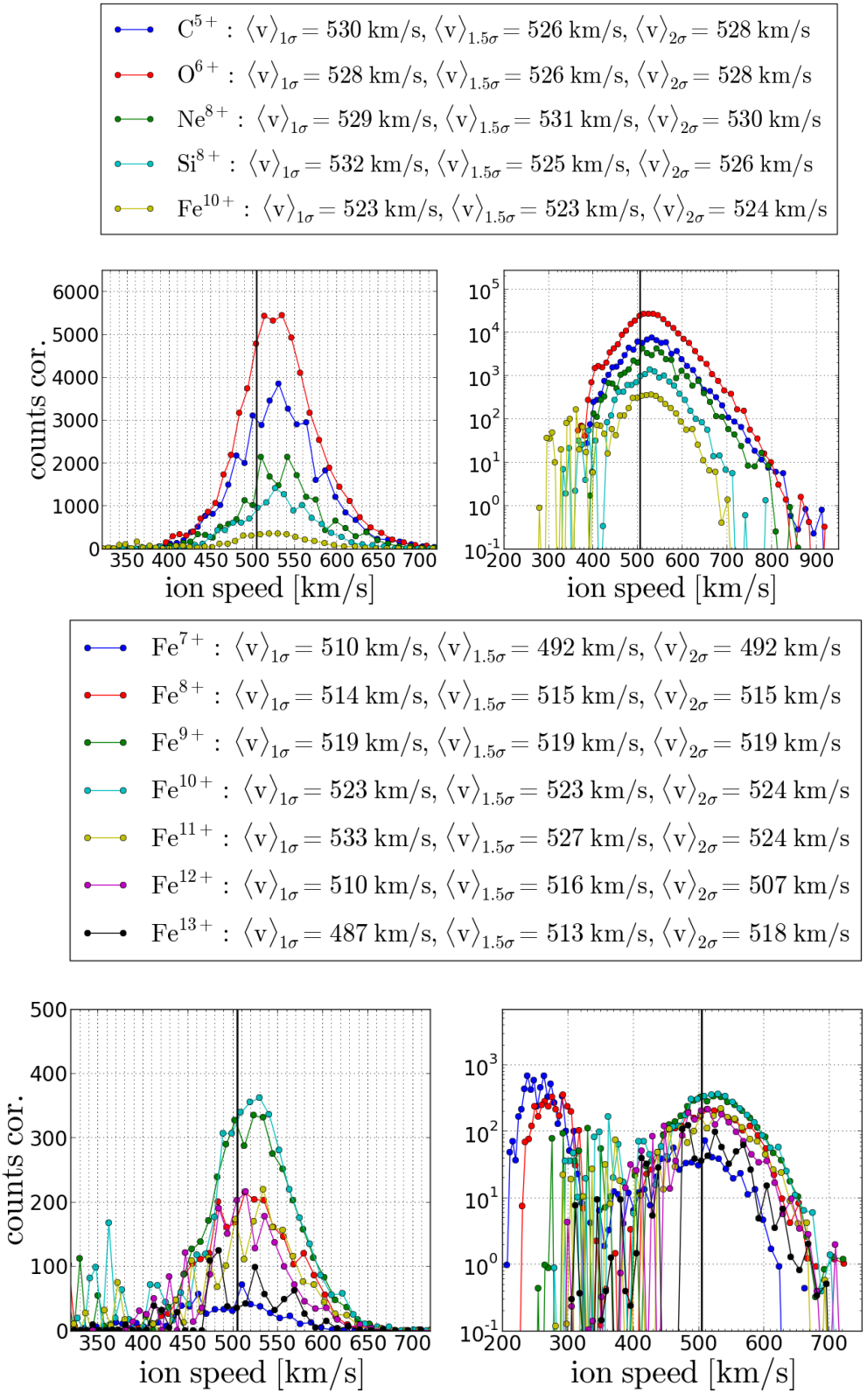

FIGURE D.35: Long-term accumulated speed spectra obtained from the Kappa-Moyal Stable Reduced response model with *tail scaling parameter* $A_C = 0.0025\,\mathrm{ch}^{-1}$ for the same ion species selection C^{5+} - Fe^{10+} as in Figure D.28 (upper panels) and Fe^{7+} - Fe^{13+} (lower panels) under the same fast wind condition $v_p \in [500\,\mathrm{km/s}, 510\,\mathrm{km/s}]$ and for the same measurement period DOY 174-220, 1996. In the linear scaling the count rates of C^{5+}, O^{6+} and Ne^{8+} (upper left panel) are scaled down with a factor of 0.5., 0.2 and 0.5, respectively. The black vertical line marks the mean proton speed.

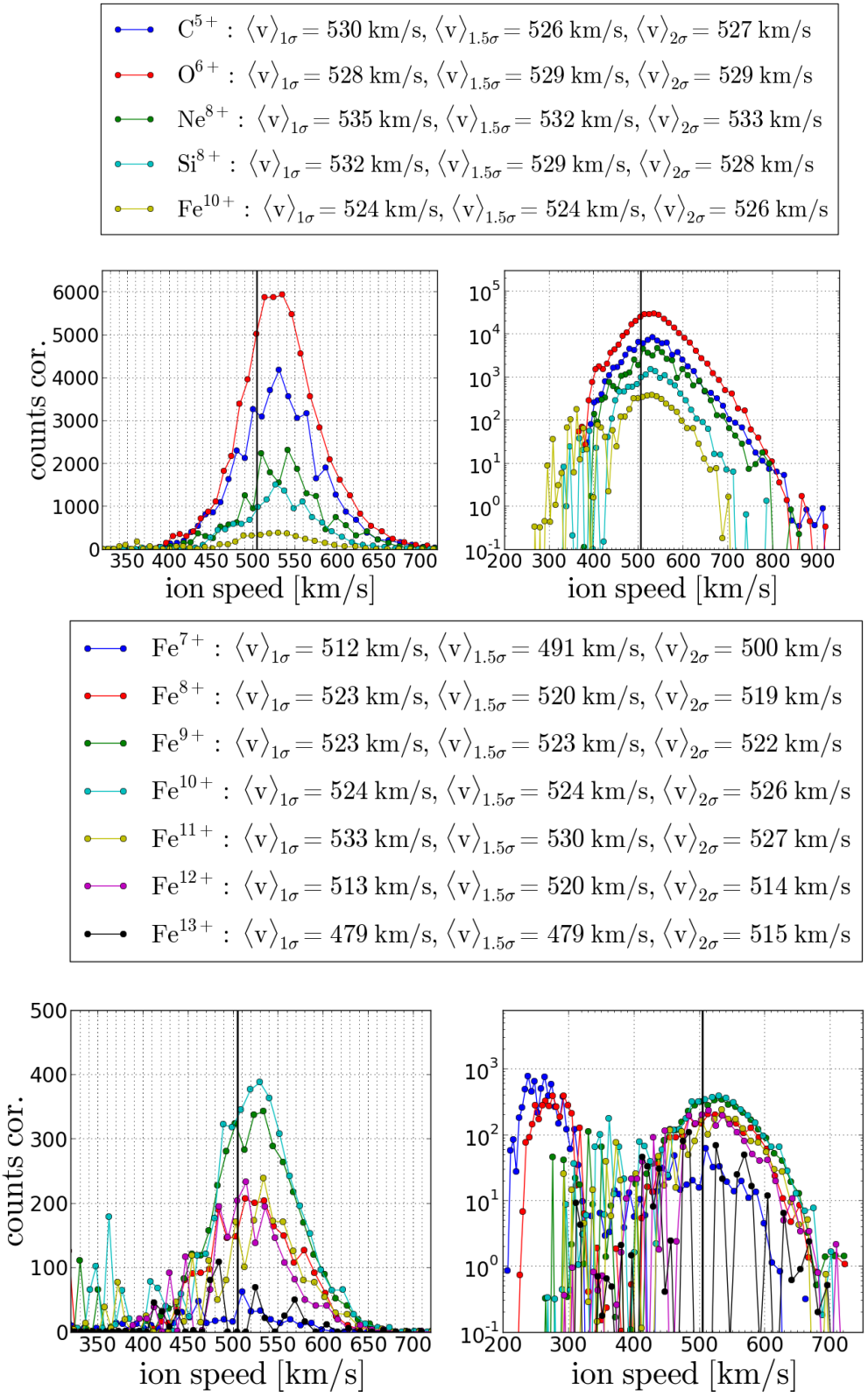

FIGURE D.36: Long-term accumulated speed spectra obtained from the Kappa-Moyal Stable Reduced response model with *tail scaling parameter* $A_C = 0.0035\,\mathrm{ch}^{-1}$ for the same ion species selection C^{5+} - Fe^{10+} as in Figure D.28 (upper panels) and Fe^{7+} - Fe^{13+} (lower panels) under the same fast wind condition $v_p \in [500\,\mathrm{km/s}, 510\,\mathrm{km/s}]$ and for the same measurement period DOY 174-220, 1996. In the linear scaling the count rates of C^{5+}, O^{6+} and Ne^{8+} (upper left panel) are scaled down with a factor of 0.5., 0.2 and 0.5, respectively. The black vertical line marks the mean proton speed.

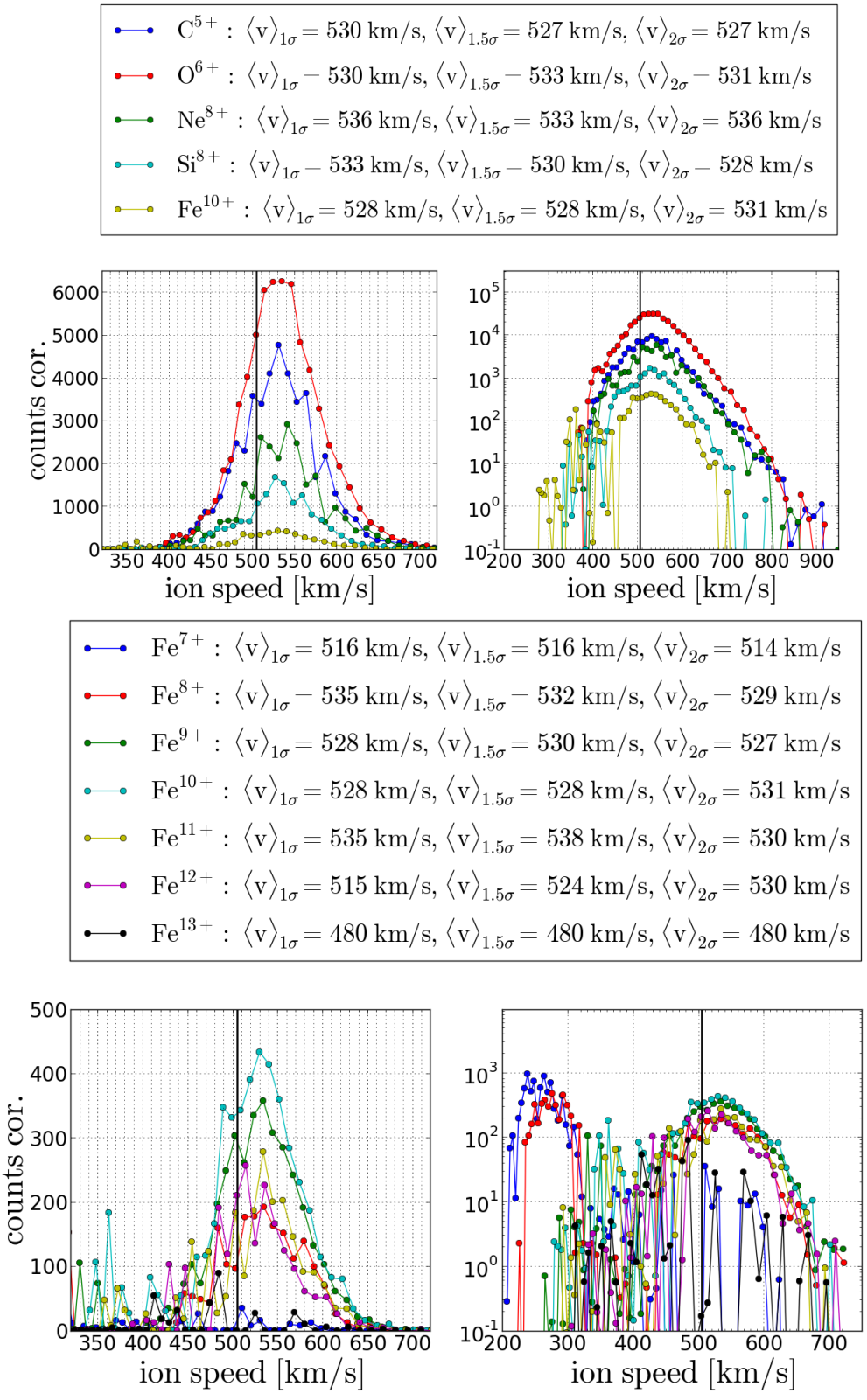

FIGURE D.37: Long-term accumulated speed spectra obtained from the Kappa-Moyal Stable Reduced response model with *tail scaling parameter* $A_C = 0.0055\,\mathrm{ch}^{-1}$ for the same ion species selection C^{5+} - Fe^{10+} as in Figure D.28 (upper panels) and Fe^{7+} - Fe^{13+} (lower panels) under the same fast wind condition $v_p \in [500\,\mathrm{km/s}, 510\,\mathrm{km/s}]$ and for the same measurement period DOY 174-220, 1996. In the linear scaling the count rates of C^{5+}, O^{6+} and Ne^{8+} (upper left panel) are scaled down with a factor of 0.5., 0.2 and 0.5, respectively. The black vertical line marks the mean proton speed.

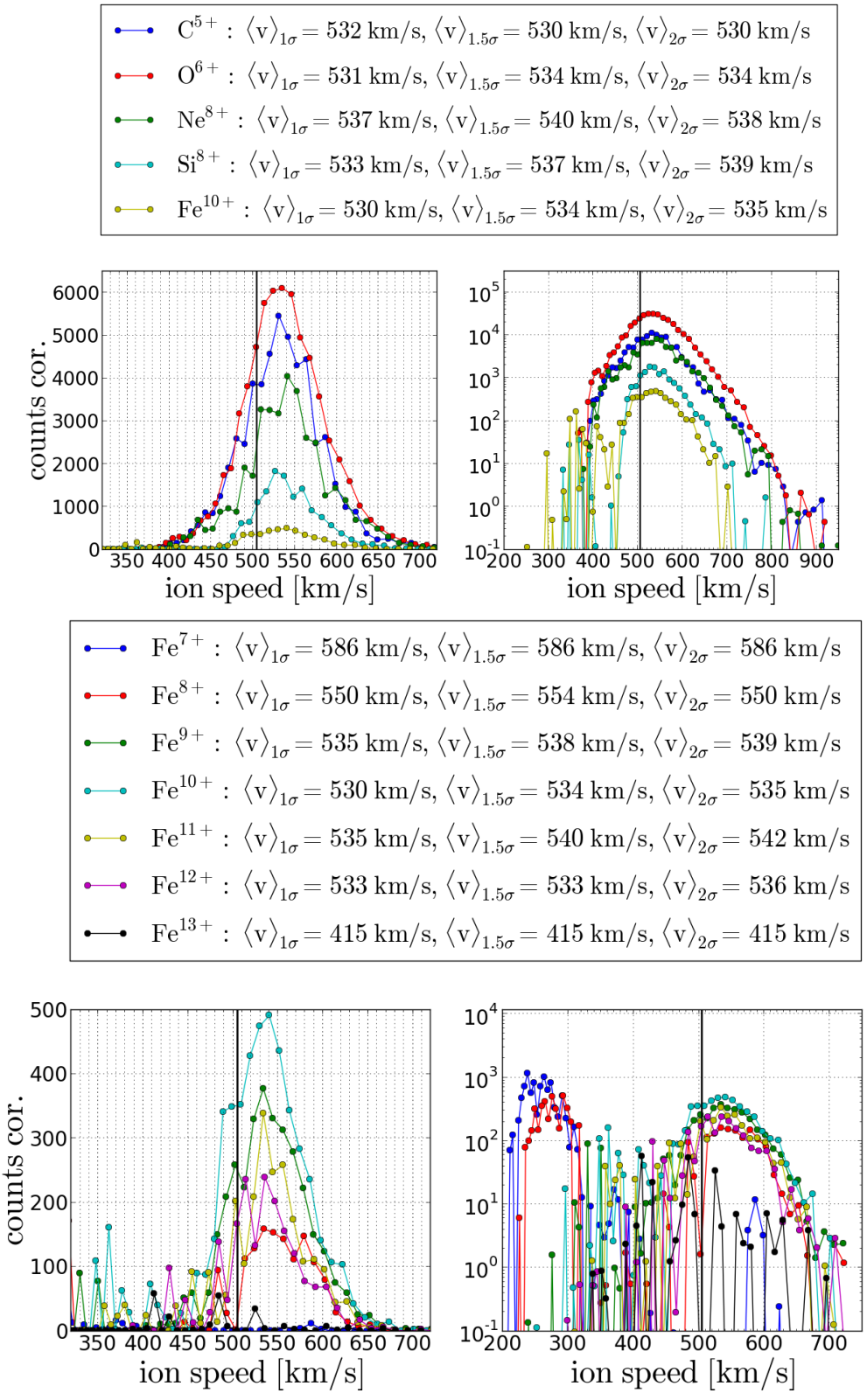

FIGURE D.38: Long-term accumulated speed spectra obtained from the Kappa-Moyal Stable Reduced response model with *tail scaling parameter* $A_C = 0.0075\,\mathrm{ch}^{-1}$ for the same ion species selection C^{5+} - Fe^{10+} as in Figure D.28 (upper panels) and Fe^{7+} - Fe^{13+} (lower panels) under the same fast wind condition $v_p \in [500\,\mathrm{km/s}, 510\,\mathrm{km/s}]$ and for the same measurement period DOY 174-220, 1996. In the linear scaling the count rates of C^{5+}, O^{6+} and Ne^{8+} (upper left panel) are scaled down with a factor of 0.5., 0.2 and 0.5, respectively. The black vertical line marks the mean proton speed.

Bibliography

L. Biermann. Kometenschweife und solare Korpuskularstrahlung. *Zeitschrift für Astrophysik*, 29:274–286, 1951.

E. N. Parker. Dynamics of the interplanetary gas and magnetic fields. *The Astrophysical Journal*, 128:664, 1958. ISSN 0004-637X. doi: 10.1086/146579.

Markus J. Aschwanden. *Physics of the Solar Corona: An Introduction with Problems and Solutions*. Springer Praxis Books. Praxis Publishing Ltd Chichester UK, Berlin, Heidelberg, 2005. ISBN 9783540307655. doi: 10.1007/3-540-30766-4.

K.I. Gringauz. Results of observations of charged particles observed out to r=100,000 km with the aid of charged-particle traps on soviet space rockets. *Astronomcheskii Zhurnal*, 37:716, 1960.

M. Snyder C. W., Neugebauer. Direct observations of the solar wind particles by the Mariner II spcecraft. *Proceedings from the 8th International Cosmic Ray Conference*, 1: 210–219, 1963.

Mausumi Dikpati and Peter A. Gilman. Global solar dynamo models: Simulations and predictions. *Journal of Astrophysics and Astronomy*, 29(1-2):29–39, 2008. ISSN 0250-6335. doi: 10.1007/s12036-008-0004-3.

G. Allen Gary. Plasma beta above a solar active region: Rethinking the paradigm. *Solar Physics*, 203(1):71–86, 2001. ISSN 00380938. doi: 10.1023/A:1012722021820.

J. Geiss. Solar wind composition experiment. *Apollo 16 Prel Sci Rep NASA Spec Pub*, 305 (14):1–10, 1972.

E. Marsch, K.-H. Mühlhäuser, H. Rosenbauer, R. Schwenn, and F. M. Neubauer. Solar wind helium ions: Observations of the Helios solar probes between 0.3 and 1 AU. *Journal of Geophysical Research: Space Physics*, 87(A1):35, 1982a. ISSN 01480227. doi: 10.1029/JA087iA01p00035.

E. Marsch, K.-H. Mühlhäuser, R. Schwenn, H. Rosenbauer, W. Pilipp, and F. M. Neubauer. Solar wind protons: Three-dimensional velocity distributions and derived plasma parameters measured between 0.3 and 1 AU. *Journal of Geophysical Research*, 87(A1):52, 1982b. doi: 10.1029/JA087iA01p00052.

J. T. Steinberg, A. J. Lazarus, K. W. Ogilvie, R. Lepping, and J. Byrnes. Differential flow between solar wind protons and alpha particles: First Wind observations. *Geophysical Research Letters*, 23(10):1183–1186, 1996. ISSN 00948276. doi: 10.1029/96GL00628.

S. Peter Gary, Lin Yin, Dan Winske, and Daniel B. Reisenfeld. Alpha/proton magnetosonic instability in the solar wind. *Journal of Geophysical Research: Space Physics*, 105 (A9):20989–20996, 2000. ISSN 01480227. doi: 10.1029/2000JA000049.

Peter Bochsler. Minor ions in the solar wind. *The Astronomy and Astrophysics Review*, 14 (1):1–40, 2007. ISSN 0935-4956. doi: 10.1007/s00159-006-0002-x.

D. J. McComas, B. L. Barraclough, H. O. Funsten, J. T. Gosling, E. Santiago-Muñoz, R. M. Skoug, B. E. Goldstein, M. Neugebauer, P. Riley, and A. Balogh. Solar wind observations over Ulysses' first full polar orbit. *Journal of Geophysical Research: Space Physics*, 105(A5):10419–10433, 2000. ISSN 01480227. doi: 10.1029/1999JA000383.

Steven R. Cranmer. Coronal holes and the high-speed solar wind. *Space Science Reviews*, 101(3/4):229–294, 2002. ISSN 00386308. doi: 10.1023/A:1020840004535.

D. J. McComas, H. A. Elliott, N. A. Schwadron, J. T. Gosling, R. M. Skoug, and B. E. Goldstein. The three-dimensional solar wind around solar maximum. *Geophysical Research Letters*, 30(10):n/a–n/a, 2003. ISSN 00948276. doi: 10.1029/2003GL017136.

Gerd W. Prölss. *Physics of the Earth's Space Environment: An Introduction*. Springer Berlin Heidelberg, Berlin, Heidelberg, 2004. ISBN 9783642059797. doi: 10.1007/978-3-642-97123-5.

U. Feldman. On the sources of fast and slow solar wind. *Journal of Geophysical Research*, 110(A7):261, 2005. doi: 10.1029/2004JA010918.

Fei Xu and Joseph E. Borovsky. A new four-plasma categorization scheme for the solar wind. *Journal of Geophysical Research: Space Physics*, 120(1):70–100, 2015. ISSN 01480227. doi: 10.1002/2014JA020412.

Verena Heidrich-Meisner and Robert F. Wimmer-Schweingruber. Solar wind classification via k-means clustering algorithm. In *Machine Learning Techniques for Space Weather*, pages 397–424. Elsevier, 2018. ISBN 9780128117880. doi: 10.1016/B978-0-12-811788-0.00016-0.

J. Geiss and G. Gloeckler. The southern high-speed stream: results from the SWICS instrument on Ulysses. *Science (New York, N.Y.)*, 268(5213):1033–1036, 1995. ISSN 0036-8075. doi: 10.1126/science.7754380.

M. R. Aellig. Solar wind iron charge states observed with high time resolution with SOHO/CELIAS/CTOF. *Correlated Phenomena at the Sun, in the Heliosphere and in Geospace. 31st ESLAB Symposium held 22-25 September, 1997, at ESTEC, Noordwijk, The Netherlands. Edited by A. Wilson. European Space Agency, ESA SP-415, 1997. ISBN: 92-9092-660-0., p.27*, 404:27–31, 1997.

R. von Steiger, N. A. Schwadron, L. A. Fisk, J. Geiss, G. Gloeckler, S. Hefti, B. Wilken, R. R. Wimmer-Schweingruber, and T. H. Zurbuchen. Composition of quasi-stationary solar wind flows from Ulysses/solar wind ion composition spectrometer. *Journal of Geophysical Research: Space Physics*, 105(A12):27217–27238, 2000. ISSN 01480227. doi: 10.1029/1999JA000358.

S. Hefti. Kinetic properties of solar wind minor ions and protons measured with SOHO/CELIAS. *Journal of Geophysical Research: Space Physics*, 103(A12):29697–29704, 1998a. ISSN 01480227. doi: 10.1029/1998JA900022.

R. von Steiger and T. H. Zurbuchen. Kinetic properties of heavy solar wind ions from Ulysses-SWICS. *Geophysical Research Letters*, 33(9):6360, 2006. ISSN 00948276. doi: 10.1029/2005GL024998.

Patrick J. Tracy, Justin C. Kasper, Thomas H. Zurbuchen, Jim M. Raines, Paul Shearer, and Jason Gilbert. Thermalization of heavy ions in the solar wind. *The Astrophysical Journal*, 812(2):170, 2015. ISSN 0004-637X. doi: 10.1088/0004-637x/812/2/170.

David H. Hathaway. The solar cycle. *Living reviews in solar physics*, 12:4, 2015. ISSN 1614-4961. doi: 10.1007/lrsp-2015-4.

Carolus J. Schrijver and George L. Siscoe, editors. *Heliophysics: Space storms and radiation : causes and effects*. Cambridge University Press, Cambridge, 2010. ISBN 9781107403994. doi: 10.1017/CBO9781139194532.

S. K. Antiochos, C. R. DeVore, and J. A. Klimchuk. A model for solar coronal mass ejections. *The Astrophysical Journal*, 510(1):485–493, 1999. ISSN 0004-637X. doi: 10.1086/306563.

Eckart Marsch. Kinetic physics of the solar corona and solar wind. *Living reviews in solar physics*, 3, 2006. ISSN 1614-4961. doi: 10.12942/lrsp-2006-1.

Jean Carlos Perez and Benjamin D. G. Chandran. Direct numerical simulations of reflection-driven, reduced magnetohydrodynamic turbulence from the sun to the

Alfvén critical point. *The Astrophysical Journal*, 776(2):124, 2013. ISSN 0004-637X. doi: 10.1088/0004-637X/776/2/124.

Ian W. Hoppock, Benjamin D. G. Chandran, Kristopher G. Klein, Alfred Mallet, and Daniel Verscharen. Stochastic proton heating by kinetic-Alfvén-wave turbulence in moderately high-beta plasmas. *Journal of plasma physics*, 84(6), 2018. ISSN 0022-3778. doi: 10.1017/S0022377818001277.

J. F. McKenzie and E. Marsch. Resonant wave acceleration of minor ions in the solar wind. *Astrophysics and Space Science*, 81(1-2):295–314, 1982. ISSN 0004-640X. doi: 10.1007/BF00676154.

Philip A. Isenberg and Joseph V. Hollweg. On the preferential acceleration and heating of solar wind heavy ions. *Journal of Geophysical Research: Space Physics*, 88(A5):3923, 1983. ISSN 01480227. doi: 10.1029/JA088iA05p03923.

Philip A. Isenberg, Martin A. Lee, and Joseph V. Hollweg. The kinetic shell model of coronal heating and acceleration by ion cyclotron waves: 1. outward propagating waves. *Journal of Geophysical Research: Space Physics*, 106(A4):5649–5660, 2001. ISSN 01480227. doi: 10.1029/2000JA000099.

C.-Y. TU and E. Marsch. Two-fluid model for heating of the solar corona and acceleration of the solar wind by high-frequency Alfven waves. *Solar Physics*, 171(2):363–391, 1997. ISSN 00380938. doi: 10.1023/A:1004968327196.

S. R. Cranmer and A. A. van Ballegooijen. On the generation, propagation, and reflection of Alfven waves from the solar photosphere to the distant heliosphere. *The Astrophysical Journal Supplement Series*, 156(2):265–293, 2005. ISSN 0067-0049. doi: 10.1086/426507.

Takeru K. Suzuki and Shu-ichiro Inutsuka. Solar winds driven by nonlinear low-frequency Alfvén waves from the photosphere: Parametric study for fast/slow winds and disappearance of solar winds. *Journal of Geophysical Research: Space Physics*, 111(A6):1089, 2006. ISSN 01480227. doi: 10.1029/2005JA011502.

Axford, W.I., McKenzie, J.F. Cosmic winds and the heliosphere: The solar wind. pages 31–66, 1997.

E. Marsch. Helios: Evolution of distribution functions 0.3–1 AU. *Space Science Reviews*, 172(1):23, 2012. doi: 10.1007/s11214-010-9734-z.

W. K. H. Schmidt, H. Rosenbauer, E. G. Shelly, and J. Geiss. On temperature and speed of He++ and O6+ ions in the solar wind. *Geophysical Research Letters*, 7(9):697–700, 1980. ISSN 00948276. doi: 10.1029/GL007i009p00697.

J. C. Kasper, A. J. Lazarus, and S. P. Gary. Hot solar-wind helium: direct evidence for local heating by Alfvén-cyclotron dissipation. *Physical review letters*, 101(26):261103, 2008. ISSN 0031-9007. doi: 10.1103/PhysRevLett.101.261103.

J. C. Kasper, K. G. Klein, T. Weber, M. Maksimovic, A. Zaslavsky, S. D. Bale, B. A. Maruca, M. L. Stevens, and A. W. Case. A zone of preferential ion heating extends tens of solar radii from the sun. *The Astrophysical Journal*, 849(2):126, 2017. ISSN 0004-637X. doi: 10.3847/1538-4357/aa84b1.

L. Berger, R. F. Wimmer-Schweingruber, and G. Gloeckler. Systematic measurements of ion-proton differential streaming in the solar wind. *Physical review letters*, 106(15): 151103, 2011. ISSN 0031-9007. doi: 10.1103/PhysRevLett.106.151103.

B. A. Maruca, S. D. Bale, L. Sorriso-Valvo, J. C. Kasper, and M. L. Stevens. Collisional thermalization of hydrogen and helium in solar-wind plasma. *Physical Review Letters*, 111(24):241101, 2013. ISSN 0031-9007. doi: 10.1103/PhysRevLett.111.241101.

M. Neugebauer, B. E. Goldstein, S. J. Bame, and W. C. Feldman. Ulysses near-ecliptic observations of differential flow between protons and alphas in the solar wind. *Journal of Geophysical Research: Space Physics*, 99(A2):2505, 1994. ISSN 01480227. doi: 10.1029/93JA02615.

Joseph V. Hollweg and Philip A. Isenberg. Generation of the fast solar wind: A review with emphasis on the resonant cyclotron interaction. *Journal of Geophysical Research: Space Physics*, 107(A7):6551, 2002. ISSN 01480227. doi: 10.1029/2001JA000270.

Bruce T. Tsurutani and Gurbax S. Lakhina. Some basic concepts of wave-particle interactions in collisionless plasmas. *Reviews of Geophysics*, 35(4):491–501, 1997. ISSN 87551209. doi: 10.1029/97RG02200.

L. Gomberoff and R. Elgueta. Resonant acceleration of alpha particles by ion cyclotron waves in the solar wind. *Journal of Geophysical Research: Space Physics*, 96(A6):9801, 1991. ISSN 01480227. doi: 10.1029/91JA00613.

C. F. Kennel and F. Englemann. Velocity space diffusion from weak plasma turbulence in a magnetic field. *Physics of Fluids*, 9(12):2377, 1966. ISSN 00319171. doi: 10.1063/1.1761629.

R. Hernandez and E. Marsch. Collisional time scales for temperature and velocity exchange between drifting Maxwellians. *Journal of Geophysical Research: Space Physics*, 90(A11):11062, 1985. ISSN 01480227. doi: 10.1029/JA090iA11p11062.

Z. Nemecek, T. Durovcova, J. Safrankova, F. Nemec, L. Matteini, D. Stansby, N. Janitzek, L. Berger, and R. F. Wimmer-Schweingruber. What is the solar wind frame of reference? *The Astrophysical Journal*, 889(163), 2020. doi: 10.3847/1538-4357/ab65f7.

S. Bourouaine, E. Marsch, and F. M. Neubauer. On the relative speed and temperature ratio of solar wind alpha particles and protons: Collisions versus wave effects. *The Astrophysical Journal Letters*, 728:L3, 2011. doi: 10.1088/2041-8205/728/1/L3.

Xing Li and Shadia Rifai Habbal. Proton/alpha magnetosonic instability in the fast solar wind. *Journal of Geophysical Research: Space Physics*, 105(A4):7483–7489, 2000. ISSN 01480227. doi: 10.1029/1999JA000259.

S. Livi, E. Marsch, and H. Rosenbauer. Coulomb collisional domains in the solar wind. *Journal of Geophysical Research: Space Physics*, 91(A7):8045, 1986. ISSN 01480227. doi: 10.1029/JA091iA07p08045.

E. Marsch, C. K. Goertz, and K. Richter. Wave heating and acceleration of solar wind ions by cyclotron resonance. *Journal of Geophysical Research: Space Physics*, 87(A7): 5030–5044, 1982c. ISSN 01480227. doi: 10.1029/JA087iA07p05030.

E. Marsch, K.-H. Mühlhäuser, H. Rosenbauer, R. Schwenn, and K. U. Denskat. Pronounced proton core temperature anisotropy, ion differential speed, and simultaneous Alfvén wave activity in slow solar wind at 0.3 AU. *Journal of Geophysical Research: Space Physics*, 86(A11):9199, 1981. ISSN 01480227. doi: 10.1029/JA086iA11p09199.

Lorenzo Matteini, Petr Hellinger, Bruce E. Goldstein, Simone Landi, Marco Velli, and Marcia Neugebauer. Signatures of kinetic instabilities in the solar wind. *Journal of Geophysical Research: Space Physics*, 118(6):2771–2782, 2013. ISSN 01480227. doi: 10.1002/jgra.50320.

Marcia Neugebauer and Conway W. Snyder. Mariner 2 observations of the solar wind: 1. average properties. *Journal of Geophysical Research: Space Physics*, 71(19):4469–4484, 1966. ISSN 01480227. doi: 10.1029/JZ071i019p04469.

Snyder C. W., Neugebauer, M. Solar particles and sun-earth relations. *Proceedings from the 8th International Cosmic Ray Conference*, 1:210–219, 1951.

L. Spitzer. Physics of fully ionized gases. *New York: Interscience*, 2nd edition, 1962.

Lyman Spitzer. *Physics of Fully Ionized Gases: Second Revised Edition*. Dover Books on Physics. Dover Publications, Newburyport, 2nd ed. edition, 2013. ISBN 9780486449821.

R. von Steiger, J. Geiss, G. Gloeckler, and A. B. Galvin. Kinetic properties of heavy ions in the solar wind from SWICS/Ulysses. *Space Science Reviews*, 72(1-2):71–76, 1995. ISSN 00386308. doi: 10.1007/BF00768756.

M. R. Aellig. Iron freeze-in temperatures measured by SOHO/CELIAS/CTOF. *Journal of Geophysical Research: Space Physics*, 103(A8):17215–17222, 1998a. ISSN 01480227. doi: 10.1029/98JA00588.

Steve Baker and Robert D. Cousins. Clarification of the use of chi-square and likelihood functions in fits to histograms. *Nuclear Instruments and Methods in Physics Research*, 221(2):437–442, 1984. ISSN 01675087. doi: 10.1016/0167-5087(84)90016-4.

C. G. Broyden. The convergence of a class of double-rank minimization algorithms 1. general considerations. *IMA Journal of Applied Mathematics*, 6(1):76–90, 1970. ISSN 0272-4960. doi: 10.1093/imamat/6.1.76.

Noel Cressie and Timothy R. C. Read. Pearson's x 2 and the log-likelihood ratio statistic g 2 : A comparative review. *International Statistical Review / Revue Internationale de Statistique*, 57(1):19, 1989. ISSN 03067734. doi: 10.2307/1403582.

Michael Oetliker. Response of a passivated implanted planar silicon (PIPS) detector for heavy ions with energies between 25 and 360 kev. *Nuclear Instruments and Methods in Physics Research Section A: Accelerators, Spectrometers, Detectors and Associated Equipment*, 337(1):145–148, 1993a. ISSN 01689002. doi: 10.1016/0168-9002(93)91147-F.

V. Domingo, B. Fleck, and A. I. Poland. The SOHO mission: An overview. *Solar Physics*, 162(1-2):1–37, 1995. ISSN 0038-0938. doi: 10.1007/BF00733425.

R. Fletcher. A new approach to variable metric algorithms. *The Computer Journal*, 13(3): 317–322, 1970. ISSN 0010-4620. doi: 10.1093/comjnl/13.3.317.

Donald Goldfarb. A family of variable-metric methods derived by variational means. *Mathematics of Computation*, 24(109):23, 1970. ISSN 0025-5718. doi: 10.1090/S0025-5718-1970-0258249-6.

N. P. Janitzek. Solar wind heavy ion measurements with SOHO/CELIAS/CTOF. *Master Thesis, University of Kiel*, 2014.

E. Landi. Ion temperatures in the quiet solar corona. *The Astrophysical Journal*, 663(2): 1363–1368, 2007. ISSN 0004-637X. doi: 10.1086/517910.

Kenneth Levenberg. A method for the solution of certain non-linear problems in least squares. *Quarterly of Applied Mathematics*, 2(2):164–168, 1944. ISSN 0033-569X. doi: 10.1090/qam/10666.

Donald W. Marquardt. An algorithm for least-squares estimation of nonlinear parameters. *Journal of the Society for Industrial and Applied Mathematics*, 11(2):431–441, 1963. ISSN 0368-4245. doi: 10.1137/0111030.

J. E. Moyal. Xxx. theory of ionization fluctuations. *The London, Edinburgh, and Dublin Philosophical Magazine and Journal of Science*, 46(374):263–280, 1955. ISSN 1941-5982. doi: 10.1080/14786440308521076.

W. Pilz, J. V. Borany, R. Grötzschel, W. Jiang, M. Posselt, and B. Schmidt. Dependence of the silicon detector response to heavy ions on the direction of incidence. *Nuclear Instruments and Methods in Physics Research Section A: Accelerators, Spectrometers, Detectors and Associated Equipment*, 419(1):137–145, 1998. ISSN 01689002. doi: 10.1016/S0168-9002(98)01151-6.

William H. Press. *Numerical recipes in C: The art of scientific computing*. Cambridge Univ. Press, Cambridge, reprinted. edition, 1991. ISBN 052135465X.

D. F. Shanno. Conditioning of quasi-newton methods for function minimization. *Mathematics of Computation*, 24(111):647, 1970. ISSN 0025-5718. doi: 10.1090/S0025-5718-1970-0274029-X.

James F. Ziegler, Jochen Biersack, and Matthias D. Ziegler. *SRIM - the stopping and range of ions in matter*. SRIM, Chester, Maryland, 2008. ISBN 978-0-9654207-1-6.

F. M. Ipavich, A. B. Galvin, S. E. Lasley, J. A. Paquette, S. Hefti, K.-U. Reiche, M. A. Coplan, G. Gloeckler, and P. Bochsler. Solar wind measurements with SOHO: The CELIAS/MTOF proton monitor. *Journal of Geophysical Research*, 103:17,205–17,213, 1998.

J. R. Asbridge, S. J. Bame, W. C. Feldman, and M. D. Montgomery. Helium and hydrogen velocity differences in the solar wind. *Journal of Geophysical Research: Space Physics*, 81(16):2719–2727, 1976. ISSN 01480227. doi: 10.1029/JA081i016p02719.

Bame, S. and McComas. The Ulysses solar wind plasma experiment. *A&AS*, 92, 1992.

N. P. Janitzek, A. Taut, L. Berger, P. Bochsler, C. Drews, B. Klecker, and R. F. Wimmer-Schweingruber. High-time resolution measurements of solar wind heavy ions with SOHO/CELIAS/CTOF. AIP Conference Proceedings, page 040006, 2016. doi: 10.1063/1.4943817.

R. A. Mewaldt. Long-term fluences of energetic particles in the heliosphere. In *AIP Conference Proceedings*, pages 165–170. AIP, 2001. doi: 10.1063/1.1433995.

R. Chhiber, A. V. Usmanov, W. H. Matthaeus, and M. L. Goldstein. Solar wind collisional age from a global magnetohydrodynamics simulation. *The Astrophysical Journal*, 821(1):34, 2016. ISSN 0004-637X. doi: 10.3847/0004-637x/821/1/34.

W. C. Feldman, J. A. Asbridge, S. J. Bame, and M. D. Montgomery. Double ion streams in the solar wind. *Journal of Geophysical Research*, 78:2017–2027, 1973.

S. P. Gary. What is a plasma instability? *Eos, Transactions American Geophysical Union*, 73(49):529, 1992. ISSN 0096-3941. doi: 10.1029/91EO00388.

Daniel J. Gershman, Thomas H. Zurbuchen, Lennard A. Fisk, Jason A. Gilbert, Jim M. Raines, Brian J. Anderson, Charles W. Smith, Haje Korth, and Sean C. Solomon. Solar wind alpha particles and heavy ions in the inner heliosphere observed with messenger. *Journal of Geophysical Research: Space Physics*, 117(A12):n/a–n/a, 2012. ISSN 01480227. doi: 10.1029/2012JA017829.

Gloeckler, G. and Geiss. The solar wind ion composition spectrometer. *Astronomy and Astrophysiscs*, 92:267–289, 1992.

D. Hovestadt, M. Hilchenbach, A. Buergi, B. Klecker, P. Laeverenz, M. Scholer, H. Gruenwaldt, W. I. Axford, S. Livi, E. Marsch, B. Wilken, H. P. Winterhoff, F. M. Ipavich, P. Bedini, M. A. Coplan, A. B. Galvin, G. Gloeckler, P. Bochsler, H. Balsiger, J. Fischer, J. Geiss, R. Kallenbach, P. Wurz, K.-U. Reiche, F. Gliem, D. L. Judge, H. S. Ogawa, K. C. Hsieh, E. Moebius, M. A. Lee, G. G. Managadze, M. I. Verigin, and M. Neugebauer. CELIAS - charge, element and isotope analysis system for SOHO. *Solar Physics*, 162(1-2):441–481, 1995. ISSN 00380938. doi: 10.1007/BF00733436.

F. M. Ipavich, A. B. Galvin, G. Gloeckler, D. Hovestadt, S. J. Bame, B. Klecker, M. Scholer, L. A. Fisk, and C. Y. Fan. Solar wind Fe and CNO measurements in high-speed flows. *Journal of Geophysical Research: Space Physics*, 91(A4):4133, 1986. ISSN 01480227. doi: 10.1029/JA091iA04p04133.

M. Arnaud and R. Rothenflug. An updated evaluation of recombination and ionization rates. *Astronomy and Astrophysics Supplement Series*, 60:425–457, 1985.

A. Taut. Pick-up ions at 1 AU. *Master Thesis, University of Kiel*, 2014.

S. Hefti. Solar wind freeze-in temperatures and fluxes measured with SOHO/CELIAS/CTOF and calibration of the CELIAS sensors. *PhD Thesis, University of Bern*, 1998b.

S. Aellig. Freeze-in temperatures and relative abundances of iron ions in the solar wind measured with SOHO/CELIAS/CTOF. *PhD Thesis, University of Bern*, 1998b.

L. Berger. Velocity distribution functions of heavy ions in the solar wind at 1 AU. *PhD Thesis, University of Kiel*, 2008.

M. Koeten. An improved efficiency model for ACE/SWICS - determination of the carbon isotopic ratio C13/C12 in the solar wind from ACE/SWICS measurements. *PhD Thesis, University of Kiel*, 2009.

L. Landau. On the energy loss of fast particles by ionization. *J. Phys.(USSR)*, 8:201–205, 1944.

Donald S. Gemmell. Channeling and related effects in the motion of charged particles through crystals. *Rev. Mod. Phys.*, 46:129–227, Jan 1974. doi: 10.1103/RevModPhys.46.129.

M. Oetliker. CTOF, a solar wind time-of-flight mass spectrometer with high charge resolution, numerical simulations and calibrations. *PhD Thesis, University of Bern*, 1993b.

R.F. Wimmer-Schweingruber, J. Geiss, G. Gloeckler, F. M. Ipavich, and B. Wilken. O5+ in high speed solar wind streams: SWICS/Ulysses results. *Solar Composition and its Evolution — from Core to Corona. Space Sciences Series of ISSI*, 5:387–396, 1998. doi: 10.1007/978-94-011-4820-7_35.

D. Verscharen, B. Chandran, S. Bourouaine, and J. V. Hollweg. Deceleration of alpha particles in the solar wind by instabilities and the rotational force: Implications for heating, azimuthal flow and the Parker spiral magnetic field. *The Astrophysical Journal*, 806(157):157–172, 2015. doi: 10.1088/0004-637X/806/2/157.

Eidesstattliche Erklärung

Ich versichere an Eides Statt, dass ich die vorliegende Dissertation in Form und Inhalt eigenständig angefertigt habe. Abgesehen von der Beratung durch meine Betreuer und der angegebenen Literatur wurde die Arbeit ohne fremde Hilfe erstellt.
Ich versichere, dass ich keine andere als die angegebene Literatur verwendet habe. Diese Versicherung bezieht sich auch auf alle in dieser Arbeit enthaltenen Grafiken und bildlichen Darstellungen. Die Arbeit wurde bisher in keinem anderen Prüfungsverfahren vorgelegt. Einige der von mir erstellten Abbildungen in der Arbeit wurden in ähnlicher Form in meinen Veröffentlichungen in Fachzeitschriften abgedruckt und sind dementsprechend gekennzeichnet.
Ich erkläre abschließend, dass die Arbeit unter Einhaltung der Regeln guter wissenschaftlicher Praxis der Deutschen Forschungsgemeinschaft entstanden ist. Es wurde mir in der Vergangenheit kein akademischer Grad entzogen.

Unterschrift: _____

Ort, Datum: _____